Martin Schmal

Heterogeneous Catalysis and its Industrial Applications

Springer

Heterogeneous Catalysis and its Industrial Applications

Martin Schmal

Heterogeneous Catalysis and its Industrial Applications

Springer

Martin Schmal
Chem.Eng. Dept.
Federal University of Rio de Janeiro (UFRJ)
Rio de Janeiro, Brazil

University of São Paulo (USP)
São Paulo, Brazil

Printed on acid-free paper

Dedicated
To my parents who greatly contributed
to my training and life.
To my wife, Victoria, who always
encouraged me, for her patience and love.
To Thaiz and Alice my daughters and
Camille, Sophie, Catarina and Hector my
grandchildren who made my life more
beautiful.

Preface

The importance of catalysis is due to the large number of applications in catalytic processes, particularly in the chemical and petrochemical industry, in power generation, in environmental preservation by reducing gas and water pollution, and in the development of new materials.

Although many important catalytic processes were mostly resolved, there is great scope for development of new processes and new efficient catalysts in various areas of industry. Known processes for several decades can be optimized by improving their performance and stability. There are good prospects for the development of new catalysts, alternative catalysts, and processes for environmental catalysis, fine chemicals, hydrotreating heavy oils, generation of hydrogen, C1 chemistry, new materials, and biomass.

The study of nanostructured materials is of great interest from the standpoint of both basic science and technological applications.

The increased process efficiency, substitution of raw materials, the development of cleaner processes, and technologies for environmental control and for alternative energy production are focal areas that illustrate the need for adjustments to existing formulations and/or development of new materials.

Specifically in the area of catalysis and materials, progress in the summary field requires a descriptive and theoretical understanding of interface phenomena and an interdisciplinary approach where the physical chemistry, modeling of processes, and surface phenomena appear with an appropriate methodological way to construction of scientific knowledge to minimize the gap between theory and application.

The following methods have had an impressive progress in recent years and consequently the basic knowledge in catalysis, facilitating the understanding of surface and interfacial phenomena. In addition to the chemical and physicochemical methods, physical methods of surface and interfaces were those which allowed the greatest advance in the knowledge of phenomena involving the chemical reaction.

This book aims to present the fundamentals of catalysis and applications illustrated with experiments performed in our laboratory, trying to understand why select the catalysts and processes. We seek to split the text into two parts. The first part presents the fundamentals addressing the activity patterns, adsorption–desorption phenomena, and advanced theories (Chaps. 1–5). The second part presents the most important conventional methods of characterizing properties (Chap. 6); the important methods of preparation with pre/posttreatment (Chap. 7); the most important traits (Chap. 8), with examples and practices; spectroscopic characterizations, even in situ (Chaps. 8–12); Nanostructured catalysts (Chap. 13) the microkinetic chemistry and surface mechanisms (Chap. 14), and finally the evaluation of an industrial catalyst process (Chap. 15).

Rio de Janeiro, Brazil   Martin Schmal

Acknowledgment

Contents

Chapter 1
Introduction

Abstract The importance of catalysis is due to the large number of applications in catalytic processes, particularly in the chemical and petrochemical industry, in power generation, the gas and water pollution to preserve the environment and the development of new materials. This book aims to present the fundamentals of catalysis and applications illustrated with experiments performed in our laboratory, trying to understand why select the catalysts and processes.

Keywords Activity Patterns • Basic concepts • Catalysts preparation • Evaluation of Industrial Catalysts • Model catalysts • Nanostructures • Surface and Structural analyses

The importance of catalysis is the large number of applications in catalytic processes, particularly in the chemical and petrochemical industry, in power generation, in the gas and water pollution to preserve the environment, and in the development of new materials. In general, the catalytic reactions can be classified as either homogeneous or heterogeneous.

Although many important catalytic processes were mostly solved, there is a great scope for the development of new processes and new, more efficient catalysts in different areas of industry, in homogeneous and heterogeneous processes or hybrids. Known processes for several decades can be optimized, improving its performance and stability compared to the agents causing the deactivation or poisoning. There are good prospects for the development of new nanocatalysts, alternative catalysts, and processes for *environmental catalysis*, *fine chemicals*, *hydrotreating heavy oils*, *generation of hydrogen*, *C1 chemistry*, *and new materials*.

Environmental catalysis is currently very much in evidence with a view to depollution of atmospheric gas and liquid waste organic or inorganic in nature. To get an idea of its importance, it is estimated that for a 5-year program are spent 5–7 billion dollars in the United States in basic research and technology development for industrial application. In addition, there is a significant increase in work published in specialized journals and patents.

In fine chemicals, there are new possibilities. What is available in the country of a large amount and variety of natural products that deserve attention highlighted in research and development? As an example, extracted from cashew oil is sold at $1.00/ton, and the extracted products, such as antioxidants, are imported by the

approximate price of \$20.00/g. The disparity is huge, all because of the lack of knowledge of the chemical transformation technology. Most of these processes make use of catalysts which are generally activated compound complex, very expensive, and difficult to reuse. There is growing concern in developing new processes hybrids, heterogenized.

The hydrotreating is very popular, and the biggest problem is associated with high consumption of catalyst and oil nature, in particular heavy oils. The classical catalysts are $CoMo/Al_2O_3$ and $NiMo/Al_2O_3$, but currently looking to other alternatives, trying to improve the process to the drastic reduction or even total elimination of nitrogenous compounds, oxygen and sulfur. The presence of such compounds in fuels causes many environmental problems due to incomplete combustion of petrol and diesel in motor vehicles.

The hydrogen generation is one of the great problems in the future. Most chemical and petrochemical processes demand large amounts of hydrogen. There are several possible alternatives, including electrowinning. However, the big problem is the generation and storage at high pressures. The use of natural gas as hydrogen alcohol chemistry-generating sources is a viable alternative, whose efficiency can be improved by producing a more efficient and selective catalyst.

For years, scientists were predicting that the use of C_1 chemistry would be a good source of feedstock for the chemical industry. Over the past 10 years, the oxidative and non-oxidative coupling of methane, using new catalysts, have been studied, primarily aimed at the production of ethylene. There are important solutions in industrial production routes for obtaining oxy-chloride products, in order to obtain polymeric compounds. The production of fuels via Fischer-Tropsch synthesis has not been fully resolved, and the problem is getting selective products such as diesel production, the demand for which has increased significantly.

Finally, within this reason, there is a need to discover new materials, such as adsorbents, targeting the gas storage volumes, and lower pressures, permitting its transport and storage.

In studying materials, nanostructured systems are of great interest, both from the point of view of fundamental science as of technological applications. Currently, in general terms, any material that contains grains, clusters, lamella, or dimension filaments inferior to 10 nm can be considered as nanostructured, provided that their properties differ of those of the solid extended.

Such materials have been extensively studied in recent years because of the small size of their primary building units (whether particles, grains, or phases) and high surface/volume ratio resulting in mechanical, optical, electronic, and magnetic individuals.

The increased process efficiency, substitution of raw materials, the development of cleaner processes, and technologies for environmental control and for alternative energy production are focal areas that illustrate the need for adjustments to existing formulations and/or development of new materials.

Specifically in the area of catalysis and materials, progress in the summary field requires a descriptive and theoretical understanding of interface phenomena and an interdisciplinary approach where surface physical chemistry, modeling of

processes, and phenomena appear with an appropriate methodological way to construction of scientific knowledge to minimize the gap between theory and application. In catalysis, the properties associated with different morphologies, activities, and selectivity which are strongly affected by the shape and particle size, and in the case of crystalline metallic phases, and the orientation of crystal faces exhibiting differentiation, should be highlighted. Behaviors such as features that make systems reduce the scale to the nanometer size are interesting from the point of view of scientific exploration and technological application. Its unique properties associated with the ability to synthesize them in different ranges of sizes and shapes make these potentially useful materials in the field of catalysis by acting as most active and selective catalysts.

The characterization methods have had an impressive progress in recent years and consequently advanced the basic knowledge in catalysis, facilitating the understanding of surface and interfacial phenomena. In addition to the chemical and physicochemical methods, but mainly physical methods of surface and interfaces were that allowed a greater advance in the knowledge of phenomena involving the chemical reaction.

To design a new catalyst is important to know the past of catalysis, which to a certain moment was quite empirical, evolving significantly after mastering the fundamental concepts. These concepts involve advanced chemical theories in order to understand the surface and interfacial phenomena of a catalyzed chemical reaction, thus explaining the design of a new catalyst and justifying the formulation of the process kinetics.

To develop a process involving heterogeneous chemical reactions. is necessary to establish some fundamental principles for predicting its experimental behavior. These principles come from thermodynamics, chemical kinetics, and quantum mechanics. Initially we need to know the reactions, the chemical equilibrium, and the various conditions of surface and interfacial phenomena involving the overall kinetics, as adsorption-desorption, diffusion, and mass transfer processes. It is important to provide the limiting steps of the process control system. But to understand the process, the microscopic level is sought more specific theories, as the kinetic collision theory, the theory of the electronic bands, and the theory of crystal field, which among others, can explain, but probably not by itself explain all phenomena involving catalysis.

On the other hand, the selection of the catalyst depends on the process engineering, particularly macroscopic engineering, such as mass and heat transfer phenomena and diffusion, and particularly type reactor or residence time. Finally, the scale factor and the technical and economic viability are decisive factors in the choice of catalyst and the existing or new process.

The idea is to know the fundamentals and phenomena that allow us to understand the different physical and chemical properties as well as the activity and selectivity and select catalysts to a chemical process, in order to design a catalyst.

There are various industrial processes which involve one or more specific reactions which may occur simultaneously or sequentially. For example, aromatization of propane in order to produce benzene by dehydrogenation can occur for propylene, which in turn is dimerized, followed by cyclization and dehydrogenation

to produce benzene. These steps may occur on the same catalyst with multifunctional characteristics.

The various catalytic reactions can be classified basically in the following categories:

- Hydrogenation
- Hydrogenolysis
- Dehydrogenation
- Total or selective oxidation
- Cracking and isomerization
- Hydrocraking
- Polymerization (involving initiation, propagation, and termination of the reaction)

On the other hand, industrial catalysts can be classified broadly into the following categories:

- Metals
- Oxides
- Acid-base solid

These categories are specific to the different functions and chemical reactions. For example, the metals are used for dehydrogenation reactions, hydrogenation, and hydrogenolysis; the solid acid-base is employed for oligomerization reactions, cyclization, cracking, and isomerization; finally, the selective oxidation is mainly employed oxides.

1.1   Nanostructured Systems

Nanostructured systems are of great interest from a basic science point of view as technological applications. Currently, in general, any material that contains grain clusters, plates, or filament size smaller than 10 nm can be regarded as nanostructures, as long as their properties differ from those of the solid extended.

Within the topic catalysis, the properties associated with different morphologies, activities, and selectivities which are strongly affected by the shape and particle size, and in the case of crystalline metallic phases, and the orientation of crystal faces exhibiting differentiation, should be highlighted. The reactions that are influenced by the factors mentioned above (morphological) are known as sensitive reactions to the catalyst structure.

This book aims to study the fundamentals of catalysis with metal oxides and systematically in order to select and/or proposition of a catalyst. Will be presented at the end of the text some applications, showing how the catalysts are selected for process, some developed in the laboratory. Finally, we present typical industrial evaluation of catalysts.

Chapter 2
Model Catalysts

Abstract The idea is to understand of the physical-chemical properties of a catalytic process that allows making the choice of a catalyst presenting the best activity and desired product selectivity.

The idea is if we have the understanding of the physical-chemical properties of a catalytic process, then it may be possible to choose a catalyst presenting the best activity and desired product selectivity. If the process is thermodynamically possible, then it may be possible to preview the reaction behavior and the catalytic performance, as well as an understanding of the reaction mechanism, which explains the intrinsic activity and product distribution or selectivity of a desired product. We may select the most efficient catalyst of a desired process based on empirical experiments; however, with this idea, one can find novel catalysts of a chemical process or of an inefficient existing process in the industry.

For a better comprehension of this model, we started with a well-known process: the production of aromatics from propene, involving different reaction mechanisms, like cyclization, oligomerization, and dehydrogenation reactions resulting in aromatics. In this process, there are several other secondary reactions, such as carbonization and cracking [1–9].

The principal reaction and the secondary reactions are presented in Fig. 2.1 [1].
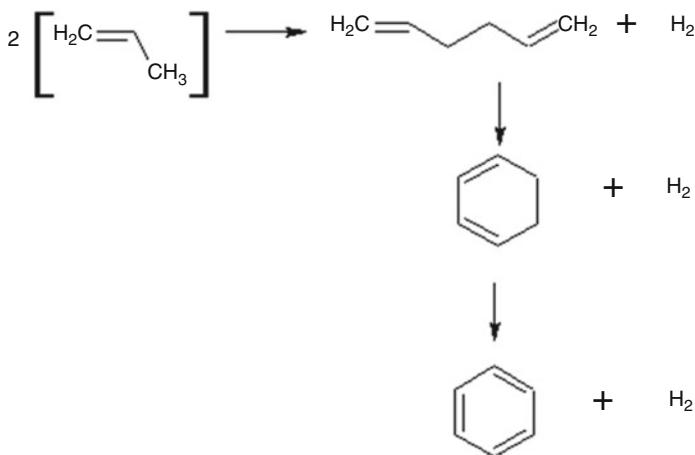
The principal reaction is thermodynamically possible and favored at high temperatures, around 300 °C, and at atmospheric pressure.

It is noteworthy that dimerization occurs in the first step, followed by the cyclization and dehydrogenation in steps 2 and 3, respectively. There are still undesired side reactions, such as dimerization and branched coking.

On the other hand, we may classify these reactions in different families. From the empirical experiments, it may be possible to select a catalyst for the specific reaction, tested separately, verifying the catalytic performance of activity and selectivity or product distribution. Depending of the reactions, the selection of a catalyst can be found through many attempts, but a general choice is practically unviable.

The dehydrogenation reaction occurs preferentially on metallic sites. The competition of molecules on sites depends on the geometrical and electronic structures;

Principal reaction

Secondary reaction
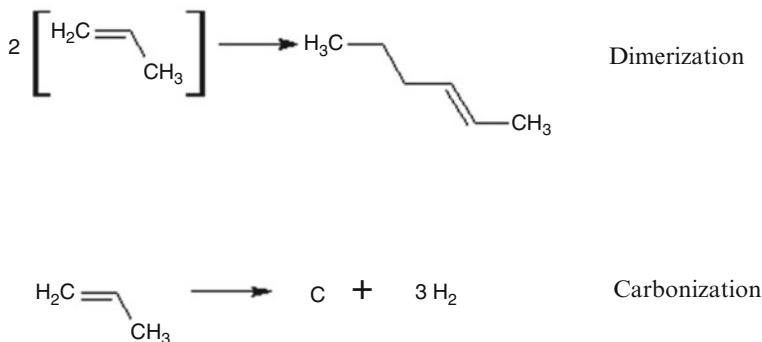
Fig. 2.1   Reaction pathway: production of aromatics from propene [1]

however, the determining step depends also on other factors which will be focused in this model. The usual metals are Ni, Co, W, Cr, Fe, Pd, Pt, and Rh, which in many cases favor coke formation. Otherwise, the cyclization and olygomerization reactions occur on acid sites or metallic oxides, such as zeolites and GaO_2 and ZnO, respectively. The protonic H-ZSM5 zeolite is the most recommended; however, supported metal oxides on zeolites are bifunctional catalysts, occurring in the dehydrogenation or hydrogenation, cyclization, and oligomerization reactions simultaneously. Specifically for aromatization of propane or propylene, Pt/HSM5, Cu/HSM5, Ga/HSM5, and Ge/HSM5 [1, 4], which have well-dispersed metallic sites and acidic sites, were done successfully.

These considerations led us to think about how to describe the surface chemical reaction mechanisms. This requires knowledge of the structure of molecules and the

Fig. 2.2 Dimerization of olefin [1]

$$2\left[H_2C = \diagup_{CH_3}\right] \longrightarrow H_2C = \diagdown\diagup_{=CH_2} + H_2$$

$$2\left[H_2C=\diagup_{CH_3}\right] \xrightarrow{O_2} H_3C\cdots\diagdown_{*\ CH_3} + H_3C-\diagdown_{*\ CH_3} + H_2 + 2\ [OH^-]$$

$$H_2C=\diagdown\diagup_{=CH_2} + H_2$$
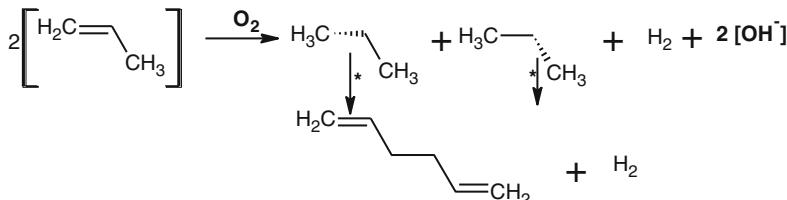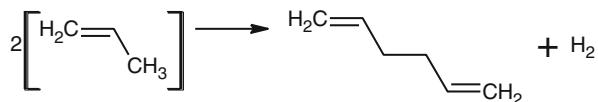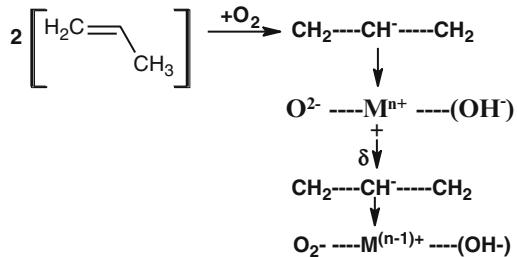
Fig. 2.3 Oxidative dehydrogenation [adapted from Trimm, D.L., "Design of Industrial Catalysis" Ed. Elsevier, Scientific Publishing Company, (1980)], where (*asterisk*) represents the active sites

Fig. 2.4 Scheme of the surface mechanism [adapted from Trimm, D.L., "Design of Industrial Catalysis" Ed. Elsevier, Scientific Publishing Company, (1980)]

$$2\left[H_2C=\diagup_{CH_3}\right] \xrightarrow{+O_2} CH_2\text{----}CH^-\text{-----}CH_2$$

$$O^{2-}\text{----}M^{n+}\text{----}(OH^-)$$

$$\overset{+}{\underset{\delta}{\downarrow}}$$

$$CH_2\text{----}CH^-\text{-----}CH_2$$

$$O_2^-\text{----}M^{(n-1)+}\text{----}(OH\text{-})$$

possible adsorption forms, as well as the likely metals and electronic structure of the molecule, known as geometric and electronic effects, which may occur simultaneously or separately [2, 3, 5–8]. As a starting point, one chooses a model surface mechanism for each reaction [1].

According to Trimm [1], starting from the olefin in the first step occurs a linear dimerization with loss of hydrogen (Fig. 2.2).

Trimm [1] suggested that the dehydrogenation at the surface may occur via an oxidative route. In this case, there is formation of intermediate π-allyl with removal of hydrogen by oxygen from the surface of the solid, forming two double bonds (Fig. 2.3).

In this mechanism, it is assumed that the hydrogen of the double bond will be removed by the available oxygen on the surface, forming intermediate π-allyl species in adjacent positions that favor the dimerization. It forms hexadiene that when desorbed releases the active sites of the surface and replenishes the surface oxygen. During the formation of intermediate π-allyl species, there is charge redistribution between the adsorbed complexes, as shown in Fig. 2.4 [1].

If the two allylic species are linked at the same ion to form a dimer, it implies that the metal M is capable of accepting two electrons. If the ion has only two separated valences, the ability of quick transfer of two successive electrons from the same ion is more difficult. Thus, the abstraction of a second electron from a second
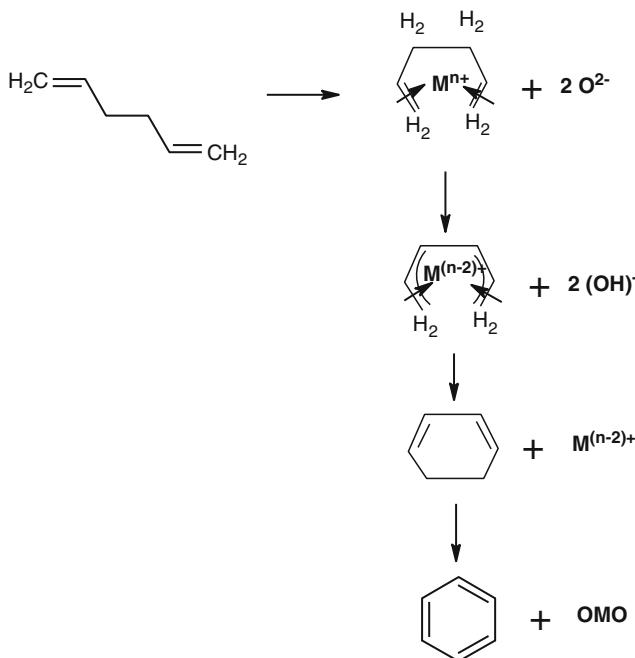
Fig. 2.5 The cyclization mechanism at the surface [adapted from Trimm, D.L., "Design of Industrial Catalysis" Ed. Elsevier, Scientific Publishing Company, (1980)]

adjacent allylic specie is easier, i.e., abstraction of electrons from two adjacent species will favor the dimerization.

Metallic oxides with separated valences in two oxidation states and can adsorb π-allylic species are Sn^{+2}/Sn^{+4} and In^{+1}/In^{+3}. The lower oxidation valence tends to be more stable and increases attraction of electrons [1, 5].

The next steps are the cyclization and dehydrogenation that behave similarly, according to the scheme shown below. During the double cyclization, the adsorbed bindings may cause charge redistribution and electron transfer of these species to the metal ion, allowing the cyclization in adjacent positions and subsequent dehydrogenation and recovery of surface-active sites [1] (Fig. 2.5).

Indeed, the adsorption of π-allylic species is possible on metal ions whose electronic structure is capable to receive electrons (d_1, d_2, d_3, d_8, d_9) and have configurations with geometric structure capable to positioning molecules in adjacent places. These properties will be studied in more detail in later chapters.

References

1. Trimm DL. Design of industrial catalysis. Amsterdam: Elsevier Scientific Publishing Company; 1980.
2. Moujijn JA, van Leeuwen PWNM, van Santen RA. Catalysis – Studies science and catalysis, vol. 79. Amsterdam: Elsevier Scientific Publishing Company; 1993.
3. Somorjai GA. Introduction to surface chemistry and catalysis. New York: Wiley; 1994.
4. Guisnet M, Gnep NS, Alario F. Aromatization of short chain alkanes on zeolite catalysts, Appl Catal A General. 1992;89:1.
5. Krylov OV. Catalysis by nonmetals. New York: Academic; 1970.
6. Bond CC. Heterogeneous catalysis and applications. Oxford: Clarendon; 1974.
7. Masel IR. Principles of adsorption and reaction on solid surfaces. New York: Wiley; 1996.
8. Van Santen RA, Niemantsverdriet JW. Chemical kinetics and catalysis. New York: Plenum; 1995.
9. Ciola R. Fundamentos em Catálise. São Paulo: USP; 1981.

Chapter 3
Activity Pattern

Abstract The influence of the kinetic parameters on the reaction rates for different processes and catalysts. The temperature and surface properties, such as, structure, morphology, texture and adsorption of molecules at the surface may influence the activity and selectivity.

Keywords Activity pattern • Kinetic parameters • Selectivity • Structure • Surface properties

The most frequent questions are:

1. Does the reaction rate in the presence of a catalyst change? Does it vary from one to another catalyst? Are there great differences in defining correctly the rate (per unit area, per weight, or per volume)? Why?
2. If there are small differences, how to distinguish one catalyst from another? What are the most important parameters that distinguish the activity and selectivity for a reaction for a specific catalyst?

One of the most important parameters is the temperature, the starting temperature, and the initial reaction rate. One can determine experimentally the initial reaction rate after elimination of diffusion and mass transport effects and then determine the Arrhenius constants, which depend on the temperature. The collision factor (k_0) and activation energy (E) parameters influence significantly the activity pattern and selectivity. Figure 3.1 illustrates the influence of the temperature on these parameters for different reactions and metallic catalysts. This effect is known as compensation effect, although empirically there are attempts on theoretical interpretations for different heterogeneous systems [1, 2].
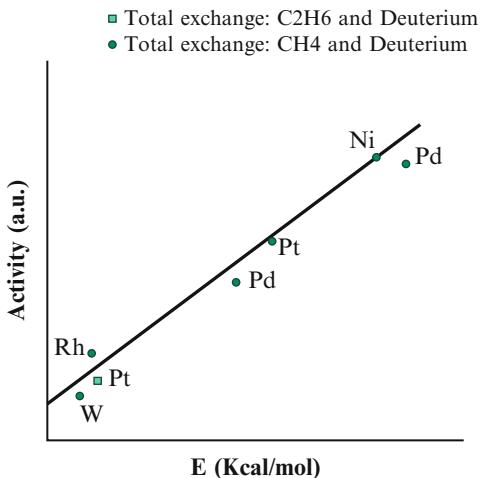
There are three different cases [2, 3]:

1. k_0 is constant and E varies (for C_2H_6 and deuterium exchange on metals):

   Pt ($E = 5.2$ kcal/mol)
   Ni ($E = 9.3$ kcal/mol)

Fig. 3.1 Influence of the
temperature on the kinetic
parameters (Adapted from
Anderson and Kemball [2])

☐ Total exchange: C2H6 and Deuterium
● Total exchange: CH4 and Deuterium

2. E is constant and k_0 varies (for ethylene hydrogenation):

$$E = 10.7 \ \text{kcal/mol}$$
$$\text{Pd} \rightarrow \log k_0 = 3.2$$
$$\text{Ni} \rightarrow \log k_0 = 1.25$$

3. E and k_0 vary, according to Fig. 3.1.
4. Note that both the temperature and the activity depend on the nature of the metal
   or the metal oxide catalysts for different reactions. Figure 3.2 shows the tem-
   perature and Fig. 3.3 the activity or rate varying with the different metal oxides
   for the oxidation of propylene [4].

These results evidence that the temperature may influence the activity, which
can be attributed to bulk and surface properties, such as, structure, morphology,
texture, and adsorption of molecules at the surface. The adsorption depends on the
bindings and strength of the activated complexes formed on surfaces. Conse-
quently, the activity is not directly proportional to the temperature. It depends on
the heat of formation, enthalpy, or heat of adsorption of the intermediate species at
the surface. Figure 3.4 shows the temperature of formation of formic varying with
the enthalpy on different metals [5].

Figures 3.5 and 3.6 show also the activity related to the heat of adsorptions of the
reactants of the ethylene hydrogenation and propylene oxidation on different metals.

Noteworthy is that the higher the heat of adsorption, the lower is the activity, which
can be assigned to the strength of adsorption bonding of the molecules at the surface.
The heat is indirectly related to the heat of formation of the unstable intermediates. The
adsorption strength depends on the metal. In fact, noble metals, like Pt, Pd, and Rh, are
more active than non-noble metals, such as Fe, Ni, and W. The adsorption strength on
noble metals is lower than on the non-noble metals and consequently the activity.

This behavior is similar for metal oxides, as shown in Fig. 3.7 for the oxidation
of hydrogen on different metal oxides.
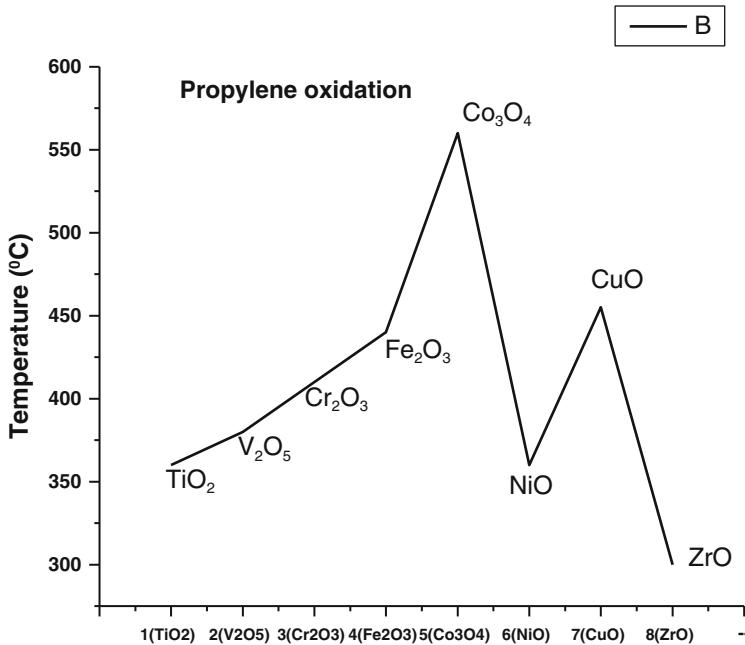
Fig. 3.2 Maximum temperature for oxidation of propylene (Adapted from Trimm [4])
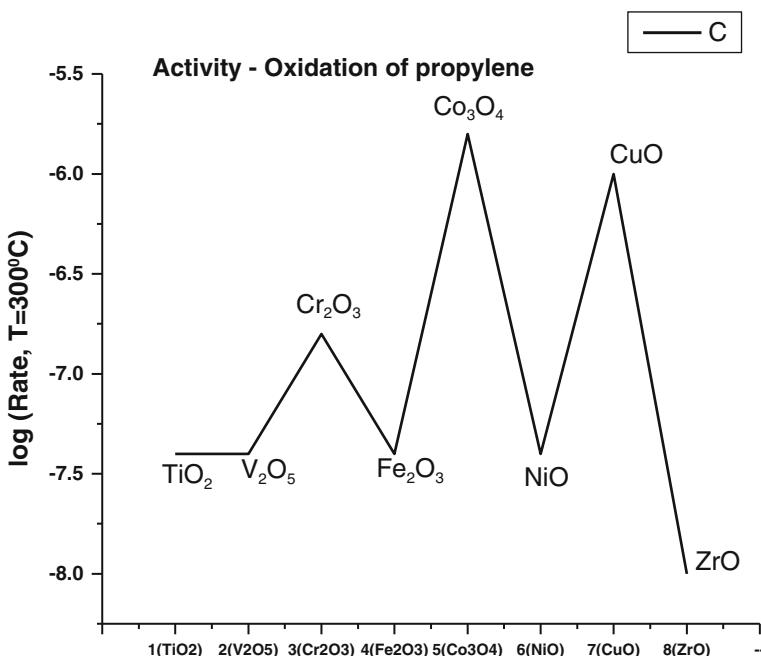
Fig. 3.3 Rates at constant temperature for the oxidation of propylene (Adapted from Trimm [4])
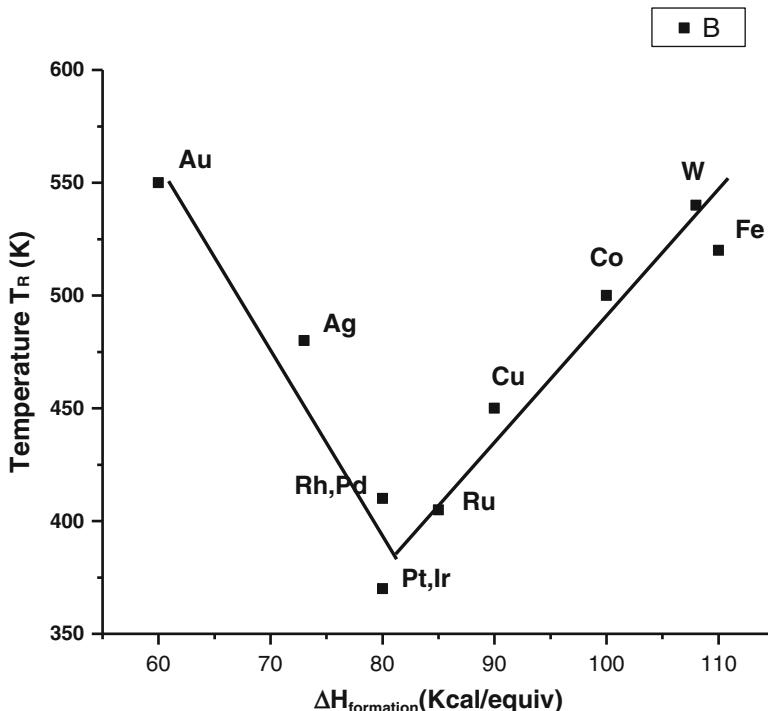
Fig. 3.4 Temperature varying with enthalpy of decomposition of acid formic (Adapted with permission from Sachtler [5])
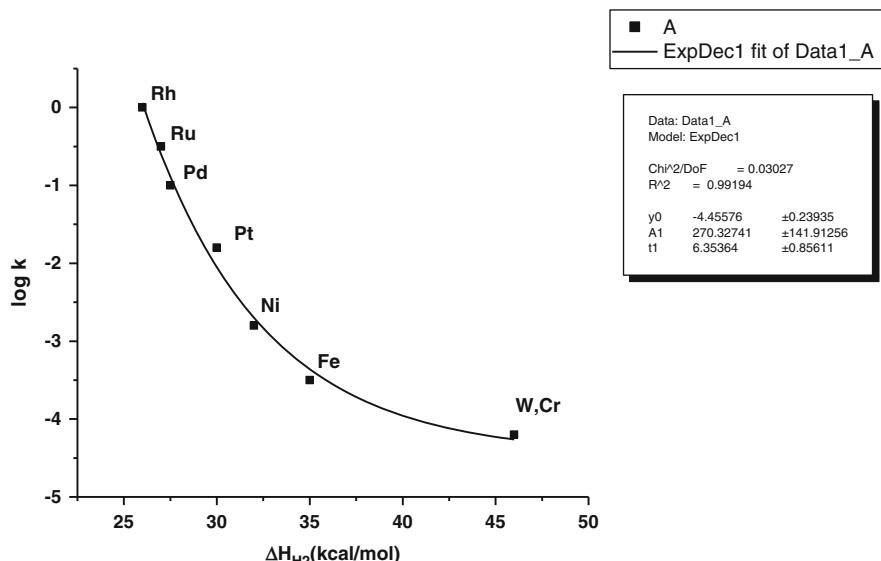
Fig. 3.5 Activity versus heat of adsorption of hydrogen (Adapted from Trimm [4])
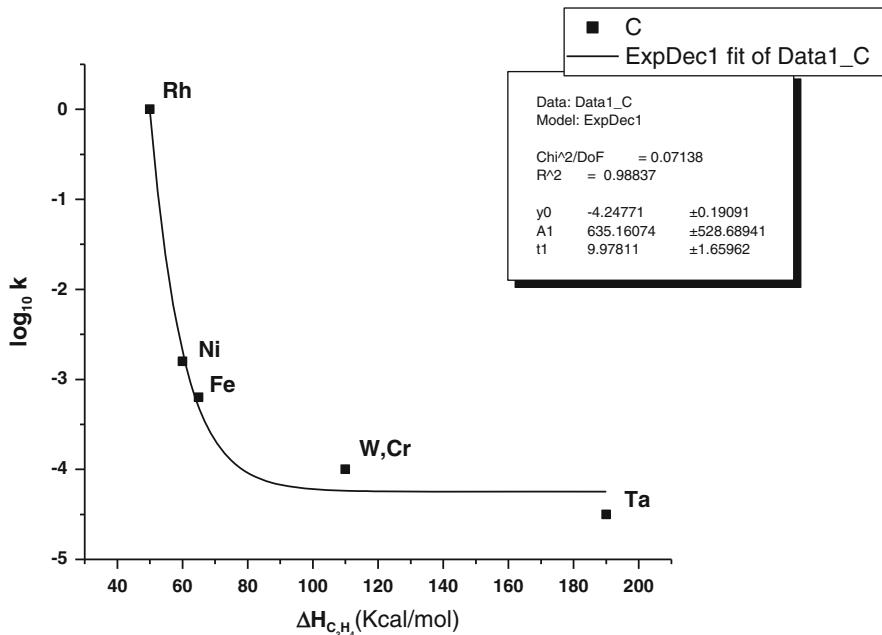
Fig. 3.6 Activity versus heat of adsorption of ethylene (Adapted from Trimm [4])
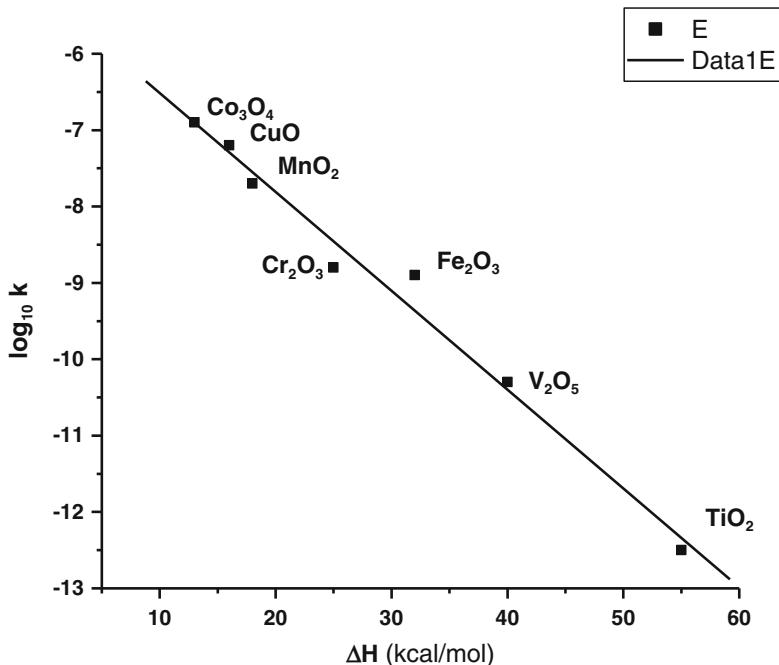
Fig. 3.7 Activity of oxidation of hydrogen as function of the enthalpy (Adapted from Trimm [4])

3.1   Influence of the Structure and of the Surface

3.1.1   Metals

Studies on flat surfaces showed that the activity is directly related to the surface atomic structure of the solids. The interatomic distances are different from metal to metal, and, consequently, the geometry of the exposed surface may influence on the adsorption of the molecules. In fact, the activity on flat surfaces varies significantly. Figure 3.8 shows the activity of the hydrogenation reaction varying with the interatomic distances on different metals.

   Moreover, the atomic structure of a metal oxide or crystal faces may also influence the activity, due to defects on surfaces, especially corners, kinks, or edges, affecting strength and forms of adsorption of molecules. An apparently spherical metal particle at the surface has different shapes or exposed faces that influence strength of adsorption. The activity changes on corners or edges and is unlike when comparing to the experimental data, as shown in Fig. 3.9. One knows that CO adsorbs as linear or bridged form over the planes [111] and [100], respectively. This is the case of the cyclopropane hydrogenolysis, which is a structure-sensitive reaction. The specific activity (TOF) varies with the crystallite sizes of the metal smaller than 4 nm of the Pt/SiO_2 catalyst, but is structure insensitive for larger particles.
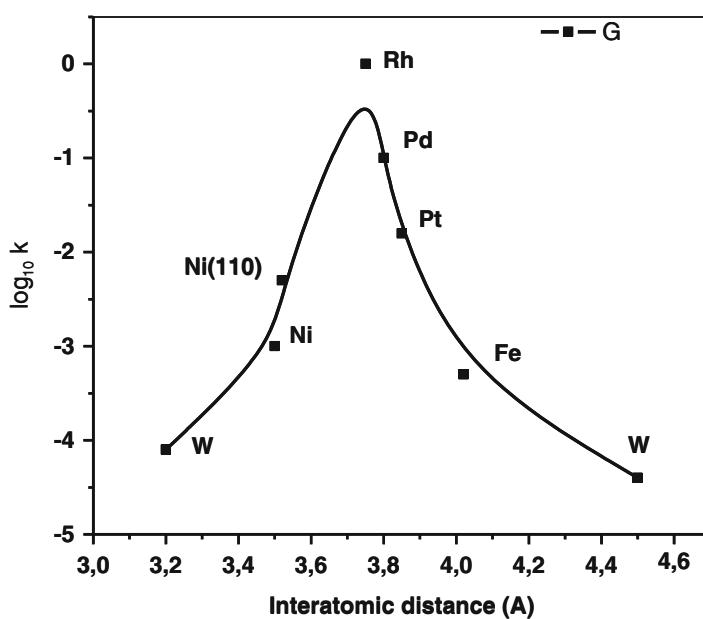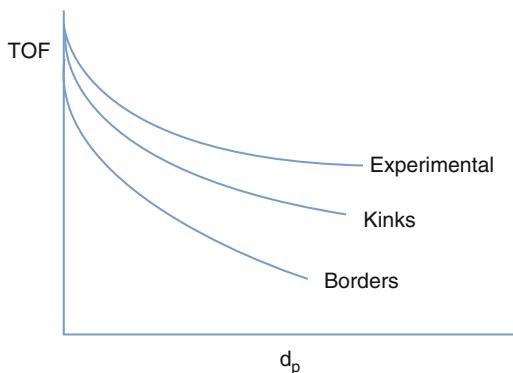
Fig. 3.8 Dependence of the interatomic distance with the activity (Adapted from Trimm [4])

Fig. 3.9 Influence of
corners and edges on
surfaces on the activity
(Adapted from Anderson
and Kemball [2])

3.1.2   Oxides

Reactions with oxides may involve the atomic oxygen of the network, especially for the selective oxidation reactions. Indeed, the oxygen anions O^{2-} have weak links with the sub-layer which during the reaction can be incorporated in the molecule.

Ionic oxides are represented by cations and anions. The formation of ionic surfaces occurs by disruption of the bonding with the formation of uncompensated charges. Having positive charge (electron acceptor) forms Lewis-type sites while with excess of negative charges forms Bronsted-type sites. In fact, the heterolytic molecules break on oxides, while on the metals they are neutral. Hence, the catalytic activity depends on the degree of extension of the unsaturated ions at the surface. Defects are associated with oxygen vacancies in the network, exposing cations that form high coordinative unsaturation and, thus, strong adsorption of molecules. For example, CO or H_2 adsorbs on defects on the surface. Oxide transition metals have more than one oxidation state and on the lowest oxidation state are highly reactive.

The mechanism of the oxidation reaction involving oxygen of the lattice is well known as Mars–Krevelen model. Thus, for example, the oxidation of carbon monoxide on oxides can be explained schematically as follows [6–9]:

a. Adsorption of CO with the formation of carbonate
b. Decomposition of carbonate with the formation of CO_2, releasing two vacancies
c. Dissociative adsorption of O_2 with the formation of O^- atom replenishing the oxygen vacancy
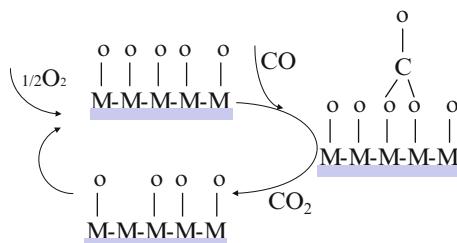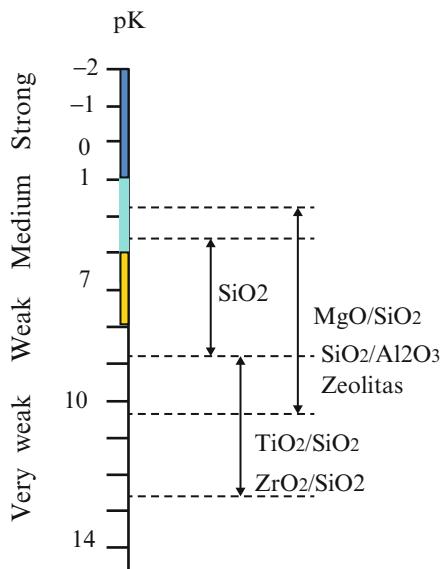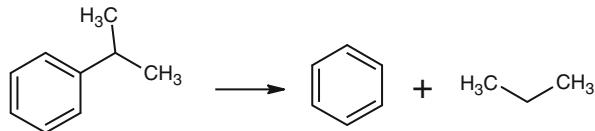
Fig. 3.10 Acidity of solids
(Adapted from Tanabe [10])

3.1.3   Acid–Base Solids

The acid–base solids are widely used in catalysis, and the activity depends on the acid strength. These acid strengths on solids are comparable to the pK of the classical solutions, according to Fig. 3.10. Noteworthy is that either natural oxides and mixed oxides or synthetic oxides, like zeolites, are mixtures of different nonstoichiometric oxides that exhibit also different acid strengths.

Cracking of cumene is a classical reaction with the disruption of the benzene ring structure, occurring on acid surfaces [10]. The reaction transforms cumene in benzene and propane, respectively, according to the following scheme.

The activity changes with the acidity. Figure 3.11 shows a nonlinear behavior of the activity with the acidity. Otherwise, the activity of propylene polymerization varies linearly with the acidity.

3.2   Model Reactions

The activity pattern and product selectivity of a reaction for a specific catalyst can be determined experimentally using model reactions [11]. However, it is worth remembering some important features of these reactions. How much is sensitive or
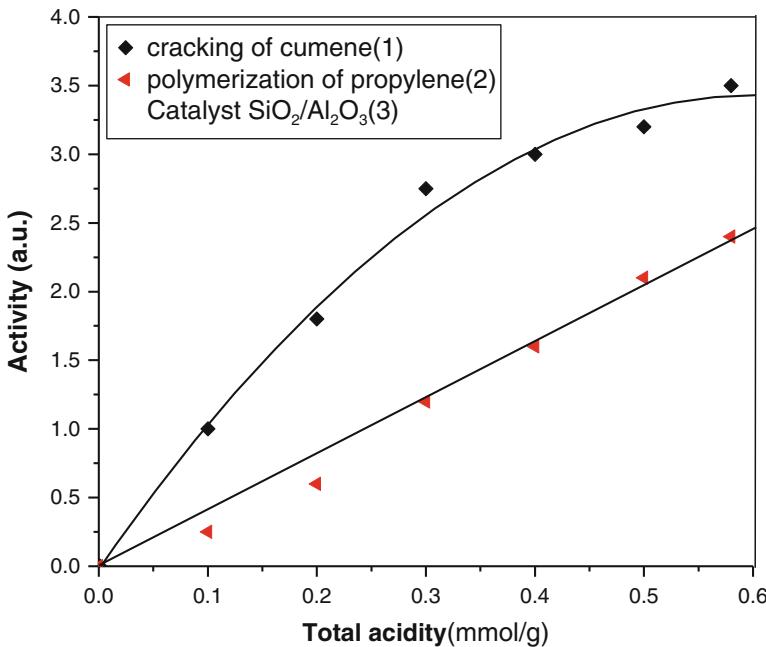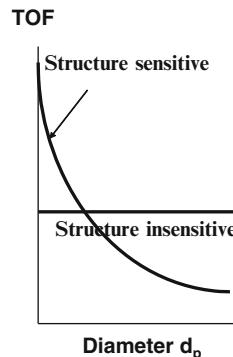
Fig. 3.11 Activity versus acidity (Adapted from Tanabe [10])

Fig. 3.12 Structure-
sensitive and structure-
insensitive reactions
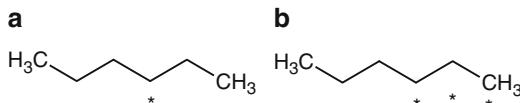
not, is the reaction with the catalyst structure. According to Boudart [1], supported catalysts are constituted by metallic particle of different sizes d. The exposed surface sites vary significantly with the particle sizes. Structure-sensitive reactions (RSS) are named when the intrinsic rates or the turnover frequency depend on the surface sites, varying with the particle sizes, while for structure-insensitive reactions (RIS) it doesn't. Thus, structure-sensitive reactions depend on the metal dispersion and on the structure of these surface sites. Structure-insensitive reactions are independent of these parameters, as shown in Fig. 3.12.

The dehydrogenation reactions are structure insensitive, while the hydrogenolysis reactions are structure sensitive. Some reactions comprise

simultaneously several steps which can be distinguished, whether they are structure sensitive or not.

These different properties of a catalyst and the effects on the activity and selectivity of the reaction, in particular for related hydrocarbon reactions, have been interpreted as two distinct phenomena: geometrical and electronic effects.

For better illustration, take, for example, the n-hexane molecule.
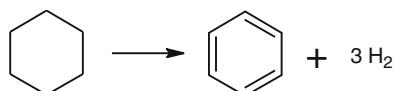
This molecule can be adsorbed on one, two, or more sites, as shown in scheme (a) and (b), and can be desorbed to form different products. So, in the first case, it can be simply dehydrogenated while in the second case can isomerize or dissociate and break in two other molecules, and therefore it is classified as hydrogenolysis.

The product distribution or selectivity changes when simultaneous reactions occur, like dehydrogenation and isomerization, or hydrogenolysis, due to the relative concentrations of mono-, bi-, or tri-adsorbed complexes on active sites. This phenomenon is named geometric effect. The dilution of an adsorbed A molecule with an inert B molecule decreases the ratio of the poly-adsorbed complexes to the mono-adsorbed, affecting the selectivity. However, the interaction of A and B not only modifies the geometric configuration or the concentration of A at the surface but also induces electronic modifications of an atom A with their neighbors. This phenomenon is known as electronic effect, caused by changes in sizes or fill of d orbitals of the metal [12–14].

3.2.1 Dehydrogenation of Cyclohexane

This reaction is structure insensitive (RIS), being the rate proportional to the number of surface active sites, and thus, the intrinsic activity (TOF) is independent of the particle size. It is also true for the reverse reaction, namely, the hydrogenation of benzene. The dehydrogenation of cyclohexane forms simple benzene and hydrogen as products, when performed at atmospheric pressure and temperatures varying between 250 and 300 °C [15].

Results of cyclohexane dehydrogenation, expressed as turnover frequency (TOF), for the Pt/Al_2O_3 and the promoted $(Pt + Sn)/Al_2O_3$ catalysts, are presented in Table 3.1. Note that the dispersion of Pt on alumina is almost 100 %, but with the addition of a second metal or promoter Sn, the dispersion decreases significantly.

Table 3.1 Dehydrogenation of cyclohexane on Pt/Al_2O_3; modified with Sn by co-impregnation (P = 1 atm H_2/C_6H_{12} = 13.2)

Catalyst	Initial rate at 543 K (10^3 mol/h/g_c)	Dispersion H/Pt[a]	TOF[b] (s^{-1})	$E_a{}^c$ (kcal/mol)
0.7 % Pt/Al_2O_3	179.5	1.1	1.2	27
0.9 % Pt/Al_2O_3	161.5	1.0	1.0	24
(Pt + Sn)/Al_2O_3	142.6	0.64	1.3	23

[a]Dispersion of Pt
[b]Activity
[c]Apparent activation energy [15]

Table 3.2 Hydrogenation of MCP on supported Pt catalysts

Catalysts	Initial rate (mol/h/g_{cat})	TOF (10^{-2} s^{-1})[a]	$nC_6{}^b$ (%)	2M[c] (%)	3MP[d] (%)	$R_1{}^e$	$R_2{}^f$
0.9 % Pt/Al_2O_3	6.3	4.1	33	42	25	1.7	0.8
(Pt + Sn)/Al_2O_3	2.6	2.4	30	43	27	1.6	0.7

[a]TOF at 573 K
[b]Selectivity to n-hexane
[c]2-methylpentane
[d]3-methylpentane
[e]Ratio 2MP/3MP
[f]Ratio nC_6/2MP

Benzene is the sole product and no deactivation was observed. Both the dispersion and the rate decreased in the presence of a second metal; however, the intrinsic activity (TOF) remained constant around 1 (s^{-1}), indicating that the rate is proportional to the surface active sites, and thus it is a structure-insensitive reaction.

The activation energy was constant equal to 24 kcal/mol. The activity (TOF) was almost constant, and therefore the promoters Sn and In do not affect the structural and surface atoms.
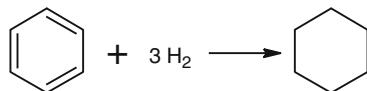
3.2.2 Hydrogenolysis of Methylcyclopentane

This is a structure-sensitive reaction (RSS), and hence the intrinsic activity or turnover frequency (TOF) depends on the particle sizes. The hydrogenolysis reaction was also tested with the Pt/Al_2O_3 and promoted with Sn. The reaction was carried out at 1 atm and 573 K and a mixture of hydrogenolysis of methylcyclopentane (MCP)/H_2 (1:10.5). The selectivity toward n-hexane, 2-methylpentane, and 3-methylpentane was determined for conversions less than 10 % and was presented in Table 3.2 [15].

Since this reaction is structure sensitive, the product distribution depends also on the particle sizes. For very small particles, the reaction presented a product distribution of about 25 % of 3-methylpentane, 42 % of 2-methylpentane, and 30 % n-hexane, which is similar to the statistical probability. For bigger particles, the ring opening presented different selectivity, producing 33 % of 3-methylpentane, 67 % of 2-methylpentane, and without any formation of n-hexane.

3.2.3 Benzene Hydrogenation

The benzene hydrogenation was selected as a model reaction for determining the metallic surface sites, because it is a structure-sensitive reaction. The sole product was cyclohexane, as shown below.

The catalysts are palladium supported on different carbons. Palladium oxide was reduced in metallic Pd^0. Table 3.3 shows the dispersions, total surface areas, metallic areas, and particle diameters of the Pd^0 on two supports [16].

The rate per site or turnover frequency was calculated based on the rate of benzene formation at 373 K and the number of surface sites after CO chemisorption, as presented in Table 3.4. Results show that the turnover frequency (TOF) changed with the different carbon supports.

The turnover frequency (TOF) results confirm that the reaction is structure sensitive (RSS). However, the catalyst with lower dispersion presented higher frequency factor k_0. Higher frequency factors indicate high effective collisions of molecules on active sites. Since the turnover frequency is a mean value and has

Table 3.3 Results from CO chemisorption at 308 K and 0.1 Kpa [16]

Catalyst	BET area [m^2/g(cat)]	Metallic area (m^2/g_{Pd})	Dispersion (%)	d_p (nm)
10 % Pd/C_V	309	89	20	5.6
9 % Pd/C_C	876	25	6	20.0

Carbon (C_V); graphite (C_C) [16]

Table 3.4 TOF and k_0 for benzene hydrogenation

Catalyst	TOF[a] (s^{-1})	k_0
10 % Pd/C_V	0.64	2.73
9 % Pd/C_C	2.84	2.90

[a]$T = 373$ K; H_2/$C_6H_6 = 14$; $P = 0.1$ MPa; Vazão Total $= 20$ mL/min [16]

$k_0 = \ln$ (linear coefficient) is directly proportional to the frequency factor
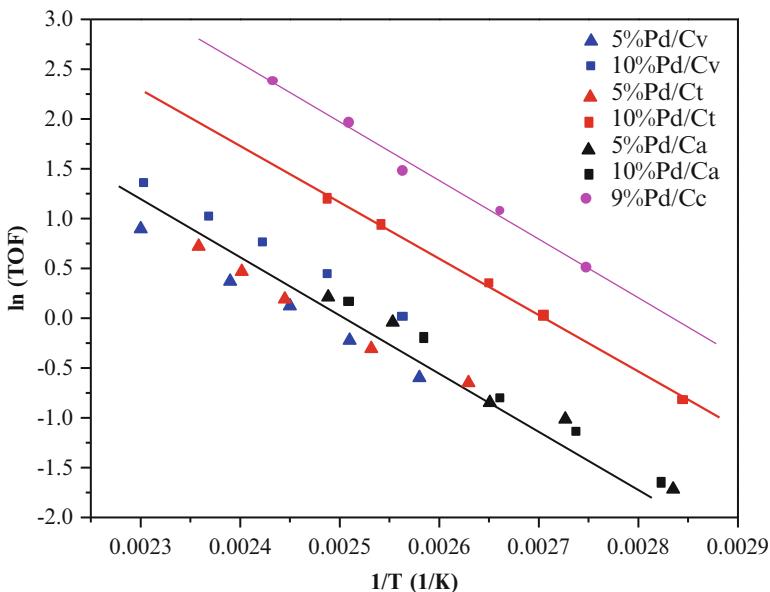
Fig. 3.13 Arrhenius plot for the hydrogenation of benzene reaction [16]

similar adsorption capacity, one can conclude that the higher the turnover frequency, the greater the concentration of surface sites. Therefore, this reaction predicts the presence of metallic surface sites.

The activation energy was calculated for different catalysts, as shown in Fig. 3.13. It was approximately equal 12 ± 1 kcal/mol. However, the frequency factor changed [16].

3.2.4 Butadiene Hydrogenation

This model reaction has been used for interpreting geometrical and electronic effects [7, 16–19]. As an example, we used the same reaction system described above; however, with a palladium-supported catalyst, fed with butadiene and hydrogen at $T = 275$ K, WHSV $= 800$ h^{-1}. Results of dispersions, activity, and selectivity are presented in Table 3.5 [16].

The activity expressed as turnover frequency (TOF) shows that this reaction is structure sensitive (RSS). The literature presents conflicting interpretations in this regard. Thus, the analysis of the performance of the catalysts will be made in terms of selectivity for the main products, as presented in Table 3.5.

The catalyst supported on graphite (GR) showed the highest *trans/cis* ratio and a lower production of butane and 1-butene. According Boitiaux et al. [17], this performance is characteristic of metals with higher electron density, which disfavors the formation of the intermediate carbene. Regarding the supported catalyst on

Table 3.5 Hydrogenation of 1,3-butadiene at isoconversion ($x_{BD} \cong 10\,\%$) and $T = 275$ K
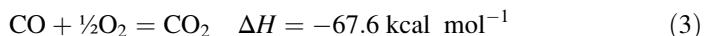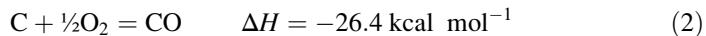
Catalyst	Dispersion (%)	Rate (mol BD/h/gcat)	TOF (s^{-1})	t/c	S_{BA}	S_{1-BE}/BE_t
1 % Pd/G	30.1	0.045	0.54	7.77	3.8	36.2
1 % Pd/C$_V$	82.2	0.122	0.54	6.11	9.6	42.5
1 % Pd/C$_T$	47.1	0.127	1.06	5.38	22.2	42.4
1 % Pd/C$_A$	21.0	0.073	1.26	4.69	40.9	46.3

WHSV = 800 h^{-1}; t/c selectivity ratio of trans-2-butene/cis-2-butene, SBA selectivity of butane, S_{1-BE}/BE_t selectivity of 1-butene relative to the total butanes [16]

activated carbon (C_T), it resulted in a lower ratio and higher production of butane and 1-butene compared to untreated coal. The C_A diluted sample generated a lower ratio and higher production of butane and 1-butene. These results indicate higher electron deficiency of palladium.

3.2.5 Carbon Monoxide Oxidation

Carbon monoxide is the main product of the incomplete combustion in many processes, especially in the FCC units, combustion of exhaust gases, and coke elimination. Coke is oxidized producing CO and CO_2 according to the following reactions:

$$C + O_2 = CO_2 \qquad \Delta H = -94 \text{ kcal mol}^{-1} \tag{1}$$

$$C + \tfrac{1}{2}O_2 = CO \qquad \Delta H = -26.4 \text{ kcal mol}^{-1} \tag{2}$$

$$CO + \tfrac{1}{2}O_2 = CO_2 \quad \Delta H = -67.6 \text{ kcal mol}^{-1} \tag{3}$$
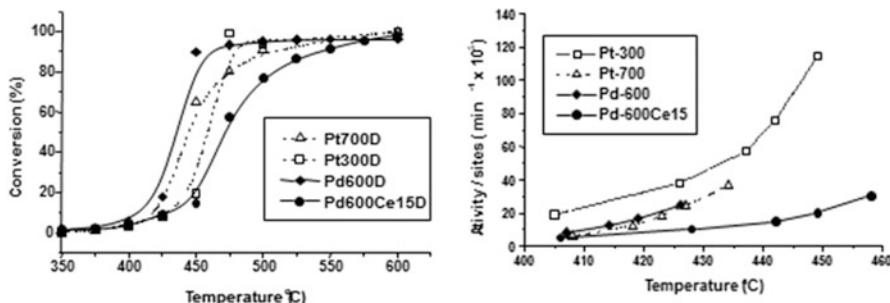
Note that the heat produced during the oxidation reaction of CO is 2.6 times greater than the heat of formation. Therefore, for maximum energy recovering, it requires complete combustion, in particular in the regeneration units.

Today there is a controversy whether the CO oxidation on supported metals is or not a structure-sensitive reaction. Although some studies have shown that the activity depends on particle sizes below 3 nm and low CO concentrations [20], Cant et al. [21] have not observed any dependence of the turnover frequency with the dispersion on Pt/SiO$_2$ catalyst. Sarkany and Gonzalez [22] observed that for some degree of dispersion, this reaction is structure insensitive; however, the turnover frequency (TOF) decreased with decreasing dispersion of the Pt/Al$_2$O$_3$ catalyst. In summary, the degree of structure sensitive depends on concentration and particle sizes on supported catalysts.

As example, the spent FCC catalysts were tested and compared for different combustion tests. The catalysts were promoted with 300 and 800 ppm Pt and Ce on alumina (220 m^2/g) and mixed oxides (1–5). Platinum was impregnated with hexachloroplatinic acid (H$_2$PtCl$_6$) and calcined at 500 °C. Then, it was treated

Table 3.6 Properties of the catalysts [23]

Additives	Content (%)			Surface area (m²/g)	Dispersion (%)
	Pt	Pd	Ce		
Pt300	0.032	–	–	218	36.5
Pt700	0.075	–	–	220	32.8
Pd600	–	0.066	–	174	56.0
Pd600Ce	–	0.061	15	176	54.6

Fig. 3.14 Conversion and activity per surface sites (TOF) for different combustion catalysts [23]

hydrothermally at 760 °C for 6 h, under atmospheric vapor at 100 % for deactivation.

The main properties are presented in Table 3.6.

The feed mixture of 20 % CO/He and 20 % O_2/He was fed at 150 and 80 mL/min, respectively, and at molar ratio CO/O_2 1.87, which means lean oxidation. The reaction temperature ranged from 300 to 700 °C.

Figure 3.14 displays the conversion and activity/sites of the different pretreated catalysts and temperatures. This behavior is similar to the fresh sample and shows that with increasing Pt content the conversion increases. The catalyst promoted with Ce presented lower conversion. Noteworthy is that the sample with 300 ppm Pt (Pt300) presented high activity at higher temperature. The addition of Ce prejudiced the activity of the catalyst.

References

1. Boudart M, Djega-Mariadassou G. Kinetics of heterogeneous catalytic reactions. Princeton, NJ: Princeton University Press; 1984.
2. Anderson JR, Kemball C. Research article catalysis on evaporated metal films. III. The efficiency of different metals for the reaction between ethane and deuterium. Proc R Soc A. 1954;223:361.
3. Boudart M. Fundamentals of industrial catalytic processes. Chem Eng Prog. 1961;57:33.
4. Trimm DL. Design of industrial catalysis. Amsterdam: Elsevier Scientific Publishing; 1980.

5. Rootsaert WJM, Sachtler WMH. Interaction of formic acid vapour with tungsten. Z Phys Chem. 1960;26:16–26.
6. Moujijn JA, van Leeuwen PWNM, van Santen RA. Catalysis—studies science and catalysis, vol. 79. Amsterdam: Elsevier Scientific Publishing; 1993.
7. Somorjai GA. Introduction to surface chemistry and catalysis. New York: Wiley; 1994.
8. Krylov OV. Catalysis by nonmetals. New York: Academic Press; 1970.
9. Masel IR. Principles of adsorption and reaction on solid surfaces. New York: Wiley; 1996.
10. Tanabe K. Solid acids and bases. New York: Academic Press; 1970.
11. Ciola R. Fundamentos em Catálise. São Paulo: EDUSP; 1981.
12. Anderson JR, Boudart M. Catalysis, science and technology, vol. 7. Berlin: Springer; 1985.
13. Bond CC. Heterogeneous catalysis and applications. Oxford: Clarendon; 1974.
14. Van Santen RA, Niemantsverdriet JW. Chemical kinetics and catalysis. New York: Plenum Press; 1995.
15. Passos FB, Aranda DAG, Schmal M. Characterization and catalytic activity of bimetallic Pt-In/Al2O3 and Pt-Sn/Al2O3 catalysts. J Catal. 1998;178:478.
16. Ramos ALD, Alves PS, Aranda DAG, Schmal M. Characterization of carbon supported palladium catalysts: inference of electronic and particle size effects using reaction probes. Appl Catal A General. 2004;277:71.
17. Boitiaux JP, Cosyns J, Vasudevan S. Hydrogenation of highly unsaturated hydrocarbons over highly dispersed palladium catalyst: Part I: behaviour of small metal particles. Appl Catal. 1983;6:41.
18. Boitiaux JP, Cosyns JP, Robert E. Additive effects in the selective hydrogenation of unsaturated hydrocarbons on platinum and rhodium catalysts: II. Influence of various compounds containing phosphorus, oxygen, sulphur and chlorine on the catalytic performance of platinum catalyst. Appl Catal. 1989;49:235.
19. Sinfelt JH. Bimetallic catalysts. New York: Wiley; 1983.
20. McCarthy E, Zahradnik J, Kuczynski GC, Carberry JJ. Some unique aspects of CO oxidation on supported Pt. J Catal. 1975;39(1):29.
21. Cant NW. Metal crystallite size effects and low-temperature deactivation in carbon monoxide oxidation over platinum. J Catal. 1980;62:173–5.
22. Sarkany J, Gonzalez RD. Support and dispersion effects on silica- and alumina-supported platinum catalysts: II. Effect on the CO-O_2 reaction. Appl Catal. 1983;5:85.
23. de Carvalho MCNA, Morgado Jr E, Cerqueira HS, de Resende NS, Schmal M. Behavior of fresh and deactivated combustion promoter additives. Ind Eng Chem Res. 2004;43:3133.

Chapter 4
Adsorption–Desorption

Abstract Adsorption-desorption studies addressing the influence of surfaces and gas molecules associated to energy concepts and different mechanisms and models based on ideal and non-uniform surface energy on metals, metal oxides and semiconductors.

Keywords Adsorption • Desorption • Mechanisms • Models • Potential energy • Surfaces

4.1 Basic Concepts

4.1.1 Introduction

The adsorption is actually the first step of a heterogeneous chemical reaction process and occurs on flat surfaces or porous solids or on smooth planes and films. Understanding this process is crucial to explain the activity and selectivity of a chemical reaction. It is a well-studied phenomenon, but initially it was differently interpreted. Berzelius [1] was one of the first to note that the adsorption is a process where the surface tension causes the condensation of gases in pores. He showed that the vapor pressure in a small drop is much larger than in the "bulk" fluid and proposed the following relation:

$$\ln\frac{P_{drop}}{P_{vapor}} = \frac{1}{kT}\frac{2\gamma V}{r} \tag{4.1}$$

where P_{drop} is the vapor pressure of the fluid, γ the surface tension, V and r the volume and radius, k the Boltzmann constant, and T the temperature in K.

This equation is commonly used to calculate the condensation of fluids in capillary pores. However, it is a limited equation depending on the properties of the different fluids and solids, mainly whether the solid is or not porous. In fact, it was observed that the amount of adsorbed gas per unit mass varied significantly.

Besides, there is a difference between the adsorption and absorption phenomena. In the first case, gas is directly linked at the surface, while in the second case, it is dissolved in the bulk. If the mass of absorbent doubles, then the amount of absorbed

gas increases twofold; unlike adsorption, the adsorbed amount of gas is directly proportional to the solid surface and not to the volume or mass.

The nature of the gas and the surface properties influence the adsorption process. Thus, for example, H_2 and CO are adsorbed in different forms on metals or oxides of Pt or Co, even on flat or porous surface solids, as reported in several experiments [1]. Actually, the advanced knowledge on surface science improved the observations on adsorption processes, either of physical or chemical nature, which depends on the adsorbed molecule and on the geometry and the adsorption form. Thus, for example, benzene and ethylene may be adsorbed on surfaces in different forms, horizontal or vertically and σ or π form, respectively, that may influence the amount of adsorption on the surface.

Generally, one can say that the gas can be adsorbed forming one layer (monolayer) or several layers, which are of physical or chemical nature, while liquids are usually condensed at the surface or in capillary pores. The nature depends on the binding energy of gases or fluids (adsorbed) and the surface (adsorbent) when:

1. The kinetic energy E_C, or thermal energy, allows the particles of the system (atoms, molecules, or ions) to have various types of motion: translational, rotational, and vibrational.
2. There is interaction energy between the particles, such as van der Waals forces and electrostatic forces.

The relationship between these energies defines the properties of the system:

(A) If $E_C \gg E_i$, then the molecules have maximum freedom, because the distance between them changes. The volume of the system depends on the temperature, pressure, and number of molecules. This system corresponds to an ideal gas.
(B) If $E_C \approx E_i$, then the molecules or atoms of the system have less freedom. The molecules move but the distance between them changes very little. The volume of the system depends on the temperature and on the number of molecules, but is virtually independent of the pressure. This system represents the liquid state.
(C) If $E_C \ll E_i$, then the volume of the system depends only on the number of molecules. In this case, the molecules or atoms have only vibration movement, and the kinetic energy is due to the vibration around the same position. This system represents the solid or molecules adsorbed on solids.

The systems (B) and (C) are called condensed states of the matter, since their volumes are defined and less sensitive to pressure variations. In the condensate system, the particles on the surfaces, or at the interface, present different situations:

1. The particles located within the system are submitted to forces in all directions, resulting in zero.
2. The surface forces of the particles are derived only from the internal particles. The balance of forces and the resulting strength F_R can be schematically represented in Fig. 4.1, considering the defect in the structure.

$$F_R = 0 \qquad\qquad F_R \neq 0$$
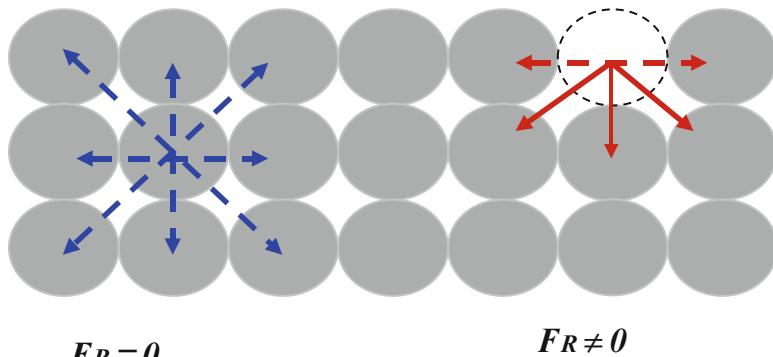
Fig. 4.1 Interaction between particles of a condensed system (solid or liquid)

Thus, as shown in Fig. 4.1, there is an excess of energy involving the particles, named superficial energy E_S. This energy is responsible for the tension in the liquid phase and for the adsorption of gases on solids.

The adsorption of molecules in multilayers occurs typically when the temperature is near the boiling point. However, when adsorbed as monolayer, there is a direct link between adsorbed and adsorbent, occurring at a higher than the boiling point temperature. For example, CO molecules can adsorb on a platinum surface at 10^{-7} torr and 400 K. In general, the adsorbed density of a monolayer looks like a liquid film, which means, the adsorbed molecules on a monolayer are very close together. Calculations show that water vapor can be adsorbed forming a layer of 3 A^0 and the number of adsorbed molecules is

$$N_a = 1 \ \left(\text{g/cm}^3\right)\left(3 \times 10^{-8} \ \text{cm}\right)\left(\frac{6 \times 10^{23} \ \text{molecules}}{10 \ \text{g}}\right)$$

$$= 1 \times 10^{15} \ \text{molecules/cm}^2$$

Thus, a water vapor monolayer contains approximately 1×10^{15} molecules/cm^2 and needs a surface area of the order of 6×10^8 cm^2 for the adsorption of 1 mol of water vapor. For example, the area of a porous activated carbon is of the order of 1000 m^2/g. Thus, for 1 g of solid, the surface area is 1000 m^2, which is significant.

The adsorption of gases at the surface does not occur immediately, since, before reaching the adsorbed state, it passes through different stages. In the first stage, the molecule collides with the surface. This surface is formed by corners, or particles with defects of different exposed faces, as shown in Fig. 4.2.

When the molecule collides on the surface, it loses energy and does not have sufficient energy to go back to its initial stage, but has sufficient energy to roll over the surface, reaching the precursor state, scatters and diffuses at the surface, and then adsorbs [2].
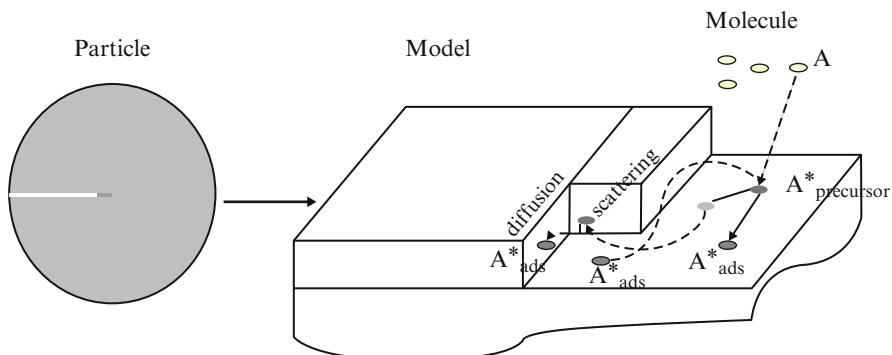
Fig. 4.2 Adsorption model on surfaces

The nature of adsorption depends on the bonding strength between the adsorbed molecule and the adsorbent (solid). If the adsorption strength is weak, there is no direct link between the molecules and the surface, and it is classified as physical adsorption. This strength is equivalent to the van der Waals force. Therefore, the physical adsorption is the polarization between molecules and not an electronic bonding. On the other hand, chemisorption represents the direct bonding between the molecules and the solid surface and is a strong bonding, characteristic of the interaction between the electrons of molecules and surface. The electronic structure of the molecules modifies, changing the bonding form. This energy involved in the chemical bonding is similar to the energy involved in the chemical reaction.

4.1.2 Energy Diagram

The chemical reaction involves physicochemical phenomena, such as adsorption and desorption, besides the chemical reaction itself. These three phenomena can be viewed in the potential energy diagram during the reaction pathway, exhibiting the catalytic cycle and therefore, qualifying the reaction as catalytic or non-catalytic.

Figure 4.3 shows a barrier which is known as activation energy. For the catalytic reaction, this barrier is much lower compared to the non-catalytic reaction, as a consequence of the adsorption and desorption phenomena of molecules occurring on the surface, besides the reaction. The adsorption is exothermic, and thus straightly bonded at the surface, which decreases the degree of freedom, and facilitates the reaction between adsorbed species and thus the reaction rate.

(a) –Non catalytic reaction
(b) –Catalytic reaction –good catalyst
(c) –Catalytic reaction –real catalyst
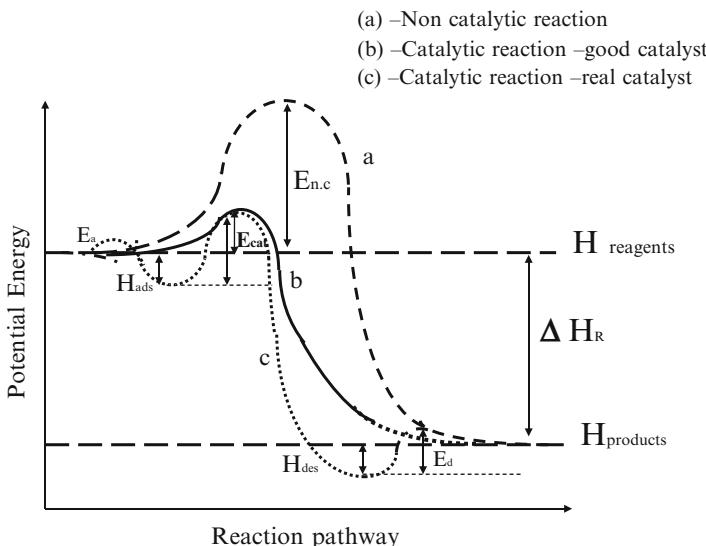
Fig. 4.3 Potential energy diagram during the reaction route, comparing catalytic and non-catalytic reactions [Adapted with permission from Masel, I.R., "Principles of Adsorption and Reaction on Solid surfaces," John Wiley & Sohns, Inc., New York, (1996)]

4.1.3 Characteristics

4.1.3.1 Thermodynamic

The adsorption of fluids on surfaces can be explained from thermodynamic point of view, using the Gibbs free energy principle. It is a spontaneous phenomenon, and thus, $\Delta G < 0$. On the other hand, the final entropy of this system also decreases, since the disorder is lower when adsorbed. From the thermodynamic, we have

$$\Delta G = \Delta H - T\Delta S \tag{4.2}$$

When the adsorption occurs, then

$$\Delta H_{ads} = \Delta G_{ads} + T\Delta S_{ads} \tag{4.3}$$

Since the free energy $\Delta G < 0$ and $\Delta S < 0$, then the enthalpy of adsorption is negative and very exothermic for more negative values. When the molecules are dissociated, then $\Delta S > 0$ and hence $\Delta H > 0$; this means that the dissociation energy of the molecules is higher than the bonding energy of formation [1, 3].

Table 4.1 Comparison of physical and chemical adsorptions

Characteristics	Physisorption	Chemisorption
Solids	All solids	Depends of the gas
Gas	All gases	Depends of the solid
Temperature	Near the boiling temperature	Above boiling temperature
Coverage	Multilayers	Monolayer
Reversibility	Reversible	In general irreversible
Activation energy	Null	Greater than zero
Heat of adsorption	Low (-0.5 to 5 kcal/mol)	High (-10 to -100 kcal/mol)

4.1.3.2   Adsorption Rate

The rate of adsorption in physisorption is small since the activation energy is small (1 kcal/mol) but reversible. However the rate of adsorption on chemisorption is very high, although the activation energy is small, but finite, or $e^{-\left(E/RT\right)} \approx 1$.

On the other hand, the collision factor of the molecules with the surface is high, of the order of $k_0 \approx 10^{17}(cm^2 \ s)$. This means that the adsorption rate occurs in a fraction of seconds, very quick [3]. Table 4.1 resumes the main characteristics.

4.1.3.3   Effect of Pressure and Temperature
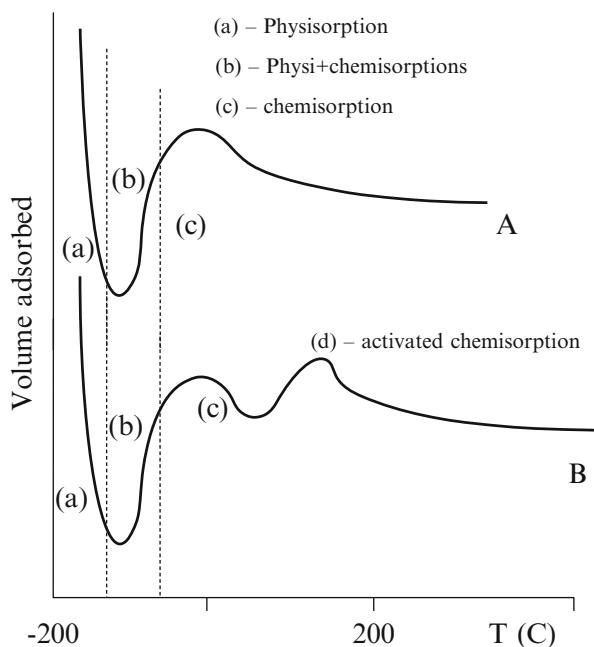
Experimentally, one measures the volume of gas adsorbed on surfaces, which depends on the vapor partial pressure in a system at a constant temperature, which are represented as *adsorption isotherms*. The pressure reference is pure liquid vapor or P_0. There are different cases:

- When $\frac{P}{P_0} \approx 0.01$, then the adsorbed volume is very low.
- When $\frac{P}{P_0} \approx 0.1$, the adsorbed volume forms a monolayer.
- When $\frac{P}{P_0} \geq 0.1$, the adsorbed volume forms a multilayer.

The effect of temperature on the adsorption of gases is significant, and, depending on the temperature range and the surface, there are different adsorption forms. Figure 4.4A shows the general behavior for an extended range of temperature [1, 4].

For low temperatures the physisorption prevails; for intermediate temperatures there are both physisorption and chemisorption. However, above 0 °C, the chemisorption is predominant but not exclusive. For example, the adsorption of N_2 occurs at -190 °C and condenses on the surface and in pores, while the adsorption of H_2 at 0 °C occurs by chemisorption.

Fig. 4.4 Effect of temperature on adsorption [Adapted with permission from Masel, I.R., "Principles of Adsorption and Reaction on Solid surfaces," John Wiley & Sons, Inc., New York, (1996)]

(a) – Physisorption

(b) – Physi+chemisorptions

(c) – chemisorption

(d) – activated chemisorption

4.1.3.4 Specificity

The physisorption is not specific and may occur on all solids, and for most gases, however, it depends only on the partial pressure. Gases such as N_2, CO_2, and Ar are frequently used for adsorptions and for surface area measurements, because they can easily penetrate in pores.

Chemisorption is specific, depending on the binding form and the nature of the surface. Figure 4.4B illustrates the adsorption curve and the activated chemisorption.

4.1.3.5 Isotherms

The amount of adsorbed gas on solid is proportional to the mass, depending on the temperature, pressure, and surface of solid or gas. Therefore, the number of moles of adsorbed gas is

$$n = f(P, T, \text{gas}, \text{solid})$$

For constant temperature, the equation is simplified as

$$n = f(P)_{T=\text{const}}. \tag{4.4}$$

which represents the *adsorption isotherm* and gives the amount of adsorbed gas at pressure equilibrium and constant temperature.
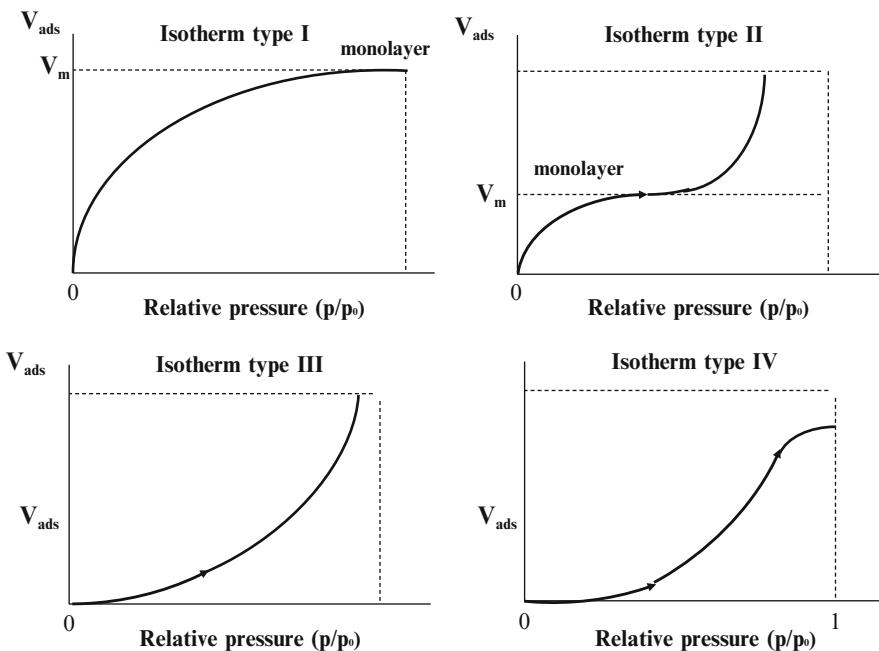
Fig. 4.5 Adsorption isotherms [Adapted with permission from Moujijn, J.A., van Leeuwen, P.W. N.M., van Santen, R.A., "Catalysis—Studies Science and Catalysis" vol 79, Ed.Elsevier, Scientific Publishing Company, (1993)]

The experimental isotherms may be classified in different forms, as shown in Fig. 4.5.

Type I represents the isotherm of chemisorption and attains saturation at low relative pressures, with the formation of a complete monolayer. This isotherm characterizes the microporous solids.

Isotherm type II represents the incomplete monolayer followed by capillary condensation: it occurs mainly on a macroporous material when $V \rightarrow \infty$.

The adsorption isotherm III tends to infinite when $P/P_0 \rightarrow 1$, which corresponds to the physisorption in superposed multilayers occurring on nonporous or macroporous materials.

Isotherm IV is similar to isotherm III, however, attains saturation with increasing pressure, and corresponds to a complete capillary condensation.

There are some specific isotherms, which depend on the angle and the surface tension, as shown in Fig. 4.6.

The isotherms in Fig. 4.6 show hysteresis during desorption, which means that the descendant curves are not equal to the ascendant adsorption curves, since the gas condensed in pores does not evaporate easily, and are recondensed due to the menisci of capillaries. These isotherms represent the macro- or mesoporous solids, and the adsorption volumes tend to a finite value, indicating pores filled out.
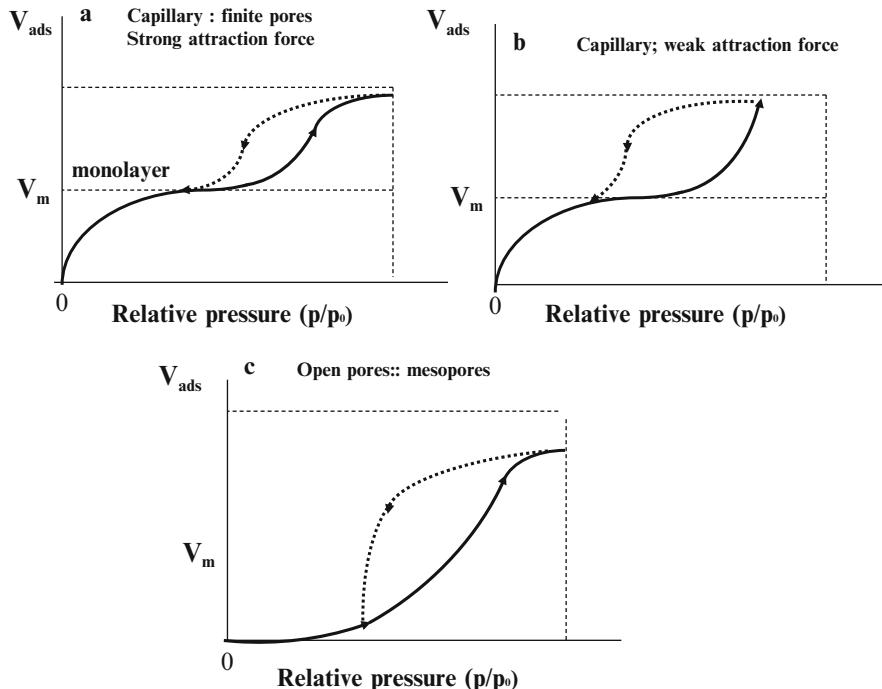
Fig. 4.6 Hysteresis curves of adsorption–desorption [Adapted with permission from Masel, I.R., "Principles of Adsorption and Reaction on Solid surfaces," John Wiley & Sons, Inc., New York, (1996)]

The explanation is given by the Kelvin equation, Eq. (4.1). Thus [1],

$$\ln\frac{P_{\text{drop}}}{P_{\text{vapor}}} = -\frac{1}{RT}\frac{2\gamma V}{r}\cos\phi \tag{4.5}$$

where

V—molar volume
r—pore radius
γ—surface tension
φ—contact angle

Example 4.1
Different methods were used for the preparation of nanosized materials. Two CeO_2 were prepared by the precipitation and hydrothermal methods, respectively, and one CeO_2 flowerlike type was prepared. The different CeO_2 oxides and mixed oxide $CeZrO_2$ showed nanosized structures and morphologies in particular distinct structural and surface properties.
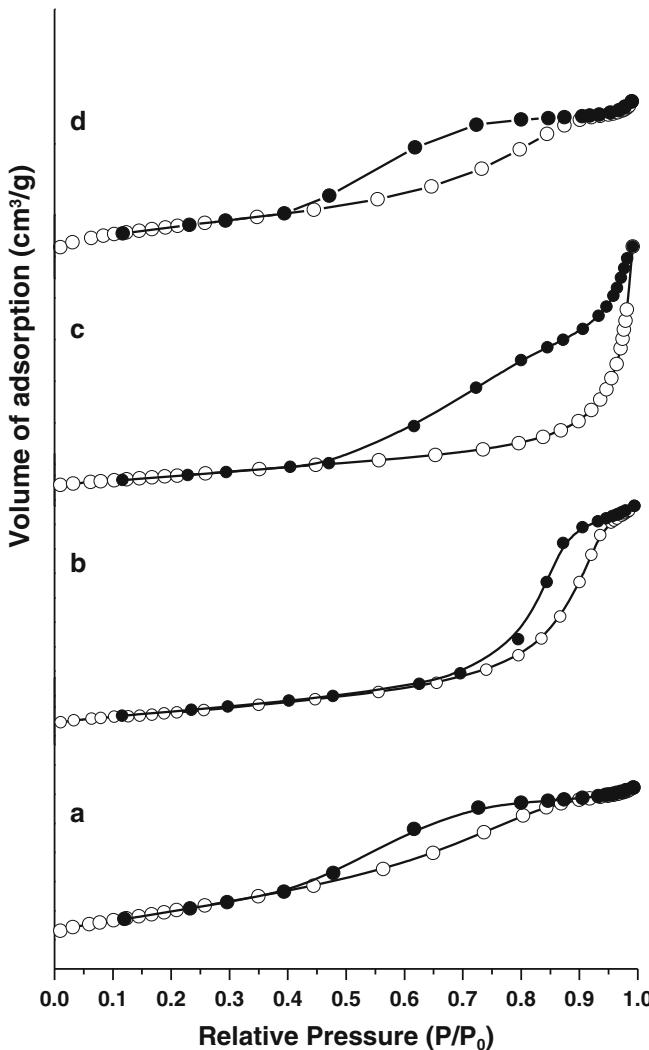
Fig. 4.7 Nitrogen adsorption–desorption isotherms for: (a) CeO_2 (P), (b) CeO_2 (F), (c) CeO_2 (H), and (d) $CeZrO_2$. Adsorption (*circle*) and desorption (*filled circle*) [5]

The isotherms of all samples are shown in Fig. 4.7, indicating adsorption–desorption profiles of type IV, associated with mesoporous solids [6].

All physisorptions show hysteresis, which are associated to this type of material due to the condensation on capillarity and geometrical morphologies [7–10]. As seen, the CeO_2 (H) displays hysteresis of type H1 associated with agglomerated solids with uniform cylindrical and not by interconnected mesopores, while the CeO_2 (F) and the mixed oxide $CeZrO_2$ (b, d) showed interconnected pores with cracks and parallel plates of type H3. Finally, the sample CeO_2 (P) shows undefined

Table 4.2 Surface area and pore distribution for (a) CeO$_2$ (P), (b) CeO$_2$ (F), (c) CeO$_2$ (H), and (d) CeZrO$_2$

Samples	Surface area (m^2/g)	Pore volume[a] (cm^3/g)	Pore diameter [b] (nm)	Type	Isotherm	Hysteresis
CeO$_2$ (P)	71	0.094	5.2	Meso	V	H2–H3
CeO$_2$ (F)	128	0.327	10.2	Meso	IV	H3
CeO$_2$ (H)	45	0.146	12.8	Meso	IV	H1
CeZrO$_2$	102	0.132	4.9	Meso	IV	H3

[a]Total volume from $P/P_0 \approx 0.98$
[b]Mean pore diameter ($4V_p/A_{BET}$)

hysteresis, which may be associated with the combination of H2 and H3 [7, 11]. Table 4.2 presents the surface area, pore volumes, and pore diameters using BET and BJH methods.

Noteworthy is the high surface area of the flowerlike CeO$_2$ (F) and of the mixed CeZrO$_2$.

4.2 Adsorption–Desorption Models

4.2.1 Introduction

There are several proposed models, which explain the adsorption–desorption phenomena. The most important models were described through the isotherms introduced by *Langmuir*, *Freundlich*, and *Temkin*.

4.2.1.1 The Langmuir Model

The first model of adsorption of gases on solids was proposed by *Irving Langmuir* in 1916. Langmuir suggested the following hypotheses for this model [6, 12]:

1. The solid surface needs definite number of sites for the adsorption of gases.
2. Each site can adsorb only one molecule.
3. All sites are energetically equivalents, that means, all sites must have the same enthalpy of adsorption.
4. The adsorption is independent on the neighboring adsorbed specie, which means that the enthalpy of adsorption does not depend of the degree of coverage.
5. At equilibrium, the rate of adsorption is equal the rate of desorption.
6. At equilibrium and for constant temperature and pressure, there are n_A moles adsorbed molecules on the surface.
7. The adsorption rate of a molecule A depends on the partial pressure p_A and of the number of free sites, at a constant temperature, and the desorption rate on the number of occupied sites.

molecules

atoms
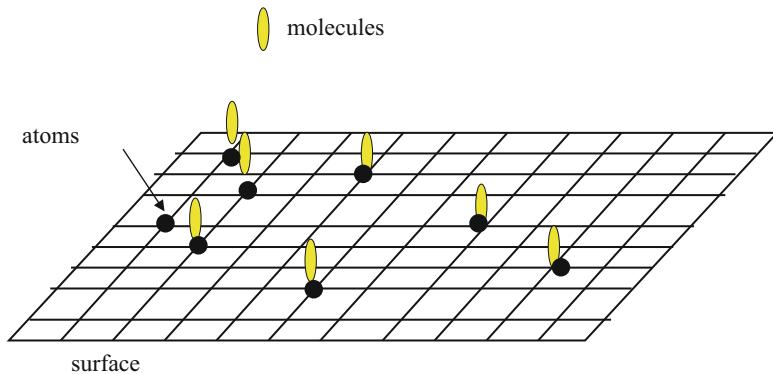
surface

Fig. 4.8 Model of adsorption of molecules on the surface [1–4, 14]

Fig. 4.9 Adsorption model
of a molecule A

A_{gas}

θ_A

$(1-\theta_A)$

surface

1a) *Single adsorption*

Consider the adsorption of a molecule A on the surface. One fraction of sites is
occupied by A, i.e., θ_A, and the other one is vacant, or $(1 - \theta_A)$ [11, 13]. Thus
(Fig. 4.8),

$$\theta_A = \frac{n_A}{n_m} \tag{4.6}$$

where n_m is the number of moles which corresponds to a monolayer.
Schematically, we have (Fig. 4.9):
The adsorption rate r_{ads} is directly proportional to the number of vacant sites at
the surface and the partial pressure of A. The proportionality factor is the
adsorption constant k_a. Thus,

$$r_{ads} = k_a p_A (1 - \theta_A) \tag{4.7}$$

Simultaneously desorption of the adsorbed of molecule A occurs, and thus, the
desorption rate r_{des} is directly proportional to the occupied fraction θ_A, where
the proportionality factor k_d is the desorption constant:

$$r_{des} = k_d \theta_A \tag{4.8}$$

The resulting rate is the difference between the adsorption and desorption rates;
however, the adsorbed species can also be desorbed, which allows new mole-
cules to be adsorbed at the surface. However, according to Langmuir, these
rates are in equilibrium, and so

$$r_{\text{ads}} = r_{\text{des}}$$

Therefore, we determine the fraction of occupied sites at the surface θ_A, equaling Eqs. (4.7) and (4.8), coming to the following equation:

$$\theta_A = \frac{k_a p_A}{k_d + k_a p_A}$$

However, from the definition of the equilibrium adsorption–desorption constant, $K_A = \frac{k_a}{k_d}$, this equation can be transformed as

$$\theta_A = \frac{K_A p_A}{1 + K_A p_A} \tag{4.9}$$

This is the Langmuir equation for the adsorption of a molecule A. In fact, the fraction of occupied surface can be obtained experimentally, by measuring the volume of adsorbed gas in a system, at a constant temperature and total pressure, according to the gas law. Thus,

$$\theta_A = \frac{V_{\text{ads}}}{V_{\text{monolayer}}} \tag{4.10}$$

The equilibrium constant K_A indicates the affinity of the gas with the surface. If K_A is high, the equilibrium goes in the direction of adsorption and vice versa. There are two extreme cases which can be considered:

1. If $K_A p_A \approx 0$, then Eq. (4.9) can be simplified as $\theta_A = K_A p_A$, which means that the surface coverage is proportional to the gas pressure. This situation occurs when $p_A \approx 0$, corresponding to the initial adsorption; when $K_A \approx 0$, the affinity of gas with the solid is very small.
2. If $K_A p_A \gg 0$, then Eq. (4.9) becomes $\theta_A = 1$, meaning that there is a complete coverage of adsorbed molecules on the surface, forming a monolayer. This situation occurs when $p_A \gg 0$, near the vapor pressure of the gas; it indicates that for $K_A \gg 0$, there is great affinity of the gas with the solid.

1b) *Symmetric dissociative adsorption*
Consider now the dissociation and adsorption of a molecule A_2 on two sites *, according to the following equation [11, 13]:

$$A_2(g) + 2*(s) \rightleftarrows 2A*_{(\text{ads})} \tag{4.11}$$
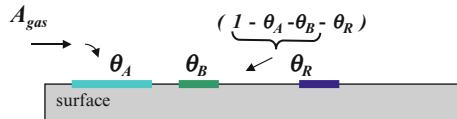
In this case, the adsorption and desorption rates are, respectively,

$$r_{\text{ads}} = k_a p_A (1 - \theta_A)^2 \tag{4.12}$$

$$r_{\text{des}} = k_d \theta_A^2 \tag{4.13}$$

Since, the dissociated molecule occupies simultaneously two sites at the surface.

A_{gas} $(1 - \theta_A - \theta_B - \theta_R)$

θ_A θ_B θ_R

surface

At equilibrium, we have

$$r_{ads} = k_a p_A (1 - \theta_A)^2 = k_d \theta_A^2$$

since

$$K_A = \frac{k_a}{k_d}$$

Thus, the fraction of occupied sites is

$$\theta_A = \frac{\sqrt{K_A p_A}}{1 + \sqrt{K_A p_A}} \tag{4.14}$$

This is the Langmuir equation of adsorption for dissociative molecules.

1c) *Adsorption of n-molecules*

When the adsorption and desorption of different molecules occur simultaneously, either reactants or products, then the situation is equivalent to following scheme (Fig. 4.10):

where θ_B and θ_R are fractions occupied by reactant B and product R, respectively.

Thus, the fraction of vacant sites is equal to

$$\theta_v = (1 - \theta_A - \theta_B - \theta_R \cdots)$$

The rates of adsorption and desorption for each component, according to Eqs. (4.7) and (4.8), are presented below as function of the adsorption–desorption equilibrium constants. Therefore,

$$
\left.
\begin{aligned}
\theta_A &= K_A p_A \theta_v \\
\theta_B &= K_B p_B \theta_v \\
&\cdots\cdots\cdots\cdots \\
\theta_R &= K_R p_R \theta_v
\end{aligned}
\right\} \quad +
$$

$$\sum \theta_i = \underbrace{(K_A \cdot p_A + K_B \cdot p_B + K_R \cdot p_R \text{-----})}_{\sum K_i p_i} \times \underbrace{\theta_v}_{(1 - \sum \theta_i)}$$

Thus,

$$\sum \theta_i = \frac{\sum K_i p_i}{\left(1 + \sum K_i p_i\right)} \tag{4.15}$$

and

$$\theta_v = \frac{1}{\left(1 + \sum K_i p_i\right)} \tag{4.16}$$

Therefore, the fraction of occupied sites for each component can be determined from the equation:

$$\theta_i = K_i p_i \theta_v$$

For the component i, we obtain

$$\theta_i = \frac{K_i p_i}{\left(1 + \sum K_i p_i\right)} \tag{4.17}$$

When one component is dissociated, one substitutes the term by including the root square. For example, if A is dissociated, then

$$\theta_A = \frac{\sqrt{K_A p_A}}{(1 + \sqrt{K_A p_A} + K_B p_B + K_R p_R)} \tag{4.18}$$

Equations (4.17) and (4.18) represent the fraction of sites occupied, whether dissociated or not, respectively. Substituting these expressions in Eqs. (4.12) and (4.13), we can calculate the adsorption and desorption rates for all components, due to simultaneous adsorption, desorption, and reaction.

4.2.1.2   Other Adsorption Models

As seen before, the adsorption–desorption equilibrium constant K_A in Eq. (4.9) can be related to the thermodynamic or free energy ΔG^0. Thus,

$$K_A = K_{A0} \exp\left(-\Delta G^0 / RT\right) \tag{4.19}$$

However,

$$\Delta G^0 = \Delta H^0 - T\Delta S^0 \tag{4.20}$$

Thus, substituting Eq. (4.20) in Eq. (4.19), we obtain

$$K_A = \underbrace{K_{A0}.\exp\left(\Delta S^0/R\right)}_{\text{Independent of the temperature}} \cdot \underbrace{\exp\left(-\Delta H^0_{\text{ads}}/RT\right)}_{\text{depends on the temperature}} \tag{4.21}$$

Consequently, the fraction θ_A of surface coverage also depends on the temperature, according to Eq. (4.17).

Therefore, the Langmuir model fails, because:

- The sites are not all equally actives.
- The sites are not all energetically equivalent, i.e., they do not have the same energy, varying with the temperature.
- The adsorption energy depends on the degree of coverage, or, in other words, the adsorbed molecules interfere on the adsorption of the neighboring sites.

Indeed, the Langmuir hypotheses are "not correct," as demonstrated in 1951 by Kummet and Emmet, suggesting that the surface is not homogeneous. The adsorption occurs on distinct sites or multisites, and therefore, the coverage varies with the fraction of sites.

In fact, K^i depends on the entropy and enthalpy of the system, varying with temperature. Thus, rewriting Eq. (4.17), we get a general expression

$$\theta_i = \frac{y_i K^i p_i}{1 + \sum y_i K^i p_i} \tag{4.22}$$

where y_i is the fraction of site i.

Understanding how the coverage varies on sites implies understanding the type of interaction existing between the adsorbed (gas) and adsorbent (surface). One knows that there is a strong interaction between the molecules and the surface, when the adsorption is of a chemical nature. The heats of adsorptions vary due to the interaction between molecules on the surface, and between the molecules and the surface, since K^i depends on the temperature and the nature of the sites. Experimental data showed that the heats of adsorptions varied with the degree of coverage and for different molecules, as, for example, CO, NO, and H_2, as shown in Fig. 4.11 [3].

Consequently, the bonding strengths between molecules and the surface and between the molecules vary. There are two forms, the direct and indirect interactions between the molecules and surface:

1. Direct interaction between adsorbed adjacent molecules
2. Indirect interaction, where the adsorbed molecules vary with the degree of surface coverage, affecting the adsorption of adjacent molecules

In the first case, the interaction is weak and similar to the interaction of molecules in the liquid, where the attraction force is of the order of the van der Waals forces, with repulsion.
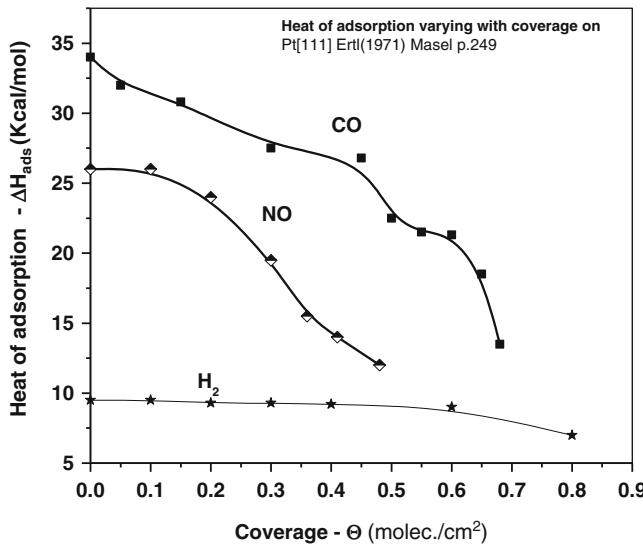
Fig. 4.11 Heat of adsorption versus surface coverage [Reproduced with permission from Masel, I. R., *Principles of Adsorption and Reaction on Solid Surfaces*, John Wiley & Sons, Inc., New York, (1996) 3, p. 249]

In the second case, the indirect interaction indicates strong bindings of adsorbed species with the surface, which are chemical bindings. There are donor electron transfer phenomena, which modify the electronic structures of the surface, changing the bondings of the adsorbed species with the surface, and thus, the surface coverage. It is very difficult to measure experimentally, but it is possible to have an idea of the interaction, using spectroscopic measurements [1].

4.2.1.3 Freundlich's Model

Freundlich suggested that the surface coverage depends on the heat of adsorption and proposed the following equation for surface coverage [15]:

$$\theta = kP^{\left(\frac{1}{n}\right)} \tag{4.23}$$

where k and n are the constants. These are empirical values, where $n > 1$; however, k and n decrease with the increasing temperature. The constant n represents the interaction between the adsorbed and adsorbent.

Freundlich's equation was originally proposed as an empirical equation based on experiments. Figure 4.12 shows the curve of the heat of adsorption as function of the coverage. Note that there are two parameters, while the Langmuir equation has only one parameter. This equation can be written assuming that the heat of adsorption decreases with the logarithm of the degree of coverage:

Freundlich's model   Tempkin's model
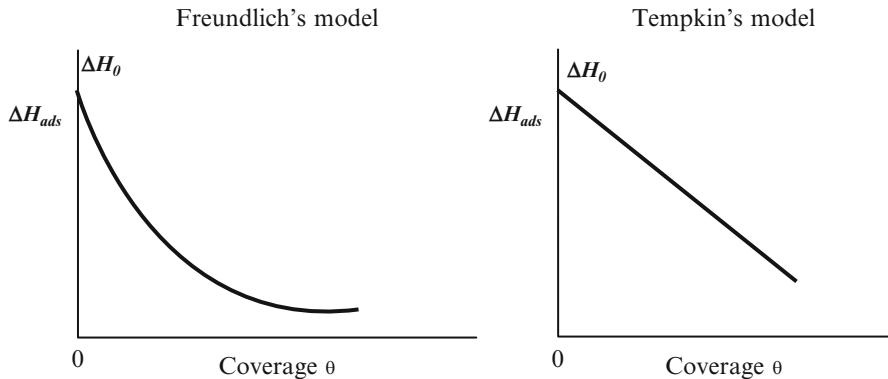
Fig. 4.12 Adsorption isotherms on surfaces [1–3, 14]

$$\Delta H_{\text{ads}} = -\Delta H_0 \ln\theta \tag{4.24}$$

where ΔH_0 is initial enthalpy or heat of adsorption when $\theta = 0$. The θ value can vary between 0.2 and 0.8.

4.2.1.4 Temkin's Model

Temkin assumed a linear relationship between the heat of adsorption and the surface fraction coverage. This model represents the indirect interaction [15, 16]:

Thus,

$$\Delta H_{\text{ads}} = \Delta H_o(1 - \alpha\theta) \tag{4.25}$$

Substituting Eq. (4.25) in Eq. (4.21), we have

$$K_A = K_{A0}.\exp\left(-\Delta H_{\text{ads}}^0 \alpha\theta_A / k_B T\right) \tag{4.26}$$

where

k_B—Boltzmann constant
α—constant

However, from Eq. (4.9):

$$\theta_A = \frac{K_A p_A}{1 + K_A p_A}$$

Table 4.3 Comparison of isothermic models

Isotherms	Advantages	Disadvantages
Langmuir	One parameter	Ignores the interaction adsorbed/adsorbent
Freundlich	Two parameters	Empirical
Multisites	Various parameters	Heterogeneous surfaces
Temkin	Interaction molecule/surface	Undefined layers
Others	Interactions	Difficult to explain

Thus,

$$K_A p_A = \frac{\theta_A}{1 - \theta_A}$$

Substituting K_A [Eq. (4.26)] in logarithmic form, we get

$$\ln(K_{A0}p_A) = \frac{\Delta H^0_{ads}\alpha\theta}{k_B T} + \ln\frac{\theta}{(1 - \theta)}$$

Figure 4.12 shows that there is an approximate linear relationship between ΔH^0_{ads} and θ up to $\theta = 0.5$. Thus, substituting $\theta = 0.5$, then the last term of the equation disappears, or

$$\theta_A = \frac{k_B T}{\Delta H^0_{ads}\alpha k_B T}\ln(K_{A0}p) \tag{4.27}$$

where ΔH^0_{ads} is the initial enthalpy of adsorption. The degree of surface coverage is expressed in the following equation:

$$\ln(K_{A0}p_A) = \frac{\Delta H^0_{ads}\alpha\theta_A}{k_B T} \tag{4.28}$$

where K_{A0} is the reference equilibrium constant.

It is important to stress that although the limitations, the Langmuir model is, for simplicity, the preferred equation used in kinetic models.

Table 4.3 shows the following limitations, advantages, and disadvantages.

4.3   Adsorption on Metals

The adsorption on metals involves physisorption and chemisorption. In the first case, the interaction is weak, like van der Waals forces, while in the second case, the interaction between the molecules and the metal is strong, involving electrons of both sides and modifying the electronic structure. Molecules can chemisorb in the

direct or dissociative form, but depend on a several parameters, such as tempera-
ture, surface structure, and the degree of surface coverage.

Adsorption studies on well-defined crystal surfaces, films, or flat surfaces were
important to explain and correlate the interaction between molecules and surfaces
of metals and supported metals. However, adsorption of molecules on crystal
surfaces is usually performed under ultrahigh vacuum, free of impurities, and
thus under ideal conditions. For example, if the molecule adheres at the surface
after each collision, under vacuum at 10^{-6} torr, it forms a monolayer in 1 s, which
corresponds to one Langmuir unit, or a monolayer.

On the other hand, these flat surfaces are meaningless for very small metallic
particles. In this case, it is better to define the coordination number i of atoms at the
surface and the number of surface sites, as shown in Fig. 4.13 [1].

In reality these structures are not reactive; however the defects on these flat
surfaces may provoke forces which attract molecules to the surface. These defects
can be holes, edges, corners, etc.

There are three stages for the adsorption of molecules on metals, as shown in
Fig. 4.14, for the dissociative adsorption of H_2 on metallic structure (fcc)
surface [2].

In the first stage, it forms independent clouds of electrons around the H atom and
the metal, which are not superimposed, and indicates a weak attraction or molecular
physisorption.

In the next stage, hydrogen is dissociated and the clouds of electrons are
superimposed forming a transition state. However, hydrogen atoms are bonded
and probably exert attraction on metal atoms.
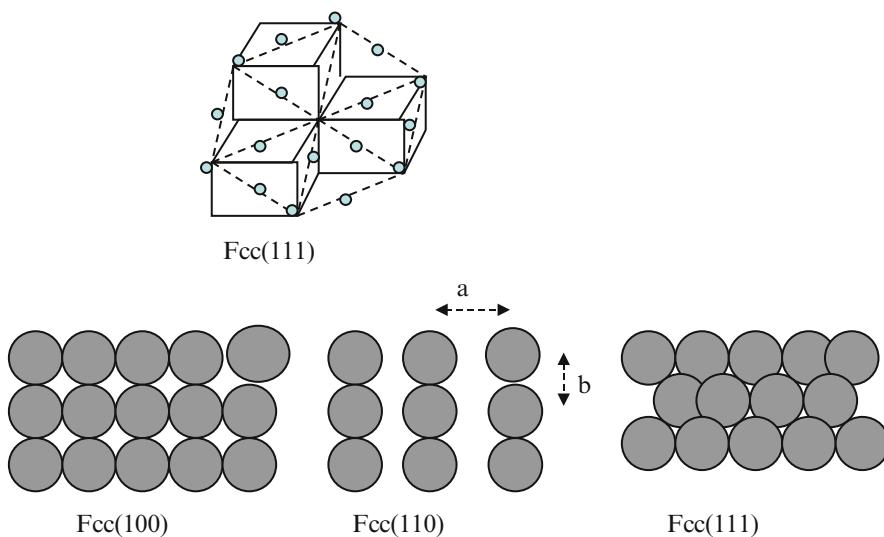
Fig. 4.13 Structure models [1, 4]
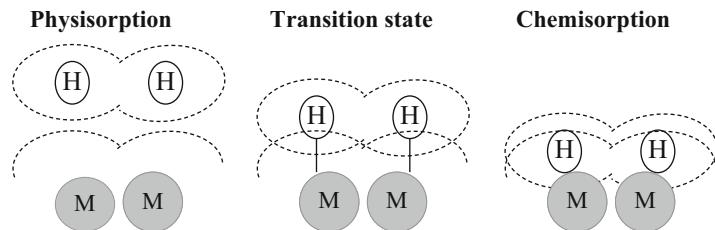
Fig. 4.14 Adsorption stages on metals [Adapted from Bond, C.C., *Heterogeneous Catalysis and Applications*, Clarendon Press, Oxford (1974)]

In the last stage, the electron clouds are superimposed forming new electronic structures, which are strong chemical bonds, characterizing the chemisorption phenomena, as shown in Fig. 4.14.

In this case, Fig. 4.14 exhibits the surface atomic structure of metallic site Me^0, representing two atoms of metal and hydrogen dissociated (H) [2]:

$$2M_s^0 + 2H \rightarrow 2MH \tag{4.29}$$

4.3.1   Lennard-Jones Diagram

After collision of the molecule with the surface, there are two successive sequences before adsorption [1, 17]:

1. The molecule adheres at the surface with the formation of a precursor state.
2. The molecule may or not be dissociated and after moves or diffuses over the surface and reaches finally the adsorption state.

The adsorption can be represented energetically through the Lennard-Jones diagram [17], displaying the potential energy of the system during the adsorption process, starting from the initial position of both the metal and of the molecule, as shown in Fig. 4.15.

The abscissa indicates the distance of the molecule from the solid and the ordinate of the potential energy, which can be positive, negative, or null. Far from the surface, these molecules are stable, and to bring them closer to the surface for dissociation, the energy needed is high (E_{H-H}). The molecules approaching the surface may interact, with the formation of bindings. In this case, the energy needed for dissociation is lower than when dissociated directly, which Lennard-Jones defined as dissociated state.

Following path (b) the molecule adsorbs initially without dissociation, releasing energy $\Delta H_f < 0$ at a distance d_f, and then forms the precursor that surpasses the energy barrier E_c, which is then strongly adsorbed at the surface, or chemisorbed, and releases an energy $\Delta H_c < 0$, which is highly exothermic. Note that the energy barrier E_c is positive, but much lower than the energy necessary to bring directly the
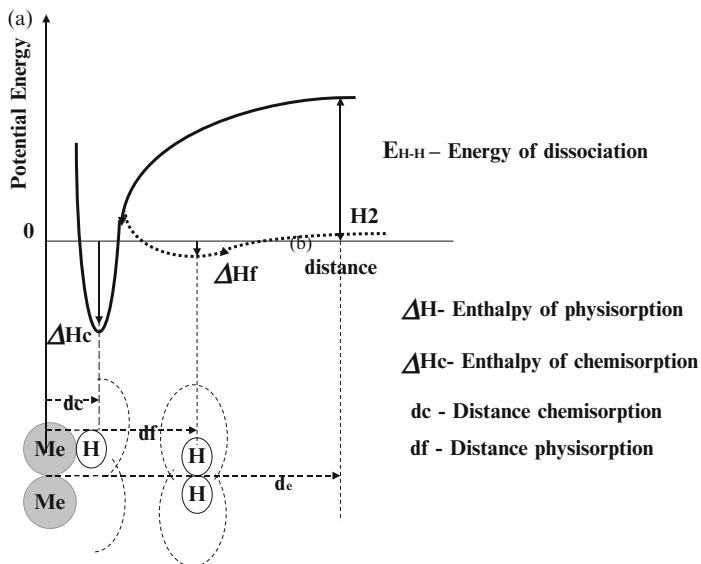
Fig. 4.15 Lennard-Jones diagram—potential energy versus distance [1–4, 6, 11–20]

molecule to the chemisorption state. Lennard-Jones distinguished the molecular adsorption and the dissociative adsorption, based on this principle. There are two other possibilities, as shown in Fig. 4.16.

Figure 4.15 (a) shows that the adsorption or chemisorption depends on the energy barrier E_c. First, molecules are physisorbed and dissociated, surpassing the energy barrier before being chemisorbed. If the energy barrier is small, then the dissociated species surpass easily on the energy barrier, prevailing chemisorption.

Figure 4.16 case (b) evidences that physisorption is predominant. The energy barrier is high, prevailing the molecular adsorption.

Finally, case (c) indicates a more complex situation where energy barrier is absent. Thus, most physisorbed molecules pass directly without dissociation to the chemisorption state. The chemisorption prevails and it is called activated dissociation.

Therefore, we conclude that there are two critical situations whether the molecules are adsorbed in molecular or dissociative form. The chemisorption is thermodynamically favored.

4.3.2 Mechanisms of Adsorption of Gases

The mechanisms of adsorption of molecules have been studied on supported metals, but mainly on well-defined crystals allowing understanding the adsorption forms and mechanisms. The main problem is quantifying the adsorption and prove such
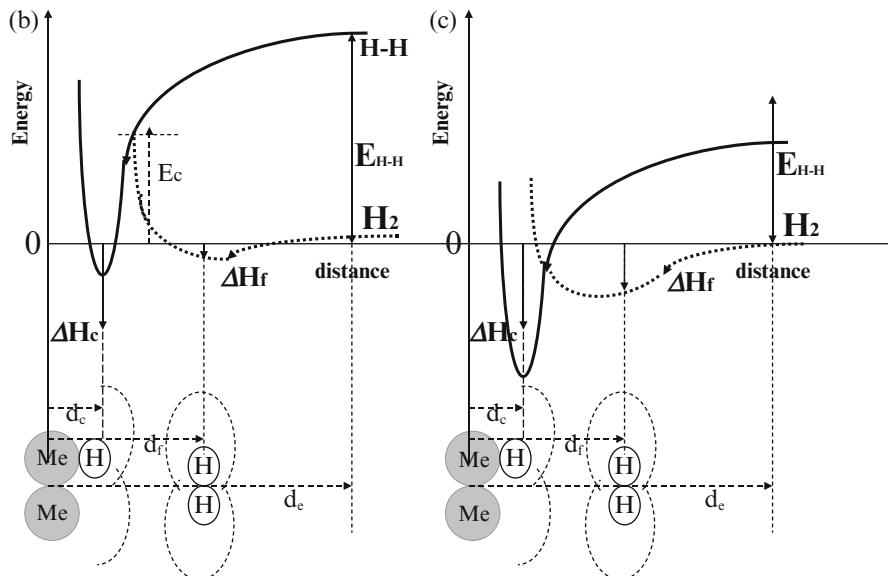
Fig. 4.16 Diagrams of energy (b) and (c) [Adapted with permission from Masel, *Principles of Adsorption and Reaction on Solid Surfaces*, p. 249, Fig. 4.7 (1996) Wiley] [1]

adsorptions forms. One easy way is measuring the total and reversible adsorption volumes. The difference corresponds to the irreversible adsorption or chemisorption. The adsorption form was understood from spectroscopic measurements and, in particular, on well-defined crystals. It has been shown that gas molecules are adsorbed in different and complex forms. However, the simple gas molecules can be adsorbed dissociative or associatively [1, 2].
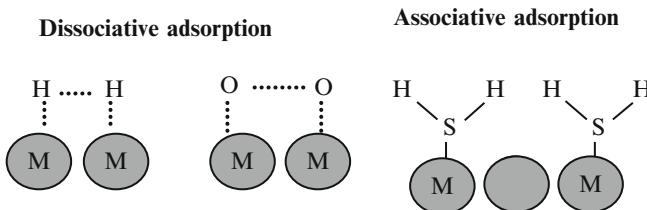
Dissociative Adsorption The molecules are dissociated on two sites (linear), as for H_2 and O_2 according to:

$$H_2 + 2^* \rightarrow 2H^*$$
$$O_2 + 2^* \rightarrow 2O^* \tag{4.30}$$

Associative Adsorption Adsorption of a the molecule on one site (*):

$$H_2S + ^* \rightarrow H_2S^* \tag{4.31}$$

or schematically:

In general, adsorbed molecules on surfaces are distorted, which are attributed to changes in the electronic structure when adsorbed, and are different from the electronic structure of the molecule in the gas phase. This has been verified for CO and C_2H_4 on flat surfaces of Pt[111] by different authors [1, 14]. In fact, they observed, through spectroscopic measurements, that there are simultaneously different adsorption forms of molecules on distinct sites, but energetically similar.

CO Adsorption

The carbon monoxide molecule (CO) can be adsorbed in different forms on distinct sites of the surface, namely, as linear, or on top adsorption, on one site, or as bridged form on two adjacent sites of the surface. It can also be adsorbed as triple bonding. In the first case, there is π interaction of the molecule with the free valence of the surface. In the second case, there is redistribution which then joins the free valence. Schematically, it is shown in Fig. 4.17 [1, 2, 14].
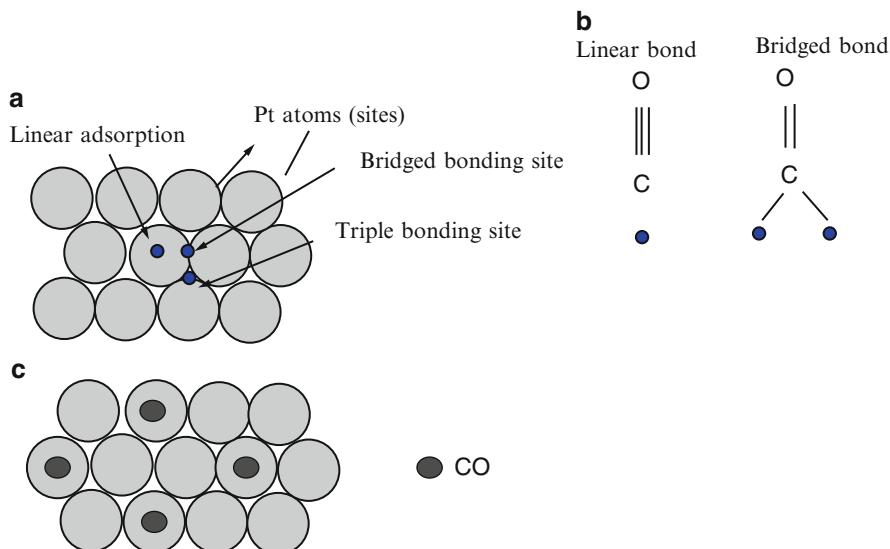
Fig. 4.17 Model of adsorption of CO on flat surfaces [1, 2, 14]
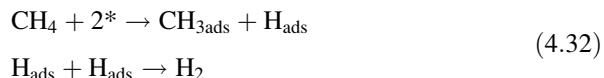
Figure 4.17a shows the atomic surface structure adsorption, displaying the linear form (central), the bridged adsorption form (at the interface), and the triple coordination form (junction between atoms). Figure 4.17b shows the scheme of the adsorption bonds and Fig. 4.17c the CO adsorption on atoms, which according to Crossley and King [21] have a structure like $\sqrt{3} \cdot \sqrt{3}$. For low coverage, the CO bond is perpendicularly at the surface, reaching complete coverage for 3.3×10^{14} molecules/cm^2. With increasing temperature, double or triple bonds occur. CO adsorbs initially as linear but, with increasing coverage, forms bridged and combined linear and bridged bindings. For other cases, this situation is more complicated.

In general, the CO molecule adsorbs on most surfaces. Adsorbs on copper at 77 K, but desorbs easily at 300 K. It does not adsorb on gold and silver. It adsorbs in the dissociative form on molybdenum and tungsten, but not on ruthenium and nickel. It was observed that CO dissociates on Ni[111] and Ni[100] at 673 K and under high vacuum.

Adsorption of Hydrocarbons

Other molecules can be adsorbed selectively on metals, but it is more complex. Hardly CH_4 and C_2H_6 can adsorb on metals. The first quantitative measurement of adsorption of methane on supported Ni was reported by Kubokawa [7]. He observed the formation of CH_x species, x varying between 0 and 3. Kuijpers et al. [8] observed dissociative adsorption on small Ni metallic particles but not on bigger particles. Methane was adsorbed in dissociative form at temperatures as low as 303 K, with simultaneous evolution of H_2 at 423 K.

The adsorption of CH_4 was also studied quantitatively by Martins et al. [9] for different supported metals. During pulses of methane, they also observed the evolution of H_2, independent of the support or the metal. The H_2 evolution resulted from the association of hydrogen atoms, due to the dissociative chemisorption of CH_4, according to the following reaction:

$$CH_4 + 2* \rightarrow CH_{3ads} + H_{ads}$$
$$H_{ads} + H_{ads} \rightarrow H_2$$

$$(4.32)$$

where (*) represent the sites.

Results showed that the adsorption capacity of the catalyst increases ten times with increasing temperature of adsorption from 423 K up to 623 K.

More complex is the adsorption of hydrocarbons and particular ethylene that forms different intermediate species. Cassuto et al. [10] showed a π adsorption form of ethylene on flat Pt[111] surface at 40 K, without significant changes of the structure in the gas phase. However, at 90 K forms a di-σ complex with hybridization sp^3 over a flat Pt[111] surface, which then passes to the ethylene–ethylene stretched bonding structure from 1.34 Å up to 1.49 Å.

a

Adsorption Π   **Adsorption di σ**

  40K   90K

$H_2C{=}CH_2$ $H_2C{=}CH_2$

b

$H_2C{=}CH_2$ $\xrightarrow{-[1/2]H_2}$ Ethylidene $\xrightarrow{-[1/2]H_2}$

Adsorption di-σ   Ethylidene   C Adsorbed

c

$H_2C{=}CH_2$ $\xrightarrow{-H_2}$ $^-$Vinilydene $\xrightarrow{-H_2}$

Adsorption di-σ $^-$Vinilydene   C Adsorbed
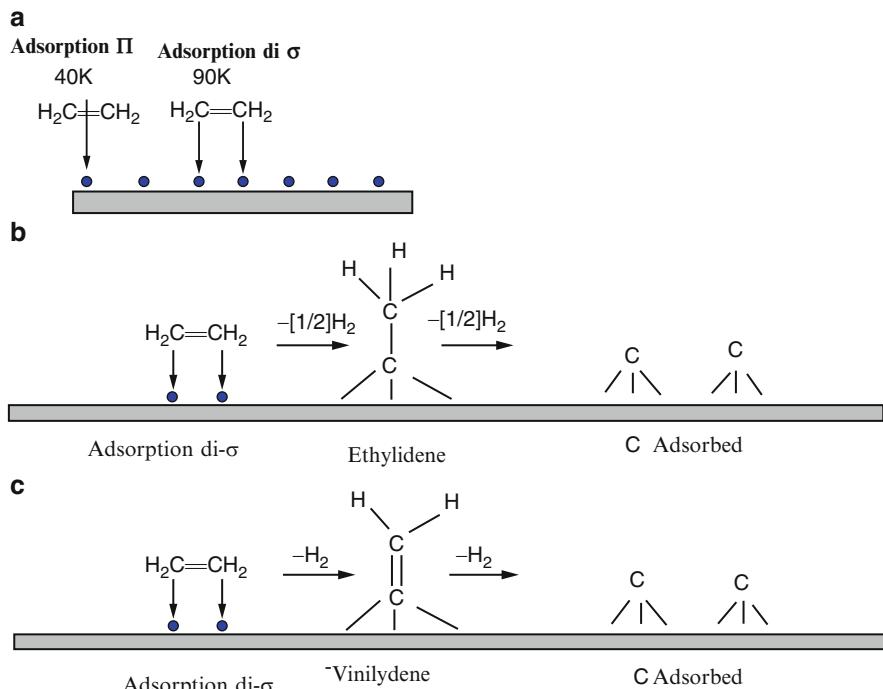
Fig. 4.18 Adsorption of ethylene on flat surfaces [Adapted with permission from Somorjai, G.A., *Introduction to Surface Chemistry and Catalysis*, John Wiley & Sons, Inc., New York, (1994)]

On the other hand, Somorjai and his group [14] demonstrated that the adsorption of ethylene on flat Pt[111] forms hydrogen atom and an intermediate complex $CHCH_2$, which can easily be transformed in ethylidene CCH_3, which dehydrogenates to CCH_2 and CCH species, at higher temperatures, indicating multiple dissociative adsorption on the metal, forming finally carbon, as shown in Fig. 4.18.

The intermediate species have different levels and energetic barriers, as shown in the Lennard-Jones diagram. However, it is impossible to represent graphically in a one-dimensional level.

It is possible to explain the adsorption phenomena for the molecular and dissociative adsorption at energetic level. For the dissociative adsorption, the energy level is low. However, when the energetic barrier is too low, molecules can easily be adsorbed. Thus, the energy barrier may predict qualitatively the chemisorbed state, according to the Lennard-Jones diagram [1, 17].

Adsorption of Oxygen

The oxygen molecule can be dissociated on practically all metals or $O_2 + 2^* \rightarrow 2O^*$. The adsorption is easy at low temperatures. However, at high temperatures, a reaction of the metal with the oxygen occurs, forming immediately an oxide.

The titration method is an example of oxygen adsorption used for determining the metallic surface sites, titrating with H_2 the superficial oxygen at low temperatures. The titration is an alternative process with adsorption of O_2 and H_2. Oxygen binds at metallic surface in the first step, and then hydrogen atoms remove the surface oxygen, forming hydrate, successively, according to the equations in this example. Starting from the platinum oxide [2]:

$$PtO_2 + 2H_2 \rightarrow Pt_s^0 + 2H_2O \tag{4.33}$$

Titration process:

(1)
$$Pt_s^0 + \frac{1}{2}O_2 \rightarrow Pt_s - O \tag{4.34}$$

(2) $Pt_s - O + \dfrac{3}{2}H_2 \rightarrow Pt_s^0 - H \ + H_2O$ $\left.\rule{0pt}{3.5em}\right\}$ n times $\tag{4.35}$

(n) $Pt_s^0 - H \ + \dfrac{3}{4}O_2 \rightarrow Pt_s - O + \dfrac{1}{2}H_2O$ $\tag{4.36}$
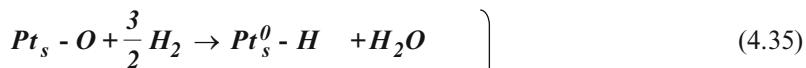
The number of moles of oxygen in the stage (n) relative to step (1) is

$$\frac{n_{On}}{n_{O1}} = 1.5 \tag{4.37}$$

However, the number of moles of hydrogen in step (n) relative to the oxygen in step (1) is

$$\frac{n_{Hn}}{n_{O1}} = 3 \tag{4.38}$$

Therefore, it needs 1.5 atoms of oxygen per metal atom. The ratio of H_2 and O_2 moles in step (n) is

$$\frac{n_{Hn}}{n_{On}} = 2 \tag{4.39}$$

Strength of Adsorption
As seen before, the adsorption of molecules on surface sites depends on the electronic structure and on the geometric congruence between molecules and the surface. During the adsorption of molecules, there are structural deformations which depend on the adsorption strength. Thus, for example, structural changes provoking deformation are shown in the following case (Fig. 4.19).

Fig. 4.19 Adsorption
model for ethylene
[Adapted with permission
from Somorjai, G.A.,
*Introduction to Surface
Chemistry and Catalysis*,
John Wiley & Sons, Inc.,
New York, (1994)]

$$H_2C{=}Ch_2 \quad 1.34A$$

Ethylene

Ethylene   Pt[111]^{at} 300K
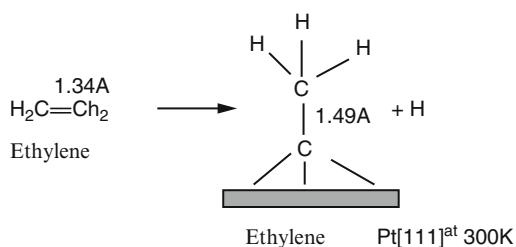
Table 4.4 Adsorption force of gases on different solids, metals, or oxides [Bond, C.C., "Hetero-geneous Catalysis and Applications" Clarendon Press, Oxford (1974)]

Group	Metal/oxides	O_2	C_2H_2	C_2H_4	CO	H_2	CO_2	N_2
I	Ti, Zr, Hf, V, Nb, Ta, Cr, MoW, Fe, Ru.Os	+	+	+	+	+	+	+
II	Ni, Co	+	+	+	+	+	+	
III	Rh, Pd, Pt, Ir	+	+	+	+	+		
IV	Mn, Cu	+	+	+	+	+		
V	Al, Au	+	+	+	+			
VI	Li, Na, K	+	+					
VII	Mg, Ag, Zn, Cd, In, Si, Ge, Sn, Pb, As, Sb, Bi	+						

The adsorption force depends on the interaction between molecules and sur-faces, but measurements are very difficult. Several experiments of different gases, and surfaces were reported in the literature and qualitatively the adsorption of gases on all surfaces, follow the order [4, 31]:

$$O_2 > C_2H_2 > C_2H_4 > CO > H_2 > CO_2 > N_2$$

The ability of interaction of a molecule with the surface on metals and oxides depends on the adsorption force, which varies from gas to gas and solids. A qualitative analysis was made based on different experiments, and Table 4.4 shows the molecules which are or not absorbed on solids [4].

One can see that oxygen is adsorbed on all metals and oxides and CO, ethane, and ethylene over the solids of groups 1–5, H_2 on solids of groups 1–4, while N_2 and CO_2 are weakly or not adsorbed on most metals or oxides.

The adsorption force is proportional to the enthalpy of formation and varies considerably on the different surfaces of metal oxides. The *enthalpy of adsorption* is defined as the *molar enthalpy when a molecule passes from the gaseous phase to the adsorbed state* and can be adsorbed or dissociated. In this later case, we consider also the heat of dissociation. The heat of adsorption and dissociation depend on different factors, such as the surface, whether flat or irregular, and the fraction of
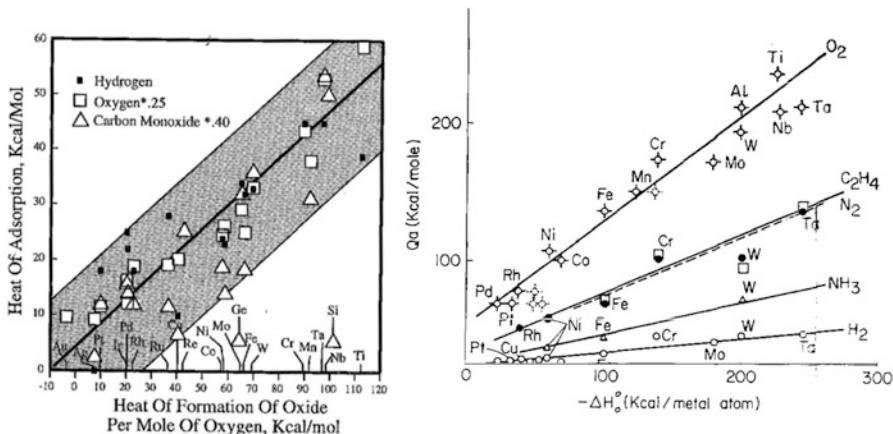
Fig. 4.20 Correlation between heat of adsorption and heat of formation [Reproduced with permission from Masel, *Principles of Adsorption and Reaction on Solid Surfaces*, p. 137, Fig. 3.23 (1996) Wiley and (b) from K. Tanaka, K. Tamaru, J. Catal., 2 (1963) 366 Fig. 6 (Elsevier)]

covered and exposed surface faces of the metal oxide. When not dissociated, the heat of adsorption is directly proportional to the heat of formation.

Brennan et al. [22] observed experimentally that the oxygen adsorption on transition metals does not confirm the model and suggested alternative models. There is no correlation between the heat of adsorption and the heat of formation of bulk metal oxides. They suggested that the heat of adsorption is equal to the chemical energy bond of the oxygen in the bulk oxides. Roberts et al. [23] correlated the heat of adsorption of oxygen with the heat of formation of oxygen–metal bonding and for hydrogen the heat of formation of bulk hydrate. Tanaka and Tamaru [24] extended this model for other metals which are or not reactive. The reactive metals may form strong bonds, and the nonreactive metals weak bonds with different molecules. Thus, strong bonds form hydroxides, nitrates, sulfates, etc. The heat of adsorption of gases can be correlated to the heat of formation of hydroxides or carbides. The conclusion is that for most gases the heat of adsorption may be correlated to the heat of formation of bulk oxides, as shown in Fig. 4.20.

This correlation shows a qualitative analysis but is quite good, although some deviations. However, it is the most significant correlation because the heat of adsorption can be measured directly.

The enthalpy of adsorption (kJ/atom) of gases depends on the transition metals and is represented in Fig. 4.21 as function of the elements of the periodic table.

Figure 4.21a shows that the enthalpy of adsorption on metal oxide of the groups 4–6 is high, suggesting the following order of adsorption force: $O_2 > CO > H_2$. The heats of adsorption of oxygen on metal oxides of groups 8–10 are relatively high, compared to CO and H_2, which are much lower and constant. In this range, we find the noble metals. The metal oxides of the group 11 indicate that the heat of
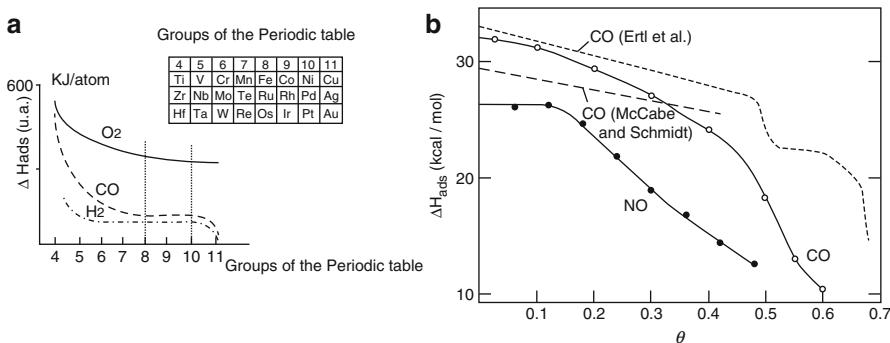
Fig. 4.21 Enthalpy of adsorption of gases on metal oxides [Adapted with permission from E.G. SEEBAUER, A.C.F. KONG and L.D. SCHMIDT, *Surface Science* 176 (1986) 134–156, p. 148, Fig. 9 (Surface Science) and from Trimm, D.L., *Design of Industrial Catalysis*, Ed. Elsevier, Scientific Publishing Company, (1980)]

adsorption of oxygen is low and very low for CO and H_2. Noteworthy is that the enthalpy of adsorption for H_2 and CO is of the order of -100 kJ/atom, but increases for metal oxides of group 4–6. The enthalpy of adsorption for oxygen varies between -300 and -600 kJ/atom. In fact, the enthalpy of adsorption is highly exothermal. Figure 4.21b displays the heat of adsorption varying with coverage similarly [25].

The adsorption force is directly related to the catalytic activity and the general rule is that the greater the adsorption force, the lower is the activity. In this case, the strongly adsorbed molecules makes the desorption more difficult and the contact time is very high, decreasing the rate of adsorption at the surface. The opposite occurs when the molecules are weakly adsorbed, i.e., the adsorption force is also too weak. The contact time is too low and the activity is also too low. As observed the activity is high or maximum in the range of not so high and not so low adsorption strength, as shown in Fig. 4.22. This was confirmed experimentally for reactions with noble metals, which are the most preferred in many industrial processes [26].

Curve (a) shows a wide range of activity, while curve (b) a selective activity, which depends on the metal, of the nature and surface properties, and in particular of the dispersion or particle sizes on supported materials. Smaller particles can expose more sites for adsorption of small molecules, which also depend on the adsorption force and thus facilitates or hinders the reaction, affecting the catalytic activity.

Simple Theoretical Model

The simplest theoretical model representing the adsorption was proposed in 1950, and was improved, as new experiments came out. It was assumed that the adsorption of molecules on surfaces is attributed to electronegativity and bond energy. Novel models have been proposed based on the quantum mechanics theory, which are more comprehensive and complete. However, this simple model is yet

Groups of the Periodic table

4	5	6	7	8	9	10	11
Ti	V	Cr	Mn	Fe	Co	Ni	Cu
Zr	Nb	Mo	Te	Ru	Rh	Pd	Ag
Hf	Ta	W	Re	Os	Ir	Pt	Au
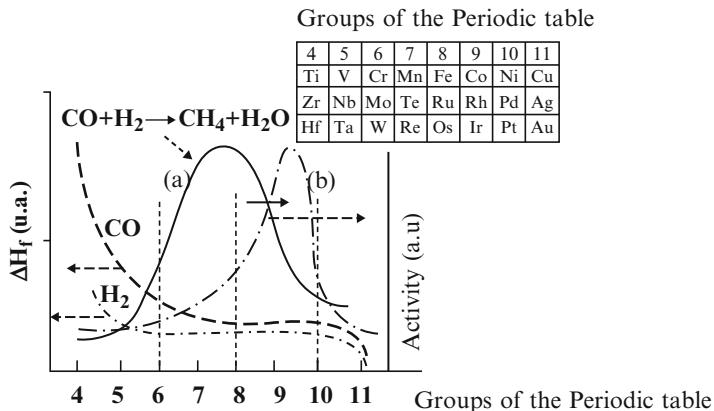
Fig. 4.22 Adsorption versus activity [Adapted from Trimm, D.L., *Design of Industrial Catalysis*, Ed.Elsevier, Scientific Publishing Company, (1980)]

appropriate for correlating experimental data. We will not deduce the formula and details can be seen in the book of R. Masel (p. 133) [1, 4]. According to L. Pauling, one assumes a model with two electrons and calculates the binding energy between two species. This equation is based on one electron of the A–B bond. When the atom A approaches atom B, it has one variable electron, as shown in the equation:

$$D(A - B) = \frac{1}{2}(D(A - A) + D(B - B)) + \gamma_{Pa}(\chi_A - \chi_B)^2 \qquad (4.40)$$

where $D(A - B)$, $D(A - A)$, and $D(B - B)$ are the binding energies between A and B, χ_A, χ_B the electronegativity, and γ_{Pa} the universal Pauling constant (1/eV).

Eley [27] employed this model to calculate the adsorption of molecules, estimating the electronegativity, based on the so-called work function (WF). The work function can be measured and represents the change of free energy when one electron is removed from the inner orbital of the metal and transferred to longer distances. In the UHV system, the emission conductor of the filament varies with the temperature, which is proportional to the work function.

If molecules are dissociated, it is possible to predict the enthalpy, according to Eley [27], based on the difference of the work function of the adsorbate and of the surface, assuming metal–metal binding [1, 4, 26, 27]:

$$\Delta H_{MX} = \frac{1}{2}(-\Delta H_{ads} + D_{XX}) \qquad (4.41)$$

where

ΔH_{MX}—bond enthalpy M–X
D_{XX}—enthalpy of diatomic molecule

The adsorption on metals has been measured experimentally and been explained theoretically through different models, although these models predict the adsorption of gases, are in discussion, but for most cases are limited.

Examples

1. *Adsorption of H_2 and CO on supported Pt catalyst*

   The comprehension of surface properties, notably the nature of sites, is of fundamental importance for developing supported metal catalysts. Therefore, understanding the surface mechanism allows to design a catalyst when investigating the nature of sites at the surface, aiming high activity and better stability. The metallic structures of platinum clusters present segregated or agglomerated atoms, which can be diluted after migration of the reduced species on the support. However, these effects can diminish the total number of surface sites exposed due to the coverage or electronic changes of the metal or, otherwise, promote the formation of new sites. Thus, it is necessary to determine the influence of the metal–support interaction on the nature of surface sites of platinum and understand the promoting effect on the mechanism.

   Table 4.5 presents the chemisorption results of H_2 and CO on metallic Pt supported on alumina and zirconia, after reduction at 500 °C. The dispersion was calculated from the irreversible H_2 adsorption, assuming a linear stoichiometry ($H/Pt_s = 1$). The stoichiometry of the CO adsorption on platinum may vary as linear ($CO/Pt_s = 1$) (linear) or bridged ($CO/Pt_s = 1/2$). Moreover, CO may interact with the support at the interface Pt–Zr. The mean particle diameter of platinum particles (d_p) was estimated from the dispersion, assuming spherical particles and using the formula:

   $$d_p = \frac{113}{D}$$

   where D is the dispersion (%) and d_p the particle diameter (nm).

   The Pt/Al_2O_3 presents high dispersion while Pt–ZrO_2 low dispersion, both reduced at 500 °C. Thus, the particle diameters are different. These results are related to the high and low surface area, respectively. The pure ZrO_2 support adsorbed only small amounts of CO, while alumina did not adsorb both H_2 and CO.

Table 4.5 Chemisorption of H_2 and CO on Pt/Al_2O_3 and Pt–ZrO_2 [28]

Catalysts	H_2 consumption (µmoles/g_{cat})	Dispersion[a] (%)	CO consumption (µmoles/g_{cat})	Ratio CO/H_2	Particle diameter d_p (nm)
Pt/Al_2O_3	22.3	87	35.7	1.60	1.3
Pt–ZrO_2	8.8	34	60.9	6.9	3.3
ZrO_2	0	–	–	1.29	–

[a]Based on platinum content (experimental)

Table 4.6 Adsorption of H_2 at 448 K and calculated dispersions, after different reduction temperatures ($m = 2$ g) [29]

Catalyst	Reduction temperature (K)	H_2 uptake (µmoles)	Dispersion (%)	Particle diameter d_p (nm)
Co/Al$_2$O$_3$	573	34.9	4.6	21.8
Co/Al$_2$O$_3$	773	34.6	4.5	22.0
Co/Nb$_2$O$_5$	573	28.9	3.8	26.3
Co/Nb$_2$O$_5$	773	5.3	1.0	104

The obtained molar ratio of **CO/H$_2$** for the **Pt/Al$_2$O$_3$** can be justified, since CO adsorbs as linear (CO/H$_2$ = 2) and bridged forms (CO/H$_2$ = 1). However, for the Pt–ZrO$_2$, this ratio is very high and means interaction of Pt–CO at the interface of **Pt–ZrO$_x$**, since the amount of CO adsorbed on zirconia is very low.

2. *Chemisorption of H_2 on cobalt supported on alumina and niobia*

The results of the irreversible hydrogen adsorption on the Co/Al$_2$O$_3$ and Co/Nb$_2$O$_5$ were obtained, according to the procedures described before [29] and are shown in Table 4.6.

Noteworthy is that the H$_2$ adsorption on Co alumina support is independent of the reduction temperature and, however, shows great effect on the Co niobia support, provoking significant decrease of adsorption with increasing reduction temperature suggesting strong metal–support interaction effects [29].

4.4 Adsorption on Semiconductor Oxides

Semiconductors are the most used in catalysis. The semiconductors have conductivity of the order of 10^{-3} a 10^{-8} Ω/cm and can be classified as intrinsic or extrinsic semiconductors, also considered as nonstoichiometric materials. The extrinsic semiconductors are natural materials [4].
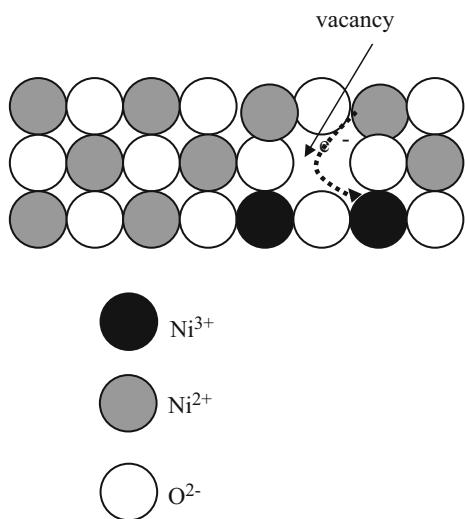
The electrons have low mobility in semiconductors. Consequently, there is no transfer of electrons and the link between the molecule and surface on a semiconductor is local. Moreover, the electronic structure of a semiconductor is unlike and so more complicated to explain the adsorption phenomena [1].

What we know is that the bindings between the molecules and the semiconductors are similar to the molecular bindings, like hybrid bindings, s–p–d, and consequently, have swinging motions. Semiconductors like NiO and TiO$_2$ present defects in the solid structure particularly associated with vacancies in the network. Heinrich [30] showed that defect on surface structures of semiconductors can adsorb, and lattice oxygen reacts with molecular gases. There are two cases:
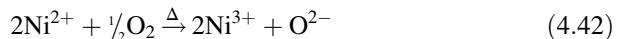
- *Semiconductors of p-type*
  Semiconductor *p-type* is positively charged and can donate electrons. Nickel oxide is a good example [4]. When heated in the presence of oxygen, it receives oxygen in the network and donates electrons. Within this type are several

Fig. 4.23 Scheme of the
NiO structure [Adapted
from Bond, C.C.,
*Heterogeneous Catalysis
and Applications*,
Clarendon Press,
Oxford (1974)]

semiconductors, such as CoO, Cu_2O, SnO, and Cr_2O_3. Schematically, the
structure of these semiconductors may be represented as follows [4]:

$$2Ni^{2+} + \tfrac{1}{2}O_2 \overset{\Delta}{\rightarrow} 2Ni^{3+} + O^{2-} \tag{4.42}$$

or in two steps

$$2Ni^{2+} \overset{\Delta}{\rightarrow} 2Ni^{3+} + 2e^- $$
$$O_2 + 2e^- \rightarrow O^{2-} \tag{4.43}$$
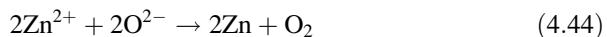
This semiconductor is classified as *p-type*.
This structure can also be schematically represented, as shown below, satisfying
the swinging bonding in the vacancies (Fig. 4.23):
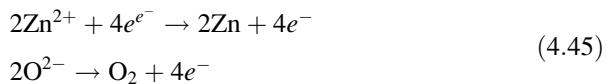
- *Semiconductors of n-type:*
  This is the opposite, where the semiconductors accept electrons and lose oxygen
  from the network and becomes negatively charged. This is the case of the oxides
  classified as type n: ZnO, TiO_2, Fe_2O_3, V_2O_5, and CuO. It is represented as

$$2Zn^{2+} + 2O^{2-} \rightarrow 2Zn + O_2 \tag{4.44}$$

or in two steps

$$2Zn^{2+} + 4e^{e^-} \rightarrow 2Zn + 4e^- $$
$$2O^{2-} \rightarrow O_2 + 4e^- \tag{4.45}$$
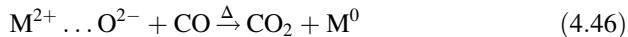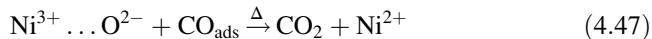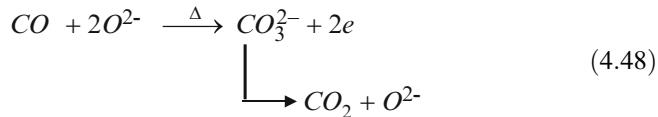
- *Chemisorption*

  In these models, gases are or not dissociated, but react with the surface oxygen ion of the nonstoichiometric structure. In a semiconductor p-type (Eq. 4.42), the CO chemisorbs first on the cation, where it reacts with an oxide ion, forms CO_2, and, consequently, leads to the reduction of the metal oxide in the metal. For example, [4]:

$$M^{2+} \ldots O^{2-} + CO \xrightarrow{\Delta} CO_2 + M^0 \tag{4.46}$$
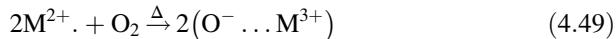
The process that occurs is actually a reaction. For the p-type semiconductor, the adsorbed oxygen ion reacts with the adsorbed CO to form CO_2 as a final product and hence regenerating the original ion structure. For example, the CO adsorption on NiO is [4]

$$Ni^{3+} \ldots O^{2-} + CO_{ads} \xrightarrow{\Delta} CO_2 + Ni^{2+} \tag{4.47}$$
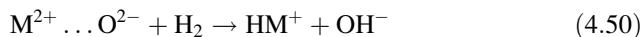
For the semiconductor type n, CO also reacts with the two oxide ions at the surface and forms carbonate, which is decomposed as CO_2, regenerating the oxygen ion:

$$CO + 2O^{2-} \xrightarrow{\Delta} CO_3^{2-} + 2e$$
$$\hookrightarrow CO_2 + O^{2-} \tag{4.48}$$

The oxygen chemisorption on p-type semiconductors involves the oxidation of ions as shown in Eq. (4.44):

$$2M^{2+}. + O_2 \xrightarrow{\Delta} 2(O^- \ldots M^{3+}) \tag{4.49}$$

In fact, it means that it represents the excess of oxygen ion in the lattice structure. The chemisorption of the hydrogen (H_2) is dissociative and irreversible. Hydrogen reacts with the surface oxygen ion, forming hydrate and hydroxyl, as follows:

$$M^{2+} \ldots O^{2-} + H_2 \rightarrow HM^+ + OH^- \tag{4.50}$$

On heating the hydroxyl ions are decomposed to form water and oxygen vacancies.

References

1. Masel IR. Principles of adsorption and reaction on solid surfaces. New York: Wiley; 1996.
2. Boudart M, Djega-Mariadassou G. Kinetics of heterogeneous catalytic reactions. Princeton, NJ: Princeton University Press; 1984.

3. Van Santen RA, Niemantsverdriet JW. Chemical kinetics and catalysis. New York: Plenum Press; 1995.
4. Bond CC. Heterogeneous catalysis and applications. Oxford: Clarendon; 1974.
5. Neto R, Schmal M. Synthesis of CeO_2 and $CeZrO_2$ mixed oxide nanostructured catalysts for the iso-syntheses reaction. Appl Catal A Gen. 2013;450:131–42.
6. Langmiur I. "Heterogeneous reactions". Chemical reactions on surfaces. Trans Faraday Soc. 1922;17:607.
7. Kubokawa M. The rate law for the adsorption of gases on catalysts. Rev Phys Chem (Japan). 1938;12:157.
8. Kuijpers EGM, Jansen JW, van Dillen AJ. The reversible decomposition of methane on a $NiSiO_2$ catalyst. J Catal. 1981;72:75.
9. Martins RL, Baldanza MAS, Souza MMVM, Schmal M. The effect of support on methane activation over Pt catalysts in the presence of MoO_3. Appl Catal A Gen. 2007;318:207–12.
10. Cassuto A, Mane M, Jupille J. Surf Sci. 1991;249:8.
11. Satterfield CN. Mass transfer in heterogeneous catalysis. Cambridge, MA: M.I.T Press; 1970.
12. Gregg GC, Sing KSW. Adsorption, surface area and porosity. 2nd ed. London: Academic; 1982.
13. Fogler S. Elements of chemical reaction engineering. 2nd ed. Prentice Hall; 2000.
14. Somorjai GA. Introduction to surface chemistry and catalysis. New York: Wiley; 1994.
15. Freundlich H. Kapillarchemie. Leipzig: Akad Verlag; 1909.
16. Tempkin MI, Pyzhev V. Kinetics of ammonia synthesis on promoted iron catalysts. Acta Physiochim. 1940;12:217.
17. Lennard-Jones JE. Processes of adsorption and diffusion on solid surfaces. Trans Faraday Soc. 1932;28:333.
18. Ramos ALD, Alves PS, Aranda DAG, Schmal M. The effect of support on methane activation over Pt catalysts in the presence of MoO_3. Appl Catal A Gen. 2004;277:71.
19. Moujijn JA, van Leeuwen PWNM, van Santen RA. Catalysis—Studies science and catalysis, vol. 79. Amsterdam: Elsevier Scientific Publishing Company; 1993.
20. Ciola R. Fundamentos em Catálise. Sao Paulo: Ed.USP; 1981.
21. Crossley A, King DA. Vibrational spectroscopy of molecules on surfaces. Surf Sci. 1980;95:131.
22. Brennan D, Hayward DO, Prapnell BMW. The calorimetric determination of the heats of adsorption of oxygen on evaporated metal films. Proc R Soc A. 1960;256:81.
23. Roberts MW. Nature. 1960;188:1020.
24. Tanaka K, Tamaru K. A general rule in chemisorption of gases on metals. J Catal. 1963;2:366.
25. Seebauer EG, Kong ACF, Schmidt LD. Surface diffusion of hydrogen. Surf Sci. 1986;176:134–56.
26. Trimm DL. Design of industrial catalysis. Amsterdam: Elsevier, Scientific Publishing Company; 1980.
27. Eley DD. Advances in atomic and molecular physics. Trans Faraday Soc. 1958;8:34.
28. Souza MMVM, Aranda DAG, Schmal M. Reforming of methane with carbon dioxide over Pt/ZrO_2/Al_2O_3 catalysts. J Catal. 2001;204(2):511.
29. Silva RRCM, Schmal M, Frety F, Dalmon JA. Effect of the support on the fischer–tropsch synthesis with Co/Nb_2O_5 catalysts. J Chem Soc Faraday Trans. 1993;89(21):3975.
30. Heinrich VE, Cox PA. The surface science of metal oxides. New York: Cambridge University Press; 1994.
31. Kessmodel LL, Dubois LH, Somorjai GA. LED analysis of acetylene and ethylene chemisorption on the Pt(111) surface: evidence for ethylidyne formation. J Chem Phys. 1979;70:2180.

Chapter 5
Basic Concepts

Abstract The adsorption phenomena on metals and oxides showed that the interaction of molecules and surfaces is associated with electronic and geometrical properties between molecules and surface sites or atoms. Basic concepts of steric and electronic phenomena.

Keywords Basic concepts • Band theory • Electronic effects • Electronegativity • Steric effects

The adsorption phenomena on metals and oxides showed that the interaction of molecules and surfaces is associated with electronic and geometrical properties between molecules and surface sites or atoms.

Before presenting some concepts which explain the electronic properties of metals and semiconductors, let's see the geometrical or steric properties that may explain the adsorption form of molecules on active surfaces.

5.1 Geometric Configurations: Steric Effects

The basic concept was proposed by Baladin [1] asserting that the adsorption and the reaction activity depend on the attraction of molecules by surface atoms. Therefore, it depends on the steric effects or relates the spatial arrangement of atoms in a molecule and of surface atoms, especially, as it affects chemical reactions. This is called multiplet theory, which assumes congruence between the molecule and the surface atoms.

The classical example is the reaction of ethanol on alumina, occurring dehydration and dehydrogenation reactions of ethanol, which depends on the interaction between the molecule and the surface atoms [2]. Besides the steric coincidence, it requires also equal energy levels or similar bonding forces. That depends on the spatial configuration. Generically, atoms of a surface flat (111) which can be represented as follows (Fig. 5.1).

The steric configuration of an adsorbate allows us to calculate the distance between atoms of the surface and of the adsorbed molecules and to determine the
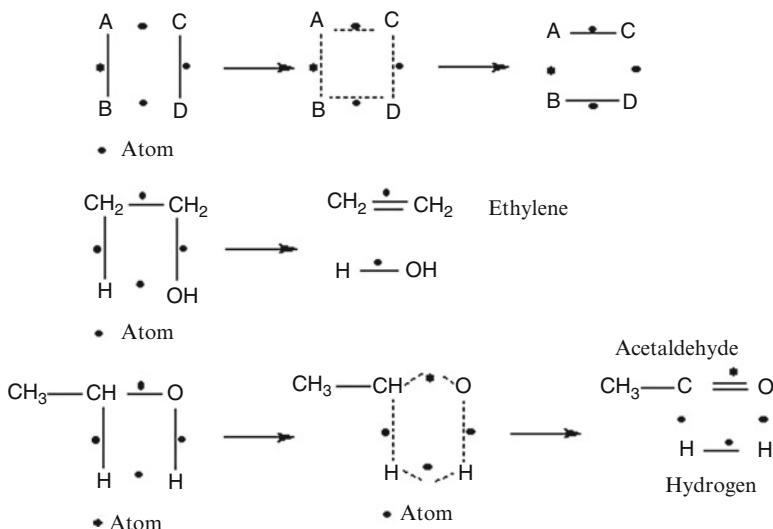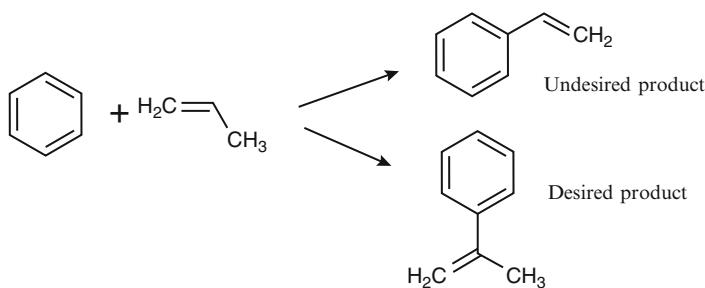
Fig. 5.1 Schematic representation of a steric configuration [Adapted from A. A. Baladin, Z. Phys. Chem. 32 (1929)289,33,167] [1].

congruence between molecules and atoms and thus the best configuration for the selectivity of desired product of the reaction.

Imagine the steric planar configuration of toluene and propylene in separate, and the configurations of o-propyl-benzene and p-propyl-benzene as the main products, one as desired and the other one as undesired [3]. Thus,

Assuming different planar configurations and adsorption forms. There are three possibilities (Fig. 5.2).

We can calculate the distances d between atoms at the surface having different adsorption forms:

- Case (A): Adsorption π (propylene) and adsorption of π-allyl (cyclohexadiene) $\rightarrow d_1 = 1.18\,\text{Å}$
- Case (B): Adsorption π (propylene) and adsorption π-(cyclohexadiene) $\rightarrow (d_1 + d_2) = 2.15\,\text{Å}$
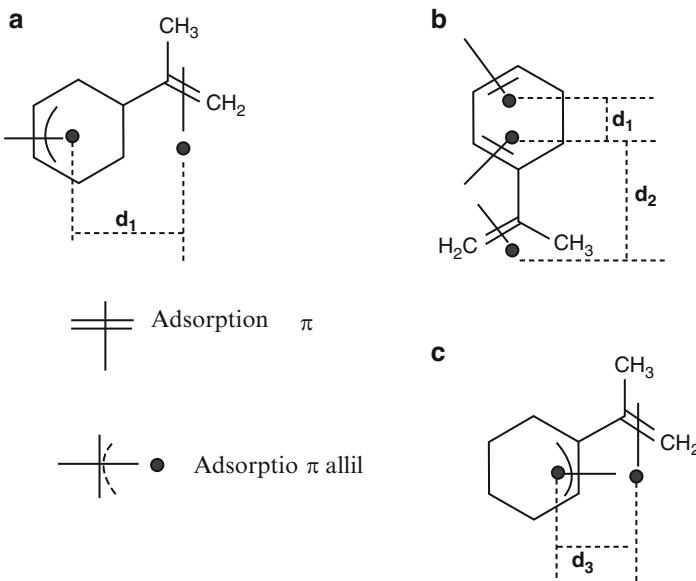
Fig. 5.2 Scheme of surface configurations [Adapted from D. L. Trimm, *Design of Industrial Catalysts*, Elsevier, (1980)] [3].

- Case (C): Adsorption π (propylene) and adsorption π-allyl (cyclohexadiene) $\rightarrow (d_1 + d_2) = 2.15\,\text{Å}$

Calculations show that for the desired product, case (B) is the most suitable. Therefore, we have to find out a metal oxide with atomic distances closest to the desired adsorbed molecule. These distances are tabulated. The atomic distance should be greater than 1.98 Å and lesser than 2.15 Å. Among the metal oxides, the nickel oxide has an atomic interplanar distance (Ni–O–Ni) of 2.09 Å and the Ni–Ni atomic interplanar structure 3.51 Å (Table 5.1).

Occurring dissociation of the molecules, we have considered different possible mechanisms, such as hydrogenolysis of methyl formate to form methanol [3] (Fig. 5.3).

There are different combination possibilities with surface atoms (Fig. 5.4).

These combinations help to suggest the most suitable adsorption form for the desired product. According to the steric parameters, we can make the choice of a catalyst with dimensions satisfying the steric congruence between molecules and surface atoms.

Table 5.1 Distances of some
metal oxides [3]

Metal oxides	Structure	Distance M–O (Å)
α-Al_2O_3	Hed	1.85
γ-Al_2O_3	Cb	1.78
Co_3O_4	Cb	1.92
CoO	Cb	2.12
CO_2O_3	Cb	1.75
CO_3O_4	Cb	1.92
Cr_2O_3	Rh	2.01
CrO_2	Tet	1.90
CrO_3	Rh	1.76
MoO_3	Rh	1.75
MoS_2	Hex	2.35
NiO	Cb	2.09
Ni_2O_3	Rh	1.80
NiS	Hex	2.56
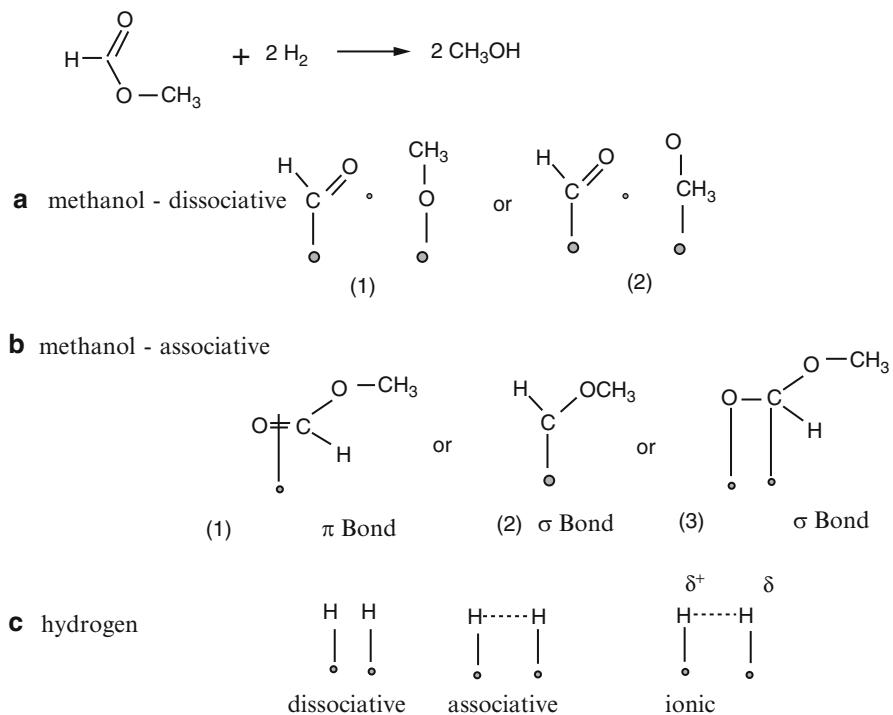
Fig. 5.3 Schemes of dissociative surface configuration [3]
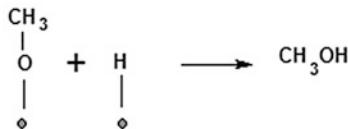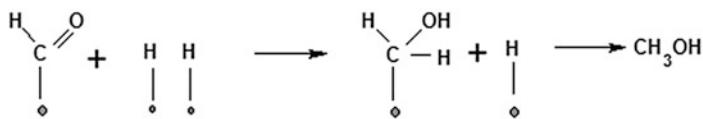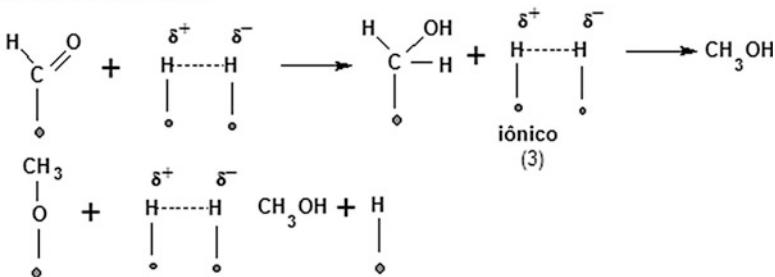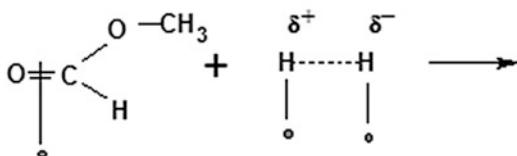
Fig. 5.4 Configuration possibilities [Adapted from D. L. Trimm, *Design of Industrial Catalysts*, Elsevier, (1980)] [3]

5.2 Electronic Configurations: Electronic Effects—Band and Orbital Theories

The ability to form bonds between molecules and surface atoms is fundamentally based on the existence of interpenetration of the orbitals and consequent energy stabilization. The simplest models which explain bindings and interactions, as shown above, do not satisfy, and several subsequent formulations have been made to adapt the models to the experiments.

The CO adsorption on oxides is very unlike on semiconductor oxides and conductive metals. The energy bindings which are directly proportional to the enthalpy of adsorption, which can be determined experimentally, are distinct. The

previous presented models are insufficient to explain distinct adsorption forms. Masel [4] and Somorjai [5] presented detailed concepts about the adsorption models and surface reactions.

The density functional theory is based on the calculations of quantum mechanics. Kohn and Sham [6] showed that the calculations can be made according to the electron density ρ_e. The total energy of the system E_T is a function of the electron density $N(E)$, being the potential associated to the interaction between atomic levels and electron layers. From these calculations a more general equation was obtained 4.40, namely,

$$D(M - S) = \frac{1}{2}(D(M - M)) + E_S^0 + \gamma_{Pa}(\chi_M - \chi_S)^2 + \Psi \qquad (5.1)$$

where

$$\gamma_{Pa} = \frac{1}{2(\eta_M + \eta_S)} \qquad (5.2)$$

η being a constant which indicates the interaction between the adsorbate and the surface, M, adsorbate, S, surface, and χ_M and η the electronegativity of the adsorbate and surface, respectively. The parameter Ψ is an integral that depends on the potential energy change associated with the interaction between the layers of the atom and electrons.

5.2.1   Band Theory

The band theory is based on the fact that each orbital of the atom represents a single energy level, but when joined, lose their identity and together form electronic bands. Thus, for example, the corresponding energy levels S and p as function of the interatomic distance is almost constant, but as they approach, they lose their identities and form bands, as shown below [7].

One observes that until a certain interatomic distance, the energy levels are independent, but from a certain distance, the electrons coexist, forming the band which increases with decreasing interatomic distance (Fig. 5.5a).

The electronic density $N(E)$ represents the number of layers or levels with electrons with energy between E and $E + dE$, which are transferred from one level to another until obtaining the maximum energy level, known as Fermi energy E_F (Fig. 5.5b).

This density $N(E)$ increases with $\sqrt{E}$ [7]. The electrons always occupy the lower levels. In general there are two bands. First, the conduction band sp. This band extends through the metal and conducts electricity. The localized bands are called d bands, which are closer to the atoms. They are usually represented by the valence band. Secondly, the valence band is the band with the highest electron occupancy level and the conduction band goes to the highest level. The electrons of the d band

Fig. 5.5 Energy as function of interatomic distances [Adapted from G.C. Bond, *Heterogeneous Catalysis: Principles and Applications*, Clarendon Press, Oxford (1974)]
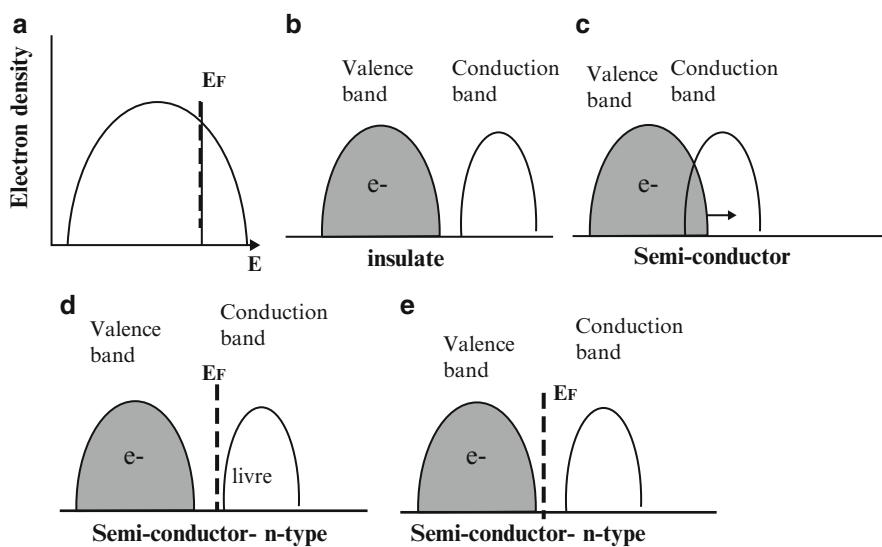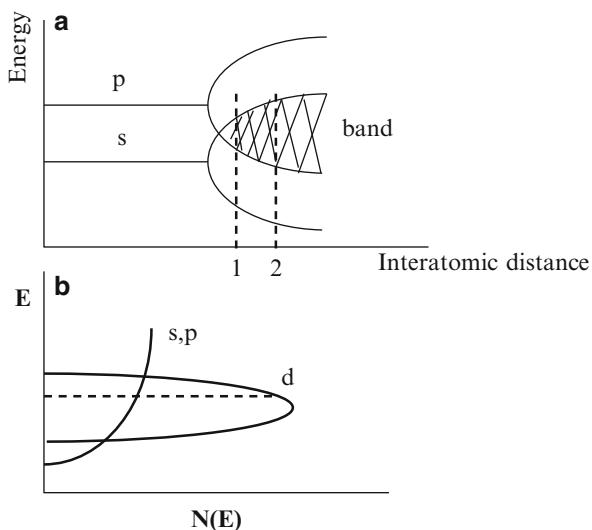
Fig. 5.6 Electron density as function of energy [Adapted from G.C. Bond, *Heterogeneous Catalysis: Principles and Applications*, Clarendon Press, Oxford (1974)]

vary. In Cu, Ag, and Au, the valence bands are all occupied by electrons and decrease with the metals like Ni, Pd, and Pt. In addition, the Fermi energy, E_F, known as work function, can change up or down, depending on the metal (periodic table). The metal bonding strength of transition metals decreases with the increasing valence band d [7].

Figure 5.6b shows that the valence band is totally occupied by electrons, while the conduction band is completely empty and separate, where electrons have no mobility between the bands, and therefore it is a solid material called an *insulator*.

The semiconductors are natural or intrinsic materials, with overlapping the valence and conduction bands and therefore, electron mobility between bands and a natural electrical conduction, which is only possible if the valence band is incomplete. The electrons are transferred from one to another level and therefore can move. Figure 5.6c shows the direction of electron motion between bands.

There are two ways to interpret the bands in the structures. First, considering the Fermi level E_F that represents the chemical potential of the electrons in the band. Below the Fermi level, the band is occupied by electrons, and above this level the band is completely empty. Second, through the electron density of the band per unit energy, because the electron distribution is not homogeneous.

Figure 5.6c–e represents the valence and conduction bands of semiconductors, which in principle have vacancies or defects in the structure. These are called nonstoichiometric oxides, by losing or accepting oxygen in the network. For example, the semiconductor ZnO loses oxygen and accepts electrons in the network and therefore has a deficiency of oxygen and is called n-type, while NiO receives oxygen in the network and donates electrons, making it nonstoichiometric with excess of oxygen, and is called p-type.

Semiconductor with defects in the structure exhibits gaps between valence and conduction bands, which do not allow the passage of electrons and thus, any electron motion or electric conduction. In the case (c), there is an overlap of valence and conduction bands and, therefore, free passage of electrons.

Introducing a dopant, it is possible to change oxide properties and the energy levels. For example, doping SiO_2 with Ga, it replaces Si atom in the network. Gallium becomes a sp^3 configuration and gets one electron less than Si. Therefore the solid has one electron less in the unoccupied valence. However, doping with *As* gets with more electrons in the unoccupied conduction band [4]. It is like changing the energy level or the Fermi level, approaching the valence or conduction levels, reducing the distance between the valence and conduction band, and allowing electron jump.

In the case of a dopant in a semiconductor p-type, like an impurity, the Fermi E_F level approaches the valence band, and there is a probability for electron jump to the conduction band or accept electrons and become electroconductive. In the case of a dopant in the semiconductor n-type, it is the opposite; the Fermi level E_F approaches the conduction band and electrons jump to the conduction band.

Dopants or impurities may transform oxides in nonstoichiometric semiconductors which can be attributed to:

- Excess of atoms in the interstices
- Gaps in the lattice

In the case of excess of atoms, as seen before, there are semiconductors of type n or p. Type n are electropositive, such as ZnO. With increasing temperature, the electrons are excited and move through the bands, and thus the solid carries electrons.

In the case of gaps in the lattice, it loses negative ions. To conserve neutral charge, the electron enters where the ion left. Therefore, the dopants modify the properties of the oxide. They add or subtract electrons to the solid, changing their electrical charge and changing their electronic bands.

5.2.2   *Theory of Molecular Orbitals*

The catalytic reactions occur on the surface, after adsorption and dissociation of molecules, and products leave after desorption. Molecules may form or break up links, due to the interaction between the molecules and the surface atoms, with formation of intermediates and complexes. Due to this interaction, there are overlapping bands of electrons from the metal surface and the molecule. With the superposition of bands, there are variations of electron density.

The dissociation and adsorption and chemical reaction depend on the activation energy barrier, according to Horiuti and Polanyi [8], which is related to the free energy changes during the reaction. The correlation deduced by Evans and Polanyi [9] is given by the following expression:
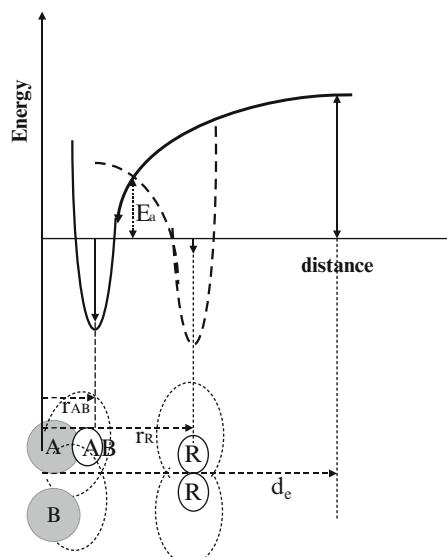
$$E_{\mathrm{a}} = \gamma_{\mathrm{P}}\big(\Delta G^0\big) + E_{\mathrm{a}}^0 \tag{5.3}$$

where γ_{P} is the transfer coefficient and E_{a}^0 the intrinsic energy barrier.

The energy barrier is shown in the Lennard-Jones potential energy graphical representation (Fig. 5.7), indicating how the energy varies with distance between molecules or atoms, as, for example, for the reaction $A + B \rightarrow R$.

Initially, the molecule A moves in the direction B, as shown in Fig. 5.8. If the distance between A and B is great, these molecules are attracted, and when they approach they are repelled. The electron cloud of A tends to overlap on cloud B, which causes electron repels (Fig. 5.8). This repulsion causes the molecules to not come closer, as van der Waals forces. With the time the adsorbed molecules form complex that decomposes only when overcoming the energy barrier E_{a}, breaking the link AB to form a new bond and the final product R [3, 4].

Fig. 5.7 Variation of the potential energy with distance [Adapted with permission from R. I. Masel, *Principles of Adsorption and Reaction on Solid Surfaces*, John Wiley & Sons (1996), 7]
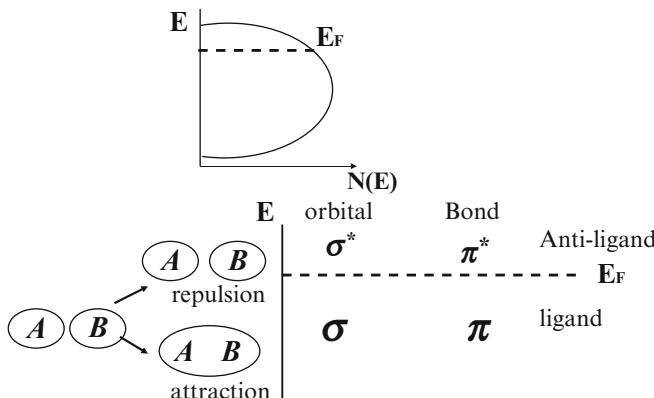
Fig. 5.8 Orbitals ligands and anti-ligands [Adapted from D. L. Trimm, *Design of Industrial Catalysts*, Elsevier, (1980)]

When the electrons of atoms combine with high density, they form a molecular orbital bonding. On the other hand, when the density is minima, they are destabilized, forming an antibonding orbital. So we have, as shown below, covalent binding σ and π levels occupied by electrons, and anti-ligands σ* and π*, above the Fermi level with levels without electrons.

In the case of bindings, the potential energy of molecules and surfaces varies. When the molecule approaches the surface, free electrons of the molecule orbital facilitate the loss of electric charge. In opposite, the free orbital of the surface facilitates the loss of electric charge of the molecule. According to Fukui [10], when molecules A and B interact, it stabilizes when the highest level of occupied orbital (HOMO) of A interacts with the lower free orbital level (unoccupied) (LUMO) of B and vice versa.

Therefore, for analyzing the metal–adsorbate system, we assume a molecular surface system, where metal bands and molecular bands are covalent bonds or anti-ligands with free electron bands.

According to Niemantsverdriet [11], we assume the adsorption of a single atom (monoatomic) at the surface, as shown in Fig. 5.9.

Figure 5.9 shows a simplified diagram of the possible links between an atom and a surface. The metal has a valence band occupied by electrons and a free electron band, where the maximum level for each metal, with orbital d (oxide or semiconductor), is the Fermi level E_F. Consider one atom away from the surface to which the energy level is constant and stable. When approaching the surface, there is an overlapping of electron densities and adsorbed metal atom, giving rise to a new pair of orbitals that are occupied by electrons and metal atom and, according to the diagram of Fig. 5.9, form covalent bonds (ligands) or anti-ligands, respectively, i.e., form bands occupied by electrons and free electron bands, due to attraction or repulsion, respectively.

Adsorption orbitals_{Atom orbitals}
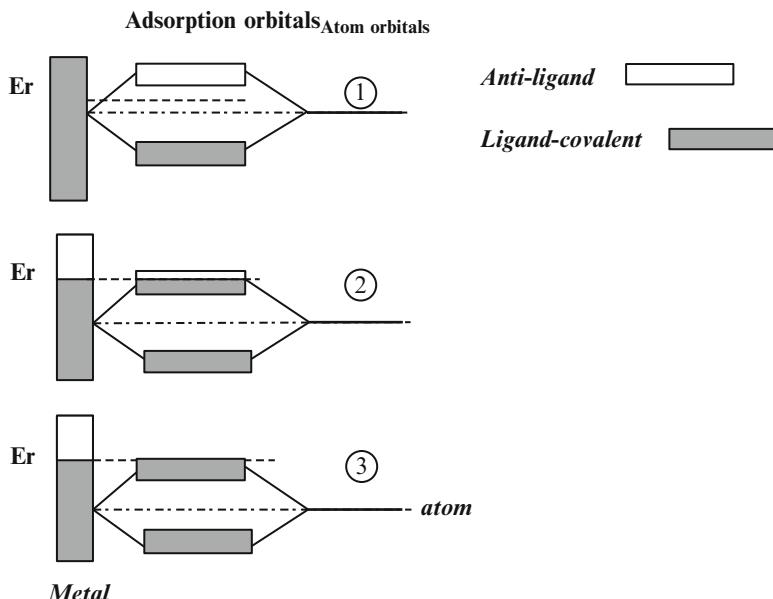
Fig. 5.9 Links between atoms and surfaces – orbital theory [Adapted with permission from R. A. van Santen, J. W. Niemantsverdriet, *Chemical Kinetics and Catalysis*, Plenum Press, New York, (1995)]

In case (1) the anti-ligand orbital of the adsorbed atom is above the Fermi level of the metal band and therefore does not accept electrons from the metal, while the covalent bond is completely occupied by electrons. Consequently, it is bonded, featuring a strong adsorption due to the strong attraction between the electrons of the atom and the metal.

In case (2), the anti-ligand band descends and is partially below the Fermi level and thus will be partly occupied by metal electrons coming. Thus, the energy is divided between the ligand and anti-ligand orbital, causing partial repulsion of electrons and not attraction. The interaction between the atom and the orbital of the metal is small, that is, a weak bond.

In case (3), both orbital ligand and anti-ligand are below the Fermi level, that is, the anti-ligand orbital is occupied by electrons coming from the metal, and hence there is total repulsion between the electrons of the metal and of the atomic molecule. The adsorption is very low.

The adsorption of diatomic molecules (CO and H_2) on metals, based on the orbital theory and, according to the above scheme, must take into account the dissociation of molecules and two orbitals of the molecule which, as mentioned earlier, can occupy the highest levels (HOMO) and the lowest level (LUMO) which allows the adsorption on surfaces.

Thus, consider a molecule with orbital ligand σ occupied by electrons and anti-ligand orbitals free of electron. When approaching the metal, interactions of these electrons with the electrons of the metal band may or not exist, depending on the
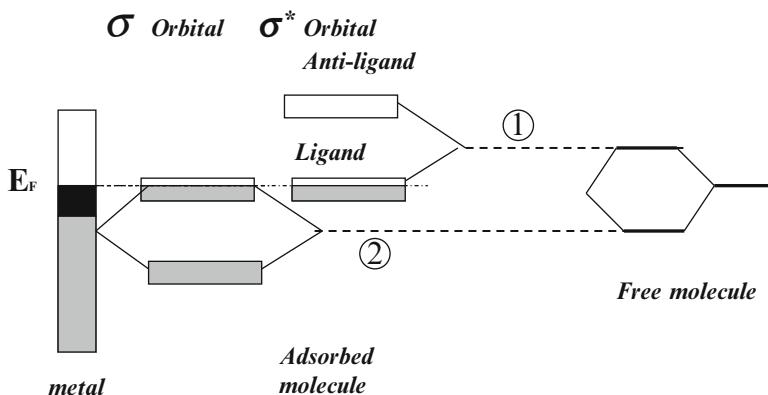
Fig. 5.10 Electron distribution for a diatomic molecule [Adapted with permission from R. A. van Santen, J. W. Niemantsverdriet, *Chemical Kinetics and Catalysis*, Plenum Press, New York, (1995) Fig. 6.2]

new configuration of the electronic levels. So, imagine for the molecule A_2 a new distribution for σ (ligand orbitals) in HOMO and also a new distribution for σ* (anti-ligand orbital) in LUMO and verify regarding the distribution of the metal band electrons the new configuration of electrons. This is shown in the diagram in Fig. 5.8. There are three cases to consider:

(a) If the electrons of the occupied σ and unoccupied σ* levels of the new configuration in HOMO (Fig. 5.10a) are below the Fermi level of the metal orbital occupied electrons, then the electrons of the metal are transferred to the free electron level and become fully occupied. Therefore, there is repulsion and no interaction occurs between the molecule and the metal surface, hence any adsorption.
(b) On the other hand, if the antibonding orbital σ* is just above the Fermi level, it will be partially occupied by electrons. In this case, a partial interaction will occur between the electrons of the molecule and the metal and adsorption, but a weak adsorption.
(c) Imagine now the new anti-ligand band σ* configuration (Fig. 5.11), where the ligand σ orbital may be above or below the Fermi level. The LUMO orbital of the molecule is anti-ligand with respect to interaction between the atoms of the molecule and if below the Fermi level then transfers electrons of metal band to σ band that will be fully or partially occupied by electrons. However, if completely occupied by electrons, then the molecule will dissociate, since the antibonding band is unoccupied or free electrons. If partially occupied then the interaction between the molecule and the surface is smaller and consequently the A–A binding of the chemically adsorbed molecule weakens.

One can make an analogy or a direct link of orbital configuration of the diatomic molecule over the metal with the potential energy, according to Lennard-Jones, as shown in Fig. 5.11 and as illustrated by Niemantsverdriet [11].
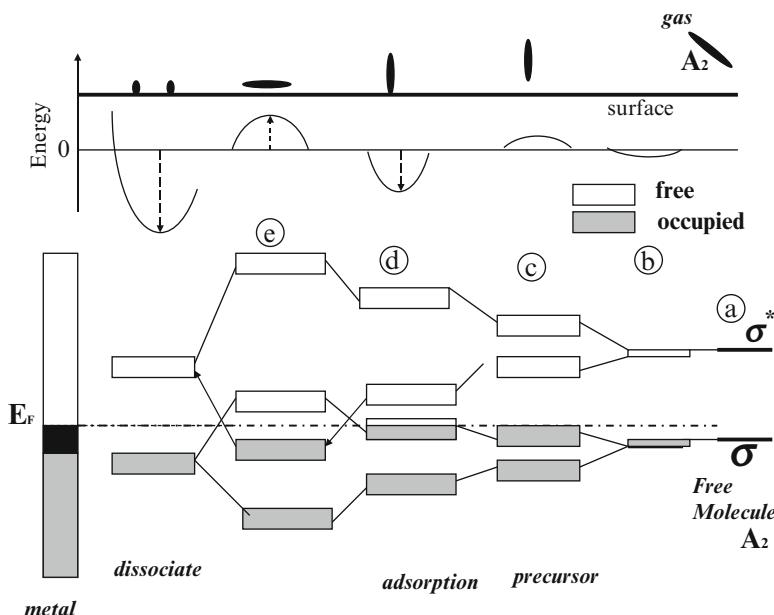
Fig. 5.11 Electronic configuration and potential energy during adsorption [Adapted with permission from R.A. van Santen, J. W. Niemantsverdriet, *Chemical Kinetics and Catalysis*, Plenum Press, New York, (1995)]

Initially, the molecule A_2 is free in the gas phase and with the corresponding ligand σ and anti-ligand σ^* orbitals. As it approaches the metal surface, it passes through different stages:

(a) Initially, the molecule collides, loses energy, and adheres (trap) passes to the precursor or physisorbed state (b). The interaction between the electrons of the molecule and the surface electrons is very low, causing only a slight and broadband energy, passing to the physisorbed state, with mild release of energy. In this condition the adsorption forces are equivalent to the van der Waals forces.

(b) Approaching the metal surface, there is an overlapping of energy bands and a higher interaction with the electrons of the metal band, forming a new molecular configuration of ligand σ and anti-ligand σ^*. If the interaction of the σ electrons and of the metal electrons is small, there arises a new configuration for σ and σ^*, because both are below the Fermi level, transferring electrons of the metal to σ^*, since both will be completely occupied by electrons. There is repulsion between the molecule and the surface atoms, causing increasing potential energy, which causes increased energy barrier that must be overcome, as shown at (c).

(c) The interaction between bands increases, and the antibonding level σ^* gains energy, moving upward the Fermi line, causing the electrons to vacate this level, while there is a loss of energy and displacement downward. Therefore,

decreases the repulsion and the molecule pass to the chemisorbed state, as shown in the figure at position (d). Note that the molecule remains unchanged, since the orbital of the chemisorption state formed from the orbital anti-ligand σ^*, forms a new configuration, but are all above Fermi level.
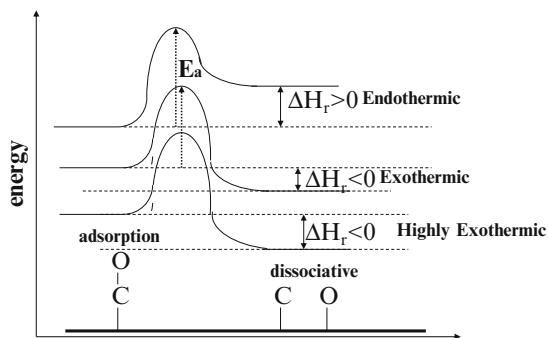
(d) With the approaching of metal increases, the interaction triggers the displacement of the ligand σ of the anti-ligand level σ^*, pushing down of Fermi level. In this new configuration, the electrons are transferred from the metal and this level will be occupied by electrons. Note that the passage of the configuration (d) to (e) causes release of electrons of anti-ligand level σ moving up the Fermi level and the displacement of the ligand further down level. In this case, due to the increased electrons in the anti-ligand σ^* level of the molecular orbital, the electrons are released, causing a backward donation (back donation) of electrons to the molecule. These conditions are favorable to overcome the energy barrier in (c) and dissociate the adsorbed molecule at a lower energy than is required to dissociate the molecule in the gaseous phase. Once separated, it passes to chemisorbed state releasing energy, causing a large release of heat.

(e) Intramolecular binding molecule undergoes elongation when approaching a metal. But this will depend upon the interatomic distance and the distance between the molecule and the surface. This implies that the energy difference between the ligand σ and anti-ligand σ^* decreases. The retroactive donation of electrons is caused by the occupation of electrons in anti-ligand orbital that expands and then releases electrons. The closer the surface largest is back donation and therefore greater is the stretching of the molecule be able to dissociate.

The concept of ligand and anti-ligand orbital formation, caused by the interaction of molecules with the surface, may explain the different adsorption forms over metal surfaces. Thus, for example, the electronic structure of different metals varies depending on the last layer and increases with increasing atomic number. The electrons of the layer d varies from d^0 to d^{10}, where layers d^0, d^5, and d^{10} are complete. For the incomplete layers, there is a decrease of electrons in the anti-ligand level, decreasing the electron density between the adsorbate and the surface, which allows a significant increase of the chemical bonding.

The binding strength of a substrate with the adsorbed molecule varies much less than they adsorbed atoms. This happens when the energy change in LUMO is small relative to the higher level of occupation of the metal electrons. Dissociation depends on how the electrons of the HOMO and LUMO orbitals of the molecule interact with the surface.

Bonding (ligand) levels formed by electrons of the metal and HOMO are fully occupied by electrons, unlike the anti-ligand levels formed with metal and the LUMO orbitals of the molecule which are empty, while ligand levels are partially occupied. If the concentration of electrons between the adsorbate and the metal surface decreases, when the electronic level d of the layer decreases, the interaction of the adsorbate with LUMO decreases, whereas with the HOMO increases. The total bonding strength does not vary.

Fig. 5.12 Energy of dissociation of CO on different metals [Adapted with permission from R.A. van Santen, J.W. Niemantsverdriet, *Chemical Kinetics and Catalysis*, Plenum Press, New York, (1995)]

This interpretation was made for diatomic molecules, and unlike with monoatomic molecules the behavior depends on other parameters.

The dissociation of adsorbed molecules depends on the thermodynamic. There is a difference between the dissociation of the molecule in the gas phase and of adsorbed molecules, where the cleavage fragments are stabilized by adsorption on the surface.

The most common case is the CO adsorption and dissociation on surfaces which depends on the type of metal and thus, on the electrons of the metal layer d. Thus, for example, during the adsorption and dissociation of CO with different metal levels d is connected directly to dissociation energy. The CO dissociation on copper is endothermic, on nickel is exothermic, and on cobalt is highly exothermic, as shown in Fig. 5.12.

The adsorption and dissociation phenomena depend on other factors such as the type of molecule and the geometrical or structural shape of the surface. But in general, we can say that the activation energy depends on the heat or dissociation enthalpy of adsorption, which according to Evans and Polanyi [9] can be simplified by the equation

$$\Delta E_a = \frac{1}{2} \Delta H_r \tag{5.4}$$

where ΔH_r is the enthalpy of reaction.

About the electron distribution of metals, the greater the electron valence of the metal atom, the greater is the distribution of electrons in the vicinity of the atom and weaker is the bonding of an atom alone.

5.2.3   The Electronegativity Theory: The Role of Electrons d

Molecules are linked to organometallics forming complex coordination with energy comparable to the adsorption energy over surfaces. The surface or chemical bindings have electron distribution in the layers s, p, and d.

Pauling [12] calculated the binding energy between two atoms, according to Eq. (5.5). This equation was compared with experimental measurements which allowed calculating the electronegativity of solids. Further studies, reported by Young and Crowell [13], improved this equation and were extrapolated for the adsorption and proven that the electronegativity concept is applicable for the adsorption theory.

As seen before, there is a transfer or sharing of electrons between a molecule and a surface, whether metal or transition metal. In the case of CO, this was achieved, especially with the back donation metal electrons to the antibonding orbital σ^* of CO. This means that there is a correlation between electronegativity of CO with the metal. The same applies to clusters with different configurations of atoms, depending on the electronegativity variation. Therefore, the role of electrons d for the adsorption of a molecule on a transition metal is very important.

The formations of complexes of transition metals with molecules depend on the structure of the orbitals. The electron layers have structures with electron densities in the three most important directions, as shown in Fig. 5.13, where the densities d_{z^2} and $d_{x^2-y^2}$ are highest and d_{xy}, d_{yz}, and d_{xz} are minimal, in the x, y, and z axis [3].

Assume that the central octahedron ion is surrounded by six bindings. There is a repulsion of electrons in d_{z^2} and $d_{x^2-y^2}$ and a new distribution of electrons between d_{xy}, d_{yz}, and d_{xz}, as shown in Fig. 5.14. The electrons tend to occupy a more stable orbital, moving to the lower levels. Furthermore, the electrons tend to spread in different orbital and there is interaction. Thus, note that the electrons are distributed in the lower , orbital d_{xy}, d_{yz}, and d_{xz}, two in each orbital, and the others in the orbital d_{z^2} and $d_{x^2-y^2}$, less stable. This causes an energy change which is represented by the electronegativity Δ, being 2/3 and 1/3 to each one. Further orthogonal deformation causes further redistribution of electrons at different levels.

Fig. 5.13 Orbital structure [Adapted from D. L. Trimm, *Design of Industrial Catalysts*, Elsevier, (1980)]
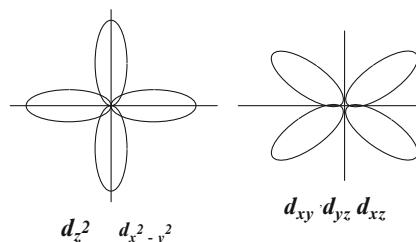
Fig. 5.14 Distribution of electrons in the layer d [Adapted from D. L. Trimm, *Design of Industrial Catalysts*, Elsevier, (1980)]
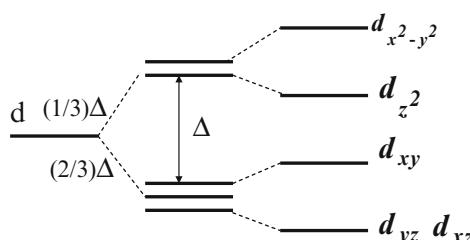
Table 5.2 Distribution of electrons for the octahedral configuration [Adapted from O. V. Krilov, *Catalysts by Nonmetals*, Academic Press, N.York, (1970)]

Layer d	Ions	t_{2g}	e_g	Δ eV)
1	Ti^{3+}, V^{4+}			0,4
2	Ti^{2+}, V^{3+}			0,8
3	V^{2+}, Cr^{4+}, Mn^{4+}			1,2
4	$Cr^{3+}, Mn^{3+}, Fe^{4+}$			0,6
5	$Mn^{2+}, Fe^{3+}, Co^{4+}$			0,0
6	Fe^{2+}, Co^{3+}			0,4
7	Co^{2+}, Ni^{3+}			0,8
8	Ni^{2+}			1,2
9	Cu^{2+}			0,6
10	Zn^{2+}, Cu^+			0,0
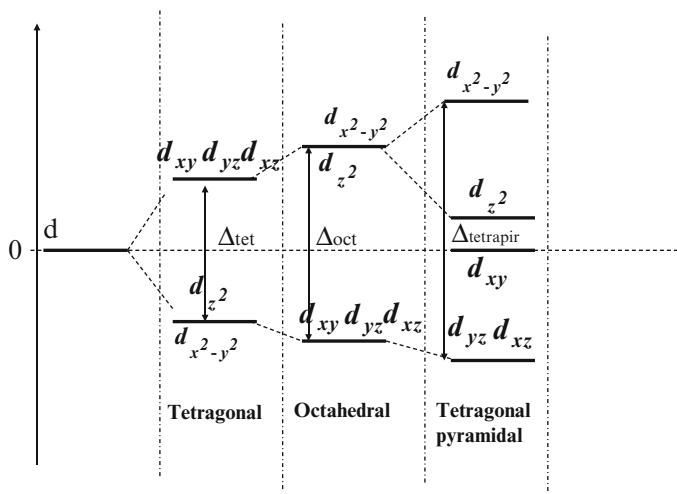
Fig. 5.15 Distribution of electrons in *d* for different configurations [Adapted from D. L. Trimm, *Design of Industrial Catalysts*, Elsevier, (1980)]

The electronegativity is a measure used to characterize the degree of interaction of the transient metal with the molecule to be adsorbed. The higher Δ, the stronger the bond, and in opposite, the low Δ, the weaker the binding to the molecule.

Table 5.2 shows electronegativity values of transient metals or oxide groups with their respective configurations in electron distribution in the layer *d* [2, 3].

Figure 5.15 displays the different geometric configurations and configuration changes, while Table 5.3, the corresponding electronegativity values.

Table 5.3 Energy varying with coordination change

Change of coordination—electronegativity Δ (kcal/mol)

d	Ion	Triangular $\rightarrow$ Tetrahedral	Tetrahedral $\rightarrow$ Tetragonal pyramidal	Tetragonal pyramidal $\rightarrow$ Octahedral	Tetrahedral $\rightarrow$ Octahedral	Triangular $\rightarrow$ Tetragonal pyramidal	Triangular $\rightarrow$ Octahedral
d^0	Ca^{2+}	0	0	0	0	0	0
d^1	Ti^{3+}	−6	−9.5	+2.9	−6.7	−3.6	−0.7
d^2	V^{3+}	+11	−18	+5.5	−13	−6.8	−1.3
d^3	V^{2+}	+27	−23	−7.0	−30	+3.2	−3.8
	Cr^{3+}	+34	−30	−9.2	−39	+4.2	−5
d^4	Cr^{2+}	+14	−29	+12	−16	−14	−2.1
	Mn^{3+}	+20	−39	+17	−22	−20	−2.9
d^5	Mn^{2+}, Fe^{3+}	0	0	0	0	0	0
d^6		+3.6	−5.7	+1.7	−4	−2.1	−0.42
	Fe^{2+}	+6.4	−10	+3.0	−7	−3.8	−0.74
d^7	Co^{3+}	+6.7	−11	+3.2	−7.4	−4.0	−0.78
d^8	Co^{2+}	+17	−15	+4.6	−19	−2.1	−2.5
d^9	Ni^{2+}	+14	−27	+12	−16	−14	−2
d^{10}	Cu^{2+}, Cu^{1+}, Zn^{2+}	0	0	0	0	0	0

According to Dowden and Wells

Adapted from D. L. Trimm, *Design of Industrial Catalysts*, Elsevier, (1980)
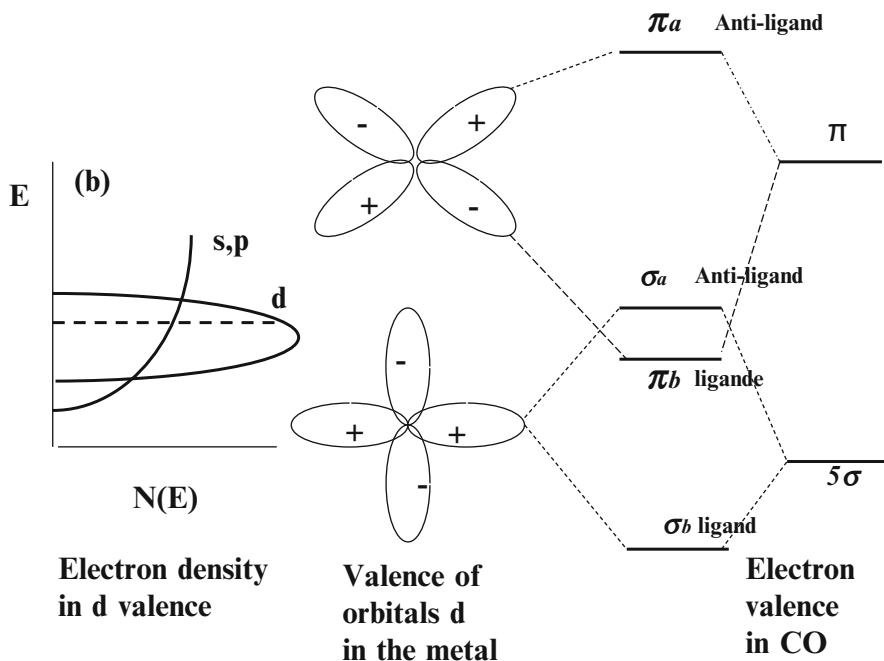
Fig. 5.16 Distribution of metal electrons in the presence of CO [Adapted with permission from J. A. Moulijn, P.W.N.M. van Leeuwen, R. A. van Santen, Catalysis, 2 Edition (1995) Elsevier, Amsterdam]

In the presence of an adsorbate, the electronic configuration changes and will also affect the Δ electronegativity. Consider, as an example, the linear adsorption of CO molecule on a surface, where the CO orbital π interacts with atomic orbitals d of the metal, but also either on p_x or p_y. The orbital 5σ will interact with d_{z^2} but also with s and p_z of the metal, as shown in Fig. 5.16. Fragments of ligand orbitals (b) and anti-ligand (a) are formed. Type ligands π are occupied and located on the metal or ligand and anti-ligands type σ will be occupied. The ligands type σ_b are located in CO while anti-ligands σ_a on the metal [14].

Unlike CO orbital σ, the energy of unoccupied orbitals π is larger than the Fermi energy. The occupied orbitals resulting from the interaction of the molecule with the metal are ligands and located in the metal.

5.2.4   Conclusion

The presented theoretical concepts explain the adsorption phenomena on homogeneous solid surfaces and the interaction through steric and electronic mainly concepts that allow us to understand the surface phenomena between adsorbate and adsorbent. In catalyst design, these concepts are fundamental to the proper choice of a catalyst without using empirical methods. The simple example, but important in the selection of catalysts, is shown below.

5.3   Examples

5.3.1   Design of a Catalyst: Alcohol Route

The goal is the selection of catalysts for reactions involving the formation of higher alcohols, following the alcohol chemistry route. This study aims to apply the theory and thus provide the selection of catalysts for the process.

This is a well-known industrial process, with suitable catalysts for each process. The catalysts for the production of crotonaldehyde and 2-ethylhexanol are different. Besides the alcohol route, the petrochemical route is used industrially. For both routes, there are four basic reactions:

- Dehydration
- Dehydrogenation/hydrogenation
- Aldolization/condensation
- Hydroformylation

In addition, there are several secondary reactions. The reactions of aldolization and hydroformylation are reactions in homogeneous phase.

Initially, one must predict all thermodynamically possible reactions, besides the desired reactions and if possible the superficial mechanisms. By alcohol route, we have

Principal Reactions

Analyzing the secondary reactions separately:

The dehydration reaction is endothermic and occurs preferably between 300 °C and 360 °C and is favored with increasing temperature and decreasing pressure.

The ethyl ether formation is favored at 190 °C, being exothermic and reversible. It is not influenced by the pressure, but this depends on the water vapor and of course the catalyst.

The ethyl ether decomposition reactions are endothermic and above 200 °C temperatures favor decomposition.

The formation of acetaldehyde takes place under endothermic conditions and is favored with decreasing pressure and increasing temperature.
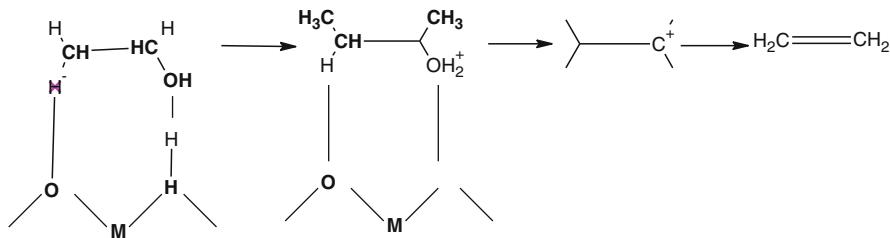
The coke formation occurs at high temperatures, since the synthesis of gas formation occurs at temperatures above 300 °C. The presence of water increases the formation of products. The ethane formation occurs at higher pressures and the presence of impurities and depends on the catalyst.

Superficial Mechanism

There are three possible reaction mechanisms.

1. Mechanism via Brønsted acid sites
   In this case, the existence of Brønsted acid sites on the surface is assumed. Adsorption occurs on two surface sites, according to the scheme below:
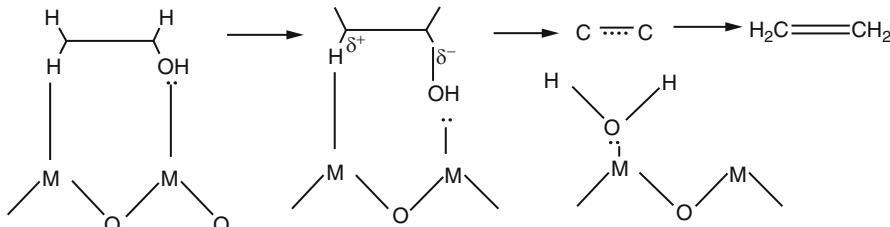
   The formation of a carbocation resulting from the dehydration of ethanol by the H surface protonated acid occurs. This arrangement forms ethylene.

2. Mechanism via Lewis acid sites
   The mechanism follows with the formation of carbon–oxygen ion on a surface of an oxide, as shown below:
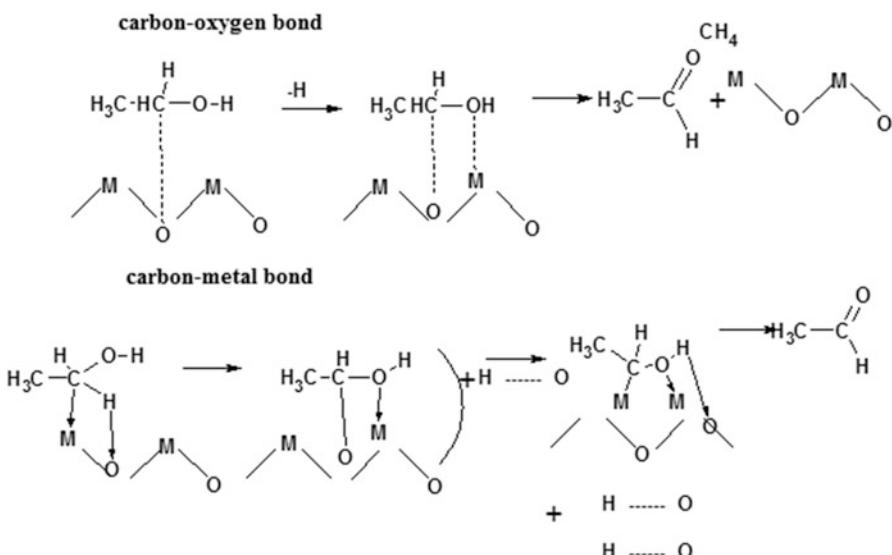
Bonds on Lewis sites

3. Dehydrogenation
   In the dehydrogenation of ethanol for the production of acetaldehyde, secondary reactions occur and by-products are formed, such as ethyl acetate, acetic acid, acetone, and butanol. Furthermore, consecutive reactions occur of acetaldehyde and ethyl acetate to crotonaldehyde, butyraldehyde acetal, and butyl acetate. These reactions are significant around 150 °C, but with increasing temperature acetaldehyde decomposes into CO and CH_4.

   Although the surface mechanism of the dehydrogenation reaction has been discussed with various propositions, the most accepted is where the adsorption occurs on two active sites through the CO and H group, as shown in the diagrams below:

carbon-oxygen bond

carbon-metal bond
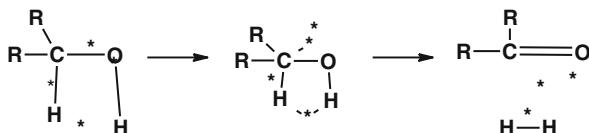
4. Selection of catalysts
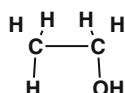
The selection of catalysts for the dehydration and the dehydrogenation is based on the surface competitive mechanisms. Higher acidity favors dehydration, while metals or base sites favors dehydrogenation. Depending of this model and based on basic concepts, we can find out a catalyst with these characteristics.

Based on what we learned from the band theory, the determining step of the dehydrogenation reaction is the donation of electrons, while dehydration takes place by accepting electrons. Therefore, it is expected that the dehydrogenation is catalyzed by p-type, while the dehydration by the n-type semiconductors.

However, from the multiplet theory, adsorption requires local and congruent active sites for the decomposition of ethanol. Thus, for the dehydrogenation of ethanol, there are adsorption bonding of C–O, C–H and O–H at the surface atoms (*), according to the following mechanism:

Otherwise, for dehydration reaction, one suggests the C–C, C–H and C–OH binding as
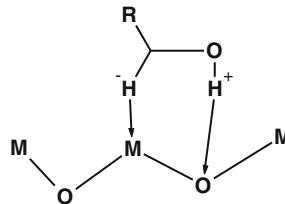
The calculated atomic distances of C–O and C–C are 1.42 and 1.54 Å, respectively. Thus, the lattice parameter of the oxide or solid metal oxide for dehydration must be greater than the dehydrogenation.

Since the dehydration occurs on acid sites, it should be catalyzed by protonic solid. The dehydrogenation .requires electron transfer and must be catalyzed by metals and semiconductors.

Krylov [2] has shown the dependence of the activity and electronegativity on metal–metal atoms. Experiments have shown that for the dehydration of isopropyl alcohol, the activity decreases with increasing .electronegativity. This premise is consistent with the mechanism for the dehydration of alcohols, since the oxides have lower electronegativity.

The same is true for the dehydrogenation.

Eucken et al. [15] showed that dehydration occurs through activated hydride complex, where the ions H^+ are polarized, according to the scheme:

However, this mechanism is the opposite of the former.

On the other hand, Krylov [2] claims that the activity of the dehydration of isopropyl alcohol is independent of the interatomic metal–nonmetal distance, which is similar for ethanol dehydration.

Tables 5.4 and 5.5 show some properties of the oxides, the interatomic distances and electronegativity, and the relative activity of dehydrationand dehydrogenation reactions.

In fact, geometric and electronic properties influence on the catalytic activity. These tables show that the n-type solids are the most active and that the interatomic distance, metal–oxygen 2 Å, and the electronegativity 2.0 eV adjust better the activity results:

5.3.2   Deoxygenation of Benzoic Acid to Benzaldehyde

Why Study Deoxygenation?

• Bio-oil resulting from the pyrolysis of biomass has a high oxygen content (30–55 %).

Table 5.4 Solid properties and relative activity for the isopropanol dehydration

- *High activity*

	WO_2	Nb_2O_5	TaO_2	Ta_2O_8
Relative activity	-	1.0	-	-
Semiconductor	n	n	-	n
Distance MeO (A^0)	2.0	2.03	2.02	2.0
Electronegativity (eV)	1.9	1.9	2.1	-

- *Intermediate activity*

	Al_2O_3	TiO_2(anatase)	Fe_2O_3	TiO_2(rutile)	MoO_3
Relative activity	1.0	0.8	0.72	0.63	0.5
Semiconductor	n	-	n	n	n
Distance MeO (A^0)	1.78	1.95	1.90	1.94	1.75
Electronegativity (eV)	2.0	1.9	1.70	1.90	1.8

\

- *Low activity*

	BaO	ZnO	CdO	Cr_2O_3	NiO
Relative activity	0.4	0.33	0.26	0.24	0.15
Semiconductor	p	n	n	n.p	p
Distance MeO (A^0)	2.76	1.99	2.35	2.01	2.09
Electronegativity (eV)	2.65	2.0	2.0	1.90	1.8

- High acidity, corrosivity, and instability due to oligomerization/condensation reactions.
- Not suitable for use in turbines and as fuel for transport.

Table 5.5 Solid properties and relative activity of isopropanol dehydrogenation

	NiO	PdO	AgO	Ag$_2$O	PbO	HgO	
Activity[a] (ln)	2.3	–	–	–	–	–	
Semiconductor	p	p	p	p	p	n	
Distance MeO (Å)	2.09	2.2	2.03	2.05	1.9	2.03	
Electronegativity (eV)	2.0	1.5	1.7	1.7	2.24	1.6	
	Cu$_2$O	CuO	Co$_2$O$_3$	ZnO	CdO	AuO	TiO$_2$
Activity[a] (ln)	2.2(2.11)	1.9(2.13)	2.0	2.0	2.13	2.0(1.84)	2.0(1.01)
Semiconductor	p	p.n	p	n	n	n	n
Distance MeO (Å)	1.84	1.95	2.12	1.75	2.35	2.22	1.94
Electronegativity (eV)	2.0	1.5	1.8	2.0	2.0	2.1	1.9
	Cr$_2$O$_3$	TeO	Co$_2$O$_3$	In$_2$O$_3$	SnO$_2$	Sb$_2$O$_5$	Sb$_2$O$_3$
Activity[a] (ln)	1.6(1.44)	(1.43)	1.85(1.52)	–	–	–	
Semiconductor	p.n	p	n	n	n	n	p
Distance MeO (Å)	2.01	2.16	1.90	2.15	2.06	–	2.22
Electronegativity (eV)	1.9	1.85	1.7	1.9	1.7	1.4	1.7
	BaO	La$_2$O$_3$	CaO	MgO			
Activity[a] (ln)	(1.03)	–	(0.99)	0.79			
Semiconductor	p	n	p.n	p.n			
Distance MeO (Å)	2.76	2.42	2.40	2.10			
Electronegativity (eV)	2.65	2.4	2.5	2.3			

[a]Activity of isopropanol dehydrogenation

- The removal of organic acids results in a bio-oil less acidic and less corrosive.
- Catalysts for deoxygenation can be used during the flash pyrolysis process.
- Reaction system rather complex.
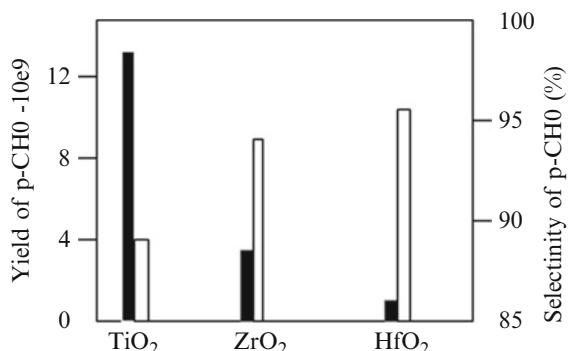
The deoxygenation of benzoic acid to benzaldehyde is an alternative process for the production of benzaldehyde. There is the formation of undesired by-products that cause environmental impact [16, 17]:

- The idea:
  Studying the selective hydrogenation (deoxygenation) of benzoic acid to benz-aldehyde in one step minimizing formation of by-products and waste.
- Reactions

  – Desired reaction

$$C_6H_5COOH + H_2 \rightarrow C_6H_5CHO + H_2O \qquad (5.5)$$

  – Undesired reactions

Fig. 5.17 Yield and selectivity to para-benzaldehyde [Adapted from C. A. Koutstaal, V. Ponec, Science and technology in Catalysis, 1994, p. 105]

Direct reduction of acid benzoic

$$C_6H_5COOH + 3H_2 \rightarrow C_6H_5CH_3 + 2H_2O \tag{5.6}$$

Hydrogenation or hydrogenolysis of benzyl alcohol

$$C_6H_5CH_2OH + H_2 \rightarrow C_6H_5CH_3 + H_2O \tag{5.7}$$

Hydrogenation (deoxygenation) of benzaldehyde

$$C_6H_5CHO + 2H_2 \rightarrow C_6H_5CH_3 + H_2O \tag{5.8}$$

Formation of benzyl alcohol

$$C_6H_5CHO + H_2 \rightarrow C_6H_5CH_2OH \tag{5.9}$$

Formation of benzene

$$C_6H_5COOH \rightarrow C_6H_6 + CO_2 \tag{5.10}$$

Formation of benzophenone

$$2C_6H_5COOH \rightarrow C_{12}H_{10}CO + CO_2 + H_2O \tag{5.11}$$

Koutstaal and Ponec [18] studied the deoxygenation of benzoic acid to benzaldehyde with four group oxides (ZrO_2, HfO_2, and TiO_2) and the effect of addition of Cu to Pt and ZrO_2 selectivity to benzaldehyde. The results of the catalytic tests are shown in Fig. 5.17.

Superficial Mechanism
Mechanism I (Fig. 5.18):
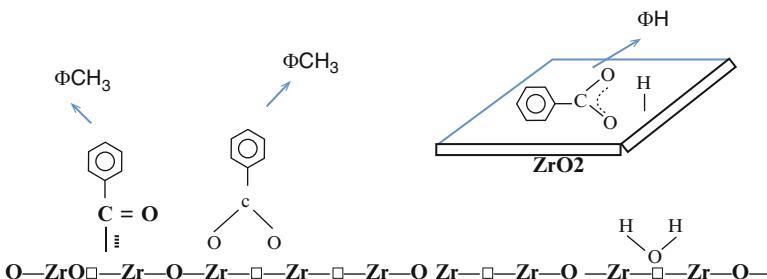
Fig. 5.18 Superficial mechanism [Adapted with permission from C. A. Koutstaal, V. Ponec, Science and technology in Catalysis, 1994, p. 105]

Thus:

- The selectivity for benzaldehyde decreased with decreasing strength binding of metal oxide (MO) in order $HfO_2 > ZrO_2 > TiO_2$.
- Reaction takes place in two stages with the participation of oxygen lattices.
- Hydrogen reduces the surface and creates oxygen vacancies.
- Subsequently benzoic acid reoxides the surface and desorbs as benzaldehyde.
- Addition of metal (Pt or Cu) resulted in decreased selectivity to benzaldehyde and the increase of by-products such as benzene, toluene, and cyclo-hexanoic acid.
- Addition of water in the reaction resulted in the reduction of oxygen vacancies resulting in decreased selectivity for toluene.
- The concentration of oxygen vacancies in the network plays an important role in the reaction.

Catalysts: Sakata et al. [19] tested the oxides MgO, PbO, Cr_2O_3, La_2O_3, Pr_6O_{11}, Yb_2O_3, MnO_2, Mn_3O_4, Fe_2O_3, Fe_3O_4, Co_3O_4, ZnO, ZrO_2, and CeO_2 for the deoxygenation of benzoic acid

Mechanism II:

Lange et al. [20] investigated the deoxygenation of benzoic acid to benzaldehyde with ZnO and ZrO_2 and proposed the following mechanism (Fig. 5.19).

Thus,

- The deoxygenation on ZnO is higher than on ZrO_2. The limiting step of the reaction is the activation of hydrogen.
- The energy barrier in forming vacancies on the ZrO_2 is greater than on ZnO, due to the greater strength of the metal–oxygen bond in ZrO_2.
- For a given reaction temperature, the concentration of oxygen vacancies in the ZnO is higher than in ZrO_2.

Lange et al. [21] confirmed the reaction mechanism proposed by Sakata (Mars & van Krevelen) (Fig. 5.20).
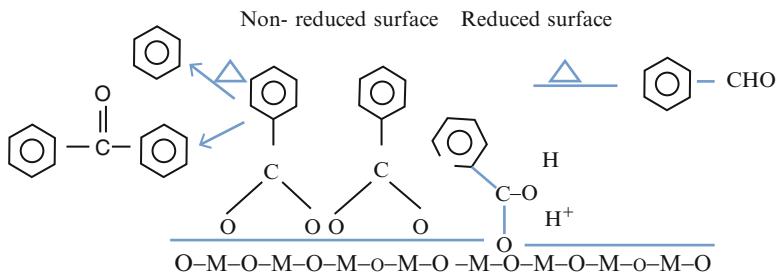
Fig. 5.19 Superficial mechanism proposed by Lange et al. [Adapted with permission from M.W. de Lange, J.G. van Ommen, L. Lefferts, Appl. Catal. A: Gen.220 (2001) 41]
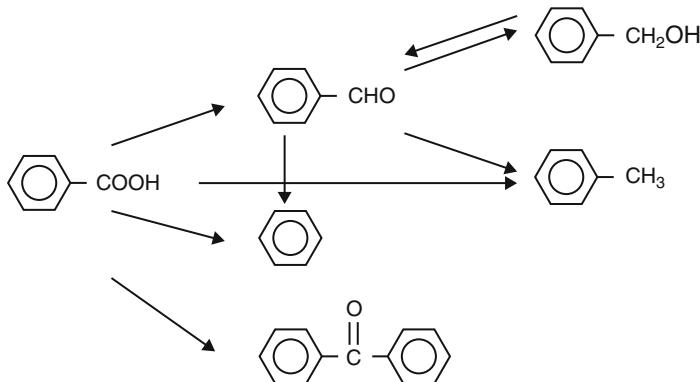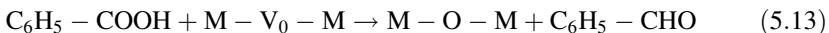
Fig. 5.20 Superficial redox mechanism superficial according to Lange et al. [Adapted with permission from M.W. de Lange, J.G. van Ommen, L. Lefferts, Appl. Catal. A: Gen.220 (2001) 41]
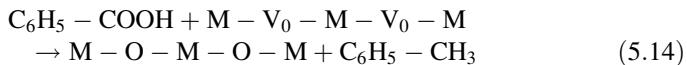
Activation of oxide in the presence of H_2

$$H_2 + M - O - M \rightarrow H_2O + M - V_0 - M \qquad (5.12)$$

Reoxidation through benzoic acid forming benzaldehyde:

$$C_6H_5 - COOH + M - V_0 - M \rightarrow M - O - M + C_6H_5 - CHO \qquad (5.13)$$

When the number of vacancies is high, toluene is formed:

$$\begin{aligned} C_6H_5 - COOH + M - V_0 - M - V_0 - M \\ \rightarrow M - O - M - O - M + C_6H_5 - CH_3 \end{aligned} \qquad (5.14)$$
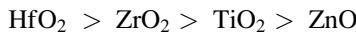
- Catalysts
  The main properties of desirable products.

- The bonding strength of the M–O: if high, then the oxygen vacancies decrease. Low strength allows formation of vacancies and favors the selectivity of toluene. In opposite, if strong then it decreases the formation of vacancies and the activity.

  – Basic character: weak or amphoteric. High basicity increases the selectivity of benzene.
  – Redox properties: metal increases the formation of benzene ring hydrogenation and creates more vacancies.

Properties of the Oxides
The main properties of the oxides are presented in the Table 5.6.

Conclusions
The catalysts satisfying the activity and selectivity based on the proposed mechanisms and oxide properties are

$$HfO_2 \; > \; ZrO_2 > \; TiO_2 > \; ZnO$$

The oxides HfO_2, ZrO_2, and TiO_2 are very selective for higher temperatures.
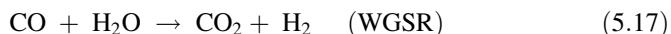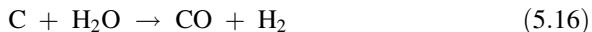
Example 5.3.3: CH_4 Reforming on Promoted Ni–YSZ Catalysts (Anodes)
Takeguchi et al. (2003) [22] studied the methane reforming on Ni–YSZ. The goal here is conceptually studying the work of Takeguchi et al. [23] and investigate the catalytic properties and electrochemical activity, prioritizing the deposition of C on the anode during the reforming of methane.

For high S/C ratio (S/C = 2.0), it starts with the decomposition of methane (limiting step):

$$CH_4 \rightarrow C + 2H_2 \tag{5.15}$$

It was found that the deposition rate of C is not proportional to the decomposition of CH_4, which means that there are other reactions involved that remove carbon, which explains the quick removal of coke precursors, such as

$$C \; + \; H_2O \; \rightarrow \; CO \; + \; H_2 \tag{5.16}$$

$$CO \; + \; H_2O \; \rightarrow \; CO_2 + H_2 \quad (WGSR) \tag{5.17}$$

By modifying the catalyst Ni–Y_2O_3–ZrO_2, adding Pt or Ru or Pd or Rh, there are changes in activity (conversion), selectivity, and stability (carbon deposition), due to geometric and electronic effects.

Unfortunately these authors didn't make specific characterizations, and this lack makes room for assumptions and considerations.

Table 5.6 Properties of the oxides [Adapted from D. L. Trimm, *Design of Industrial Catalysts*, Elsevier Sci. Publ. Company, 1980]
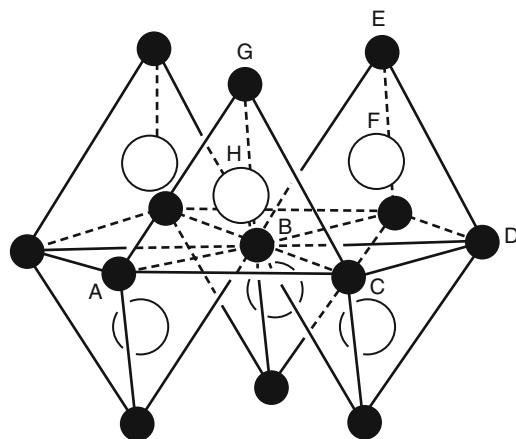
Oxide	M-O (A)	Semi-conductor	Structure	Electro-negativity	ΔH_f oxide/0 (KJ/mol)	Enthalpy M-O bond (KJmol	Lattice Energy (KJ/mol)	Reduction Potential (E/V)
ZnO	1.39	n	hex	2.0	351	159.0	4142	-0.79
TiO_2	1.95/1.94	-/n	tet	2.1	470	672.4	12150	-0.86
ZrO_2	2.20/2.04	n/-	--/mn	2.1	550	776.1	11183	-1.55
HfO_2		n,p	cb	2.2	559	801.7		-1.70
CeO_2	2.21	n	cb	2.3	544	795.0	9627	
Fe_2O_3	2.34	n	rh	1.7	274	390.4	14309	-0.04
Fe_3O_4	1.91	n	cb		279			-0.44
Co_3O_4	1.93	p	cb	1.6	220	384.5		
MnO_2	1.92	n	tet	1.9	261	402.9	12970	
Mn_3O_4	1.87		cb		347		15146	
MgO	2.05	n,p,ion	cb	2.3	602	363.2	3795	-2.36
PbO	2.1	n,p/n	tet/rh	1.2	215	332.0	3520	
Cr_2O_3	2.30/2.24	p,n	rh	1.9	376	429.3	15276	-0.74
La_2O_3	2.01	n	rh	2.3	598	799.0	12452	
	2.42							

Oxides	Conversion (%)	Enthalpy (KJ/mol) (atO)	Basicity	Semi-conductor	Electro-negativity(eV)	M-O (A)
HfO_2,ZrO_2,TiO_2,ZnO	>95	-350;-560	Weak	n	2.0-2.2	1.94-2.21
$MnO_2,Mn_3O_4,Fe_2O_3,Fe_3O_4$	10-50	-250;-349		n	1.7-1.9	1.87-2.05
	5	-220		n	1.6	1.92
$Co_3O_4,$	90	-214			1.2	2.24-2.30
PbO	5	-602	Strong	n	2.3	2.1
MnO	98	-598	Moderate	n	2.3	2.42
La_2O_3	86	-544			2.3	2.34
Ce_2O_3	2	-376	Moderate		1.9	2.01
Cr_2O_3				n		

Table 5.7 Electronic properties of metals [Adapted from J. R. Anderson, *Structure of Metallic Catalysts*, Academic Press, 1975]

Metal	Group	Electronic distribution	Electronegativity (eV)	Interatomic distance (Å)
Ni	4/10	$3d^0, 4s^4$	1.91	3.51
Ru	5/8	$4d^6, 5s^2$	2.2	3.53
Rh	5/9	$4d^7, 5s^2$	2.28	3.8
Pd	5/10	$4d^8, 5s^2$		3.9
Pt	6/10	$5d^8, 6s^2$	2.28	3.9

Fig. 5.21 Structure of ZrO_2 in the tetragonal transition, *open circle* oxygen, *filled circle* zirconia [Adapted from J. R. Anderson, *Structure of Metallic Catalysts*, Academic Press, 1975]

We assume that these different catalysts were prepared similarly and that the addition of noble metals reached similar dispersions, for example. Some specific properties of transition metals, which are of interest, are presented in Table 5.7.

5.3.2.1 Electronic Properties of Metals

Zirconia, part of the catalyst, or anode, has a monoclinic structure at room temperature, but transitions to tetragonal or cubic, at higher temperatures, while yttria (Y_2O_3), another component, stabilizes the tetragonal and/or cubic phases (Fig. 5.21).

Furthermore, Y_2O_3 has high stability and mechanical strength at high temperatures. The presence of yttria causes modification of the crystalline structure and generates vacancies to replace cations Zr^{4+} by less loaded cations, Y^{3+}. This causes an electronic effect, i.e., change in the charge density, which is dominated by oxygen atoms, and setup channels, generating noncontinuous surfaces [24].

Electronic modifications of Ni, i.e., changes in electron density, can be induced by the formation of an alloy or an interaction with the promoter (Table 5.8).

Table 5.8 Electronic changes on metals [25]
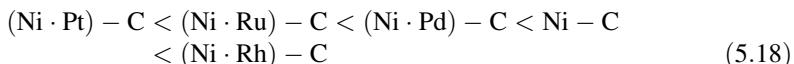
$Ni^{\circ} - Pt^{\circ}$ or $Ni^{+\delta} - Pt^{-\delta}$
$Ni^{\circ} - Ru^{\circ}$ or $Ni^{+\delta} - Ru^{-\delta}$
$Ni^{\circ} - Pd^{\circ}$ or $Ni^{+\delta} - Pd^{-\delta}$
$Ni^{\circ} - Rh^{\circ}$ or $Ni^{+\delta} - Rh^{-\delta}$

Table 5.9 Effect of metals on rate deposition [24]

Catalyst	Rate of C deposition (C/g_{cat} min)
Ni–YSZ Pt	0.027
Ni–YSZ Ru	0.030
Ni–YSZ Pd	0.037
Ni–YSZ	0.045
Ni–YSZ Rh	0.062
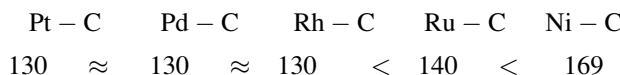
Both situations can generate different interactions between active site and reactants. There may be a weaker bond strength M–C, which can influence the activity and the stability of the catalyst.

The bonding force of the M–C follows the tendency:

$$(Ni \cdot Pt) - C < (Ni \cdot Ru) - C < (Ni \cdot Pd) - C < Ni - C \\ < (Ni \cdot Rh) - C \tag{5.18}$$
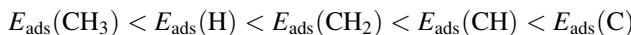
This is consistent with the results of carbon deposition, where rates increase in sequence (Table 5.9).

Trimm [3] suggested the following sequence of bonding energies in Kcal/mol:

$$\begin{array}{ccccc} Pt - C & Pd - C & Rh - C & Ru - C & Ni - C \\ 130 & \approx \quad 130 & \approx \quad 130 & < \quad 140 & < \quad 169 \end{array}$$

On the other hand, from the point of view of electronic structure, according to the band theory, it can be represented in the following (Fig. 5.22) [26].

Thus,

$$E_{ads}(CH_3) < E_{ads}(H) < E_{ads}(CH_2) < E_{ads}(CH) < E_{ads}(C)$$

When the number of H atoms bonded to C increases, the bonding strength decreases Pd–C and Pd–C and the distance increases.

According to Bengaard et al. [27], structural defects, such as steps and folds, play an important role in the dissociation of water. As studied before, defects facilitate interaction of electronic effects, which in this case favors the dissociation of H_2O. In addition, intermediaries without hydrogen carbon tend to make strong interactions with metallic sites due to electronic effects, and thus we can predict that most likely will face carbon deposition problems. Additional papers related to this chapter are presented in the references [28–31].
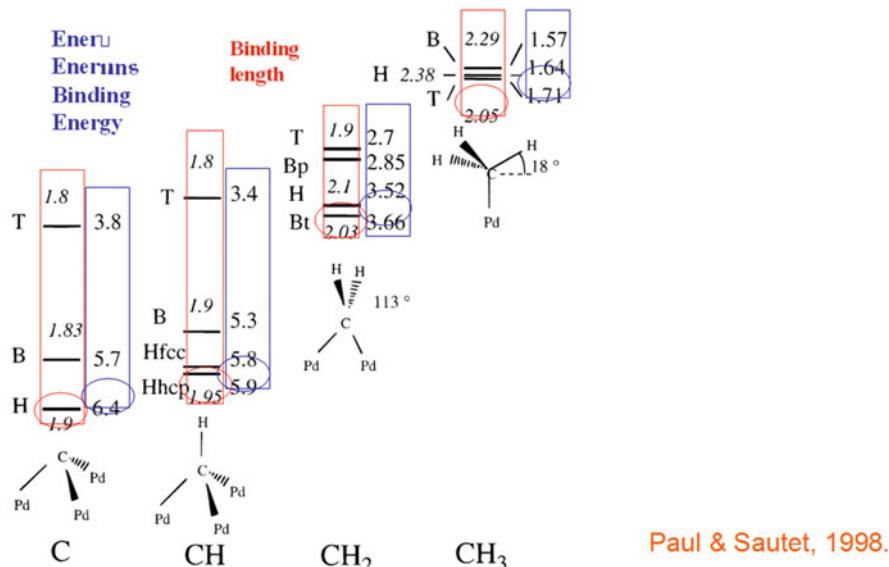
Fig. 5.22 Electronic bands for each species [Adapted with permission from J.-F. Paul and P. Sautet, J. Phys. Chem. B, 1998, 102, pp 1578–1585, Copyright © 1998 American Chemical Society]

References

1. Baladin AA. The Nature of Active Centers and the Kinetics of Catalytic Dehydrogenation, Z Phys Chem. 1929;32:289,B3,167.
2. Krilov OV. Catalysts by non-metals. New York: Academic Press; 1970.
3. Trimm DL. Design of industrial catalysts. Amsterdam: Elsevier; 1980.
4. Masel I. Principles of adsorption and reaction on solid surfaces. New York: Wiley; 1996.
5. Somorjai GA. An introduction to surface chemistry and catalysis. New York: Wiley; 1994.
6. Kohn W, Sham L. Self-Consistent Equations Including Exchange and Correlation Effects. J. Phys Rev. 1965;140:1133.
7. Bond GC. Heterogeneous catalysis: principles and applications. Oxford: Clarendon Press; 1974.
8. Horiuti J, Polanyi M. Exchange reactions of hydrogen on metallic catalysts. Trans Faraday Soc. 1934;30:1164.
9. Evans MG, Polanyi M. Further considerations on the thermodynamics of chemical equilibria and reaction rates. Trans Faraday Soc. 1936;32:1333.
10. Fukui K. Theory of orientation and stereoselection. Berlin: Springer; 1975.
11. van Santen RA, Niemantsverdriet JW. Chemical kinetics and catalysis. New York: Plenum; 1995.
12. Pauling L. The nature of the chemical bond. New York: Cornell University Press; 1938, 1960.
13. Young DM, Crowell AD. Physical adsorption of gases. New York: Butterworth; 1962.
14. Moulijn JA, van Leeuwen PWNM, van Santen RA. Catalysis. 2nd ed. Amsterdam: Elsevier; 1995.
15. Faith WL, Keyes DB, Clark LR. Industrial chemicals. 3rd ed. New York: Wiley; 1965.

References (Examples)

16. Yokoyama T, Setoyama T, Fujita N, Nakajima M, Maki T, Fujii K. Novel direct hydrogenation process of aromatic carboxylic acids to the corresponding aldehydes with zirconia catalyst. Appl Catal A. 1992;88:149–61.
17. Marlon Almeida—Fund. da Catálise em Metais e Óxidos – Coppe/UFRJ. 2007.
18. Koutstaal CA, Ponec V. Science and technology in catalysis. 1994. p. 105.
19. Sakata Y, Koutstaal CA, Ponec V. Novel direct hydrogenation process of aromatic carboxylic acids to the corresponding aldehydes with zirconia catalyst. J Catal. 1997;169:13.
20. de Lange MW, van Ommen JG, Lefferts L. Novel direct hydrogenation process of aromatic carboxylic acids to the corresponding aldehydes with zirconia catalyst. Appl Catal A Gen. 2001;220:41.
21. de Lange MW, van Ommen JG, Lefferts L. Deoxygenation of benzoic acid on metal oxides: 2. Formation of byproducts. Appl Catal A. 2002;231:17–26.
22. Toniolo FS. Fund. da Catálise em Metais e Óxidos – Coppe/UFRJ. 2007.
23. Takeguchi T, Kikuchi R, Yano T, Eguchi K, Murata K. Effect of precious metal addition to Ni-YSZ cermet on reforming of CH4 and electrochemical activity as SOFC anode. Catal Today. 2003;84:217.
24. Santoyo-Salazar J, Gonzalez G, Ascencio JA, Tartaj-Salvador J, Chávez-Carvayar JA. Novel yttria-stabilised zirconia–alumina tetragonal phase obtained by co-precipitation. J Crystal Growth. 2006;290:307–12.
25. Anderson JR. Structure of metallic catalysts. London: Academic; 1975.
26. Paul F, Sautet P. Chemisorption and transformation of CHx fragments (x = 0–3) on a Pd(111) surface: a periodic density. J Phys Chem B. 1998;102:1578–85.
27. Bengaard HS, Nørskov JK, Sehested J, Clausen BS, Nielsen LP, Molenbroek AM, Rostrup-Nielsen JR. Novel yttria-stabilised zirconia–alumina tetragonal phase obtained by co-precipitation. J Catal. 2002;209:365–84.
28. Wang X, Shen M, Wang J, Fabris S. Enhanced oxygen buffering by substitutional and interstitial Ni point defects in ceria: a first-principles DFT+U study. J Phys Chem C. 2010;114:10221–8.
29. Yang Z, Woo TK, Hermansson K. Effects of Zr doping on stoichiometric and reduced ceria: a first-principles study. J Chem Phys. 2006;124:224704.
30. Wyckoff RWG. Crystal structures, vol. 1. New York: Wiley; 1965. p. 85–92.
31. De Souza EF, Chagas CA, Manfro RL, Souza MMVM, de Alencastro RB, Schmal M. Combined DFT and experimental study of the dispersion and interaction of copper species in Ni-CeO$_2$ nanosized solid solutions. RSC Adv. 2016;6:B5057–67.

Chapter 6
Textural and Thermochemical Characterizations

Abstract Textural and thermo-chemical methods of characterizations of solid materials, metals and oxides.

6.1 Part I: Adsorption Methods for Determination of Surface Areas and Pore Volumes

Adsorption method for application in heterogeneous catalysis is very important for determining the surface area, metallic areas, and volume and distribution of pores whether on porous solid materials or not. This method allows determining the texture and the active area of solids, oxides, or supported metallic catalysts. The solid texture is defined as the spatial dimensions that are within the range of 0.3 and 1 mm, involving both the external surface and internal pores. One must distinguish texture and structure of the catalyst, because in the latter case is crystallographic material. However, the catalytic properties depend significantly on both and, therefore, should be known. There are significant differences between the surface and mass properties. The adsorption method allows to determine the surface properties.

As seen before, there are two distinct types of adsorption which depend on the nature and the adsorption forces involved.

6.1.1 Physical Adsorption or Physisorption

Physisorption is a process having low degree of interaction between the adsorbed molecules and the solid surface. The forces involved are of the same order of magnitude as the van der Waals forces and the enthalpy of adsorption is in the range of the condensation or evaporation enthalpy of the gases (from 0.5 to 5 kcal/mol). In this type, the molecular adsorption can form overlapping layers, and the adsorption force decreases with increasing number of layers.

According to London–van der Waals, the strengths between molecules and atoms can be represented in function $\left(\frac{a}{V^2}\right)$, as equation [1]

$$\left(p + \frac{a}{V^2}\right)(E_i - V) = RT \tag{6.1}$$

where V is the volume of the gas, $\left(\frac{a}{V^2}\right)$ is the correction factor for the strengths between molecules, and a is the gas constant.

The total energy between the molecules is the contribution of dipole–dipole interaction and dipole-induced interaction, which is a function of radius, that is, $E_i = -C \times r^{-6}$, where E_i is the energy of interaction and r the radius of the molecule. Care should be taken when the interaction is of atoms or ions with the surface.

In conclusion, the majority of molecules interact with the surface atoms and between the molecules.

The physisorption takes place at low temperatures and is high when the temperature is close to the condensation temperature of the gas. Due to the low energy of interaction with the surface and the absence of activation energy, the physisorption quickly reaches equilibrium and is a reversible process. However, in the materials with very small pores (zeolites, carbons), the physisorption is slow and thus, the process is limited by the rate of gas diffusion into pores.

The physisorption of gases on solids is used for determining the textural properties of catalysts, such as surface area and pore size distribution.

6.1.2   Chemical Adsorption or Chemisorption

The chemisorption is characterized by the high degree of interaction between the gas molecules and solid surfaces. The chemisorption enthalpies are of the order of 10–100 kcal/mol and thus of the same order of magnitude as the chemical bonds.

Unlike the physisorption, the chemisorption is an irreversible process and takes place at higher temperatures, compared to physisorption temperature, and since it is a specific interaction between the gas and the solid, it forms a single layer.

The chemisorption requires long periods of time to reach the equilibrium, especially at low temperatures. There are two types of chemisorption: activated or not. In the activated chemisorption, the rate of adsorption varies with temperature and depends on the activation energy, expressed by Arrhenius equation. In the not activated, the adsorption occurs rapidly, since the activation energy is practically nil.

Adsorption Isotherms

The adsorption isotherm is represented by the amount of gas adsorbed as a function of the partial equilibrium pressure, $\frac{p}{p^0}$, for a constant temperature.

The amount of gas adsorbed by a solid is expressed in terms of weight of sample (g) or volume of gas at STP standard conditions (pressure and temperature), but
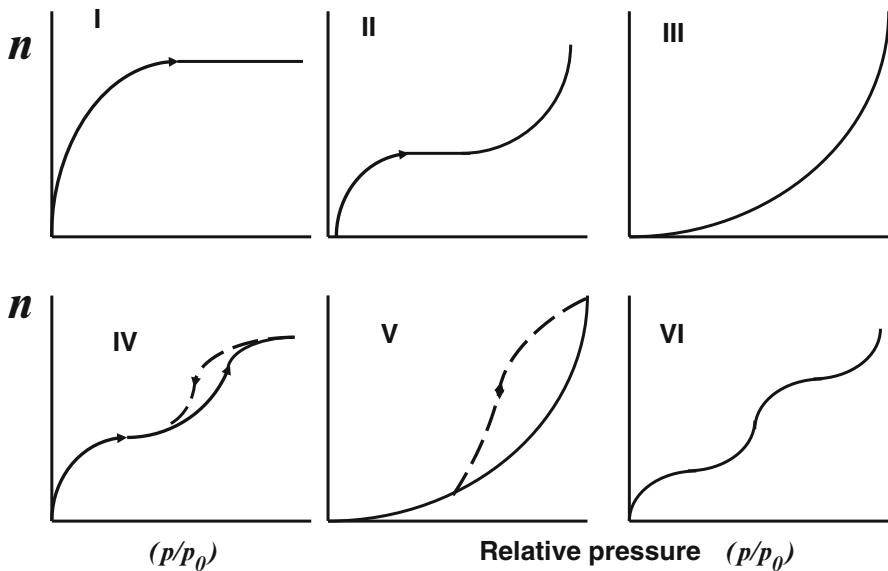
Fig. 6.1 Adsorption isotherms [Adapted from S.J. Gregg. K.S.W. Sing. "Adsorption. Surface Area and Porosity". 2 Edition. (1982) Academic Press. London]

depends on the temperature, pressure, and type of gas and solid. Thus, the amount of gas adsorbed on a solid is given by

$$n = f(p, T, \text{gas}, \text{solid})$$

For a specific gas and constant temperature, the equation becomes

$$n = f\left(p/p^0\right)_{T,\ \text{gas, solid}} \tag{6.2}$$

Most adsorption isotherms can be grouped into six typical types, as shown in Fig. 6.1.

The isotherm (I) represents microporous materials, generally found in zeolites and activated carbons. The isotherm (II) is the multilayer physisorption on a flat surface (usually nonporous). The isotherms (III) and (V) are characteristic of gas–solid weak interactions, and the isotherm (IV) is the most frequent in heterogeneous catalysts, representing multilayer adsorption and capillary condensation in mesoporous materials. The isotherm (VI) shows the behavior of nonporous materials, energy uneven.

6.1.3 Porosity

The method of measuring the porosity depends on the type of material, pore sizes, and shapes. According to Dubinin [2, 3], the present micropores in the solids have

diameters ranging from 0.3 to 2 nm while on mesopores varied from 2 to 50 nm. The macropores have pore diameters over 50 nm up to 105 nm. Meso-, micro-, and macropores can be determined experimentally by N_2 adsorption or Ar, but also by Hg porosimetry [4]. Here we present only the adsorption methods.

The simplest method for determining pore volume is pycnometry. The porosity is defined as

$$\Phi = \frac{V_p}{V_t} \times 100 \quad (\%) \tag{6.3}$$

where V_p is the pore volume (cm^3/g) and V_t the total volume of the pores in the solid.

From the adsorption isotherm type I or for a complete monolayer, when the adsorbent fills all pores, forming a complete monolayer on 1 g of solid, we can calculate the surface area:

$$S = n_m a_m N_A \tag{6.4}$$

where S is the specific surface area (m^2/g); n_m the maximum moles for a complete monolayer (moles/g_{cat}); a_m mean area occupied by molecules on a monolayer, and N_A the number of Avogadro (6.023×10^{23} mol^{-1}).

Experimental results are done by N_2 adsorption at 77.4 K. The a_m value was calculated by Brunauer and Emmett [5], which corresponds to liquid nitrogen density. Thus,

$$a_m = 1.091 \times \left(\frac{M}{\rho_L} \times N_A \right)^{2/3} \tag{6.5}$$

where

$$M = 28; \quad \rho_L = 0.81 \quad (g/cm^3);$$

Therefore,

$$a_m(N_2) = 16.2 \ A^0 \quad \text{or}$$
$$a_m(Ar) = 13.85 \ A^0$$

6.1.4 Specific Surface Area: BET Method

Qualitative and quantitative analysis of the adsorption–desorption of molecules on surfaces has been discussed in Chap. 4. For a given adsorbent, the fraction θ of the surface occupied by adsorbed molecules is given by the equation

$$\theta = \frac{k_a p_r}{k_d + k_a p_r} \tag{6.6}$$

This equation represents the type I isotherm, which corresponds to the adsorption of molecules on an energetically uniform surface, where A is the adsorbent, k_a and k_d are the adsorption and desorption constants, and $p_r = p/p_0$ is the relative partial pressure. Considering the adsorption–desorption equilibrium constant $K = \frac{k_a}{k_d}$, this equation becomes

$$\theta = \frac{Kp_r}{1 + Kp_r} \tag{6.7}$$

This is known as the Langmuir equation [6] for a gas. If θ is the fraction of the surface occupied by adsorbed molecules, then

$$\theta = \frac{n}{n_m} \tag{6.8}$$

where

n—number of moles adsorbed per gram of catalyst
n_m—number of moles of a complete monolayer

Rearranging, we have

$$\frac{1}{n} = \frac{1}{n_m} + \frac{1}{n_m K} \left(\frac{1}{p_r} \right) \tag{6.9}$$

Plotting $(1/n)$ vs. $(1/p_r)$, we obtain a straight line, which allows calculating the number of moles of the monolayer n_m and from the slope the equilibrium constant $K = \frac{k_a}{k_d}$.

However, this correlation is not real, first, because the surface energy is not uniform and secondly, it doesn't form a complete monolayer, but several layers. Thus, there is interaction between the gas molecules and the adsorbed molecules at the surface, besides a great mobility of the molecules, which doesn't meet the Langmuir hypotheses. However, for low coverages and low relative pressures, this equation can be used allowing to calculate the fraction of adsorption at the surface or the volume of adsorbed molecules.

The most successful model was proposed by Brunauer, Emmet, and Teller [7] and is known as BET method. Different from the original model, takes in account the adsorption of molecules in multilayers, keeping all other hypothesis. Moreover, Gregg and Sing [4] assumed that the heat of adsorption varies, decreasing with increasing layers. The heat of adsorption is similar to the latent heat of condensation. Based on these assumptions, Brunauer, Emmet, and Teller deduced the equation. The number of molecules n of the gas phase coming to the surface is given by the kinetic theory of gases:

$$\frac{n}{(2\pi MR)^{1/2}} p$$

where p is the partial pressure, M molecular weight, and R gas constant. If θ_0 is the free fraction of the surface, then the condensation rate of the molecules in the first layer is

$$r_1 = \frac{n}{(2\pi MRT)^{1/2}} p \times \alpha_1 \times \theta_0 \qquad (6.10)$$

where α_1 is a correction factor indicating that only a fraction of molecules in the gas phase condenses in the first layer on the surface.

The reverse process, that is, the evaporation of the first layer, is essentially an activated process, since each molecule needs an energy E_1 to break the attraction force linked at the surface.

The probability of a molecule to desorb, considering the oscillation frequency of the adsorbed molecule in the direction of the surface, is

$$e^{-\left(E_1/RT\right)}$$

where E_1 is the desorption activation energy.

It is difficult to determine α_1 but can be assumed equal the vibration frequency of adsorbed molecules, between 1012 and 1014 s^{-1}. Thus, the number of molecules that desorbs per site and per second is given by the expression

$$\alpha_1 \times e^{-(E_1/RT)}$$

The sites occupied in the first layer are equal to $z_m\theta_1$, where z_m is the total number of molecules adsorbed in the first layer and θ_1 the fraction of the surface occupied by adsorbed molecules. Thus, the rate of desorption of molecules of the first layer is

$$r_1' = z_m\theta_1\alpha_1 \times e^{-\left(E_1/RT\right)} \qquad (6.11)$$

At equilibrium

$$r_1 = r_1'$$

or

$$\frac{n}{(2\pi MRT)^{1/2}} p\alpha_1\theta_0 = z_m\theta_1\alpha_1 \times e^{-\left(E_1/RT\right)} \qquad (6.12)$$

Calling

$$\frac{n}{(2\pi MR)^{1/2}} = K \qquad (6.13)$$

We obtain in analogy for the ith layer:

$$Kp\alpha_i\theta_{i-1} = z_m\theta_i\alpha_i \times e^{-\left(E_i/RT\right)} \tag{6.14}$$

The number of molecules adsorbed in a monolayer can be related to the volume of adsorbed gas:

$$\frac{V_{ads}}{V_m} = \frac{z}{z_m} \tag{6.15}$$

According to Gregg et al. [4], the fraction of adsorbed molecules on the surface is given by the following equation:

$$\theta_A = \frac{V_{ads}}{V_m} = \frac{c \times p_A}{(p_o - p_A)\left[1 + \frac{(c-1)p_A}{p_o}\right]} \tag{6.16}$$

where

$$c = e^{(H_1 - H_2)/RT} \tag{6.17}$$

where

$H_1 \equiv$ Enthalpy of the formation of the first layer
$H_2 \equiv$ Condensation heat of the gas
$p_A \equiv$ Pressure of gas A on gas–solid interface
$p_o \equiv$ Vapor pressure of gas A at constant temperature T

Equation (6.16) can be rearranged, which is known as the BET equation, allowing to calculate V_m, the adsorbed volume of gas in a monolayer and the constant c. It is also possible to calculate the adsorption enthalpy of the first layer.

Inverting Eq. (6.16), we have

$$\frac{V_m}{V} = \frac{(p_o - p_A)\left[1 + \frac{(c-1)p_A}{p_o}\right]}{cp_A}$$

Or in another form,
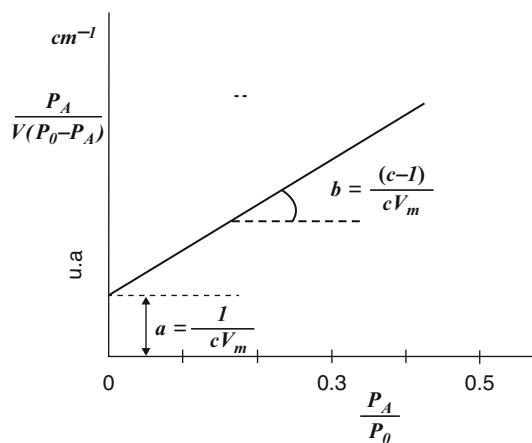
$$\frac{p_A}{V(p_o - p_A)} = \frac{1}{cV_m} + \frac{(c-1)}{cV_m}\frac{p_A}{p_o} \tag{6.18}$$

This represents a linear equation, like $y = ax + b$, plotting in the graph (Fig. 6.2)

$$p_A/V(p_o - p_A)\text{vs.}p_A/p_o.$$

for n experiments.

Fig. 6.2 BET graphical
representation

Supposed a is the angular coefficient and b the linear coefficient, or:

$$a = \frac{1}{cV_m}$$

$$b = \frac{(c-1)}{cV_m}$$

but:

$$c = \frac{1}{aV_m}$$

Thus, substituting c in the expression of b and determining the linear coefficient, we get

$$V_m = \frac{1}{a+b}$$

That is, the inverse of the sum of linear and angular coefficients provides the volume of gas adsorbed as monolayer on the solid.

Therefore, the number of molecules n required to form a monolayer is

$$n = V_m \frac{N_A}{V_M}$$

where

$N_A \equiv$ Number of Avogadro
$V_m \equiv$ Volume of a monolayer at NTP
$V_M \equiv$ Molar volume at NTP

Thus,

$$n = \frac{6.023 \times 10^{23}}{22,400} V_m$$

$$n = 2.68 \times 10^{19} V_m$$

Since the area occupied by a gas molecule is α, then the area occupied by n molecules is the specific area of the solid:

$$S_g = 2.68 \times 10^{19} \ V_m \ \alpha \tag{6.19}$$

The α value is calculated for the N_2 molecule, according to the formula

$$\alpha = 1.09 \left[\frac{M}{\rho N_A} \right]^{2/3}$$

Substituting the values, we get

$$\alpha = 16.25 \times 10^{-16} \ cm^2 = 0.162 \ nm$$

Substituting in Eq. (6.1.22), we obtain

$$S_g = 2.68 \times 10^{19} \times 16.25 \times 10^{-16} \times 10^{-4} \frac{V_m}{m_{cat}}$$

$$S_g = 4.37 \frac{V_m}{m_{cat}} \ \left(\frac{m^2}{g_{cat}} \right) \tag{6.20}$$

These equations are valid for most cases and fall within the isotherms II and IV, but limited at pressures between 0.05 and 0.3, according to Sing et al. [4].

However, the equation is invalid, for instance, for microporous materials and combinations of micro-, meso-, and macropores, such as zeolites, activated charcoals, and several others. Therefore, a new standard isotherm was proposed, known as t-plot. In this case the adsorption isotherms can be represented by a single curve.

The main problem was attributed to capillary condensation phenomenon in the mesoporous solids and the formation of a layer thickness on the surface. These cases were solved using Kelvin's equation, as proposed by Barret, Jayner, and Halenda [8], by developing the BJH method. It allows determining volumes and areas of mesoporous materials, through the distribution of pore radii with increasing pressure. However, Lippens de Boer [9] developed the t-plot method that allows determining the volume of micropores and mesoporous and the outside area.

The pore radius is defined as

$$r = r_K + t \tag{6.21}$$

where t is the thickness near to the wall and r_K is the Kelvin radius.

The Kelvin radius can be calculated from thermodynamics and the following formula was found:

$$r_K = \frac{2\sigma V_M \cos\theta}{RT\ln\left(\frac{P_0}{P}\right)} \tag{6.22}$$

where V_M is the molar volume and θ contact angle with the surface.

Making $\cos\theta = 1$ in the Kelvin equation, we have

$$r_K = \frac{0.414}{\ln\left(\frac{P_0}{P}\right)} \quad (\text{nm}) \tag{6.23}$$

and

$$t = 0.35\left[\frac{5}{\log(P/P_o)}\right]^{1/2} \tag{6.24}$$

The abscissa represents a statistical thickness of multilayers. Values can be calculated as follows:

The number of adsorbed nitrogen molecules on a monolayer of 1 m^2 represents 0.23 cm^3 N$_2$ at standard conditions (STP). Therefore, a solid with an area $A(t)$ has a volume

$$V_m = 0.23 \times A(t) \ \left(\text{cm}^3 \ N_2\right) \tag{6.25}$$

If V_{ads} is the adsorbed volume of N$_2$, then the number of layers formed is statistically $\frac{V_{ads}}{V_m}$. Since the thickness of the layer is equal to 0.354 nm, the thickness corresponding to $\frac{V_{ads}}{V_m}$ layers is as follows:

$$t = \frac{V_{ads}}{V_m} \times 0.354 \ \text{nm} = \frac{V_{ads} \times 0.354}{A(t) \times 0.23}$$

Thus,

$$A(t) = 1.54 \times \frac{V_{ads}}{t \times 0.23} \ (\text{m}^2) \tag{6.26a}$$

Figure 6.3 displays the volume of adsorption V_{ads} as function of t for a nonporous material, according to Eq. (6.24). From the slope we calculate $A(t)$.

In general, for solids, the calculation of $A(t)$ follows the procedure [1]:

- Experimental measurements of the volume of adsorption at 78 K.
- Converting in t-plot, by substituting for each P/P_o the corresponding t value.
- The t values are plotted in the figure and calculated using the following equation:

Fig. 6.3 Graphical representation of the *t*-plot [1].
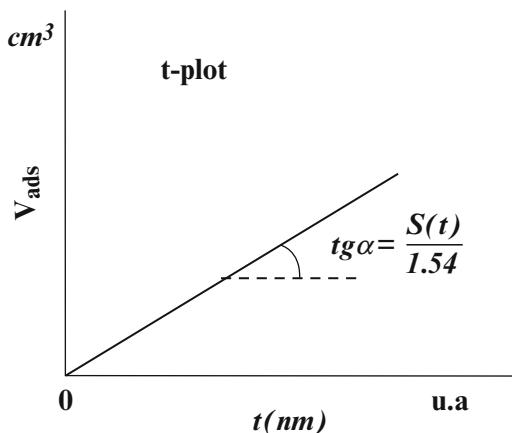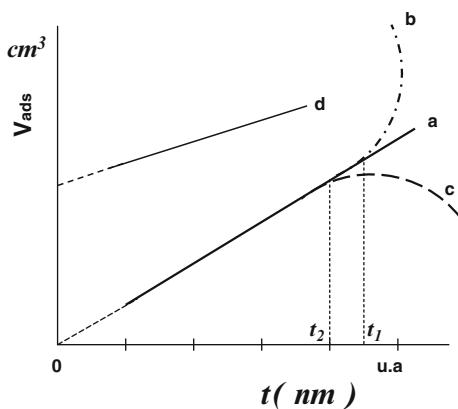
Fig. 6.4 Deviation of the *t*-plot for porous solids [Adapted with permission from Moujijn, J.A., van Leeuwen, P.W.N.M., van Santen, R.A., "Catalysis—Studies Science and Catalysis" vol 79, Ed. Elsevier, Scientific Publishing Company, (1993)]
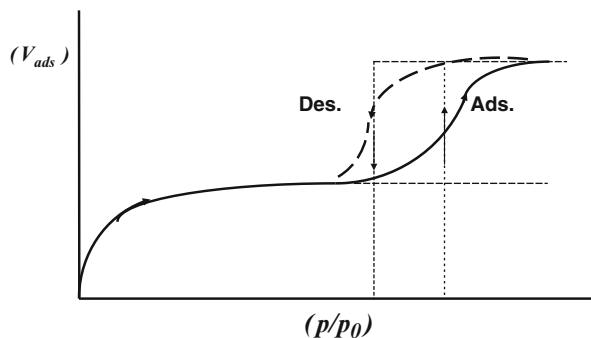
$$t = 0.1 \left[\frac{13.99}{-\log(P/P_o) + 0.034} \right]^{1/2} \tag{6.26b}$$

This equation is valid for relative pressures between 0.1 and 0.8.

In practice, there are deviations, as shown in Fig. 6.4.

The straight line (a) shows the behavior of a porous solid. The curve (b) indicates that above a specific pressure (P/P_o) or above a t_1 value, it grows, indicating higher adsorption volumes than expected, suggesting that above t_1 there is a capillary condensation, besides the adsorption. In contrast, the curve (c) shows that from t_2, there is no more adsorption, suggesting that very small pores, and in the neighbors these pores are covered by multilayered and do not allow more N_2 adsorption.

The straight line (d) is similar as line (a), however, intersects the ordinate at a point corresponding to the volume adsorbed at very low pressures, indicating strong adsorption in the micropores. One can calculate the amount adsorbed in the micropores. Thus, it is possible to calculate the total area $A(t)$ deducting the area of the micropores.

Fig. 6.5 Hysteresis curve

The microporous solids, like zeolites and activated carbon, with sizes of the order of 2 nm, are represented by isotherms of type I. The adsorbed volume is large already at very low pressures, around $P/P_o = 0.05$, showing a strong inclination around 0.15 and reaching a level for $P/P_o = 0.95$. The amount corresponding to this saturation is equal to the volume adsorbed in micropores.

Finally, we should consider the hysteresis phenomenon, as shown in Fig. 6.5. This means that the increase of the capillary condensation occurs on the walls toward the interior of the pore.

As shown, hysteresis occurs during the desorption due to the capillary condensation when $P/P_o = 0.8$ and ends at $P/P_o = 0.64$.

Dubinin–Radushkevich [10] also developed a theory based on the assumption that the surface energy of adsorption varies. Thus, de Dubinin–Radushkevich indicated that the adsorption occurs at low pressures, yet underestimated. The de Dubinin–Radushkevich equation introduces a new relative parameter accounting the energy heterogeneity of the surface.

Based on this assumption, the author suggests the following Eq. (6.27) of the characteristic curve, for any vapor in the adsorption space which is filled and thus the distribution of the volume of the micropores V_{po}:

$$\ln N_A = \ln\left(\frac{V_0}{b}\right) - \frac{BT^2}{\beta^2}\left[\log_{10}\left(\frac{\tau^2 P_c}{P}\right)\right]^2 \tag{6.27}$$

where

N_A = Number of moles of adsorbed gas
V_0 = Volume of micropores (cm^3)
b = van der Waals constant (cm^3/mmol)
$B = \frac{2.303^2 R^2}{k}$ (atm cm^3/gmol K)^2
k = Distribution parameter (solid)
T = Temperature of the isotherm (K)
P = Pressure (mmHg)
β = Affinity coefficient = 0.33 (dimensional)
$\tau = T/T_c$ (nondimensional)

Table 6.1 Surface area and pore volume [11]

Sample	S_{BET} (m^2/g_{cat})	S_{BJH} (m^2/g_{cat})	S_{D-R} (m^2/g_{cat})	V_{BJH} (cm^3/g_{cat})	V_{D-R} (cm^3/g_{cat})	% micropores
Charcoal						
C_V	664	355	755	0.426	0.268	38.6
C_T	651	326	747	0.339	0.265	39.9
C_A	646	336	760	0.403	0.257	38.9

S_{BET} = total surface area estimated by the BET equation
S_{BJH} = surface area estimated by BJH equation
S_{D-R} = surface area estimated by Dubinin–Radushkevich
V_{BJH} = pore volume estimated by BJH
V_{D-R} = pore volume estimated by Dubinin–Radushkevich
% Micropores $= V_{D-R}/(V_{D-R} + V_{BJH})$

Thus, plotting $\left[\log_{10}\left(\frac{r^2 P_c}{P}\right)\right]^2 \times \ln N_A$, we calculate the volume of the micropores (V_{po}) and the distribution parameter (k).

Example Comparing the Methods The N_2 adsorption measures for different coals, virgin (CV), and pretreated by thermal (TC) and chemical (CA) procedures, were obtained, as shown in Table 6.1.

The surface area, pore volume, and pore diameter were calculated using the BHJ method and the Dubinin–Radushkevich equation [10]. So the V_{D-R} relationship/ $(V_{D-R} + V_{BJH})$ can indirectly express the percentage of micropores.

6.1.5 Other Adsorption Models

The main existing models are the Langmuir, Freundlich, and Temkin, previously seen in Chap. 4. Resuming the Langmuir hypotheses:

1. The surface of a solid contains a defined number of sites, z_m, for the adsorption.
2. Each site can only adsorb a molecule.
3. All sites are energetically equivalent, i.e., all have the same enthalpy of adsorption.
4. The adsorption is independent of the presence or absence of adsorbed species in the vicinity, i.e., the enthalpy of adsorption depends on the degree of coverage.
5. At equilibrium, the adsorption rate is equal to the desorption rate.
6. At equilibrium at a certain temperature and pressure, there is a z_A number of adsorbed molecules. The fraction of sites occupied by a molecule A is

$$\theta_A = \frac{z_A}{z_m}.$$

7. At a given temperature, the rate of adsorption of a molecule of a gas depends on the partial pressure of A and the number of empty sites. The desorption rate depends on the number of occupied sites.

The Langmuir model fails [12] because not all sites are equally active and the enthalpy of adsorption depends on the degree of coverage; in other words, the adsorbed molecules interfere with the adsorption of neighboring sites. The finding that the first hypothesis is not true was demonstrated in 1951 by Kummet and Emmet [13].

However, the dependence of the degree of coverage with the heat of adsorption was found by two other models, proposed by Freundlich and Temkin.

Freundlich [14] found experimentally that the degree of coverage varies with the pressure as follows:

$$\theta = kP^{\left(1/n\right)} \tag{6.28}$$

where k and n are constants (>1).

$$\Delta H_{ads} = -A \times \ln\theta \tag{6.29}$$

where θ assumes values between 0.2 and 0.8.

Temkin [14] assumed that the heat of adsorption decreases *linearly* with the surface coverage, i.e.,

$$-\Delta H_{ads} = \Delta H_o(1 - \beta\theta) \tag{6.30}$$

where ΔH_o is the initial enthalpy of adsorption. In this case the surface coverage was determined:

$$\theta = -\frac{RT}{\beta\Delta H_o}\ln(A \times P) \tag{6.31}$$

where A is a constant related to the enthalpy of adsorption.

It is important to stress that although there are limitations on the Langmuir model, it is the simplest but generally the preferred and accepted model in the heterogeneous kinetics.

6.1.6   Chemisorption
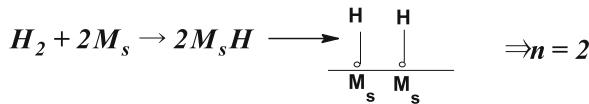
Initially, we must define the active surface sites or accessible surface atoms to molecules. The total number of atoms is different from the number of active surface sites:

- N_s—number of active sites $=$ number of chemisorbed molecules multiplied by n, the stoichiometric factor

$$N_s = \frac{V_{ads}}{V_M} \times \frac{N_A}{m_{cat}} \times n = \frac{V_{(NTP)}}{22,400} \times \frac{6.023 \times 10^{23}}{m_{cat}} \times n \quad \left(^{atoms}/_{g_{cat}}\right) \tag{6.32}$$
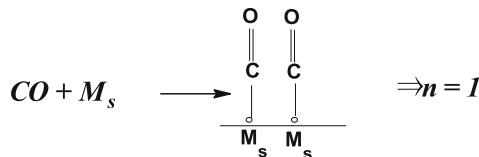
This stoichiometric factor depends on the adsorption form, if dissociated or associated. We have the following cases:

- Dissociative: H_2

$$H_2 + 2M_s \rightarrow 2M_sH \longrightarrow \quad \Rightarrow n = 2$$
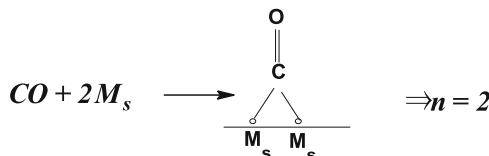
- Associative: CO: linear and bridged

  - Linear:

$$CO + M_s \longrightarrow \quad \Rightarrow n = 1$$

  - Bridged:

$$CO + 2M_s \longrightarrow \quad \Rightarrow n = 2$$
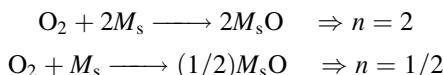
where M_s represents the metallic surface sites.

- Oxygen:

$$O_2 + 2M_s \longrightarrow 2M_sO \quad \Rightarrow n = 2$$
$$O_2 + M_s \longrightarrow (1/2)M_sO \quad \Rightarrow n = 1/2$$
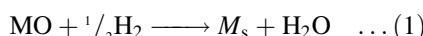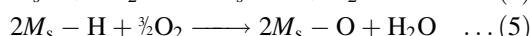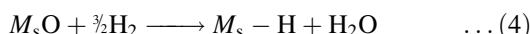
- **By titration O_2 and H_2:**
  This method was proposed by Boudart et al. [15] and consists of adsorbing successively O_2 and H_2 on the surface sites:

- Reduction of metal oxide, chemisorption of H_2, and surface oxidation:

$$MO + {}^1/_2H_2 \longrightarrow M_s + H_2O \quad \ldots (1)$$
$$M_s + \tfrac{1}{2}H_2 \longrightarrow M_s - H \quad \ldots (2)$$
$$M_s + \tfrac{1}{2}O_2 \longrightarrow M_sO \quad \ldots (3)$$

- Titration of the surface at 25 °C:

$$M_sO + \tfrac{3}{2}H_2 \longrightarrow M_s - H + H_2O \quad \ldots (4)$$
$$2M_s - H + \tfrac{3}{2}O_2 \longrightarrow 2M_s - O + H_2O \quad \ldots (5)$$
$$\ldots \ldots$$
$$2M_sO + \tfrac{3}{2}O_2 \longrightarrow 2M_s - O + H_2O \quad \ldots (n)$$

where

MO—metal oxide
M_s—metal surface sites

Let n_H be the number of moles of H_2 adsorbed and n_O the number of moles of oxygen adsorbed.
Thus,

$$(n_H)_n = (n_H)_1 = \ldots\ldots$$
$$(n_O)_n = (n_O)_2 = \ldots\ldots$$

Combining equations (5), (3), and (4) with (2), we have

$$(n_O)_n = 1.5(n_O)_2$$
$$(n_O)_n = 3(n_{H_2})_2$$

Thus,

$$\frac{(n_H)_n}{(n_O)_n} = 3$$

This means that we need three hydrogen atoms for titration of the oxygen at the surface.

6.1.7   Calculation of Metal Surface Area, Dispersion, and Particle Diameter

The metal surface can be calculated through the following formula [14, 16]:

$$S'_m = \frac{N_s}{[L]}$$

where $[L]$ is the maximum site density or metal surface atoms per m^2.
   The density depends on the crystal face and plans, and for the metals, it is tabulated:

Cupper $[L] = 1.7 \times 10^{19}$ atoms/m^2
Iridium $[L] = 1.35 \times 10^{19}$ atoms/m^2
Platinum $[L] = 0.96 \times 10^{19}$ atoms/m^2

   It is important to include the metal content, and thus,

$$S_m = \frac{N_s}{y \times [L]} \quad \left(m^2/g_{metal}\right) \tag{6.33}$$

where N_s is given in Eq. (6.1.31).

The dispersion can be calculated, according to the definition

$$D(\%) = \frac{\text{number of accessible atoms}}{\text{number of total atoms}} \times 100$$

or

$$D(\%) = \frac{N_s}{N_t} \times 100 \qquad (6.34)$$

where N_s is given in Eq. (6.32); thus,

$$N_t = n_t \times N_A = \frac{y \cdot m_{\text{cat}}}{M} \times N_A \qquad (6.35)$$

and

n_t—number of total atoms, N_A—Avogadro's number, m_{cat}—mass of catalyst (g) M—molecular weight, and y—mass fraction of supported metal.
Calculate the particle diameters considering

$$d_p = f \times \frac{V_{\text{solid}}}{S_m}$$

where factor f depends on the geometry, with $f = 6$ for a spherical geometry and $f = 4$ for a cylindrical geometry:

$$d_p = f \times \frac{y m_{\text{cat}}}{\rho_{\text{metal}} S_m (m^2)} \times 10^{-4} \ (m) \qquad (6.36)$$

Or from the dispersion,

$$d_p = \frac{f}{D} \ (nm)$$

Fo Pd, Ir, $d_p = \frac{0.9}{D}$ (nm)
For Ni, $d_p = \frac{101.2}{D}$ (nm)

Example 1 Calculate the metal area, dispersion, and the particle diameter of the catalyst Ir / Al$_2$O$_3$. We measured the total volume adsorbed H$_2$ at standard conditions, $V_{\text{H}_2} = 1.225 \ cm^3$. It is known that $[L] = 1.15 \times 10^{19}$ atoms/m^2. The mass of the sample was 1 g and the concentration of Ir is equal to 2.8 %.

From Eq. (6.32) we have

$$N_s = \frac{V_{(CNTP)}}{22,400} \times \frac{6.023 \times 10^{23}}{m_{cat}} \times n$$

$$= \frac{1.225}{22,400} \times \frac{6.023 \times 10^{23}}{1} \times 2 = 6.73 \times 10^{19} \ \ (atoms/g)$$

Thus, the metal area from Eq. (6.33):

$$S_m = \frac{N_s}{y \times [L]} = \frac{6.73 \times 10^{19}}{1 \times (0.028) \times 1.5 \times 10^{19}} = 209 \ \ (m^2/g_{metal})$$

Calculating the dispersion from Eqs. (6.34) and (6.35),

$$D = \frac{6.73 \times 10^{19}}{1 \times (0.028/192) \times 6.023 \times 10^{23}} = 0.766 = 76.6 \ \%$$

Calculating the particle diameter:

$$d_p = \frac{0.9}{D} \ \ nm = \frac{0.9}{0.766} = 1.17 \ \ nm$$

Example 2: Comparing the Methods A comparison of the adsorption by chemisorption of H_2, CO, or titration methods depends not only on metal but also of interaction of the metal with support. Without the influence of the support, the dispersion values should be equivalent, assuming the same stoichiometry. The difference is attributed to the stoichiometry, especially for the adsorption of CO.

The H_2 chemisorption and O_2 titration were performed for a Pt/Al_2O_3 catalyst, without the influence of the support. For comparison the results are presented in Table 6.2 [17].

The results show high dispersion (100 %) for the same Pt concentration. Further, both the adsorption with H_2 and titration H_2/O_2 confirm the same stoichiometry.

Table 6.2 Chemisorption on Pt/Al_2O_3

Catalyst	H_2[a] (μmoles/g_{cat})	H/Pt[b]	Titration[c] (μmoles/g_{cat})
0.7 % Pt/Al_2O_3	20.4	1.1	60.1
0.9 % Pt/Al_2O_3	21.4	1.0	52.0

[a]Irreversible a 300 K
[b]Dispersion
[c]Titration—H_2 (irreversible) and titration with He/O_2

Table 6.3 Hydrogen chemisorption

		(μmoles H_2/mgPd)	Ratio Q_{H2}	T_{red}573 K	T_{red}773 K
Catalyst	$T_{red} = 573$ K	$T_{red} = 773$ K	573/773 K	D (%)	D (%)
Pd	2.41	2.35	1.03	51.36	50.07

Q : H_2, chemisorption; D, dispersion

Table 6.4 Titration $O_2 - H_2$ of Pd catalyst reduced at different temperatures

	O_2/H_2 (μmoles H_2/mgPd)	O_2/H_2 (μmoles H_2/mgPd)	Dispersion (%)	Ratio Tit/Q_{H2}	Dispersion 773 K (%)	Ratio
Catalyst	$T_{red} = 573$ K	$T_{red} = 773$ K	$T_{red} = 573$ K		$T_{red} = 773$ K	Tit/Q_{H2}
Pd	7.52	5.75	46	2.71	41	2.45

Table 6.5 Irreversible H_2 and CO adsorptions (μmoles/gcat) after reduction at 300 and 500 °C

	H_2	H_2	D (%)	D (%)	CO	CO	CO/H	CO/H	d_p (nm)
Catalyst T_{red}(° C)	300	500	300	500	300	500	300	500	500
PtAl	19.0	22.3	74	87	27.3	35.7	1.44	1.60	1.3
PtZr	14.6	8.8	57	34	57.1	60.9	3.92	6.92	3.3

[a]Based on experimental Pt content (AA)
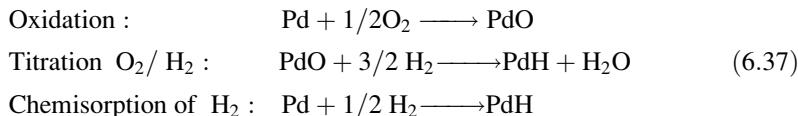
Comparative chemisorptions were performed for a catalyst Pd/Al$_2$O$_3$ (1 % Pd), reduced at different temperatures, as presented in Table 6.3. The stoichiometry was $H/Pd_s = 1$.

Note worth is that the ratio of hydrogen chemisorption on catalyst reduced at 573 and 773 K is approximately similar, which suggests that the reduction temperature didn't affect the dispersion of this catalyst.

The results of the O_2/H_2titration method are presented in Table 6.4.

The dispersion values for the palladium catalyst determined by titration at temperatures of reduction at 573 and 773 K are close to the values obtained by H_2chemisorption. The difference is about 15 % and can be attributed to experimental error.

The ratios between the moles of H_2 adsorbed in during the titration O_2/H_2 and H_2 chemisorbed on the Pd catalyst were approximately equal the value corresponding to stoichiometry of the reactions in Eq. (6.37), which indicates that the H_2 adsorbed by titration is three times greater than the H_2 adsorbed by chemisorption:

$$\text{Oxidation}: \quad\quad Pd + 1/2O_2 \longrightarrow PdO$$
$$\text{Titration } O_2/ H_2: \quad PdO + 3/2 H_2 \longrightarrow PdH + H_2O \quad\quad (6.37)$$
$$\text{Chemisorption of } H_2: \quad Pd + 1/2 H_2 \longrightarrow PdH$$

Example 3: *H_2 and CO Chemisorption* H_2 and CO adsorption on the Pt/Al$_2$O$_3$, and Pt/ZrO$_2$ catalysts, after reduction at 300 and 500 °C, are shown in Table 6.5 [18].

The dispersion was calculated from the H_2 chemisorption, assuming linear stoichiometry (H / Pt_s = 1). However, CO may interact with the zirconia support and platinum and at the same time with Pt–ZrO_2 interface. The dispersion was estimated from the mean diameter of platinum particles (d_p), assuming spherical particles, and using the following formula [19]:

$$d_p = \frac{113}{D(\%)} \text{ nm}$$

The PtAl catalyst exhibits high dispersion after reduction at 500 °C [18]. After reduction at 300 °C, the H_2 chemisorption diminished, which can be associated with incomplete reduction of platinum. The CO chemisorption also decreases after reduction at 300 °C.

The PtZr catalyst showed lower dispersion, especially after reduction at 500 °C. This result may be related not only to the low specific area of zirconia but also to the partial coverage of platinum, due to the migration of reduced zirconium species on Pt, when compared to the H_2 adsorption at a reduction temperature of 300 °C. However, the CO adsorption was not influenced by the reduction temperature.

The difference of CO/H_2 molar ratio for the PtAl catalyst can be explained by the fact that the CO adsorption may occur in the linear (CO/H_2 = 2) or bridged forms (CO/H_2 = 1) or both. For the PtZr catalyst, the high CO/H_2 ratio cannot be justified solely by this argument. It is clear that the zirconia is able to modify the nature of the Pt–CO interaction, due to the interaction itself of the support with platinum. Since the amount of CO adsorbed on pure zirconia is extremely small, it can be stated that the CO interacts with the Pt–ZrOx interface.

Example 4: Experimental Measurements by N_2 Adsorption (BET) and H_2 Chemisorption (Metallic Area) The adsorption measurements are essential for the determination of total and metal areas, volumes, and dispersions. Of course, experimental methods can be classified into static and dynamic. There are commercial devices (ASAP) that measure the isotherms allowing to calculate all parameters mentioned above. We intend here to illustrate an experiment.

Volumetric Method

The method is known as static volumetric method, where measurements are made in a temperature-controlled unit.

We calculate the initial moles using the equation:

$$n_{01} = \frac{P_1 V_2}{RT}.$$

Then the moles at equilibrium:

$$n_{01}^{'} = \frac{P_1(V_1 + V_2)}{RT} \tag{6.38}$$

Thus the moles adsorbed for the first experiment is
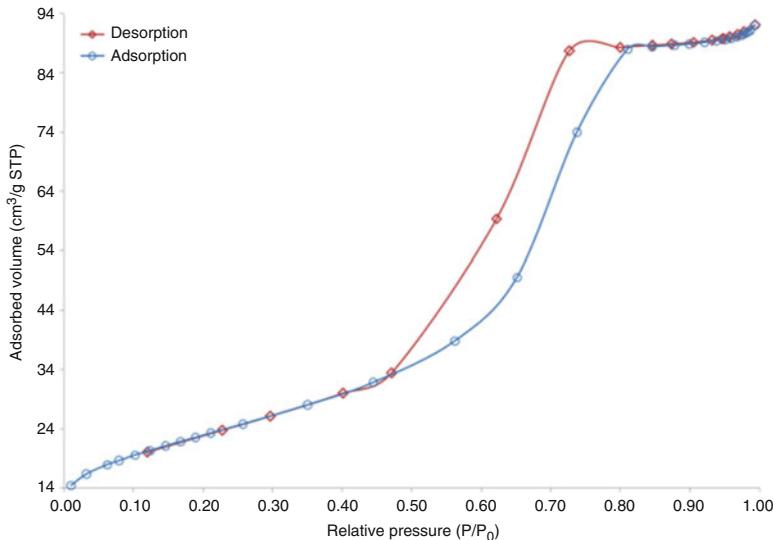
Fig. 6.6 Total and reversible adsorption—BET method
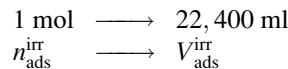
$$n_{ads}^1 = n_{01} - n_{01}' \tag{6.39}$$

And successively varying the pressure and measuring the volume.

The moles adsorbed irreversibly are

$$n_{ads}^{irr} = n_{ads}^{total} - n_{ads}^{reversible} \tag{6.40}$$

Determination of V_{ads}^{irr}, as plotted in the figures:

$$1 \text{ mol} \longrightarrow 22,400 \text{ ml}$$
$$n_{ads}^{irr} \longrightarrow V_{ads}^{irr}$$

Results are plotted in Fig. 6.6 as shown below.

Figure 6.6 illustrates the isotherm of adsorption–desorption and the distribution of pores for CeO_2 calcined at 500 °C, which were obtained from the nitrogen adsorption, using the BET method. The curve of adsorption–desorption (hysteresis loop) features is characteristic of type IV. Typical adsorbed mesoporous with strong and weak affinity and size of pores between 2 and 50 nm, indicating formation of cylindrical pores open and closed with narrowing, resulting in an irregular morphology of the "bottle."

Figure 6.7 shows the isotherm of H_2chemisorption of a 5 % Co/Al_2O_3 catalyst, indicating the Langmuir type I isotherm, forming a complete monolayer [17].
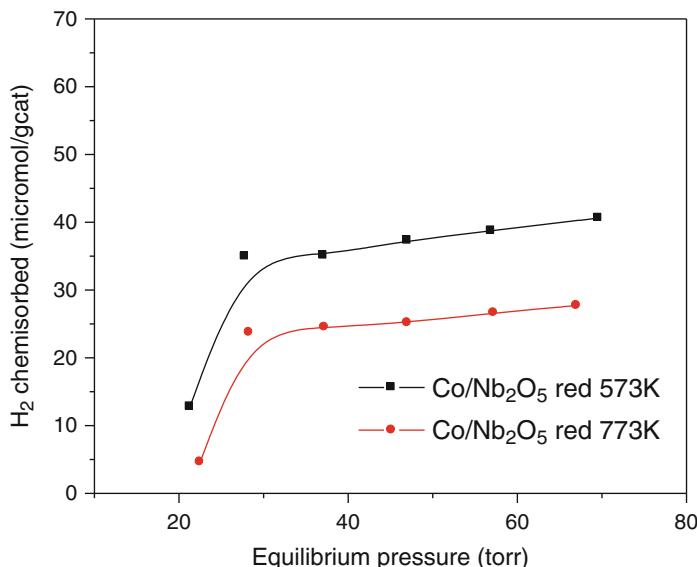
Fig. 6.7 Hydrogen chemisorption

6.2   Part II: Thermal-Programmed Methods

6.2.1   Introduction

These methods are significant in applied chemical processes, serving as basis for defining the process conditions, but also in basic studies. There are three main approaches.

First, the phenomena occurring on the surfaces, the adsorption, desorption, and the surface reactions, are fundamental for determining the kinetics and mechanisms of the reactions in chemical processes. It is also a way to identify active sites and determine the nature and strengths of adsorption–desorption on surfaces.

Second, one needs to know the structure of the catalyst, the oxidation states, and the interaction between the metal and the support, besides the degree of reduction or oxidation of oxides or metals, respectively. Finally, for the activation process of the catalysts, gases, such as H_2, O_2, CO, and CH_4, or other molecules, like H_2S and CS_2, are used for sulfidation. These techniques with temperature programming allow predicting the conditions used in an industrial process.

Third, by using these techniques, determine the conditions for the decomposition of the precursors during the preparation of the catalyst and the identification of coke, poisons, or impurities after reaction, in addition to the possibility of removing these compounds.

The programmed temperature techniques may be performed by gravimetric and volumetric methods, which will be treated in the following order of subitems:

- *Temperature programmed desorption (TPD)*
- *Temperature programmed reduction (TPR)*
- *Temperature programmed oxidation (TPO)*
- *Differential scanning calorimetry (DSC)*
- *Thermogravimetric and thermo-differential (TG-DT)*
- *Activation processes–reduction and sulfidation*
- *Temperature programmed surface reaction (TPSR)*

These methods provide qualitative results, predicting pre- and post-treatment conditions, but also quantitative results, giving basic information about the kinetic parameters and reaction mechanisms. There are kinetic models for the different cases and we will see some specific models.

They are also significant for determining bulk and particularly surface properties, namely, surface sites, such as metallic and acid–base sites. However, these are still complementary to spectroscopic methods, as we shall see in another chapter.

These processes depend on a number of other parameters, such as concentration of gases, initial temperature, mass of catalyst, active phases, and of the thermodynamic. The choice of conditions is not trivial and currently there are methods of experimental design for selecting the most important variables.

6.2.2   Apparatus

Currently, there are all types of commercial equipment's that perform simultaneously all procedures; however, the basic principles are schematized below (Figs. 6.8 and 6.9):
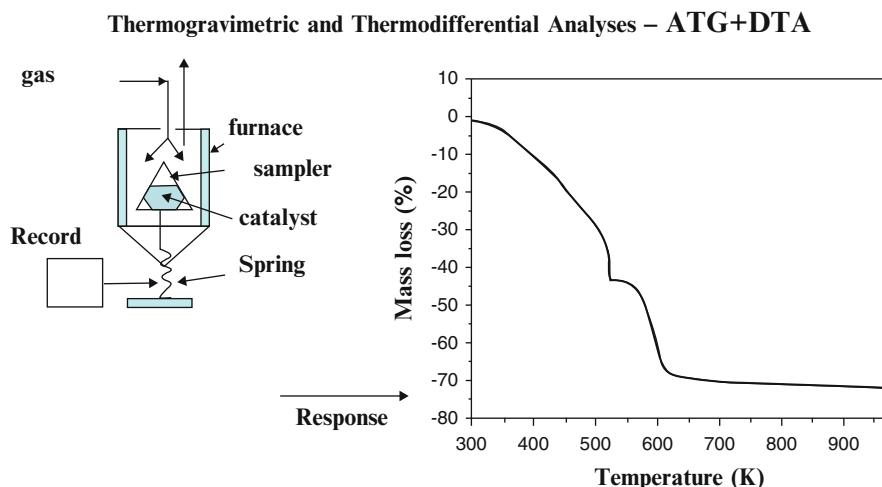
Fig. 6.8 Schematic thermogravimetric and thermo-differential methods
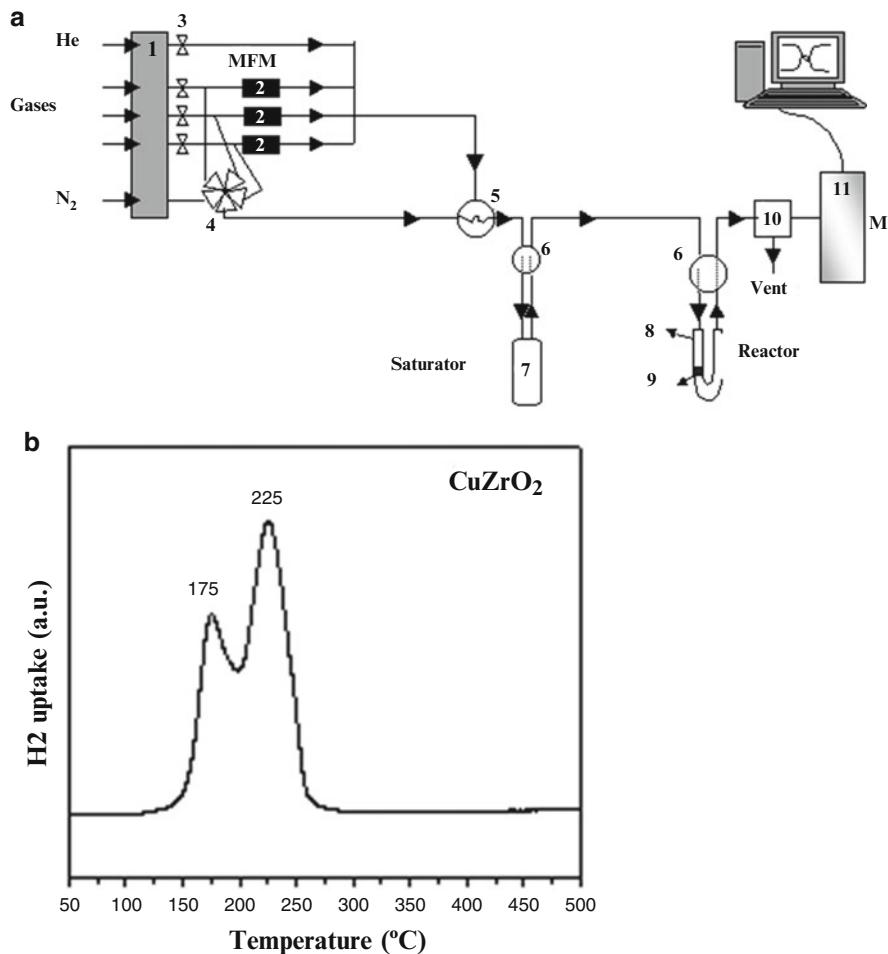
Fig. 6.9 (**a**)- Multipurpose unit; (**b**) –TPR - reduction profile of CuZrO$_2$

6.2.3 Quantitative Analyses

A quantitative analysis is necessary for calculating surface sites, degree of reduction, or oxidation, or the amount of gas uptake or desorption during the temperature programming processes. Calculations are presented later.

6.2.3.1 Experimental Planning Design

This technique involves a number of variables that must be selected to find the parameters that best represent the phenomena. However, to date, experiments are done without a more detailed analysis and only after many experiences are defined
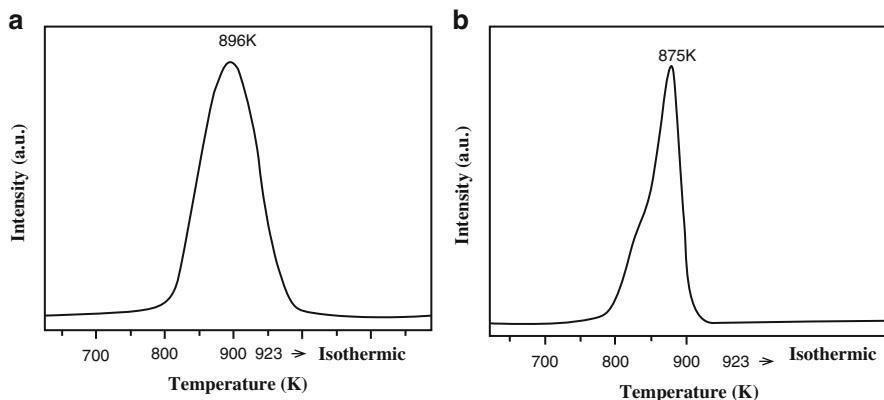
Fig. 6.10 (**a**, **b**) *mass/ratio cat/PM* 95:1, *rate*, 20 K/min, (**a**) *Flow rate* 5 ml/min (**b**) *Flow rate 11* 5 ml/min

the variables. This requires time, material, and cost. In the measurements of TPD, TPR, and TPO, the choice of variables is critical, and misuse affects the interpretation of experimental results. Experimental results of TPR and of TPO showed that depending on the flow rate, mass, and the heating rate, the corresponding maximum peak temperature is shifted, and the profiles may change. Figure 6.10 shows an example of carbon particulate combustion experiments, varying only the flow rate of the reaction mixture containing oxygen [20].

We observe that the maximum temperature peak varied and the profiles changed, varying the gas flow rate, keeping the other variables constant.

Therefore, the knowledge of the experimental precision is critical for all parameter estimation procedures, and the design of experiments is an important tool for selecting these parameters.

The essence of good planning is to design an experiment so that it is able to provide exactly the type of information sought. To do this, one must define the aim of such trials and thus choose the most suitable technique. At first, in a situation of lack of knowledge about the system to be studied, one must make a screening of the variables that exist in this system; the most advisable would be to conduct experiments to follow a full factorial design [21].

In general, the system can be represented by a function, which is in principle unknown, but one knows that it connects the factors (input variables) and responses (output variables). When we want to know whether certain factors have any influence on the response, but not known how to describe very precisely this possible influence, the minimum requirement is the factorial design. This type of planning is very simple to perform.

In addition to the experiments determined by planning, one should estimate the error to be able to assess whether there are significant effects on the system that can be attributed to the factors. With this in mind, it should be noted the standard deviation. An assumption is reasonable for most cases, but should always be assessed; it is assumed that the experimental error is the same for all experiments. An example is shown in practice.

6.2.4 Temperature Programmed Desorption

This technique serves to determine the surface properties of the catalyst and determine qualitatively and quantitatively the irreversibly adsorbed molecules at the surface of a porous or nonporous solid or even of crystals or models. It allows us to observe the influence of these parameters on the adsorption of the molecules and on the kinetics of the process. It is also useful to verify the formation of intermediate molecular states, which are difficult to identify. A general scheme is shown in Fig. 6.11.

The system is a multipurpose unit, coupled to a mass spectrometer. The temperature rises from the room up to a final temperature at a specific heating rate. It identifies and measures the volume of desorption of molecules with increasing temperature. If properly calibrated, their compositions or mole fractions can be calculated. One obtains a profile which is the desorption rate of the molecules as a function of temperature. From this profile it is possible to determine the surface sites, assuming that one molecule adsorbs on one surface site, which is proportional to the strength of adsorption varying with the temperature.

The choice depends on the type of molecules and strength or interaction with the surface sites. Carbon monoxide (CO) and hydrogen (H_2) are the most often used but also NO, N_2O, ethanol, and methanol. It gives us information about the dispersion of surface active sites, the nature and morphology of the metal sites, as well as metal–support interactions. The desorption profiles may be accompanied by several other profiles of products formed during the desorption.

The TPD profiles do not represent multiple adsorbed states on the surface, but multiple kinetic processes during the desorption. So the kinetics of the desorption process on a surface solid is important and was presented the first time by Redhead [22] and later expanded by Anderson and Boudart [14] and Masel [23].
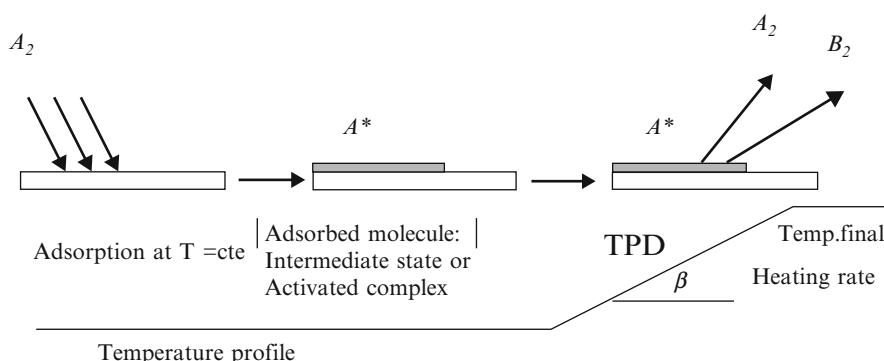
Fig. 6.11 Scheme of adsorption–desorption of molecules

6.2.4.1 Kinetic Models

Redhead [22] proposed a simple kinetic model of n order for the desorption rate. It should be noted that this model is based on Langmuir's model. Thus, the desorption rate is as follows:

$$r_d = -N_s \frac{d\theta_A}{dt} = k_0 \theta_A^n \times \exp\left(-\frac{E_A}{RT}\right) \qquad (6.41)$$

where

r_d—desorption rate of A (molecules/cm^2)
N_s—concentration of sites (number/cm^2)
θ_A—fraction of surface coverage of specie A
n—desorption order
k_0—pre-exponential factor
E_A—activation energy of desorption

Assuming that the temperature varies linearly with time,

$$T = T_0 + \beta t \qquad (6.42)$$

where

T_0—initial temperature
β—heating rate

Combining both, we have

$$\frac{r_d}{N_s \beta} = -\frac{d\theta_A}{dT} = \frac{k_0}{\beta} \theta_A^n \times \exp\left(-\frac{E_A}{RT}\right) \qquad (6.43)$$

Therefore, the desorption of A can be determined experimentally and directly from TPD desorption curves. Figure 6.12 shows the desorption profiles, the surface fraction coverage, and the desorption rate, varying with the temperature, calculated from Eq. (6.43) [23].

The desorption profile follows a Gaussian type curve. At low temperatures the desorption rate is small, but when temperature raises the rate increases exponentially. However, the thermodesorption process is not stationary. At the beginning, the surface coverage is high, and with increasing temperature, the molecules desorb and the surface coverage diminishes. The desorption reaches the maximum at a temperature T. However, the surface fraction is still sufficient to desorb all molecules. Moreover, the desorption rate increases exponentially.

The desorption rate depends on the desorption order n. Integration of Eq. (6.43), for different orders (n), assuming the initial coverage θ_0 is the same, shows different profiles, as displayed in Fig. 6.13. Note that for $n = 1$, the curves are asymmetrical, but the maximum peak is the same, independent of the initial coverage. However,

Fig. 6.12 TPD profiles, surface coverage, and rate as function temperature [Reproduced with permission from R.I. Masel, "Principles of Adsorption and Reaction on Solid Surfaces", John Wiley & Sons (1996). Masel, p. 510]
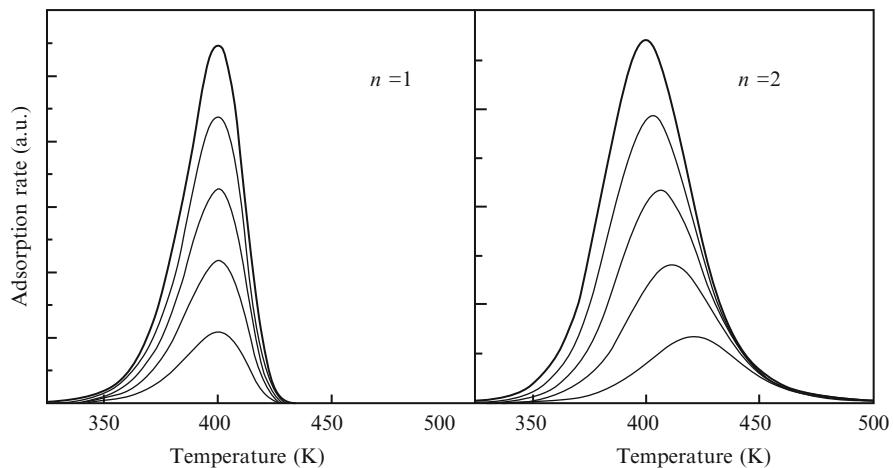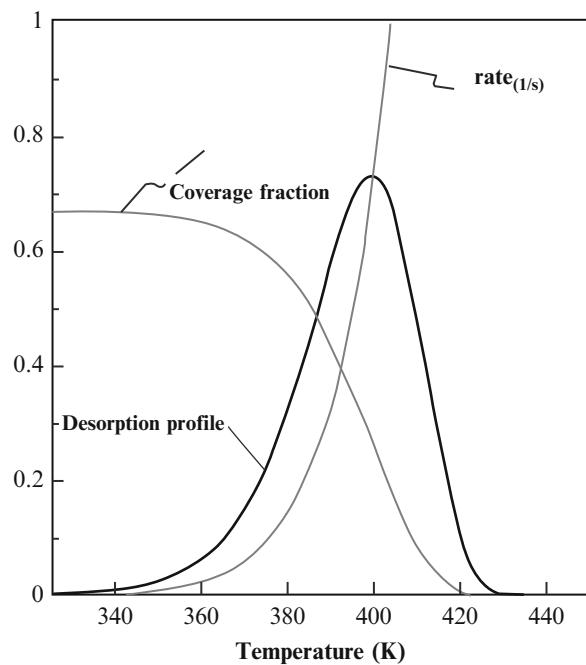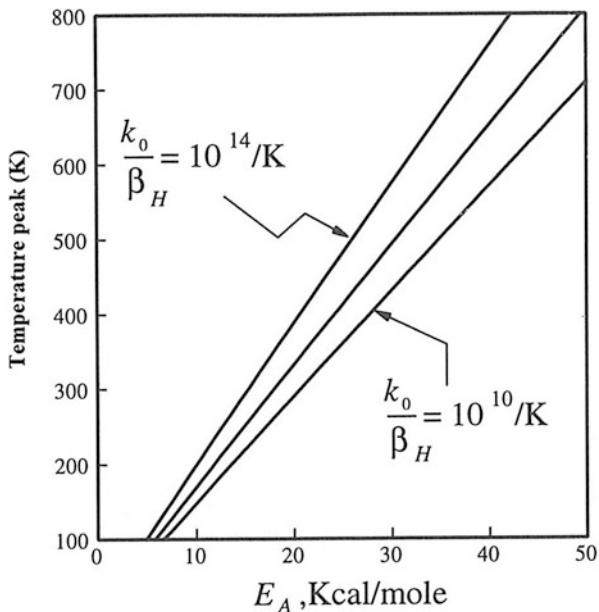
Fig. 6.13 TPD profiles—effect of desorption order [Reproduced with permission from R.I. Masel, "Principles of Adsorption and Reaction on Solid Surfaces", John Wiley & Sons (1996), 511]

for a different orders ($n = 2$), the curves are symmetrical, and the maximum peaks depend of the initial coverage θ_0.

The activation energy and pre-exponential factor may influence the desorption rate, as shown in Fig. 6.14. Note that when the activation energy is high, the peak moves toward higher temperatures. With increasing heating rate, peaks are shifted

Fig. 6.14 Maximum temperature desorption [Reproduced with permission from R.I. Masel, "Principles of Adsorption and Reaction on Solid Surfaces", John Wiley & Sons (1996). Masel, 510]

toward higher temperatures, but if the pre-exponential factor increases, the peaks are shifted toward lower temperatures. Calculations show that the maximum peak occurs when the desorption constant is of the order of 0.5 s^{-1} and the rate is 0.5 monolayer(s). This maximum can be calculated when:

$$\frac{dr_{\mathrm{a}}}{dT} = 0 \qquad (6.44)$$

Substituting Eq. (6.43) in Eq. (6.44) and differentiating, we obtain after rearrangement [23]:

$$\frac{E_{\mathrm{A}}}{RT_{\mathrm{m}}} = \ln\left(\frac{k_0 T_{\mathrm{m}} n}{\beta} \theta_{\mathrm{m}}^{n-1}\right) - \ln\left(-\frac{E_{\mathrm{A}}}{RT_{\mathrm{m}}}\right) \qquad (6.45)$$

where

T_{m}—maximum peak temperature
θ_{m}—fraction coverage for maximum temperature peak

Note that for $n = 1$, the coverage θ is null. When $n = 2$, it becomes $\theta_{\mathrm{m}} = \frac{\theta_0}{2}$.

We can calculate the desorption activation energy using Eq. (6.45). This calculation is iterative. Thus, by approximation we have

$$E_{\mathrm{A}} = 0.06 \; T_{\mathrm{m}} \qquad (6.46)$$
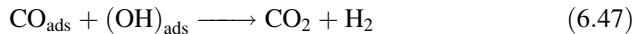
Unit is given by kcal/(moles K).

Figure 6.14 shows the maximum temperature peak varying with the activation energy and for different heating rates.

For low temperatures, around 100 K, the activation energies are low increasing gradually with temperature. These results were calculated for low pre-exponential factor k_0.

6.2.4.2 Deviation from the Ideal Behavior

The real kinetic profiles are quite different and exhibit more than one peak at different temperatures, which represent different intermediate steps. Thus, there are changes on the surface coverages, and previous models are not anymore valid, as for example, for the reaction:

$$CO_{ads} + (OH)_{ads} \longrightarrow CO_2 + H_2 \tag{6.47}$$

Another model was suggested by Taylor and Weinberg [24], which relates the activation energy of desorption with the enthalpy of adsorption and assuming reversibility. Under these conditions we have a relationship between the adsorption and desorption constants with the equilibrium constant, varying only with temperature:

$$K = \frac{k_A}{k_A'} \tag{6.48}$$

where

k_A—adsorption constant: $k_A = k_{A0}e^{-(E_A/RT)}$ (6.49)

k_A'—desorption constant: $k_A' = k_{A0}'e^{-\left(E_A'/RT\right)}$ (6.50)

K—equilibrium constant ads-des.: $K = K_o e^{(\Delta H_A/RT)}$ (6.51)

E_A—activation energy of adsorption

E_A'—activation energy of desorption

ΔH_A—enthalpy of adsorption

Substituting Eqs. (6.49) and (6.50) in Eq. (6.48) and after logarithm transformation, we have

$$\Delta H_A = E_A - E_A' \tag{6.52}$$

Assuming that the activation energy of adsorption is negligible,

$$E_A = 0$$

We get

$$\Delta H_A = -E_A' \tag{6.53}$$

Thus, the activation energy of desorption is directly related to the enthalpy of adsorption–desorption, which can be determined from TPD experiments. Since the enthalpy varies with the surface coverage, then the desorption energy also varies. Experimentally it was found that this activation energy does not varies even up to $\theta = 0.5$. One can thus admit that it is constant.

The TPD technique is appropriate for determining active sites and acid–base sites, when the system is coupled to a mass spectrometer. We will see some specific cases.

6.2.4.3   Qualitative Analyses and Interpretation of Experimental Data

- *TPD of NO*
  The Cu/ZSM5 catalyst exhibits excellent selectivity for NO decomposition, one of the major environmental problems of interest. The catalyst consists of a zeolite $(SAR = 26)$ where copper was introduced by ion exchange at a ratio $Cu/Al = 0.498$, i.e., 100 % exchange in the form of Cu^{2+} [25]. TPD profiles of NO are shown in Fig. 6.15.
  Figure 6.15 shows single peak of NO desorption at 416 K with the simultaneous formation of N_2 and N_2O at 560 K. The NO conversion was 78.5 %, and the selectivity of N_2 and N_2O was 78.1 and 21.9 %, respectively.
- *TPD of CO*
  TPD profiles of CO on Pt/Al$_2$O$_3$ and Au/ Al$_2$O$_3$ are displayed in Figs. 6.16 and 6.17 showing product profiles due to the CO decomposition at the surface at different temperatures [26].
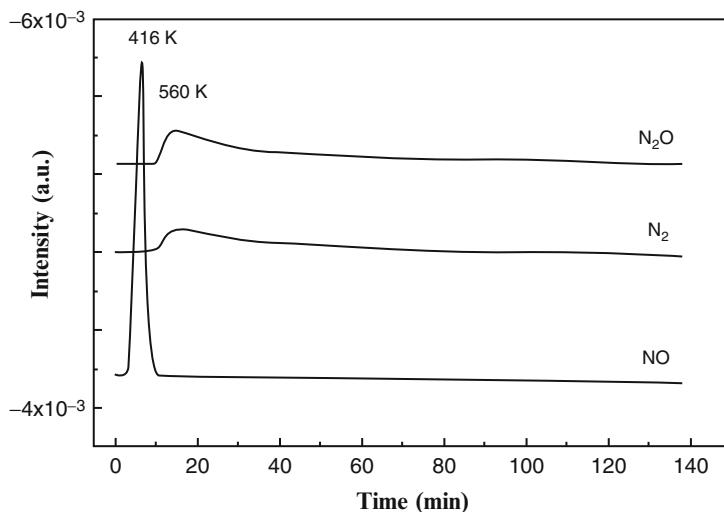
Fig. 6.15   TPD of NO on Cu/ZSM5
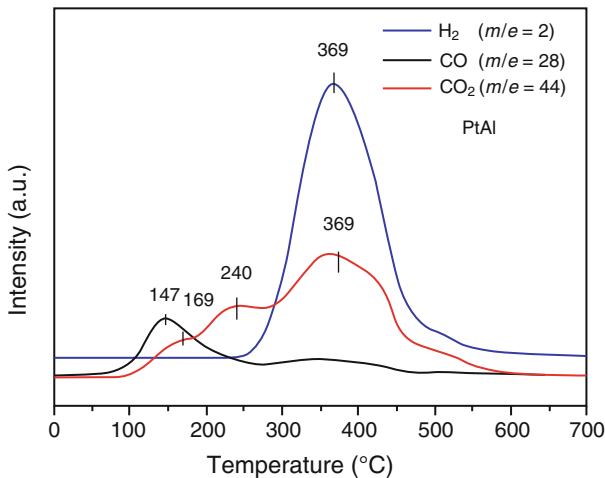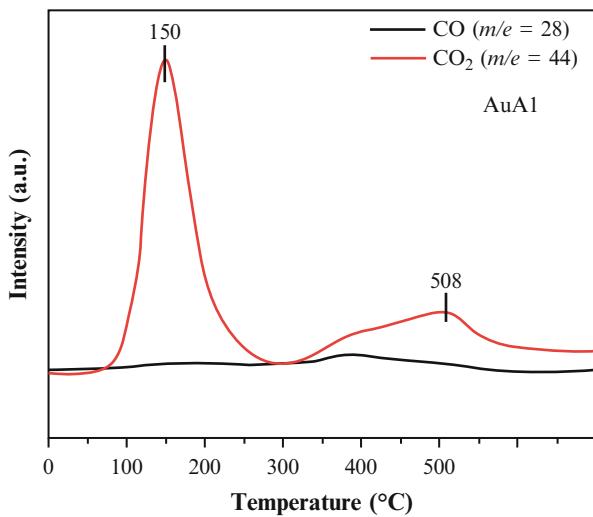
Fig. 6.16 TPD of CO on Pt/Al$_2$O$_3$

Fig. 6.17 TPD de CO on Au/Al$_2$O$_3$

We observe the formation of H$_2$ and CO$_2$ due to the decomposition reaction. The low temperature peak indicates lower energy barrier, while for higher temperature it has higher energetic barrier during the desorption process [27].

The formation of CO$_2$ is attributed to the disproportionation reaction of carbon monoxide. The CO desorption is significant on platinum sites, and the disproportionation reaction is low. The CO$_2$ formation occurs simultaneously with the formation of H$_2$ at higher temperature (~ 370 °C). Aranda and Schmal [28] suggested that adsorbed CO leads to the formation of formate species which decomposes at high temperatures. The adsorbed CO on platinum may react with
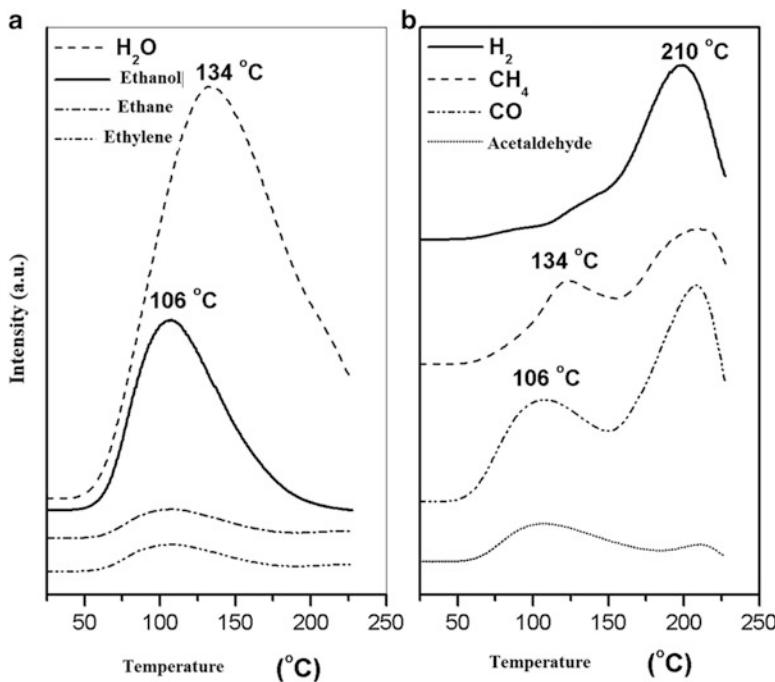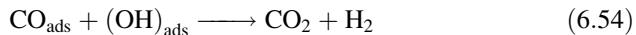
Fig. 6.18 TPD of ethanol on Pt/Al$_2$O$_3$ (a, b)

the surface hydroxyls of the support. This mechanism can be described as the water gas shift reaction, according to Eq. (6.2.14):

$$CO_{ads} + (OH)_{ads} \longrightarrow CO_2 + H_2 \tag{6.54}$$

- *TPD of ethanol*
  The TPD profiles of ethanol on the supported Pt/Al$_2$O$_3$ are shown in Fig. 6.18a, b [29].
  We observe that besides the ethanol desorption profile (a), there are other profiles related to the formation of water, acetaldehyde, hydrogen, CO, and methane at different temperature ranges (Fig. 6.18b). This suggests dehydrogenation and decomposition reactions of ethanol. Dehydrogenation and decomposition reactions occur on the metallic sites while dehydration on the support [30].
- *TPD of ammonia and* CO$_2$
  This analysis aims to evaluate the interaction and the adsorption force between the molecule and the surface of the catalyst [31, 32]. The acidic and basic properties of the catalysts may be determined by temperature programmed desorption of NH$_3$ and CO$_2$, respectively. Figure 6.19 displays the TPD profile of CO$_2$ on modified zirconia [33].
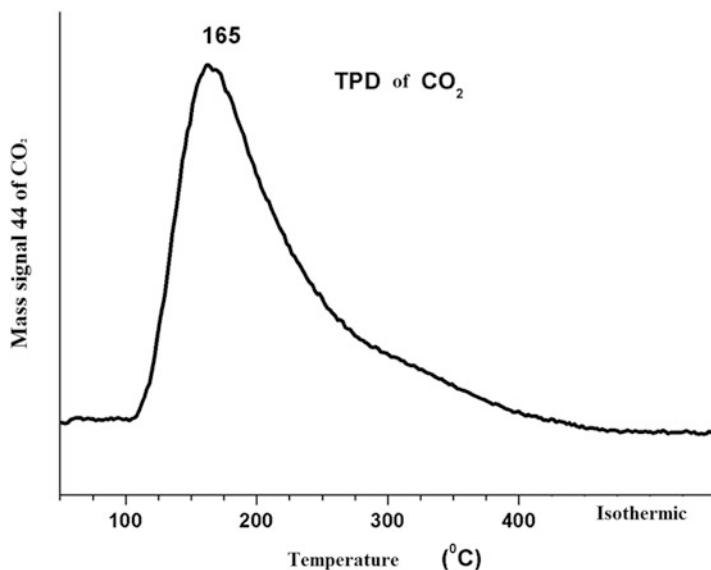
Fig. 6.19 TPD of CO_2 on modified zirconia [33]

Table 6.6 Quantitative results of acid and base sites

Sample	Acidity (µmol/g)	Basicity (µmol/g)
ZrSTBas	126	139
ZrSTAci	57	79

The quantitative results in Table 6.6 present the amounts of acid sites, as measured by the desorption of NH_3 (not shown), and of the base sites (CO_2) on the modified zirconia.

The ratio of acid–base sites is 0.9 on the ZrSTBas sample, while on the ZrSTAci sample, it is 0.72. Furthermore, it was found that the sample ZrSTBas presented higher amount of acidic sites, i.e., 2.2 times larger than the ZrSTAci oxide.

6.2.5   Temperature Programmed Reduction

A common method used in the characterization of catalysts is the temperature programmed reduction. This method consists in passing a reducing gas (usually H_2 diluted in an inert) with increasing programmed temperature. The reduction rate can be determined by the H_2 consumption needed for the reduction of the oxide to a metal or to some intermediate phase, by measuring continuously the unreacted H_2 in the exit gas. The reduction depends on the composition and structure of the reducible oxide and can be identified by one or more peaks at different temperatures. The results provide also information about the reduction of bimetals, oxidation state, and the interaction between the metal oxide and the support, besides the
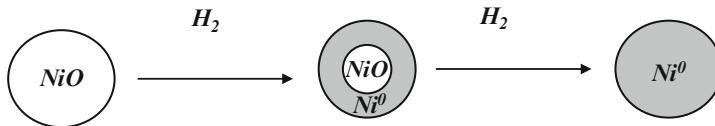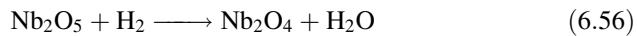
Fig. 6.20 Scheme of reduction of oxides

formation of alloys and, more importantly, the kinetics of reduction for different parameters. The profiles indicate the maximum temperature reduction peak and the amount of hydrogen consumption.

Thus, for example, (Fig. 6.20):

$$NiO + H_2 \longrightarrow Ni^0 + H_2O \tag{6.55}$$

$$Nb_2O_5 + H_2 \longrightarrow Nb_2O_4 + H_2O \tag{6.56}$$

The reduction is thermodynamically possible, since the free energy change, as given by Eq. (6.57), depends on the oxide and the reaction conditions, namely,

$$\Delta G = \Delta G^0 + RT\ln\left(\frac{p_{H_2O}}{p_{H_2}}\right) \tag{6.57}$$

The Gibbs free energy of most oxides, like PdO and CuO, is negative. However, other oxides, such as V_2O_5 and Fe_2O_3, have positive energy. Even for these cases, the partial pressure is so low, especially at high temperatures, that the equilibrium is dislocated by removing constantly water which favors the reduction. The Gibbs free energy values are known [1].

Quantitative analysis allows calculating the degree of reduction. This calculation is shown in Appendix quantifying the H_2 consumption during the reduction.

The degree of reduction is the ratio of the number of moles of hydrogen consumed for the reduction of a metal oxide and the stoichiometric number of moles of hydrogen needed to reduce it to the metal, or:

$$\alpha = \frac{n_{H_2}}{n_{H_2(teórico)}} \times 100 \ (\%) \tag{6.58}$$

6.2.5.1 Examples of Reduction Profiles of Metal Oxides

Figure 6.21a,b shows examples of reduction of simple bulk metal oxides, particularly NiO and CuO, and shows the profiles of hydrogen consumption with increasing temperature for a given heating rate. We observe the same Gaussian behavior as found in the TPD profiles. With increasing temperature the rate of reduction increases exponentially, reaching a maximum at a temperature T, and then
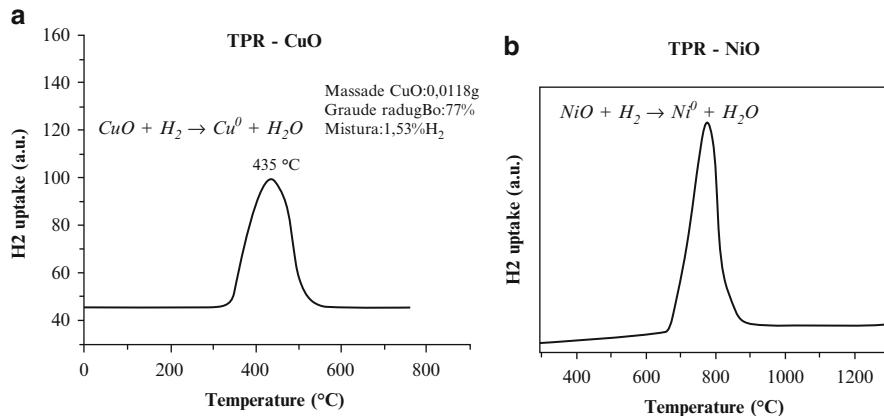
Fig. 6.21 TPR of CuO and NiO as reference
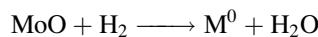
decreasing until the end, when all the oxide was reduced to metal. These profiles depend on a number of parameters as we shall see.

The profiles have different maximum temperatures. For the bulk NiO, the maximum is about 750 K, which is in accordance with the literature [25, 34, 35]. For the bulk CuO, the maximum is about 708 K.
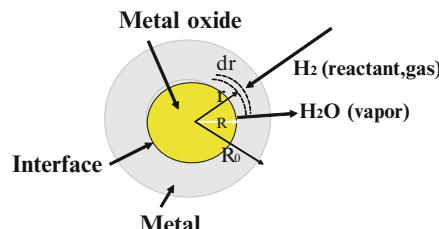
The reduction degrees of CuO and NiO were calculated according to Eq. (6.58), resulting in 78 % and 100 % to Cu^0 and Ni^0, respectively.

6.2.5.2 Kinetic Model

The most usual model was presented by Kissinger [36] for reaction types like solid $\longrightarrow$ gas + solid. However, this model can be used for the reduction of metal oxides, like

$$MoO + H_2 \longrightarrow M^0 + H_2O$$

The Kissinger [36] method is basically a shrinking core model gas–solid reaction as shown in the following scheme.

One obtains the following rate expression for the kinetic of reduction of order n and varying with temperature. Thus, the rate of reduction or H_2 consumption is [1]

$$\frac{dS}{dt} = \frac{dn_H}{dt} = -k_0 \times S^n \overline{C}^m e^{\left(-\frac{E}{RT}\right)} \tag{6.59}$$

where

S—rate of reduction of the solid (μmol)
$\frac{dn_H}{dt}$—rate of H_2 consumption (μmol/s)
k—specific rate constant
$\overline{C}$—mean concentration of H_2 (μmol/cm^3) $= \overline{C} = \frac{C+C_0}{2}$
C_0, C—input and output concentrations

If $\alpha = 1 - S$ is the reduction degree and considering the mean H_2 concentration, we obtain

$$\frac{d\alpha}{dt} = k_0(1-\alpha)^n e^{\left(-\frac{E}{RT}\right)} \tag{6.60}$$

where

k_0—pre-exponential factor $\left(\text{min}^{-1}\right)$
α—reduction degree
n—reaction order
E—activation energy (J/mol)
T—temperature (K)
$R = 8.314$ J/mol K—gas constant

Assuming that the temperature increases linearly with time,

$$T = T_0 + \beta t \tag{6.61}$$

where $\beta = \frac{dT}{dt}$ heating rate (K/s).
Combining the equation we have,

$$\frac{d\alpha}{dT} = \frac{k_0}{\beta}(1-\alpha)^n e^{\left(-\frac{E}{RT}\right)} \tag{6.62}$$

This equation can be solved for different cases. The solution for a monolayer nucleation model is simple. Separating variables we obtain,

$$-\ln(1-\alpha) = \frac{k_0}{\beta} \int_{T_0}^{T} e^{\left(-\frac{E}{RT}\right)} dT \tag{6.63}$$

From the TPR profile, we can determine the activation energy. To do it we must do several experiments, varying the heating rate and using the maximum peak value of the TPR profile, where the reaction rate is zero. The maximum occurs at a temperature T_m, when

$$\frac{d}{dT}\left(\frac{d\alpha}{dT}\right) = 0 \tag{6.64}$$

or

$$\frac{d}{dT}\left(\frac{E}{RT_m^2} - k_0 \times n \times (1-\alpha)^{n-1} \times e^{\left(-\frac{E}{RT}\right)}\right) = 0 \tag{6.65}$$

Thus,

$$\frac{E\beta}{R \times T_m} = A_0 \times n \times (1-\alpha)_m^{n-1} \times e^{\left(-\frac{E}{RT_m}\right)}. \tag{6.66}$$

Kissinger [36] shows that the $n(1-\alpha)_m^{n-1}$ is not only independent of β, but close to one. Therefore, one can simplify the equation to

$$\frac{\beta}{T_m^{\,2}} = \frac{k_0 R}{E}\ e^{\left(-\frac{E}{RT_m}\right)} \tag{6.67}$$

In logarithmic form, we obtain

$$\ln\left(\frac{\beta}{T_m^2}\right) = -\frac{E}{R}\frac{1}{T_m} + \ln\left(\frac{k_0 R}{E}\right) \tag{6.68}$$

Knowing β and T_m and plotting $\ln\left(\frac{\beta}{T_m^2}\right)$ versus $\frac{1}{T_m}$, we obtain a straight line and thus the parameters k_0 and E from the angular and linear coefficients.

From TPR profile one determines the amount of H_2 consumption for the reduction of the oxide as a function of time and temperature and thus the degree of reduction with time. The temperature T_m corresponds to the maximum at $\frac{d\alpha}{dT}$. Also, from the DTA curves varying the heating rates β, one obtains T_m and thus the kinetic parameters k_0 and E.

This method has been tested for different kinetic models $f(\alpha)$ varying the heating rates [1].

The kinetic model is also valid for other systems with temperature programming, such as temperature programmed oxidation (TPO), differential scanning calorimetry (DSC), and thermogravimetric or differential analysis (ATG, ATD), as we shall see.

6.2.5.3   Influence of the Variables

The influence of variables on the reduction profiles of supported metal oxides is more complex than for bulk oxides, due to the interaction between them. In fact, these profiles depend on the reducing conditions, especially:

- Gas concentration
- Heating rate
- Flow gas
- Catalyst mass
- Particle sizes
- Effect of water

The kinetic parameters of the reduction should take in consideration the mass balance for the reducing gas (reagent) on the surface and in the fluid gas. Much of the models, as seen above, do not take into account inter- and intra-particle diffusion effects, which can significantly modify the reduction profile. The conditions under which these effects can be neglected must be determined.

Monti and Baiker [37] proposed the kinetic model for the reduction considering these effects.

The mass balance for H_2:

$$v_0 C_0 = vC + kS^m \overline{C}^n \tag{6.69}$$

where v_0 and v are input and output volumetric flow rates (cm^3/s), respectively.

Combining Eqs. (6.59) and (6.69), one can relate the experimental parameters v_0, C_0, β, S with the kinetic parameters k_0, E. Thus, we obtain the following expression, assuming a first-order kinetics [37]:

$$\frac{dS}{dt} = \frac{dn_H}{dt} = -\frac{2C_0 \times v_0}{\beta} \left[\frac{1}{\left(1 + \frac{2v_0}{S \times k_0 \times e^{\left(-\frac{E}{RT}\right)}}\right)} \right] \tag{6.70}$$

With the initial conditions,

$S = S_0$ and $T = T_0$

The solution of Eq. (6.70) provides the concentration of reducible species as function of the temperature.

The concentration of hydrogen in the reducing mixture can be calculated from the following relationship:

$$C = \frac{C_0 \left(v_0 - \frac{kS}{2}\right)}{v_0 + \frac{kS}{2}} \tag{6.71}$$

Monti and Baiker [37] defined a characteristic parameter K which allows determining optimum reduction conditions:

$$K = \frac{S_0}{v_0 C_0} \tag{6.72}$$

The minimum and maximum values of K are equal to 55 and 140 s, respectively. Below or above these limits, the sensitivity is very low.

If other reducible species are present in the oxides, they can be correlated from the reduction profiles. Theoretically we can have various species S_i and kinetic parameters k_{0i} and E_i. Equation (6.70) can be modified generically [37]:

$$\frac{dS_i}{dt} = -\frac{2C_0 \times v_0}{\beta} \left[\frac{1}{\left(1 + \frac{2v_0}{S_i \times k_{0i} \times e^{\left(\frac{E_i}{RT}\right)}}\right)} \right] \tag{6.73}$$

With the initial condition:

$$S = S_{0i} \quad T = T_{0i}$$

These equations can be solved numerically for two or more reducible species, with different parameters and initial conditions.

Monti and Baiker [37] solved Eq. (6.73) for a reducible species, with the following conditions and parameters:

$$
\begin{aligned}
C_0 &= 2.46\,\mu\text{moles/cm}^3 & T_0 &= 300\,^\circ\text{C} \\
v_0 &= 1.25\,\text{cm}^3/\text{s} & S_0 &= 200\,\mu\text{moles} \\
\beta &= 0.2\,\text{K/s} & K &= 65\,\text{s} \\
E &= 129\,\text{kJ/mol} & k_0 &= 1.73 \times 10^{12}\ (1/\text{mol\,s})
\end{aligned}
$$

Figure 6.22 displays the concentration profile of H_2 with increasing temperature and the maximum temperature at $T_M = 580$ K. As observed, there are no significant diffusion effects.

The profiles of two reducible species S_1, S_2, with the corresponding kinetic parameters, are shown in Fig. 6.23 [37]:

$$
\begin{aligned}
E_1 &= 129\,\text{kJ/mol} & k_{01} &= 1.73 \times 10^{12}(1/\text{mol\ s}) \\
E_2 &= 145\,\text{kJ/mol} & k_0 &= 1.94 \times 10^{12}(1/\text{mol\ s})
\end{aligned}
$$

The reduction profiles are independent and the hydrogen consumptions are different.
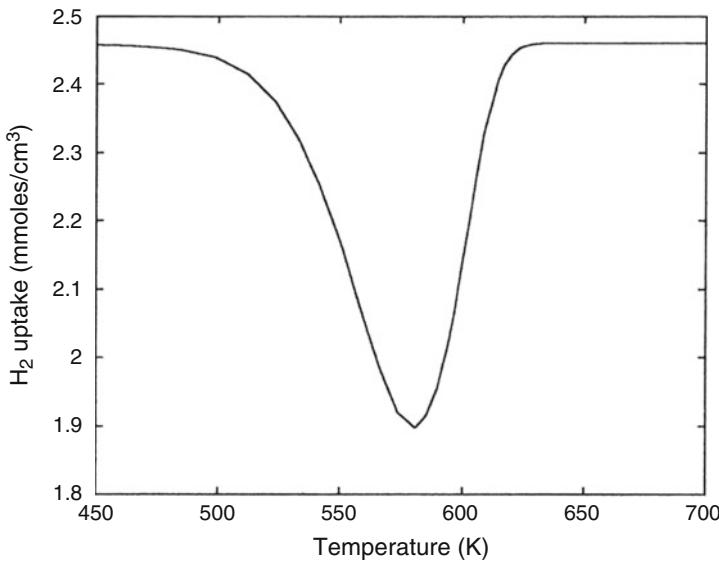
Fig. 6.22 Concentration profile of H_2(TPR) [Reproduced with permission from Kissinger, H. E., Analytical Chemistry, 29, 11 (1957) 1702 with PERMISSION/LICENSE]
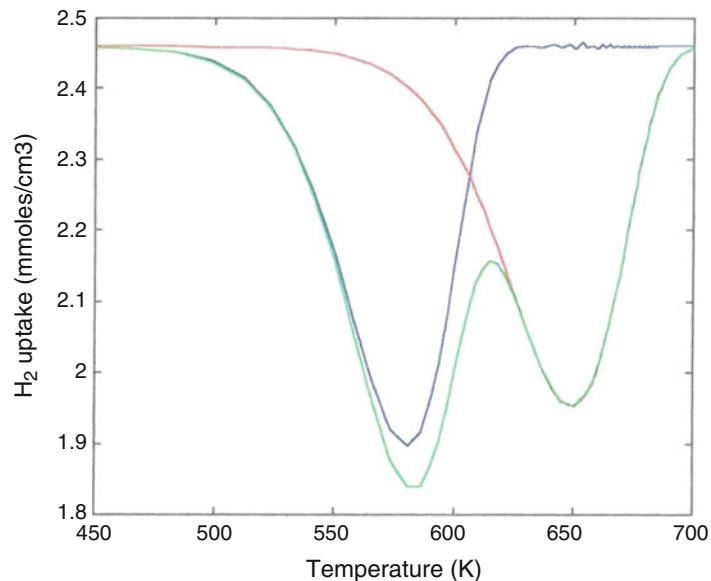
Fig. 6.23 Concentration profiles of two species [Reproduced from Kissinger, H. E., Analytical Chemistry, 29, 11 (1957) 1702 with PERMISSION/LICENSE]

Influence of the Parameters

This example shows the influence of these parameters on the reduction of NiO supported on alumina (13.2 % NiO/Al$_2$O$_3$).

First, we studied the effect of the hydrogen concentration using mixtures of 1.53 % H$_2$/Ar and 10 % H$_2$/Ar, with or without water vapor, as shown in Figs. 6.24 and 6.25. The displacement of the peak indicates that the higher the concentration
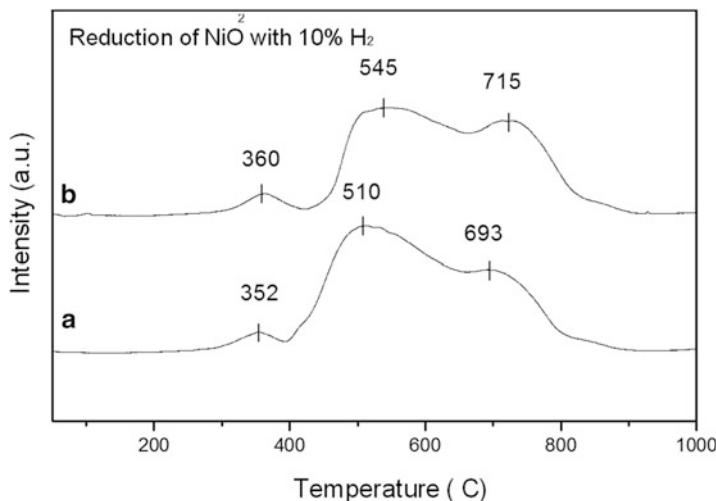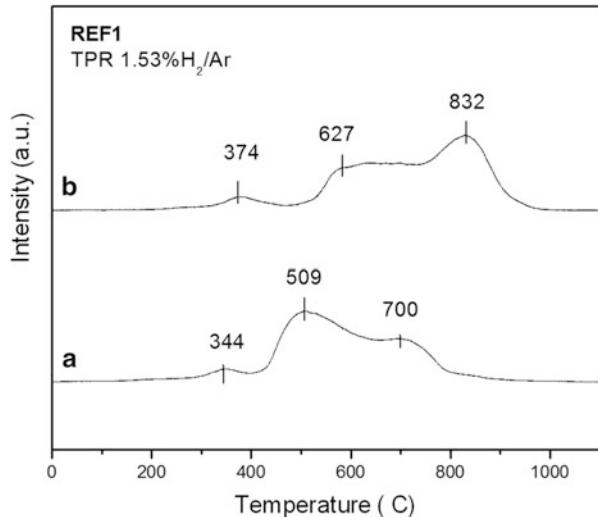
Fig. 6.24 TPR profiles of sample NiO/Al$_2$O$_3$ mixture with 10 % H$_2$/Ar, in the absence (*a*) and presence (*b*) of water vapor

Fig. 6.25 TPR profiles of sample NiO/Al$_2$O$_3$ mixture with 1.53 % H$_2$/Ar, in the absence (*a*) and presence (*b*) of water vapor

is, the easier is the reduction, but higher concentrations may cause sintering, due to exothermic reaction [38].

The presence of water vapor displaces the reduction of peak toward higher temperatures, and the influence is more significant when the reducing gas mixture is low (1.53 % H_2/Ar).

There are limits of concentrations levels, of gas flows, and of heating rates that allow eliminating diffusion, mass, and adsorption effects on the surface.

H_2 Concentrations
The literature recommends H_2 concentrations in the range 5–10 % in Ar or He. The reduction process is extremely exothermic, which increases significantly the temperature in the reactor, causing hot spots, sintering, or interaction of the metal with the support at higher concentrations [39, 40].

H_2 Flow Rates
The H_2 flow rate should be high to prevent diffusion effects and mass transfer. In general, it must be greater than >50 mL/min for a mass of about 50 mg. The space velocity should be high (about > 100 mL/g min).
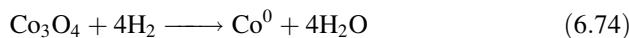
Heating Rates
Finally, the heating rate must be high to eliminate residual adsorption of the reducing gas. In general must be greater than 10 K/min, but are recommended rates above 20 K/min.

The reduction profiles show that the first peak is clearly associated with the reduction of NiO with weak interaction with the support, while the second and third peaks, which are partially overlapped, can be related to the reduction of NiO interacting with the support or the reduction of nickel aluminate or even partial reduction of La_2O_3 dissolved in the alumina matrix [41, 42].

The degrees of reductions were calculated from the integration of the reduction profiles. The degree of reduction of the first peak, around $500\,^\circ C$, was similar in both cases, indicating that approximately 7 % of NiO is reduced to Ni metal.

6.2.5.4 Reduction of Bulk Oxides, Supported Oxides, and Reducible Oxides

The oxides with different oxidation states, like Co_3O_4, exhibit different reduction peaks, which represent intermediate oxidation states. The bulk oxide, after calcination of the precursors, forms Co_3O_4 and CoO. The theoretical stoichiometry is

$$Co_3O_4 + 4H_2 \longrightarrow Co^0 + 4H_2O \tag{6.74}$$

Usually, Co_3O_4 can be reduced in two steps:

$$Co_3O_4 + H_2 \longrightarrow 3CoO + H_2O \tag{6.75}$$
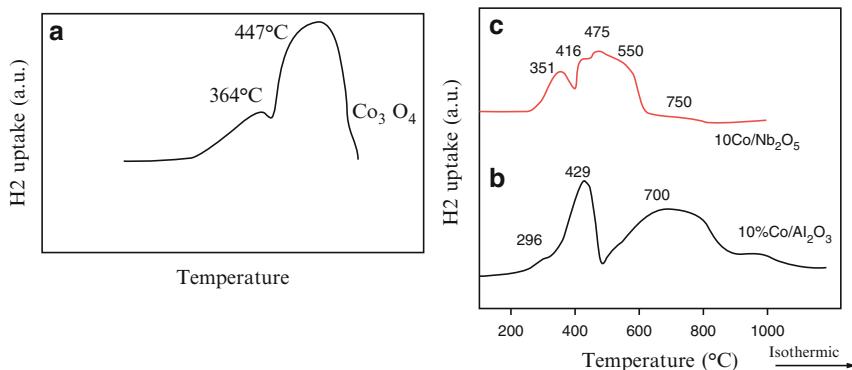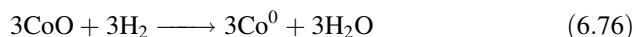
Fig. 6.26 TPR profiles of (a) bulk Co_3O_4, (b) Co/Al_2O_3 ($H_2 : Co = 1.33$) and (c) Co/Nb_2O_5 ($H_2 : Co = 1.49$)

$$3CoO + 3H_2 \longrightarrow 3Co^0 + 3H_2O \tag{6.76}$$
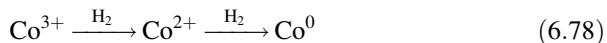
The reduction of Co_3O_4 follows in sequence, according to

$$Co_3O_4 \xrightarrow{H_2} CoO \xrightarrow{H_2} Co^0 \tag{6.77}$$
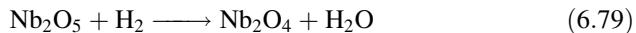
Figure 6.26a exhibits the TPR profile of bulk oxide Co_3O_4 showing two different peaks at 364 °C and 447 °C. From this profile we calculate the ratio H_2/Co of 1.30, which is close to the theoretical value of bulk oxide Co_3O_4 [43, 44].

Figure 6.26a displays the reduction of the unsupported Co_3O_4 sample. The reduction peaks occur at 364 °C and 447 °C, transforming the cobalt oxide in the metallic form, namely:

$$Co^{3+} \xrightarrow{H_2} Co^{2+} \xrightarrow{H_2} Co^0 \tag{6.78}$$

Profiles (b) show that the supported metal oxide (Co/Al_2O_3) reduces at 429 °C and at higher temperature, which suggests the interaction of the metal oxide with the support. However, the experimental ratio is close to the theoretical value 1.33.

However, reducible supports with lower oxidation states, also reduce partially, like Nb_2O_5 [43]:

$$Nb_2O_5 + H_2 \longrightarrow Nb_2O_4 + H_2O \tag{6.79}$$

Peaks above 420 °C indicate the influence of metallic cobalt in the partial reduction of the niobia, which also facilitate reduction of cobalt itself. The reduction of bulk niobia occurs at higher temperatures at 750 °C. However, for the catalyst Co/Nb_2O_5, the ratio H_2/Co is 1.44, much higher, which indicates the partial reduction of Nb_2O_5 [45, 66].
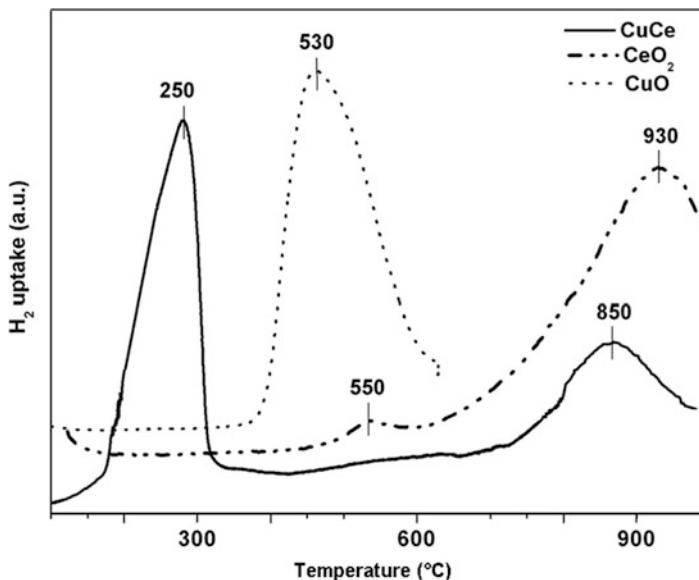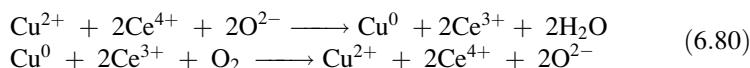
Fig. 6.27 TPR profiles of the mixed oxide and reference samples CuCe, CuO, and CeO$_2$ [48]

6.2.5.5 Reduction of Mixed Oxides

We studied the reduction of a mixed oxide CuO‑CeO$_2$, forming a solid solution Cu$_x$Ce$_y$O$_z$, called CuCe, and of pure oxides as reference [47]. The profiles of the samples CuCe and CeO$_2$ and of the reference sample CuO are shown in Fig. 6.27. The CeO$_2$ sample shows a reduction peak at 550 °C and 900 °C [48].

In the case of mixed oxide catalyst CuCe, the peak shows the facile reduction of the mixed oxide into Cu^0 and of Ce^{4+} in Ce^{3+} at the surface layer. It shows that even at higher temperatures, Ce facilitates the reduction of Cu^{2+}, and in parallel, the copper facilitates the reduction of ceria, by lowering the temperature, around 850 °C. The reduction temperature of CuO decreased from about 375 °C on the reference sample to 250 °C on the CuCe sample. The presence of a shoulder at lower temperatures indicates that there is probably intermediate reduction of isolated Cu^{2+} into Cu^{+1} and into Cu^{0}particles, in accordance with the literature [49, 50].
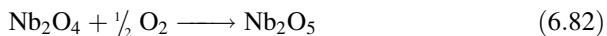
Thus, according to Bera et al. [49], there may occur the following reaction cycles:

$$Cu^{2+} + 2Ce^{4+} + 2O^{2-} \longrightarrow Cu^0 + 2Ce^{3+} + 2H_2O$$
$$Cu^0 + 2Ce^{3+} + O_2 \longrightarrow Cu^{2+} + 2Ce^{4+} + 2O^{2-} \qquad (6.80)$$
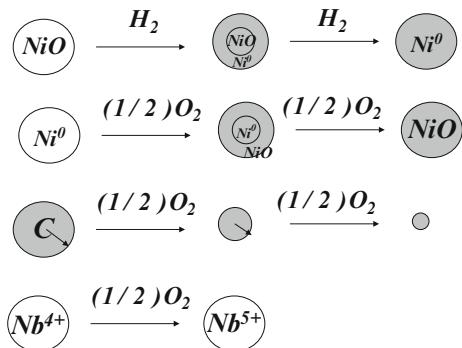
XRD results suggest that Cu is present as highly dispersed CuO phase. CuO does not react with O$_2$; therefore, part of Cu ions were incorporated into the CeO$_2$ matrix due to the interaction between Cu^{2+} and CeO$_2$, which leads to decreasing the reduction temperature of both ions.

6.2.6   Temperature Programmed Oxidation
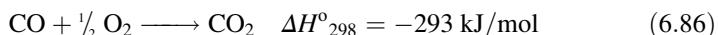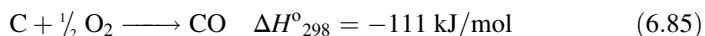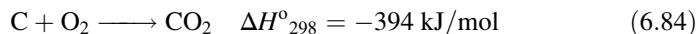
The temperature programmed oxidation is the inverse of the programmed reduction and serves to oxidize the metal and to transform the metal oxide in the lower oxidation state to the highest state. It is used in carbon combustion, coke and diesel particulates. As examples we have the oxidation of metals, oxides and carbon as follows:

$$Ni^0 + \tfrac{1}{2}\,O_2 \longrightarrow NiO \tag{6.81}$$

$$Nb_2O_4 + \tfrac{1}{2}\,O_2 \longrightarrow Nb_2O_5 \tag{6.82}$$

$$C + \tfrac{1}{2}\,O_2 \longrightarrow CO_2 \tag{6.83}$$

Transformations occur as shown in the scheme below, indicating the oxygen consumption with the increase of temperature.

Thermodynamically these transformations are possible, given that the free energy change is negative ($\Delta G^0 < 0$). The main reactions are known and highly exothermic, such as

$$C + O_2 \longrightarrow CO_2 \quad \Delta H^\circ{}_{298} = -394\ \text{kJ/mol} \tag{6.84}$$

$$C + \tfrac{1}{2}\,O_2 \longrightarrow CO \quad \Delta H^\circ{}_{298} = -111\ \text{kJ/mol} \tag{6.85}$$

$$CO + \tfrac{1}{2}\,O_2 \longrightarrow CO_2 \quad \Delta H^\circ{}_{298} = -293\ \text{kJ/mol} \tag{6.86}$$

The temperature programmed oxidation is done using the same experimental multipurpose unit, coupled to a quadrupole mass spectrometer or a thermal conductivity detector (TCD), as shown in scheme Fig. 6.9. In addition we can use the thermo-differential method (TGA-DTA), as shown in Fig. 6.8.

Different TPO analysis procedures can be made, depending on the objectives, i.e., metal oxidation and combustion (carbon, coke, or diesel).

The degree of oxidation can be calculated similarly, determining the oxygen consumption, or weight loss, according to item 6.2.3.
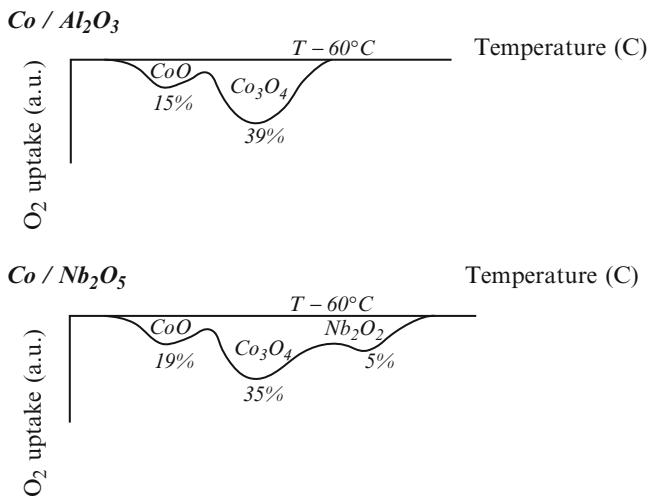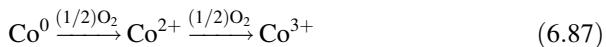
Co / Al₂O₃

Co / Nb₂O₅

Fig. 6.28 Temperature Oxidation profiles (TPO) of Co/Al_2O_3 and Co/Nb_2O_5

6.2.6.1   Oxidation

The oxidation of the metal, for example, Co^0, follows the reverse path of reduction, so

$$Co^0 \xrightarrow{(1/2)O_2} Co^{2+} \xrightarrow{(1/2)O_2} Co^{3+} \tag{6.87}$$

Or even for the bulk oxide

$$Nb_2O_4 + (1/2)O_2 \longrightarrow Nb_2O_5 \tag{6.88}$$

The profiles are similar, as shown in Fig. 6.28. One observes that there are sequential stages of intermediate to final oxides. The oxidation of Nb^{4+} passes to the oxide form Nb_2O_5. The degree of oxidation is calculated considering the consumption of oxygen, resulting in different degrees for each oxidation step.

6.2.6.2   Decomposition by Calcination

In the preparation of a catalyst, calcination is performed prior to the step of the reduction process of the final catalyst. This calcination is performed with air or in continuous flow oven with temperature programming oxidation. When coupled to mass spectrometry, one can follow the formation of gases during decomposition. The final temperature of calcination occurs when there is no more evolution of decomposition gases.
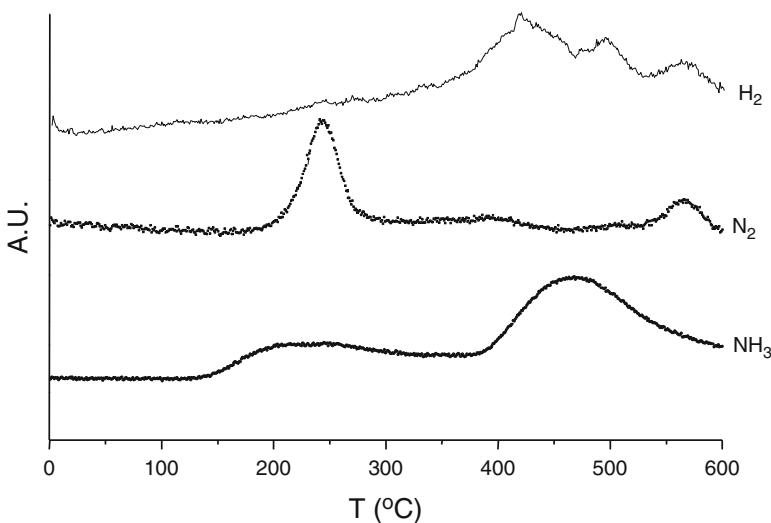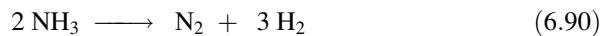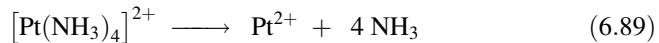
Fig. 6.29 Temperature programmed helium profiles (TPHe) after calcination at 350 °C [51]

Thus, for example, in the preparation of the Pt/ZSM-5 catalyst, we use the $Pt(NH_3)_4Cl_2$ precursor in solution and after drying was calcined at 350 °C. To verify whether there is residual gas usually one passes a He flow with temperature programming up to 550 °C. Figure 6.29 shows the NH_3 formation profile during the treatment with He into two distinct regions. A huge amount was observed between 400 °C and 500 °C and a small fraction between 150 and 350 °C. We also observed the formation of H_2 and N_2 at 200 °C. The maximum N_2 peak was at 200 °C with another lesser peak at 550 °C. However, the H_2 profile showed a broad band above 350 °C. This is attributed to the decomposition of the platinum complex. However, after calcination above 550 °C, all residual gases have been removed [51].

One can conclude that besides the decomposition of the complex, part of the H_2 serves to reduce the Pt^{2+}, as shown below:

$$\left[Pt(NH_3)_4\right]^{2+} \longrightarrow Pt^{2+} + 4\,NH_3 \tag{6.89}$$

$$2\,NH_3 \longrightarrow N_2 + 3\,H_2 \tag{6.90}$$

$$Pt^{2+} + H_2 \longrightarrow Pt^\circ + 2\,H^+ \tag{6.91}$$

6.2.6.3   Combustion

The graphitic carbon (coke) is formed in most chemical processes and causes deactivation of catalysts or clogging in the reactors. Moreover, huge amounts of soot particles are released from vehicle engines due to the incomplete combustion

of diesel. The particulate materials (or soot) consist, in general, a chain of carbonaceous cores (0.1–10 μM). Both must be eliminated by burning.

The temperature of combustion can be found experimentally, using the temperature programming oxidation methodology (TPO) in a multipurpose unit. The gases resulting from the oxidation of carbon (coke or particulates) can be determined by using a mass spectrometer coupled to the system. Thus, it is possible to quantify the consumption of carbon or gases formed.

Coke Combustion

Deactivation of Pt/Al_2O_3 catalysts has been studied, with the main focus on the kinetics [52], the influence of additives to prevent coke formation [53], the amount of coke deposition on surfaces [54], and the nature of carbon [55], as well as of the coke composition [56]. We studied the deactivation of Pt/Al_2O_5 and Pt/Nb_2O_5 catalysts during the dehydrogenation of n-heptane, due to the coke formation, by using the temperature programmed oxidation (TPO) technique, by burning the carbon or coke and measuring the resulting gas, with increasing temperature [57].

The main properties before and after reaction are presented in Table 6.7.

Figure 6.30 shows the O_2 consumption and the CO_2 profiles during TPO of the spent catalysts. The profiles are similar, which suggest that the O_2 consumption is

Table 6.7 Textural properties and coke formation

	Fresh catalyst		After reaction	
	Pt/Nb_2O_5	Pt/Al_2O_3	Pt/Nb_2O_5	Pt/Al_2O_3
Surface area BET (m^2/g)	58	200	56	195
Pore volume (cm^3/g)	0.131	0.600	0.128	0.650
Coke (%)	–	–	3.6	3.1
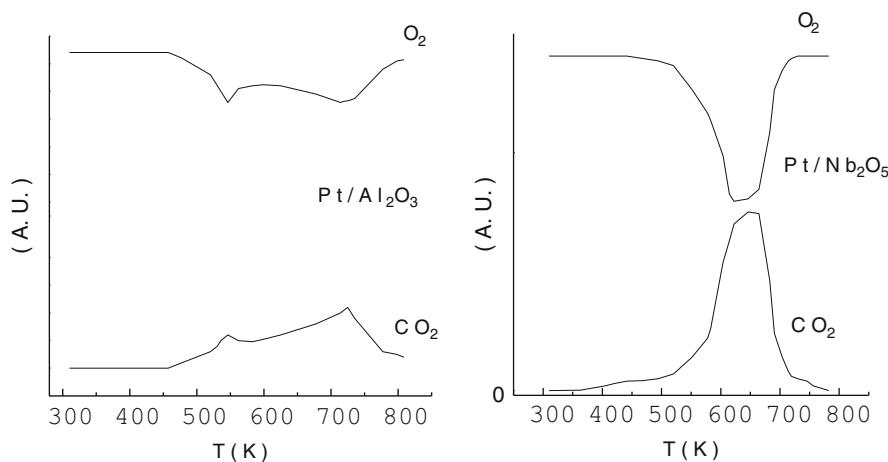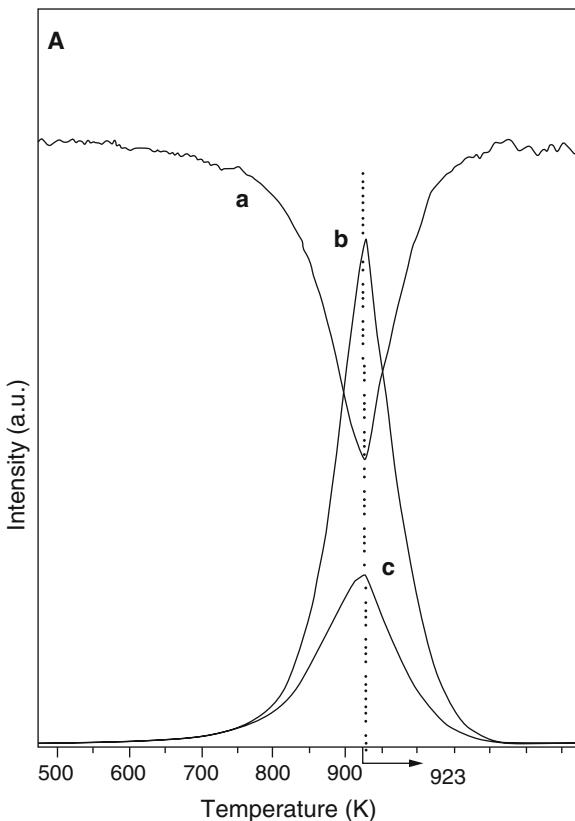
Fig. 6.30 Oxidation profiles during TPO of carbon on Pt/Al_2O_3 and Pt/Nb_2O_5 [57]

Fig. 6.31 Oxidation profiles of PM samples (A) (a) O$_2$, (b) CO, (c) CO$_2$. Conditions: 10 K/min 15 % O$_2$/He without addition of water, catalyst: $M = 2 : 1$ mixture poor contact, MW = 10 mg [58]

due to the carbon burning, forming CO$_2$ and not for re-oxidizing the metallic particles or for reducing niobia. The catalyst Pt/Al$_2$O$_3$ exhibits two peaks at 538 and 606 K, while the Pt/Nb$_2$O$_5$ one broad peak around 650 K.

According to Barbier et al. [19], the first region at low temperatures is attributed to the burning of carbon material deposited on metal particles, while at higher temperatures, the oxidation of carbon is assigned to the coke formation on the acid sites over the support.

Soot Combustion

This is a good example of carbon combustion or partial combustion of carbon in the presence of a catalyst. Leocadio et al. [58] studied the combustion of diesel particulate on Mo$_2$O$_3$ catalysts. Figure 6.31 shows the profiles of consumption of O$_2$ (a) and formation of CO (b) and CO$_2$ (c), with increasing temperature during the TPO experiments in the system coupled to a mass spectrometer.

As seen the combustion of carbon particulates without catalyst was complete above 923 K. Results showed that combustion produced about 62 % CO and 28 % CO$_2$. Thus, there are parallel reactions besides the carbon combustion. Stanmore

et al. [59], Du et al. [60], and Ahmed et al. [61] observed that catalyzed combustion of particulates occurs in two basic steps. The first is the adsorption of O_2 on the surface of the carbon, coexisting two adsorption sites, yielding two superficial oxidized complexes (SOC): a more reactive, which is responsible for the formation of CO and other less reactive, for the formation of CO_2. In the second stage, the oxidation is completed and the adsorbed complexes are decomposed, consuming the carbon atoms on the surface.

6.2.7   Differential Scanning Calorimetry

This analysis helps to evaluate catalytic properties even under reaction conditions. The *differential scanning calorimetric* is specific for calorimetric analysis for determining the reaction enthalpy (ΔH) for samples when submitted at a heating rate with increasing temperature under synthetic air flow.

The reaction enthalpy (ΔH) can be calculated using the following equation:

$$\Delta H = \frac{KA}{m} \, [\text{cal/g}] \tag{6.92}$$

where K is a constant equal to 1.06, m mass (mg), and A heat (mcal) which correspond to the area of the DSC profile ((cal/s). s).
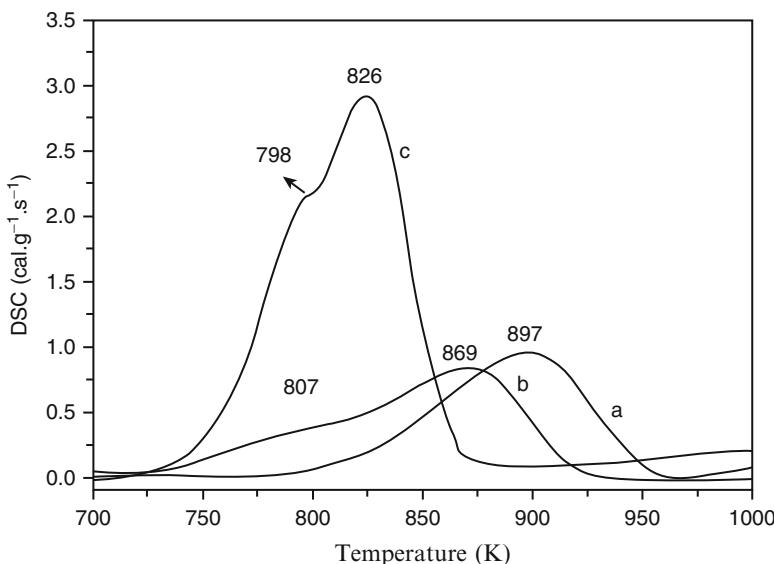
Fig. 6.32 DSC profiles of samples PM : Al_2O_3 (*a*), C5Mo catalysts (*b*) and C15Mo (*c*). Rate: 10 K/min under synthetic air (50 mL/min) (γ - Al_2O_3 is reference: the average mass of the sample equal to 1.5 mg [58])

Table 6.8 Heat of reaction (ΔH) and activation energy (E) found by DSC for PM/Al$_2$O$_3$, PM/C5Mo, and PM/15Mo [58]

Samples	E (kJ/mol)	ΔH (kJ/mol)
PM/Al$_2$O$_3$	180	-86
PM/C5Mo	100	-108
PM/C15Mo	96	-189

For the same example as above, Fig. 6.32 shows the DSC profiles of the particulate/Al$_2$O$_3$ (a) and of the sample in the presence of the catalyst PM/Mo (b, c).

The temperature at maximum peak on the DSC profile, referred to as combustion temperature T_c, is the parameter used for evaluation of the catalytic performance. The temperature T_c of PM/Al$_2$O$_3$ (a) is 896 K and equals to the PM without alumina. However, the temperature T_c of the DSC profile of the particulate in the presence of 15 % molybdenum catalyst decreased to about 826 K. In conclusion, there is a significant effect on the catalytic activity. The maximum temperature decreased to 60 K.

Table 6.8 presents the calculated activation energy (E) and reaction enthalpy (ΔH), according to Eq. (6.32).

It may be noted that the Mo catalyst diminished substantially the activation energy by a factor of 2. This variation is significant.

6.2.8 Thermogravimetric and Thermo-Differential Analyses

The gravimetric methods permit determining the loss or weight gain during heating with temperature programming. About 10 mg is placed in a crucible, passing an inert gas or reactant gas stream, measuring the weight loss in a sensitive microbalance. It also allows determining thermal variations during the temperature rise, indicating phase changes occurring at different temperatures. The apparatus used is the thermo-microbalance, and the basic design is shown in Fig. 6.8. When coupled to a mass spectrometer can monitor the evolution of exit gases. Special care must be taken with diffusion and mass transfer, controlling the gas flow and the heating rate.

The objectives are different and can be classified in:

- *Decomposition—mass loss during calcination*
- *Combustion—mass loss by carbon burning*
- *Formation of coke—mass gain by carbon deposition*
- *The reduction of oxides in the presence of hydrogen or oxidation in the presence of oxygen*

We will present some examples. The calculation or conversion degrees of the transformations can be made analogously as described before.
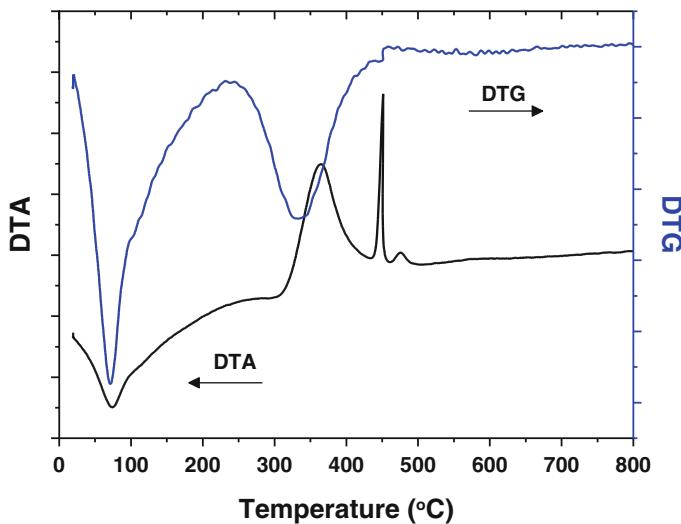
Fig. 6.33 Differential thermal analysis (DTA) and derivative thermogravimetric analysis (DTG) for the sample (ZrSTAci) not calcined [33]

6.2.8.1   Decomposition

In the decomposition of precursors, one determines the mass loss of the samples due to the removal of water and precursors or due to phase transformation during heating under an oxidizing atmosphere (O_2) at a rate of about $10\,°C$/min up to $1000\,°C$.

In general, materials are prepared by the precipitation method. For example, zirconium hydroxide obtained by hydrolysis of zirconium acetate ($[CH_3COO]_4^-$ $[Zr]^+$) with ammonium hydroxide (**NH$_4$OH**). (NH$_4$OH). Calcination of the hydroxides give rise to zirconium oxide (ZrO_2) [62].

The DTG and DTA profiles for the zirconium hydroxide decomposition are shown in Fig. 6.33 [33]. It can be seen, an endothermic region, loss of mass in the temperature range between 30 and $230\,°C$, corresponding to water and structural water. A second exothermic region between 240 and $430\,°C$ was observed. Together with a large heat release, one observes a marked weight loss, which is attributed to the thermal decomposition of the precursors. A high exothermic peak at $450\,°C$ gives rise to the crystallization process to form oxides, with tetragonal structure, as identified by XRD analysis.

6.2.8.2   Combustion

The deactivation test was performed with reforming of ethanol (H$_2$O/EtOH) at different temperatures for long test life. There was high formation of coke after
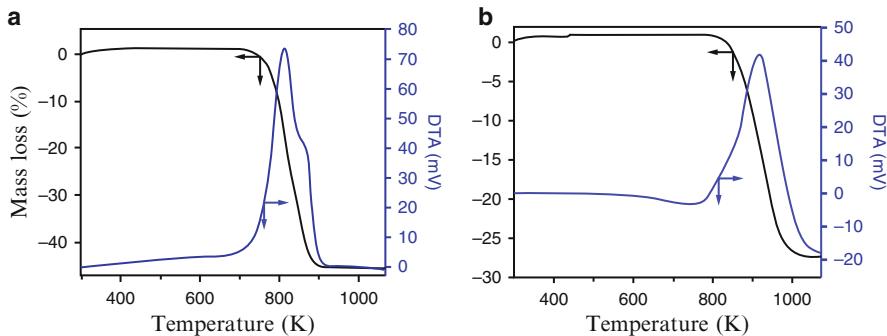
Fig. 6.34 TG/DTA analyses at (**a**) $T = 623$ K, (**b**) $T = 963$ K [34]
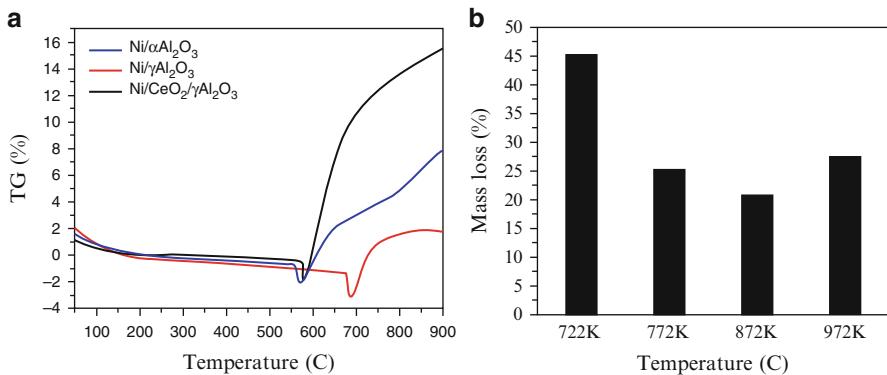
Fig. 6.35 (**a**) Thermogravimetric analysis "in situ" during the partial oxidation reaction mixture of 90 % methane and 10 % ethane for the catalyst, 15 % Ni /αAl$_2$O$_3$, 15 % Ni / γ - Al$_2$O$_3$ and Ni / CeO$_2$/ γ - Al$_2$O$_3$ [63]. (**b**) Weight loss after TG analyses [63]

3 h life test [34]. Spent catalysts were collected and analyzed by ATG/DTA and SEM/EDS.

Figure 6.34 shows the TG/DTA results for the spent catalysts after reforming at 663 K (a) and 963 K (b). It is not possible to differentiate the type of coke deposited on the catalyst. The mass loss of the catalyst tested at 663 K was 45 %, while that at 963 K about 28 %. DTA profiles show that the catalyst tested at 663 exhibited one peak at 820 K and a shoulder around 860 K, which suggest the presence of two different types of coke formations. On the other hand, the catalyst tested at 963 K exhibited only one peak at around 950 K and indicates the presence of only one coke type formation.
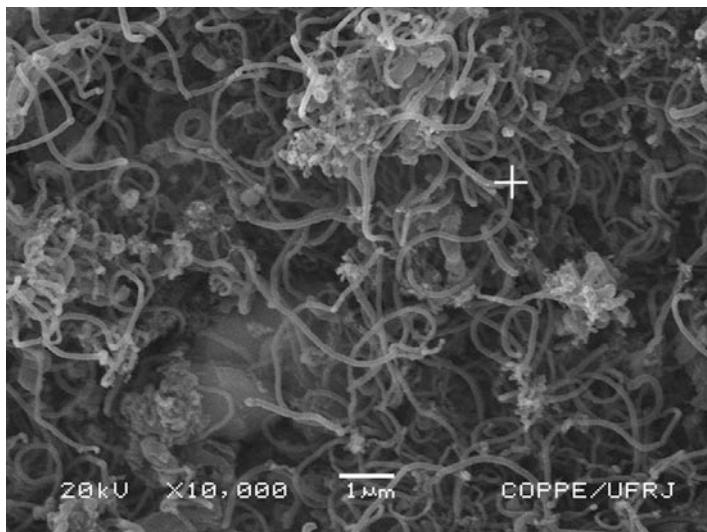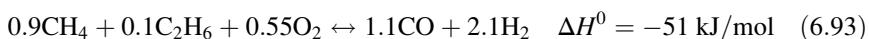
Fig. 6.36   Micrographs after test at 623 K [34]

6.2.8.3   Thermogravimetric Analysis "In Situ": Carbon or Coke Formation

The thermogravimetric analysis "in situ" allows determination of weight gain during heating with temperature programming. How the coke or carbon are formed can be visualized in this example during the partial oxidation of hydrocarbons on a catalyst 15 % Ni /γAl$_2$O$_3$, and promoted with CeO$_2$, using a mixture of O$_2$/mixing HC = 0.55. This relationship corresponds to the stoichiometric required amount of oxygen for the partial oxidation of hydrocarbon according to the equation [63]:

$$0.9CH_4 + 0.1C_2H_6 + 0.55O_2 \leftrightarrow 1.1CO + 2.1H_2 \quad \Delta H^0 = -51 \text{ kJ/mol} \quad (6.93)$$

The weight gain in carbon after different reaction temperatures is shown in Fig. 6.35, which depends on the catalyst. Figure 6.35a displays the amount of carbon formed, varying with the temperature. The mass gain on Ni / γ - Al$_2$O$_3$ is lower (4.9 %) than on Ni / CeO$_2$/ γ - Al$_2$O$_3$ (16.3 %) and decreases with the reaction temperature.

The carbon formation on nickel catalysts is attributed to the formation of carbon filaments and coke, which explains the mechanism proposed by Rostrup-Nielsen [64].

One way of verifying the type of carbon is the analysis by scanning electron microscopy (SEM) after the use of the catalysts; Fig. 6.36 shows carbon filaments, featuring carbon nanotubes. These filaments may carry metallic Ni through the tubes [34].

6.2.9   Temperature Programmed Surface Reaction

This technique allows analyzing qualitatively and quantitatively the reaction between adsorbed molecules and the formation of products with programmed temperature in situ [65].

The same multipurpose unit (Fig. 6.9), already described, is used, coupled to mass spectrometer (quadruple) and infrared spectroscopy (DRIFTS). Here we present some examples using this technique. In the next chapter, we will present specifically the infrared spectroscopy.

The principle of this method is:
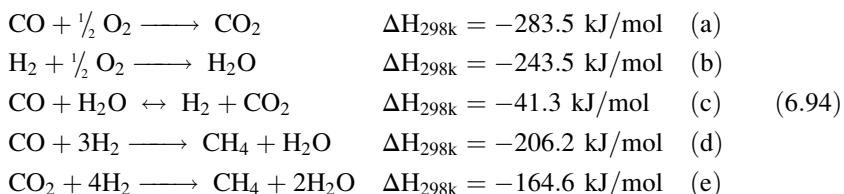
- First, adsorbing reactant A on the surface under continuous flow or by pulses.
- Second, after cleaning the surface with He flow, reactant B is added continuously at a constant flow rate with increasing temperature and constant heating rate up to the final temperature. Reactants and products are measured by mass spectrometry or infrared spectroscopy with time and temperature.
- The third way is passing both reactants flowing simultaneously with increasing temperature and constant heating rate up to the final temperature or introducing reactants by pulses.

  Examples

6.2.9.1   Partial Oxidation of Methane

Temperature programmed surface reactions (TPSR) were carried out with $LaCoO_3$ perovskite-type in a multipurpose unit equipped with a quadrupole mass spectrometer (Balzers Prisma-QMS 200). The signal intensity of masses 2, 15, 18, 28, 32, and 44 corresponding to H_2, CH_4, H_2O, CO, O_2, and CO_2, respectively, was monitored continuously. The reaction gas mixture consisted of 1 vol.% CO, 1 vol.% O_2, 60 H_2 vol.%, and He balance [64].

PROX reaction is characterized by CO oxidation and quite a number of thermodynamically allowed reactions summarized in Eq. (6.94):

$$
\begin{array}{lll}
CO + \tfrac{1}{2}\,O_2 \longrightarrow CO_2 & \Delta H_{298k} = -283.5 \text{ kJ/mol} & \text{(a)} \\
H_2 + \tfrac{1}{2}\,O_2 \longrightarrow H_2O & \Delta H_{298k} = -243.5 \text{ kJ/mol} & \text{(b)} \\
CO + H_2O \leftrightarrow H_2 + CO_2 & \Delta H_{298k} = -41.3 \text{ kJ/mol} & \text{(c)} \quad (6.94) \\
CO + 3H_2 \longrightarrow CH_4 + H_2O & \Delta H_{298k} = -206.2 \text{ kJ/mol} & \text{(d)} \\
CO_2 + 4H_2 \longrightarrow CH_4 + 2H_2O & \Delta H_{298k} = -164.6 \text{ kJ/mol} & \text{(e)}
\end{array}
$$

Reactions a and c in Eq. 6.94 are the desired ones, whereas reactions (b), (d), and (e) are undesired. Figure 6.37 shows that the equilibrium conversion (dashed line) decreases with increasing temperature.
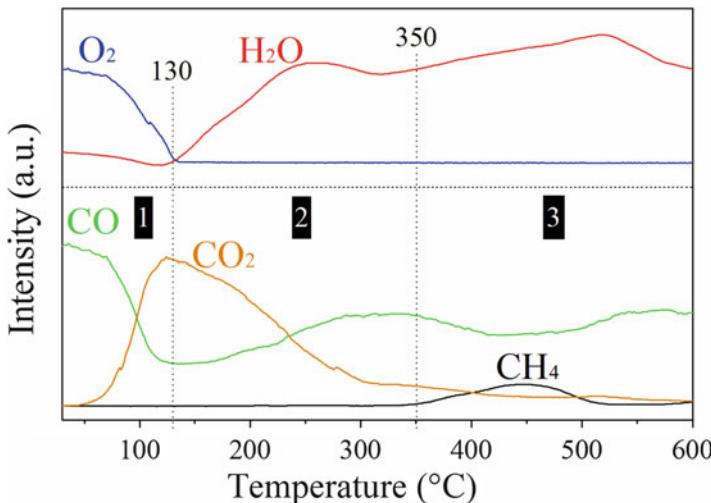
Fig. 6.37 TPRS profiles of the partial oxidation of LaCoO$_3$

According to Mul et al. [66], the CO oxidation is favored when compared to the H$_2$oxidation and much more favored than methanation (d) and water gas shift reaction (WGSR), because the sequence of values of the equilibrium constants is CO oxidation $>$ H$_2$ oxidation $\gg$ CO methanation $>$ WGSR. That shows that selective CO oxidation is practical from the thermodynamic perspective, since the equilibrium constant of CO oxidation is larger than the side reactions (b), (c), and (d). These reactions can be analyzed simultaneously through TPRS experiments, whose profiles are illustrated in Fig. 6.37 for the LaCoO$_3$ catalyst.

The main products were CO$_2$, H$_2$O, and CH$_4$ depending on the temperature range. In accordance with the reported results in the literature [41], three distinct regions were also observed during increasing temperature.

For LaCoO$_3$ sample, the first region shows CO signal decreasing as the temperature raised, together with the O$_2$ signal until total consumption up to 130 °C and an increasing formation of CO$_2$, without water signal.

Region 2 shows an increase in the CO and H$_2$O signals, whereas CO$_2$ decreases as the temperature is raised. This observation indicates the extent of CO oxidation to CO$_2$ is disfavored in benefit of reactions in which H$_2$O is the product and O$_2$ is the main reactant, since it is still totally consumed. Thus it is proposed that the hydrogen oxidation takes important place in this step.

Another possibility is the occurrence of the reverse water gas shift reaction (RWGS). It was investigated by Woods et al. [41] in the range of 100–275 °C, and they found minimal CO$_2$conversion below 200 °C, suggesting that the extent of reverse water gas shift reaction (RWGS) is negligible below this temperature and also that above 200 °C the methanation is more favored than RWGS. In agreement with these findings, the H$_2$oxidation probably has more influence than RWGS in region 2 for our results.
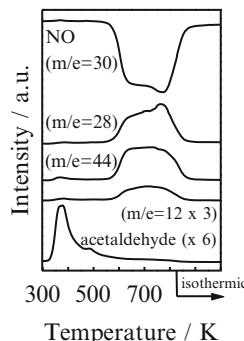
Region 3 shows an unsteady CO signal together with raising H_2O formation and decreasing CO_2 signal. The main product was CH_4, possibly formed according to reactions (4) and (5) and whose initial formation temperature and profile varied for the catalysts. The $LaCoO_3$perovskite presented higher initial temperature to methanation (350 °C). At these temperatures Co^{n+} species coexist with metallic Co^0 which favors the undesirable methanation reaction. This hypothesis is supported by the TPR experiment that showed the highest extent of reduction at the temperature range of 300–500 °C leading to reduction of all Co^{3+} to Co^{2+} and part of Co^{2+} to Co^0. These results evidence that Co^{3+} in perovskite matrix are more resistant to reduction when compared to typical supported cobalt catalysts, what explains higher temperatures to methanation reaction over perovskite oxides [67]. The coexistence of Co^{n+} and metallic cobalt in region 3 could favor the occurrence of dry reforming causing drop in CH_4. Since the initial CO signal is not reestablished, there is formation of CO_2 in the reaction environment that would justify its consumption in the dry reforming and even in the RWGS, given that CO_2 signal is minimum [64].

6.2.9.2   Reduction of NO with Acetaldehyde

The reduction of NO with acetaldehyde was performed on Pd/Al_2O_3 catalyst [68, 69]. The sample was purged with helium flow (50 cm^3/min) from room temperature up to 823 K (10 K/min), cooled to room temperature and reduced under flowing H_2(30 cm^3/min) up to 773 K (5 K/min). Acetaldehyde was adsorbed at room temperature until saturation, then purged with He. The 1 % NO/He mixture (50 cm^3/min) with temperature raising at 20 K/min until 823 K. The reaction products were monitored using a quadrupole mass spectrometer (Balzers, PRISMA), as described before [27, 30].

Figure 6.38 shows the profiles for the Pd/Al_2O_3 catalyst. A small amount of acetaldehyde desorption was detected at 375 and 485 K. The NO desorption was observed at 630 and 775 K, with simultaneous formation of $N_2(m/e = 28)$, CO ($m/e = 28$ and 12) and/or CO_2 ($m/e = 44, 28$ and 12). Additional papers related to this topics are presented in the references [70–91].

Fig. 6.38 TPSR profiles of NO^+ acetaldehyde reaction on Pd/Al_2O_3

References

1. Moulijn JA, van Leeuwen PWNM, van Santen RA. Catalysis. 2nd ed. Amsterdam: Elsevier; 1995.
2. Dubinin MM. Surface and nanomolecular catalysis. Zhur Phys Chem. 1960;34:959.
3. Dubinin MM. The potential theory of adsorption of gases and vapors for adsorbents with energetically nonuniform surfaces. Chem Rev. 1960;60:235.
4. Gregg SJ, Sing KSW. Adsorption. Surface area and porosity. 2nd ed. London: Academic; 1982.
5. Brunauer S, Deming LS, Deming WS, Teller E. On a theory of the van der Waals adsorption of gases. J Am Soc. 1940;62:1723.
6. Langmuir I, Langmuir I. The constitution and fundamental properties of solids. J Am Chem Soc. 1929;6:451.
7. Brunauer S, Emmett PH, Teller E. Dissolution rates of cadmium and bismuth tellurides as a function of pH, temperature and dissolved oxygen. J Am Soc. 1938;60:309.
8. Barret EP, Jayner LS, Halenda PP. The determination of pore volume and area distributions in porous substances. I. Computations from nitrogen isotherms. J Am Chem Soc. 1951;73:373.
9. Lippens BC, Linsen BG, de Boer JH. Studies on pore systems in catalysts I. The adsorption of nitrogen; apparatus and calculation. J Catal. 1964;3:32.
10. Dubinin MM. Adsorption in micropores. J Coll Interf Sci. 1967;23:487.
11. Dantas Ramos AL, da Silva AP, Aranda DAG, Schmal M. Appl Catal A Gen. 2004;277:71.
12. Langmuir I. Advances in catalysis, volume 9. J Am Chem Soc. 1916;38:2267.
13. Kummer JT, Podgursk HH, Spencer WB, Emmett PH. Synthesis. The addition of radioactive alcohol. J Am Chem Soc. 1951;73(2):564–9.
14. Boudart M, Mariadassu GD. Kinetics of heterogeneous catalytic reactions. Princeton, NJ: Princeton University Press; 1982.
15. Benson JE, Boudart M. Hydrogen-oxygen titration method for the measurement of supported platinum surface areas. J Catal. 1965;4:704.
16. Aben PC. Palladium areas in supported catalysts: determination of palladium surface areas in supported catalysts by means of hydrogen chemisorption. J Catal. 1968;10:224.
17. Silva RRCM, Schmal M, Frety F, Dalmon JA. Effect of the support on the fischer-tropsch synthesis with Co/Nb_2O_5 catalysts. J Chem Soc Faraday Trans. 1993;89(21):3975.
18. Souza MMVM, Aranda DAG, Schmal M. Palladium areas in supported catalysts: determination of palladium surface areas in supported catalysts by means of hydrogen chemisorption. J Catal. 2001;204(2):498.
19. Barbier J. Deactivation of reforming catalysts by coking—a review. Appl Catal. 1986;23:225.
20. Leocadio ICL, Minana CV, Braun S, Schmal M. Effect of experimental conditions on the parameters used for evaluating the performance of the catalyst Mo/Al_2O_3 in diesel soot combustion. Appl Catal B Environ. 2008;84:843–9.
21. Alberton AL, Schwaab M, Schmal M, Pinto JC. Experimental errors in kinetic tests and its influence on the precision of estimated parameters. Part I—Analysis of first-order reactions. Chem Eng J. 2009;155:816–23.
22. Redhead PA. Thermal desorption of gases. Vacuum. 1963;12:203.
23. Masel RI. Principles of adsorption and reaction on solid surfaces, Wiley series in chemical engineering. New York: Wiley; 1996.
24. Taylor TL, Weinberg WH. A method for assessing the coverage dependence of kinetic parameters: application to carbon monoxide desorption from iridium (110). Surf Sci. 1978;78(2):259.
25. de Carvalho MCNA, Passos FB, Schmal M. The behavior of Cu/ZSM-5 in the oxide and reduced form in the presence of NO and methanol. Appl Catal A. 2000;193:265.
26. Ribeiro NFP, Mendes FMT, Perez CAC, Souza MMVM, Schmal M. Selective CO oxidation with nano gold particles-based catalysts over Al_2O_3 and ZrO_2. Appl Catal A Gen. 2008;347(1):62.

27. Anderson JR, Foger K, Breakspere RJ. Adsorption and temperature-programmed desorption of hydrogen with dispersed platinum and platinum-gold catalysts. J Catal. 1979;57(3):458.
28. Aranda DAG, Schmal M. Ligand and geometric effects on Pt/Nb_2O_5 and $Pt–Sn/Nb_2O_5$ catalysts. J Catal. 1997;171(2):398.
29. Schmal M, Vargas DC, Souza MMVM, Guarido CE. Can J Chem Eng. 2011;89(5):1166–75.
30. Yee A, Morrison SJ, Idriss H. A study of ethanol reactions over Pt/CeO_2 by temperature programmed desorption and in situ FT-IR spectroscopy: evidence of benzene formation. J Catal. 2000;191:30.
31. Mishra BG, Rao GR. Mol J Catal A. 2006;243:204–13.
32. Pokrovski KA, Bell AT. J Catal. 2006;244:43–51.
33. Neto RC, Schmal M. Synthesis of CeO_2 and $CeZrO_2$ mixed oxide nanostructured catalysts for the iso-syntheses reaction. Appl Catal A Gen. 2013;450:131.
34. Alberton AL, Souza MMVM, Schmal M. Carbon formation and its influence on ethanol steam reforming over Ni/Al_2O_3 catalysts. Catal Today. 2007;123:257.
35. Rodriguez JA, Hanson JC, Frenkel AI, Kim HY, Perez M. Experimental and theoretical studies on the reaction of H_2 with NiO: role of O vacancies and mechanism for oxide reduction. J Am Chem Soc. 2002;124:346.
36. Kissinger HE. Reaction kinetics in differential thermal analysis. Anal Chem. 1957;29 (11):1702.
37. Monti DAM, Baiker A. Temperature-programmed reduction. Parametric sensitivity and estimation of kinetic parameters. J Catal. 1983;83(2):323.
38. de Souza MMVM, Clavé L, Dubois V, Perez CAC, Schmal M. Temperature-programmed reduction. Parametric sensitivity and estimation of kinetic parameters. Appl Catal A. 2004;272:133.
39. Li C, Chen YW. Temperature-programmed-reduction studies of nickel oxide/alumina catalysts: effects of the preparation method. Thermochim Acta. 1995;256:457.
40. Richardson JT, Twigg MV. Reduction of impregnated $NiO/\alpha-A1_2O_3$ association of A13+ ions with NiO. Appl Catal A. 1998;167:57.
41. Richardson JT, Lei M, Thrk B, Forester K, Twigg MV. Reduction of model steam reforming catalysts: $NiO/\alpha-Al_2O_3$. Appl Catal A. 1994;110:217.
42. Pompeo F, Nichio NN, Souza MMVM, Cesar DV, Ferretti OA, Schmal M. Study of Ni and Pt catalysts supported on $\alpha-Al_2O_3$ and ZrO_2 applied in methane reforming with CO_2. Appl Catal A. 2007;316:175.
43. Mendes FMT, Perez CAC, Noronha FB, Souza CDD, Cesar DV, Freund HJ, Schmal M. Fischer–Tropsch synthesis on anchored $Co/Nb_2O_5/Al_2O_3$ catalysts: the nature of the surface and the effect on chain growth Fischer–Tropsch synthesis on anchored $Co/Nb_2O_5/Al_2O_3$ catalysts: the nature of the surface and the effect on chain growth. J Phys Chem B. 2006;110:9155–63.
44. Mendes FMT, Perez CAC, Noronha FB, Schmal M. TPSR of Co Hydrogenation on $Co/Nb_2O_5/Al_2O_3$. Catal Today. 2005;101:45–50.
45. Haller G, Resasco DE. The changes in the catalytic properties of Rh/TiO_2 caused by raising the reduction. Adv Catal. 1989;36:173.
46. Hu Z, Kunimori K, Uchijima T. Interaction of hydrogen and oxygen with niobia-supported and niobia-promoted rhodium catalysts. Appl Catal A Gen. 1999;69:253.
47. Rodas-Grapain A, Arenas-Alatorre J, Gómes-Cortés A. Catal Today. 2005;107–108:168–74.
48. Schmal M, Perez CA, da Silva VT, Padilha LF. Hydrogen and ethylene production from partial oxidation of methane on CuCe, CuZr mixed oxides and ZrO_2 catalysts. Appl Catal A Gen. 2010;375:205–12.
49. Bera P, Priolkar KR, Sarode PR. Structural investigation of combustion synthesized Cu/CeO_2 catalysts by EXAFS and other physical techniques: formation of a Ce1-x Cu x O2-δ solid solution. Chem Mater. 2002;14(8):3591.
50. Rodas-Grapain A, Arenas-Alatorre J, Gómes-Cortés A. Catalytic properties of a $CuO–CeO_2$ sorbent-catalyst for de-SOx reaction. Catal Today. 2005;107–108:168.

51. Araujo LRR, Schmal M. The calcination effects on Pt/HZSM-5 catalysts in the aromatization of propane. Appl Catal A. 2000;203(2):275.
52. Barbier J, Marecot P, Martin N, Elassal L, Maurel R. Deactivation and poisoning of catalysts. Catal Deactiv. 1980;53
53. Margitfalvi J, Szedlacsek P, Heged M, Nagry F. Reaction kinetic approach to study activity, selectivity and deactivation of Pt/Al$_2$O$_3$ in n-hexane conversion. Appl Catal. 1985;15:69.
54. Espinat D, Freund E, Dexpert H, Martino G. Localization and structure of carbonaceous deposits on reforming catalysts. J Catal. 1990;126:496.
55. Wolf EE, Alfami F. Catalyst deactivation by coking. Catal Rev Sci Eng. 1982;24:329.
56. Afonso JC, Schmal M, Cardoso JN, Frety R. Hydrotreatment of Iraty shale oil. Behavior of the aromatic fraction. Ind Eng Chem Res. 1991;30:2133.
57. Aranda DAG, Afonso JC, Frety R, Schmal M. Temperature programmed oxidation of deactivated Pt/Nb$_2$O$_5$ catalysts. Stud Surf Sci Catal. 1997;3:335.
58. Leocadio ICL, Braun S, Schmal M. Diesel soot combustion on Mo/Al$_2$O$_3$ and V/Al$_2$O$_3$ catalysts. Investigation of the active catalytic species. J Catal. 2004;223:114–21.
59. Stanmore BR, Brilhac JF, Gilot P. The oxidation of soot: a review of experiments, mechanisms and models. Carbon. 2001;39:2247.
60. Du Z, Sarofim AF, Longwell JP. Activation energy distribution in. . . modeling and application to the soot-oxygen system. Energy Fuels. 1990;4:296.
61. Ahmed S, Back MH, Roscoe JM. A kinetic model for the low temperature oxidation of carbon. Combust Flame. 1987;70:1.
62. Schmal M, Perez CA, Silva VT, Padilha LF. Appl Catal A Gen. 2010;375:205–12.
63. Mori H, Wen C, Otomo J, Eguchi K, Takahashi H. Appl Catal A. 2003;245:79.
64. Rostrup-Nielsen JR. Science and technology, vol. 5. Berlin: Springer; 1984.
65. Hoffer T, Dobos S, Guczi L. Structure and methanol activation: niobia promoted Pt/Al$_2$O$_3$ catalysts. Catal Today. 1993;16:435.
66. Mul G, Neeft JPA, Kapteijn F, Makkee M, Moulijn JA. Nanophase catalytic oxides: I. Synthesis of doped cerium oxides as oxygen storage promoters. Appl Catal B. 1995;6:339.
67. Liu S, Obuchi A, Uchisawa J, Nanba T, Kushiyama S. An exploratory study of diesel soot oxidation with NO$_2$ and O$_2$ on supported metal oxide catalysts. Appl Catal B. 2002;37:309.
68. de Mello LF, Noronha FB, Schmal M. Interaction of hydrogen and oxygen with niobiasupported and niobia-promoted rhodium catalysts. J Catal. 2003;220:358.
69. Idriss H, Diagne C, Hindermann JP, Kiennemann A, Barteau MA. Reactions of acetaldehyde on CeO$_2$ and CeO$_2$-supported catalysts. J Catal. 1995;155:219.
70. Jin R, Chen Y, Li W, Cui W, Ji Y, Yu C, Jiang Y. Mechanism for catalytic partial oxidation of methane to syngas over a Ni/Al$_2$O$_3$ catalyst. Appl Catal A. 2000;201:71.
71. Aneggi E, Boaro M, De Leitenburg C, et al. Insights into the redox properties of ceria based oxides and their implications in catalysis. J Alloys Compounds. 2006;408–412:1096–102.
72. Cagnoli MV, Alvarez AM, Gallegos NG, et al. Mossbauer and XPS spectroscopies studies of SMSI effect on Fe/Nb$_2$O$_5$ catalysts for the Fischer–Tropsch synthesis. Appl Catal A Gen. 2007;326:113–9.
73. Chary KVR, Lakshmi KS, Rao PVR, et al. Characterization and catalytic properties of niobia supported nickel catalysts in the hydrodechlorination of 1,2,4-trichlorobenzene. J Mol Catal A Chem. 2004;223:353–61.
74. Helali Z, Markovits A, Minot C, et al. First row transition metal atoms adsorption on rutile TiO$_2$ (110) surface. Struct Chem. 2012;23:1309–21.
75. Hong WJ, Iwamoto S, Inoue M. Direct NO decomposition over a Ce-Mn mixed oxide modified with alkali and alkaline earth species and CO$_2$-TPD behavior of the catalysts. Catal Today. 2011;164:489–94.
76. Hong WJ, Ueda M, Iwamoto S, et al. Effect of Fe content on physical properties of BaO-CeOx-FeOy catalysts for direct NO decomposition. Appl Catal B Environ. 2011;106:142–8.
77. Jasik A, Wojcieszak R, Monteverdi S, et al. Study of nickel catalysts supported on Al$_2$O$_3$, SiO$_2$ or Nb$_2$O$_5$ oxides. J Mol Catal A Chem. 2005;242:81–90.

78. Laguna OH, Centeno MA, Boutonnet M, et al. Fe-doped ceria solids synthesized by the microemulsion method for CO oxidation reactions. Appl Catal B Environ. 2011;106:621–9.
79. Liu J, Xue D, Li K. Single-crystalline nanoporous Nb_2O_5 nanotubes. Nanosc Res Lett. 2011;6:138–45.
80. Liu L, Cao Y, Sun W, et al. Morphology and nanosize effects of ceria from different precursors on the activity for NO reduction. Catal Today. 2011;175:48–54.
81. Qiao D, Lu G, Liu X, et al. Preparation of Ce1-xFexO$_2$ solid solution and its catalytic performance for oxidation of CH_4 and CO. J Mater Sci. 2011;46:3500–6.
82. Quinelato AL, Longo E, Leite ER, et al. Synthesis and sintering of ZrO_2-CeO_2 powder by use of polymeric precursor based on Pechini process. J Mater Sci. 2001;36:3825–30.
83. Rojas E, Guerrero-Pérez MO, Bañares MA. Niobia-supported nanoscaled bulk-NiO catalysts for the ammoxidation of ethane into acetonitrile. Catal Lett. 2013;143(1):31–42.
84. Shen Q, Lu G, Du C, et al. Role and reduction of NOx in the catalytic combustion of soot over iron-ceria mixed oxide catalysts. Chem Eng J. 2013;218:164–72.
85. Sudarsanam P, Mallesham B, Reddy PS, et al. Nano-Au/CeO$_2$ catalysts for CO oxidation: Influence of dopants (Fe, La and Zr) on the physicochemical properties and catalytic activity. Appl Catal B Environ. 2014;144:900–8.
86. Wang J, Shen M, Wang J, et al. Preparation of FexCe1-xOy solid solution and its application in Pd-only three-way catalysts. J Environ Sci. 2012;24(4):757–64.
87. Wang J, Zhang B, Shen M, et al. Effects of Fe-doping of ceria-based materials on their microstructural and dynamic oxygen storage and release properties. J Sol-Gel Sci Technol. 2011;58:259–68.
88. Wojcieszak R, Jsaik A, Monteverdi S, et al. Nickel niobia interaction in non-classical Ni/Nb_2O_5 catalysts. J Mol Catal A Chem. 2006;256:225–33.
89. Yan C, Xue D. Formation of Nb_2O_5 nanotube arrays through phase transformation. Adv Mater. 2008;20:1055–8.
90. Yao X, Tang C, Ji Z, et al. Investigation of the physicochemical properties and catalytic activities of Ce0.67 M0.33O2 (M = Zr4+, Ti4+, Sn4+) solid solutions for NO removal by CO. Catal Sci Technol. 2013;3:688–98.
91. Yue L, Zhang XM. Structural characterization and phtocatalytic behaviors of doped CeO_2 nanoparticles. J Alloys Compounds. 2009;475:702–5.

Chapter 7
Catalyst Preparation

Abstract Catalyst preparation is not an attempt of a series of experiments. Different methodologies of preparations and the influence of the parameters. The influence of pre and post treatments, and chemical properties of the materials

Keywords Impregnation • Metals • Mixed oxides • Oxides • Precipitation

7.1 Introduction

Catalyst preparation is not an attempt of a series of experiments, but requires a basic knowledge of the chemical and physicochemical phenomena and process engineering. There are two stages for preparing a catalyst, which are not independent. The first one involves the chemical phenomena, reactions and the kinetics, and the second one covers the thermal treatment processes, principally conformation and resistance.

Catalyst preparation can be made tentatively or empirically and requires knowledge and experience, but it can also be optimized through experimental design. On the other hand, the preparation can be made from basic knowledge (theoretically), like surface phenomena, physicochemical properties, morphology, texture, and structure of the different materials involved in the preparation [1–8].

The main question is: what parameters are involved? The more practical and usual is to obtain the preparation parameters as precursor salts, methodology, impregnation or precipitation, pH, aging time, contact time, temperature, agitation, concentrations, etc. In the experimental design, as we shall see, these parameters can be selected and optimized to be used in the experience. On the other hand, the theory (Chap. 5) allows us to identify the interfacial and surface physicochemical, geometrical, and electronic parameters. In general, it is desired to know about the adsorption and desorption phenomena, the bond strengths, forces of attraction or repulsion, geometric and electronic phenomena, which provide reasonable accuracy optimization of the preparation process.

In industrial processes, heterogeneous and homogeneous catalysts are used. The processes are different, and here we want to address only the heterogeneous catalysts. The powdered catalysts can be metals, metal oxides, mixed oxides, zeolites, and nanostructured materials. These materials can be synthetic or naturals.

For example, zeolites are used in different processes, but especially in the catalytic and thermal cracking to produce gasoline from petroleum. Another example is a well-known powdered catalyst of iron–silica (kieselguhr) promoted with K, applied in the Fischer–Tropsch synthesis to obtain hydrocarbons, in a wide range of light hydrocarbons, gasoline, and diesel.

The second most widely used catalyst type is constituted by two phases, the support and the active material, obtained by impregnation, precipitation, or deposition–precipitation. In general, the support is not an active phase, but it serves to increase the area and to disperse the active phase. The active phase can be a metal or oxide which is the active component to interact with the molecules during the chemical reaction. The most used supports are alumina, silica, carbons, and other inert oxides. Often, the material known as support can also be active, so that there are two active phases, with different functionalities, for example, Pt/Y, in which both are active for isomerization processes. The difference is that the Pt concentration is very small, but it plays a preponderant role [1].

The third type of catalyst are clusters or alloys, which consist of a mixture of support and active mass. It is generally obtained by deposition–precipitation, in which the active phase is highly dispersed throughout the system, not just on the surface. There are also the catalysts constituted by active oxides finely deposited on an inert material, constituting a much dispersed active phase on an inert material.
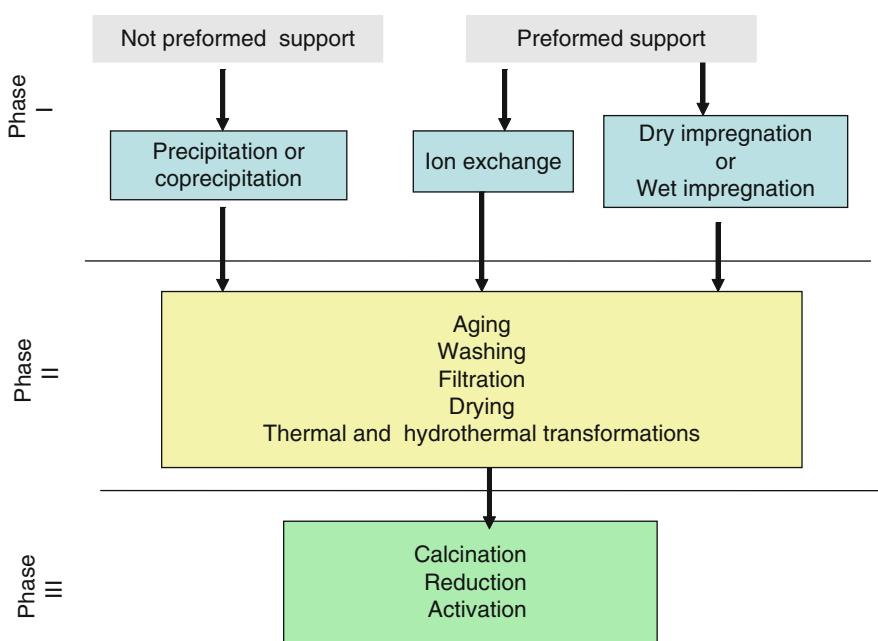
Currently, nanostructured catalysts have been developed, such as nanoparticles on supports with average particle sizes in the range of 2–20 nm, which are highly dispersed on a support, besides nanotubes, nanofibers, graphenes, and nanostructured non-stoichiometric oxides, which are very active and selective with specific properties [19–30]. As examples, we have, in the first case (nanostructured catalysts), Au/Al_2O_3 nanoparticles of Au for selective oxidation reactions. In the second case, there are carbon nanotubes, nanorods, and graphene which allow the incorporation of metallic nanoparticles, such as Pt/C, used in catalytic membranes. In the third case, we have the nanocompounds, like lamellar-type potassium niobate ($K_4Nb_6O_{17}$), which possess strong acidic properties, being promising for hydrogenation of biodiesel.

We will see in detail these types of catalyst preparation, however, before we will present the main variables and a general preparation scheme [1–9].

The main variables that compose a catalyst are:

- Grain size
- Pore size
- Surface area or specific area
- Location of the active phase
- Interaction of the active phase with the support
- Particle size
- Mechanical properties
- Thermal stability

In the general preparation scheme, we have:

7.1.1 Materials for the Preparation

Generally, organic and inorganic water-soluble materials are used. These materials are not pure and contain about 2–5 % of impurities; some are harmful and others generally inert, but which are difficult to remove. They are divided into cations and anions.

Anions

Sulfates of the type	SO_4^-
Nitrates	NO_3^-
Carbonates	CO_3^-
Chlorides	Cl^-

The sulfates are problematic as they are not easy to be removed during calcination. On the other hand, nitrates are more soluble, volatile, and easily removed during the thermal treatment, but can interact with the support and retained as nitrate or nitrite residues.

In turn, carbonates, which are relatively soluble, can easily decompose in CO_2 during the heat treatment or calcination, but can also be retained as residue of coke and carbon, which depends on interaction with the used support. This coke can only be eliminated under specific conditions.

Finally, the chlorides have strong bonds with the support, and so retain chlorine that is difficult to be removed at low temperatures.

Cations
NH_4^+, Na^+, and K^+

The ammonium ions are soluble and are readily decomposed into NH_3, forming complexes. The sodium or potassium ions are retained in the support and are not easily removed.

Examples:
Metals:
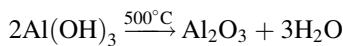
Pt   Precursors such as H_2PtCl_2 or $Pt(NH_3)_4Cl_2$ solutions
Pd   Solutions of $PdCl_2$ or $Pd(NO_3)_2$
Ni   Solutions of $Ni(NO_3)_2.6H_2O$
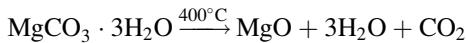
Oxides: Mo_2O_3, Al_2O_3, Nb_2O_5, and SiO_2
Hydroxides:

$$2Al(OH)_3 \xrightarrow{500°C} Al_2O_3 + 3H_2O$$

Carbonates:

$$MgCO_3 \cdot 3H_2O \xrightarrow{400°C} MgO + 3H_2O + CO_2$$

Nitrates:

$$Ni(NO_3)_2 \xrightarrow{500°C} NiO + N_2O_4 + \tfrac{1}{2}O_2$$

Supports: The support is very important, must be stable, and must be resistant to acid attack and thermal treatments. In general, commercial supports (natural and synthetic) having well-defined properties are used. Thus, the supports can be classified as:

Naturals: Diatomite or kieselguhr are based on silica. Carbon or activated carbon is based on coal. In general, diatomites and kieselguhr have relatively small areas, while carbons have very high surface areas.

Synthetics: These materials can be manufactured in large scales and have well-defined properties. The most used are alumina (Al_2O_3), silica (SiO_2), MgO, ZnO, zeolites, and others, which have surface areas in the range of 100–300 m^2/g and are very stable. As we shall see, these materials may be amorphous or crystalline of different structures and depend on the calcination or pretreatment, resulting in high or low surface areas. Silica and alumina are important supports, but serve also as raw material to synthesize other materials, such as zeolites. These zeolites are materials exhibiting variable Si/Al ratios and, depending on this ratio, have different pore sizes, i.e., micropores on ZSM5. zeolites and macropores on MCM materials. Finally, silica–magnesia can also be used as support for polymers.

7.2   Precipitation and Coprecipitation

Initially, we need to know the thermodynamic properties or particularly the constant of solubility, besides the energy involved and verify if the process is thermodynamically possible. It is also very important to know about the kinetics of precipitation for determining the precipitation rates.

There are two types of materials resulting from the precipitation, i.e., amorphous and crystalline, or mixed, which have different properties.

To obtain crystalline materials, the precipitation occurs in two steps [1–8]:

1. *Nucleation*—Germs are formed in solution in homogeneous phase. There is interaction between ions and molecules in solution that form clusters, groups, or curls, and the crystallization begins. If precipitation occurs in the presence of a support, it occurs in a heterogeneous phase; germs are formed due to the interaction of ions with the surface to form crystal nucleus.
2. *Growth*—This is a physicochemical process at the solid–solution interface, growing crystal nuclei, but the growth rate depends on the kinetics.

Nucleation is a discrete event that may be defined as "A phase transition whereby a critical volume of a semi-organized network is transformed into a structure that is sufficiently well-organized to form a viable center of growth from which the crystal lattice will grow" [1].

Nucleation may occur by means of homogeneous or heterogeneous mechanisms, either through primary or secondary route. In the primary homogeneous mechanism, nuclei are generated from the solution, while in the heterogeneous mechanism, the solid surface promotes the nucleation. In the heterogeneous nucleation or secondary route, two situations may occur: the first one is adding crystal seeds of the same phase and the second one is the formation of new crystals by fragmenting the crystallites and by breaking mechanically large particles and generating new nucleus. This occurs preferentially under certain conditions of supersaturation, when the preferential growth in a specific direction can form tips and edges breaking, generating new nuclei, the dendritic nucleation [1–8].

7.2.1   Thermodynamic Analyses

From the viewpoint of the classical approach, the nucleation can be understood from the concept of a critical nuclei size (r_c). In the first phase, it is the thermodynamics that tells us what work is required to create the interface solid–liquid to determine the binding energy by the passage of solute to the cluster [1–8]. Thus,

$$\Delta G^0_{nucleation} = \Delta G^0_{superficial} + \Delta G^0_{volume} \tag{7.1}$$

The superficial free energy is endothermic, and the energy of transformation solute—cluster, or volume energy is exothermic. So, we must find out a nucleation energy which is thermodynamically possible, that is,

$$\Delta G^0_{\text{nucleation}} < 0 \tag{7.2}$$

Consider i the number of ions in the germ, so we have

$$\Delta G^0_{\text{volume}} = i\Delta G^0_i < 0 \tag{7.3}$$

It is assumed that the germ is a spherical particle. In this case, we have

$$\Delta G^0_{\text{g}} = 4\pi r^2 \sigma + \frac{4}{3}\pi r^3 \frac{N_A}{M} \Delta G^0_{\text{v}} \tag{7.4}$$

where, g is the germ (nucleate) and v is the volume.

Note that the first term contains the area of a sphere $4\pi r^2$ multiplied by the surface tension between the solute and the solution. The second term contains the volume of the crystallite $\frac{4}{3}\pi r^3$ and the ratio of Avogadro number and molecular weight.

The free energy of germ (nucleation) formation depends on the radius of the crystallites, which is represented in Fig. 7.2.

Note that, initially, the germination-free energy is positive, or thermodynamically unfavorable, until a critical agglomeration radius r_c, corresponding to activation-free energy barrier ΔG^*. It corresponds to the formation of an activated state, which is unstable or metastable, and may undo easily. Then the nucleation begins, forming very small crystallites, but also unstable. Once past the barrier, it forms crystal clusters, and the free energy ΔG decreases until attaining radius r_0, which corresponds to a spontaneous nucleation and to a negative free energy, and thus thermodynamically favorable (Fig. 7.1).

If $r > r_c$, we have

$$\Delta G = \Delta G_i - \Delta G^* \tag{7.5}$$

But

$$\Delta G_i < \Delta G^*$$

Thus,

$$\Delta G^0_{\text{g}} < 0 \tag{7.6}$$

This condition favors the nucleation or germination.

If

$$r > r_0$$

Fig. 7.1 Free energy of
nucleation process
[Adapted from J.F. Le Page,
J. Cosyns, P. Courty,
E. Freud, J.P. Franck,
Y. Joaquin, B. Jugin,
G. Marcelly, G. Martino
et al., Catalyse de Contact,
Technip (1978)] [1]
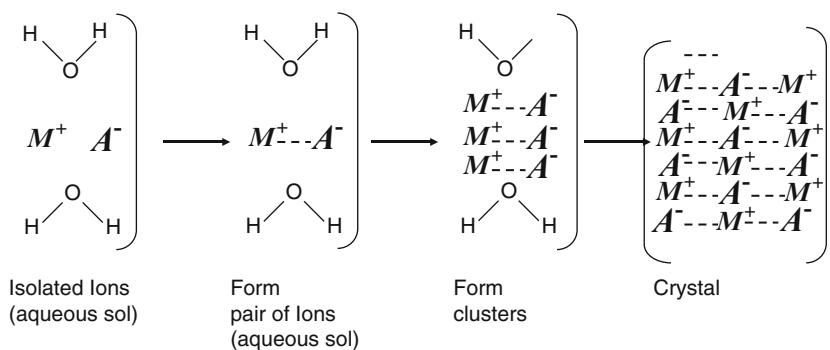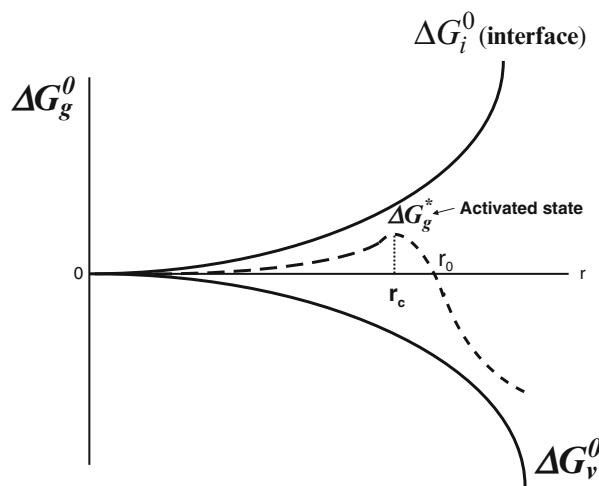
Fig. 7.2 Nucleation [Adapted from J.F. Le Page, J. Cosyns, P. Courty, E. Freud, J.P. Franck, Y. Joaquin, B. Jugin, G. Marcelly, G. Martino et al., Catalyse de Contact, Technip (1978)]

then according to the thermodynamic, we get

$$\Delta G_g^0 = -k_B T \, \ln \frac{C}{C_{s0}} \tag{7.7}$$
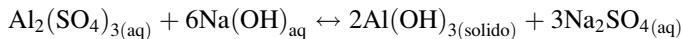
where
k_B—Boltzman constant
C_{s0}—saturation concentration
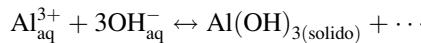
Equilibrium Condition
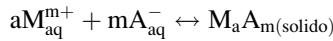
Consider the reaction of aluminum sulfate with sodium hydroxide to precipitate
aluminum hydroxide and a solution of sodium sulfate, according to

$$\mathrm{Al_2(SO_4)_{3(aq)}} + 6\mathrm{Na(OH)_{aq}} \leftrightarrow 2\mathrm{Al(OH)_{3(solido)}} + 3\mathrm{Na_2SO_{4(aq)}}$$

This can be simplified as

$$\mathrm{Al^{3+}_{aq}} + 3\mathrm{OH^-_{aq}} \leftrightarrow \mathrm{Al(OH)_{3(solido)}} + \cdots$$

or represented generically as [5, 6]

$$a\mathrm{M^{m+}_{aq}} + m\mathrm{A^-_{aq}} \leftrightarrow \mathrm{M_aA_{m(solido)}}$$

Thus, at equilibrium,

$$[\mathrm{A^{a-}}]^m [\mathrm{M^{m+}}]^a > K_{ps} \tag{7.8}$$

where K_{ps} is the solubility constant, $\mathrm{A^-}$ is the anion, and $\mathrm{M^+}$ is the cation.

$$\text{Defining} \quad s = \frac{C}{C_{s0}} \tag{7.9}$$

then we have the following possibilities:

$s = 1$—saturated solution
$s < 1$—unsaturated solution
$s > 1$—supersaturated solution, when precipitation occurs.

If $s \gg 1$, then it precipitates forming homogeneous crystalline nuclei. Schematically, we have

We can monitor the process of nucleation and crystal formation using the phase diagram. Figure 7.3 shows the phase diagram.

Curve (a) shows the saturation solubility constant varying with temperature and concentration of the solute, beginning the nucleation, and forming metastable germs. Curve (b) shows the supersaturation solubility constant, where the nucleation is spontaneous, forming heterogeneous solutions of micelles and small crystallites. This occurs for crystal sizes of radius r_0 where the free energy is negative ($\Delta G_g^0 < 0$) and the process is thermodynamically favorable.

Consider two situations, following paths 1 and 2, under isothermal conditions. In the first case, increasing the solute concentration at a constant temperature up to curve K_{ss}, it forms micelles spontaneously, but the concentration of the solute will decrease until reaching equilibrium conditions and forms crystals. Following path 2 at different temperature, the solute concentration surpasses the equilibrium curve and reaches supersaturation curve, which is thermodynamically favorable for spontaneous formation of crystals, which are substantially homogeneous. The concentration of the solute decreases then toward an equilibrium concentration, as shown in Fig. 7.3.
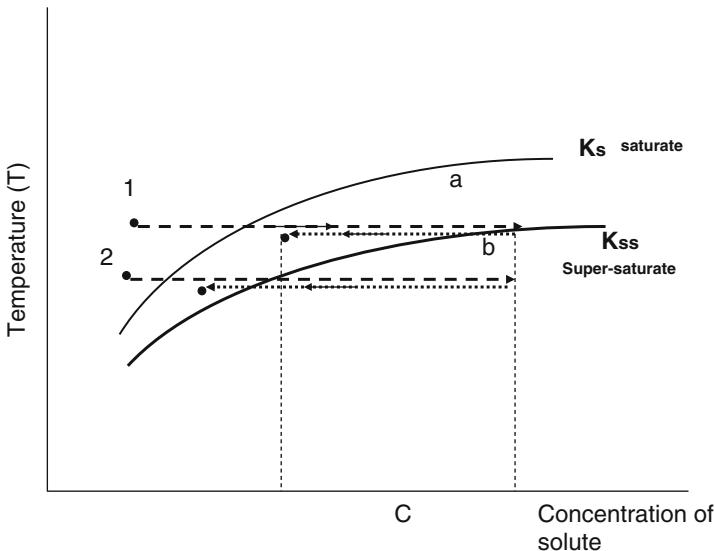
Fig. 7.3 Phase diagram [Adapted from J.F. Le Page, J. Cosyns, P. Courty, E. Freud, J.P. Franck, Y. Joaquin, B. Jugin, G. Marcelly, G. Martino et al., Catalyse de Contact, Technip (1978)]

7.2.2 Kinetics of the Precipitation

Growth This is a physicochemical process, where crystal nuclei grow up at the solid–solution interfaces and the growth rates depend on the kinetics. The rate growth during the nucleation process depends on the concentration of the solute and the temperature. Initially, it is slow, but then grows exponentially up to the supersaturation concentration. Figure 7.4 shows the growth rate of the cores as a function of concentration $s = \frac{C}{C_{s0}}$.

The growth rate is very small during the induction period up to the supersaturated concentration, but then it grows exponentially, as a sigmoidal curve. However, with decreasing solute concentration the rate decreases, as shown in Fig. 7.4.

The growth can be represented as a rate of first order, namely [1],
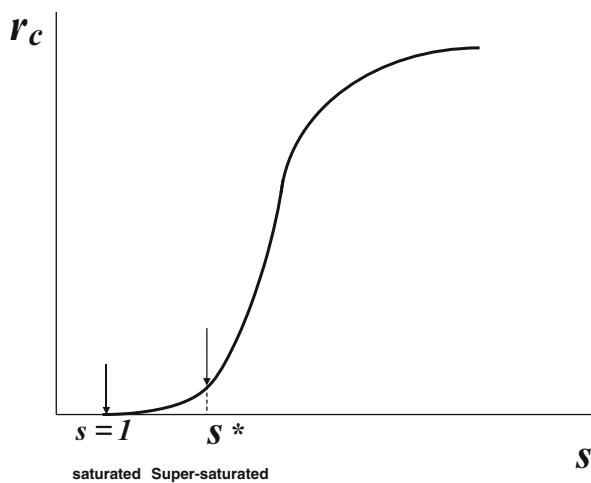
$$r_c = kC \tag{7.10}$$

where k is the kinetic constant, C is the concentration of the solute and

$$k = k_0 \exp\left(-\frac{\Delta G^0}{k_B T}\right) \tag{7.11}$$

or

$$r_c = C_{s0}k_0\exp\left(-\frac{\Delta G^0}{k_B T}\right)s \tag{7.12}$$

where k_B is the Boltzmann constant, $\Delta G *$ the nucleation-free energy, and C_{s0} the initial concentration of the solute.

Substituting Eqs. (7.11) and (7.12) in (7.10) and if $s = \frac{C}{C_{s0}}$, then

$$-\frac{dC}{dt} = kC$$

$$-\frac{dC}{C} = kdt$$

$$-\ln\frac{C}{C_{s0}} = k_0\exp\left(-\frac{\Delta G^*}{k_B T}\right)t \tag{7.13}$$

In general, one defines the nucleation rate as

$$r_c = r_{c0}s*N* \tag{7.14}$$

Here, r_{c0} is the initial rate which corresponds to the saturation, $s *$ the supersaturation concentration, and $N *$ the number of critical nuclei, corresponding to supersaturation.

It is possible to induce rapid precipitation, by adding seeds to the solution, which increases the concentration of the solution at the interface. It is a heterogeneous nucleation. The number of crystal particles present in the solution depends on the number of cores or germs in the solution.

The rate growth r_{ch} around the core depends on the diffusion of ions at the solution–solid interface; thus, [1],

$$r_{ch} = k_d(C_\infty - C_s)^n \tag{7.15}$$

where k_d is the diffusion constant and n is an exponent varying between 1 and 2.

Substituting the concentration by the saturation s, we have

$$r_{ch} = k_d(C_\infty - C_s)^n = k_d C_s^n(s-1)^n \tag{7.16}$$

For supersaturation, the exponent is approximately 1; thus, when $s \gg 1$, then $n \approx 1$.

As shown in the following figure:

Figure 7.5 shows the rate growth of crystals after nuclei formation. Note that the nucleation rate increases exponentially, whereas the rate of crystal growth increases linearly with different ramps r_{ch}^1 and r_{ch}^2.

Region I shows that the crystal rate growth is always greater than the nucleation rate, $r_{ch}^1 > r_c$, thus forming a few large crystals. Unlike, region II shows that the crystal rate growth is always smaller than the nucleation rate $r_{ch}^1 < r_c$, and hence it forms many and smaller crystals. Thus, for example, starting from (1), where the concentration is at saturation, it begins to form crystals. With increasing saturation concentration, the rate growth passes the nucleation curve and thus forms other nuclei around the crystal and increases the growth of many smaller crystals. Starting from (1) to (3), the crystal growth is linear, forming larger crystals.

Figure 7.6 shows the crystallite sizes depending on the saturation in the heterogeneous nucleation. Note, when saturated, crystals grow, reaching a maximum, but

Fig. 7.5 Heterogeneous nucleation [Adapted from J.F. Le Page, J. Cosyns, P. Courty, E. Freud, J.P. Franck, Y. Joaquin, B. Jugin, G. Marcelly, G. Martino et al., Catalyse de Contact, Technip (1978)]
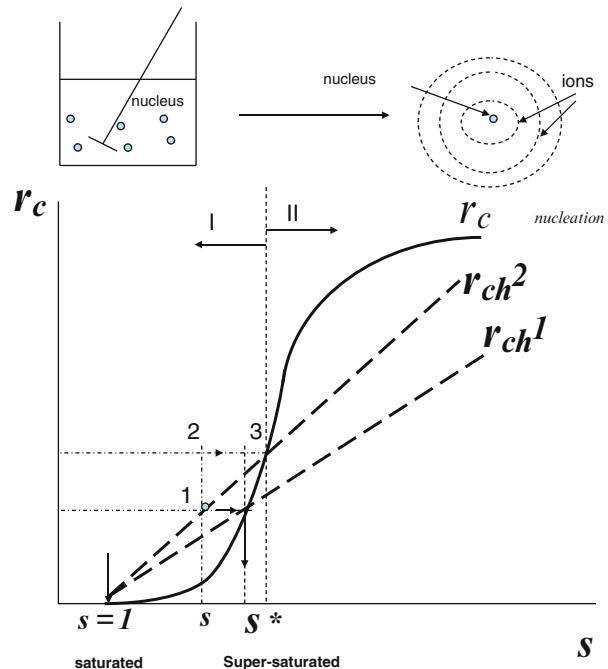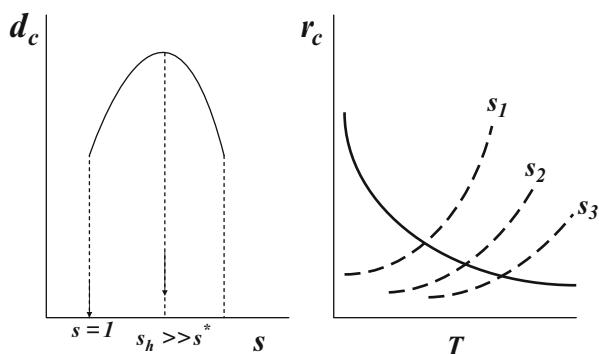
Fig. 7.6 Influence of parameters on crystal growth [Adapted from J.F. Le Page, J. Cosyns, P. Courty, E. Freud, J.P. Franck, Y. Joaquin, B. Jugin, G. Marcelly, G. Martino et al., Catalyse de Contact, Technip (1978) and D. Cardoso, Introdução a Catálise Heterogênea, U.F.S. Carlos (1987)] [5]

decrease after reaching the supersaturation concentration, where nucleation predominates, forming smaller crystals.

The growth of crystals is influenced mainly by:

- Stirring—High stirring favors formation of small crystals, since the concentration at the interface increases.
- Temperature—High temperature decreases the rate growth of crystals and thus increases crystal sizes.

7.2.3 Amorphous Solids

The amorphous *solids* are obtained by sol–gel precipitation. Sol is a dispersed homogeneous phase. Colloidal solutions are constituted by micelles. The micelles are formed due to electric charges, whose repulsive force prevents coagulation. Micelles are formed by polycondensation [1].

The electrostatic potential varies with distance, which can be associated with van der Waals forces. The electrostatic potential is generated by the surface with ions concentrated near the wall and diffusion of ions in both directions of the liquid. The electrostatic potential can be represented by the following equation: $\psi = \psi_\delta e^{-kx}$ where ψ is the electrostatic potential, δ the layer thickness at the interface, and x the interface distance, k being a constant. The negative ions at the interface and the positive ions in the layer δ near the liquid phase form the set of micelles as outlined in Fig. 7.7 [1]. Note that the maximum potential is at the interface ψ_0. The ions are distributed in the liquid phase reducing its concentration with increasing x.

An example is the preparation of silica, schematized in Fig. 7.8. The following steps occur:

- Formation of silanols after lowering the pH of the solution by adding an acid (H_2SO_4) [1]:
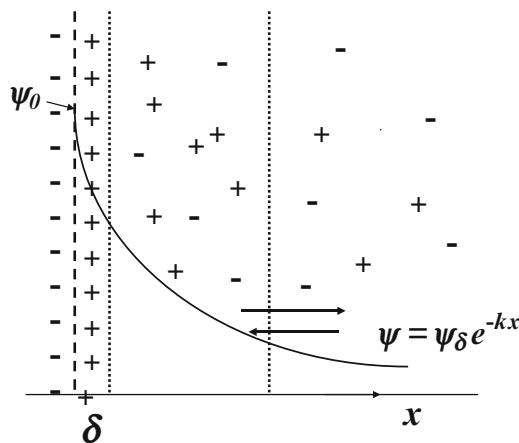
Fig. 7.7 Electrostatic potential of the ion interface [Adapted from J.F. Le Page, J. Cosyns, P. Courty, E. Freud, J.P. Franck, Y. Joaquin, B. Jugin, G. Marcelly, G. Martino et al., Catalyse de Contact, Technip (1978)]
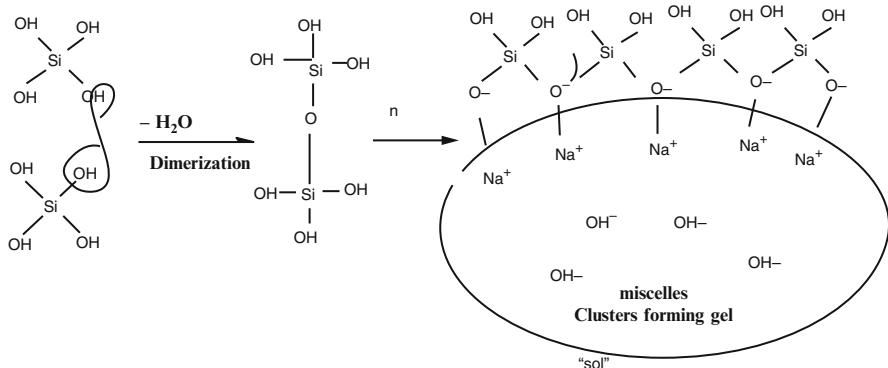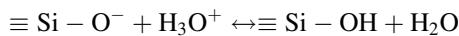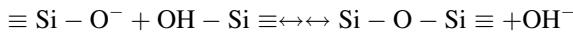
Fig. 7.8 Scheme of micelles sol–gel [Adapted from J.F. Le Page, J. Cosyns, P. Courty, E. Freud, J.P. Franck, Y. Joaquin, B. Jugin, G. Marcelly, G. Martino et al., Catalyse de Contact, Technip (1978)]

$$\equiv Si - O^- + H_3O^+ \leftrightarrow \equiv Si - OH + H_2O$$

- Silanols tend to polymerize with maximum Si–O–Si bonds and minimal noncondensable Si–OH groups, namely,

$$\equiv Si - O^- + OH - Si \equiv \leftrightarrow \leftrightarrow Si - O - Si \equiv +OH^-$$

The formation of hydrogel depends on the gelation time which comprises of 90 % water inside.

There are clusters forming gel in the gelling process. This gel is formed by three-dimensional structures, namely [1] (Fig. 7.9),
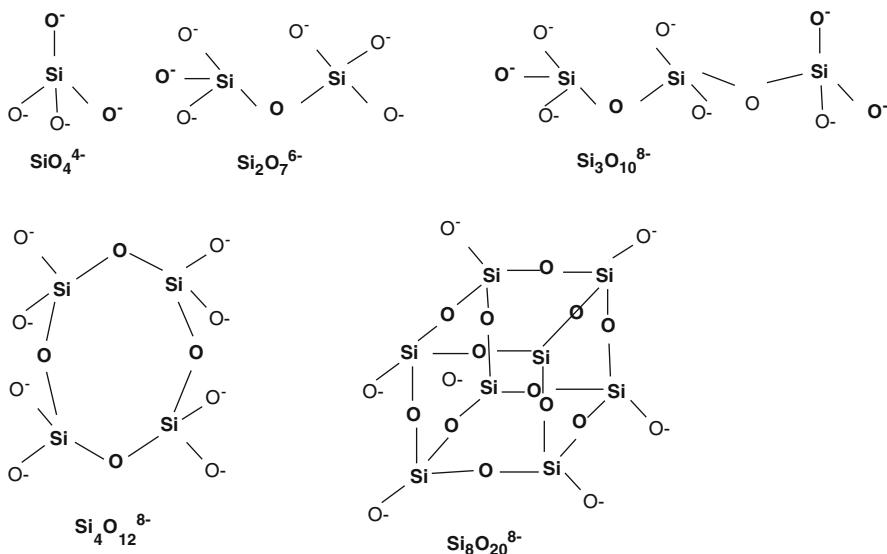
Fig. 7.9 Scheme of gelification [Adapted from J.F. Le Page, J. Cosyns, P. Courty, E. Freud, J.P. Franck, Y. Joaquin, B. Jugin, G. Marcelly, G. Martino et al., Catalyse de Contact, Technip (1978)]

It can be seen that during the polymerization, it forms loop structures due to the oligomerization process, which are two- and three-dimensional molecules. When condensed, it forms more compact and well-defined structures [1, 5].

The hydrogel depends on the gelling time. The hydrogel may form flocculate which depends on rate drying. If too quick, it forms flocculate of the order of 1μ or 100μ [1].

The product formed depends on the chemical nature, the concentration of micelles, temperature, pH, and ionic strength, as we shall see.

7.2.4 Coprecipitation

Preparation by coprecipitation forms two active phases. This is based on two different precursors and a precipitating agent. As examples, we consider the preparation of copper chromite and Co–Cu spinel, using different coprecipitation methods.
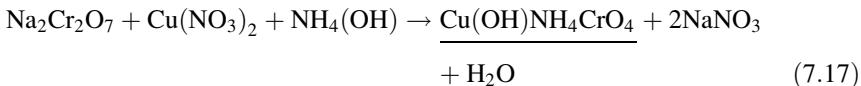
Examples

1. *Preparation of* $CuCrO_3$
   The solutions $Na_2Cr_2O_7$ and $Cu(NO_3)_2$ are mixed in stoichiometric amounts and precipitated in the presence of a precipitant agent $NH_4(OH)$. The reactions are as follows [10]:

Table 7.1 Composition of the mixed oxides $Cu_xCo_yO_4$: coprecipitation (C) [10]

Precursor	Nominal (%)		Real (%)		Formula	Ratio Cu/Co
	Cu	Co	Cu	Co		
$CuCo_2O_4$	25	48	21.98	46.36	$Cu_{0.9}Co_{1.9}O_4$	0.5

$$Na_2Cr_2O_7 + Cu(NO_3)_2 + NH_4(OH) \rightarrow \underline{Cu(OH)NH_4CrO_4} + 2NaNO_3$$
$$+ H_2O \qquad (7.17)$$
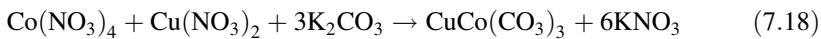
This precipitate is calcined, and we obtain $CuCrO_3$.

2. *Preparation of a mixed oxide* $Cu_xCo_yO_4$

   Preparing mixed oxides having different ratios of Cu/Co by coprecipitation, starting from the solutions $Co(NO_3)_4, Cu(NO_3)_2$, we obtain oxides with spinel-type structure $Cu_xCo_yO_4$ [10].

   The temperature is constant at 70 °C, and pH varies between 8 and 9 during the precipitation process. Nitrate concentrations are equal to 0.5 M and precipitant equal to 1 M. The following reaction occurs:

$$Co(NO_3)_4 + Cu(NO_3)_2 + 3K_2CO_3 \rightarrow \underline{CuCo(CO_3)_3} + 6KNO_3 \qquad (7.18)$$

   The precipitate should be washed repeatedly to remove the ions, dried at 110 °C/ 15 h, and calcined at 350 °C/6 h under flowing air at 30 ml/min. The calcined precipitate showed different mixed oxides, as presented in Table 7.1.

   The oxide prepared by direct coprecipitation presents segregation of CuO phase. The real composition is $Cu_{0.9}Co_{1.9}O_4$.
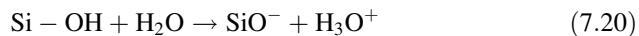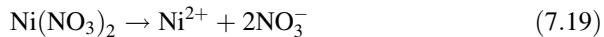
7.2.5   Deposition–Precipitation

This method allows obtaining surface with homogeneous active and highly dispersed phases. It is a hybrid method known as deposition–precipitation, when carriers may be added to the precipitant solution. The precipitating precursor is deposited on this support in suspension. This preparation depends on various parameters, such as, pH of the solution and mainly of the external surface of the support. The main problems are the onset of nucleation and crystal growth over the surface, thus nucleation and formation of small particles over the surface.
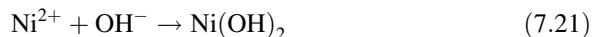
When the concentration exceeds the limit of solubility or at supersaturation, crystals begin to form and grow. It is important that nucleation occurs over the support and not in the solution, forming small crystal evenly distributed at the surface, preventing the growth of large crystals. So it should be added slowly and with vigorous stirring of the precipitating solution. This method seems to be best suited for distribution of small crystals on predefined surfaces or precast. A general

scheme can be seen in the following sequence, in order to obtain a nickel precipitate on silica or alumina [1, 2]:
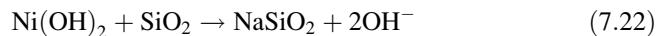
Step 1—Starting from nitrate, it forms Ni^{2+} ions and the silica provides hydroxyls:

$$Ni(NO_3)_2 \rightarrow Ni^{2+} + 2NO_3^- \tag{7.19}$$

$$Si - OH + H_2O \rightarrow SiO^- + H_3O^+ \tag{7.20}$$

The silica ions SiO^- attract Ni^{2+} ions, which are adsorbed and in turn react with the hydroxyls, forming the precipitate:

$$Ni^{2+} + OH^- \rightarrow Ni(OH)_2 \tag{7.21}$$

In addition to this precipitate, there is the possibility of forming silicates, releasing the hydroxyl again

$$Ni(OH)_2 + SiO_2 \rightarrow NaSiO_2 + 2OH^- \tag{7.22}$$

In this process, it enhances the interaction between the ion and the support, resulting better metal dispersion and higher competition between the rate growth and nucleation rate on the surface, as shown in Fig. 7.10.
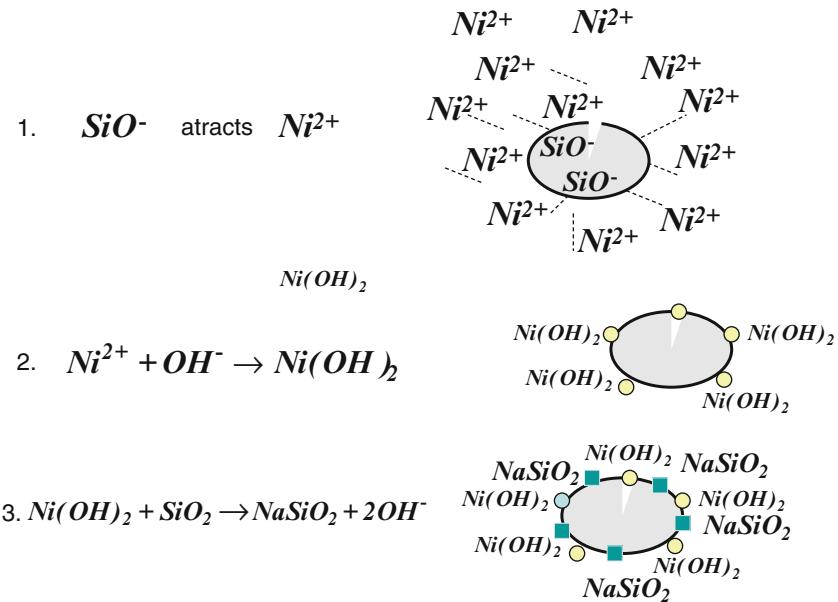
Fig. 7.10 Deposition–precipitation [Adapted from J.F. Le Page, J. Cosyns, P. Courty, E. Freud, J.P. Franck, Y. Joaquin, B. Jugin, G. Marcelly, G. Martino et al., Catalyse de Contact, Technip (1978)]

There are several other ways of precipitation, for example, formation of anionic species that may be deposited on the surface of the suspension, varying certain parameters, particularly the pH of the solution.

7.3 Impregnation

First, preparing a metal solution with a specific concentration to achieve a given content on a support, and then impregnating, by varying time, temperature, and pH, to adsorb the active phase, such that after drying and calcining, metal is fixed and stable. The support may be inert or partially active, but with well-defined properties. The most important is that the support is molded or extruded, impregnating the precursor thereon. In this case, the impregnation is carried out with a solution to fill the pores, by knowing beforehand the volume thereof. It is called dry impregnation. When the carrier is in powder, the required volume is significantly larger than the volume of the pores, and the impregnation is called wet impregnation. Thus, the impregnation can be classified in two types [1–7]:

- Without interaction with the support
- With interaction with the support

7.3.1 Impregnation Methods

In the first case, we have a solution that contains the active substance, and the carrier is inert or partially active. The impregnation may be dry or wet (Fig. 7.11).

$$V_{\text{pores}} = V_{\text{solution}} \Rightarrow \text{dry-impregnation}$$

$$V_{\text{solution}} \gg V_{\text{pores}} \Rightarrow \text{wet-impregnation}$$

Solution concentration:

$$C_{\text{solution}} = \frac{n}{V} = \frac{n}{V_{\text{p}}.m_{\text{cat}}} = \frac{\frac{m_{\text{precursor}}}{M_{\text{precursor}}}}{V_{\text{p}}.m_{\text{cat}}} = \left[\text{moles} / \text{cm}^3 \right] \tag{7.23}$$
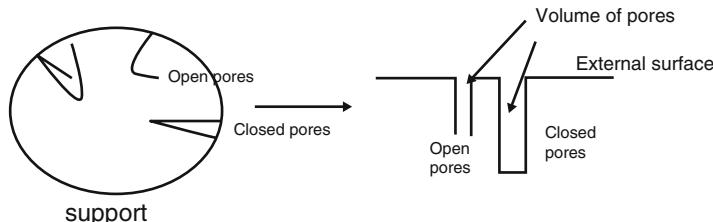
Fig. 7.11 Scheme of porous particles

The impregnation occurs by diffusion or wetting. When by diffusion one estimates the time, i.e. [9],
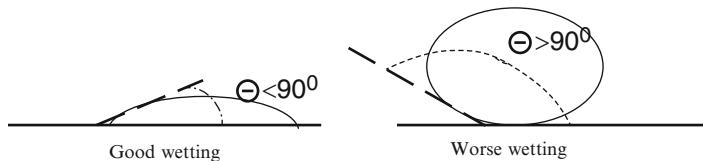
$$t_{\text{diffusion}} = t_d = \frac{x^2}{D} \tag{7.24}$$

where x is the distance from the pore to the surface and D the diffusion coefficient (cm^2/s).

The soaking time should always be longer than the diffusion time:

$$t_{\text{soaking}} > t_d$$

The impregnation mechanism is capillary and consequently depends on the capillary forces and surface wettability. There are two limiting cases:

Good wetting   Worse wetting

We may consider three situations:

The pressure difference can be calculated:

$$\Delta p = p_A - p_B = \frac{2\sigma \cos \theta}{r} \tag{7.25}$$
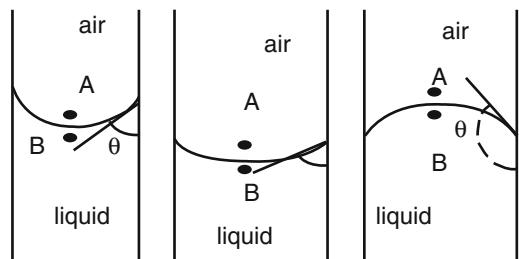
where σ is the surface tension, r the capillary radius, and θ the angle liquid–gas interface (Fig. 7.12).

Some common cases:

$$\text{Water—}\theta \approx 90° \quad p_A > p_B$$
$$\text{Liquids in general—}\theta < 90° \quad p_A \gg p_B$$
$$\text{Quicksilver} - \text{Hg—}\theta > 90° \quad p_B > p_A \tag{7.26}$$

The impregnation time can be estimated through equation

Fig. 7.12 Scheme of liquid contact-surface pores of the particle [2]
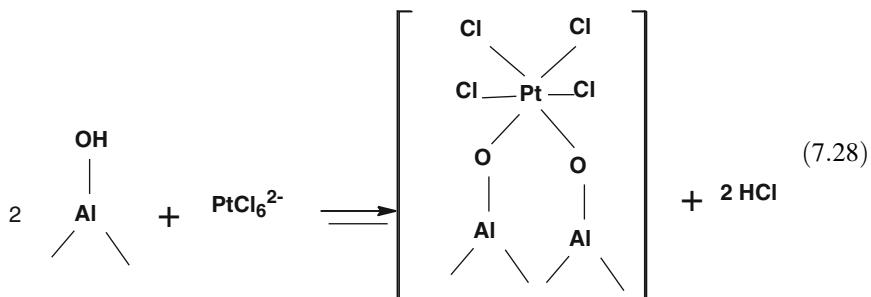
$$t = \frac{4\mu \cdot x^2}{\sigma \cdot r} \tag{7.27}$$

where μ is the dynamic viscosity [9].

7.3.1.1 Without Interaction with the Support

Usually, there are three methods as represented in Fig. 7.13.

The most common example is the impregnation of Pt on a support. Hexachloroplatinic acid H_2PtCl_6 adsorbs strongly on the surface of γ-Al_2O_3 and is practically irreversible, as shown in scheme [Adapted from J.F. Le Page, J. Cosyns, P. Courty, E. Freud, J.P. Franck, Y. Joaquin, B. Jugin, G. Marcelly, G. Martino et al., Catalyse de Contact, Technip (1978)].

$$\tag{7.28}$$

The Al–OH groups are almost equal the basic sites, since the adsorption is analogous to hydrolysis of $PtCl_6^{2-}$, which occurs in solutions of high pH.
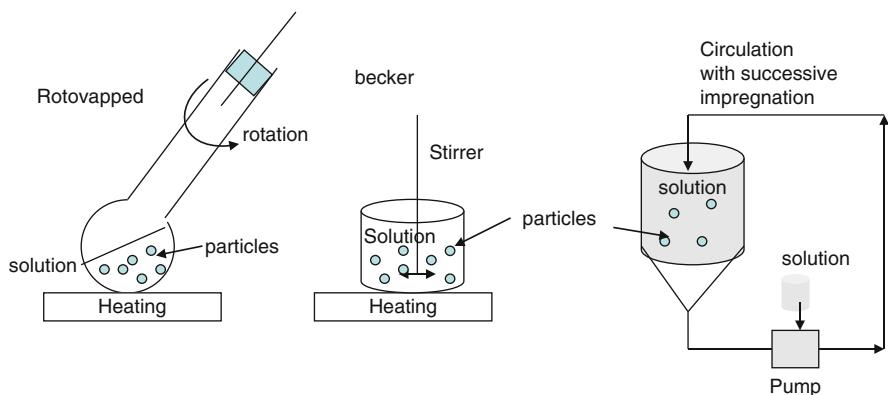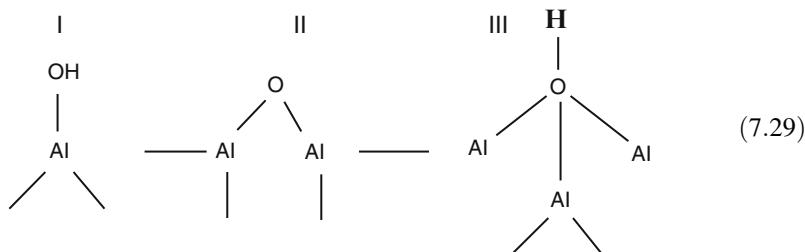
Fig. 7.13 Scheme of preparation by impregnation
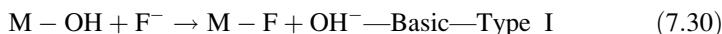
7.3.1.2   Impregnation with Interaction with the Support

When the impregnation occurs with interaction with the support, there are ionic and covalent bonds. As observed by infrared spectroscopy, there are different types of hydroxyl bonds on oxides surfaces, having low, high, and intermediate frequencies, as shown below [9]:
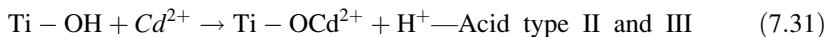
For *alumina*, there are following cases:

$$(7.29)$$
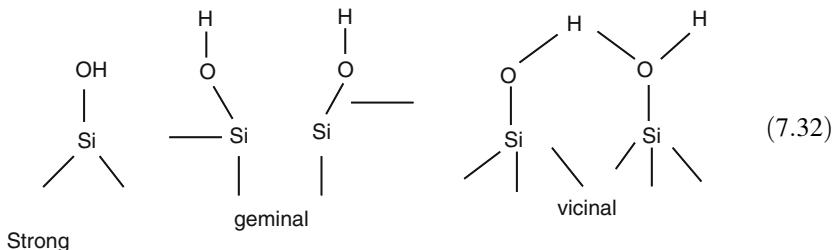
While alumina has three types, titania presents type I (basic) and bridged type II (acid). The acid or basic features can be observed through ion exchange with specific ions. Thus, the anionic character of type I can be identified when the hydroxyl ions can exchange, for example [9],

$$M - OH + F^- \rightarrow M - F + OH^- \text{—Basic—Type I} \qquad (7.30)$$
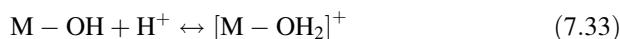
But the acid character can be observed with the ion exchange of the hydroxyl of titania with cations, for example,

$$Ti - OH + Cd^{2+} \rightarrow Ti - OCd^{2+} + H^+ \text{—Acid type II and III} \qquad (7.31)$$
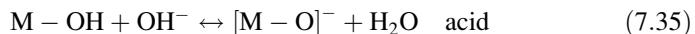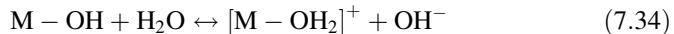
On *silica*, the bindings are different and represented as follows [1, 9]:

$$(7.32)$$

The strong bindings are the most common on surfaces and may interact with metals and oxides. When these oxides come in contact with an aqueous solution, there are different reaction forms, as [9]

$$M - OH + H^+ \leftrightarrow [M - OH_2]^+ \qquad (7.33)$$

$$M - OH + H_2O \leftrightarrow [M - OH_2]^+ + OH^- \tag{7.34}$$

$$M - OH + OH^- \leftrightarrow [M - O]^- + H_2O \quad \text{acid} \tag{7.35}$$
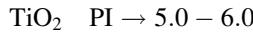
In fact, there are electric charges on the surface, which depend on the pH of the solution and the oxide type.
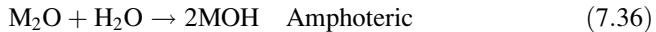
Isoelectric Point

The pH value at electric charge zero is called the point zero charge, identified as isoelectric point, where electric charges are compensated. In this state, either the solution or the colloidal system does not carry electric charges [1, 9].
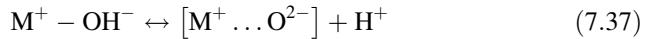
If the pH value is lower than the isoelectric point (PI), the surface or solution is positively charged and attracts anions, canceling the total charge. In the colloidal solution, we obtain amorphous material (like boehmite). If the pH is greater than the isoelectric point (PI), the surface or solution is negatively charged and attracts cations which are compensated. In a colloidal solution, it forms precipitate (like barite). All oxides have set its isoelectric point or zero charge [1–9]:

$$Al_2O_3 \quad PI = 8.0$$
$$TiO_2 \quad PI \rightarrow 5.0 - 6.0$$
$$SiO_2 \quad PI \rightarrow 2.0$$

In short:

$$M_2O + H_2O \rightarrow 2MOH \quad \text{Amphoteric} \tag{7.36}$$
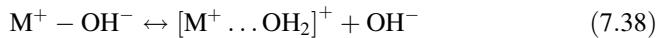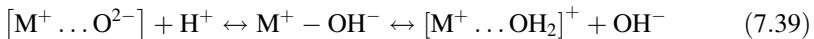
If acid (proton donor):

$$M^+ - OH^- \leftrightarrow [M^+ \ldots O^{2-}] + H^+ \tag{7.37}$$

If basic (hydroxyl donor):

$$M^+ - OH^- \leftrightarrow [M^+ \ldots OH_2]^+ + OH^- \tag{7.38}$$

Or generically [2]:

$$[M^+ \ldots O^{2-}] + H^+ \leftrightarrow M^+ - OH^- \leftrightarrow [M^+ \ldots OH_2]^+ + OH^- \tag{7.39}$$

$$\text{If acid} \rightarrow \text{surface}(+) \rightarrow \text{anion exchange}$$
$$\text{Surface}(-) \leftarrow \text{If basic}$$
$$\text{Cation exchange}$$
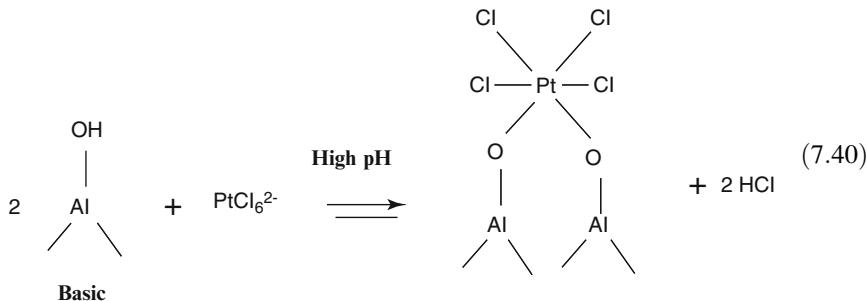
Thus, H^+ proton exchange with cations: $Ni^{2+}, Pd^{2+}, Pt^{2+}$ and hydroxyls OH^- exchange with complex anions.

In the case of Pt on SiO_2, the isoelectric point (PI) is equal to 2 and allows high adsorption, which increases with increasing pH. Since the silica has negative

charges, it attracts cations. If the pH can increase up to the limit value of 9 and above, it dissolves silica.

For Pt/Al_2O_3, where $PI = 8.0$, there is exchange as shown [9]:

$$(7.40)$$

Example 1

Preparation of Pt/Al_2O_3 catalyst by impregnation was performed using as the precursor hexachloroplatinic (H_2PtCl_6). The support was a γ-alumina from Harshaw (Al3996). The alumina was calcined at a rate of 10 °C/min to 550 °C for 2 h. The surface area was 200 m^2/g [12].

The platinum hexachloroplatinic acid was used as precursor (Aldrich), usually employed in the preparation of supported catalysts. The aqueous solution was prepared shortly before impregnation and kept in dark bottle due to the instability of the platinum solution when exposed to light. Figure 7.14 shows the platinum particles of the $Pt/Al_2 O_3$ catalyst observed by TEM [12] and particle sizes as shown in Table 7.2.

7.3.2 Ion Exchange

Ion exchange occurs between an A ion of the solid (MO) and an ion B of the solution (S) according the reaction [5, 6, 11]

$$A_{MO} + B_S \leftrightarrow B_{MO} + A_S \tag{7.41}$$

At equilibrium, we have

$$K = \frac{[B_{MO}][A_s]}{[A_{MO}][B_s]} \tag{7.42}$$

But from the stoichiometry, we have

Fig. 7.14 Platinum particles of the Pt/Al$_2$O$_3$ catalyst observed by TEM [12]
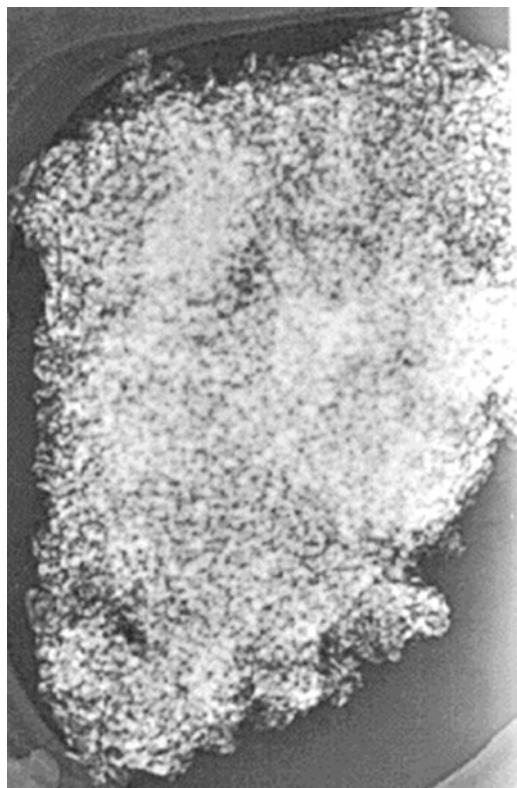
Table 7.2 Particle sizes after TEM [12, 13]

Catalyst	Dispersion (%)	d_p (nm)
PtAl	87	1, 3
ZrO$_2$	–	–

on the solid

$$[B_{MO}] + [A_{MO}] = [MO] \tag{7.43}$$

and in the solution

$$[B_S] + [A_S] = [S] \tag{7.44}$$

From these equations, we obtain

$$[A_{MO}] = [MO] - [B_{MO}] \tag{7.45}$$

$$[A_S] = [S] - [B_S] \tag{7.46}$$

Substituting Eqs. (7.38) and (7.46) in (7.42), we obtain

$$K = \frac{[B_{MO}]([S] - [B_S])}{[B_s]([MO] - [B_{MO}])} \tag{7.47}$$

or

$$[B_{MO}] = \frac{K[MO][B_S])}{[S] + [B_S](K - 1)} \tag{7.48}$$

The molar fractions are, respectively,

$$y_{B_{MO}} = \frac{[B_{MO}]}{[MO]} \tag{7.49}$$

and

$$y_{B_S} = \frac{[B_S]}{[S]} \tag{7.50}$$
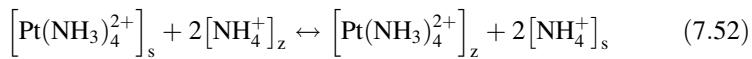
Substituting Eqs. (7.49) and (7.50) in Eq. (7.48), we have

$$y_{B_{MO}} = \frac{K.y_{[B_S]}}{1 + (K - 1)y_{[B_S]}} \tag{7.51}$$

Figure 7.15 displays the molar fractions of the ions as a function of the equilibrium K constant and shows that high K values promote better ion exchange with the ions of the solid.

Example 2

Ion exchange between the $Pt(NH_3)_4^{2+}$ solution and NH_4^+ ions of zeolites occurs according to the following reaction:

$$\left[Pt(NH_3)_4^{2+}\right]_s + 2\left[NH_4^+\right]_z \leftrightarrow \left[Pt(NH_3)_4^{2+}\right]_z + 2\left[NH_4^+\right]_s \tag{7.52}$$

Using an excess of NH_4^+ in the solution, we obtain higher exchange due to the displacement of the equilibrium. One obtains maximum exchange after 3 days at a $pH = 7$ and at 220 C. Often, to enhance the Pt content, we use several sequential exchanges [14].

XPS results of the calcined Pt catalysts at $350\,^{\circ}C$ showed the presence of $Pt(NH_3)$ $4Cl_2$ species. This suggests that the calcination temperature was not sufficient for complete decomposition of the Pt complex. After calcination at 550-CA results
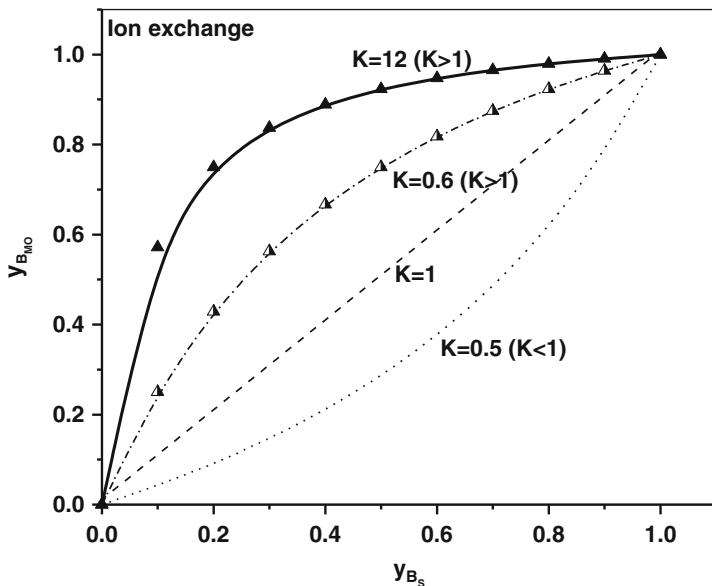
Fig. 7.15 Graphical representation of ion exchange (Adapted from Le Page et al. [1])
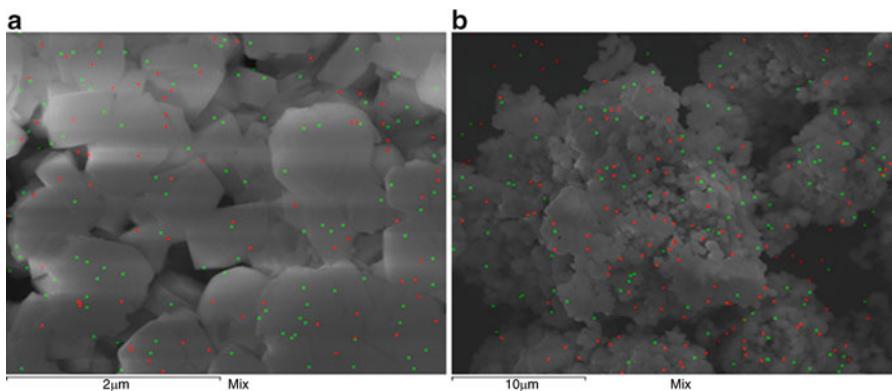
Fig. 7.16 TEM results for 1Pt1Mo catalyst with two different scales (**a**) 2 μm and (**b**) 10 μm. The *red points* corresponding to Pt atoms and *green points* to Mo atoms [12]. Additional papers related to this subject are presented in references [15–18].

presented PtO, besides metallic Pt^0, suggesting complete decomposition of the precursor.

Example 3

The Pt/Y was prepared with NaY zeolite (SAR = 5). Platinum was incorporated by ion exchange with a solution of $Pt(NH_3)_4Cl_2$ for 1 % Pt (w/w), according to Gallezot et al. [14]. The desired Pt content was obtained by balancing the solution containing Pt and zeolite NaY. Electron microscopy (TEM) shown in Fig. 7.16, indicates small particles well distributed with diameters of the order of 5 nm [11].

References

1. Le Page JF, Cosyns J, Courty P, Freud E, Franck JP, Joaquin Y, Jugin B, Marcelly G, Martino G, et al. Catalyse de Contact, Technip (1978).
2. Bond CC. Heterogeneous catalysis and applications. Oxford: Clarendon; 1974.
3. Satterfield CN. Heterogeneous catalysis in practice. New York: McGraw Hill; 1980.
4. Ciola R. Fundamentos em Catálise. São Paulo: Editora Moderna; 1981.
5. Cardoso D. Introdução a catálise heterogênea. U.F.S. Carlos (1987).
6. Figueiredo JL, Ramôa Ribeiro F. Catálise heterogênea. Lisboa: Fundação Calouste Gulbekian; 1987.
7. Anderson RB. Experimental methods in catalytic research. New York: Academic; 1968.
8. Trimm DL. Design of industrial catalysis. Amsterdam: Elsevier, Scientific Publishing Company; 1980.
9. Moujijn JA, van Leeuwen PWNM, van Santen RA. Catalysis – Studies science and catalysis, vol. 79. Amsterdam: Elsevier, Scientific Publishing Company; 1993.
10. Cesar DV, Perez CA, Salim VMM, Schmal M., Stability and Selectivity of the Bimetallic Cu-Co/SiO2 Catalysts for the Cyclohexanol Dehidrogenation, Appl Catal A General. 1999;205:176.
11. Colman RC, Baldanza MAS, Schmal M. Influence of Mo Species on the Pt/NaY Catalyst and the Effect of Sulfur Content on theHydrodenitrogenation Reaction, J Phys Chem C. 2010;114:18501–8.
12. Schmal M, Souza MMMVM, Aranda DAG, Perez CAC. Promoting Effect of Zirconia Coated on Alumina on the Formation of Platinum Nanoparticles – Application on CO2 Reforming of Methane, Stud Surf Sci Catal. 2001;132:695.
13. Souza MMMVM, Aranda DAG, Schmal M. Reforming of Methane with Carbon Dioxide over Pt/ZrO2/Al2O3 Catalysts, J Catal. 2001;204(2):498.
14. Gallezot P, Alarcon-Diaz A, Dalmon JA. Renouprez AJ, Imelik B. Location and Dispersion of Platinum in PtY Zeolites, J Catal. 1975;39:334.
15. Campo, B., Santori, G., Petit, C., et al., 2009, "Liquid phase hydrogenation of crotonaldehyde over Au/CeO2 catalysts", Applied Catalysis A: General, v. 359, n. 1-2, p.79-83.
16. De Lima, S. M., Da Silva, A. M., Da Costa, L. O. O., et al., 2009, "Study of catalyst deactivation and reaction mechanism of steam reforming, partial oxidation, and oxidative steam reforming of ethanol over Co/CeO2 catalyst", Journal of Catalysis, v. 268, n. 2, p.268-281.
17. Khaodee, W., Tangchupong, N., Jongsomjit, B., et al., 2009, "A study on isosynthesis via CO hydrogenation over ZrO2-CeO2 mixed oxide catalysts", Catalysis Communications, v. 10, n. 5, p.494-501.
18. Kim, Y. T., Park, E. D., Lee, H. C., et al., 2009, "Water-gas shift reaction over supported Pt-CeOx catalysts", Applied Catalysis B: Environmental, v. 90, n. 1-2, p.45-54.
19. Mai, H.-X., Sun, L.-D., Zhang, Y.-W., et al., 2005, "Shape-selective synthesis and oxygen storage behavior of ceria nanopolyhedra, nanorods, and nanocubes", The Journal of Physical Chemistry B, v. 109, n. 51, p.24380-24385.
20. Panagiotopoulou, P., Kondarides, D. I. e Verykios, X. E., 2009, "Selective methanation of CO over supported Ru catalysts", Applied Catalysis B: Environmental, v. 88, n. 3-4, p.470-478.
21. Silveira, E. B., Perez, C. A. C., Baldanza, M. A. S., Schmal, M., 2008. Performance of the CeZrO2 mixed oxide in the NOx decomposition. Catalysis Today 133–135 (2008) 555–559.
22. Sun, C., Li, H. e Chen, L., 2007, "Study of flowerlike CeO2 microspheres used as catalyst supports for CO oxidation reaction", Journal of Physics and Chemistry of Solids, v. 68, n. 9, p.1785-1790.
23. Wang, Z. L. e Feng, X., 2003, "Polyhedral shapes of CeO2 nanoparticles", The Journal of Physical Chemistry B, v. 107, n. 49, p.13563-13566.
24. Zhao, M. W., Shen, M. Q. e Wang, J., 2007, "Effect of surface area and bulk structure on oxygen storage capacity of Ce0.67Zr0.33O2", Journal of Catalysis, v. 248, n. 2, p.258-267.

25. Zhong, L.-S., Hu, J.-S., Cao, A.-M., et al., 2007, "3D flowerlike ceria micro/nanocomposite structure and its application for water treatment and CO removal", Chemistry of Materials, v. 19, n. 7, p.1648-1655.

26. ECHCHAHED, B., KALIAGUINE, S., ALAMDARI, H., 2006, "Well dispersed Co0 by reduction of LaCoO3 perovskite", International Journal of Chemical Reactor Engineering, v. 4, n. A29.

27. GELLINGS, P. J., BOUWMEESTER, H. J. M., 2000, "Solid state aspects of oxidation catalysis", Catalysis Today, v. 58, n. 1 (Apr), pp. 1-53.

28. LIN, J., YU, M., LIN, C., LIU, X., 2007, "Multiform Oxide Optical Materials via the Versatile Pechini-Type Sol-Gel Process: Synthesis and Characteristics", Journal of Physical Chemistry C, v. 111, pp. 5835-5845.

29. PEÑA, M. A., FIERRO, J. L. G., 2001, "Chemical Structures and Performance of Perovskite Oxides", Chemical Reviews, v. 101, n.7 (Jul), pp. 1981-2017.

30. QUINELATO, A. L., LONGO, E. R., LEITE, M. I., et al., 2001, "Synthesis and sintering of ZrO2-CeO2 powder by use of polymeric precursor based on Pechini process", Journal of Materials Science, v. 36, pp. 3825-3830.

Chapter 8
Variables Influencing Final Properties of Catalysts

Abstract Variables influencing the preparation methods and the final properties of the catalysts.

Keywords Metals, oxides • Preparation • Properties • Supports • Variables

Variables influencing the preparation by precipitation, coprecipitation, precipitation–deposition, and impregnation can transform the chemical and physical properties, approaching to the equilibrium conditions. The main variables are as follows [1–11]:

- pH
- Aging time
- Temperature
- Precursors

8.1   Influence of pH

The pH values may influence significantly on the formation of intermediate complexes during the preparation by precipitation or precipitation–deposition. For example, gold catalysts are prepared with a gold precursor ($HAuCl_4$ solution), and pH affects the formation of gold complexes, the maximum content, and the presence of chlorine. The ions $[AuCl_4]^-$ form different complexes, as shown in Fig. 8.1. Complexes like $[AuCl_{4-x}(OH)_x]^-$ ($x = 1$–3) are adsorbed at the surface with the formation Au(OH)3 species, which are the precursors of gold nanoparticles [8, 12–14].

8.2   Autoclaving

Autoclaving is performed in a batch reactor under high pressure and different temperatures. There are thermal and hydrothermal transformations when in the presence of steam, resulting in structural changes. In the presence of a solvent, the precipitated solid suffers structural and textural modifications, but in principle the main steps are [15]:
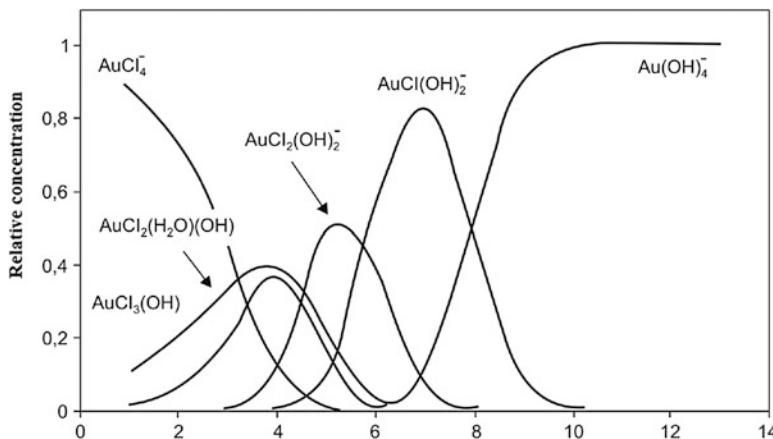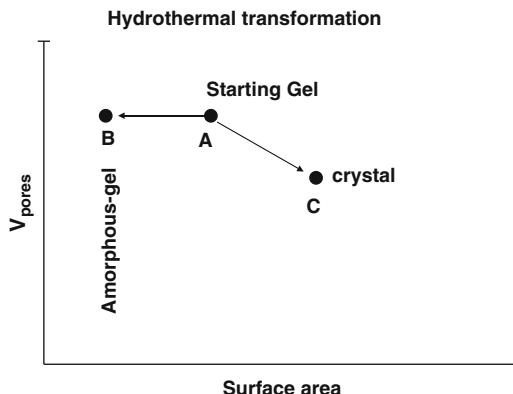
Fig. 8.1 Gold complexes from a solution of 2.5×10^{-3} M HAuCl$_4$ (adapted with permission from Lee and GAVRIILIDIS, J. of Catal. 206 (2002) 305 2002) Elsevier) [12]

Fig. 8.2 Hydrothermal transformations [adapted from J.F. Le Page, J. Cosyns, P. Courty, E. Freud, J.P. Franck, Y. Joaquin, B. Jugin, G. Marcelly, G. Martino et al., Catalyse de Contact, Technip (1978)]

1. *Dissolution*—part of the solid in the presence of a solvent or water undergoes solvation of the metallic ions with the rupture of bindings and formation of new bonds with the solid.
2. *Diffusion*—transfer of the solvated ion from the solid to the final solid.
3. *Desolvation*—the inverse phenomena of the first step, where the ion goes to the solid and is incorporated in the structure, occurring again precipitation.

The transformations occurring are:

- Small crystallites → large crystallites.
- Small amorphous particles → large amorphous particles
- Amorphous solid → crystalline solids
- Crystallites (1) → crystallites (2)

Starting from a gel (A) may be passed to an amorphous gel (B) or crystal (C) with different textural properties, as shown in Fig. 8.2.

8.3   Influence of Time, Concentration, and Impregnation Cycles

There are maximum concentrations that can be deposited on the surface. Difficult is to impregnate high metal concentrations in one step. When the support is pre-shaped, such as cylinders or spheres, the impregnation time is important. For short times, the metal distribution is concentrated at the external surface. Long impregnation times improve the metal distribution inside pores of the pellet or extruded, as shown in Fig. 8.3.

For higher metal concentrations, the successive impregnation is employed, or several cycles, until the desired concentration is reached. The metal distribution must be homogeneous. In practice, higher concentrations can be reached with 3–5 cycles (Fig. 8.4).

8.4   Thermal Treatments

8.4.1   Drying

During the drying process, the residues and solvents are eliminated, transforming gels in xerogels. The mass loss depends on the heating rate and involves heat and mass transfer phenomena:
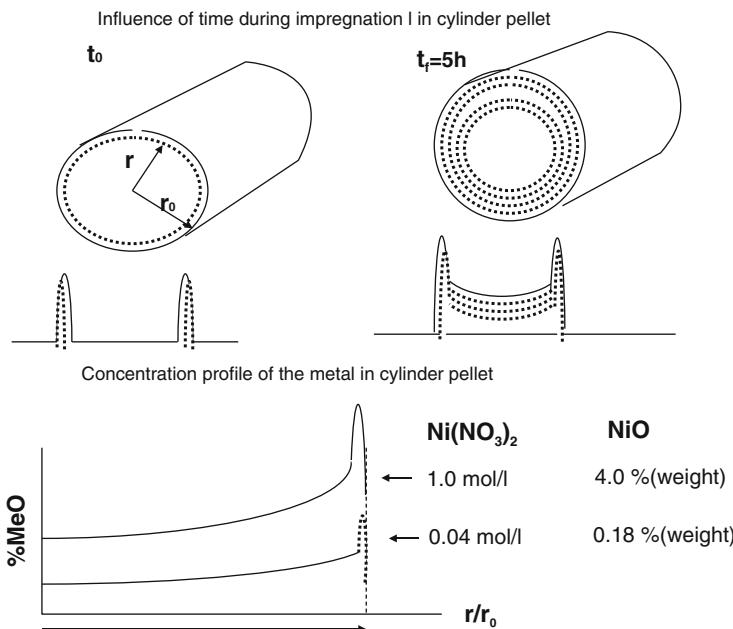
Fig. 8.3   Influence of time and concentration on pellets/extruded

Influence of impregnation cycles in a cylinder pellet
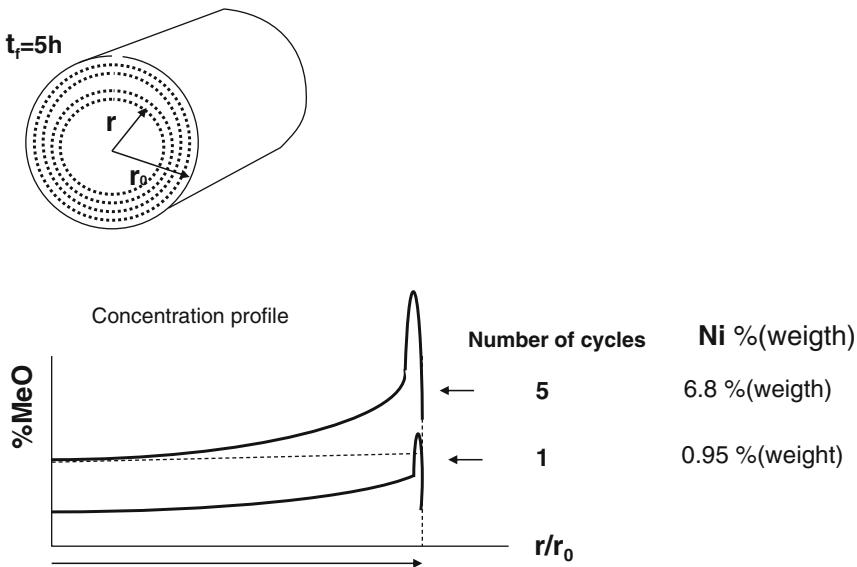
Fig. 8.4 Impregnation cycles—metal concentration

$$m = ak_m(p_s - p_g) \tag{8.1}$$

$$q = a'h(T_g - T_s) \tag{8.2}$$

Where a and a' are the interface areas; k_m, h the mass and heat transfer coefficients, respectively; and p, T the pressure and temperature of the gas (g) and solid (s), respectively. Figure 8.5a shows the mass loss and drying rates and the temperature of the different transformation phases.

The rates and the temperatures increase on the surface until they reach the temperature of equilibrium, remaining then constants. Drying proceeds into the inner and the heating rate, as well as the rate of mass transfer decreases significantly, while the temperature increases till the end. The heat transfer rate is significant to obtain a homogenous drying. In the drying processes, usually the heating rate is of the order of 10 °C/min.

The drying process is also very important in wet impregnation for the elimination of solvents, and the higher the heating rate, the less is the contact of gas with the surface, which favors the formation of smaller particles and in opposite, and the slower the heating rate, the higher is the contact time of drying gas with surface and consequently bigger particles are favored, as shown in Fig. 8.5b.
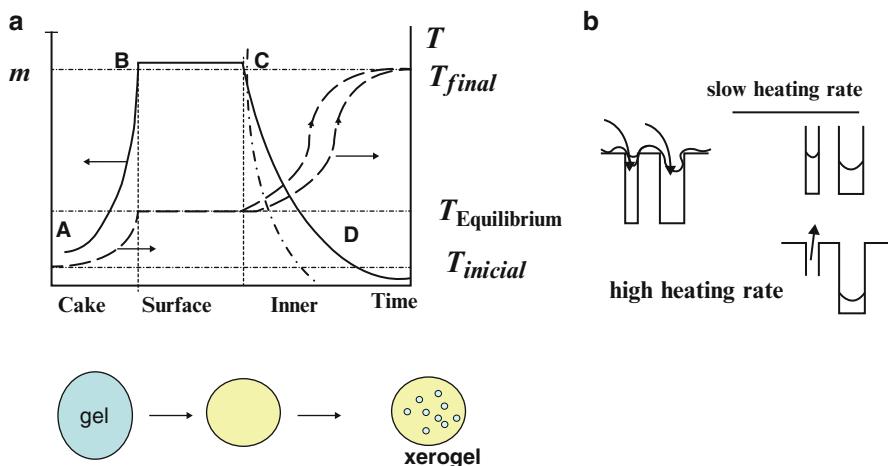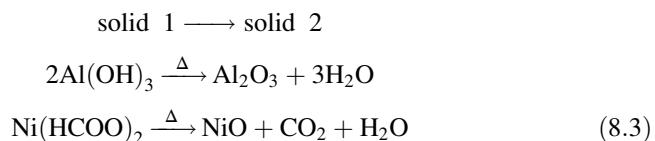
Fig. 8.5 Drying of cake (**a**) and pores (**b**)
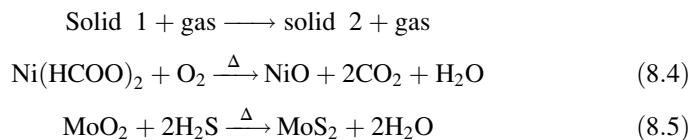
8.4.2 Calcination

During the calcination with or without gases, there are decompositions of hydroxides, carbonates (gel, xerogel) transforming into oxides which are chemical reactions, transforming one compound into other compounds. During thermal treatments, there are following cases:

(a) Decomposition:

$$solid\ 1 \longrightarrow solid\ 2$$

$$2Al(OH)_3 \xrightarrow{\Delta} Al_2O_3 + 3H_2O$$

$$Ni(HCOO)_2 \xrightarrow{\Delta} NiO + CO_2 + H_2O \tag{8.3}$$

(b) Presence of gas:

$$Solid\ 1 + gas \longrightarrow solid\ 2 + gas$$

$$Ni(HCOO)_2 + O_2 \xrightarrow{\Delta} NiO + 2CO_2 + H_2O \tag{8.4}$$

$$MoO_2 + 2H_2S \xrightarrow{\Delta} MoS_2 + 2H_2O \tag{8.5}$$
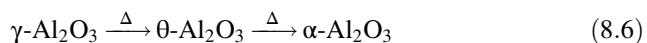
(c) Phase transformation:

$$\gamma\text{-}Al_2O_3 \xrightarrow{\Delta} \theta\text{-}Al_2O_3 \xrightarrow{\Delta} \alpha\text{-}Al_2O_3 \tag{8.6}$$

Phase transformation can be followed by thermogravimetry, measuring the mass loss and the temperature difference with increasing temperature, as shown in Fig. 8.6.

Fig. 8.6 Thermal
treatments—TGA and TDA
[adapted from J.F. Le Page,
J. Cosyns, P. Courty,
E. Freud, J.P. Franck,
Y. Joaquin, B. Jugin,
G. Marcelly, G. Martino
et al., Catalyse de Contact,
Technip (1978)]
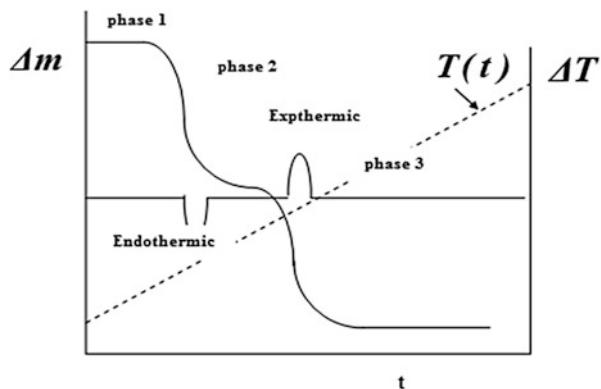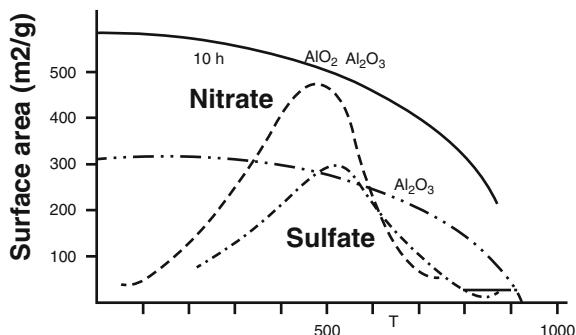
Fig. 8.7 Specific surface
area as function of the
calcination temperature
(adapted from Le
Page et al.)

The effects of calcination are significant, modifying textural and morphological properties, affecting the surface area, pore volumes, and structures. There are also differences between bulk and supported materials. In the first case, one observes from Fig. 8.7 how these parameters change with increasing calcination temperature.

It shows that the specific surface area decreases with increasing temperature of calcination.

Starting from precursors, like nitrates or sulfates, the specific surface area modifies drastically, reaching high values, and then decreases due to structural crystalline rearrangement. Starting from crystals, like alumina or silica-alumina, with increasing the calcination temperature, the specific surface area decreases due to sintering or agglomeration of crystallites. The classical case is the alumina. Starting from γ-Al_2O_3, that with a surface area around 200 m^2/g is transformed into α-Al_2O_3 which presents a surface area of the order of 20 m^2/g.

On supported catalysts, the effect of calcination is significant on the particle sizes, dispersions, and crystallite sizes. Measurements of particle sizes or metal dispersions after calcination and reduction of supported catalysts indicate different situations, and there are three cases that are illustrated bellow.

8.4.2.1 Effect of Calcination and Digestion over Reduction and Metallic Surface Area

The first case illustrated in Table 8.1 shows how the calcination temperature and digestion time affect the metallic area and degree of reduction of the alumina-supported NiO for different Ni contents.

Results indicate that the reduction without calcination presented higher reduction of NiO and higher metallic area for different Ni contents. After calcination both reduction and metallic area decreased significantly, independent of the digestion time, which suggests agglomeration of particles or interaction with the support during the calcination step. The digestion time did not affect the metallic area and the reduction.

Figure 8.8a displays the effect of calcination and reduction temperature on the metallic Ni^o area. The precursors were calcined separately at 300 and 500 °C and reduced with H_2. When calcined at 500 °C, the metallic area increases with increasing reduction temperature, allowing the reduction of big and small particles at the surface. However, when calcined at 300 °C, the metallic area indicates two different situations as shown in Fig. 8.8b.

(a) In the initial situation between range A and B, there are big NiO particles which are reduced to metallic Ni^o: $NiO \rightarrow Ni^0$.
(b) In the range B and C, the metallic area decreases because NiO interacts with the support and the reduction of these particles is more difficult.

Table 8.1 Influence of calcination temperature and digestion time

Ni (%)	$T_{calcination}$ (°C)	$t_{digestion}$ (h)	S_{metal} (m^2/g$_{Ni}$)	Reduction (%)
9	400	1	4.3	7
9	Without calcination	–	10	16
15	400	4	5.2	5
15	Without calcination		14.6	14
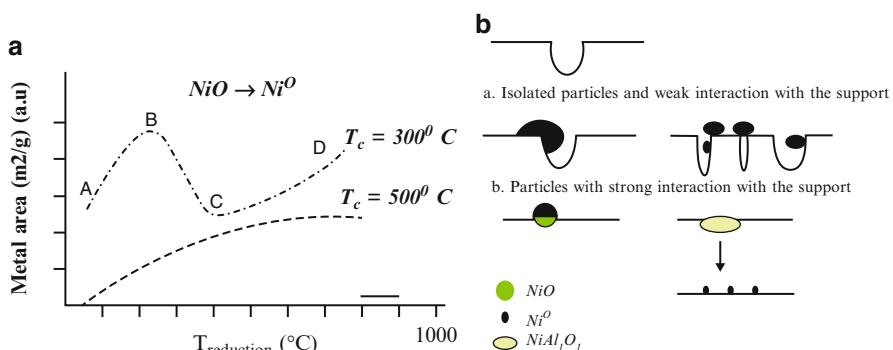
Fig. 8.8 (**a**) Effect of the calcination temperature over the metal area (adapted from Le Page [1]). (**b**) Scheme of particles sizes

(c) In between C and D, the metallic area increases due to the reduction of nickel particles with strong interaction with the support and the reduction of nickel aluminate: $NiAl_2O_3 \rightarrow Ni^0 + Al_2O_3$. These particles are not easily reduced to metallic Ni_o.

8.4.2.2 Influence of Calcination Temperature over Dispersion and Particle Sizes
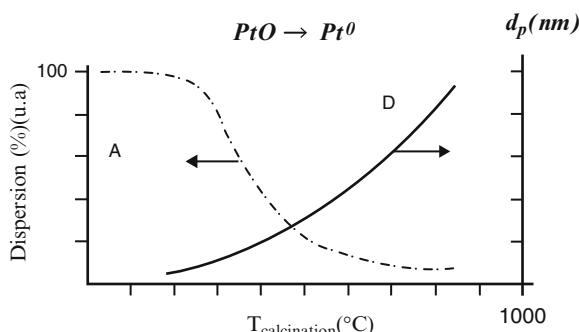
The effect of calcination temperature on particle diameters of a Pt/SiO_2 catalyst after reduction is displayed in Fig. 8.9. The precursor was calcined and presents PtO_2 or PtO. After reduction, it is transformed in metallic Pt^o.
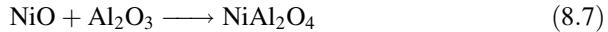
The dispersion decreases drastically, whereas particle diameters increase with increasing temperature. It is assigned to crystal growth or strong interaction with the support or sintering and therefore formation of silicates which are difficult to reduce. With increasing temperature, there are migrations of particles or growth from smaller to bigger particles [16].

8.5 Effect of Reduction Temperature on Interaction and Sintering
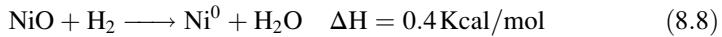
The reduction temperature influences the metal–support interaction and agglomeration, which occurs frequently on supported catalysts and will be illustrated for the nickel supported catalyst. It depends on the support, the metal concentration, the calcination temperature, the reducing agent, the H_2 concentration, and water. When promoted with potassium, lanthanum or any other promoter improves the reducibility and the metal distribution. After calcination, nickel is an oxide, but can also be Ni_2O_3, as suboxide, or as aluminate [17]:

Fig. 8.9 Effect of calcination temperature on particle diameters [adapted from J.F. Le Page, J. Cosyns, P. Courty, E. Freud, J.P. Franck, Y. Joaquin, B. Jugin, G. Marcelly, G. Martino et al., Catalyse de Contact, Technip (1978)]

$$NiO + Al_2O_3 \longrightarrow NiAl_2O_4 \tag{8.7}$$

The reduction of nickel oxide occurs as follows:

$$NiO + H_2 \longrightarrow Ni^0 + H_2O \quad \Delta H = 0.4\,Kcal/mol \tag{8.8}$$

However, the direct reduction of the nitrate precursor may also occur:

$$Ni(NO_3)_2 + 2H_2 \longrightarrow Ni^0 + H_2O + 2NO_2, \quad \Delta H = 11.9\,Kcal/mol \tag{8.9}$$

$$Ni(NO_3)_2 + 4H_2 \longrightarrow Ni^0 + 4H_2O + 2NO_2, \quad \Delta H = -86.5\,Kcal/mol \tag{8.10}$$

$$Ni(NO_3)_2 + 9H_2 \longrightarrow Ni^0 + 6H_2O + 2NH_3, \quad \Delta H = -261.5\,Kcal/mol \tag{8.11}$$

8.6   Influence of the Support and the Metal Concentration on the Reduction

The supports γ-Al$_2$O$_3$ and α-Al$_2$O$_3$ have different structures and specific surface areas, around 200 m^2/g and <10 m^2/g, respectively. Typical reduction profiles of NiO at 8 and 16 % are shown in Fig. 8.10a, b.

There are two reduction peaks, which are attributed to the reduction of NiO. At higher temperature, the NiO species linked to Al^{+3} species are more difficult to be reduced due to the strong interaction with the alumina support.

The reduction peaks of NiO on the α-Al$_2$O$_3$ support are shifted to lower temperatures with increasing metal content, when compared to the bulk NiO. Thus, the reduction is facilitated with increasing metal content. The degrees of
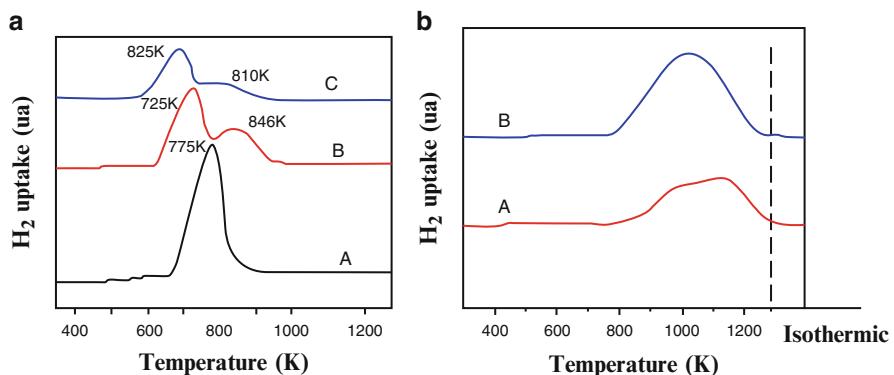
Fig. 8.10   (a) TPR profiles of Ni/α-Al$_2$O$_3$: (A) NiO, (B) 8 % Ni, and (C) 16 % Ni. (b) TPR profiles of Ni/γ-Al$_2$O$_3$: (A) 8 % Ni and (B) 16 % Ni [17]
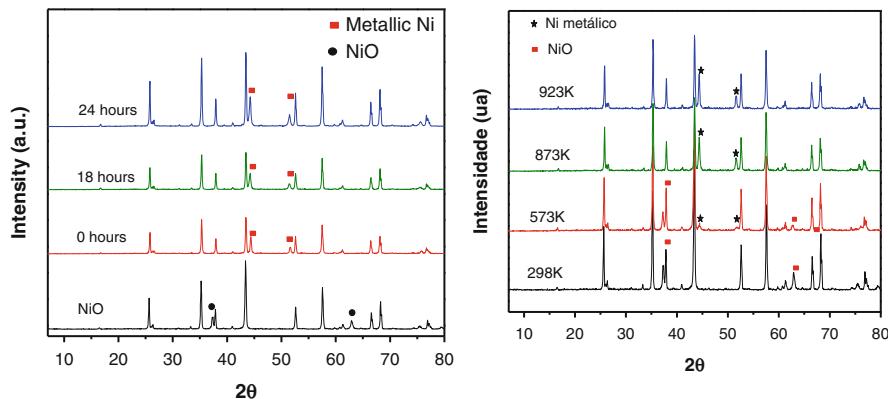
Fig. 8.11 XRD in situ reduction of 8 % Ni/αAl$_2$O$_3$ catalyst with time and different reduction temperatures

Table 8.2 Effect of heating rate

$T_{calcination}$ (°C)	Heating rate (°C)/min	Metallic area S_{metal} (m^2/g)
400	15	3.2
400	5	4.3
–	15	6.5
–	5	14.6

reduction of NiO for the 8 and 16 % Ni/α-Al$_2$O$_3$ were 59.4 % and 22.0 %, respectively. In fact, significant amounts of Ni species were not reduced.

Figure 8.11 shows the XRD diffraction pattern after in situ reduction of 8 % Ni/α-Al$_2$O$_3$, with time and reduction temperature.

The NiO was not observed after reduction above 500 °C but only metallic Ni. From the diffraction line (111) at 44.5°, we calculated the crystal sizes (d_{Ni}) 45A° and the dispersion (D_{Ni}) 1.9 % [17].

8.7 Influence of the Heating Rate

The influence of the heating rate of reduction after calcination and direct reduction on the metallic area and dispersion of the Ni/Al$_2$O$_3$ catalyst is presented in Table 8.2.

Heating rates do not affect the metallic area after calcination, but significantly after direct reduction at 550 °C.
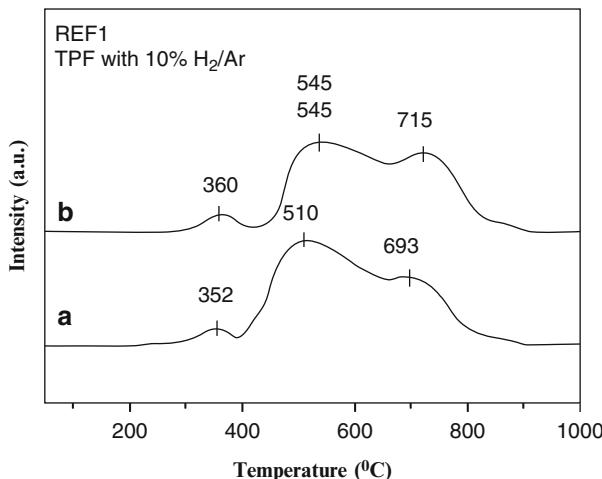
Fig. 8.12 TPR profiles of a nickel sample and with 10 % H_2/Ar, without (**a**) and with steam (**b**) [16].

8.8 Influence of Steam

The influence of steam on the reduction of nickel supported catalysts is shown in Fig. 8.12. The reduction was performed with steam and 10 % H_2/Ar. The reduction temperature with steam shifts the maximum peak to higher temperature but is not significant.

The first peak is associated to the reduction of NiO without interaction with the support, while the second and third peaks are associated to the reduction of NiO interacting with the support, probably due to the reduction of nickel aluminate. The reduction degree was 100 % and the particle sizes of the order of 200 A^0.

8.9 Effect of Temperature and Reaction Time

The reaction temperature, mainly for exothermic reactions, affects the structure and textural properties of the catalysts which causes deactivation. The consequences are structural modifications or sintering of the catalyst. The most important identification of sintering is crystal sizes or particle sizes before and after reaction.

Frusteri et al. [18] measured the particle sizes by TEM analysis of Ni/MgO sample, for ethanol reforming at 650 °C with H_2O/EtOH after 20 h reaction, as well as the influence of alkaline metals. Figure 8.13 displays the particle size distribution before and after reaction, showing the presence of big particles evidencing sintering. When doped with Li and K, the deactivation is less affected.

a

b
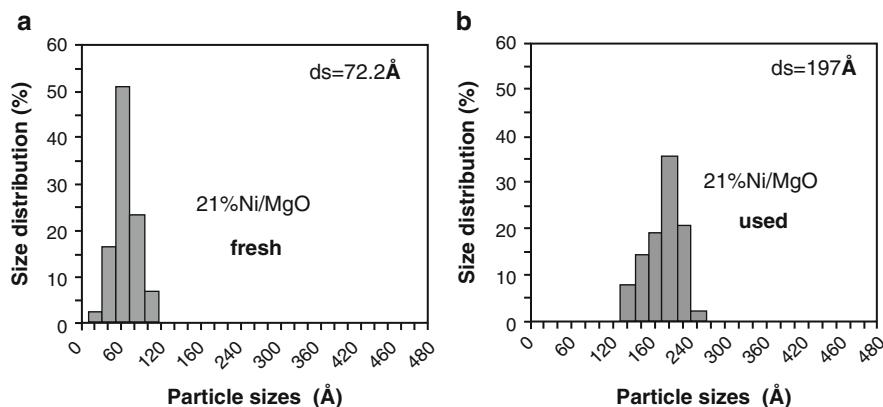
Fig. 8.13 Particle size distribution for Ni/MgO before and after 20 h reaction. Conditions: $(GHSV_V = 667 \ mL_{EtOH} \ min^{-1} \ mL_{cat}^{-1}$, $T = 923$ K e ratio $H_2O/EtOH = 3)$ (Reproduced with permission from Frusteri et al., 2004a)

8.10   Strong Metal Support Interaction

Transition metal oxides are easily reduced, promoting interaction with metals of group VIII. This phenomenon was designated by Tauster [19] as strong metal support interaction (SMSI) [20]. The main characteristic of the interaction is the lower metal surface exposition, decreasing drastically the chemisorption capacity of H_2 above 500 °C [21]. The TiO_2 is an **n**-type semiconductor, with defects in the lattice conferring special conditions for interactions and hence geometrical or electronic effects.

Horsley [22] assigned the SMSI effect of Pt/TiO_2 to charge electric transfer from titanium to platinum atoms in the covalent bonding Pt–Ti that becomes stronger than the bonding between Pt and Pt atoms. When reduced with H_2, it forms oxygen vacancies producing Ti^{+3} ions which attract platinum atoms, modifying the electronic density.

The reduction profiles of platinum-supported catalyst (1 % Pt w/w) are displayed in Fig. 8.14. The Pt/Al_2O_3 catalyst exhibits a maximum peak at 250 °C with a shoulder at 370 °C, in agreement with the literature. The hydrogen consumption is presented in Table 8.3 and corresponds to the reduction of Pt^{+4} to Pt^{+0}.

However, the Pt/TiO_2 catalyst exhibits reduction at room temperature and at 112 °C, 372 °C, and above 500 °C, besides peak shift to lower temperatures due to the reduction of PtO. Partial reduction of TiO_2 to TiO_{2-x} occurs at higher temperatures which are attributed to the strong metal support interaction (SMSI). The presence of Pt atoms promoted the reduction of titanium which in turn facilitates the reduction of platinum at the surface.

The calculated dispersion of Pt atoms at the surface of alumina was 54 %, considering the reduction degree of 82 % of platinum oxide (Table 8.3). On the

Fig. 8.14 TPR profiles of 1 % de platinum supported on Al_2O_3 and TiO_2
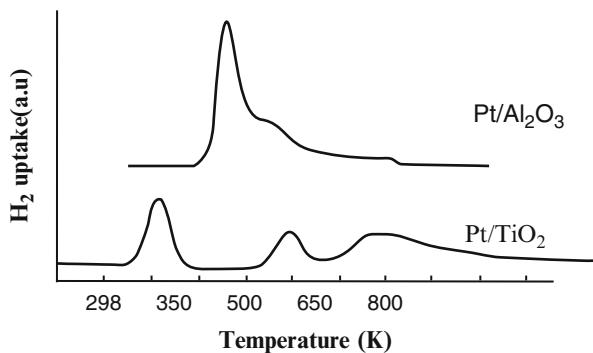
Table 8.3 H_2 consumption [23]

Catalyst % Pt[a] (weight)		TPR μmol de H_2/gcat	Chemisorption dynamic[b] μmol de H_2/gcat	H/M
Pt/Al_2O_3	1.01	84.70	11.3	0.54[c]
Pt/TiO_2	1.03	182.90	4.4	0.17

[a]After atomic absorption
[b]At 300 K
[c]82 % reduction

Table 8.4 Mean particle sizes (d_p) from CO chemisorption and microscopic analyses (TEM) [23]

		573 K[a]		773 K		773 K
	Pt (%peso)	$Sg_{Pt} \times 10^{-2}$ (m^2/g)	$d_{p\,CO}$ (nm)	$Sg_{Pt} \times 10^{-2}$ (m^2/g)	$d_{p\,CO}$ (nm)	$d_{p\,MET}$ (nm)
Pt/Al_2O_3	1.01	0.94	3.0	0.82	3.4	2.0–4.0
Pt/TiO_2	1.03	1.95	1.4	0.60	4.7	1.8–4.0

[a]After reduction

other hand, the Pt/TiO_2 catalyst presented two times more hydrogen consumption than the alumina-supported catalyst, indicating reduction of TiO_2 and thus interaction with metallic Pt^0. The H_2 chemisorption is three times less (17 %) than the Pt/Al_2O_3 catalyst and confirms the strong metal support interaction effect after reduction at 500 °C [23].

Jiang and co-workers [20] claim that the Ti^{+3} cations may adsorb hydrogen and then diffuses through the support, decreasing the adsorption rate of hydrogen dissociation.

Table 8.4 presents the mean particle sizes of metallic Pt^0 from CO chemisorption and TEM analyses of these samples. The results are in good agreement and in accordance with XRD analyses, suggesting mean particles sizes less than 5 nm.

TPR and chemisorption results confirm the SMSI effect after reduction with H_2 above 500 °C. Indeed, oxygen vacancies are formed, producing Ti^{+3} ions, attracting Pt atoms. This effect is caused by charge transfer of TiO_2 atoms to platinum atoms through the covalent bonding Pt–Ti.

8.11   Conclusion

The main goal of this chapter was to present the catalytic properties under influence of different variables before and after treatments. It shows how industrial catalysts are affected and modified during pre- and posttreatment or reaction conditions. Additional papers related to this subject are presented in references [24–65].

References

1. Bond CC. Heterogeneous catalysis and applications. Oxford: Clarendon; 1974.
2. Satterfield CN. Heterogeneous catalysis in practice. New York: McGraw Hill; 1980.
3. Ciola R. Fundamentos em Catálise. São Paulo: Editora Moderna; 1981.
4. Cardoso D. Introdução a Catálise Heterogênea. U.F.S. Carlos; 1987.
5. Figueiredo JL, Ramôa Ribeiro F. Catálise heterogênea. Lisboa: Fundação Calouste Gulbekian; 1987.
6. Anderson RB. Experimental methods in catalytic research. New York: Academic; 1968.
7. Trimm DL. Design of industrial catalysis. Amsterdam: Elsevier Scientific Publishing; 1980.
8. Kung HH, Kung MC, Costello CK. Supported Au catalysts for low temperature CO oxidation. J Catal. 2003;216:425–32.
9. Moujijn JA, van Leeuwen PWNM, van Santen RA. Catalysis – Studies science and catalysis, vol. 79. Amsterdam: Elsevier Scientific Publishing; 1993.
10. Araujo LRR, Schmal M. The calcination effects on Pt/HZSM-5 catalysts in the aromatization of propane. Appl Catal A. 2000;203(2):275.
11. Gallezot P, Alarcon-Diaz A, Dalmon JA. Location and dispersion of platinum in PtY Zeolites. J Catal. 1975;39:334.
12. Lee S-J, Gavriilidis A. Supported Au catalysts for low-temperature CO oxidation prepared by impregnation. J Catal. 2002;206:305.
13. Haruta M. Nanoparticulate gold catalysts for low-temperature Co oxidation. J New Mater Electrochem Syst. 2004;7:163.
14. Wolf A, Schuth F. A systematic study of the synthesis conditions for the preparation of highly active gold catalysts. Appl Catal A Gen. 2002;226:1.
15. Le Page JF, Cosyns J, Courty P, Freud E, Franck JP, Joaquin Y, Jugin B, Marcelly G, Martino G, et al. Catalyse de Contact, Technip (1978).
16. Schmal M, Souza MVM, Aranda DAG, Perez CAC. Promoting effect of zirconia coated on alumina on the formation of platinum nanoparticles – application on CO_2 reforming of methane. Stud Surf Sci Catal. 2001;132:695–700.
17. Alberton AL, Souza MMVM, Schmal M. Carbon formation and its influence on ethanol steam reforming over Ni/Al_2O_3 catalysts. Catal Today. 2007;123:257.
18. Frusteri F, Freni S, Chiodo V, Spadaro L, Bonura G, Cavallaro S. Steam reforming of bio-ethanol on alkali-doped Ni/MgO catalysts: hydrogen production for MC fuel cell. Appl Catal. 2004;270:1.
19. Tauster SJ, Fung SC. Strong metal-support interactions: occurrence among the binary oxides of Groups IIA-VB. J Catal. 1978;55:29.
20. Jiang X-Z, Hayden TF, Dumesic JA. Evidence for slow uptake of hydrogen by titania-supported metal samples: consequences for estimating metallic surface areas. J Catal. 1983;83:168.
21. Haller G, Resasco DE. Metal–support interaction: Group VIII metals and reducible oxides. Adv Catal. 1989;36:173.

22. Horsley JA. A molecular orbital study of strong metal-support interaction between platinum and titanium dioxide. J Am Chem Soc. 1979;101(11):2870.

23. Resende NS, Eon JG, Schmal M. Pt–TiO$_2$–Al$_2$O$_3$ catalyst I. Dispersion of platinum on alumina-grafted titanium oxide. J Catal. 1999;183:6.

24. Bao H, Chen X, Fang J, et al. Structure-activity relation of Fe$_2$O$_3$-CeO$_2$ composite catalysts in CO oxidation. Catal Lett. 2008;125:160–7.

25. Bensalem A, Bozon-Verduraz F, Delamar M. Preparation and characterization of highly dispersed silica-supported ceria. Appl Catal A Gen. 1995;121(1):81–93.

26. Cant NW, Angove DE, Patterson MJ. The effects of residual chlorine on the behaviour of platinum group metals for oxidation of different hydrocarbons. Catal Today. 1998;44:93–9.

27. Chafik T, Kameoka S, Ukisu Y, et al. In situ diffuse reflectance infrared Fourier transform spectroscopy study of surface species involved in NOx reduction by ethanol over alumina supported silver catalyst. J Mol Catal A Chem. 1998;136:203–11.

28. Chary KVR, Lakshmi KS, Rao PVR, et al. Characterization and catalytic properties of niobia supported nickel catalysts in the hydrodechlorination of 1,2,4-trichlorobenzene. J Mol Catal A Chem. 2004;223:353–61.

29. Damyanova S, Pawelec B, Arishtirova K, et al. Study of the surface and redox properties of ceria-zirconia oxides. Appl Catal A Gen. 2008;337:86–96.

30. Cesara DV, Peréz CA, Salima VMM, Schmal M. Stability and selectivity of bimetallic Cu–Co/SiO$_2$ catalysts for cyclohexanol dehydrogenation. Appl Catal A Gen. 1999;176:205–12.

31. Noronha FB, Baldanza MAS, Monteiro RS, Aranda DAG, Ordine A, Schmal M. The nature of metal oxide on adsorptive and catalytic properties of Pd/MeOx/Al$_2$O$_3$ catalysts. Appl Catal A Gen. 2001;210:275–86.

32. Gaki A, Anagnostaki O, Kioupis D, et al. Optimization of LaMO$_3$ (M: Mn, Co, Fe) synthesis through the polymeric precursor route. J Alloys Compounds. 2008;451:305–8.

33. Guimaraes AL, Dieguez LC, Schmal M. Surface sites of Pd/CeO$_2$/Al$_2$O$_3$ catalysts in the partial oxidation of propane. J Phys Chem B. 2003;107:4311–9.

34. Herrmann JM, Ramaroson E, Tempere JF. Semiconductivity study of ceria-supported nickel related to its methanation catalytic activity. Appl Catal A Gen. 1989;53(2–3):117–34.

35. Hong WJ, Iwamoto S, Inoue M. Direct NO decomposition over a Ce-Mn mixed oxide modified with alkali and alkaline earth species and CO$_2$-TPD behavior of the catalysts. Catal Today. 2011;164:489–94.

36. Hong WJ, Ueda M, Iwamoto S, et al. Effect of Fe content on physical properties of BaO-CeOx-FeOy catalysts for direct NO decomposition. Appl Catal B Environ. 2011;106:142–8.

37. Hoost TE, Otto K. Temperature-programmed study of the oxidation of palladium alumina catalysts and their lanthanium modification. Appl Catal A Gen. 1992;92(1):39–58.

38. Khamman O, Yimnirun R, Ananta S. Effect of calcination conditions on phase formation and particle size of nickel niobate powders synthesized by solid-state reaction. Mater Lett. 2007;61:639–43.

39. Ko EI, Weissman JG. Structures of niobium oxide and their implications on chemical behavior. Catal Today. 1990;8:27–36.

40. Kongzhai L, Hua W, Yonggang W, et al. Preparation and characterization of Ce1-xFexO$_2$ complex oxides and its catalytic activity for methane selective oxidation. J Rare Earths. 2008;26(2):245–9.

41. Kunimori K, Oyanagi H, Shindo H. Nickel-niobia interaction induced by the reduction of NiNb$_2$O$_6$ supported on SiO$_2$. Catal Lett. 1993;21:283–90.

42. Laguna OH, Centeno MA, Boutonnet M, et al. Fe-doped ceria solids synthesized by the microemulsion method for CO oxidation reactions. Appl Catal B Environ. 2011;106:621–9.

43. Lee JH, Schmieg SJ, Oh SH. Improved NOx reduction over the staged Ag/Al$_2$O$_3$ catalyst system. Appl Catal A Gen. 2008;342:78–86.

44. Loof P, Kasemo B, Keck KE. Oxygen storage capacity of noble-metal car exhaust catalysts containing nickel and cerium. J Catal. 1989;118(2):339–48.

45. Marcelo M, Pereira A, Evandro B, Pereira B, Lam Yiu Lau C, Schmal M. The nickel–niobia–silica interactions at low nickel contents. Catal Today. 2000;57:291–6.
46. Marécot P, Fakche A, Kellali B, Mabilon G, Prigent M, Barbier J. Propane and propene oxidation over platinum and palladium on alumina. Effects of chloride and water. Appl Catal B Environ. 1994;3:283–94.
47. McCabe RW, Jen HW, Chun W, Grahan GW, Haack LP, Straccia A, Benson D. Evaluation of low-grade ceria as a Pd-catalyst support material. Appl Catal A Gen. 1999;184:265–72.
48. Monteiro RS, Dieguez LC, Schmal M. The role of Pd precursors in the oxidation of carbon monoxide over Pd/Al_2O_3 and $Pd/CeO_2/Al_2O_3$ catalysts. Catal Today. 2001;65:77–89.
49. Noronha FB, Aranda DAG, Ordine AP, Schmal M. The promoting effect of Nb_2O_5 addition to Pd/Al_2O_3 catalysts on propane oxidation. Catal Today. 2000;57:275–82.
50. Nowak I, Ziolek M. Niobium compounds: preparation, characterization and application in heterogeneous catalysis. Chem Rev. 1999;99:3603–24.
51. Orge CA, Órfão JJM, Pereira MFR. Ceria and cerium-based mixed oxides as ozonation catalysts. Chem Eng J. 2012;200–202:499–505.
52. Otto K, Andino JM, Parks CL. The influence of platinum concentration and particle size on the kinetics of propane oxidation over Pt/g-alumina. J Catal. 1991;131:243–51.
53. Peña MA, Fierro JLG. Chemical structures and performance of perovskite oxides. Chem Rev. 2001;101(7):1981–2017.
54. Pérez-Alonso FJ, Granados ML, Ojeda M, et al. Chemical structures of coprecipitated Fe-Ce mixed oxides. Chem Mater. 2005;17:2329–39.
55. Popa M, Calderon-Moreno JM. Lanthanum cobaltite nanoparticles using the polymeric precursor method. J Eur Ceram Soc. 2009;29(11):2281–7.
56. Quinelato AL, Longo ER, Leite MI, et al. Synthesis and sintering of ZrO_2-CeO_2 powder by use of polymeric precursor based on Pechini process. J Mater Sci. 2001;36:3825–30.
57. Salasc S, Perrichon V, Primet M, Chevrier M, Mathis F, Moral N. Magnetic study of the interaction of hydrogen with a Pt/CeO_2-$Al2O_3$ catalyst: influence of the presence of chlorine. Catal Today. 1999;50:227–35.
58. Schmal M, Aranda DAG, Noronha FB, Guimareas AL, Monteiro RS. Oxidation and reduction effects of propane-oxygen on Pd-chlorine/alumina catalysts. Catal Lett. 2000;64:163–9.
59. Schmal M, Pereira MM, Lam YL. The nickel-niobia-silica interactions at low nickel contents. Catal Today. 2000;57(3):291–6.
60. Trovarelli A. Catalysis by ceria and related materials, vol. 2. 1st ed. London: Imperial College Press; 2002.
61. Veser G, Wright A, Caretta R. On the oxidation-reduction kinetics of palladium. Catal Lett. 1999;58:199–206.
62. Wang D, Monnet F, Mirodatos C. Reaction kinetics and product selectivity in the oxidation of methane over Pd/Si_3N_4. Stud Surf Sci Catal. 2000;130:3561–6.
63. Wang J, Zhang B, Shen M, et al. Effects of Fe-doping of ceria-based materials on their microstructural and dynamic oxygen storage and release properties. J Sol-Gel Sci Technol. 2011;58:259–68.
64. Wojcieszak R, Jsaik A, Monteverdi S, et al. Nickel niobia interaction in non-classical Ni/Nb_2O_5 catalysts. J Mol Catal A Chem. 2006;256:225–33.
65. Ziolek M. Niobium-containing catalysts - the state of the art. Catal Today. 2003;78:47–64.

Chapter 9
Structural Analyses: X-ray Diffraction

Martin Schmal and Carlos André C. Perez

Abstract Structural analyses of materials are presented using x-ray diffraction techniques. Rietveld method was applied for determining cell parameters.

Keywords Crystallite sizes • Rietveld • Structure • X-ray parameters

Few scientific events have had such an impact on humanity as the discovery of X-rays by Röntgen in November 1895. At that time, even before the nature of these rays was fully understood, there were immediate industrial and medical applications. The first radiographs appeared as early as 1896. The exact nature of X-radiation was only established in 1912, when Max von Laue discovered the phenomenon of diffraction by crystals. He proved that X-rays are in fact electromagnetic waves and, at the same time, he discovered a rather powerful method for studying the structure of materials. In practice, diffraction is applicable to a vast array of scientific problems and technologies. All structures known to date have been determined by diffraction data from X-rays, neutrons, or electrons. Some notable examples are: the double-helix structure of DNA, the structures of hemoglobin, vitamins, proteins, minerals, polymers, metals, and ceramics [1].

X-ray diffraction is not only applicable to determining material structures. It is frequently used in the laboratory to identify phases in samples of unknown materials, to quantitatively analyze phases, and to determine the size of crystallites and the crystallinity of a material. It may also be applied to measure micro-deformation and stress in steel parts, to characterize metallic substrates and deposits in microelectronics, and to study property variations of materials with regard to temperature, pressure, and atmosphere.

9.1 Concepts and Parameters Influencing X-ray Diffraction

All the potential for X-ray diffraction for the analysis of materials is due to one simple fact: the wavelength of X-radiation is of the same order of magnitude of separation between atoms in matter in a condensed state. X-rays are electromagnetic waves with wavelengths of the order of magnitude of 10^{-10} m, 1 Å, or 0.1 nm.
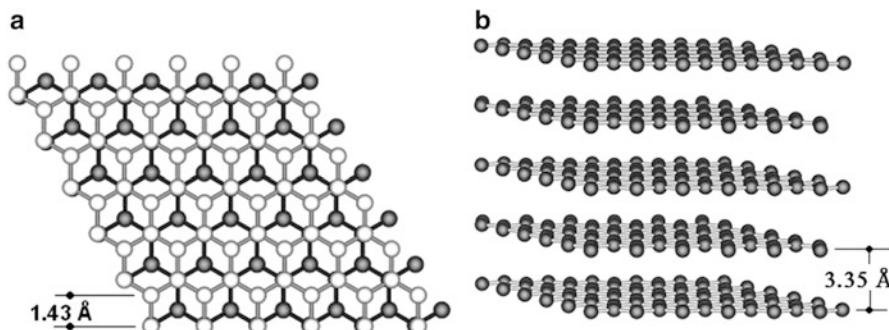
Fig. 9.1 Crystalline arrangement of graphite. View along [001] (**a**) and [100] (**b**). The distances between the atoms are of the same order of magnitude as the X-ray wavelengths. For comparison, the wavelength of Cu Kα emission is 1.5418 Å

This is the same order of magnitude as the bonds between atoms in liquid or solid matter. Thus, the condensed material serves as a kind of diffraction grating for X-rays (Fig. 9.1).

When it comes to characterizing catalysts, applying diffraction requires special attention. Many catalysts are formed by small active-phase particles supported in porous solids. These structures have a very limited spatial order. In these cases, the aspect of the diffraction pattern is very diffuse, which makes interpretation quite difficult. The application of X-ray diffraction to characterize catalysts may range from simple identification of the phases through comparison with a database of reference patterns to simulation and refinement of nanostructures. Accordingly, it is essential to know the foundations of diffraction that contribute to the understanding of catalyst structures.

X-rays interact with matter because they produce oscillations in the charges that comprise it. Several processes may occur: photoelectric effect, fluorescence, emission of Auger electrons, Compton effect, and coherent elastic scattering, to mention but a few examples. One interesting process for understanding diffraction is elastic scattering. In this process, the oscillating electric charges produce radiation. Accordingly, each charge in an irradiated material starts to behave like a new source of X-radiation, with the same wavelength and a defined *phase* relationship compared to the incident radiation.

Figure 9.2 represents a plane-polarized wave that propagates in the x direction (at light speed), incident on an electron situated at the origin. In this wave, the electric field oscillates on a vertical plane, with *amplitude* E_y, and the magnetic field oscillates on a horizontal plane, with amplitude B_z. Classic electromagnetic theory shows that the charge suffers an alternate force and oscillates at the same frequency as the incident wave. When it oscillates, the charge also produces radiation, which is *scattered* in all directions. The wave fronts are represented in Fig. 9.2 as concentric spheres propagating from the charge. In the figure, the scattered wave has the same wavelength as the incident wave.
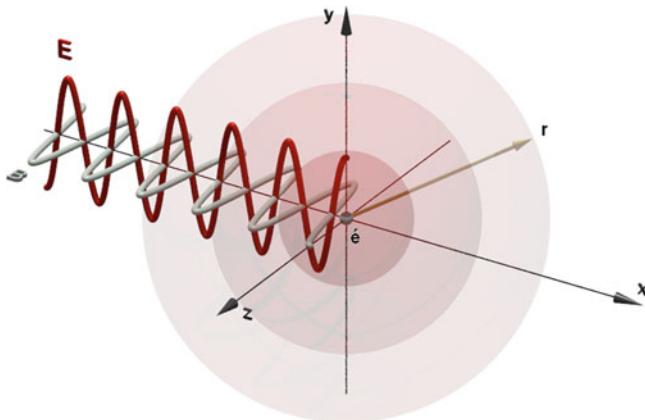
Fig. 9.2 Interaction of a plane-polarized X-ray wave with an electron at the origin

The amplitude of the electric field $\mathcal{E}(r)$ in a given position r may be calculated with Eq. (9.1):

$$\mathcal{E}(r) = \frac{\mu_o}{4\pi} \frac{e^2}{mr} \, \text{sen}(\varphi)E \tag{9.1}$$
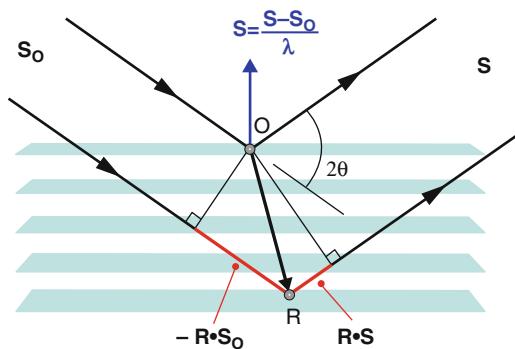
where μ_o is $4\pi \times 10^{-7}$, e is the charge of the electron $= 1.6 \times 10^{-19}$ C, r is the distance from the origin in meters, and φ is the angle between r and E. Note that the mass m of the scattering object is in the denominator. Thus, electrons are a lot more efficient at *scattering* the radiation than protons, since their mass is around 1840 times smaller. Accordingly, the X radiation scattered will be completely influenced by the distribution of the electrons in the material. In fact, the unit of reference in quantitative studies is the amplitude produced by the radiation scattered by one electron, known as $\mathcal{E}$. It is important to emphasize that the amplitude $\mathcal{E}$ is not measurable by radiation detectors, which measures *intensity*, proportional to $|\mathcal{E}|^2$.

If radiation is applied to a scatter comprising of more electrons, then the amplitudes of the waves originating from the different electrons are added together. The simplest case is a scatterer comprising two electrons, one at the origin O and the other in a vector position R, according to Fig. 9.3. The incident direction of the wave is given by the unit vector S_o and the direction of the observation detector by the unit vector S. The angle between S and S_o is defined as 2θ. The wave scattered by the electron of origin takes a path that passes through O, since the one from the other electron takes an additional path that passes through R, which is possible to calculate by the projection of R in S_o and in S, as $-R \cdot S + R \cdot S_o$.

The scattering vector is defined as $s = (S - S_o)/\lambda$, with module $|s| = 2\text{sen}\theta/\lambda$ and direction given by the bisectrix between S and $-S_o$. The phase difference between the two waves, when they emerge, is given by $2\pi(s \cdot R)$.

The sum of the two amplitudes is thus:

$$E(s) = \mathcal{E}\left(1 + e^{i(2\pi(s \cdot R))}\right) \tag{9.2}$$

Note that when $s \cdot R = 0$, i.e., when $R \perp s$, the resulting amplitude will be maximum and equal to $2\mathcal{E}$. If the second electron is on the plane that passes through O, orthogonal to s, the first plane indicated in blue in the diagram, then the amplitudes of the waves scattered by the two electrons add *coherently*. As the function is periodic, the same will happen when $-s \cdot R$ is a whole number n. The locus of all points whose positions vectors R satisfies $-s \cdot R = n$ is a set of parallel planes, highlighted in blue. The distance between these planes is given by d, which is the projection of R in the $-s$ direction. If the other electron is situated on any of these planes, the amplitude will be maximum and equal to $2\mathcal{E}$. The equation:

$$R \cdot s = d|s| = 2d\,\text{sen}(\theta)/\lambda = n \tag{9.3}$$
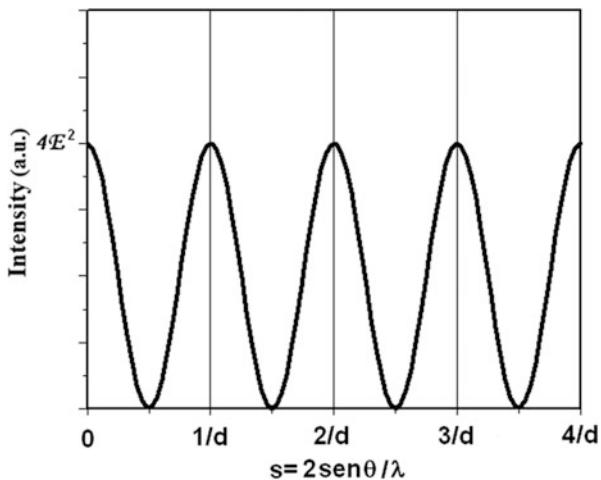
is called *Bragg's law*.

   X-ray diffraction experiments are normally done using radiation with a well-defined wavelength and scanning the possible s values by moving the detector. The curve obtained by recording the intensity as a function of the angular position of the detector, $I(s)$, is called *diffractogram*. The hypothetical diffractogram for the system of two electrons separated by a vector position R, shown in Fig. 9.3, is

$$I(s) = |E(s)|^2 = \mathcal{E}^2\left(1 + e^{i(2\pi(s \cdot R))}\right) * \left(1 + e^{i(2\pi(s \cdot R))}\right) = 4\mathcal{E}^2 \cos^2(\pi(s \cdot R)) \tag{9.4}$$

The diffractogram of two point scatterer system has the appearance shown in Fig. 9.4. Note that the curve oscillates, with zeros for $s = 1/2d$, $3/2d$, $5/2d$ and maximums for $s = 0$, $1/d$, $2/d$, …. The profile of the curve forms very "wide" peaks—centered at s values that satisfies the Bragg's law: $|s| = n/d$ ($n = 0, 1, 2, …$). The peak width at half height, normally referred to as Full Width at Half Maximum, or FWHM, in this case is $1/2d$.

Fig. 9.4 Hypothetical diffractogram for a system of two electrons

This X-ray interference pattern is related to the distance R between the electrons. The projection d of the distance R in s direction is the inverse of s that corresponds to the first maximum, $d \sim 1/s_{max1}$. One can thus obtain structural information about this simplest system by looking at its X-ray interference pattern.

The rationale used for the two-electron system may be extended to calculate the amplitude scattered by a set of N electrons, whose positions are R_n ($n = 1, 2, \ldots N$). In this case, it will be the sum of the individual amplitudes:

$$A_N(s) = \mathcal{E} \sum_n e^{i2\pi(s \cdot Rn)} \tag{9.5}$$

Similarly, for a continuous distribution, the amplitude is determined by the volumetric density of electrons (ρ):

$$A_\rho(s) = \mathcal{E} \int \rho(r) e^{i2\pi(s \cdot r)} dv \tag{9.6}$$

The scattering amplitude is obtained by a *Fourier* transformation of the electron density $\rho(r)$. Equation (9.6) is general and may be applied to any kinds of structures: atoms, ions, molecules, crystals, or even nanoclusters of atoms. In case of the scattering by an atom, electrons are distributed in orbitals such that the volumetric density of the electrons is given by $\psi^*\psi$, where ψ is the total electronic wave function of the atom. In order to simplify calculations, the X-ray scattering amplitudes for the atoms and ions are calculated, tabled, and denominated *atomic scattering factors (f)* [1]. For $s = 0$, i.e., in the direction of the incident beam, the scattering factor coincides with the number of electrons of the atom or ion; in this situation, all the waves that come from the multiple electrons are added constructively. For s values greater than zero, this interference is not perfectly constructive, causing a decrease in the atomic scattering factor, as shown in Fig. 9.5.
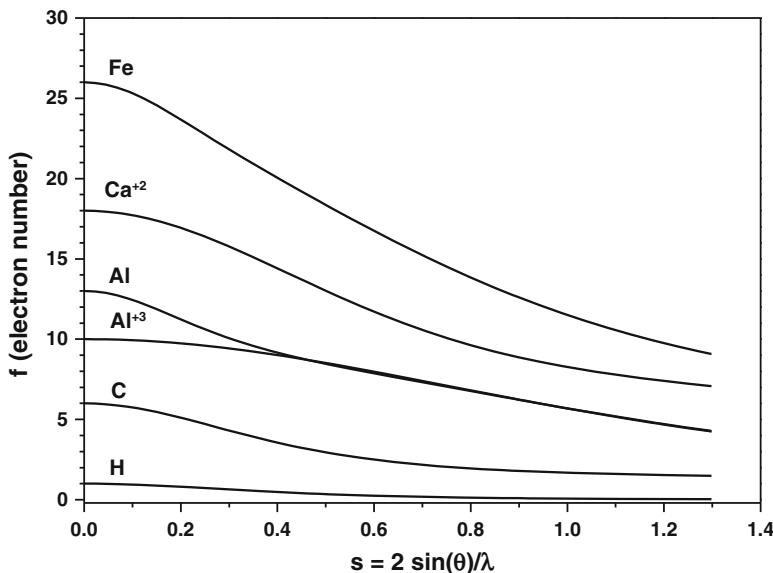
Fig. 9.5 X-ray scattering factors for some atoms and ions [2]. Note that for $2\theta = 0$ ($s = 0$), the f value corresponds to the number of electrons of the ion or the atom in question

In the case of a molecule or cluster with N atoms or ions, each one situated in R_n, the distribution of electrons will be the sum:

$$\rho(r) = \sum_n \rho_{at(n)}(r - R_n) \tag{9.7}$$

In the case of a crystal, the positions of the atoms are determined by a law of repetition of a content of a *unit cell*. A unit cell is described by the parallelepiped having base vectors $\mathbf{a}$, $\mathbf{b}$, $\mathbf{c}$. The atoms that belong to the unit cell are indicated by their position vectors $R = x\mathbf{a} + y\mathbf{b} + z\mathbf{c}$ within that cell. The x, y, and z values are the *fractional coordinates*. Inside the cell, the x, y, z values are limited to the 0–1 interval. One example, for the cubic unit cell of Nickel, which contains 4 atoms at positions:
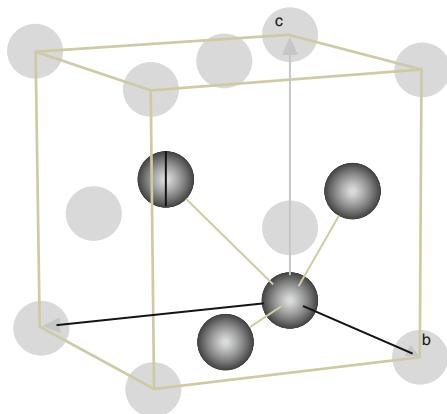
$$R_{Ni\ 1} = 0; \quad R_{Ni\ 2} = \tfrac{1}{2}\mathbf{a} + \tfrac{1}{2}\mathbf{b}; \quad R_{Ni\ 3} = \tfrac{1}{2}\mathbf{a} + \tfrac{1}{2}\mathbf{c}; \quad R_{Ni\ 4} = \tfrac{1}{2}\mathbf{b} + \tfrac{1}{2}\mathbf{c}.$$

Or, using the language of fractional coordinates x, y, z:

$$Ni_1 \text{ at } 0,0,0; \quad Ni_2 \text{ at } \tfrac{1}{2}, \tfrac{1}{2}, 0; \quad Ni_3 \text{ at } \tfrac{1}{2}, 0, \tfrac{1}{2}; \quad Ni_4 \text{ at } 0, \tfrac{1}{2}, \tfrac{1}{2}. \tag{9.8}$$

Nickel atoms form a face-centered cubic array (fcc). In fact, using a simpler notation, we can describe the crystalline array of nickel only with the coordinates

Fig. 9.6 Face-centered
cubic unit cell of nickel.
The four atoms belonging to
the cell are included in
darker tones. The other
atoms are equivalent by
translational symmetry of
the lattice

of the atom of the asymmetric unit and with the operations of its *space-group
symmetry* [2]. It is common to find the following in the structure databases:

Nickel: space-group symmetry: Fm3m

Cell parameter $a_o = 3.52$ Å.

Nickel atom is at x, y, $z = 0$, 0, 0 (Fig. 9.6).

The density of electrons in the nickel crystal may be calculated in the same way
as that for molecules:

$$\rho(r) = \sum_n \rho_{Ni}(r - R_n) \tag{9.9}$$

Where, the sum runs over the N atoms of the crystal. The crystal is a
periodic structure; one can thus decompose $R_n = R_{unit\ cell} + (n_a \cdot \mathbf{a} + n_b \cdot \mathbf{b} + n_c \cdot \mathbf{c})$,
where n_a, n_b and n_c are integer numbers that define the crystal size. $N =
(na + 1) \cdot (nb + 1) \cdot (nc + 1)$.

The Fourier transformation of the electron density of the unit cell is called
structure factor. The Laue function L is the Fourier transformation of the point
lattice, and it doesn't depend on the unit cell content. For small crystals, the Laue
function shows broad peaks, however, for a finite and relatively large crystal, it has
sharp peaks at s values that satisfies the simultaneous equations: $s \cdot a = h$, $s \cdot b = k$, and
$s \cdot c = l$ (here, h, k, and l are all integer numbers called Miller indexes), and they are
related geometrically to a set of "planes" of the structure. When these conditions are
met, a considerable intensity of radiation will strike the detector in order to reveal
peaks. For s values in the neighborhood of these peaks, the intensity falls more
steeply the larger is the crystal. Accordingly, it is possible to determine the
crystallite size by examining these peak profiles. If they are broad, the coherent
domain within the solid is small. The inverse also holds: peaks are sharp for larger
crystallites.
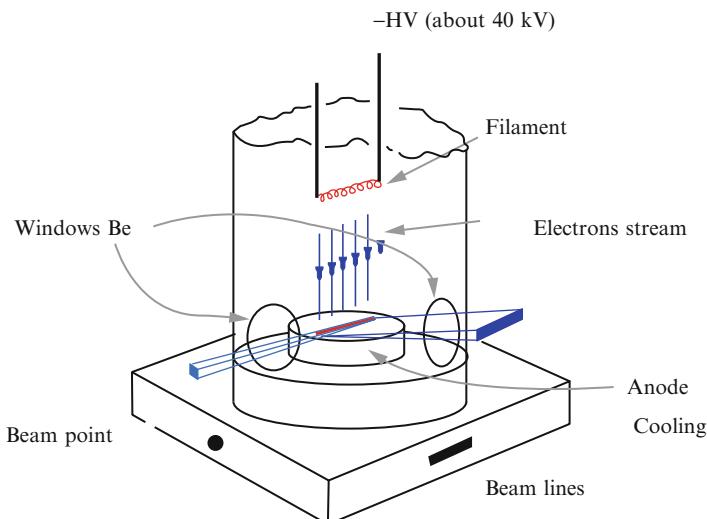
Fig. 9.7 Diagram of an X-ray tube

9.1.1 Instrumentation

In the laboratory, X-rays are produced by X-ray tubes. A typical one is shown in Fig. 9.7:

The high voltage accelerates electrons emitted by a filament toward a metallic target (anode) that can be made of copper, cobalt, chromium, iron, molybdenum, silver, or tungsten. When they collide with the target, they emit radiation, a process called "bremsstrahlung."

The radiation from a tube consists of a mixture of different wavelengths, and the distribution of these wavelengths depends on the voltage applied to the tube. Below a certain critical voltage, the tube produces only "white" radiation, which is a continual distribution of wavelengths, from a minimum λ_{swl}. Above a critical voltage, the tube also emits characteristic radiation by fluorescence of the anode atoms. To produce fluorescent X-radiation, the energy supplied to the tube must be sufficient to ionize the inner shells of the anode atoms. For example, series K will be emitted when the energy applied to the tube is sufficient to remove electrons from the K shell. Thus, series L, M, N, etc. may also be emitted. The emission process of fluorescent X-rays is outlined in the diagram in Fig. 9.8. This radiation has a well-defined wavelength and thus is convenient for use in diffraction experiments. The most commonly used radiation in laboratories is Cu Kα, which is produced when a copper atom's K shell with subsequent transition of electrons from the L shell to screen the K "hole." There are also devices called filters or monochromators that attenuate white radiation and other undesired emissions, such as Kβ, providing a best wavelength definition for doing diffraction experiments.
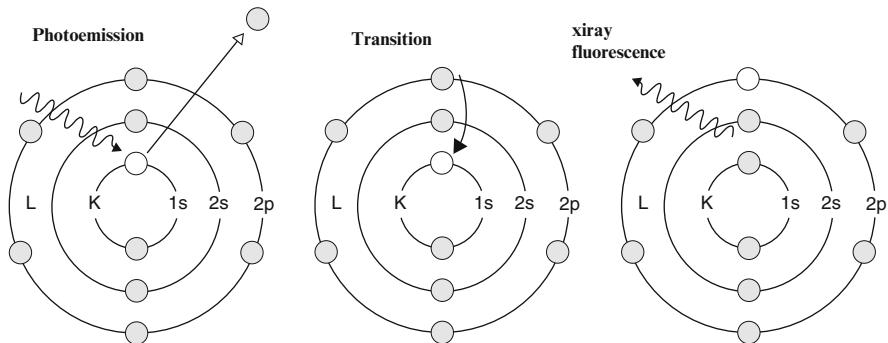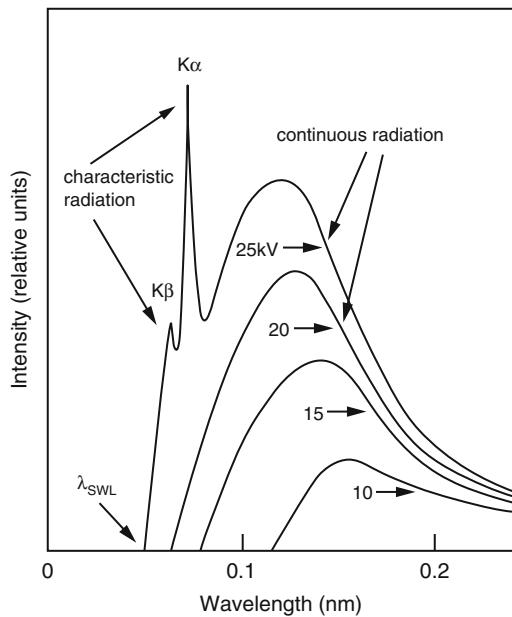
Fig. 9.8 Process of emission of characteristic X-rays

Fig. 9.9 Distribution of wavelengths of a molybdenum X-ray tube (adapted with permission from Cullity et al., Elements of X-ray Diffraction, Prentice Hall, 2001) [12].

X-Rays can be also produced at synchrotron facilities. Although an XRD experimental station is not available full time for a specific user, a typical synchrotron source has the advantages of high flux of photons and choice of its X-Ray wavelength, by tuning its monochromator settings.

Figure 9.9 shows the typical distribution obtained for a molybdenum tube:

The most frequently used device for obtaining X-ray diffraction experiments is the polycrystal diffractometer or powder diffractometer. It is shown in Fig. 9.10. On one side, it has an X-ray tube and a DS slit system that irradiates the sample, which is placed at the center of a goniometer. The tube and the DS slit system defines the direction of the incident beam S_o. On the other side, it has a detector that
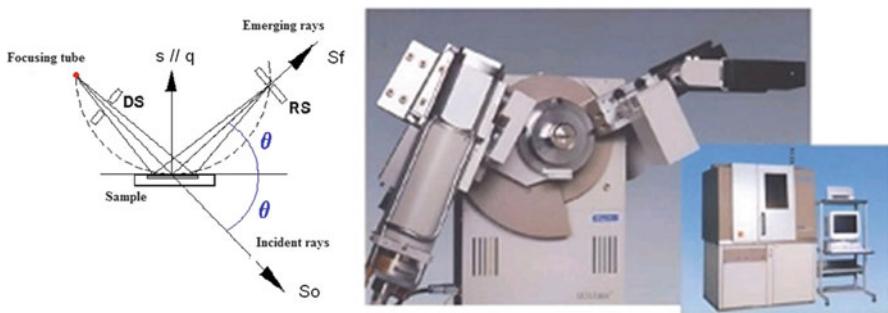
Fig. 9.10 Diagram of a powder Bragg–Brentano diffractometer geometry

is arranged to count the X-ray photons that come in at an angle of 2θ in relation to the incident beam and emerge in direction S. Throughout the experiment, the angle 2θ varies from a minimum value to a maximum value, either in steps or continuously.
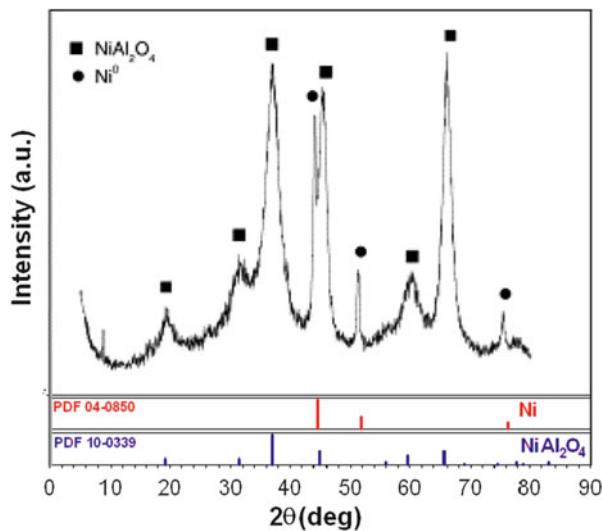
The sample is arranged in powder form on a sample plate. As the particles of the pulverized sample are arranged in random directions (in ideal cases), there is always a chance for an arbitrary plane (hkl) to produce diffraction in its respective angle 2θ.

The graph obtained from the intensity register due to 2θ is called a diffractogram. It may be plotted as a function of $|s| = 2\sin\theta/\lambda$ or 2θ. As $\sin\theta$ grows with θ in the $\theta < 90°$ interval, the overall appearance of graphs would be the same. The advantage of using $s = 2\sin(\theta)/\lambda$ is that the x-scale does not depend on the wavelength used in the experiment, since it has the dimension of inverse length. Accordingly, s is a measurement in reciprocal space.

9.1.2 Interpretation of X-ray Diffractograms: Phase Identification

Powder diffraction may be used to identify the phases that comprise a crystalline material. By Eq. (9.3), the values of the peak positions depend on the lattice geometry, and the intensities depend on the species and the arrangement of the atoms within the cell. It is clear that these characteristics may be used as a kind of "fingerprint" of each crystalline phase. The phase identification is obtained by comparison with single-phase diffractogram obtained experimentally and/or calculated and stored as references on some databases. The most usual is PDF-2 of ICDD [3] that lists, for each phase, the positions and intensities pertaining to the peaks of the pure phases. Searches in this extensive database may also be executed in subsets only, such as: set of inorganic phases, minerals, common phases, materials of forensic interest, pigments, phases with a certain color, etc. Currently, searches

Fig. 9.11 XRD identification of the Ni and NiAl$_2$O$_3$ phases in a catalyst for carbon dioxide reforming of methane. The respective reference patterns PDF2 are plotted in the ribbons [4]

are executed automatically by a software program, but long time before the computer era, Hanawalt proposed a procedure to execute them manually [5]. An example of nickel catalyst phase identification supported in transition alumina is shown in Fig. 9.11.

The phases were identified as Nickel metal and NiAl$_2$O$_4$, a mixed oxide structure spinel. The identification of the phases showed that the active phase reacted with support throughout the reaction. Since a correct identification depends on the relative positions and heights of peaks, the diffractogram must be obtained with care in order to minimize errors. Very often, failure in phase identification is due to misalignment of the goniometer or the incorrect position of the sample on the sample plate (it should not be located below or above the reference surface, because in these cases the peaks will be displaced when using the common Bragg–Brentano configuration). Moreover, the preferred direction of some grains also affects the recorded intensities. In these cases, it is necessary to use a resource that minimizes the preferential orientation of the grains, such as: side loading of the sample plate, "spray drying," and rotation/oscillation of the sample during analysis.

9.1.3 Interpretation of the X-ray Diffractograms: Crystallite Size

Determination of crystallite sizes:

Crystallite size represents the spatial extent of coherent domains in a solid. We see that the size of the coherent domain is related to the width of the diffraction peaks in reciprocal space. The Scherrer equation, which relates this size to peak width, assumes an extremely simple form in reciprocal space:
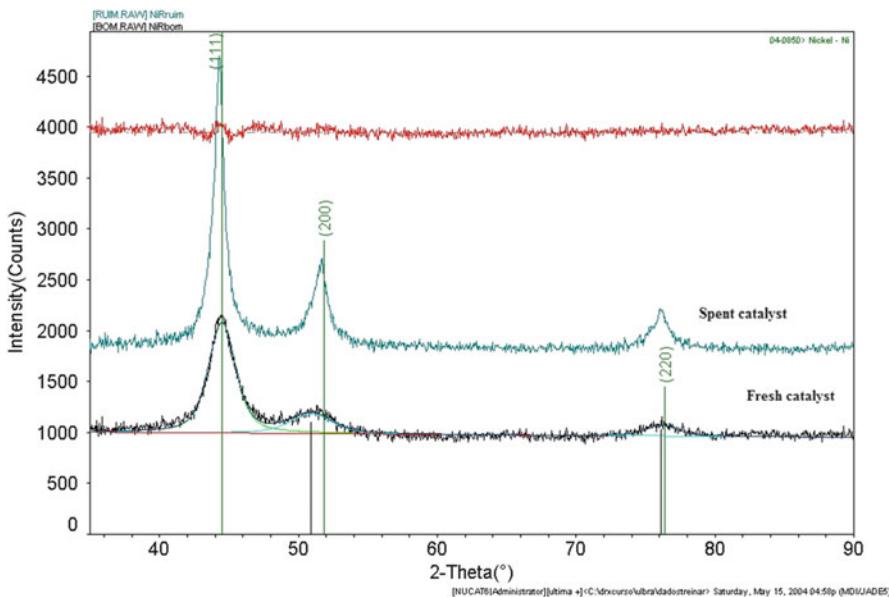
Fig. 9.12 Interpretation of the X-ray diffractograms—the Rietveld method

$$L_{(hkl)} = K/\Delta(s) = K/\Delta\left(2\mathrm{sen}\left(\theta_{(hkl)}\right)/\lambda\right) = K\lambda/\left(\cos\left(\theta_{(hkl)}\right)\Delta 2\theta_{(hkl)}\right) \quad (9.10)$$

where K is the Scherrer constant and one assume the value 0.89 when using the full width at half maximum (FWHM) as the peak broadening metrics and assuming also a spherical shape for the crystallites.

In catalysis, the average size of the crystallites is intimately linked to the dispersion; the greater the dispersion, the smaller the average size of the crystallites. One example where measurement of crystallite sizes gives useful information is in the deactivation study of Raney nickel catalysts; one diffractogram showed in Fig. 9.12 is of the recently prepared catalyst and the other is of the catalyst already used in a hydrogenation process for a long time until deactivation. There is only one identified phase: metallic nickel. The diffractogram of the used catalyst presents much narrower peak than the fresh catalyst. The measured width of the $Ni_{(111)}$ reflection went from 2.34° in the fresh catalyst to 0.93° in the spent. This means that the deactivation occurs by sintering of nickel. Calculation with the Scherrer equation provides, as presented in Table 9.1:

A typical powder diffraction pattern of a crystalline material contains the following information:

- The angular position of the peaks depends on the crystalline phases that form the sample. Each phase contributes with a series of peaks that appears at corresponding Bragg angles to their interplanar distances d_{hkl}. The list of d_{hkl} and their angular positions may be easily generated from the lattice type and the space-group symmetry.

Table 9.1 X-ray parameters of the Nickel–Raney catalyst

For the fresh catalyst:
$2\theta_{(111)} = 44.55°$, $FWHM_{(111)} = 2.342°$
$L_{(111)} = K\lambda / \left(\cos \left(\theta_{(111)} \Delta 2\theta_{(111)} \right) = (0.89 \times 1.5418\,\text{Å} \times 57.3) / (\cos (44.55/2) \times 2.342) = 36\,\text{Å} \right.$
For the spent catalyst:
$2\theta_{(111)} = 44.31°$, $FWHM_{(111)} = 0.933°$
$L_{(111)} = K\lambda / \left(\cos \left(\theta_{(111)} \Delta 2\theta_{(111)} \right) = (0.89 \times 1.5418\,\text{Å} \times 57.3) / (\cos (44.31/2) \times 0.933) = 91\,\text{Å} \right.$

- The overall intensities of the peaks are related to the abundance of each phase in the sample. For each phase, the relative intensities may be determined by the calculation of structure factors, multiplicity factors, preferred orientation, and Lorentz/polarization factors. The latter two are normally tabled as a function of the scattering angle. The atomic arrangement within the cell also influences individual peak intensities via structure factor.
- The widths of the peaks are related to crystallite size, possible lattice micro-deformations, and the diffractometer optics used in experiments.

All these factors may be rigorously determined and/or calculated. The math calculation performance of current microcomputers facilitates this work enormously. Thus, once the constituent phases in a powder diffractogram have been identified, it is possible to simulate it mathematically. Here, it must be emphasized that the relationship between structure and the diffractogram is direct; once the structure is known, its diffraction pattern can be easily determined.

The inverse relation is not so direct. As the X-ray detector only measures intensity, not amplitude, the information is not sufficient to obtain the structure factors. In general, only its module $|F_{hkl}|$ can be determined, not its phase ϕ_{hkl}. This fact is referred as "the phase problem in crystallography" and until now it limits our ability to reconstruct images of the structure from diffraction data. Once the phase problem is solved, we can think about x-ray microscopes, which could in principle "see" crystals and clusters at atomic scale. Accordingly, obtaining the structure from diffraction data is generally a much more elaborate task and is a challenge of solving crystal structures.

H.M. Rietveld developed a practical method to analyze powder diffraction data. The Rietveld refinement method [6] is based on modeling a diffraction pattern according to structural information available for the phases previously identified in the pattern. This model is calculated by computer software after introduction of some crystallographic data: space group symmetry, atomic species and positions within the cell, occupancies, lattice parameters, line broadening parameters, and experimental conditions. The term "refinement" refers to the cyclic "improvement" process used in the estimation of the set of parameters that can model the diffraction pattern as close as possible to the observed pattern. Usually, the Rietveld refinement is accomplished by minimizing the sum of the differences of calculated and observed intensities for each angular step of the diffraction pattern and by a

nonlinear least-squares method. Some examples of programs that can perform Rietveld analysis (and are free for noncommercial use) are Fullprof [7] and GSAS [8].

The idea of the Rietveld method is to do a step-by-step "refinement" of the whole powder diffraction pattern. One can construct an initial structural model from a partial knowledge of the phases detected in a pattern and, gradually and progressively, improve the model in order to compare it to the experimental diffraction pattern. One of the main advantages of the method is, in principle, that it can deal with heavily overlapped peak patterns. There is no need to separate peaks, since the scattering contributions from the various phases are all summed up to calculate the intensities at each diffractogram step, not attributing a particular peak to a specific phase or a crystal "plane."

In catalysis, the Rietveld method is extensively used to determine the quantitative phase composition of a sample and to calculate its average size of crystallites with the aid of the Scherrer equation. Also, it can give information on the lattice parameter changes and microstructural and size effects that may occur in the sample synthesis or after its catalytic use.

Figure 9.13 shows an example of the Rietveld procedure. The catalyst is a platinum-exchanged Y zeolite. As a starting model, we consider a single-phase
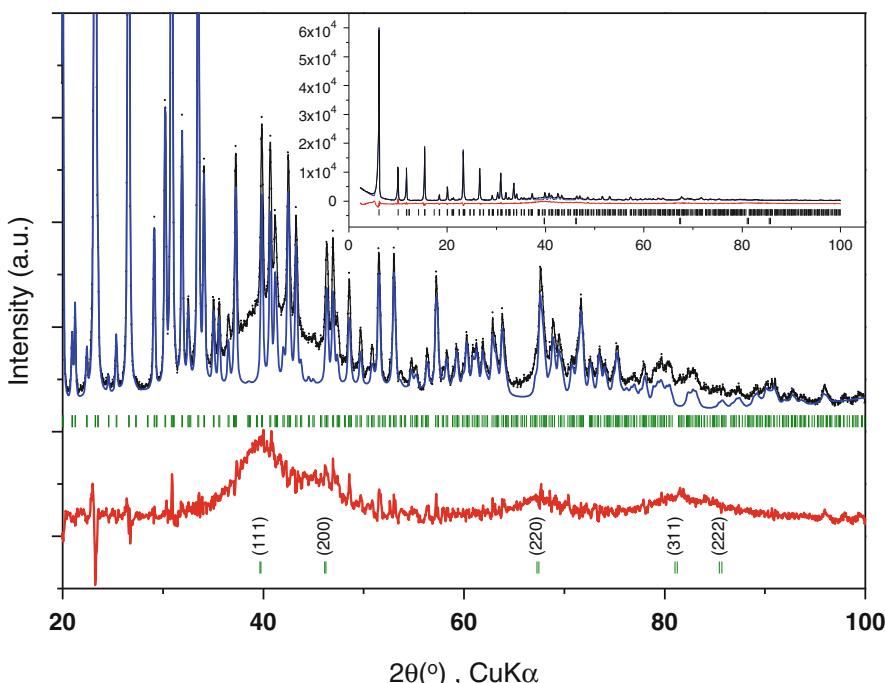
Fig. 9.13 Rietveld refinement of faujasite containing Pt nanoparticles in its cavities. Initial model is a single-phase faujasite , and the difference pattern (plotted in *red*) shows a scattering due to the presence of small (~1.1 nm) platinum crystallites

zeolite with faujasite structure, its space-group symmetry is Fd3m, its cell parameter is $a = 24.8$ Å, and its asymmetric unit is the TO_4 tetrahedron (T = Si, Al). The x, y, z fractional positions of the T and O atoms can be found on structure databases. The difference pattern shows a scattering due to 1.1 nm platinum crystallites. A possible improvement for the Rietveld model may be done by including the platinum crystal as another phase.

Another selected application of the Rietveld method is for studying oxide catalysts before and after the partial oxidation of methane [9]: The composition of CuCe catalyst is presented in Table 9.2, and the diffractograms for different conditions are shown in Fig. 9.14.

Table 9.2 Composition of oxides catalyst

Samples	Real (%)	Nominal (%)
CuCe	$5.1 - CuO$	$6 - CuO$
	$94.9 - CeO_2$	$94 - CeO_2$
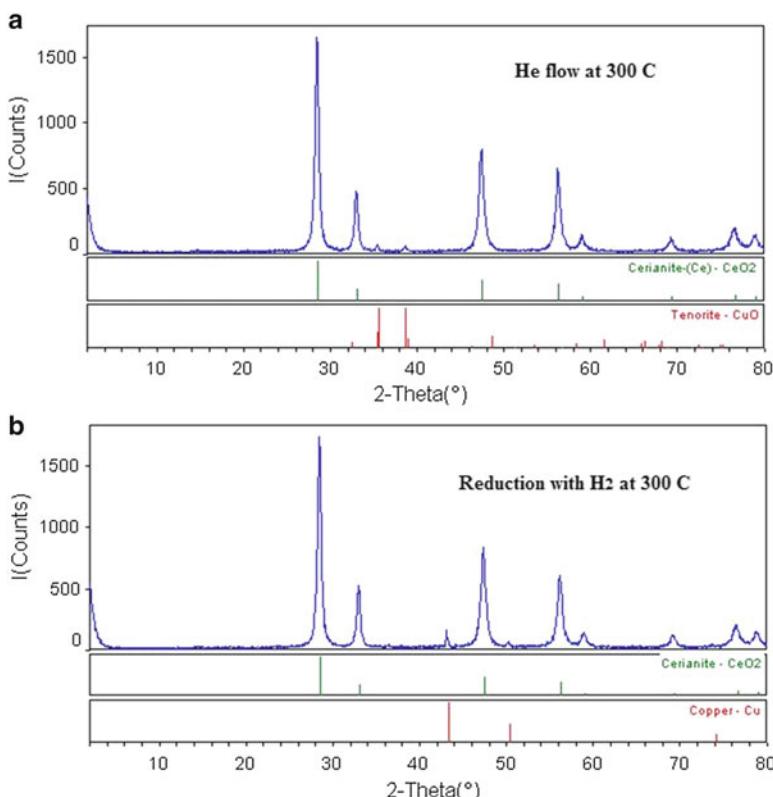
Fig. 9.14 X-ray diffractogram for the CuCe (**a**) sample in an He flow at 300 °C and (**b**) an He flow after reduction at 300 °C [9]
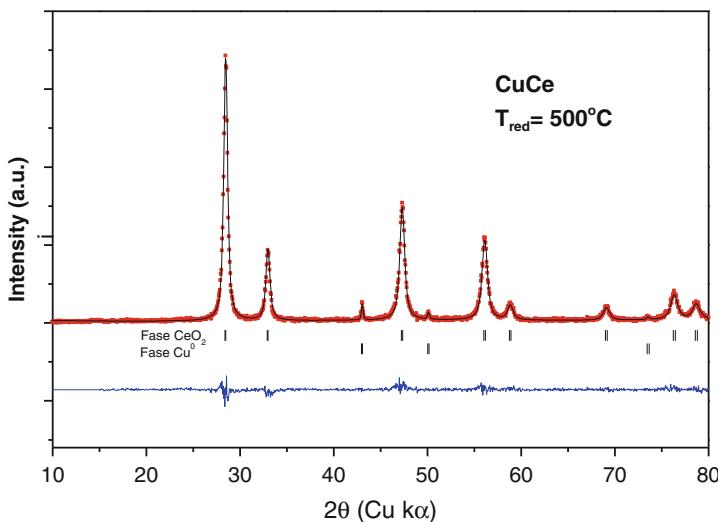
Fig. 9.15 X-ray diffractogram for the CuCe sample after reduction at 500 °C [9]

The diffractograms of CuCe oxide for different reduction temperatures were obtained with the purpose of ascertaining the influence of pretreatment conditions. Subsequent re-oxidization was undertaken after sampling of the reduction to evaluate whether the oxide has the capacity to return to its previous state.

Figure 9.14a, b show the diffractograms after pretreatment of the sample with an inert atmosphere and after the reduction with H_2 at 300 °C. The two phases are of cubic cerium oxide, with fluorite-like structure (cerianite), and after reduction, dispersed tenorite (CuO) crystallites were reduced to metallic Cu.

Figure 9.15 shows the diffractogram of the catalyst reduced at 500 °C and in that the entire CuO phase was reduced to metallic Cu^0, as verified by Rietveld quantitative phase analysis. The copper phase content in the reduced sample is 3.8 ± 0.2 %, meaning that all the copper is reduced, since this catalyst has 4 % by weight of copper, according to the chemical analysis previously done by X-ray fluorescence.

Figure 9.16 shows the diffractograms when the reduced sample was reoxidized. Note that when reoxidized at room temperature, the reflection lines of Cu^0 are still present, indicating that this metal was not completely reoxidized. However, when reoxidized at 500 °C it formed a new phase, indicating that all the Cu^0 present was reoxidized, partly in the form of cuprite (Cu_2O—1.9 ± 0.3%) and partly as tenorite (CuO—2.1 ± 0.2 %).

Table 9.3 shows the Bragg angles θ, the diffraction angles 2θ, the full widths at half height FWHM of the diffraction lines, and the crystallite sizes for the CeO_2 and CuCe samples. It can be ascertained that the diffraction angle for reflection of the most intense peaks for the CeO_2 phase is approximately equal in all cases, as well as for the CuO phase, indicating the presence of two separate phases; i.e., a mixture of oxides.
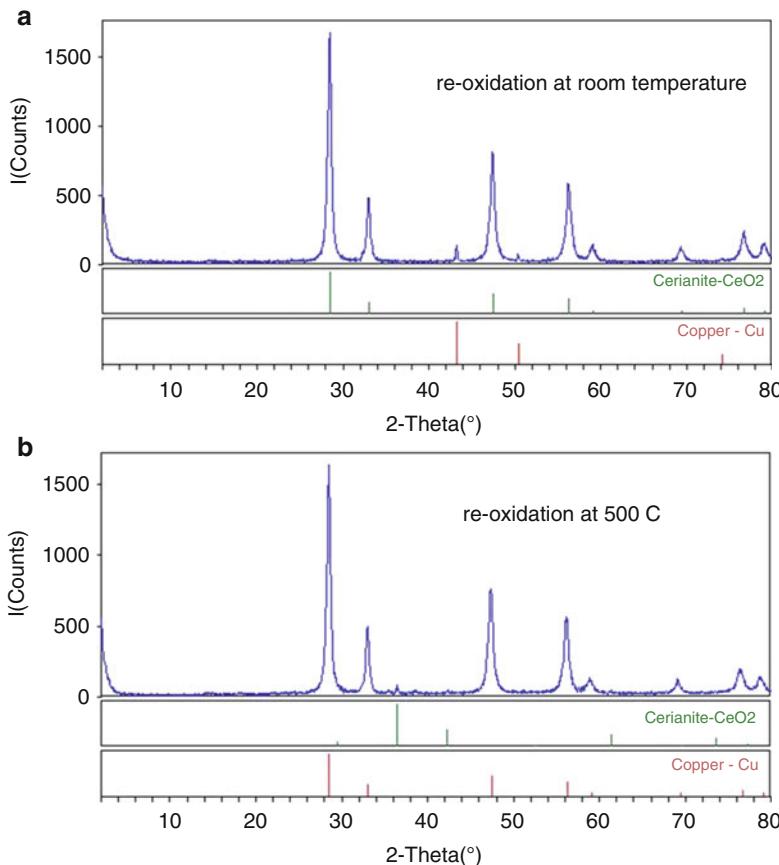
Fig. 9.16 X-ray diffractogram for the CuCe (**a**) sample in an He flow after re-oxidization at room temperature and (**b**) in an He flow after re-oxidization at 500 °C [9]

Table 9.3 Crystallite sizes obtained by Scherrer Equation [9]

	h	k	l	D (Å)	2θ(°)	θ(°)	FWHM	L (Å)
CeO₂ pure	1	1	1	3.12	28.55	14.28	0.22	365
CuCe-inert-500								
CeO₂ phase	1	1	1	3.13	28.49	14.24	0.51	158
Phase CuO	1	1	1	2.33	38.59	19.29	0.29	281
CuCe-oxi-red-500								
CeO₂ phase	1	1	1	3.14	28.39	14.19	0.49	165
Phase Cu	1	1	1	2.10	42.96	21.48	0.17	491
CuCe-reoxi-amb								
CeO₂ phase	1	1	1	3.12	28.56	14.28	0.49	165
Phase Cu	1	1	1	2.08	43.35	21.67	0.15	545
CuCe-reoxi-500								
CeO₂ phase	1	1	1	3.14	28.41	14.21	0.49	163
Phase Cu₂O	1	1	1	2.46	36.43	18.21	0.19	424
Phase CuO	1	1	1	2.34	38.49	19.24	0.20	412

The addition of copper to ceria reduced the apparent crystallite size of CeO_2 and/or increased the micro-deformations in the lattice, as can be seen in Table 9.3 by the size L. The thermal treatment increased crystallite size of the CuO phase, indicating a possible sintering of the Cu particles.

9.2 X-ray Diffraction Analyses: In Situ Analyses

9.2.1 Structure Analyses: XRD

9.2.1.1 Ex Situ

The X-ray diffraction technique is widely used for routine characterization of solids and applied for determining crystalline phases of the compounds and evaluate possible changes in the crystal structure thereof.
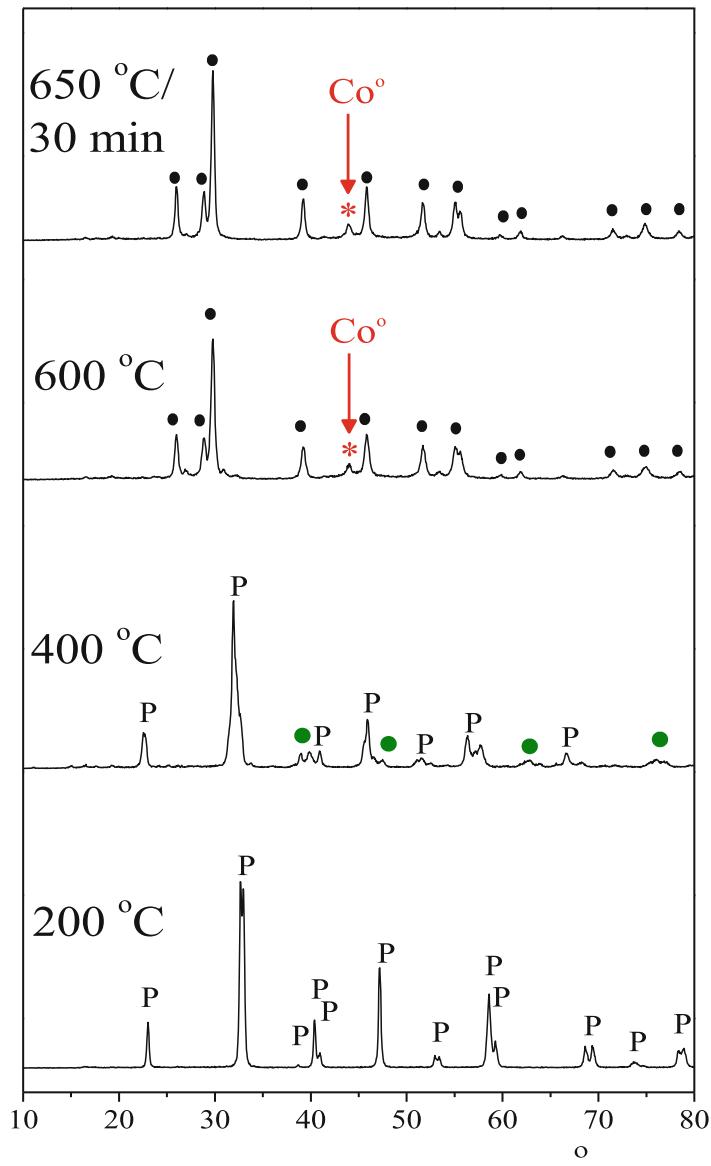
One can do X-ray diffraction experiments under non-ambient conditions. The X-ray diffractometer can be equipped with a reaction chamber, where the powder sample can be analyzed under the presence of gases, pressure, and/or vacuum. Sometimes, it is also possible to perform reactions. The "in situ" analyses were initiated with reduction or oxidation processes. The reaction can be carried out in the presence of the reaction mixture.

Detecting and measuring the size of nanoparticles in supported metal catalysts is of utmost importance for the overall characterization of the system, a factor that is related to the catalytic behavior. Some properties of nanomaterials can be inferred by modeling its cluster structure and size, and a model is used to simulate the scattering of rays by the sample. In general, the parameters involved in the model are optimized until the theoretical pattern fit the experimental results.

9.2.2 Reducibility of Oxide (LaCoO₃) by In Situ XRD

This example shows clearly the transformation during the reducibility of an oxide, in particular of the $LaCoO_3$ catalyst (LC), using temperature programmed reduction at different temperature and under reducing H_2 atmosphere, undergoing in the XRD chamber, aiming to investigate the differences in behavior in the reducibility of the oxide [10].

The in situ diffractograms for different reduction temperatures are displayed in Fig. 9.17, showing the collapse of oxide structure and appearance of new phases with increasing reduction temperature. Up to 300 °C, the oxide is resistant to reduction. It is a single-phase $LaCoO_3$ perovskite. At 400 °C, perovskite transforms to an intermediate structure brownmillerite $La_2Co_2O_5$. This behavior is also reported by Hansteen et al. [11]. At 500 °C, this structure still holds, but collapses before reaching 600 °C, temperature at which cobalt metal is identified with La_2O_3

Fig. 9.17 Structural evolution LC under a reducing atmosphere of 10 % H$_2$/He and programmed temperature of 10 °C/min. The main peaks Co^0 (JCPDS 15-0806) and La$_2$O$_3$ (JCPDS 37-1132) are indicated by (*) and (●), respectively. Peaks at 500 °C are related to the La$_2$Co$_2$O$_5$ ICSD 51198 (Hansteen et al. [11])

Table 9.4 Structural changes as a function of temperature

Temperature (°C)	Phases	Content (w%)	Unit cell parameters (Å) a	b	c	Cell volume (Å³)	L_{hkl} (nm)
25	$LaCoO_3$	100	5.4368	5.4368	13.101	335.37	$L_{012} = 45.0$
200	$LaCoO_3$	100	5.4578	5.4578	13.183	340.09	$L_{012} = 47.7$
300	$LaCoO_3$	100	5.4706	5.4706	13.229	342.88	$L_{012} = 61.5$
400	$La_2Co_2O_5$	100	5.5125	15.949	5.6979	500.98	$L_{040} = 19.1$
500	$La_2Co_2O_5$	100	5.5045	15.957	5.6903	499.83	$L_{040} = 41.6$
600	La_2O_3	73.8	3.9569	3.9569	6.1848	83.86	$L_{101} = 23.5$
	LaHO	5.9	8.1148	8.1148	5.6364	371.16	$L_{201} = 11.0$
	Co	20.3	3.5653	3.5653	3.5653	45.32	$L_{111} = 11.1$
650	La_2O_3	67.8	3.9599	3.9599	6.1915	84.08	$L_{101} = 29.0$
	LaHO	12.4	8.2385	8.2385	5.3380	362.31	$L_{201} = 3.1$
	Co	19.8	3.5685	3.5685	3.5685	45.44	$L_{111} = 11.1$

oxide and lanthanum oxyhydride LAHO. Therefore, this last phase may be responsible for part of the H_2 consumption during the reduction.
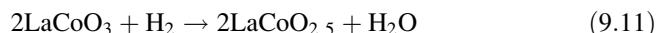
When the temperature reached 650 °C, and a vacuum level is maintained for 30 min, there is enough time to achieve a 100 % reduction. At the end of this time, the X-ray diffraction confirmed the formation of metallic Co, coexisting with La_2O_3 and LaHO.

Refinements by Rietveld are shown in Table 9.4, which allows comparison of the lattice parameters and crystallite size versus temperature.
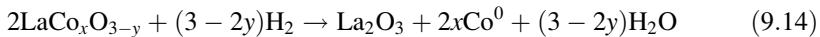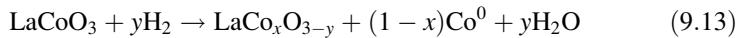
It shows increasing lattice parameters and crystallite L_{012} with increasing temperature up to 300 °C. From the cell parameters obtained after calcination and at room temperature, it can be inferred that the structure is rhombohedral perovskite $LaCoO_3$ or during the synthesis step was deformation or distortion diverting structure of cubic ideality.

The crystallographic parameters used in the calculation of the average crystallite size using Scherrer's equation [Eq. (5.8)] and the results obtained are given in Table 9.4. With collapse and emergence of $La_2Co_2O_5$ brownmillerite, there is an expansion of the unit cell parameters, in accordance with Hansteen et al. [11], attributed to the larger size of the divalent cobalt atoms of high spin. With increasing temperature, also $La_2Co_2O_5$ sinters until collapsing to form metallic cobalt of nanosized crystallites, i.e., $L_{(111)} = 11.1$ nm, which remains until ending the experiment.

Therefore, the reduction of Co^{3+} in $LaCoO_3$ in two steps is evident, as suggested by Crespin and Hall (1981) cited Huang et al. (2005):

$$2LaCoO_3 + H_2 \rightarrow 2LaCoO_{2.5} + H_2O \tag{9.11}$$

$$2LaCoO_{2.5} + 2H_2 \rightarrow 2Co^0 + La_2O_3 + 2H_2O \tag{9.12}$$

However, some authors claim that cobalt metal can be formed from 300 °C during reduction of $LaCoO_3$ with 10 % H_2/N_2, due to the appearance of an intermediate structure deficient in oxygen according to the following equations (SIS et al. 1973):

$$LaCoO_3 + yH_2 \rightarrow LaCo_xO_{3-y} + (1-x)Co^0 + yH_2O \tag{9.13}$$

$$2LaCo_xO_{3-y} + (3-2y)H_2 \rightarrow La_2O_3 + 2xCo^0 + (3-2y)H_2O \tag{9.14}$$

Refined XRD patterns showed good agreement between the observed experimental data (red symbols) and the calculated curve (solid black line), whose difference results in line in blue. The latter is mostly a straight line, with some noise in extent; however, in visual terms the adjustment can be considered satisfactory. Papers related to this subject are presented in references [13–26].

References

1. Guinier A. X-ray diffraction in crystals, imperfect crystals, and amorphous bodies. New York: Dover; 1994.
2. Waasmaier D, Kirfel A. New analytical scattering-factor functions for free atoms and ions. Acta Crystallogr A. 1995;51(3):416–31.
3. Hahn T. International tables for crystallography, space-group symmetry. New York: Wiley; 2005.
4. International Center for Diffraction Data, Powder Diffraction Database (1–42); 1992.
5. Hanawalt JD, Rinn HW, Frevel LK. Chemical analysis by X-ray diffraction: classification and use of X-ray diffraction patterns. Powder Diffr. 1986;1:2–14.
6. Young RA (ed). The rietveld method. International Union of Crystallography Monographs on Crystallography. Oxford: Oxford University Press; 1995.
7. Carvajal JR. FULLPROF: A program for rietveld refinement and pattern matching analysis. 1990. Abstracts of the Satellite Meeting on Powder Diffraction of the XV Congress of the IUCr.
8. Larson AC, Von Dreele R. General structure analysis system (GSAS). Los Alamos National Laboratory Report LAUR 86–748; 2000.
9. Schmal M, Perez CA, da Silva VT, Padilha LF. Hydrogen and ethylene production from partial oxidation of methane on CuCe, CuZr mixed oxides and ZrO_2 catalysts. Appl Catal A Gen. 2010;375:205–12.
10. Souza FT, Magalhães RNS, Perez CAC, Schmal M. Structural investigation of $LaCoO_3$ and $LaCoCuO_3$ perovskite-type oxides and the effect of Cu on coke deposition in the partial oxidation of methane. Appl Catal B Environ. 2012;117–118:156–66.
11. Hansteen OH, Fjellvåg H, Hauback BC. Crystal structure and magnetic properties of La2Co2O5. J Solid State Chem. 1998;141(2):411–7.
12. Cullity B, Stock S. Elements of X-ray diffraction. Prentice Hall: Upper Saddle River, NJ; 2001.
13. BIAŁOBOK, B., TRAWCZYŃSKI, J., MIŚTA, W., ZAWADZKI, M., 2007, "Ethanol combustion over strontium- and cerium-doped LaCoO3 catalysts", Applied Catalysis B: Environmental, v. 72, n. 3-4 (Mar), pp. 395-403.

14. Hernández-Alonso, M. D., Hungría, A. B., Martínez-Arias, A., et al., 2004, "EPR study of the photoassisted formation of radicals on CeO2 nanoparticles employed for toluene photooxidation", Applied Catalysis B: Environmental, v. 50, n. 3, p.167-175.
15. Hori, C. E., Permana, H., Ng, K. Y. S., et al., 1998, "Thermal stability of oxygen storage properties in a mixed CeO2-ZrO2 system", Applied Catalysis B: Environmental, v. 16, n. 2, p.105-117.
16. HUANG, L., BASSIR, M., KALIAGUINE, S., 2005, "Reducibility of Co3+ in perovskite-type LaCoO3 and promotion of copper on the reduction of Co3+ in perovskite-type oxides", Applied Surface Science, v. 243, pp. 360–375.
17. Mai, H.-X., Sun, L.-D., Zhang, Y.-W., et al., 2005, "Shape-selective synthesis and oxygen storage behavior of ceria nanopolyhedra, nanorods, and nanocubes", The Journal of Physical Chemistry B, v. 109, n. 51, p.24380-24385.
18. Matsumoto, S. I., 2004, "Recent advances in automobile exhaust catalysts", Catalysis Today, v. 90, n. 3-4, p.183-190.
19. Rabelo Neto RC, , Schmal M,, Synthesis of CeO2 and CeZrO2 mixed oxide nanostructured catalysts for the iso-syntheses reaction, Applied Catalysis A: General 450 (2013) 131– 142.
20. Magalhães RNSH. ,Toniolo FS ,da Silva V T , Schmal M, Selective CO oxidation reaction (SELOX) over cerium-doped LaCoO3 perovskite catalysts, Applied Catalysis A: General 388 (2010) 216–224.
21. Sun, C., Li, H. e Chen, L., 2007, "Study of flowerlike CeO2 microspheres used as catalyst supports for CO oxidation reaction", Journal of Physics and Chemistry of Solids, v. 68, n. 9, p.1785-1790.
22. Faria WLS, Perez CAC , Cezar DV, Dieguez LC, Al2O3 catalysts for oxidative steam reforming of propane, Applied Catalysis B: Environmental 92 (2009) 217–224.
23. Zhang, F., Chan, S.-W., Spanier, J. E., et al., 2002, "Cerium oxide nanoparticles: Size-selective formation and structure analysis", Applied Physics Letters, v. 80, n. 1, p.127-129.
24. SIS, L. B., WIRTZ, G. P., SORENSON, S. C., 1973, "Structure and properties of reduced LaCoO3", Journal of Applied Physics, v. 44, n. 12 (Dec), pp. 5553-5559.

Chapter 10
Spectroscopy in the Infrared Region

Martin Schmal and Deborah C. Vargas

Abstract Infrared is one important spectroscopic tool for elucidating molecular structure and qualitatively and quantitatively determining organic and inorganic compounds. Among these, spectroscopy in the infrared region stands out for analyses of molecules absorbed in a surface. Diffuse reflectance measures the energy spread diffusely after interaction with electromagnetic radiation in the infrared region with a discontinuous matrix.

Analytical spectroscopic methods are based on interaction between radiating energy and matter, wherein the amount of energy emitted or absorbed by atomic or molecular species is measured. The different methods may be classified in accordance with the region of the electromagnetic spectrum involved in the measurement (Fig. 10.1). The interaction of radiation occurs by different mechanisms and supplies different kinds of data.

Therefore, spectroscopic methods constitute an important tool for elucidating molecular structure and qualitatively and quantitatively determining organic and inorganic compounds. Among these, spectroscopy in the infrared region stands out. This is based on transitions between two vibrational levels of molecules in their fundamental electronic state, which are normally observed as an absorption spectrum.

Electromagnetic radiation may be described as a wave with properties such as frequency (ν), wavelength (λ), and propagation velocity (c), formed by energy packets called photons or quanta [1–3]. The wave number ($\overline{\nu}$) is another means of describing electromagnetic radiation, and it is equivalent to $1/\lambda$.[1]

The energy content of the photon, in accordance with quantum theory, is expressed by

$$E = \frac{\hbar c}{\lambda} = hc\overline{\nu} \tag{10.1}$$

where $\hbar$ = Planck constant = 6.63×10^{-34} J s^{-1}.

---

[1] The wave number is defined as the number of waves per centimeter, and by definition, its unit of measurement is cm^{-1}. In texts that deal with infrared spectroscopy, the term frequency is commonly used to refer to $\overline{\nu}$.
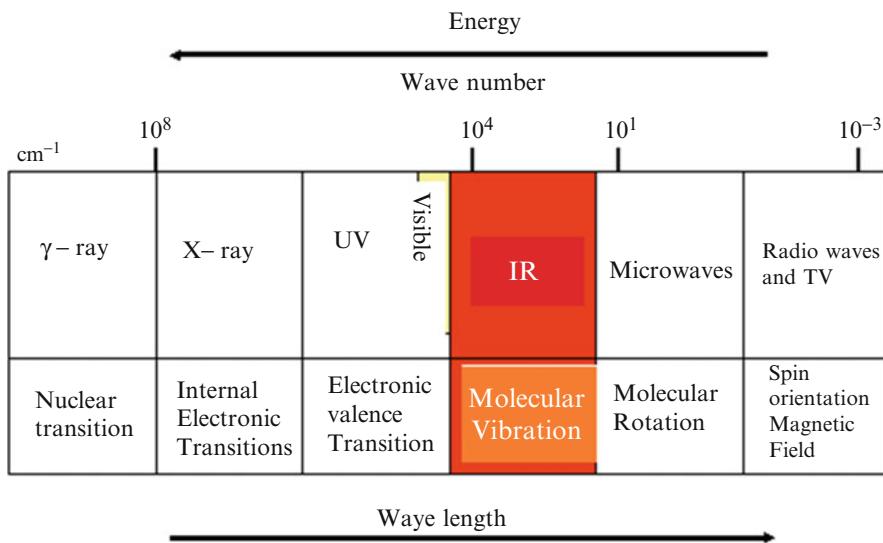
Fig. 10.1 Electromagnetic spectrum and atomic and molecular transitions resulting from interaction between radiating energy and a sample

In order to absorb radiation in the infrared region, molecules must undergo a change in their dipole moment as a result of their vibrational and rotational motions. Under these conditions, the alternating electric field of the radiation interacts with molecules and produces a change in the amplitude of one of their motions. In a molecule or polar bond, vibration causes a fluctuation in its dipole moment, producing a field that may interact with the electric field associated with electromagnetic radiation, thus generating absorption of energy which is observed in the form of bands in the infrared spectrum.

In homonuclear diatomic compounds (O_2, N_2, H_2), where there is no change in dipole moment during vibration or rotation, radiation is not absorbed in the infrared region.
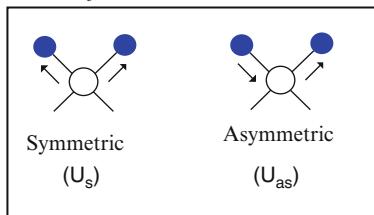
Transitions between vibrational levels correspond to certain normal vibration modes of molecules or groups of atoms, which are, in turn, related to the degree of freedom presented by molecules.

In polyatomic molecules containing N atoms, the number of independent vibrational modes is calculated by assuming that the motion of each atom may be described in terms of displacement along three perpendicular directions in space (x, y, z). Molecules have *3N* possibilities called *degrees of freedom*.
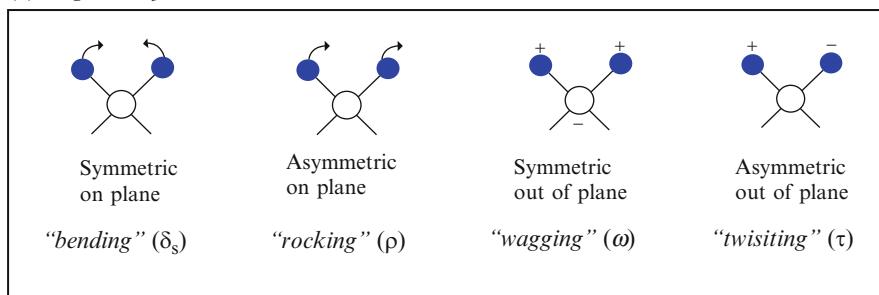
In nonlinear molecules, there are also three displacement combinations related to molecular rotation (three degrees of freedom) and three degrees due to the translational motions of the molecular centers of mass (x, y, z), forming a total of *3N-6* degrees of freedom. Thus, if the degenerate mode does not occur, *3N-6* fundamental vibrational modes are expected, and there will be *3N-6* fundamental frequencies.

For linear molecules, there will be *3N-5*, because there is no rotation on the axis. Each of these vibrational modes has a specific symmetrical relationship. After a

(1) *Axial deformations:*

(2) *Angular deformations:*
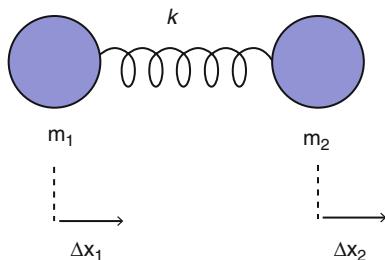
Fig. 10.2 Nonlinear molecular vibrational modes

symmetrical operation, the nature of the normal vibrations may or may not be modified; when unaltered or altered, it is called *symmetrical* and *asymmetrical*, respectively [2, 4–6].

Basically, there are two types of molecular vibrations: axial (stretch) and angular. Axial vibrations result in variation of the interatomic distance along the bond axis between two atoms. In angular deformation, variation in the angle of the bond between atoms or groups of atoms occurs in the lowest energy state. Angular modes are also divided into *rocking* (ρ), *wagging* (ω), and *twisting* (τ). Figure 10.2 presents the fundamental vibration modes.

The vibration of diatomic molecules may be related to the motion of two masses joined by a spring of negligible mass r_0 in length and a force constant of k, such as a simple harmonic oscillator. A small displacement of the particle from its equilibrium position will require a restoring force that obeys Hooke's law:

$$F = -k \cdot \Delta x \tag{10.2}$$

With the Schrödinger equation and the combination of this model with potential and kinetic energies, we obtain the vibration frequency of the oscillator, which is given by

$$\frac{1}{\lambda} = \frac{1}{2\pi c} \left(\frac{k}{\mu}\right)^{1/2} = \bar{\nu} \tag{10.3}$$

where $m_i =$ reduced mass, equivalent to

$$\mu = \frac{m_1 m_2}{m_1 + m_2} \tag{10.4}$$

Therefore, the model enables an estimation of the force constant of a chemical bond (k) by ascertaining the frequency of absorption of this bond in the infrared region or by stimulating the vibrational frequencies of the bond. In general, there is satisfactory concordance between the calculated values and experimental values of the wave numbers. One example is the C–O bond in methanol, whose calculated wave number value is 1113 cm^{-1}, and the band observed for this bond occurs at 1034 cm^{-1}. It is worth noting that this calculation did not take into consideration the interactions that may occur in the molecule.

The region of the electromagnetic spectrum corresponding to the infrared region varies between wave numbers of 12,800–10 cm^{-1} or $\lambda = 0.108$–1000 μm. This region is divided into three parts, called near-, mid-, and far-infrared [32].

Infrared Absorption Regions

- **Near-IR (12,800–4000 cm^{-1})**: more appropriate for quantitative analyses of compounds containing functional groups formed by hydrogen bonded to C, N, and O. However, these compounds may be determined more accurately by *visible UV* spectroscopy. Applications of *near$_{IV}$* include the determination of water in glycerol, organic films, and hydrazine; quantitative determination of phenol, alcohols, organic acids, and hydroperoxides based on the first overtone of the bond stretching vibration O–H; and differentiation between amines (only primary amine absorbs in this region).
- **Mid-IR (4000–200 cm^{-1})**: this region presents the characteristic vibrations of group frequencies, enabling the identification of small differences in molecule structure, and will be described in greater detail throughout this chapter.
- **Far-IR (200–10 cm^{-1})**: especially useful for studies of inorganic matter, because the absorptions related to stretching vibrations and angular deformations of bonds between metallic atoms and other organic and inorganic bonds are observed at frequencies lower than 600 cm^{-1}.

The mid-infrared region is divided into two main subregions: the *group frequency region*, which corresponds to the part of the spectrum between 4000 and 1200 cm^{-1}, and the so-called fingerprint region (1200–600 cm^{-1}). Interpretation of results involves identification of the function group to which the sample belongs

and a detailed analysis of the fingerprint region, which supplies information on the characteristics of the compound being analyzed. Small modifications in molecular structure are observed through band changes in this region. The bond C–O can be cited as an example; this presents a band in the region between 1300 and 1100 cm^{-1}, enabling an ester to be differentiated from a ketone, which does not present this band [2, 4].

10.1 Interpretation of Infrared Spectra

The use of infrared for the identification of organic compounds dates back to the 1950s and is still widely applied for the structural analysis of organic, inorganic, and biological compounds.

Current literature features a series of tables containing the characteristic vibrations of several functional groups, which enable a detailed investigation in order to identify the compound [5, 6]. By way of example, Table 10.1 presents the values of characteristic group frequencies.

Some phenomena, such as combination bands, overtones, vibrational coupling, and hydrogen bonds, may influence the position of the bands and cause interpretation errors.

Overtones are multiples of a fundamental absorption frequency and occur at frequencies two or three times greater than the fundamental frequency.

Vibrational coupling occurs between two bonds that vibrate at similar frequencies, producing absorption bands with close frequencies.

Coupling vibrations may result from fundamental coupling vibrations (in this case, AX_2) or a fundamental vibration may couple to an overtone band of another vibration, thus generating Fermi resonance, which normally leads to the formation of two close bands where only one band should appear. When an AX_2-type group

Table 10.1 Characteristic group frequencies for organic compounds

Frequency ($\bar{v}$) (cm^{-1})	Bond	Compound
3100–3200	O–H, N–H	Alcohol, phenol, carboxylic acid
3100–3000	C–H	Alkenes and aromatics
3000–2800	C–H	Alkanes
2100–1500	C=C	Alkenes and aromatics
	C≡C	Alkynes
	C–N	Amines and amides
	C≡N	Nitriles
	C=O	Aldehyde, ketone, carboxylic acid, and ester
	NO_2	Nitro compounds
1500–600	C–H	Alkanes, alkenes, and aromatics
	C–O	Alcohol, ester, carboxylic acid, and ether
	NO_2	Nitro compounds

presents vibrational coupling, it generates two symmetrical (ν_s) and asymmetrical (ν_{as}) stretch absorption bands, such as:

1. $-CH_2^- = 3000$ cm^{-1} (ν_{as}) and 2900 cm^{-1} (ν_s)
2. $-NO_2 = 1500$ cm^{-1} (ν_{as}) and 1400 cm^{-1} (ν_s)
3. $SO_2^= = 1350$ cm^{-1} (ν_{as}) and 1150 cm^{-1} (ν_s)

The hydrogen bonds, especially in compounds containing **–OH** and **–NH** groups, are affected by polar solvents or inter- and intramolecular interactions in alcohols, phenols, and carboxylic acid. Widening of the **–OH** (~3500 cm^{-1}) band and displacement to the region with the lowest wave number are observed. In **R–OH**-type compounds, there is a reduction of approximately 300 cm^{-1} [2, 4]. One way of attenuating this effect is to work with low concentrations of appropriate samples and solvents, such as CCl_4 or any other that does not favor the formation of hydrogen bonds and that also does not have band that will override those of the analyzed sample.

10.2   Sample Handling: Analysis of Solids, Liquids, and Gases

In general, samples to be analyzed by infrared absorption spectroscopy require adequate support (infrared cells) in such a way as to enable the acquisition of the spectrum in the apparatus. There are different types of cells, and the choice among them depends on the sample characteristics and the objective of the analysis, such as surface characterization studies or chemical reaction monitoring. Commercially available cells are of the sealed, collapsible, and variable thickness kinds, for gas, flow, high-vacuum and -pressure and micro-cells.

The sealed cell, shown in Fig. 10.3, is used in the analysis of liquid samples and comprises optical windows of KBr, NaCl, CsI, CaF_2, and ZnSe, among others. However, the choice of the material to be used depends on the type of study, the frequency range, and the nature of the sample. KBr windows are suitable for nonaqueous solutions and, due to their high solubility in water (65.2 g/100 g H_2O), are transparent to infrared in the 40,000–400 cm^{-1} range. CaF_2 is insoluble (0.151 g/100 g H_2O) and enables aqueous solutions to be analyzed; however, it absorbs in the region below 1100 cm^{-1}, and its range of use is between 1000 and 1100 cm^{-1} [7]. The windows are separated with spacers whose thickness varies according to the material analyzed. For aliphatics, a 0.05 mm spacer is used, while a 0.015 mm spacer is used for ethers and ketones.

The high-vacuum cell is employed in studies of catalysts and absorbed molecules. The choice of window also depends on the range of interest, but care must be taken with the pressure applied, because CaF_2, for example, can support pressures of up to 1200 atm.
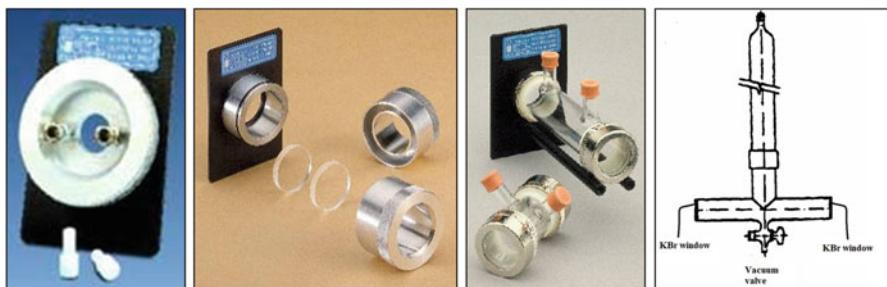
Fig. 10.3 Cells for infrared analyses: sealed, collapsible, for gas and high vacuum

Liquid Analysis A sealed cell is used for volatile pure liquids or liquids in the solution. In case of dilution, the solvent must be as nonpolar as possible, in order to minimize solute–solvent interactions, and it cannot absorb strongly in the region of interest.

Solid Analysis Finely divided and dispersed solids in alkali halides (KBr is the most widely used). The mixture in the proportion of 1 mg of sample: 300 mg of KBr is pressed, forming a clear and transparent pellet. Material that may form films, such as polymers and resins, is directly analyzed and the film must be as thin as possible. For surface characterization the sample is prepared in a the form of a self-supported pellet, where a small quantity of solid (~20 mg) is pressed in order to obtain a thickness of decimals of millimeters.

Gas Analysis Requires cells with an optical pathway that is greater or equal to 10 cm and pressures of between 5 and 400 torr in order to produce an absorption spectrum with a reasonable level of absorbance. This is applied in atmospheric pollution studies, as well as to identify reaction intermediaries and evaluate gas purity.

Quantitative analysis is based on the maximum absorption measurement of an analytical band, which needs to be free of interferences for absorption of the solvent, or other components or contaminants. The analytical band is specific to the species to be quantified, and it must be very sensitive to small concentration variations and obey Lambert–Beer law (quantitative treatment of energy absorption by the compound). The equations below are the expressions of Lambert–Beer law [1–3]:

$$A = a \cdot b \cdot c \tag{10.5}$$

where a is the absorptivity (L g^{-1} cm^{-1}), b the optical pathway covered by the radiation (cm), and c the species concentration (g L^{-1})

When the concentration is expressed in (mol L^{-1}), absorptivity is called molar absorptivity (ε) and the unit of measurement is (L mol^{-1} cm^{-1}).

The classical method for measuring absorbance (A) uses the height measurement of its maximum absorption. Integration of the analytical band area, however, supplies more significant measurements.

It is important to observe that Lambert–Beer law is only valid when absorbance is a linear function of concentration (c) and the optical pathway (b). Intermolecular associations result in deviations in Lambert–Beer law, which may be avoided using diluted solutions.

The solids diluted in KBr or in the form of films present difficulties in the measurement of its thickness. In this case, an internal standard is used that consists of adding a known quantity of a material that is not present in the sample and that does not interact with it. The internal standard must be pure, have an intense band, be well resolved, and not interfere with the analytical band. The concentration is obtained directly, as long as the absorptivity and the optical pathway are known. Another widely used method is the calibration curve, suitable for cases where the concentration of the sample varies within a wide range of limits.

10.3   Surface Characterization of Solids Using Probe Molecules

Infrared was one of the first techniques applied to the analysis of molecules absorbed in a surface, and the first studies were conducted by Terenin and Kasparov in 1940, where ammonium was absorbed in the surface of a catalyst consisting of iron dispersed in silicone gel. Subsequently, the chemisorption study of CO in metals and metallic oxides was studied in the literature [7, 8, 32].

This methodology is an important tool in surface studies, with the characterization of heterogeneous catalysts, supplying information on the state and chemical environment of the metal or transition ion at the surface of the catalyst, including changes in the surface due to thermal treatment, reactions among other components, acidity, and others [7].

Interaction between the probe molecule and the site must be specific and be spectrally sensitive to variations in the electronic state at the site of adsorption, and it cannot influence the characteristics of the solid analyzed by causing modifications at the surface.

The different samples are mostly inorganic solids. The preparation method consists of pressing the powder sample (~25 mg) in order to form a self-supporting disk (pellet). Experiments should be performed under conditions where the surface is completely contaminant free [2–4].

The empirical interpretation of the adsorbed molecular spectra is based on determining the differences between the absorption profile of pure substances in the gas or liquid phases and of the adsorbed molecules. However, interpretation may be more than this comparison; spectroscopic adsorption studies attempt to

determine the interaction mechanisms, their energy, and the types of elements and molecules that are part of the surface interactions.

An example of empirical interpretation would be to determine the presence of adsorbed olefines and aliphatic compounds, where bands at frequencies above 3000 cm^{-1} (bond characteristic =C–H, 3020 cm^{-1}) indicate the presence of olefines, while bands in the region below 3000 cm^{-1} are suggestive of the presence of aliphatic compounds (–C–H, 2960 cm^{-1}) [9].

Several studies in literature demonstrate the use of different probe molecules for surface studies, such as pyridine, ammonium, CO, methanol, NO, and propene.

Adsorption of molecules such as ammonium and organic bases is used in the study of chemical surface properties of oxide catalysts. The acidity of an oxide can be evaluated based on the classic Brönsted and Lewis concepts, i.e., according to their capacity to donate a proton and accept electrons, respectively. Thus, spectroscopic evidence of the presence of these sites on the surface of oxides is obtained from the adsorption of molecules capable of adsorbing at the acidic sites on the surface of the oxide.

The adsorption of pyridine for the identification of acidic sites was applied [9] in the 1960s, where it was ascertained that it was possible to distinguish between pyridine coordinated to the pair of electrons isolated at Lewis sites and adsorbed at Brönsted sites, thus forming a pyridinium ion (Fig. 10.4). Since pyridine (pK_B ~9) is a weaker base than ammonium ($pK_B = 5$), it is generally more widely used, because it only reacts with strong acidic sites [9]. Thus, the use of pyridine as a probe molecule to selectively study acidic surface sites has become a routine practice in laboratories for catalyst characterization.

Pyridine is the most widely studied probe molecule, capable of interacting with acidic Brönsted sites, as well as Lewis sites, which absorb at different frequencies in the infrared region. This analysis enables the presence of these sites to be identified and quantified, thus permitting an evaluation of the influence of acidity on cracking, isomerization, alcohol dehydration, and alkylation reactions, as well as the polymerization of hydrocarbons, which are catalyzed by acidic sites.

The vibrational modes of pure, physisorbed, and aluminosilicate-adsorbed pyridine are listed in Table 10.2 [9].

The diagram in Fig. 10.4 shows the forms of adsorption of pyridine at the Brönsted and Lewis sites. Acidity is measured by observing bands at **1545 cm^{-1}** for *Brönsted sites* and **1450 cm^{-1}** for *Lewis sites*.

When the objective is solely to determine protonic acidity, the use of bases that are sterically prevented from reacting with Lewis sites is recommended, for

Fig. 10.4 Adsorption of the Lewis molecule of pyridine at Brönsted (B$^-$) and Lewis (L) acidic sites
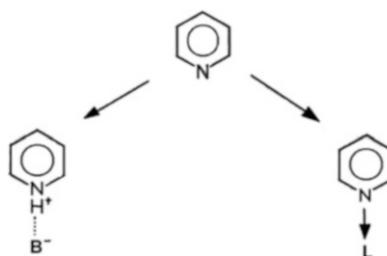
Table 10.2 Frequencies associated with the vibrational modes of aluminosilicate-adsorbed pyridine

Frequencies (cm^{-1})				
Py	Py/L	PyB	MPy	Vibrational mode
		3260		ν_{NH}
		3188		
3083	(3147)	(3147)		ν_{CH}
3054	(3114)	(3114)	3065	
(3054)	(30,810)	(30,810)	3043	
1580	1620	1638	1614	ν_{CC}
15,102	151,010	1620	1593	
1482	1482	1490	1490	
1439	1450	1545	1438	

Py = pyridine; Py/L = coordinated with a Lewis site; PyB = protonated pyridine; MPy = adsorbed at the molecular level through hydrogen bonds with superficial hydroxyl groups [9]
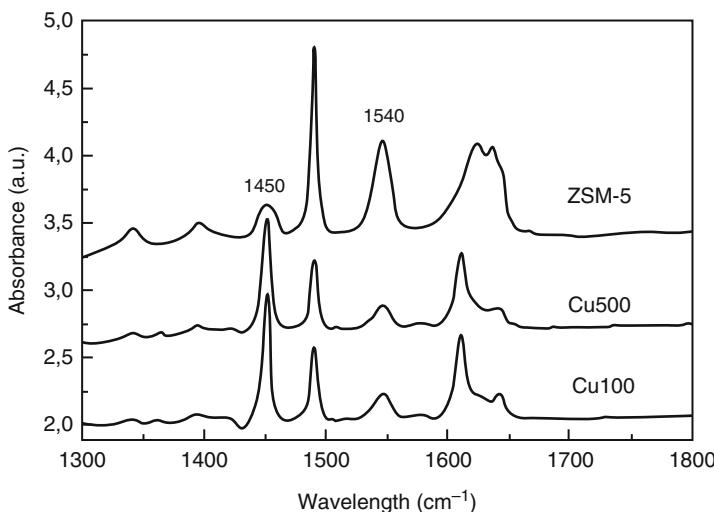
Fig. 10.5 Pyridine spectra in adsorbed in the ZSM-5 and Cu/ZSM-5 catalysts: Cu100—dried at 100 °C and Cu500—calcined at 500 °C [10]

example, 2,6-dimethylpyridine, whose 1630 cm^{-1} and 1650 cm^{-1} bands characterize protonic acidity.

Besides identifying the sites, it is possible to calculate their concentrations from the integration of the area of characteristic Brönsted and Lewis bands and the knowledge of the molar absorptivity of the sample and the self-supporting area of the pellet, by applying Lambert–Beer law.

The effect of adding copper with regard to the acidity of ZSM-5-type zeolites applied in the reduction of NO with methanol was studied by Carvalho et al. [10] and illustrates the application of the technique to catalyst studies. The 1540 cm^{-1} band in the ZSM-5 sample demonstrates the presence of acidic Brönsted sites

Table 10.3 Acidity of ZSM-5 and Cu/ZSM-5 catalysts [10]

Catalyst	Lewis sites (µmol/mg)	Brönsted sites (µmol/mg)	Total of acidic sites (µmol/mg)
ZSM-5	0.23	1.17	1.40
Cu100	1.14	0.33	1.47
Cu500	0.99	0.33	1.32

ε (1540 cm^{-1}) = 0.059 cm^2/µmol
ε (1450 cm^{-1}) = 0.084 cm^2/µmol

(Fig. 10.5); with the addition of Cu, there was a significant increase in the intensity of this band, thus confirming that there was an ion exchange during the preparation stage. The increase in intensity of the band of the Lewis sites (1450 cm^{-1}) in the exchanged sample is indicative of the presence of Cu^{2+} ions at the surface.

The concentration of Brönsted and Lewis acidic sites (Table 10.3) was calculated based on the intensity of the respective bands and their corresponding molar extinction coefficients (ε) by applying Lambert–Beer law. The quantification of sites showed that the total number of acidic sites of the zeolite did not change after addition of Cu and that a modification in the nature of the acidic sites occurs, wherein Brönsted sites are transformed into Lewis sites. An evaluation of the methanol oxidation catalysts, used as a reaction model, showed that activity and selectivity are influenced by the distribution of acidic sites.

The catalysts used in the heterogeneous catalytic processes are systems where a variety of active components (metals) is deposited on more or less inert supports (SiO_2, Al_2O_3, TiO_2). Characterization of these metallic sites is normally undertaken using probe molecules, such as CO and NO.
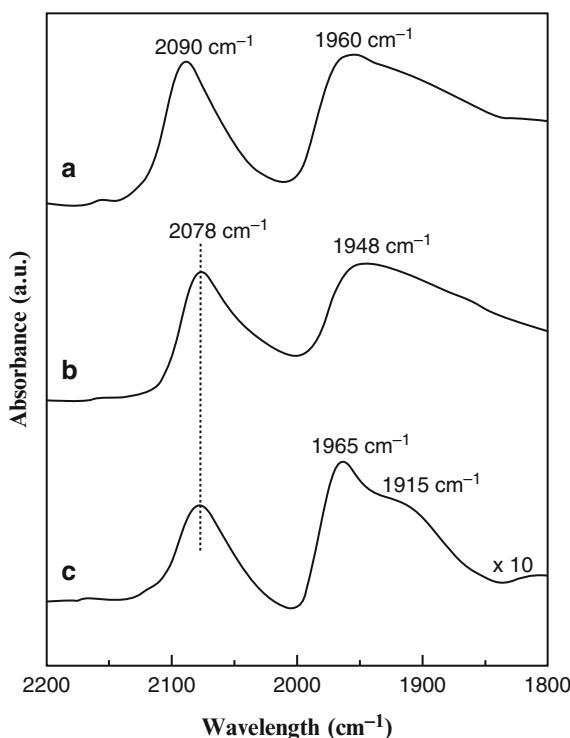
The adsorption stoichiometry of CO in metals occurs in two ways, linear and bridged-bonded, producing characteristic bands in different regions of the spectrum. The linear form produces bands at frequencies above 2000 cm^{-1} and below this value in bridge-bonded form. The CO adsorbed in Pt, for example, is characterized by an intense and moderately broad band at 2020–2100 cm^{-1}, related to CO linearly bounded to Pt and a weak band of around 1900–1800 cm^{-1}, due to CO bonded to two Pt atoms (bridge-bonded).

It is important to observe that several factors may affect the absorption frequency of an adsorbed molecule, such as degree of coverage, inductive effect of the ligands, the exposed face of the crystallite, and particle size.

CO adsorption was used to study the nature of Pd sites of %Pd/Al$_2$O$_3$ catalysts prepared from different precursors (chloride, nitrate, and acetylacetonate) by Monteiro, Chaloub, and Schmal [8]. The monometallic catalysts Pd–Cl, Pd–acac and Pd–N present two bands in the region between 2000 and 1800 cm^{-1}, characteristic of CO adsorbed in the linear form (above 2000 cm^{-1}) and bridge-bonded form (below 2000 cm^{-1}), as observed in Fig. 10.6.

The greatest intensity of linear bands CO for Pd–Cl and Pd–acac catalysts is in accordance with the greatest metallic dispersion observed for these samples (51 %), measured by chemisorption of H$_2$. Bands related to CO bridge-bonded adsorption were observed in a higher frequency for the Pd–N sample (1960 cm^{-1}) than for

Pd–acac and Pd–Cl. This difference is indicative of the influence of precursors in the distribution of Pd particle size.

The vibration frequency variation of the C–O bond is explained by the retro-bond, from Pd filled *d* orbitals to the $2\pi^*$ empty antibonding orbital of CO. At - low-coordination sites, availability of electrons for the retro-bond is lower than that for sites with an elevated coordination number. Accordingly, at the low-coordination sites, the bond Pd–CO is weaker and the infrared band is located at lower frequencies, while for elevated coordination, the C–O bond is stronger and the vibration frequency is higher [11].

The existence of two bridge-bonded adsorption bands of CO in the Pd–N (1965 cm^{-1} and 1915 cm^{-1}) sample is associated with different faces of the particle, demonstrating the lower metallic dispersion in this sample ($D = 16\,\%$).

Similar studies on the characterization of surfaces using different probe molecules are available in literature and enable a greater understanding of the different catalytic systems.

Infrared spectrometers also enable the use of accessories for more specific purposes, such as attenuated total reflectance (ATR) used, for example, to analyze aqueous solutions that are incompatible with the material of the commercial cell windows and diffuse reflectance infrared fourier transform spectroscopy (DRIFTS) , which enables in situ analyses to be performed.

10.4   Diffuse Reflectance Infrared Fourier Transform Spectroscopy (DRIFTS)

Diffuse reflectance measures the energy spread diffusely after interaction with electromagnetic radiation in the infrared region with a discontinuous matrix (powder-, solid-, plate-, or film-type samples) and reflects by charging spectral information that is dependent on the concentration of the sample. As shown in Fig. 10.7, the beam of light takes a random path suffering several reflections and is partially absorbed. The spectrum produced is similar to that obtained through the infrared technique by transmittance using potassium bromide (KBr) or self-supported pellets.

The difference between transmittance and reflectance is due to the difference in the optic path taken; in transmission, the optic path is constant for the entire wave number, while in reflectance it may be variable. The differences observed by comparing the spectra obtained by transmittance and diffuse reflectance are in the relative intensities of the bands. This occurs because in some regions of the spectrum, the sample absorbs weakly and the light penetrates more deeply into the matrix; the opposite happens when there is strong absorption. Thus, the weak bands in the transmittance spectrum will appear stronger in reflectance. Furthermore, another phenomenon observed is specular reflection (Fig. 10.7), which occurs at the faces of the particles and influences in the intensity and width of the bands. The factors, such as elevated refraction index, particle size, packaging, and concentration, favor the increase in specular reflection and must be taken into account during the analysis. One way of minimizing these effects is to reduce particle size and dilute the sample in a nonabsorbent matrix, such as KBr.

The results of the *DRIFTS* analysis are expressed in % *R*, which shows the quantity of energy reflected and is equivalent to % *T* (transmittance):

$$\%R = \left(\frac{I_S}{I_B}\right) \times 100 \tag{10.6}$$

where

I_s = intensity of infrared radiation reflected by the sample

I_B = intensity of infrared radiation reflected by a reference (mirror, KBr), also called background[2]
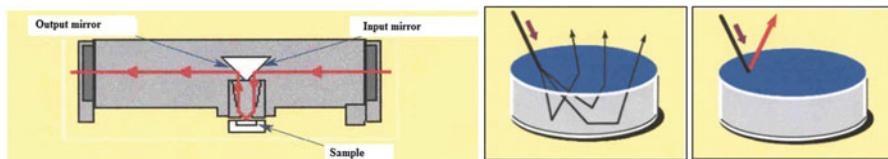
Fig. 10.7 Accessory diagram for diffuse reflectance, interaction of radiation with the sample, and specular reflection, respectively

---

[2] Background is a reference spectrum obtained with the purpose of measuring the contributions of the instrument and the environment.

The results of the DRIFTS analyses reported in literature are also expressed in **% A** (*absorbance*) and **Kubelka–Munk (K–M)**, which relates $f(R_\infty)$ functions with concentration and the scattering factor of the samples, and it is used for quantitative analyses:

$$\log\frac{1}{R} = A \tag{10.7}$$

$$F(R_\infty) = k \cdot c \tag{10.8}$$

while

$$F(R_\infty) = \frac{(1 - R_\infty)^2}{2R_\infty} \tag{10.9}$$

where $k =$ scattering coefficient and $R_\infty =$ ratio between diffuse reflectance of an infinitely thick sample[3] and that of a selected standard.

Analyses performed by DRIFTS have the advantage of minimum sample preparation, without requiring pellets. It may be applied to analyze samples in powder form or those deposited in a matrix, and some examples of material analyzed may be cited, such as medicinal products, high molecular weight organic material, plastics, crystals, and dyes (whose pigments usually cause transmittance distortions).

This technique has proven to be a valuable tool for characterizing catalysts. The accessory with a chamber for heating and gas flow enables the in situ analysis of the different catalytic systems. This analysis enables the acquisition of information about the modifications that occur at the surface of catalysts during chemical reactions, as well as the identification and formation of intermediate species and gas phases [12–16].

In situ DRIFTS studies of propane steam reforming over $Pd/CeO_2/Al_2O_3$ catalyst were carried out by Faria, Dieguez, and Schmal [16]. The DRIFTS measurements were performed under static and dynamic conditions in samples reduced at 500 °C. Figure 10.10 shows the spectra obtained in reactional conditions for $Pd/CeO_2/Al_2O_3$ catalyst. The bands in the 2030–1900 cm^{-1} range reveal the presence of CO adsorbed in Pd^0. The adsorption of CO in the triple-bridge mode presents values that are characteristic in the 1850–1800 cm^{-1} range. Accordingly, absorption bands obtained at 2031 and 1896 cm^{-1} refer to the adsorption of CO in metallic palladium in the linear and bridge modes, respectively.

Characteristic bands centered on 2353 and 2143 cm^{-1} are related to the presence of CO_2 and CO, respectively, in the gas phase. No characteristic bands of CO adsorbed either at oxidized cerium sites (Ce^{4+}, 2170 cm^{-1}) or in reduced cerium particles ($\sim$2115 cm^{-1}) were observed. In accordance with the catalytic evaluation

---

[3] Infinitely thick sample means a depth beyond which the signal does not change (~5 mm).
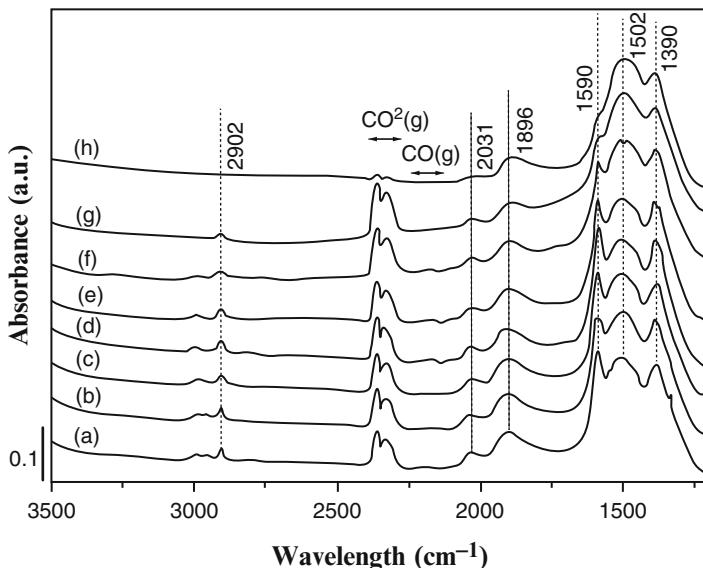
Fig. 10.8 DRIFTS spectra for the Pd/CeO$_2$/Al$_2$O$_3$ catalyst collected in O$_2$/C$_3$H$_8$ flow ($R = 2.5$) for 5′ (**a**), 15′ (**b**), and 20′ (**c**). Subsequent closing of the chamber for 1′ (**d**), 5′ (**e**), 15′ (**f**), and 20′ (**g**) under a O$_2$/C$_3$H$_8$ atmosphere. Cleaning of the surface after He flow for 10′ (**h**) [11]

under the same experimental conditions, the formation of CO$_2$ and CO was ascertained in the outtake gas, along with hydrogen production.

Formate species adsorbed in the support are observed at 1380 (ν_s OCO), 1390 (δ C–H), 1590 (ν_{as} COO), and 2902 cm^{-1} (δ CH), while bands of around 29,100 cm^{-1} are related to propane in the gas phase. Monodentate carbonate exhibits bands in the ranges 1530–1470 cm^{-1} (ν_{as} COO$^-$), 1370–1300 cm^{-1} (ν_s COO$^-$), and 1080–1040 cm^{-1} (ν C–O), while bidentate presents bands in the ranges 1620–1530 cm^{-1} (ν C–O), 1270–1250 cm^{-1} (ν_{as} COO), and 1030–1020 cm^{-1} (ν_s COO). Thus, it can be inferred that the bands exhibited in the 1550–1420 cm^{-1} range (Fig. 10.8) are characteristic of the presence of carbonates, very probably in monodentate form [17].

Therefore, the joint adsorption of O$_2$/C$_3$H$_8$ in the catalyst Pd/CeO$_2$/Al$_2$O$_3$ generates carbonate and formate species at the surface, CO adsorbed in Pd^0, as well as the presence of CO$_2$ and CO in the gas phase. After closure of the chamber (Fig. 10.7e–g), there is a reduction in intensity of the characteristic formate bands concomitant with an increase in the formation of gaseous CO$_2$ over time. This is indicative that a formate is an intermediate species in propane reforming. Admission of a pure He flow into the chamber (Fig. 10.8h) did not remove the carbonated surface species, providing evidence of the stability of these species in the experimental conditions used.

DRIFTS analyses in conjunction with in situ X-ray diffraction, diffuse reflectance in the visible UV region, thermal propane desorption, and catalytic tests

permitted the proposal of a reactional mechanism. Propane is adsorbed in the metal–support interface, decomposing into smaller hydrocarbon fragments and reacting with superficial hydroxyls of γ-Al_2O_3 of oxygen of the CeO_2 network, generating $HCOO^-$ (formate) and/or monodentate carbonate. CO_x species are formed by the combustion of these carboxylate species (formate and carbonates) in the presence of oxygen.

The use of DRIFTS has been growing in recent years, not only due to its greater simplicity but also due to the possibility of coupling it to other techniques, such as mass and visible UV spectrometry.
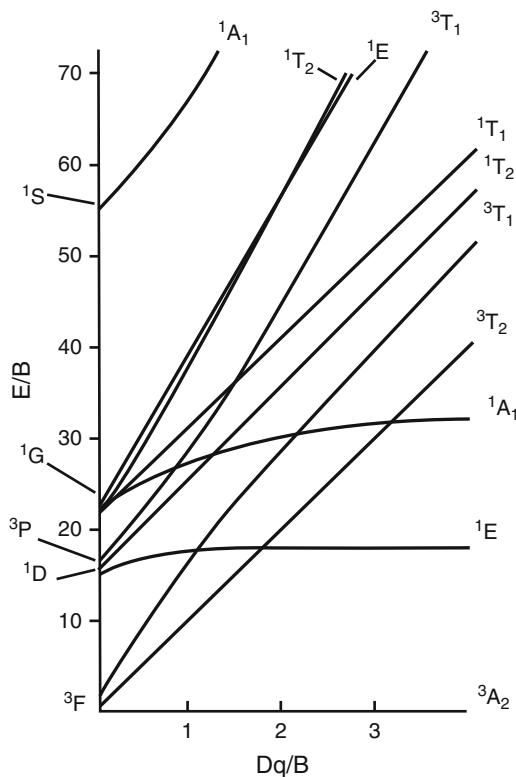
10.5   Diffuse Reflectance Spectroscopy (DRS) in the Visible UV Region

The optic characterization technique for the absorption of radiation in the ultraviolet (190–380 nm) and visible (380–800 nm) regions is widely used to characterize catalysts, where absorption of light is directly related to the change in the energetic state of the valence electrons that are promoted in their fundamental state and more elevated energy states. Since absorption of radiation results in excitation of the electrons that participate in the chemical bond, the λ wavelengths of the absorption peaks may be related to the types of bonds of the species being studied. Furthermore, transitions related to the metallic centers that involve metals of the first and second transition series (they possess electrons in partially occupied d orbitals) occur in the visible range and are called d–d transitions. These metals are part of the composition of several catalysts, and therefore, knowledge of the oxidation states and coordination geometry is extremely important in order to understand the properties and performance of a catalyst.

The effects of alterations in the energies of the d orbitals of the metal by the atoms bound to it may be predicted and offer information that helps explain the *UV* and *visible* spectra. The crystalline field theory is used for this purpose and evaluates the loss of degeneration of energy levels of the d orbitals of the metal when this combines with a ligand. This generates an energy deployment, forming new orbitals (t_{2g} and e_g) for the octahedral crystal field, and the energy difference between these orbitals corresponds to the energy to execute the electronic transition between the sets of orbitals [18].

It is important to remark that the distribution of electrons in an orbital may occur in different ways, where the electron occupies a specific orbital d called a microstate, whose energies vary according to distribution. Thus, depending on the number of electrons, several configurations are generated (t_{2g} and e_g), which deploy in function of the applied crystalline field (strong or weak), with its multiplicities. When microstates of the same energy are grouped, spectroscopically distinguishable energy levels called *spectral term* are obtained; these are defined by $(2S+1)_L$

Fig. 10.9 Energy diagram (Tanabe–Sugano) for d^8 ion in an octahedral field (Adapted with permission from Advances in Materials Characterization, Amarendra G. M. H. Manghnani, University Press Series in Metallurgy and Material Science, India, 2009, [19])

(L = total orbital angular momentum quantum number; $(2S + 1)$ = term spin multiplicity) [19].

In a d^2 configuration, for example, the spectral terms will be ^3F, ^3P, ^1G, ^1D, ^1S, and in the same way that the d orbitals deploy in function of the field, so too do the spectrals. Thus, we have $S \rightarrow A_{1g}$, $P \rightarrow T_{1g}$, $F \rightarrow A_{2g} + T_{1g} + T_{2g}$, and the component terms keep their original spin multiplicity (e.g., $^3F \rightarrow {}^3A_{2g} + {}^3T_{1g} + {}^3T_{2g}$). The diagrams generated (see Fig. 10.9) are called *Tanabe–Sugano diagrams*, which permit the study of transition energies involving the orbitals d.

The possibility of transition occurring is determined by spin selection rules ("transitions between different multiplicity terms are prohibited," e.g., singlet $\rightarrow$ triplet) and the Laporte rule ("transition between terms of the same parity, $\mathbf{g} \rightarrow \mathbf{g}$ and $\mathbf{u} \rightarrow \mathbf{u}$, are prohibited"). It is important to emphasize that a prohibited transition means that the possibility of it occurring was restricted and, therefore, its intensity is reduced.

Accordingly, the compound spectra formed by transition metals in the solid state (polycrystalline) are formed by a set of low-intensity bands, generally broad and situated at wavelengths between 350 and 1000 nm, attributed to transitions d–d.

Bands observed in wavelengths that are smaller than 350 nm are very intense and are related to the permitted transitions, called load transfer (LT) bands. These result

from the load density redistribution process between the metal and its ligand, and it is due to the fact that electrons move from one orbital with the predominant contribution of the ligand to a molecular orbital with the main contribution of the metal. The transfer may be from the ligand → metal (more common, TCLM) or metal → ligand (TCML). The LT bands are permitted by the selection rule and the Laporte rule; thus they are intense.
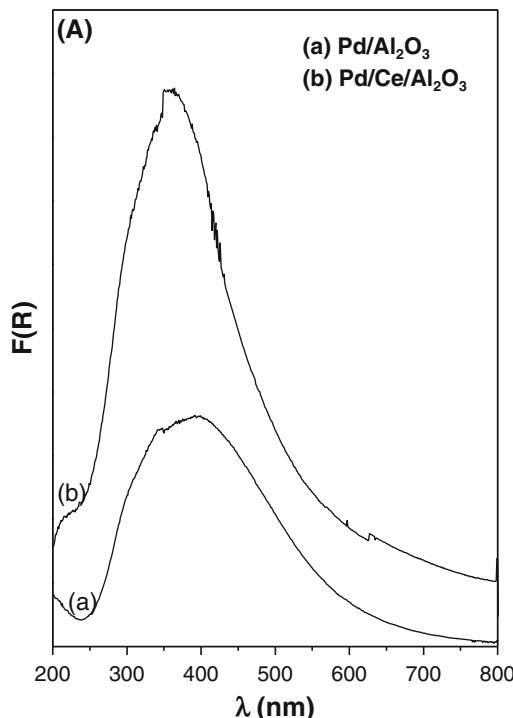
Quantitative measurements are based on Lambert–Beer Law, related to total absorbance of light where the wavelength depends on the absorption coefficient. Standard absorption coefficients are generally used to quantify them.

The information regarding the characteristics of semiconductors is striking, indicating the corresponding free bands and excitation spectra [19].

The solid samples generate many disturbances in the absorption spectra, due to the scattering of light, and for studies of these types of samples, a spectrophotometer containing a Praying Mantis diffuse reflectance accessory is used. The spectral range varies from 190 nm to 800 nm, with a speed of 1800 nm min^{-1}. The sample may or may not be pretreated, depending on the material. In the case of samples containing cerium, pretreatment is necessary. With this analysis, the intention is to determine the valence of metals and to qualitatively analyze dispersion over the support.

The absorption spectrum of the fresh **Pd/Al$_2$O$_3$** catalysts after reactional cycles are presented in Fig. 10.10. The Schuster–Kubelka–Munk (SKM) function,

Fig. 10.10 Diffuse reflectance spectra (UV–vis) in Pd/Al$_2$O$_3$ and Pd/Ce/Al$_2$O$_3$ catalysts [8, 23]

expressed by Eq. (10.10), is used to present all the spectra, rather than apparent absorbance, where R_∞ is the reflectance defined at $1/(10^{absorbance})$ [20, 21]:

$$F(R_\infty) = \frac{(1 - R_\infty)^2}{2R_\infty} \qquad (10.10)$$

All the spectra present $F(R_\infty)$ values that are lower than the unit, indicating the absence of specular reflectance in the samples. γ-Al_2O_3 was used as a reference in all the spectra, thus enabling an evaluation of the chemical state of palladium and cerium.

For the fresh **Pd/Al$_2$O$_3$** catalyst [curve (a)], the spectrum is characteristic of PdO, with a peak centered at 400 nm, attributed to the *d–d* transition of palladium. Furthermore, a small kink is observed at around 290 nm due to metal–ligand load transfer [21–23].

The presence of Pd in its metallic form in conjunction with PdO may be evidenced by a peak centered at 400 nm. This characteristic enables a distinction between the two oxidation states of the catalyst.

The wavelength corresponding to absorption (*UV–vis*) of a semiconductor such as cerium may be used to prove the presence of nanocrystals that may potentially escape detection by DRX. According to Faria et al. [23] and Bensalem et al. [18], pure cerium consists of medium-sized crystals ≥20 nm, with strong absorption in UV at $\lambda = 400$ nm. The absorption bands of CeO_2 are centered at around 350 nm, thus indicating the presence of cerium nanoparticles. Furthermore, a kink is observed at around 280 nm due to the transfer of $Ce^{4+} \rightarrow O^{2-}$ load [24–26], probably superimposed on the palladium *d–d* transition band.

Although the position of the peak is usually the method employed to identify the catalyst spectrum, this measurement is limited by the influence of the vibrational state of each sample, and the energy of the empty band of an insulator or semiconductor is best represented by the absorption edge energy. Thus, Weber [28] suggested an empirical linear correlation comparing the edge energy with the number of adjacent neighbors to the "cluster." The edge energy could be found by the intersection of the straight line $[F(R_\infty) \cdot h_\nu]^2$ vs h_ν with the axis of the abscissae, traced to low values of $[F(R_\infty) \cdot h_\nu]^2$, where $F(R_\infty)$ is the Kubelka–Munk function and h_ν is the energy of the incident photon. Through values pertaining to edge energy, obtained by means of *polyoxo-molybdate* spectra with well-defined structures (Fig. 10.11), Weber [28] observed a reduction in edge energy with an increase in the number of adjacent Mo neighbors.

Caldeira and Schmal [27] also observed a reduction of this energy associated with an increase in size (i.e., with an increase in the number of neighbors) in molybdenum catalysts supported in aluminum oxide, with a layer that corresponds to sizes varying between 0.1 and 6.3 μmol Mo m^{-2}.

According to Fournier et al. [29], with the increase in the size of the Mo cluster in supported catalysts, the bands were broadened and displaced to greater wavelengths. On the other hand, they noted a thinning and displacement of same bands to smaller wavelengths, with an increase in Mo dispersion.
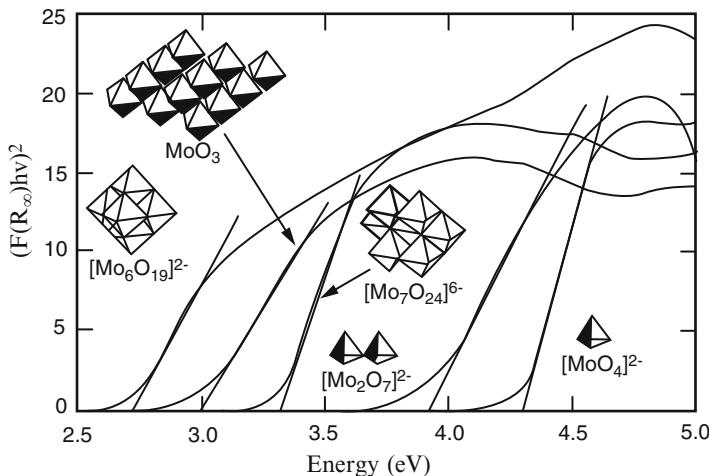
Fig. 10.11 UV absorption edges for standard Mo compounds (Reproduced with permission from Weber, J Catal. 151, (1995) 4100, [28])

Fig. 10.12 Transformation of DRS spectra of the 6.3 µmol Mo m^{-2} catalyst to obtain absorption edge energy [27]
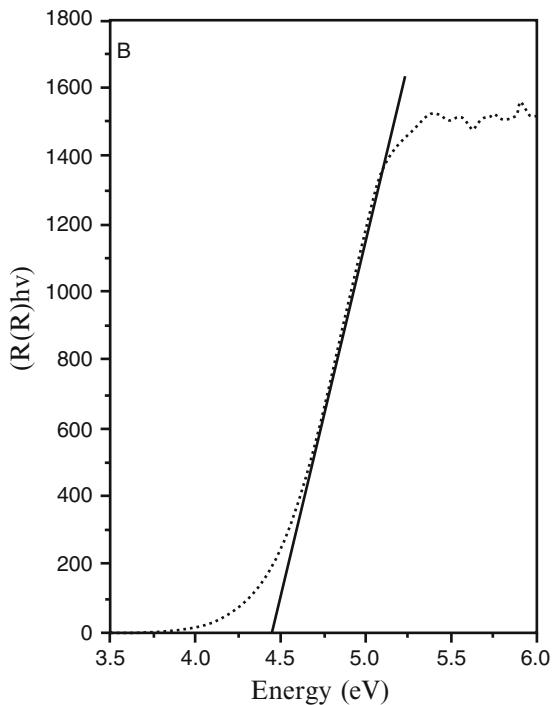
Figure 10.12 shows the UV–DRS spectra of the catalyst containing 6.3 µmol Mo m^{-2}, using the mathematical transformation of DRS curves, proposed by Weber. The spectrum pertaining to the 6.3 µmol Mo m^{-2} catalyst presents a broad band; however it is more intense and seemingly the result of the

composition of the other two, one with maximum intensity of around 210 nm and the other at 240 nm.

Abello et al. [30] and Xiaong et al. [31] attributed the 260–280 nm bands to the electronic absorption of the Mo=O bond of tetrahedral species of molybdate in supported molybdenum catalysts. Fournier et al. [29] showed that the size of the clusters and the distance between them have greater influence in the position of the bands than the local symmetry of Mo. Accordingly, Weber [28] calculated the value of edge energy and, thus, inferred the number of adjacent neighbors to the Mo clusters.

The energy encountered was 4.46 eV. Comparing the values found by Weber for standard Mo compounds (Fig. 10.9), it can be ascertained that the energies are close to that of the anion $[MoO_4]^{2-}$, without neighbors and with tetrahedral coordination, indicating that the catalysts contain Mo clusters with a low agglomeration grade.

With regard to the foregoing, the location and relative high intensity of the bands observed for the catalysts indicate the existence of Mo^{6+} species dispersed in the catalyst. Furthermore, edge energies in the order of 4 eV appeared as additional evidence of the occurrence of thermal scattering of MoO_3 over the surface of aluminum oxide, indicating the presence of disperse species and small Mo clusters, similar to the $[MoO_4]^{2-}$ anion. Additional references on the subject [33–60].

References

1. Ewing GW. Instrumental methods of chemical analysis. New York: McGraw-Hill; 1985.
2. Silverstein RM, Bassler GC, Morril TC. Identificação Espectrométrica de Compostos Orgânicos. Rio de Janeiro: Guanabara-Koogan; 1994.
3. Skoog DA, Holler FJ, Nieman TA. Princípios de Análise Instrumental. São Paulo: Bookman; 2002.
4. Colthup NB, Daly LH, Wiberley SE. Introduction to Infrared and Raman spectroscopy. 2nd ed. New York: Academic Press; 1975.
5. Nakamoto K. Infrared spectra of inorganic and coordination compounds. New York: Wiley; 1963.
6. Ryczkowski J. IR spectroscopy in catalysis. Catal Today. 2001;68:263–381.
7. Miller RGJ, Stace BC. Laboratory methods in infrared spectroscopy. London: Heyden; 1972.
8. Monteiro R, Dieguez LC, Schmal M. The Role of Pd Precursors in the Oxidation of Carbon Monoxide over Pd/Al2O3 and Pd/CeO2/Al2O3 Catalysts. Catal Today. 2001;65:1010.
9. Little LV, Kiselev AV, Lygin VI. Infrared spectra of adsorbed species. New York: Academic Press; 1965.
10. Carvalho MCA, Passos FB, Schmal M. The behavior of Cu/ZSM-5 in the oxide and reduced form in the presence of NO and methanol. Appl Catal A. 2000;193:265.
11. Blyholder G. J Phys Chem. 1964;68:210102.
12. Pompeo F, Nichio NN, Souza MMVM, Cesar DV, Ferretti OA, Schmal M. Study of Ni and Pt Catalysts Supported on a-Al2O3 and ZrO2 Applied in Methane Reforming with CO2. Appl Catal A. 2007;316:1105.
13. Múnera JF, Irusta S, Cornaglia LM, Lombardo EA, Cesar DV, Schmal M. Kinetics and reaction pathway of the CO2 reforming of methane on Rh supported on lanthanum-based solid. J Catal. 2007;245:25.

14. Faria RMB, Cesar DV, Salim VMM. Surface reactivity of zinc-modified hydroxyapatite. Catal Today. 2008;133–135:168.
15. Demoulin O, Navez M, Ruiz P. Investigation of the behaviour of a Pd/γ-Al₂O₃ catalyst during methane combustion reaction using in situ DRIFT spectroscopy. Appl Catal A. 2005;295:59.
16. Faria WLS, Perez CAC, César DV, Dieguez LC, Schmal M. In situ characterizations of Pd/Al2O3 and Pd/CeO2/Al2O3 catalysts for oxidative steam reforming of propane. Appl Catal B. 2009;92:2110–224.
17. Pielaszek JJ, Kepinski L, Kazachkin DV, Kovalchuk VI, d' Itri JL. Characterization and catalytic activity of differently pretreated Pd/Al₂O₃ catalysts: the role of acid sites and of palladium–alumina interactions. J Catal. 2004;227:11.
18. Bensalem A, Bozon-Verduraz F, Delamar M, Bugli G. Preparation and characterization of highly dispersed silica-supported ceria. Appl Catal A. 1995;121:81.
19. Amarendra G, Baldeve Raj, Manghnani MH. Advances in materials characterization, University Press Series in Metallurgy and Material Science. Hyderabad: Universities Press; 2009.
20. Appel LG, Eon JG, Schmal M. The CO2-CeO2 interaction and its role in the CeO2 reactivity. Catal Lett. 1998;56:199.
21. Gaspar AB, Dieguez LC. Dispersion stability and methylcyclopentane hydrogenolysis in Pd/Al2O3 catalysts. Appl Catal A. 2000;201:241.
22. Mishra BG, Rao GR, Mishra BG, Rao GR. Promoting effect of ceria on the physicochemical and catalytic properties of CeO₂–ZnO composite oxide catalysts. J Mol Catal A. 2006;243:204.
23. Faria WLS, Dieguez LC, Schmal M. Autothermal reforming of propane for hydrogen production over Pd/CeO2/Al2O3 catalysts. Appl Catal B Environ. 2008;85:1010.
24. Martinez-Arıas A, Fernandez-Garcia M, Salamanca LN, Valenzuela RX, Conesa JC, Soria J. Structural and redox properties of ceria in alumina-supported ceria catalyst supports. J Phys Chem B. 2000;104:4038.
25. Rakai A, Tessier D, Bozon-Verduraz F. New J Chem. 1992;16:869.
26. Zaki MI, Hussein GAM, Mansour SAA, Ismail HM, Mekhemer GAH. Colloids Surfaces A. 1997;127(1):47–56.
27. Leocadio ICL, Braun S, Schmal M. Diesel soot combustion on Mo/Al2O3 and V/Al2O3 catalysts. Investigation of the active catalytic species. J Catal. 2004;223(1):114.
28. Weber RS. Diesel soot combustion on Mo/Al2O3 and V/Al2O3 catalysts. Investigation of the active catalytic species. J Catal. 1995;151:470.
29. Fournier M, Louis C, Che M, Chaquin P, Masure D. Polyoxometallates as models for oxide catalysts: Part I. An UV-visible reflectance study of polyoxomolybdates: Influence of polyhedra arrangement on the electronic transitions and comparison with supported molybdenum catalysts. J Catal. 1989;119:400.
30. Abello MC, Gomez MF, Ferretti O. Mo/γ-Al2O3 catalysts for the oxidative dehydrogenation of propane.: Effect of Mo loading. Appl Catal A. 2001;207:421.
31. Xiong G, Li C, Feng Z, Ying P, Xin Q, Liu J. Surface Coordination Structure of Molybdate with Extremely Low Loading on γ-Alumina Characterized by UV Resonance Raman Spectroscopy. J Catal. 1999;186:234.
32. Hiselev AV, Lygin VI. Infrared spectra of surface compounds. New York: Wiley; 1975.
33. Baidya T, Marimuthu A, Hegde MS, Ravishankar N, Madras G, 2007, "Higher catalytic activity of nano-Ce1-x-yTixPdyO2-δ compared to nano-Ce1-xPdxO2-δ for CO oxidation and N2O and NOreduction by CO: role of oxide ion vacancy", The Journal of Physical Chemistry C, v. 111, pp.830-839.
34. Bensalem A., Bozon-Verduraz F., Delamar M., Bugli G., "Preparation and characterization of highly dispersed silica-supported ceria", Applied Catalysis A v. 121, pp. 81-93, 1995.
35. Bensalem A., Muller J.C., Bozon-Verduraz F., "From bulk to supported cerium-oxygen clusters: A diffuse reflectance approach", J. Chem. Soc. Faraday Trans. v. 88, pp. 153-154, 1992.

36. Craciun R., Shereck B., Gorte R.J., "Kinetic studies of methane steam reforming on ceria supported Pd", Catalysis Letters v. 51, pp. 149-153, 1998.
37. Demoulin O. Navez M., Ruiz P., "Investigation of the behaviour of a Pd/g-Al2O3 catalyst during methane combustion reaction using in situ DRIFT spectroscopy", Applied Catalysis A, v. 295, pp. 59-70, 2005.
38. Fanson, PT., Hortin, M. R., Delgass, W. N., Lauterbach, J., 2003, "FTIR analysis of storage behavior and sulfur tolerance in barium-based NOx storage and reduction (NSR) catalysts", Applied Catalysis B, v. 46, pp. 393–413.
39. Faria WLS, Perez CAC, Cesar, DV, Dieguez LC, Schmal M, In situ characterizations of Pd/Al2O3 and Pd/CeO2/Al2O3 catalysts for oxidative steam reforming of propane, Applied Catalysis B: Environmental 92 (2009) 217–224.
40. Guglielminotti, E, Boccuzzi, F., 1996, "Study of the NOχ reaction with reducing gases on Fe/ZrO2 catalyst", Applied Catalysis B, v. 8, pp. 375-390.
41. Guimarães A.L., Dieguez L.C., Schmal M., "The effect of precursor salts on surface state of Pd/Al2O3 and Pd/CeO2/Al2O3 catalysts", Annals of the Brazilian Academy of Sciences v. 76, pp. 825-832, 2004.
42. Hadjivanov, KI, 2000, "Identification of neutral and charged NxOy surface species by ir spectroscopy", Catalysis Reviews, v. 42, pp. 71–144.
43. Hadjivanov, KI, 2000, "Use of overtones and combination modes for the identification of surface NOx anionic species by IR spectroscopy", Catalysis Letters, v. 68, pp. 157-161.
44. Kantcheva, M, Ciftlikli, E Z, 2002, "FTIR Spectroscopic Characterization of NOx Species Adsorbed on ZrO2 and ZrO2−SO4 2-" Journal of Physical Chemistry B, v. 106, pp. 3941-3949.
45. Little L.H., Infrared of adsorbed species, New York, Academic Press, 1966.
46. Liu , L J, Cao , Y, Sun , W J, Yao , Z J, Liu , B, Gao , F, Dong L, 2011, "Morphology and nanosize effects of ceria from different precursors on the activity for NO reduction", Catalysis Today, v. 175, pp. 48-54.
47. Lyubovsky M., Pfefferle L., "Complete methane oxidation over Pd catalyst supported on a-alumina. Influence of temperature and oxygen pressure on the catalyst activity", Catalysis Today v. 47, pp. 29-44, 1999.
48. Mello LF, Noronha FB, Schmal M, NO reduction with acetaldehyde on alumina-supported Pd–Mo catalysts, Journal of Catalysis 242 (2006) 48–57.
49. Mello, L. F. de, Baldanza, M. A. S., Noronha, F. B., Schmal M, "NO reduction with ethanol on MoO3/Al2O3 and CeO2-ZrO2-supported Pd catalysts", Catal. Today v. 85, pp. 3-12, 2003.
50. Mello, LF, Noronha, FB, Schmal, M, 2003, "NO reduction with ethanol on Pd–Mo/Al2O3 catalysts", Journal of Catalysis, v. 220, pp. 358-371.
51. Nova, I, Castoldi, L, Prinetto, F, Dal Santo, V, Lietti, L,Tronconi, E, Forzatti, P, Ghiotti, G, Psaro, R, Recchia, S, 2004, "NOx adsorption study over Pt–Ba/alumina catalysts: FT-IR and reactivity study", Topics in Catalysis, v. 30-31, pp. 181-186.
52. Roseno, KTC, Baldanza, MAS, Cesar, DV, Schmal, M, 2009, "NOx reduction by ethanol on Pd/Sulphated Zirconia", Catalysis Letters, v. 129, pp. 85-92.
53. Schmal M., Souza M.M.V.M., Alegre V.V., Silva M.A.P., César D.V., Perez C.A.C., " Methane oxidation – effect of support, precursor and pretreatment conditions – in situ reaction XPS and DRIFT", Catalysis Today v. 118, pp. 392-401, 2006.
54. Seldmair, C, Seshan, K, Jentys, A, Lercher, J A, 2003, "Elementary steps of NOx adsorption and surface reaction on a commercial storage-reduction catalyst", Journal of Catalysis, v. 214, n.2, pp. 308-316.
55. Shen, Q, Lu, G, Du, C, Yankin UG, 2013, "Role and reduction of NOx in the catalytic Combustion of soot over iron-ceria mixed oxide catalysts", Chemical Engineering Journal, v.218, pp. 164-172.
56. Skotak M. Karpínski Z., Juszczyk W., Rielaszek J., Kepínski L., Kazachkin D.V., Kovalchuk V.I., d'Itri J.L., "Characterization and catalytic activity of different pretreated Pd/Al2O3

catalysts: the role of acid sites and of palladium-alumina interactions", Journal of Catalysis v. 227, pp. 11-25, 2004.

57. Vieira FT, Baldanza MAS, Pinto JC, Schmal M, Use of ethanol in the catalytic abatement of NOx, Applied Catalysis A: General 403 (2011) 192– 198.

58. Wang, X., Spivey, JJ., Lamb, HH, 2005, "NO decomposition over a Pd/MgO catalyst prepared from [Pd(acac)2]", Applied Catalysis B, v. 56, pp. 261-268.

59. Yao, X, Tang, C, Ji, Z, Dai Y, Cao Y, Gao F,Dong, L, 2013, "Investigation of the physico-chemical properties and catalytic activities of Ce0,67M0,33O2 (M=Zr4+, Ti4+, Sn4+) solid solutions for NO removal by CO", Catalysis Science & Technology , v. 3, pp. 688-698.

60. Zhang J.H., Yang Y.Q., Shen J.M., Wang J.A., "Mesostructured CeO2 and Pd/CeO2 nanophases: Template synthesis, crystalline structure and catalytic properties", Journal of Molecular Catalysis A v. 237, pp. 182-190, 2005.

Chapter 11
X-Ray Photoelectron Spectroscopy
(ESCA: XPS/ISS)

Martin Schmal and Carlos André C. Perez

Abstract The photoemission spectroscopy is one of the most important techniques for the study of surfaces and interfaces, enabling you to determine the oxidation state, the dispersion of the phases and the dependence of the atomic concentration with depth. It allows determining the chemical state and several other surface informations.

Keywords Dispersion, oxidation state • ESCA • ISS • Surface

11.1 Introduction

The photoemission spectroscopy is one of the most important techniques for the study of surfaces and interfaces, enabling you to determine the chemical composition, the oxidation state, the dispersion of the phases, and the dependence of the atomic concentration with depth. This information is relevant to areas such as microelectronics, pharmacy, metallurgy, materials, and chemistry. Some examples of applications that rely on this study are biocompatibility of bone implants, drug coating technology of thin films, polymers, construction of nanostructured materials, and the development of new catalysts for the industry and for the environmental area.

Experimentally, by XPS surface analysis involves irradiation on the solid under vacuum with X-ray photons and emitted by electron classification of energy. The sample is prepared in ultrahigh vacuum environment (pressure $<10^{-9}$ Torr) and excited by a beam of X-rays with magnesium or aluminum anode. Since the mean free path of electrons is very small, the detected electrons originate from the outermost atomic layers of the material analyzed, giving superficial sensitivity technique.

This technique is very sensitive when radiation or particles to be detected undergo no more than a few atomic distances through the solid. Low energy electrons or ions are appropriate to investigate a surface. Experimentally, it works with electrons when done under high vacuum (10^{-10} mbar) since otherwise the particles leaving the surface do not reach the detector. These conditions are necessary to obtain significant results in surface characterization of solids and catalysts, which is of fundamental importance, since only the first atomic layers are involved.

The photoelectron spectroscopy for chemical analysis (ESCA, also known as photoelectron spectroscopy XPS) uses the photoelectric effect for information on the chemical composition and the structure of a surface [1–3].

11.2   Concepts

The X-ray photoelectron spectroscopy (XPS) is based on the photoelectron effect: an atom adsorbs a photon with energy h_ν; when a photon source (e.g., X-rays) is directed on a sample, the photons may interact with electrons in the sample. If the photon has enough energy, then an electron is emitted from its orbit with kinetic energy E_c, according to Eq. (11.1) and Fig. 11.1:

$$E_c = h_\nu - E_b \tag{11.1}$$

where E_c is the kinetic energy of the emitted photoelectrons, h_ν is the photon energy, and E_b is the binding energy of the electrons. As the photon energy h_ν is known and the kinetic energy (E_c) is measured in the experiment, the binding energy (E_b) can be calculated, revealing the energy the electron had in its atomic or molecular environment. The scheme of the experiment is shown in Fig. 11.2.

For the photoemission of solids, the term work function should be added to this equation. The original work function is established for each XPS instrument. This term expresses the additional energy required after the ionization process for the electron emitted from the surface, in vacuum. Thus, the electron binding energy is an indicative of the element from where it came and from the chemical environment of the element.

For XPS analysis, the sample is placed in an ultrahigh vacuum environment (UHV), typically less than 10^{-9} Torr. The sample is then irradiated with low-energy X-rays. The radiation causes the emission of atomic layers of photoelectrons of the elements present in the sample. These electrons have a characteristic energy of the

Fig. 11.1 Photoelectronic scheme: atom absorbs X-ray photon with energy and emits a photoelectron with kinetic energy $E_c = h_\nu - E_b$
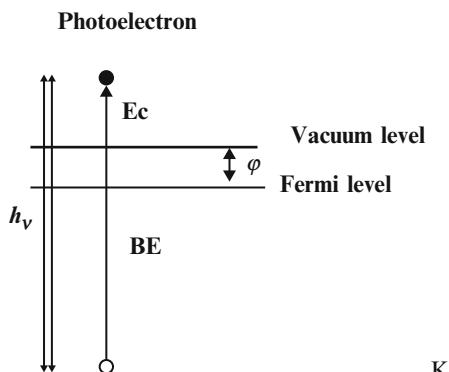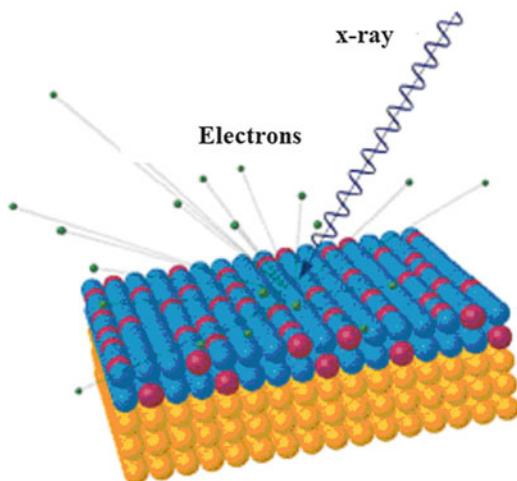
element and molecular orbitals from which they are issued. Counting the number of electrons detected at each energy value generated a spectrum of peaks corresponding to the elements on the surface. The area under the peaks is a measure of the relative amount of each element present as the shape and position of the peaks reflect the chemical environment of each element.

Routinely, one uses the X-ray sources Mg Kα type ($h_\nu = 1253.6\,\text{eV}$) and Al Kα ($h_\nu = 1486.3\,\text{eV}$). One measures the intensity of the photoelectrons $N(E)$ as function of E_c. The XPS spectrum is given by $N(E)$ vs. E_c or more often by the binding energy E_b, usually named BE. Remind that usually the photoelectrons have kinetic energy ranging from 0.2 to 1.5 keV and reach the outer layer of the surface.

XPS analysis is sensitive at the surface because only the electrons can leave the surface without losing a considerable amount of energy and reach the detector. An electron emitted in the deeper layers of a solid must cross higher path and will inevitably lose their energy. The amount that determines the ability of an electron crossing the solid without losing its energy is called inelastic mean free path (IMFP), as shown in Fig. 11.3.

Electrons can emerge from the solid without losing energy, called elastically scattered electrons, as well as lose some of its initial energy. In this latter case, it is called inelastic scattered electrons, which contribute to the "background" of the XPS spectrum.

The mean free path of electrons on the surface of a solid depends on the kinetic energy. Optimal surface sensitivity is obtained for the electrons with kinetic energy between 250 eV and 50, where 50 % of the electrons come from the outermost surface layer [4].

XPS spectra were obtained on a Perkin Elmer 1257 spectrometer using Mg Kα ($h_\nu = 1253.6$ eV) ($h_\nu = 1253.6$ eV) radiation as the excitation source with the tube operating at 15 kV/200 W. The kinetic energy of the photoelectrons was measured
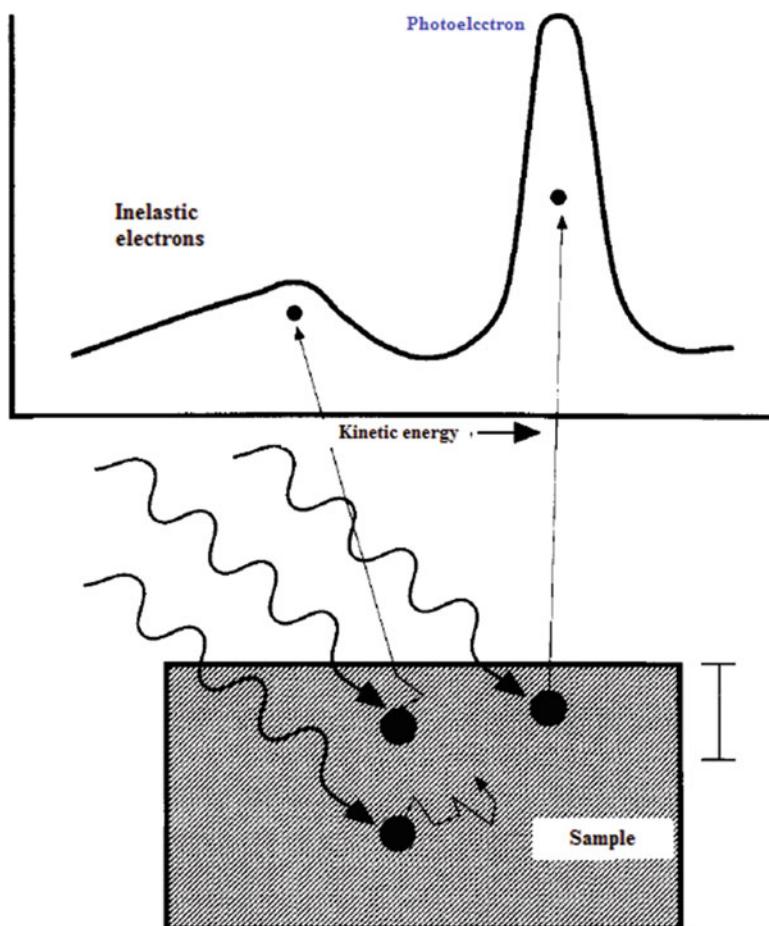
Fig. 11.3 Mean free path of electrons

in a hemispheric analyzer, with energy pass of 46.95 eV/step. The vacuum chamber was about 10^{-9} Torr, and the correction was obtained using as reference the C 1s line at 284.6 eV.

Surface composition are analyzed by X-ray photoelectron spectroscopy (XPS) using a SPECS electron spectrometer with a PHOIBOS hemisphere analyzer. All results presented here correspond to the use of Al K alfa radiation. Pass energy (Epass) of 50 eV was used to obtain the wide-scan spectra, while 15 or 25 eV (depending on signal intensity) was used for the high-resolution (HR) spectrum of Au 4f. The full width at half maximum (FWHM) in the HR spectra was about 1.0–1.5 eV (Epass: 15–25). Each spectrum was calibrated by using C 1s signal with a FWHM of (2.9278 ± 0.001) eV and peak position of (284.64 ± 0.04) eV. Au 4f envelopes were analyzed and peak fitted after subtraction of a Shirley background using a Gaussian–Lorentzian peak shape obtained from the CasaXps software package.

11.3   Surface Chemical Composition

As an example, we present the surface structure of the sample perovskite $LaCoO_3$ catalyst [5] to identify the presence of chemical species, in particular, the oxidation state and the relative concentration of the elements at the surface, measuring the kinetic energy of the electrons emitted by the sample when excited by photoelectron X-ray.

The XPS spectra (Fig. 11.4) are referred to the internal levels of La3d, Co2p, and O1s. The $LaCoO_3$ displays one peak for Co $2p_{3/2}$ centered at 781.39 eV, which is assigned to Co^{3+}. Lanthanum for $4d_{5/2}$ is centered at 104.59 eV, which according to Hueso et al. [6] belongs to the lattice of the perovskite structure.
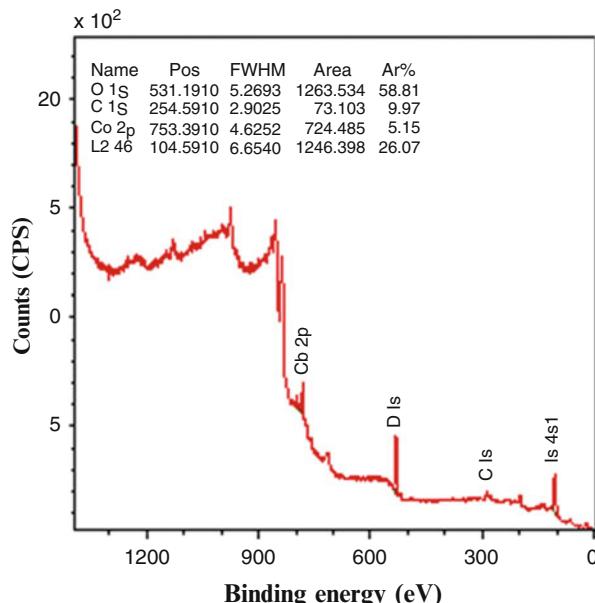
The O 1s signal of the substituted perovskite is displayed in the spectra of Fig. 11.5. The La95Ce5 shows a binding energy centered at 528.34 eV which is assigned to oxygen species belonging to the perovskite lattice, and another band at 530.38 eV attributed to segregated oxides type, according to Hueso et al. [6].

Data relative to the O 1s indicate one peak at 531.19 eV, which is assigned to the oxygen of hydroxide or carbonate species [5]. These carbonate ion structures are present at the surface due to the carbonation of the La^{3+}cations [6].

Schmal et al. [5] analyzed results of perovskite under different treatments and showed that the binding energy of the different oxygen species on the surface is associated species such as oxygen in the perovskite lattice, segregated oxides, and carbonates and oxygen below state coordination.

The quantification of surface species, taking into account the area of each peak of the components and sensitivity factors of each chemical species, is presented in

Fig. 11.4 XPS spectrum of $LaCoO_3$perovskite

Name	Pos	FWHM	Area	Ar%
O 1S	531.1910	5.2693	1263.534	58.81
C 1S	254.5910	2.9025	73.103	9.97
Co 2p	753.3910	4.6252	724.485	5.15
L2 46	104.5910	6.6540	1246.398	26.07

Name	Pos.	FWHM	L.Sh.	Area	%Area
O1s1	528.3382	2.4948	GL(30)	2242.147	44.03
O1s2	530.3846	3.9048	GL(30)	2853.880	55.97
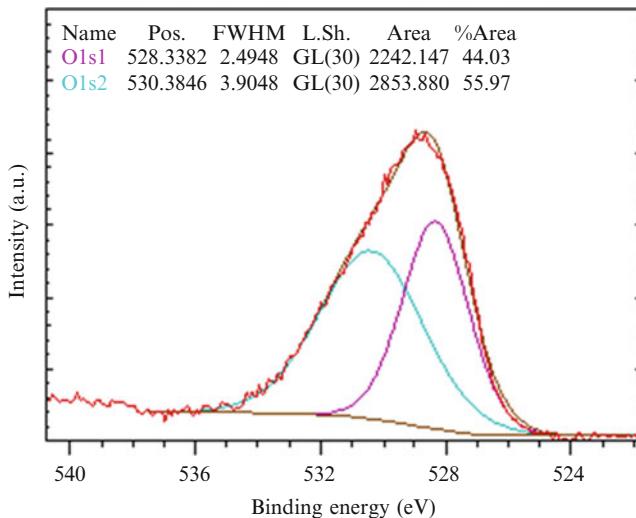
Fig. 11.5 XPS oxygen spectrum of $LaCoO_3$perovskite

Table 11.1 Surface composition of the substituted perovskites promoted by Ce [5].

Sample	La	Co	Ce	C	O	$\dfrac{La}{Co}$	$\dfrac{Co}{S^*}$	$\dfrac{Co}{Co + S^* + La}$
La95Ce5	22.50	7.27	1.12	14.36	54.73	3.09	20.00	0.23

S^* = substituent (Ce)

Table 11.1 for the modified perovskites. The results indicate that the surface of the synthesized perovskite is quite enriched with lanthanum and the La/Co ratio differs substantially from the bulk. The promoted isostructural substitutions did not change the surface composition relative to the cobalt, independent of the substituent.

11.4   Oxidation State

The binding energies BE are not specific only for the elemental analyses, but allows determining the chemical state and several other surface informations. The electron energy levels in the layer depend on the chemical state of the atom. There are shifts that can vary between 0 and 3 eV, which correspond to different metallic or oxidation states. In general, the binding energy increases with increasing oxidation state. The binding energy by XPS measurements is not necessarily equal to the orbital energies emitted by the photoelectrons. The difference is caused by the reorganization of the remaining electrons when an electron is removed from an inner layer. The binding energy of the photoelectron contains information about the
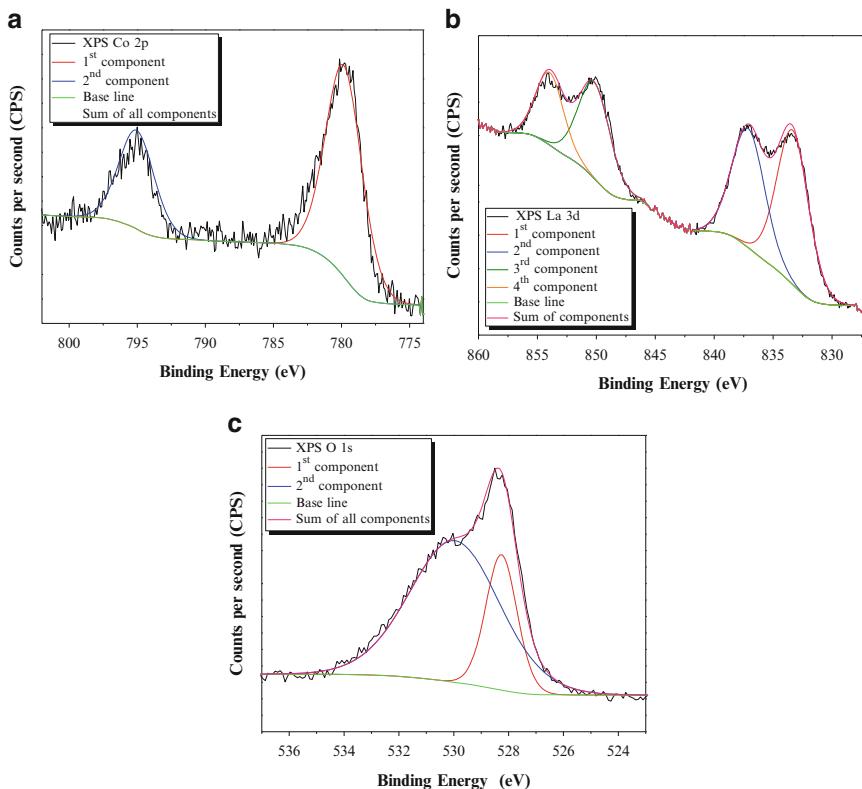
Fig. 11.6 XPS spectra of the powdered LaCoO$_3$perovskite: (**a**) Co 2p, (**b**) La 3d, and (**c**) O 1s (Schmal et al., Top Catal (2014) 57:1103–1111) [5].

initial atomic state and after the emission of an electron, i.e., final state. Thus, it is correct to interpret the spectra shifts related to the initial state.

The surface composition was determined on the perovskite-type sample. Figure 11.6 displays the Co 2p, La 3d, and O 1s spectra.

As shown, the Co 2p spectrum (a) exhibits two peaks, identified at BE 779.82 and 795.04 eV, which are associated to the doublet 2p$_{3/2}$ and 2p$_{1/2}$, respectively. The energy difference of the doublet is 15.22 eV, in agreement with the literature [6], which is assigned to the LaCoO$_3$ mixed oxide.

The satellite peak around 790 eV assigned to the Co^{+2} species was not detected at the surface, which indicates that this method was efficient to diffuse cobalt ions in the La$_2$O$_3$ structure for the formation of the LaCoO$_3$ perovskite [7].

The spectrum of La 3d is displayed in Fig. 11.6b and shows two peaks associated to the doublet La 3d$_{5/2}$ and La 3d$_{3/2}$ at BE 832.98 and 850.08 eV, respectively.

The O 1s spectrum showed on peak at 528.5 eV (Fig. 11.6c), revealing the existence of two contributions. The first one centered at 528.26 eV is assigned to the oxygen in lattice, and the other one at 529.96 eV is attributed to the adsorption of oxygen species as hydroxyls or carbonate.

Table 11.2 Surface chemical composition of the LaCoO$_3$perovskite obtained by XPS [7]

Element	Component spin–orbit	Binding energy (eV)	Area (CPS.eV)	FWHM (eV)	Surface composition (molar %)
C	1s	284.64	332.3	2.17	22.08
O	1s	528.5	2413.0	3.53	54.72
Co	2p$_{3/2}$	779.82	1476.5	3.15	
Co	2p$_{1/2}$	795.04	667.8	3.05	15.76
La	3d$_{5/2}$	832.98	7168.2	6.70	
La	3d$_{3/2}$	850.08	4127.6	6.37	7.44

The surface composition of the LaCoO$_3$ perovskite is presented in Table 11.2.

The Co/La ratio was 0.47, lower than the stoichiometric value (1.0) for the LaCoO$_3$ structure, probably due to the segregation of La^{+3} ions at the surface and the formation of La(OH)$_3$.

11.5 ISS Spectra

Although the XPS technique is important for determining the composition and oxidation states, also is for the metal dispersion of supported catalysts. Indeed, the ISS and XPS techniques have been used in order to obtain a better measure of the distribution of an oxide or metallic phase onto a porous structure support and so also determine the degree of coverage.

As example, ZrO$_2$/Al$_2$O$_3$ samples were prepared with different ZrO$_2$ contents [1, 5, 10, and 20 % (W)] onto alumina support. On these samples 1 % Pt was impregnated and submitted for XPS and ISS analyses [8].

The relative intensities of IAl/ IZr, determined by XPS and ISS, are displayed in Fig. 11.7, as function of the atomic bulk ratio Zr/Al. The intensity ratio of IAl/IZr increased linearly with increasing concentration of zirconia on the alumina surface up to 10 % (weight) and then decreases due to nucleation of zirconia crystallites. That suggests the formation of a zirconia monolayer on the alumina surface for concentrations between 10 and 20 % of zirconia.

ISS and XPS results show the formation of monolayer of zirconia on alumina for ZrO$_2$ content between 10 and 20 % ZrO$_2$. That is, the maximum surface concentration of zirconia on the alumina is not related to how the zirconia is impregnated, but of formation of crystals which is strongly dependent on the preparation method.

The binding energy of Zr 3d$_{5/2}$ in pure zirconia (182.4 eV) is consistent with the bond energy values of the zirconia Zr^{4+} reported in the literature [9–12]. The small decrease in the binding energy with increasing ZrO$_2$ coverage must be related to the change in the coordination of zirconia, due to the interaction of zirconium atom with alumina through the Zr–O–Al bonds.
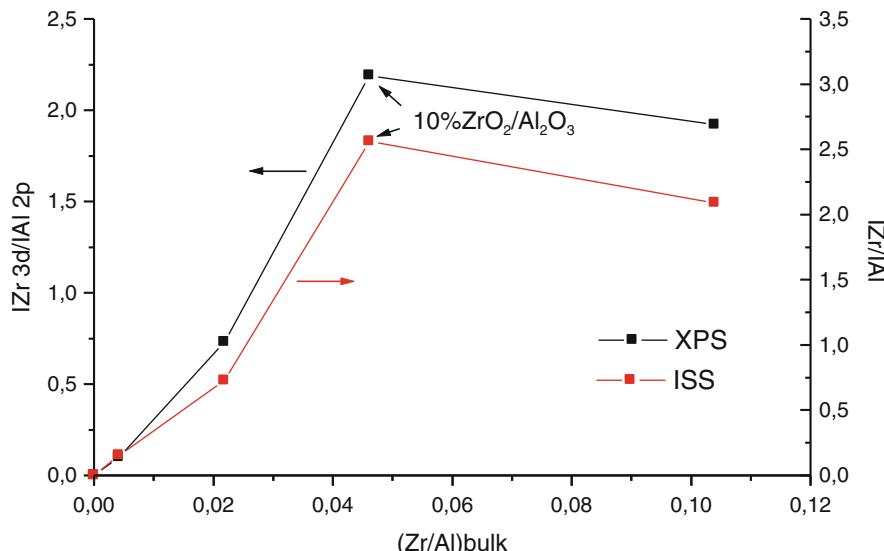
Fig. 11.7   XPS and ISS intensity ratios of Zr and Al on the ZrO_2/Al_2O_3 sample (Souza, D.A. et al., J. of Catal., 204, 2 (2001) 498)

11.6   Surface Analyses XPS "In Situ"

The science of catalysis and surface science have developed over the years in friendly contact, though to a large extent independently [13]. There are, however, examples where key information for our understanding of catalytic processes has been gained from studies in surface science, one example being ammonia synthesis (Schlögl 2008) [14]. Thus, is there anything fundamental to be discovered through this interplay between catalysis and surface science?

The answer is YES, the field is wide open, and there are many fundamental questions to be answered.

They may be grouped into those connected with understanding the complex materials active as catalysts and those connected with operating conditions.

Complexity often does not only lead to qualitative changes but to new phenomena that do not occur in simpler systems, and they need to be understood to be able to describe catalytic phenomena reliably.

Considerable progress has been made in model catalysts of planar well-ordered extended surfaces, but under UHV conditions. Atomic structure and electronic properties of many metal surfaces or metal oxide-supported materials are now accessible, related to the physical and chemical properties of adsorbate species on surfaces, in particular binding sites. However, there are several problems related to the application of models with real catalysts, such as metal–support interactions and
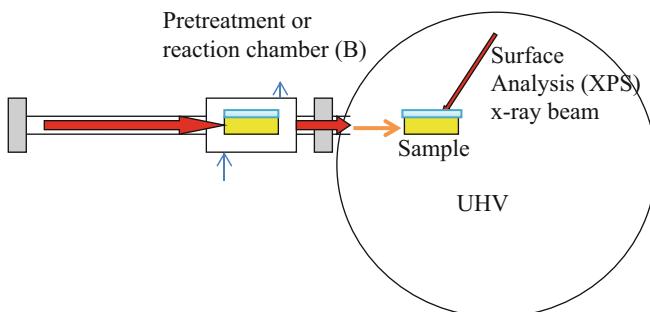
Fig. 11.8 Scheme of experiment: pre-chamber (heating and gas flow) + UHV

particle size effects, which are not clearly settled. These effects influence the reactivity and selectivity of the catalyst. There are three different cases:

- Metal single crystals—surface area of 1 cm^2
- Metal clusters on planar oxide supports—surface area of 0.1 cm^2
- Metal supported on oxides (real catalyst)—surface area of 100 m^2/g.

The bridge gap between single crystal models and real supported catalyst is still not resolved. In modeling, the interested metal is deposited by vapor deposition, controlled, and then analyzed under UHV related to questions about structure, sizes, and coverage or bindings. The pressure gap has been addressed by using high pressure cells or micro-reactors into high vacuum equipments. This later case is suitable for XPS surface analysis.

The photoelectron X-ray spectra of the catalysts are obtained using a spectrometer with radiation X-ray tubes. The samples are subjected to a primary vacuum for 1 h at room temperature and subsequently be introduced in the ultravacuum analysis chamber on the order of 10^{-9} Torr. To this end, we use a step of 0.2 eV with a scan time of 100 ms per step and a total of 10, 100, 50, 30, and 10 scans for the selected elements.

As shown in Fig. 11.8, the powder is placed in sample holder in a pre-chamber and pretreated under normal pressure, or under reactant gases, and at high temperature, evacuated, and then transferred in the UHV chamber for surface analysis.

To identify the *oxidation and metallic state* during the reaction, the catalysts of the catalytic tests can be analyzed by XPS. The intensity measurements are used to evaluate the structure of the surface metals or oxides and the dispersion. One can calculate the surface atomic ratios of the elements [13].

11.6.1   *XPS Spectra of Calcined and Reduced Catalyst*

The XPS spectra of Pd 3d5/2 for the calcined and reduced catalysts are displayed in Fig. 11.9 [15]. The binding energy of the catalyst calcined and reduced Pd/Al$_2$O$_3$ are 336.8 and 335.4 eV, respectively, attributed to PdO and metallic Pd^0. The peaks

Pd 3d Calcined
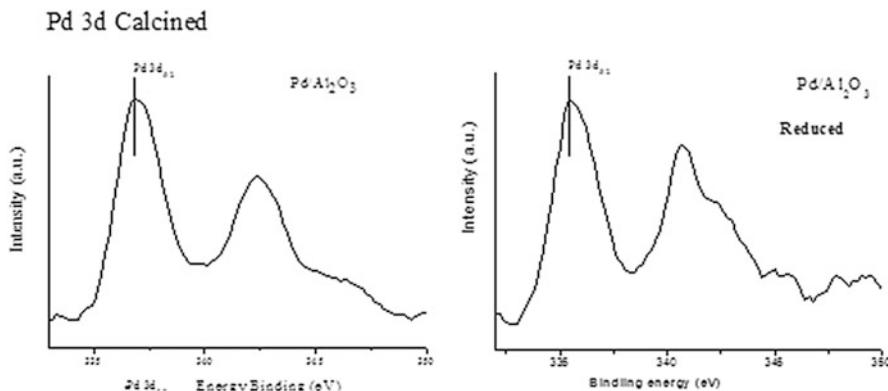
Fig. 11.9 Spectra of Pd after calcination and reduction (Franchini et al. Catal Lett (2010) 137:45–54)

relative to the binding energy of Pd $3d_{5/2}$ are symmetric and correspond to metallic Pd^0 [15]. All the palladium oxide at surface was reduced to metal. The Pd/Al ratios for the calcined and reduced samples were 1.1×10^{-3} and 0.58×10^{-3}, respectively.

The theoretical Pd/Al ratio calculated for Pd/Al$_2$O$_3$ catalyst is 5×10^{-3}. When compared to the total amount of Palladium, it shows that 22 % lays at the surface and 52.7 % was reduced. After reduction, the decrease of Pd/Al values is associated to sintering under hydrogen atmosphere [12].

11.6.2 XPS In Situ Reaction: Methane Oxidation

We observed during the stability test of the Pd/Al$_2$O$_3$ and Pd/ZrO$_2$ catalysts for the total oxidation of methane a significant induction period. The activity of the Pd/ZrO$_2$ increased suddenly 10 times after 3 h and then remained constant for 25 h. Unlikely was the behavior of the Pd/Al$_2$O$_3$, as shown in Fig. 11.10 [16].

The question is why? These results suggested searching for an explanation of the surface properties and the effects of the metal–support interaction, the affecting of the induction periods, and stability of the Pd/Zirconia catalysts.

The only way to explain it was to find out possible modifications occurring at the surface, using XPS equipped with a pre-chamber. The reaction was performed in the pre-chamber with $T = 400$ °C and O$_2$/CH$_4 = 2$ and with time on stream. After vacuum it was transferred in the ultrahigh vacuum chamber for analysis. For palladium (Pd 3d), for example, 30–200 scans will be held in order to verify the occurrence of Pd photoreduction by prolonged exposure of the samples to X-rays. For the connection of energy, correction was used as the reference peak C 1s at 284.6 eV. The calculation of the atomic ratio (e.g., Pd/Al, O/Al, and O/Ce) was
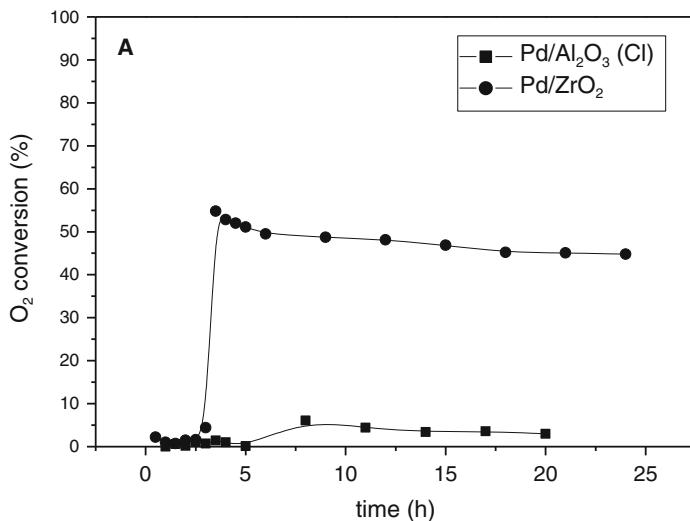
Fig. 11.10 Activity test of methane combustion on Pd/Al_2O_3 and Pd/ZrO_2 catalysts

made by combining the curves and normalized by the number of scans using the sensitivity factors of each element [16].

However, what about the catalyst? A commercial γ-Al_2O_3 from Harshaw (BET area, 200 m^2/g) and ZrO_2 (BET area, 62 m^2/g), obtained by calcination of zirconium nitrate (Aldrich) in air at 550 °C for 2 h, were used as supports. Pd was added from a $PdCl_2$ (Aldrich) precursor by incipient wetness impregnation of the supports. The precursor was dissolved in concentrated HCl to generate tetrachloride palladium acid (H_2PdCl_4), heated to eliminate chlorine, dissolved in distilled water, dried, and again diluted until the final volume. The samples were dried overnight in an oven and then calcined in air at 550 °C for 2 h. Palladium contents were close to 1 wt%.

Figure 11.11a shows the XPS results of Pd/Al_2O_3 without reduction but under reaction conditions. Spectra were taken after 2 and 10 h, without any modification of the surface. However, the Pd/ZrO_2 displayed a visible satellite peak at 337.6 eV only after 10 h exposition, suggesting the formation of PdO_x species, indicating a real modification of palladium at the surface. These results suggest that the oxidation of methane affected strongly the oxidation state PdO at the surface, modifying both the metal oxide and the ZrO_x species at the surface above 10 h reaction. Figure 11.11b shows also the spectra $Zr3p_{1/2}$ and $Zr3p_{5/2}$ after 3 h reaction, without modification compared to the calcined sample.

Table 11.3 presents the binding energy values of $Pd3d_{5/2}$ and $Pd3d_{3/2}$ and the Pd/Al atomic ratios at the surface with time on stream. The bond energy up to 6 h is 336.9 eV, which corresponds to the PdO species at the surface. After 10 h the bonding is shifted to 337.1 eV. The Pd/Al atomic ratios decreased and are half of the initial PdO particles at the surface after 10 h reaction, which suggests agglomeration of the initial PdO particles.
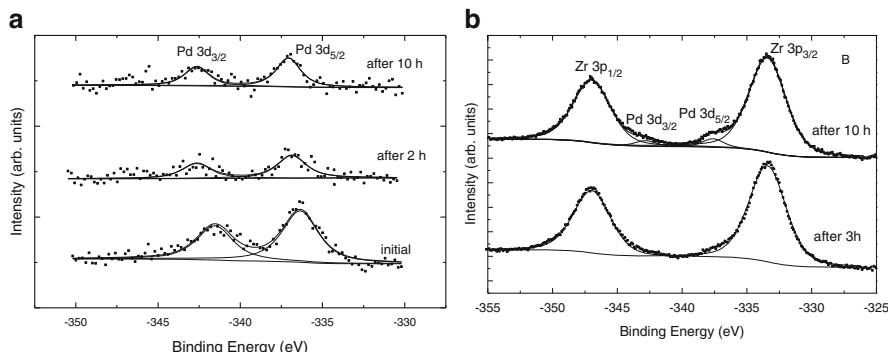
Fig. 11.11 XPS in situ reaction on Pd/Al$_2$O$_3$ (**a**) and Pd/ZrO$_2$ (**b**) catalyst (Schmal et al., Catal. Today 118 (2006) 392) [16].

Table 11.3 Electron binding energies and atomic ratios for Pd/Al$_2$O$_3$ catalyst

Time (h)	Energy (eV)		Area		
	Pd3d$_{5/2}$	Pd3d$_{3/2}$	Al2p	Pd3d	Pd/Al
0	336.3	341.6	1907	243.2	5.6×10^{-3}
2	336.9	342.6	1663	35.3	9.3×10^{-4}
6	336.9	342.6	1448	71.0	2.1×10^{-3}
10	337.1	342.6	1796	95.4	2.3×10^{-3}

Table 11.4 Electron binding energies and atomic ratios for Pd/ZrO$_2$ catalyst

Time (h)	Energy (eV)		Area		
	Pd3d$_{5/2}$	Pd3d$_{3/2}$	Zr3d	Pd3d	Pd/Zr
10	337.6	342.8	9642	534	2.7×10^{-2}

Table 11.4 presents the binding energy Pd/ZrO$_2$ catalyst after 10 h. The binding energies up to 6 h with time on stream (not shown) were absolutely similar to the Pd/Al$_2$O$_3$ catalyst. However, suddenly after 10 h reaction, the binding energy of Pd3d$_{5/2}$ increased to 337.6 eV and according to the literature corresponds to a higher oxidation state of PdO$_x$ or PdO$^{\delta+}$. The Pd/Zr surface atomic ratio is 2.7×10^{-2} and when compared to the Pd/Al$_2$O$_3$ catalyst increased 10 times, indicating a pronounced augment of palladium at the surface with a higher oxidation state of Pd$^{2+\delta}$.

The induction time is approximately 3–5 h, which corroborates with the hypothesis of rearrangement of the PdO in a higher oxidation state and stabilization of this oxidation state at the surface and due to the interaction of PdO$_x$/ZrO$_y$ interface.

11.6.3   ISS: CO Adsorption In Situ

However, it is not possible to verify the reduction of zirconia oxide by XPS. ISS is more sensitive and permits to analyze only the first atomic layer, while the sample depth in XPS is about 4 nm. Figure 11.12 shows the ISS spectra of the PtZr after reduction at 300 and 500 °C and subsequently by CO adsorption [17].
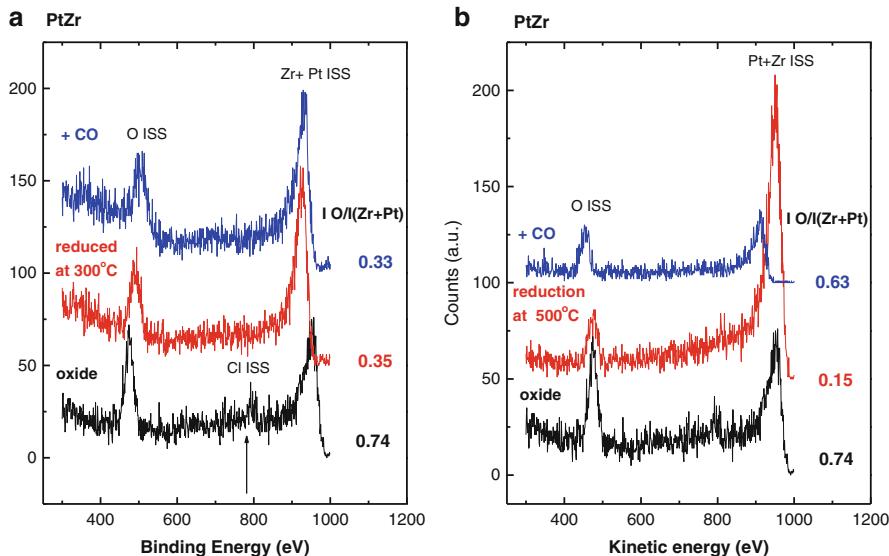
Fig. 11.12 ISS spectra of the PtZr after reduction at 300 and 500 °C and after CO adsorption (Phys. Status Solidi A, vol. 187, n. 1, pp. 297–303) [17].

Note that the peak corresponding to the Pt atoms and Zr basically represents the Zr atoms, since the platinum content is only 1 %. Thus, a lower ratio between the intensities of the peaks of O and Zr + Pt (ratio $I_O/I_{(Pt+Zr)}$) after reduction indicates an increase in Zr^{n+} population at the surface. The decrease is higher after reduction at 500 °C, due to the higher degree of reduction of zirconia at this temperature.

The CO adsorption at room temperature on the reduced sample at 300 °C, (Fig. 11.12a) does not show significant changes, which suggests no interaction of CO with zirconia. However, adsorption of CO on the reduced sample at 500 °C (Fig. 11.12b) indicates that there are exposed zirconium cations on the surface interacting strongly with CO, thus causing a decrease in the intensity of Zr + Pt peak and consequently increasing ratio $I_O/I_{(Pt+Zr)}$) intensity [18–34]. Additional references related to this subject [91–107].

References

1. Wagner C, Riggs W, Davis L, Moulder J, Muilenberg G. Handbook of X-ray photoelectron spectroscopy. Eden Prairie, MN: Perkin Elmer; 1979.
2. Meijers ACQM, de Jong AM, Van Gruijthuijsen LMP, Niemantsverdriet JW. Preparation of zirconium oxide on silica and characterization by X-ray photoelectron spectroscopy, secondary ion mass spectrometry, temperature programmed oxidation and infra-red spectroscopy. Appl Catal. 1991;70:53–71.

3. Morant C, Sanz JM, Galan L, Soriano L, Rueda F. An XPS study of the interaction of oxygen with zirconium. Surf Sci. 1989;218:331–45.

4. Shustorovich E. The bond-order conservation approach to chemisorption and heterogeneous catalysis: applications and implications. Advances in catalysis, Vol. 37. London: Academic Press; 1990. p. 101.

5. Schmal M, Perez CAC, Magalhaes RNSH. Synthesis and characterization of perovskite-type oxides La1-2xMxCoO3 (M= Ce, Sr) for the selective CO oxidation. Top Catal. 2014;57:1103.

6. Hueso JL, Caballero A, Ocana M, Gonzalez-Elipe R. Reactivity of lanthanum substituted cobaltites toward carbon particles. J Catal. 2008;257:334.

7. Natile MM, Ugel E, Maccato C, Glisenti A. LaCoO$_3$: Effect of synthesis conditions on properties and reactivity. Appl Catal B. 2007;72:351.

8. Souza MMVM, Aranda DAG, Schmal M. Reforming of methane with carbon dioxide over Pt/ZrO2/Al2O3 catalysts. J Catal. 2001;204(2):498.

9. Martins RL, Schmal M. Methane activation on superacidic catalysts based on oxoanion modified zirconium oxide. Appl Catal A. 2006;308:143D.

10. Engel T, Ertl G. Elementary steps in the catalytic oxidation of carbon monoxide on platinum metals. Adv Catal. 1979;28:1.

11. Akubuiro EC, Verykios XE, Lesnick L. Dispersion and support effects in carbon monoxide oxidation over platinum. Appl Catal. 1985;14:215.

12. Bitter JH, Seshan K, Lercher JA. The state of zirconia supported platinum catalysts for CO$_2$/CH$_4$ reforming. J Catal. 1997;171:279.

13. Somorjai GA. Introduction to surface chemistry and catalysis. New York: Wiley; 1994.

14. Schlögl R. Handbook of heterogeneous catalysis, 12.1 Ammonia synthesis. London: Wiley.

15. Franchini CA, Cesar DV, Schmal M. The interaction of oxides of the Pd/Ce/Zr/Al2O3 catalysts prepared by impregnation over alumina and promoting effects on surface properties. Catal Lett. 2010;137:45–54.

16. Schmal M, Souza MMVM, Alegre VV, da Silva MAP, Cesar DV, Perez CAC. Methane oxidation – effect of support, precursor and pretreatment conditions – in situ reaction XPS and DRIFT. Catal Today. 2006;118:392.

17. Souza MVM, Schmal M. Surface characterization of zirconia-coated alumina as support for Pt particles. Phys Status Solidi A. 2001;187:297–303.

18. Boschini F, Rulmont A, Cloots R. Colloidal stability of aqueous suspensions of barium zirconate. J Eur Ceram Soc. 2005;25:3195–201.

19. Craciun R, Daniell W, Knözinger H. The effect of CeO$_2$ structure on the activity of supported Pd catalysts used for methane steam reforming. Appl Catal A. 2002;230:153.

20. Damyanova S, Bueno JMC. Effect of CeO$_2$ loading on the surface and catalytic behaviors of CeO$_2$-Al$_2$O$_3$-supported Pt catalysts. Appl Catal A. 2003;253:135.

21. Frydman A, Campbell CT, Castner D, Schmal M. A method for accurate quantitative XPS analysis of multimetallic or multiphase catalysts on support particles. J Catal. 1995;157:133–44.

22. Frydman A, Campbell CT, Castner D, Schmal M. Particle and phase from XPS analysis of supported bimetallic catalysts: calcined Co-Rh/Nb$_2$O$_5$. J Catal. 152:164–78.

23. Guo Q, Liu Y. MnOx modified Co$_3$O$_4$-CeO$_2$ catalysts for the preferential oxidation of CO in H$_2$-rich gases. Appl Catal B. 2008;82:19–26.

24. Holgado JP, Alvarez R, Munuera G. Interplay at copper oxide-(Ce, Zr) Ox interfaces: influence of the presence of NO on the catalytic activity for CO oxidation over CuO/CeZrO$_4$. Appl Surf Sci. 2000;161:301.

25. Kluener T, Schmal M, Kuhlenbeck H, Shaikhutdinov S, Freund HJ. Preparation and characterization of well-ordered, thin niobia films on a metal substrate. Surf Sci. 2005;599:14–26.

26. Malpartida I, Larrubia Vargas MA, Alemany LJ, Finocchio E, Busca G. Pt–Ba–Al$_2$O$_3$ for NOx storage and reduction: characterization of the dispersed species. Appl Catal B Environ. 2008;80:214–25.

27. Reddy B, Sreekanth P, Yamada Y, Kobayashi T. Surface characterization and catalytic activity of sulfate-, molybdate- and tungstate-promoted Al_2O_3–ZrO_2 solid acid catalysts. J Mol Catal A Chem. 2005;227(1–2):81–9.
28. Roncolatto RE, Cardoso MJB, Cerqueira HS. Lam Y L, Schmal M, XPS Study of Spent FCC Catalyst Regenerated under Different Conditions. Ind Eng Chem Res. 2007;46:1148–52.
29. Schmitz P, Otto K, de Vries J. An X-ray photoelectron spectroscopy investigation of palladium in automotive catalysts: binding energies and reduction characteristics. Appl Catal A. 1992;92:59.
30. Shyu J, Otto K, Watkins W, Graham G. Characterization of Pd/γ-alumina catalysts containing ceria. J Catal. 1998;114:22.
31. Starr DE, Mendes FMT, Middeke J, Blum RP, Niehus H, Lahav D, Guimond S, Uhl A, Kluener T, Schmal M, Kuhlenbeck H, Shaikhutdinov S, Freund HJ. Preparation and characterization of well-ordered, thin niobia films on a metal substrate. Surf Sci. 2005;599:14–26.
32. Villoria JA, Alvarrez-Galvan MC, Al-Zahrani SM. Oxidative reforming of diesel fuel over $LaCoO_3$ perovskite derived catalysts: influence of perovskite synthesis method on catalyst properties and performance. Appl Catal B Environ. 2011;105:276–88.
33. Wang P, Yao L, Wang M, Wu W. XPS and voltammetric studies on La1−xSrxCoO3−δ perovskite oxide electrodes. J Alloys Compounds. 2000;311:53.
34. Wen Y, Zhang C, He H, Yu Y, Teraoka Y. Catalytic oxidation of nitrogen monoxide over La1−xCexCoO3 perovskites. Cat Today 2007;126:400–5. J Mol Catal A. 2005;227:81.

Chapter 12
Electronic Microscopy: General and Specific Notions

Martin Schmal and Sonia M.R. Vasconcelos

Abstract Electronic microscopy (EM) plays a key role in the characterization of catalysts. The understanding of some aspects of these techniques becomes a "sine qua non" condition in catalysis. Although the literature is relatively wide in fundamentals and applications.

Electronic microscopy (EM) plays a key role in the characterization of catalysts. The understanding of some aspects of these techniques becomes a "sine qua non" condition in catalysis [1]. Although the literature is relatively wide in fundamentals and applications [2], this chapter will present a brief summary on scanning electronic microscopy (SEM) and transmission electronic microscopy (TEM).

Increase and resolution are important concepts in microscopy. No use obtains large increases if there is no good resolution. But one has to distinguish "resolution" of "resolving power." While "resolution" means the smallest distance that one can distinguish between two points, "resolving power" is, for a given instrument, the ability to resolve details of the observed material, and it is represented as the inverse of resolution measure.

Electronic microscopy (EM) uses electron beam and no light radiation [3]. Thus, considering the wave properties of the electron, a thin beam of particles interacting with a sample under appropriate conditions sets a high resolving power, about 10 nm for conventional SEMs, reaching the range of 1–2 nm for high-resolution SEM. For conventional TEM and high resolution (HRTEM), these values can reach in optimal operating conditions, about 1 nm and between 0.1 and 0.05 nm, respectively [4].

12.1   Imaging in SEM: Basic Principles

Figure 12.1 shows the electron beam generated on the cathode, typically a tungsten filament (W) or lanthanum hexaboride (LaB$_6$),[1] which is heated by an electric current. By thermionic effect, it creates an electron beam that is accelerated by an
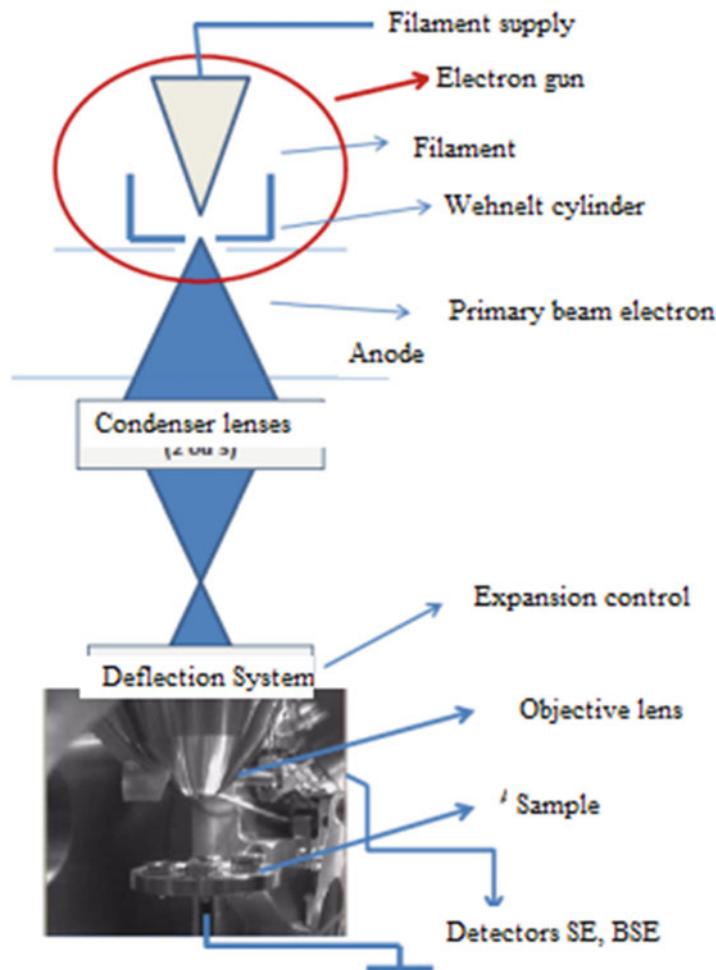
Fig. 12.1 SEM of a representative diagram (photo scheme is conjugated to the interior of the sample chamber of a SEM, model FEI Quanta 400 Company, used in NUCAT/PEQ/COPPE/UFRJ). PHOTO combined this QUANTA MANUAL scheme 400 FEG-SEM FEI

---

[1] The temperature emission for tungsten filament, commonly used in conventional SEM and TEM, is about 2500 C. It is a suitable material for its high melting point and low vapor pressure. His lifetime (40–100 h) is, however, lower compared to the LaB6 (200–1000 h), which is even
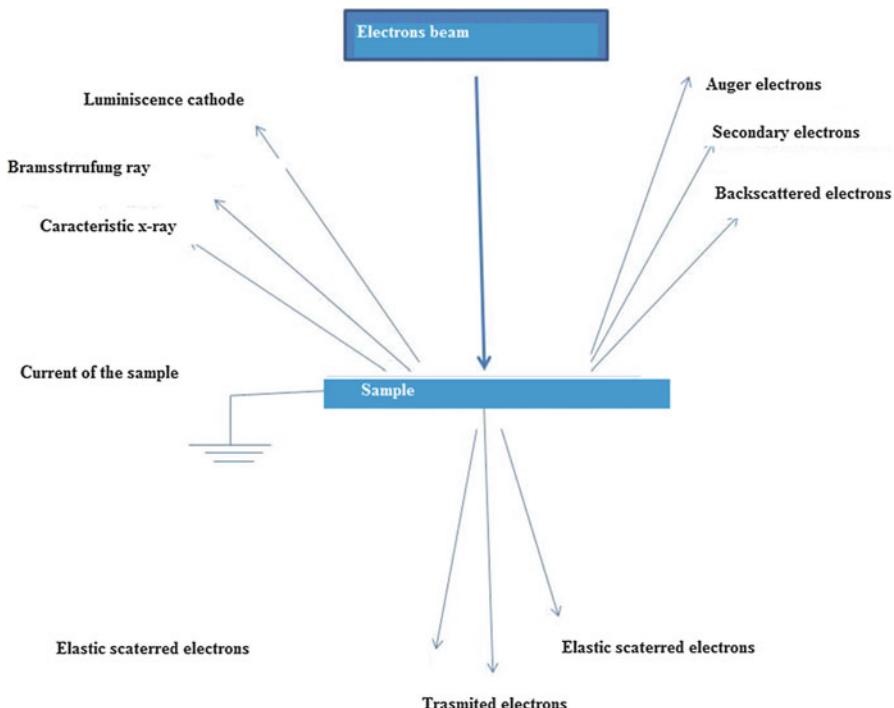
Fig. 12.2 Sample–beam interaction (the direction of the arrows does not necessarily represent the direction of radiation)

electrode system, called electron gun. This primary beam is then collimated by condenser lenses which greatly reduce their diameter—the reduction is carried out using two or more magnetic lenses in series before it is focused on the sample by the objective lens [5, 6].

When focusing on the sample, the primary beam interacts with the atoms of the material and causes scattering and various emissions, including secondary electrons (SE), backscattered electrons (BSE), and characteristic X-rays (Fig. 12.2, [7, 8]).

These three types of radiation are usually significant for SEM analyzes, and the apparatus are equipped with detectors, able to collect the signals.

These signals are associated with different types of information from microscopy. The volume of electron beam interaction with the material is associated with the energy of the incident beam, the type of material, and the atomic number of the elements [9].

---

much more expensive and produces about $10\times$ brighter than the tungsten. In the case of SEM by field emission (FEG-SEM—"field emission gun scanning electron microscopy"), the required temperature is much lower than that used in thermionic emission. For the FEG-SEM, which is a high-resolution SEM, a strong electric field (about 109 V m^{-1}) is applied to the "tip" metallic for issuing eléctrons. The FEG surpasses the previous two in life and also in performance. Regarding tungsten, for example, the FEG produces about $1000\times$ more electrons.

12.2   Secondary Electrons

The secondary electrons are very important in SEM and more recently in STEM. TEM uses electrons passing through the sample (transmitted). Among signals of the inelastic interactions with the sample (loss of energy with little change of direction), the secondary electrons (SE) are equivalent to the low kinetic energy electrons (about 5–50 eV). These electrons are generated throughout the interaction volume, but because of low energy, only the surface is issued with exhaust depth of nanometric order (<10 nm). Thus, near the surface of the material these secondary electrons may easily escape into the vacuum environment, while those coming from deeper layers are lost; much of them are absorbed by the own atoms of the analyzed sample. The amount of SE emitted depends, among other factors, on the acceleration and on the characteristic voltage of the material (e.g., topography of the sample). These signals are responsible for information on the surface of the sample, the morphology, and topography [10, 11].

The depth field is determined by how much the analyzed material remains in focus during the observation [12]. This characteristic can be observed in the micrograph below (Fig. 12.3). What we see is a high-resolution image generated in SEM by field emission. The analyzed material is an untreated $Co_3O_4/Al_2O_3/$ cordierite catalyst, where the secondary electron images were obtained at 20 kV.
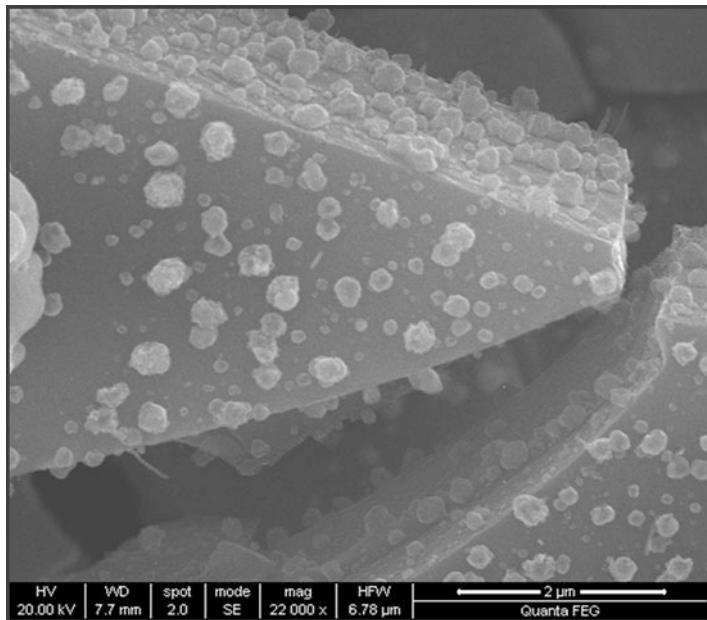
Fig. 12.3 Image of secondary electrons (high-resolution SEM, FEI Quanta 400) of fissures on the $Co_3O_4/Al_2O_3/$cordierite catalyst (NUCAT/PEQ/COPPE/UFRJ) [13].

12.3   X-Ray Analysis
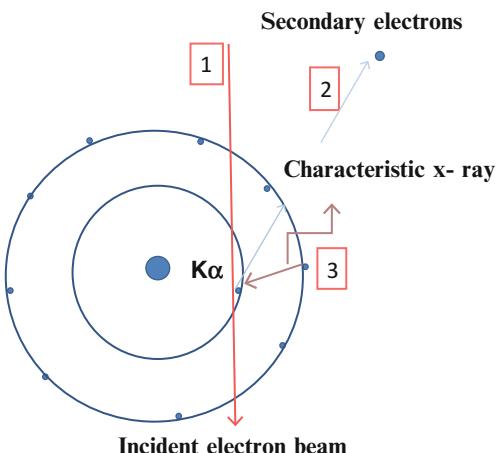
The X-rays generated in the sample–beam interaction are classified as continuous X-rays ("bremsstrahlung" braking radiation), secondary X-rays, and characteristic X-rays. The latter is of most interest for chemical microanalysis by using the energy-dispersive X-ray spectroscopy (EDS). "Bremsstrahlung" is part of the inelastic interactions of the electron beam with the atoms of the material. In this case, electrons are decelerated, whose energies are issued in the form of continuous X-rays with wide energy range, which hinder the identification of characteristic X-rays of low energy [14].

The characteristic X-rays are generated when an electron from an inner shell of the atom is ejected by interaction with the primary beam: it creates a hole that is filled by an electron from an outer layer. The energy difference between the initial and final state of the transition is equivalent to the characteristic X-ray of a given element (Fig. 12.4).

The EDS detector is a crystal, usually Si (Li)—although most current systems use SDD ("silicon drift detector")—which absorbs the energy of the X-ray, generated by elements of the sample, producing electrical pulses corresponding to the characteristic X-rays. In a typical microanalysis characteristic X-rays, it generates an EDS spectrum (energy-dispersive X-ray spectroscopy) [15, 16].

As an example, Fig. 12.5 shows the SEM analysis of the alumina completely overlaid on the cordierite surface, including macropores and cavities present in the structure, after deposition of six cycles of the secondary support, indicating homogeneous size distribution on the support [17]. Figure 12.5a shows the changes of surface morphology over the same inert support during the deposition cycles. Figure 12.5b displays the peaks of the elements present in the sample. The spectra illustrate the relationship between count (number of photons received) and keV energy peaks, related to those elements.

Fig. 12.4 Graphical representation of the emission of X-rays in the atom

12.4   Preparation of Catalyst Samples for SEM Analyses

The preparation of most samples for SEM analysis is usually straightforward. For most of the metal catalyst, the sample can be analyzed without any pretreatment ("as it is"). However, it is important that the sample be dry, including preservation in a vacuum chamber, and be conductive. For catalysts in powder form, the material
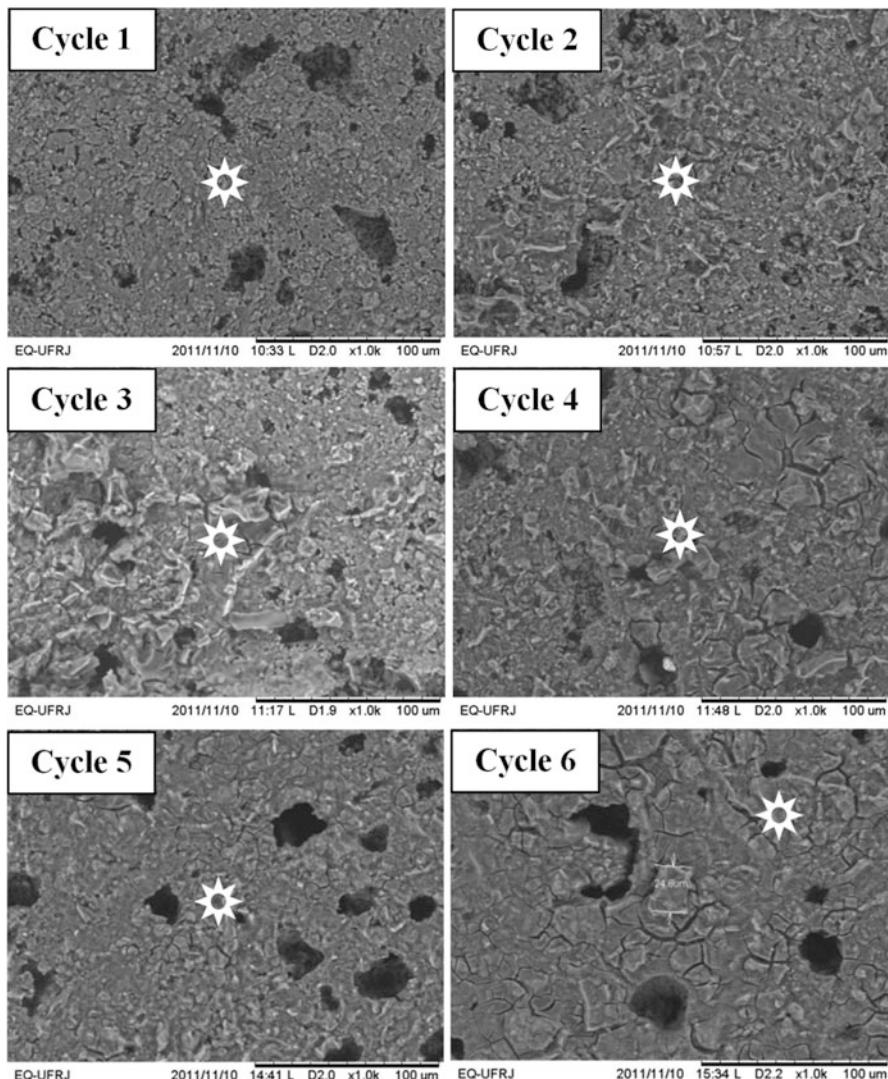
Fig. 12.5 SEM-EDS cordierite after 6 alumina deposition cycles (**a**). EDS spectra are in the same order corresponding to those shown SEM images (**b**). The *blank spots* indicate the locations analyzed by EDS (NUCAT/PEQ/COPPE/UFRJ) [17]
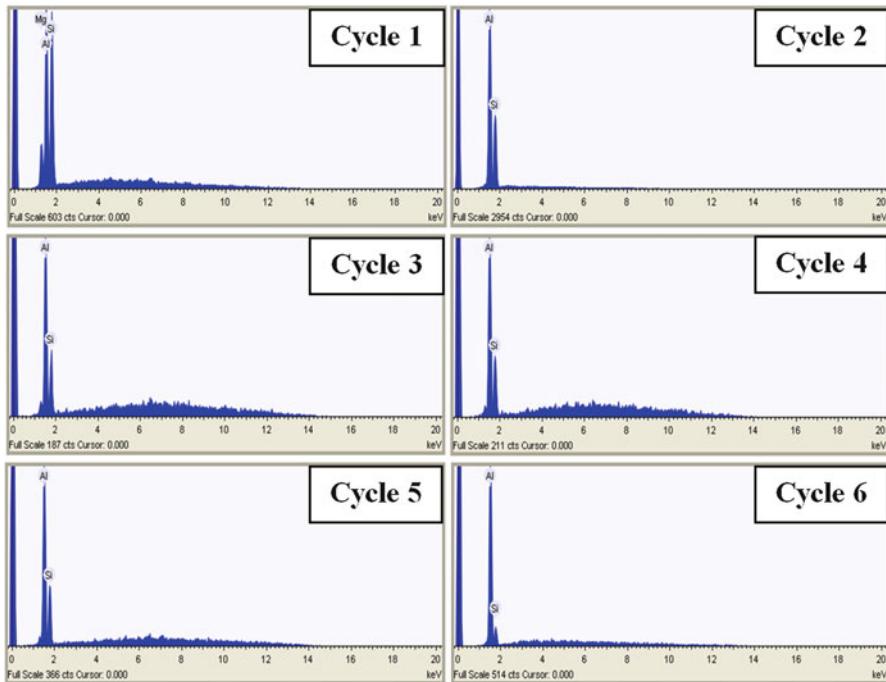
Fig. 12.5 (continued)

may be deposited on a double-sided carbon tape stuck to a stub of aluminum, brass, or even polyethylene. Analysis of the material without treatment already allows the generation of images with good quality, since under optimized conditions.

For a conventional SEM analysis, the uncoated sample analysis is especially harder than in a SEM field emission (which operates at ultrahigh vacuum of 10^{-8} Torr order), especially for obtaining good results at low kV. For the conventional, depending on the vacuum conditions in the chamber, the static charges—due to low emission or bad grounding of the sample—may hinder the acquisition of images with an acceptable resolution. The reduction of acceleration voltage ("low kV") is an alternative, because it can reduce the loading effects. But there is a significant loss of contrast, increasing aberrations of lenses, especially for conventional SEM.

In many cases, gold may be used for the coating, which is usually done by sputtering. A thin film of Au is deposited on the catalyst, which occurs by means of plasma, by applying a voltage (usually 1–2 kV) to a gas, which may be air, under very low pressure.

The thickness of the deposited metal must be controlled (in the range of 10–30 nm, depending on the material), which is relevant for catalysts. A very thin but heterogeneous layer may lead to insufficient emission amount of secondary electrons and may change the interpretation of the analysis of the surface material. A thick layer, however, can generate artifacts and mask details and/or change the
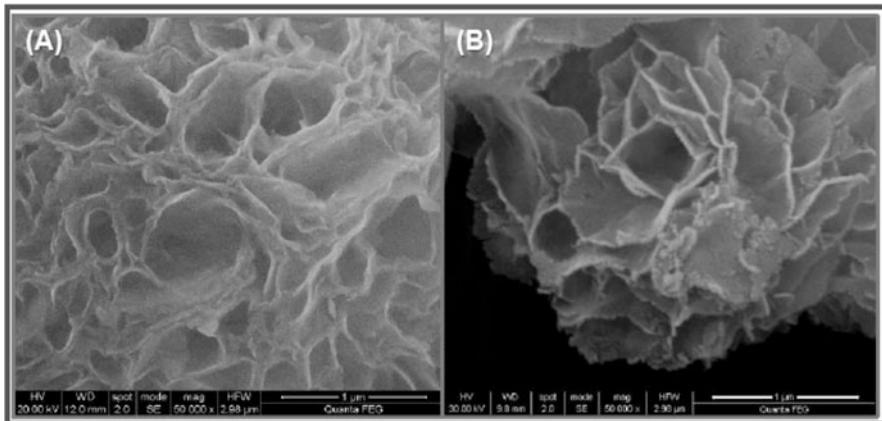
Fig. 12.6 (**a**) CeO$_2$ catalyst with nanoflower morphology (high-resolution SEM, FEI Quanta 400) powered. Images of secondary electrons of the material as such (high-resolution SEM, FEI Quanta 400); (**b**) even analyzed material coating with Au. NUCAT/PEQ/COPPE/UFRJ [18]

image resolution at the surface. Preferably, SEM by field emission layer must have the same thickness of resolution and for that one must use "sputtering" at UHV.

This problem may be more critical for SEM analysis at high voltage (30 kV) where edge effects, for example, are typically more pronounced. The micrographs below show (Figs. 12.6a, b) a high-resolution analysis generated in a SEM by field emission. The sample was analyzed as such, without coating with Au. The same coated sample (even slightly lower magnification) showed the evidence of artifacts masking the morphological details of the surface. In the literature, these effects have been described as the "orange peel effect" and can be observed in micro- and nanostructures analysis [19].

12.5   Transmission Electronic Microscopy

As described in Sect. 12.2, the electron beam in electronic microscopy is generated in a cathode, heated by electric current. As shown, the electron beam is accelerated by an electrode system, the electron gun. The three cannon components are the filament (cathode), the cylinder Wehnelt, and the anode.

As can be seen in Fig. 12.7, the cylinder Wehnelt causes the electrons that are ejected from the cathode to form a thin beam of electrons to the anode.

In TEM, the acceleration voltage applied will determine the velocity of the electrons in the beam to be collimated by the condenser lenses, which also occurs in the SEM. In fact, the basic distinction between SEM and TEM is closely related to the electron beam. It is the intensity of the beam and how it is controlled by optical-electronic column that define much of what can be achieved in scanning analysis or transmission [12].
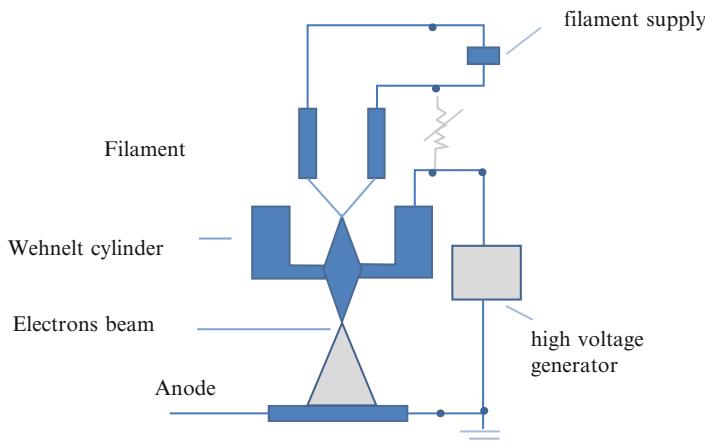
Fig. 12.7 Schematic cross section of the electron gun in an electron microscope (schema adaptation presented by FEI Company and used with permission of the company)

Unlike SEM, the inelastic scattered electrons, secondary electrons, for example, are not significant for image contrast in the TEM (if we disregard the imaging mode for STEM—"scanning transmission electron microscopy") and are excluded from analysis through the lens objective.

In addition, the speed with which the electrons pass through the electron optic column in TEM is typically much larger than in SEM, since the former operates at higher accelerating voltages, which can vary depending on the analysis conditions between 80 and 200 kV in a conventional TEM.

In Fig. 12.8, the acceleration voltage applied to the cylinder was 200 kV. The electrons focused on the material at a speed close to $200,000 \, \mathrm{km \, s^{-1}}$ [20]. This speed allows electrons to pass through the material, which is not possible by conventional configuration SEM, but only for high-resolution with STEM accessory.

However, high acceleration voltages used in the TEM must be combined with some important features relating to the material being observed. For the electrons that penetrate the material, it is necessary that the material be electron transparent. Thus, samples with a thickness greater than 100 nm may limit the beam penetration.

Different types of interactions with the sample define different contrast images, which can be controlled via the lens system. Basically, two types of contrast are of most interest in TEM: amplitude contrast (or diffraction contrast) and phase contrast. In the first case, electrons are elastically scattered by the atoms of an amorphous or crystalline or diffracted material as the Bragg condition. In this type of contrast include the thickness contrast/mass Z and the diffraction. In phase contrast, occurs the elastic scattering of electrons atoms of a crystal [12, 21]. In contrast range, bright-field or dark-field images are the most common types in TEM analysis, especially bright field.

The diffraction contrast is widely used to identify structural defects and lattice parameters ("lattice parameters"). Information about the nature of these defects can be obtained by diffraction contrast, where multiple Bragg reflections can assist in
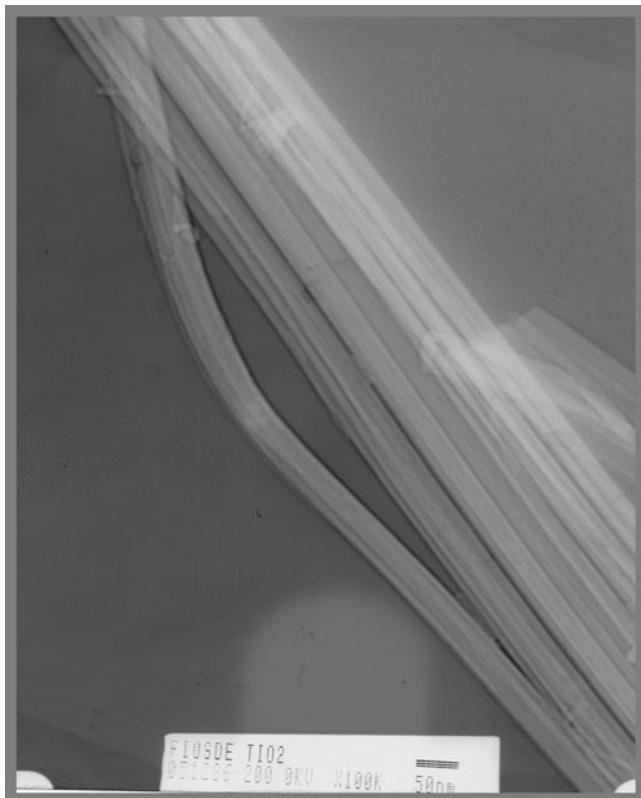
Fig. 12.8 Bright-field image of TiO$_2$ wires (TEM, JEOL Model 2010) (NUCAT/PEQ/COPPE/ UFRJ

the study of the displacement vector set these oxides and defects for three-dimensional geometry crude crystals [22, 23].

The phase contrast originates from elastic scattering of electrons through the specimen [12]. The phase contrast is the basic TEM ("high-resolution transmission electron microscopy"—HRTEM), since variations at the atomic level can be better observed—as a structural periodicity of crystalline samples—in the conventional TEM. However, in general, all TEM can generate atomic resolution images when properly operated and before a sample whose spacing between atoms is higher than its resolution.

In catalysis, HRTEM analyses are particularly important [24] for in situ observations in the structure of materials and allow monitoring of chemical processes at the atomic level. HRTEM fitted with chambers allows the in situ reaction and gives information of structural dynamics during the reaction in real time under the influence of temperature and reactive atmosphere. Figure 12.9 shows an HRTEM analysis in situ during the reaction, revealing such modifications on Cu/ZnO catalyst under different gaseous atmospheres [25].
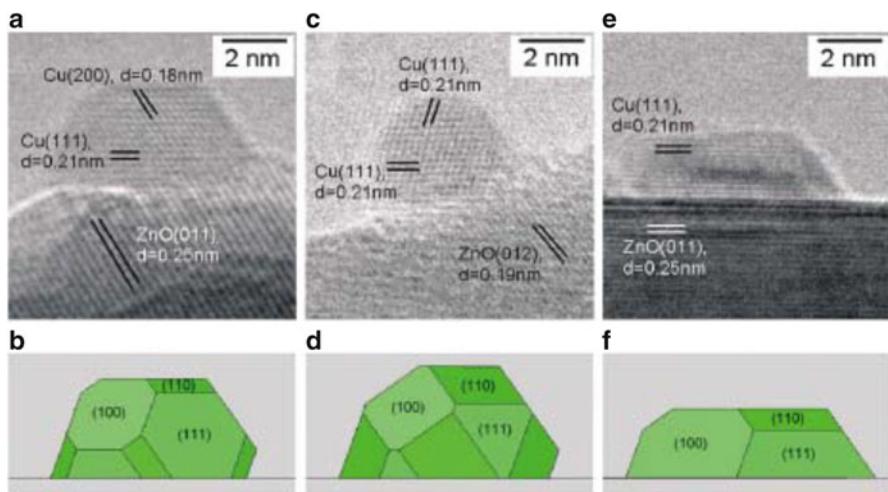
Fig. 12.9 Transmission electronic microscopy images (**a**, **c**, and **e**) of Cu/ZnO catalysts, under different gaseous atmospheres. The image was obtained at 1.5 mbar H_2 at 220 °C; C for mixture H_2/H_2O equal to 3:1 total pressure of 1.5 mbar at 220 °C and H_2; and the mixture H_2/CO (95:5) total pressure of 1.5 mbar H_2 at 220 °C (Reproduced by permission from Topsoe et al. Journal of Catalysis, 216, 2003, 155–164)

12.6 Examples

Example 1: Pd/Al$_2$O$_3$ Catalyst TEM analyses were performed after calcination of the Pd/Al$_2$O$_3$ catalyst [26]. Figure 12.10a–c show particles with uniform sizes, which are of the order of 0.8–1.4 nm. EDX results indicate uniform distribution of Pd. Note that with higher magnification in Fig. 3b, the particles contain clusters of Pd particles at the surface of the alumina support. The particles are of the order of 2 nm.

Thus, the Pd/γ-Al$_2$O$_3$ catalysts prepared by coprecipitation presented homogenous microstructure but different particle sizes.

Example 2: Au/Al$_2$O$_3$ Catalyst Contrast TEM has a particularly important role in the characterization of supported metal nanoparticles catalyst. Figure 12.11a, b show the micrographs and particle distribution histogram of the catalyst Au/Al$_2$O$_3$, respectively. It can be clearly seen that the gold particles (white dots in the image) are homogeneously distributed on the surface of the catalyst. The excellent contrast obtained made it possible to estimate the size and distribution of Au particles. The count showed a bimodal particle size distribution in a narrow range. The average particle size was calculated to be 2.1 ± 0.8 nm.

Example 3: Perovskite Catalysts After Consecutive TPSR Experiments The synthesis of LaCoO$_3$ (LC) using a simple Pechini method assigned as polymerizable complex route was analyzed by TEM after the TPSR under CH$_4$/O$_2$/He = 5/1/64, as

shown in Fig. 12.12a–c. TEM images still showed many metal particles carried inside the carbon nanotubes like those pointed out in Fig. 12.12b. Figure 12.12c shows the XRD analysis of metallic cobalt **Co(100).**

According to Pyrz and Buttrey [27], it is possible to obtain significant levels of contrast by varying the accelerating voltage of TEM. They showed that by increasing the voltage, it reduces the likelihood of scattering of heavier elements, such as a
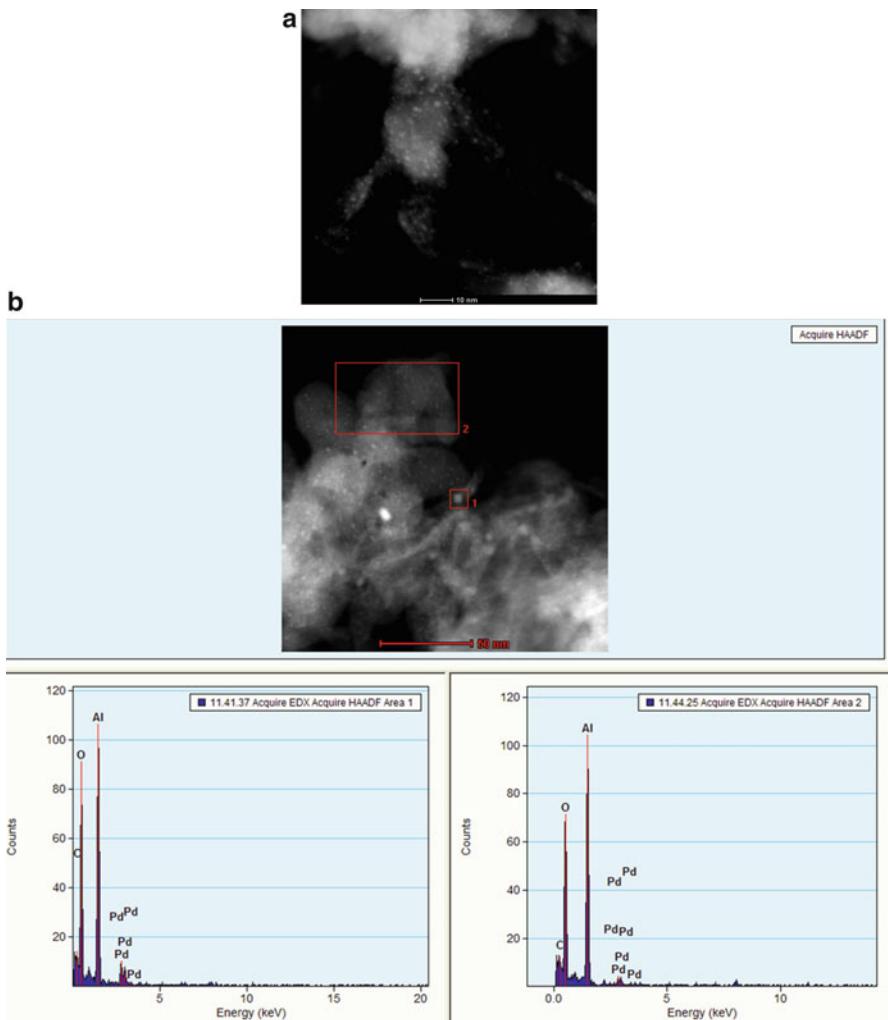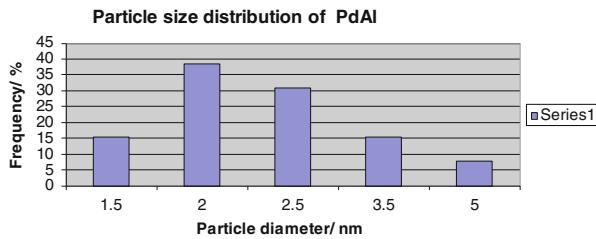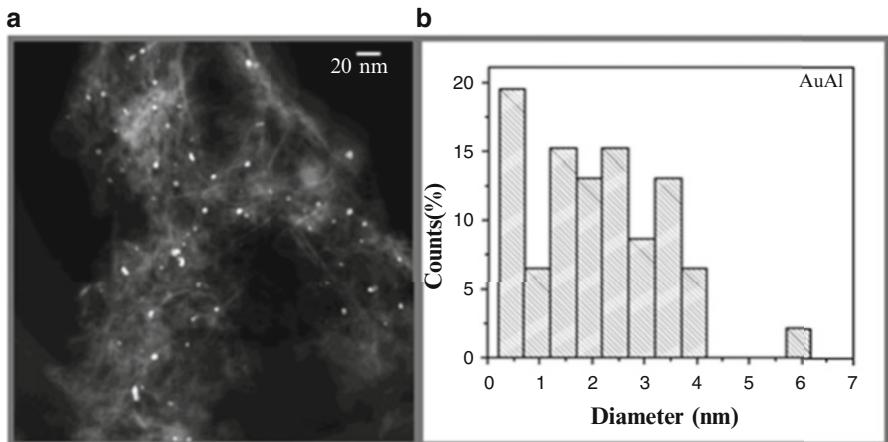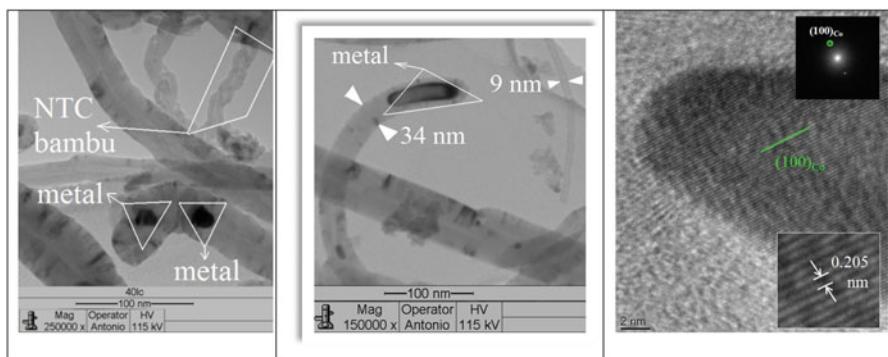
Fig. 12.10 (**a**) High-resolution transmission electronic microscopy (HRTEM) of the Pd/Al$_2$O$_3$ catalyst (Toniolo et al., Advanced Chemistry LettersVol. 1, pp. 1–8, 2012). (**b**) EDX analyses of the Pd/Al$_2$O$_3$ catalyst (Toniolo et al., Advanced Chemistry LettersVol. 1, pp. 1–8, 2012). (**c**) Particle size distribution of the 1.5 % Pd/Al$_2$O$_3$ catalyst (PdAl) (Toniolo et al., Advanced Chemistry Letters Vol. 1, pp. 1–8, 2012) [26]

Fig. 12.10 (continued)

Fig. 12.11 (**a**) TEM analyses at high-resolution image (HRTEM) of a Au/Al$_2$O$_3$ catalyst; (**b**) histogram distribution of the average size of Au particles [28]

Fig. 12.12 Micrographs of LC catalyst (**a**, **b**, **c**) after consecutive TPSR experiments under CH$_4$/O$_2$/He $=$ 5/1/64 mixture [29]
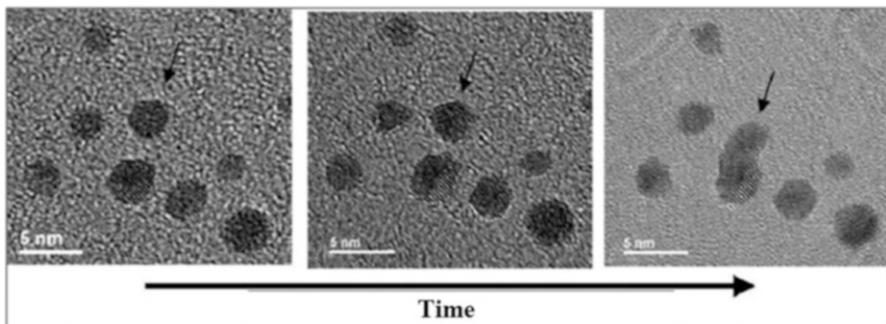
Fig. 12.13 High-resolution TEM images resulting from phase contrast (with increasing exposure time), showing the Au nanoparticle mobility and coalescence effects induced by the energy of the incident beam in the material. Acquiring the first image for the third (from *left* to *right*), the elapsed time was 1 min (Pyrz & Buttrey Langmuir. 2008;24:11350–60 (Adapted with permission) [27]

metal catalyst supported on Carbon. In this case, the scattering for C will be much lower than for the metal. However, the operator should have caution because some materials, including nanostructured catalysts, may be damaged when exposed to very high voltages.

Moreover, the observation of nanoparticles in a conventional TEM and high resolution must be done very carefully and held in various magnifications, in order to avoid a particle selection bias. This bias can distort the interpretation of the morphological and structural material, which can be avoided by a prior analysis in SEM.

In addition to these limitations, the authors highlight problems with artifacts: In the analysis of nanoparticles in TEM, the instability observed during exposure to the beam can cause artifacts arising from mobility of the particles, the material decomposition, and coalescence, as shown in Fig. 12.13.

12.7   Preparation of Catalyst Samples for TEM

Sample preparation for TEM analysis is not trivial. For powder, the material is dispersed in ethanol or isopropyl alcohol, and the suspension should be agitated by ultrasound for several minutes. One or more drops of this suspension are deposited on a holder, called grid (after evaporation of alcohol, it is ready for testing), with diameter varying from 2 to 3 mm. For powdered samples, grids of Co, Ni, or Mo may be used. The material bars should be opaque to electrons and to minimize the distortion of the magnetic field of the objective lens. The particle size of these sieves must be typically between 100 and 400 mesh and preferably coated with a thin film of carbon or Formvar® (polyvinyl formal resin, $R = C_3H_7$). The grids may be coated by a carbon film on one side and by a thin layer of another Formvar® [30].
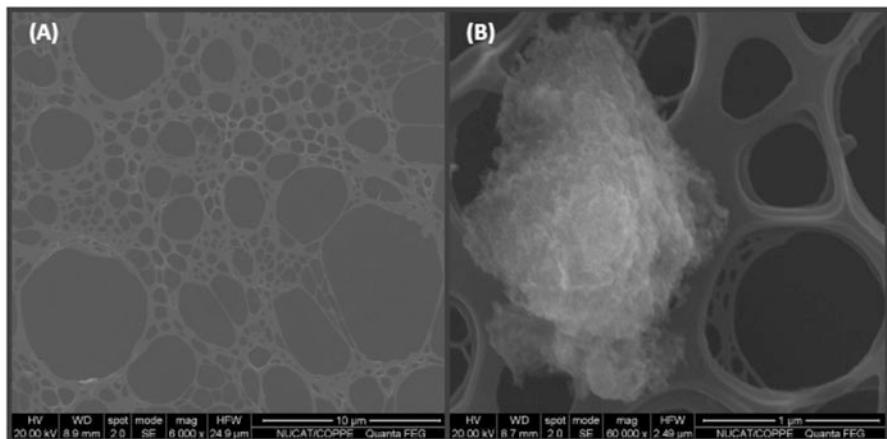
Fig. 12.14 (**a**) Image of secondary electrons (high-resolution SEM, FEI Quanta 400) of a detail of a grid with carbon film; (**b**) secondary electron image of a catalyst sample of Au/Al_2O_3 on a 400 mesh grid with carbon film ("holey film"). Material developed in NUCAT/PEQ/UFRJ, 2008

Grids with carbon films are widely used, and among the advantages is the high thermal and electrical conductivity. This feature helps to reduce the thermal expansion and loading effects during exposure of the sample to the electron beam [10]. It is important that the material is deposited on a thin film transparent to electrons; the thickness may vary from about 10 to 30 nm, depending on the manufacturer.

The thickness of a film Formvar® 100 mesh layer on a grid is more robust than for one with a smaller apertures, such as a 400 mesh, for example (SPI Supplies). Typically, the so-called holey films are the most suitable for the analysis of powder catalysts. Figure 12.14a, b show images of a 400 mesh grid coated with a thin carbon layer sample without and one with a catalyst sample of Au/Al_2O_3, respectively, by the deposition method of alcohol droplets.

For high-resolution TEM analysis, the most appropriate materials are "holes" in the range of about 0.2–10 μm, which reduces the absorption and scattering of the electron beam and help to improve the quality of the signal. For particles with little contrast, "holey films" coated with an extra layer, ultrathin of carbon can improve the quality of images. The so-called lacey films are quite recommended for electron diffraction images [31].

The correct preparation of the sample and the use of adequate grids to support the material for analysis are important for observing two-dimensional images with high quality and resolution. However, an alternative is the ultramicrotome. The particles are embedded in a polymer resin and cut in thin sections of about 20 nm with a diamond knife. It is specially recommended for zeolite materials. The observation of these thin sections allows to observe the internal morphology of the particles and the dispersion of metals on the microporous structure material [32].

The careful choosing of the appropriate method of sample preparation is very important. Proper sample preparation is one of the key points for successful analysis of materials by electronic microscopy.

References

1. Abhaya J, Datye K. Electronic microscopy of catalysts: recent achievements and future prospects. J Catal. 2003;216:144–54.
2. Gai PL. Developments of electronic microscopy methods in the study of catalysts. Curr Opin Solid State Mater Sci. 2001;5:371–80.
3. Nobelprize.org. Ernst Ruska: The Nobel Prize in Physics 1986. http://nobelprize.org/nobel_prizes/physics/laureates/1986/ruska-autobio.html.
4. SPI Supplies. http://www.2spi.com/catalog/grids/cusctgrd.php.
5. Jaksch H. Low loss BSE imaging with the EsB detection system on the Gemini Ultra FE-SEM. 14th European microscopy congress (1–5 Setembro, 2008, Aachen, Germany, pp. 555–556), I3; 2008.
6. Oldfield R. Light microscopy: an illustrated guide. London: Academic Press; 1994.
7. Steigerwald M. ESB detection low voltage. BSE imaging. 2004. http://www.iptonline.com/articles/public/TECHNICA1.pdf.
8. Richards RG, Owen GR, Gwynn I. Low voltage backscattered electron imaging (<5 kV) using field emission scanning electron microscopy. Scann Microsc. 1999;12(1):55–60.
9. Goldstein J, Newbury DE, Joy DC, et al. Scanning electronic microscopy and X-ray micro-analysis. 3rd ed. New York: Kluwer Academic/Plenum; 2005.
10. Zhou W, Wang ZL. Scanning microscopy for nanotechnology: techniques and applications. New York: Springer; 2007. 522 p.
11. Lyman CE, et al. Scanning electronic microscopy and X-ray microanalysis and analytical electron microscopy: a laboratory workbook. New York: Plenum; 1996.
12. Williams DB, Carter CB. Transmission electron microscopy: a textbook for materials science. 2nd ed. New York: Springer Science; 2009. 832 p.
13. Rodrigues CP, da Silva VT, Schmal M. Partial oxidation of ethanol over cobalt oxide based cordierite monolith catalyst. Appl Catal B Environ. 2010;96:1.
14. Griffin J, Suvorova AA. Charge-related problems associated with X-ray microanalysis in the variable pressure scanning electron microscope at low pressures. Microsc Microanal. 2003;9:155–65.
15. Whallon H, Flegler ST, Klomparens KL. Energy-dispersive x-ray microanalysis. Bioscience. 1989;39(4):256–9.
16. Eades A. Reflections on sum peaks in EDS spectra. Acta Microsc. 2008;17:20–33.
17. Brackmann R, Perez CA, Schmal M. $LaCoO_3$ perovskite on ceramic monoliths – Pre and post reaction analyzes of the partial oxidation of methane. Int J Hydrog Energy. 2014;39:13991–4007.
18. Martins RL, Schmal M. Activation of methane on NiO nanoparticles with different morphologies. J Braz Chem Soc. 2014;25(12):2399–408.
19. Liu Y, Jehanathan N, Yang H, Laeng JJ. SEM observation of the "orange peel effect" of materials. Mater Lett. 2007;61:1433–5.
20. FEI Company. All you wanted to know about electron microscopy. 2006. http://www.fei.com/uploadedFiles/Documents/Content/2006_06_AllYouWanted_pdf.

21. Mannheimer WA. Microscopia dos materiais. Sociedade brasileira de microscopia e microanálise. Rio de Janeiro: E-papers Serviços Editoriais; 2002. 221 p.
22. Fultz B, Howe JM. Transmission electronic microscopy and diffractometry of materials. 3rd ed. Heidelberg: Springer; 2008. 758 p.
23. Gai PL, Boyes ED, editors. Electronic microscopy in heterogeneous catalysis. London: Institute of Physics Publishing; 2003. 233 p.
24. Kiely C. New views of catalysts. Nat Mater. 2010;9:296–7.
25. Topsoe H. Developments in operando studies and in situ characterization of heterogeneous catalysis. J Catal. 2003;216:155–64.
26. Toniolo FS, Moya S, Schmal M. Syntheses of nanostructured supported palladium catalysts—non-oxidative methane coupling II. Adv Chem Lett. 2013;1:1–8.
27. Pyrz WD, Buttrey DJ. Particle size determination using TEM: a discussion of image acquisition and analysis for the novice microscopist. Langmuir. 2008;24:11350–60.
28. Ribeiro NFP, Mendes FMT, Perez CAC, Souza MMVM, Schmal MM. Selective CO oxidation with nano gold particles-based catalysts over Al_2O_3 and ZrO_2. Appl Catal A Gen. 2008;347:62–71.
29. Toniolo FS, Magalhães RNSH, Perez CAC, Schmal M. Structural investigation of $LaCoO_3$ and $LaCoCuO_3$ perovskite-type oxides and theeffect of Cu on coke deposition in the partial oxidation of methane. Appl Catal B Environ. 2012;117–118:156–66.
30. Dedavid BA, Gomes CI, Machado G. Microscopia Eletrônica de Varredura Aplicações e Preparação de Amostras Materiais Poliméricos, Metálicos e Semicondutores Edição do CEMM – Centro de Microscopia e Microanálises do IDÉIAPUCRS – Instituto de Pesquisa e Desenvolvimento. Porto Alegre: EDIPUCRS; 2007. 60 p.
31. Ted Pella, Inc. http://www.tedpella.com/grids_html/grids.htm 284 12 Electronic microscopy: general and specific notions.
32. Gallezot P, Leclercq C. Characterization of catalysts by conventional and analytical electronic microscopy. In: Imelik B, Vedrine JC, editors. Catalyst characterization, physical techniques for solid materials, fundamental and applied catalysis. Heidelberg: Springer; 1994. p. 509–58.

Chapter 13
Nanostructured Catalysts

Martin Schmal and Silvia Moya

Abstract Nanostructured systems are of great interest from points of view of basic science and technological applications. Within the topic of catalysis, should be highlighted the properties associated with different morphologies, activities and selectivities, which are strongly affected by the shape and particle size; in the case of crystalline metallic phases are oriented crystal faces. The reactions that are influenced by these factors (morphological) are known as structure sensitive reactions.

Keywords Grapheme • Metals • Nanostructure • NCT • Oxides

13.1 Part I: Introduction

Nanostructured systems are of great interest from points of view of basic science and technological applications. Currently, in general, any material that contains grain clusters, plates, or filament size smaller than 10 nm can be regarded as nanostructure, as long as their properties differ from those of the bulk solids. These materials have been extensively studied in recent years, because the small size (particles, grains, or phases) and high surface/volume ratio (S/V) resulted in mechanical, optical, electronic, and natural magnetic properties in important applications.

In the transition metal nanoparticles, new behaviors arise deriving from effects related to the size reduction. Changes in its electronic structure provide the development of new reactivity characteristics, in addition to other previously cited properties with respect to those presented by the bulk structure. These behaviors are also related to surface effects as superplasticity, dynamic differential sintering, and catalysis.

The size and surface characteristics are related through the S/V ratio. For spherical particles, the S/V ratio is inversely proportional to its radius R, ($S/V = 3/R$). Clusters of type complete layer (full shell) are formed with atoms packed in closed hexagonal structure (hcp) and cubic (ccp). This model assumes that the particles are constructed by adding densely packed layers around a central atom. The number of atoms per layer is represented by $Ns = 10n^2 + 2$, where n is the layer number in question. The total number of atoms (N) in a structure consisting of N layers is $N = (10n^3 + 15n^2 + 11n + 3/3)$. The S/V ratio can be

Full-Shell "Magic Number" Clusters					
Number of shells	1	2	3	4	5
Number of atoms in cluster	M_{13}	M_{55}	M_{147}	M_{309}	M_{561}
Percentage surface atoms	92%	76%	63%	52%	45%

Fig. 13.1 Scheme of cluster-type full-layer hexagonal packing (Adapted from Aiken, J. Mol. Catal. A, vol. 145, pp. 1–44, 1999)

obtained, so the ratio of surface atoms to the total atoms constituting the cluster, Ns/N [1, 2].

Most of these clusters assume complete layer structures, as shown in Fig. 13.1, since the optimal number of metal–metal atom bonds for each leads to higher stabilization of the system.

This configuration allows higher stability of the clusters; it provides a structure whose atoms have the largest possible number of neighbors. The cluster growth decreases the amount of surface atoms [1, 2].
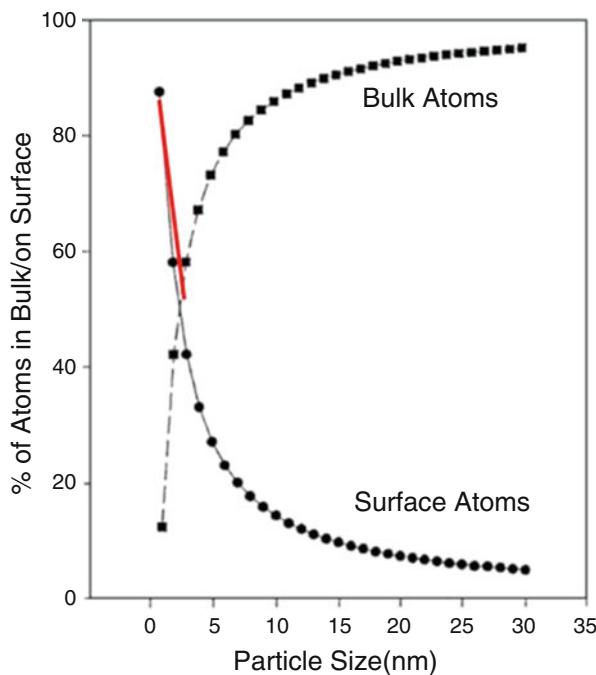
In a few hundred of nano atoms, the major fraction of them is located at the surface. Because of the tendency that surface atoms are coordinately unsaturated, high surface energy has great contribution to the total energy of the system. Also, a high ratio S/V, that is, the particle size and its shape, influences the electronic structure of cluster levels. These properties have been reported in the literature in different aspects of nanoscience.

Within the topic of catalysis, the properties associated with different morphologies, activities, and selectivities should be highlighted, which are strongly affected by the shape and particle size; in the case of crystalline, metallic phases are oriented crystal faces. The reactions that are influenced by these factors (morphological) are known as structure-sensitive reactions. The high performance of nanostructured catalysts is explained by the high concentration of atoms at the surface, due to the small particles. The variation of surface atoms relative to the solid volume, as a function of particle size, is illustrated in Fig. 13.2.

Note that the percentage of surface atoms increases the smaller the particle size and decreases with increasing particle size. But the opposite is true in the bulk, indicating that the larger the size of particles, the greater the concentration of atoms in the bulk phase. Catalytic reactions are surface phenomena, and the size reduction of the active phase may favor them as follows:

- The reactions occur at lower temperatures due to the high ratio of surface atoms/ volume changes in the electronic levels.
- Increased yield and selectivity due to greater surface active area available and morphology.
- Increased mechanical strength.

Fig. 13.2 Surface atoms versus bulk atoms (Adapted from Aiken 1999, *J. Mol. Catal. A, vol. 145*, pp. 1–44, 1999; Burda et al. *Chem. Rev., vol. 105*, pp. 1025–1102, 2005)

There are excellent reactivity characteristics, as a result of the decreasing size high surface/volume ratio, compared to bulk materials.

It is well known from studies of model catalysts (single crystal), under conditions of ultrahigh vacuum (UHV), that the selectivity is significantly influenced by the crystal face. The catalytic activity of metal nanoparticles of different shapes was quite reasonably correlated with the fraction of atoms located at vertices and edges of the crystalline metal structures [3]. Its unique properties associated with the ability to synthesize in different size ranges and shapes make these materials potentially useful in catalysis, which are more active and selective than the conventional catalysts.

Nowadays, materials which are of great interest are the carbon nanotubes (CNT) and graphene, which were invented the first time in (1962) and present new properties which can be applied in catalysis [4]. They present high chemical resistivity and are resistant to oxidation and to temperatures. CNT presents electric transport like metals, semiconductors, or superconductors, besides mechanical resistance and flexibility, which can be applied in sensors, polymers, ceramics, and of course catalysis, in particular for hydrogen storage and fuel cells [5].

13.1.1   *Synthesis of Nanostructured Catalysts*

The syntheses of nanostructured materials are of different natures, such as:

- Metals
- Oxides

- Sulfites or carbides
- Carbon nanotubes and oxide nanotubes
- Nanostructured oxides and mixed oxides

Nanostructured materials for metals or supported oxides, oxides and mixed oxides, and in particular graphenes will be focused. The most important requirements that should guide the choice of a method of synthesis for these classes of materials are:

- Control of particle size
- Control of the particle size distribution
- Control of morphology or particle shape
- Homogeneous distribution of particulate material supported thereby including the largest number of surface active sites available for reaction, adsorption, etc.

There are several routes that can be chosen for the synthesis of nanostructured systems. The method may involve the preparation of novel compounds from a precursor that is called chemical synthesis or may involve only a vaporization process and cooling the material under controlled condensation conditions; it is classified as physical preparation.

The *physical methods* of preparation of nanostructured materials are basically of gas phase synthesis, which allows getting a flexible composition and a high degree of homogeneity in the generation of "nanoclusters," ranging from refractory materials to multicomponent alloys. The following are among the physical methods that are noteworthy:

- Chemical vapor deposition (CVD) or sputtering
- Lithography by electron beam
- Plasma

Chemical methods, on the other hand, exert the main role in the synthesis of nanomaterials. The advantage of chemical synthesis methods is the variety of methods and versatility in the design characteristics such as structures and compositions, in addition to increased operational simplicity. The materials obtained by chemical processes have greater homogeneity, because the chemical synthesis allows interaction between the components of the reaction mixture at the molecular scale. Consequently, understanding how matter interacts and organizes this dimension allows the understanding of its effect on the macroscopic properties of the desired products. Figure 13.3 shows a general scheme of nanomaterial synthesis.

Among the chemical methods, we have [1, 6]:

- In situ precipitation of metal precursors
- Synthesis in confined spaces—microemulsion
- Sonochemical synthesis
- Deposition–precipitation
- Sol–gel method
- Thermal decomposition

Nanostructured Catalysts - Sunthesis
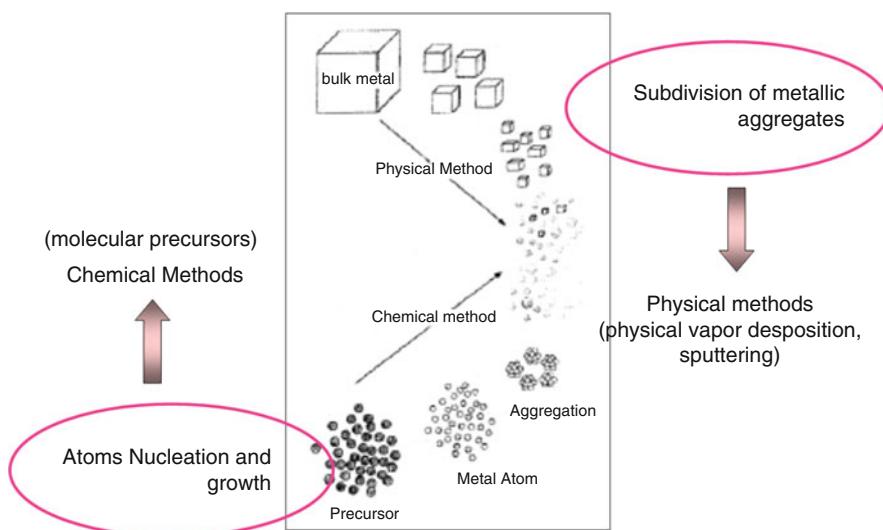
Fig. 13.3 Schematic representation of physical and chemical methods
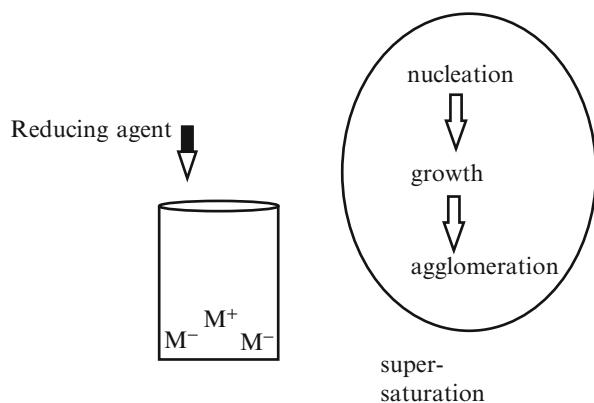
- Photochemical synthesis
- Reduction or decomposition of binders of organometallic compounds
- Chemical vapor decomposition

13.1.2   In Situ Precipitation of Metal Precursors

The precipitation process is basically a nucleation followed by growth and agglomeration of poorly soluble products generated in supersaturation condition. To obtain nanostructured materials, one must control the growth stage and prevent agglomeration in the reaction medium, which may be aqueous or organic. As in most precipitation processes, the supersaturation condition must be reached; in this case, the reduction of the metal precursor is obtained by adding a reducing agent which is added to the reaction medium. Figure 13.4 shows a simplified scheme of synthesis of precipitation conditions.

In the precipitation method, one should pay attention on the choice of the parameters for controlling the precipitation reactions for the increased growth of the particles of desired characteristics (size and morphology). The first step is the nucleation, which must occur at a high degree of supersaturation of the solution, in order to form a large number of nucleation centers (very small crystals), in a short period of time. To ensure uniformity in size of the crystals, it is necessary that only the nuclei are formed in the first stage and then should only grow via molecular mechanisms until the precipitate of the equilibrium concentration is achieved.

Fig. 13.4 Scheme of the precipitation method

Reducing agent ■

nucleation

⇩

growth

⇩

agglomeration

super-
saturation

M^+

M^- M^-

The reaction for extended periods of time can result in the total reagent shortage. Thereafter, in the period called aging reaction, begins the digestion of solid formed. The digestion of the precipitate occurs with the growth of larger particles due to the consumption of the smaller particles which decrease in size until complete dissolution, in a process known as Ostwald digestion [2]. This process also leads to the formation of larger particles and a solution with broad size distribution.

Deposition on Supports

The deposition of the active phase on a support depends on the surface charges of the support and of precursor in suspension. The surfaces of the particles in a polar medium develop loadings caused by ionization process in which functional groups are present in the material or even ionized by the ion adsorption. This affects the distribution of the charge near ions, increasing the concentration of counter ions near the surface. Thus, an electrical potential is generated, which decreases exponentially away from the surface, as expressed by Eq. (13.1). The adsorbed ions cause decreasing electric potential, as illustrated in Fig. 13.5a:

$$\psi = \psi_0 \cdot e^{-\kappa \cdot x} \tag{13.1}$$

where ψ is the electric potential at a distance x from the surface, ψ_0 is the potential on the particle surface, and κ is the Boltzmann constant $\left(\kappa = 1.38 * 10^{-23} J / K\right)$.

The adsorption of charged ions on the surface leads to the formation of the so-called electrical double layer, which can be divided into two regions, the Stern layer and the diffusion layer as shown in Fig. 13.5a. The Stern layer indicates ions strongly adsorbed at the surface, while the diffusion layer is a region in which the distribution of the ions is determined by the balance between the electrostatic forces and thermal motion.

This phenomenon is known as electrophoresis. The particles and ions strongly adsorbed (Stern layer) move as a unit, and the electric potential at the border of the unit where the sliding takes place between the phases is known as the zeta potential (Setz 2009). The zeta potential is influenced by the pH of the system since the H^+ and OH^- ions affect the surface charge of the particle and thus the zeta potential
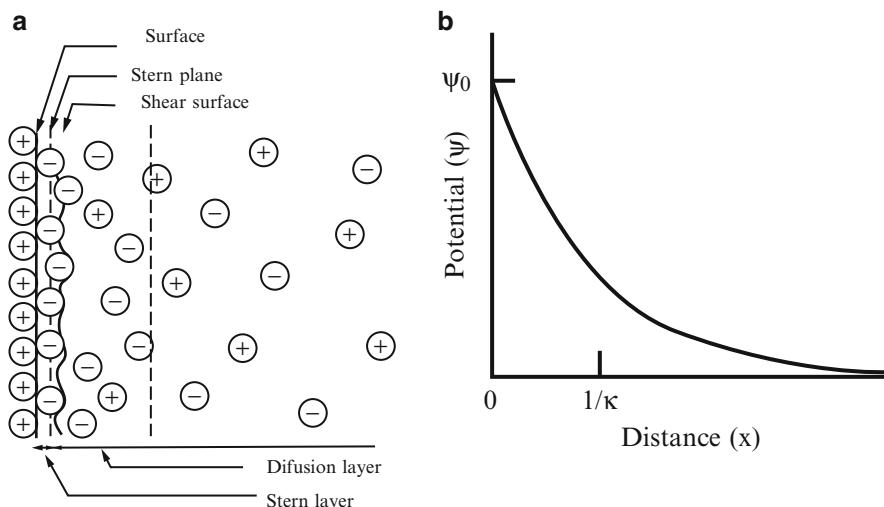
Fig. 13.5 (**a**) Representation of the electric double layer in a positively charged surface; (**b**) the variation of the electric potential as a function of distance from the surface positively charged. The variable $1/\kappa$ is called the "thickness of the electrical double layer" (Adapted from Roucoux A., Schulz J., Patin H., *Chem. Rev., vol. 102*, pp. 3757–3778, 2002) [7]

(Adamson 1997). The pH value of suspension at which the zeta potential is zero is known as the isoelectric point (IEP). In this case, the electrostatic repulsion between particles is negligible, and van der Waals forces act to promote the approach of the ions and subsequently the coagulation. Where both the zeta potential of the particle as the surface load is null, there is the so-called point of zero charge (PZC). This can be performed using the zeta potential analyses (IEP) in order to promote greater electrostatic interaction between the support and the precursor of the active phase, allowing better adherence of the active phase.

Figure 13.6 illustrates the behavior of the alumina surface at different pH values. Note that at pH values below 13 (PIE alumina), its surface becomes positively charged due to exposure OH_2^+ groups. At pH 13, the alumina is electrically neutral, and at higher values, it is negatively charged.

13.1.3 Synthesis of Stabilized Nanoparticles: Colloidal Nanoparticles

Virtually, all grades of colloidal inorganic nanocrystal well-defined structure may be synthesized by a variety of methods, including [8]:

- Coprecipitation in aqueous phase
- Power coprecipitation
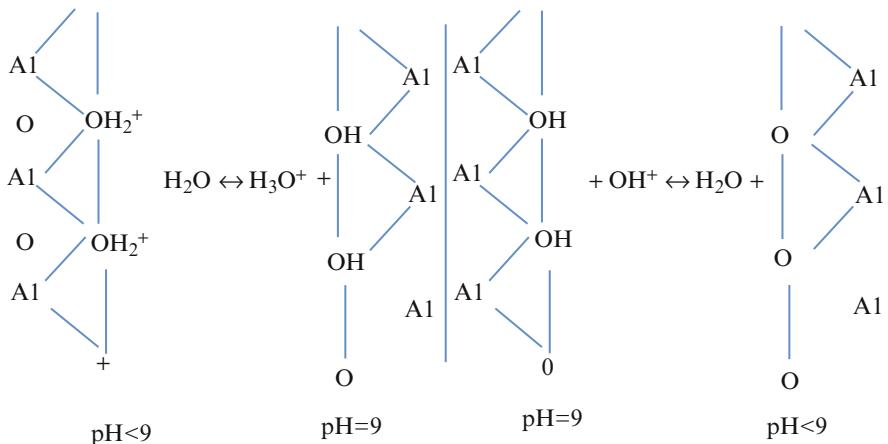
Fig. 13.6 Hydrated alumina surface at different pH values

- Microemulsion
- Hydrothermal and thermal–solvent synthesis

The usual route for the preparation of colloidal nanoparticles is the precipitation. The production of stabilized metal nanoparticles requires the reduction in aqueous or organic solution, in the presence of a stabilizing agent. The main components of systems for the synthesis of colloidal nanoparticles are:

- Metallic precursor
- Reducing agent (alcohol, H_2, hydrates, $NaBH_4$)
- Stabilizing agent (organic/inorganic binders, polymers, and surfactants)

There are two ways for stabilization of nanoparticles:

- *Electrostatic*: as a result of adsorption of ions (most commonly chloride, hydroxide and hydronium) on the surface of the nanoparticle forming a double layer (EDL)
- *Spatial repulsion*: due to species with long organic chains that involve metallic particle, which is the most common

Figure 13.7 shows schematically both ways of stabilizing colloidal nanoparticles.

The stabilization using inorganic colloid method is limited to aqueous solutions and some polar protonic solvents. Due to the dynamic nature of the electrical double layer (EDL), these systems are extremely susceptible to environmental conditions (temperature, concentration, pH), reducing considerably its stability compared to other forms of stabilization.

According to another way of stabilizing colloids, the presence of bulky organic chains around the nanoparticles prevents agglomeration due to van der Waals force interparticle. The organic interface (hydrophilic or hydrophobic character) colloid stabilizes both in water and in nonpolar solvents. The steric stabilization is the most
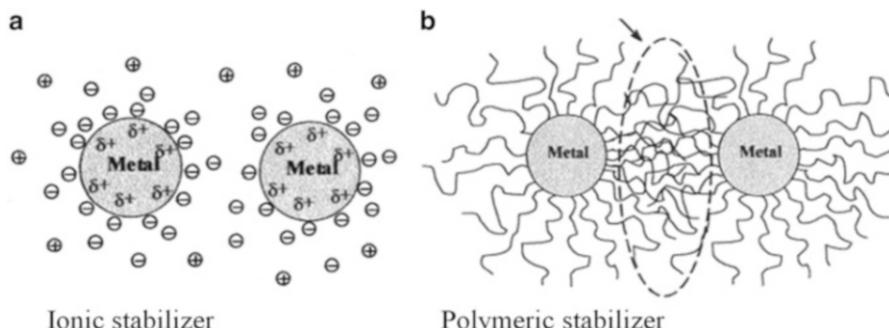
Fig. 13.7 Scheme of stabilizing nanoparticles: (**a**) DCE; (**b**) Spatial repulsion (Adapted from Novoselov, Nature Materials 6 (2007) 183–191). (**a**) Ionic stabilizer. (**b**) Polymeric stabilizer

common due to the colloid stability characteristics in wide pH ranges and in solvents of different polarities [9]. A variety of compounds are used as stabilizers. The most effective agents in the stabilization of inorganic colloids are surfactants or polymer-coordinating ligands or "capping ligands". All these substances must have polar groups (electron density donors), as phosphines [10], carboxylates [11] [190], sulfates [12, 13] [48], neutral amines [14] [232], and nitrogen heterocycles [15] [23]. These groups interact with the surface of nanoparticles in order to coordinate to metal atoms surface electron deficient. The organic chain-extending molecule provides physical isolation of the solvent and governs the nanocrystal solubility properties of the material.

Characteristics such as particle diameter, morphology, and size distribution are strongly influenced by the composition of the precursor solution during the precipitation.

So important as the nature of the reducing agent and reaction conditions are the type and amount of the stabilizer to obtain specific morphological properties. Besides, the manipulation of the concentration of the metallic precursor relative to the stabilizer is another way to control size of nanoparticles. The high-ratio stabilizer/metal cations lead to the formation of smaller crystallites during nucleation. During growth, the binder adsorbs reversibly at the particle surface and in the case of stabilization, by space constraints, produces a dynamic organic coating which stabilizes crystals in solution mediating growth. Larger molecules provide greater shielding nanoparticle, resulting in a smaller average size of the system.

Impregnation on the Support

The nanoparticles can be used as catalysts in liquid phase or impregnated on supports. In this case, it follows by drying, calcination, and activation steps.

In gas–solid catalytic systems, the precursor of the catalyst previously supported passes through the calcination process, owing to the shielding around the metal particles, so that the metal layer can be exposed to the reactants. The use of binders with low decomposition temperatures permits the removal of stabilizers which can be carried out under mild temperature conditions and does not cause damage to the

particle structure. It is extremely important that the calcination procedure impedes the formation of carbon deposits on the surface, blocking active sites.

Influence of Temperature on Supported Nanoparticles

Wang et al. [8] studied the thermal behavior Pt supported on SiO_2 amorphous nanocrystals in a transmission electron microscope in situ reaction chamber. The authors followed the heating process performed in the microscope and observed that increasing the temperature above 350 °C induces morphological deformation of nanocrystals. The continuous heating promotes fusion of the surface of the nanoparticles and their spreading on surface of the carrier rather than the sintering material inducing the change in the morphology thereof. In Fig. 13.8 it is possible to observe this process. When the particles are close enough, the coalescence becomes unavoidable Fig. 13.8.

El-Sayed [16] observed through TEM in situ the images of Pt nanocrystals at different temperatures, as shown in Fig. 13.9. The triangular shapes are preserved at temperatures up to 350 °C, without truncation of vertices and edges. The morphology changed from triangular shape to the spherical at 500 °C, due to melting of surface atomic layers; however, the inner particle maintains the
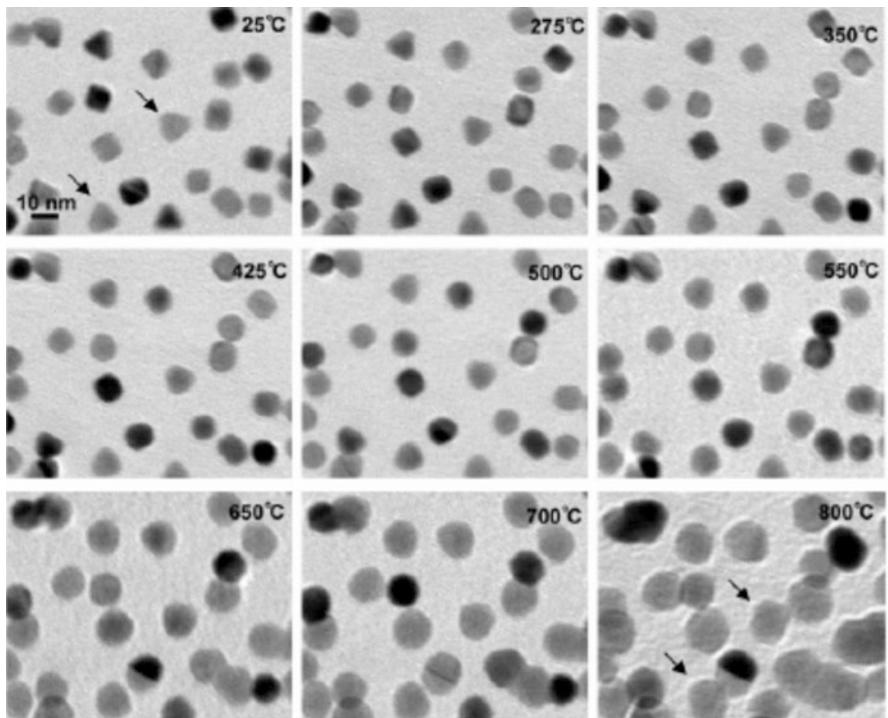
Fig. 13.8 Micrographs from TEM of the Pt/SiO_2 in situ treatment with increasing temperature, cubic and tetrahedral particles (Wang X., Zhuang J., Peng Q., Li Y., Nature, vol. 437, pp. 121–124, 2005, reproduced with permission)
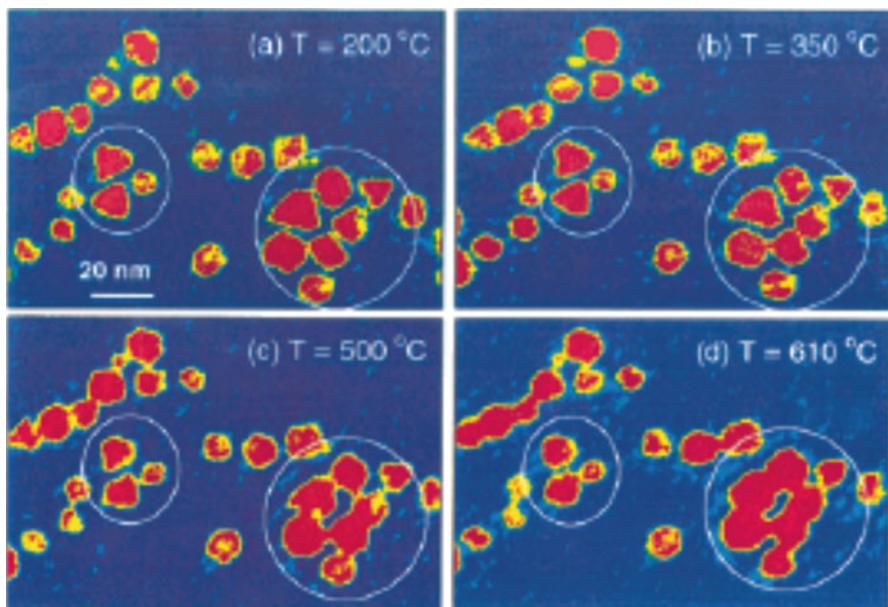
Fig. 13.9 TEM in situ images of Pt nanocrystals at different temperatures (El-Sayed M. A., Acc. Chem. Res., vol. 34, 257–264 (2001) reproduced with permission)

crystalline structure. The fusion at 600 °C becomes clear, leading to coalescence of the particles. Authors also observed differences in the stability of the different morphologies and concluded that the tetrahedral particles were the most stable, followed by the cubic and the triangular shapes [8, 16].

The regions marked with small circles represent changes of shape, and nanocrystals marked by large circles represent the merger of the crystals of the group. The blue color represents the background of the substrate, red the approximate projection of higher atomic density region of Pt, and yellow the projection of lower atomic density [8, 16].

13.1.4   Metal Nanostructures [8, 17–53]

Clusters, grains, lamellar structures, or filaments with dimensions smaller than 10 nm can be considered as nanostructured materials. These systems present a high ratio of surface area and volume with singular properties. In catalysis, changes in the surface and bulk electronic structure, caused by nanostructuring, may influence the reactivity, causing it to differ substantially from the conventional systems. Therefore, structure-sensitive reactions are strongly influenced by particle sizes

and, thus, on the method of preparation of the supported metal catalyst [30, 54], for example, in the FT synthesis, using Fe/SiO$_2$.

Nanoparticles of Pd supported on Al$_2$O$_3$ were synthesized by Okitsu et al. [55] using as precursor $(PdCl_4)^{2-}$. The authors claim that the particles supported were first nucleated as reduced Pd species, followed by growth in the solution, and finally anchoring on the support. Compared to the conventional impregnation method of preparation, the activity for hydrogenation was 20 times better.

Colloidal Method

Miyazaki et al. [56] prepared Pt nanoparticles using *colloids* with different morphologies, using K$_2$PtCl$_4$ in the presence of hydrogen and three different stabilizers, and obtained nanocrystallites of average diameters of 6.13 nm, 13.6 nm, and 13.6 nm, using also polyvinylpyrrolidone (PVP) polymer, poly(*N*-isopropylacrylamide polymer) (PNIPA), and sodium polyacrylate (SPA), respectively. As observed, there are great differences between particle sizes and morphologies. Duteil et al. [57] synthesized nickel particles stabilized by colloidal phosphines from Ni (acac) 2 (nickel acetylacetonate, C$_{10}$H$_{13}$NiO$_4$) in diethyl ether solutions using diethyl aluminum hydride as a reducing agent at -40 °C and obtained particles with an average diameter of 4 nm order. Miyazaki et al. [56] obtained particles on the order of 7–15 nm, using polyvinylpyrrolidone (PVP), poly(*N*-isopropylacrylamide) (PNIPA), and sodium polyacrylate (SPA), as stabilizers, respectively, as shown in Fig. 13.10.

Besides the difference between the observed particle sizes, its shape was greatly altered. Figure 13.10 gives the morphology of the synthesized materials [56].
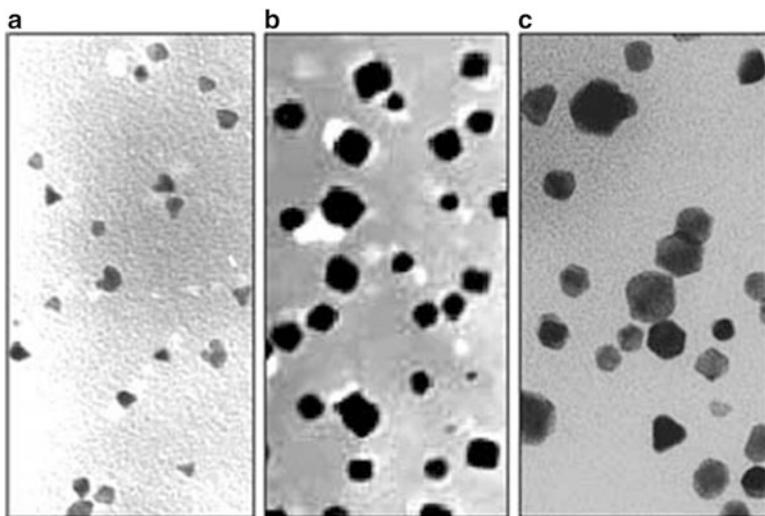
Fig. 13.10 Pt nanoparticles using different stabilizers (Miyazaki A., Balint I., Nakano Y., J. Nanop. Res., vol. 5, pp. 69–80, 2003, reproduced with permission)
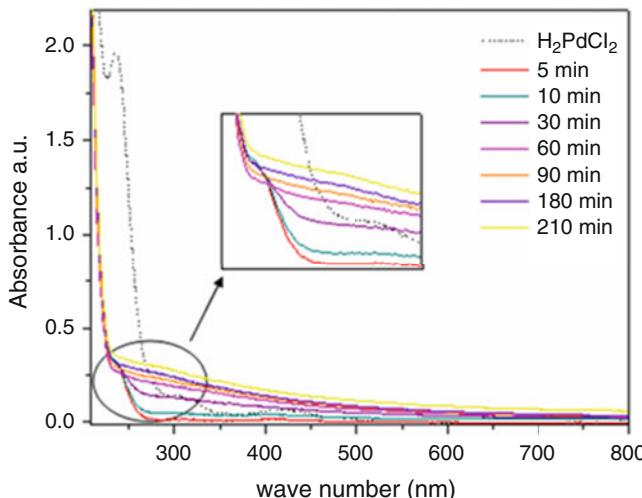
Fig. 13.11 UV–Vis spectra during reduction of Pd forming colloidal solution [17]

The Pd catalysts supported on α-Al_2O_3 using the colloidal method was also prepared by the colloidal method. The reduction of transition metals with ethanol is a widely used method for producing colloidal nanoparticles. In this process, ethanol acts both as a solvent and as a reducing agent. During the reduction, the alcohol is oxidized to aldehyde, yielding acetaldehyde. The reduction of Pd to the formation of the nanoparticles was monitored by spectroscopy in the UV–Vis region, which showed a rapid decrease of the concentration of Pd^{+2} ions from the solution as a result of the reduction process for the formation of the metal colloid. The solution prior to refluxing showed pale yellow color with a peak in the UV–Vis spectrum at 235 nm, a band that can be attributed to absorptions for the transfer of load from the binder metal ions $[PdCl_4]^{2-}$, as shown in Fig. 13.11. It was also observed by the color change from pale yellow to brown solution [19, 29].

The solution was analyzed by transmission electron microscopy, and the results are shown in Fig. 13.12. It was found in this case that the synthesis has led to obtain a solution having a large size distribution with dimensions ranging between 2 nm and 20 nm. The particles have not yet submitted various morphologies; particles were found from so close to spherical and even cubic tetrahedral triangular with maximum size limited to less than 20 nm, due to the action of the stabilizing polymer.

This solution was impregnated on α-Al_2O_3 and submitted to the usual pretreatment conditions. During the impregnation process and drying, the stabilizer was not decomposed, being submitted to calcination to remove the PVP, such that the metal is located at the external surface of the support. Figure 13.13 shows the images of the sample after calcination and reduction. There is a tendency of aggregating particles on the surface. This behavior is frequently seen on highly

Fig. 13.12 Micrograph of a colloidal solution of palladium [11]
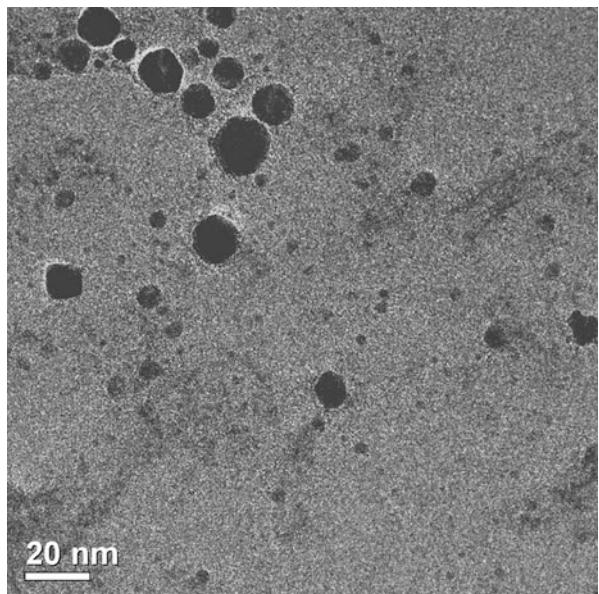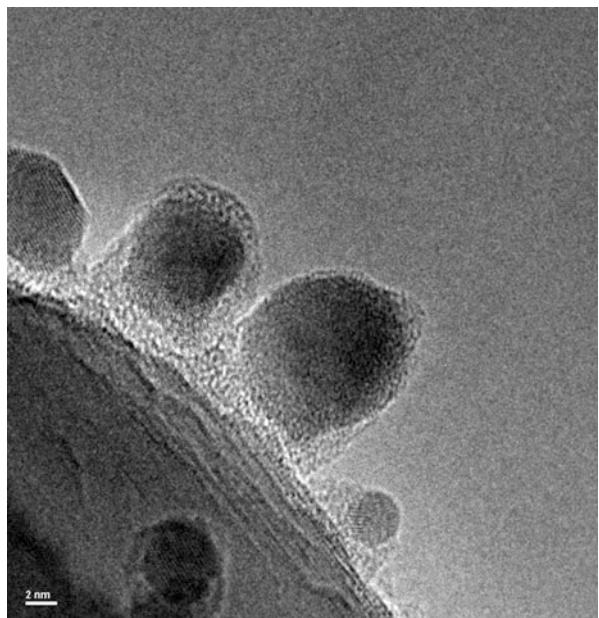
Fig. 13.13 Micrograph of TEM image of the palladium catalyst after calcination and reduction. Scale bar, 2 nm [18]

dispersed metal particles, because in nanometric scale the surface energy is high and tends to aggregate, decreasing the total energy. It is possible to see a trend of clustering of the particles on the surface of alumina. These clusters are made up of several metallic particles down to 10 nm.

Sonochemical Method

The *sonochemical* term is used to describe the use of ultrasound as a preparation tool. Ultrasound makes up a region of the electromagnetic spectrum between the frequencies of 20 kHz to 1000 MHz.
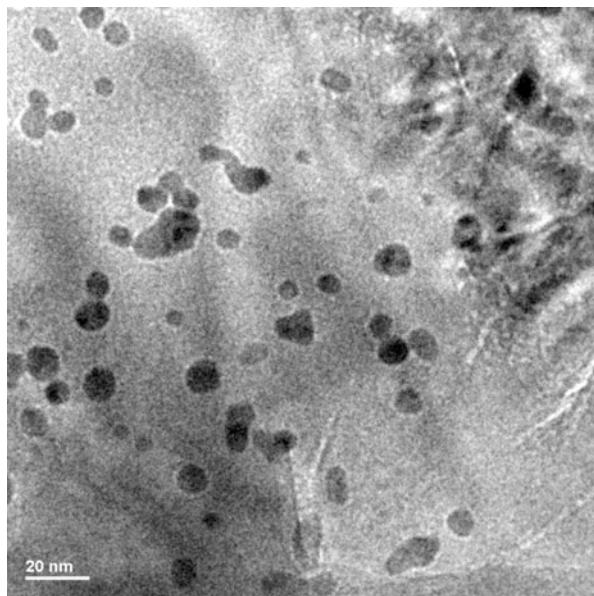
The synthesis of nanostructured inorganic materials by sonochemical had already been synthesized a large number of nanostructures of different compositions with comparable or better than the properties of the same when summed with other preparation methods. The versatility of this method also extends to the relative flexibility of reaction conditions such as the nature of the precursors and their solutions, the possibility of addition of auxiliaries, and the presence of "traps" (species immobilized) to the nanoparticles. All types of metallic nanostructured materials synthesized by *sonochemical* described (powders, colloids, or nanoparticles supported) can also be obtained for other classes of compounds such as oxides [58–60], sulfides [61], Suslick [20, 62], and more recently selenides [63, 64] and tellurides [65].

The acoustic cavitation phenomenon is responsible for disturbances caused by the components of a liquid medium during sonication. This phenomenon is the formation, growth, and implosive collapse of microbubbles associated with the propagation of sound waves in the liquid medium. The sound is transmitted via a fluid like a wave alternated with periods of compression and rarefaction. Cavitation is a result of the overlap of the sinusoidal sound pressure with the constant pressure of the medium. During periods of negative pressure (rarefaction wave period), the expanding gas is dissolved in solution (and volatile components) for the formation of microbubbles. The growth of the bubble extends to a distance many times greater than their nucleation radius. When its maximum distance is reached, immediately before the collapsing, the internal pressure becomes lower than the pressure of the liquid medium, resulting in an implosion. At this time, the acoustic pressure amplitude is maximum, the period of bubble compression by the wave sound [66].

The sonochemical method is similar to the precipitation process, using a metal precursor solution (ionic), a reducing agent, and a compound that prevents agglomeration which is a molecular stabilizer and/or a support.

Okitsu et al. [55], carried out the sonochemical synthesis of crystalline nanoparticles of Au, Ag, Pd, and Pt stabilized with polyethylene glycol monostearate (MS-PEG), sodium dodecyl sulfate (SDS, $NaC_{12}H_{25}SO_4$), and polyvinylpyrrolidone (Okitsu 1996a, b) [233, 234]. The metal particles were produced from 5 nm order and are stable for months.

Fig. 13.14 TEM images of
Pd/α-Al$_2$O$_3$ prepared by
sonochemical method.
Scale bar, 20 nm [18]

The synthesis in the presence of inorganic supports (such as silica and alumina)
gives rise to highly active heterogeneous nanostructured catalysts [20, 55, 67, 68].
The precursors may be inorganic or organometallic.
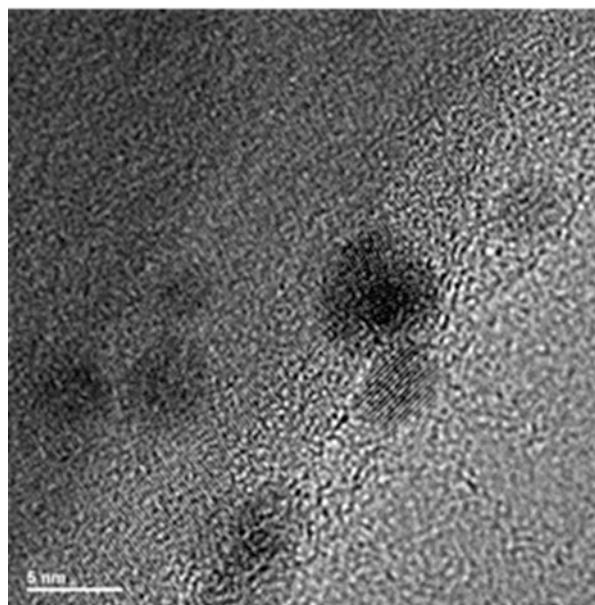
TEM images were obtained for the supported Pd/α - Al$_2$O$_3$ catalyst (PdSON), as
displayed in Figs. 13.14 and 13.15, showing clusters at the surface with mean size
of 10 nm. Images with higher magnification, Fig. 13.15, show that these clusters are
palladium crystallites with diameters less than 5 nm [18, 29].

Precipitation–Coprecipitation

To further investigate the aforementioned particle size effect, the aim is to develop
a synthesis concept to obtain size-controlled Pd nanoparticles. In this approach,
hydrotalcite-like compounds (HTlcs) are used as well-defined precursor materials,
whose general formula is [M$_{2+1-x}$ M$_{3+x}$(OH)$_2$] (An-)x/n.mH$_2$O [2, 3]. In general,
the flexibility of the choice of metal ions is quite high, and all cations in the
range of 0.5–0.8 Å, such as M^{2+} = Mg^{2+}, Mn^{2+}, Co^{2+}, Ni^{2+}, Cu^{2+}, Zn^{2+} and
M^{3+} = Al^{3+}, Ga^{3+}, Fe^{3+}, Cr^{3+}, are capable of HTlc formation [69]. Divalent and
trivalent metal cations are incorporated in brucite-like layers, and between these
positively charged layers, charge-balancing anions, typically carbonate, maintain
the electroneutrality of the lattice. Furthermore, the M^{2+}/M^{3+} ratio can be varied
from approximately 0.2 to 0.4 to gain phase-pure materials.

Upon heating, HTlcs decompose into mixed oxides exhibiting high specific
surface area, homogeneous metal distribution, and strong interaction between the
individual elements. During reduction in H$_2$, noble metals such as Pd segregate out
of the mixed-oxide matrix to form well-defined nanoparticles, whose size tends to
depend on metal loading. PdMgAl hydroxycarbonates have already been studied by

Fig. 13.15 TEM images of higher magnification of the Pd/α-Al$_2$O$_3$ prepared by sonochemical method. Scale bar, 5 nm [18]

several groups and were found to be active in phenol hydrogenation, oxidation of toluene, acetone condensation, hydrodechlorination of 1,2,4-trichlorobenzene, and total oxidation or coupling of methane [19, 25, 27].

The PdMgAl HTlcs can be synthesized by controlled coprecipitation at pH = 8.5 and a temperature of 55 °C, by co-feeding appropriate amounts of mixed metal nitrate and sodium carbonate solutions. A sodium carbonate solution was used as precipitating agent. Both solutions were added simultaneously dropwise, as described elsewhere [19]. Transmission electron microscopy (TEM) images of Pd nanoparticles were acquired using a FEI TITAN microscope as displayed in Fig. 13.16.

After reductive treatment, the material has preserved the platelet-like morphology of the HTlc precursor, and small spherical particles were formed. HAADF-STEM micrographs were used to determine the particle size distribution. The good contrast between the metallic particles (white spots in Fig. 13.16b) and the MgO/MgAl$_2$O$_4$ support allowed for measuring of individual particles. It can be clearly seen that the particles are well dispersed and below 5 nm in size. Particles even smaller than 1 nm are also present. HRTEM images (Fig. 13.16c) show the presence of small Pd metal particles on the surface of the disordered oxide support. The average particle sizes of ≤3.5 nm are quite small considering the thermal treatment at 500 °C. Thus, some control over the particle size distribution of Pd is possible using the HTlc precursor approach for the preparation of supported Pd nanoparticles. The more the Pd^{2+} ions are diluted in the precursor lattice, the smaller the resulting Pd metal particles are after thermal reduction. These particles are thermally stable up to 500 °C and their size can be controlled to some extent
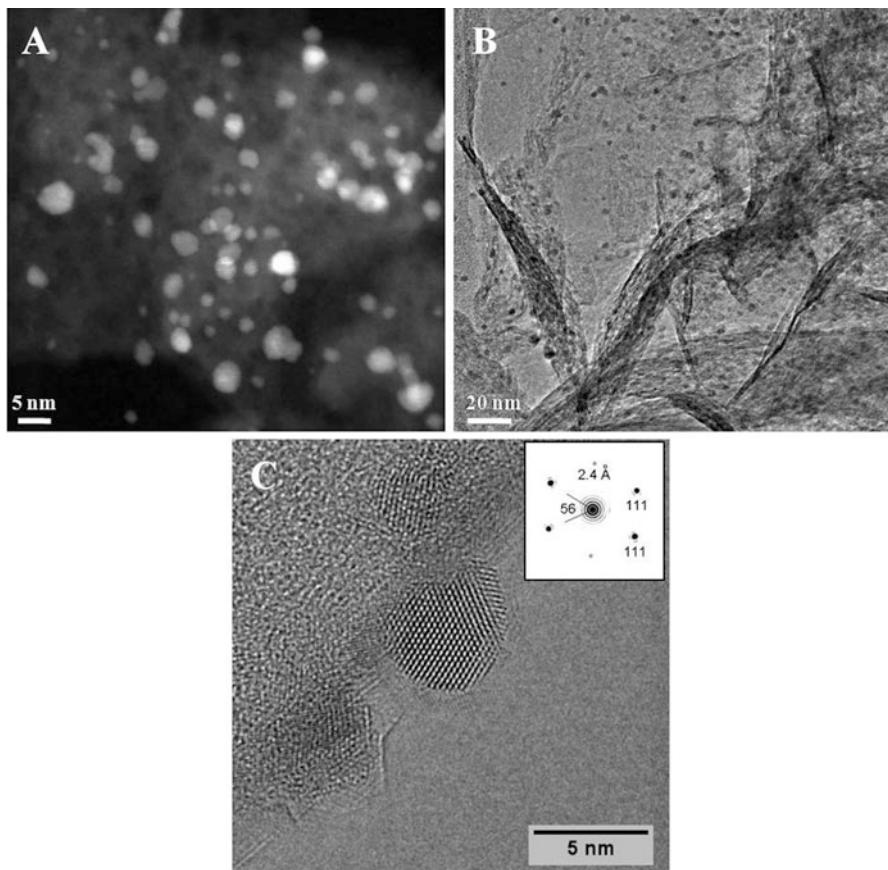
Fig. 13.16 (**a**) HAADF-STEM, (**b**) overview micrograph, (**c**) HRTEM of metallic Pd supported on MgO/MgAl$_2$O$_4$ (2.5 mol% ex-PdMgAl is shown) (Reproduced with permission from Moya et al., Applied Catalysis A: General 411–412 (2012) 105–113, 15)

between < 1.13 and 3.5 nm by adjusting the Pd content during synthesis (Fig. 13.17).

The sample with the lowest Pd loading of 0.33 wt% shows a much higher Pd dispersion compared to those samples with Pd contents between 1.5 and 8 wt%.

Activity Tests

In catalysis, there are also some examples of the dependence of activity and selectivity with the particle size and morphology of the active phase of the catalysts.

Iron catalysts supported on silica were synthesized by Suslick et al. [20]. The Fe / SiO$_2$ catalysts amorphous nature and particle size in the range 3–8 nm and were submitted to catalytic tests Fischer–Tropsch reactions, and their activities were compared with those of a catalyst Fe / SiO$_2$ prepared by dry impregnation of the
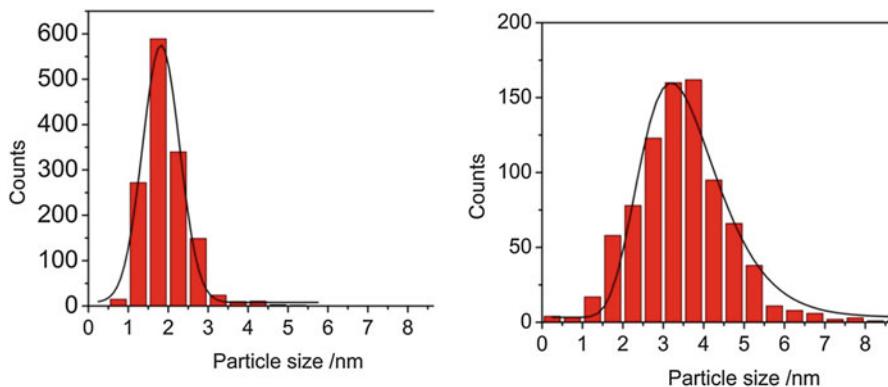
Fig. 13.17 Particle size distribution of Pd05 (**a**) and Pd25 (**b**) from TEM images [19]
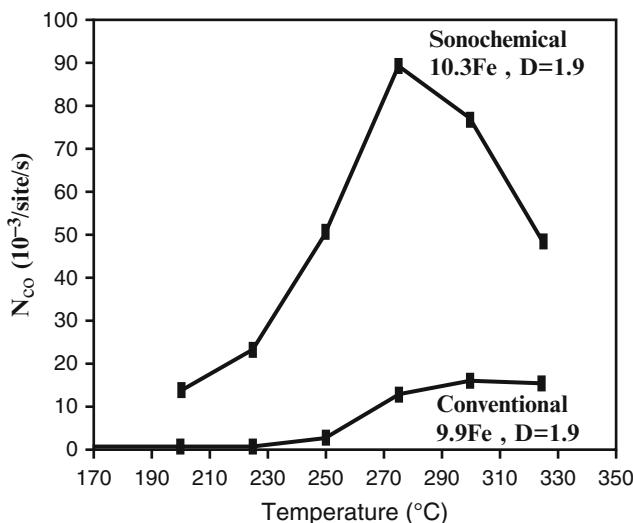
Fig. 13.18 Activity of Fe/SiO$_2$ for the Fischer–Tropsch reaction; sonochemical versus impregnation method preparation (Adapted with permission from Suslick et al., Mater. Sci. Eng. A, vol. 204 (1995) pp. 186–192)

same dispersion. The results of the activity as a function of temperature can be seen in Fig. 13.18.

El-Sayed and Narayanan [70, 71] observed that colloidal Pt catalysts have different rates for electron transfer reactions between ions and thiosulfate ferrocyanide. Kinetic studies were carried out, and the results were compared to the number of surface atoms in the vertices and edges of the nanocrystal structures for three different morphologies: cubic, tetrahedral, and spherical (the authors used the approach of cube–octahedral geometry for the calculation of the number of
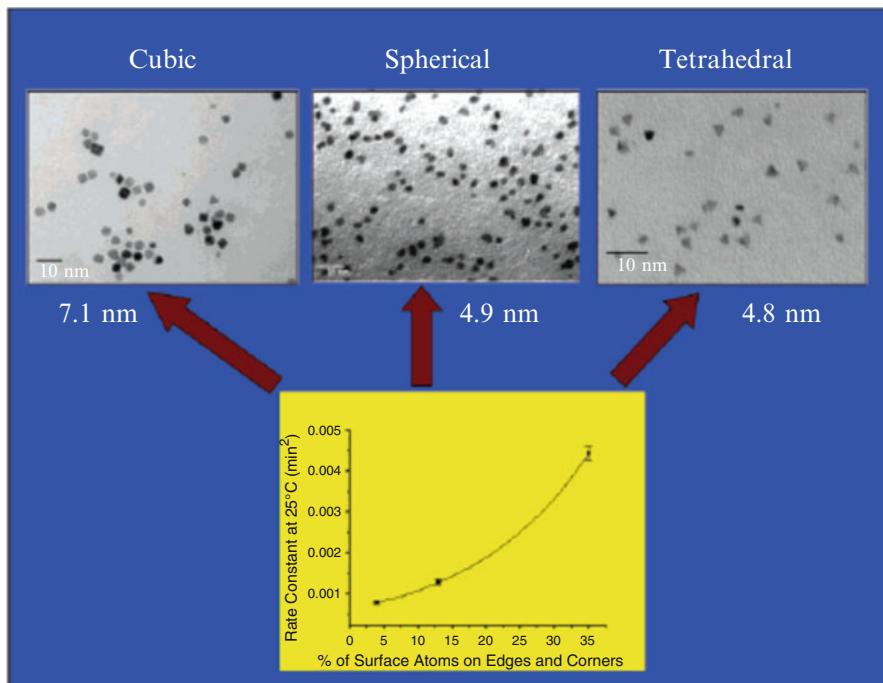
Fig. 13.19 Correlation of the catalytic activity with the fraction of surface atoms on surfaces and vertices (Narayanan, R., El-Sayed, M. A., J. Phys. Chem. B, vol. 109, 2005, 12663–12676, reproduced with permission)

sites, since these are, in fact, nearly spherical). The number of sites they occupy positions described interest can be obtained since characterized the exposed surfaces of the nanocrystals.

The plot of specific rate constant or activity versus percentage of surface tetrahedral atoms suggests that catalytic particles are the most active, followed by spherical and cubic, respectively (Fig. 13.19). This behavior shows a direct dependency of the activity to the amount of highly reactive sites. These results were corroborated with the determination of the reaction activation energy, which followed the order Pt tetrahedral Ea < Ea spherical Pt < Ea Pt Cubic.

13.1.5 *Oxide Nanocrystals [18, 19, 24, 44, 51, 53, 63, 72–152]*

Practices lead to the formation of nanocrystals with a wide range of sizes and shapes displaying a distribution of surface sites capable of promoting many different reactions. No molecular control on the nature of the active sites is expected, and only limited control on the selectivity of reactions can be achieved. Controlling the

size of the nanocrystals used for catalysis can lead to huge changes in catalytic behavior. The importance of nanocrystallites and nanostructure to the performance of catalysts has stimulated wide efforts to develop methods for their synthesis and characterization, making this area of study an integral part of nanoscience [73]. Fortunately, metal nanoparticles can now be made with quite narrow size distributions by using, besides others, colloidal- [52] or dendrimer [53]-based chemistry. The morphology of these materials depends on the synthesis conditions and has been described by different authors as nanotowers, nanocone, nanobottle, nanoflowers, nanoarrows, nanorod, nanowires, and so on. The challenge is to disperse the colloidal nanoparticles on high surface area supports and to activate them without losing the original size and shape distribution. As a matter of fact, the control of the morphology of the nanoparticles, perhaps, seems to be more important than monitoring the performance of catalysts by controlling the size of the nanoparticles of the active phase. It has been known that some catalytic processes are structure sensitive, meaning that their activity or selectivity changes significantly with the method used for the catalyst preparation [73].

Cerium Oxide Nanocrystals

In the first example, we investigated the CeO_2 and CeO_2-based materials. The higher performance of cerium oxide is assigned to the redox property $(Ce^{4+} \leftrightarrow Ce^{3+})$ promoting oxygen vacancies in the lattice, which are responsible for the high oxygen atom mobility. This is one of the important characteristics of ceria, allowing fluctuation between oxidant and reductant conditions due to the oxygen storage capability in the lattice structure [122]. However, Zhu and He [124] observed that pure CeO_2 is poorly thermostable and loses easily oxygen at high temperatures. Therefore, many authors added other metal ions or dopants to increase the stability and oxygen capability storage. The substitution of Ce^{4+} by dopants favored the reduction of the oxidation state of the Ce^{4+} to Ce^{3+} that maintains neutrality in the lattice and reduces the link stress bonding, depending on the dopant cation, which indeed favors the formation of new oxygen vacancies [115, 116, 125].

Different methods were used for the preparation of nanosized materials. CeO_2 is prepared by the precipitation and hydrothermal methods [126, 127]. The crystallite sizes are quite different depending of preparation methods [92]. These oxides present different oxidation states and evidence the presence of oxygen vacancies.

The EPR spectra are shown in Fig. 13.20 displaying signals between 3500 and 3600 Gauss attributed to the paramagnetic centers with axial symmetry $g\perp$ and $g\parallel$ associated to the Ce^{3+} cation (ion 4f1) with unpaired electrons [143, 144]. This signal is related to the Ce^{3+} cation. The intensity band may be associated to concentration of these species. Indeed, the oxygen vacancies are related to the reduction ability of the cation Ce^{4+} to Ce^{3+}, according to Adamski et al. [145], Wang et al. [146], and Appel et al. [147] as follows:

$$2\,Ce^{4+} + \; O^{2-} \; \leftrightarrow \; 2\,Ce^{3+} + \; V_O + \; \tfrac{1}{2}\,O_2 \qquad (13.2)$$
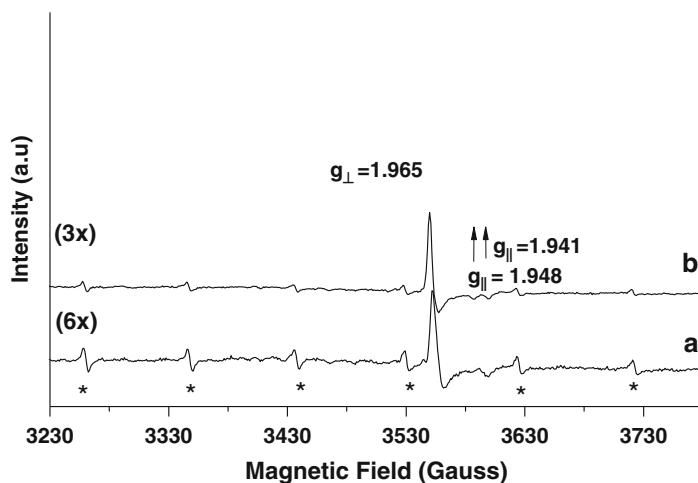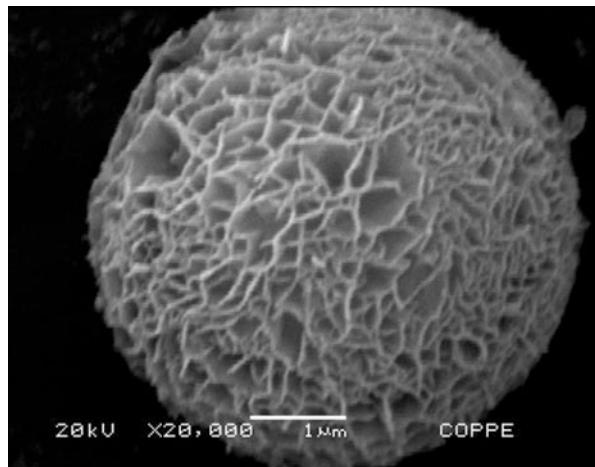
Fig. 13.20 EPR spectra of catalysts [115]

Fig. 13.21 SEM images of the CeO$_2$ (Flowerlike) [115]

where the ion O^{2-} is present in the lattice of ceria and V_O is the oxygen vacancy double charged with protons. This equation suggests that Ce^{3+} can be correlated to the concentration of the oxygen vacancies. Therefore, it also reveals strong defects in the crystalline lattice.

SEM observations displayed in Fig. 13.21 show that the CeO$_2$ flowerlike sample is nicely porous material with intercalated structured framework shapes.

Nickel Nanocrystals

In the second example, we prepared nickel nanocrystals with different morphologies which were synthesized by different methods:
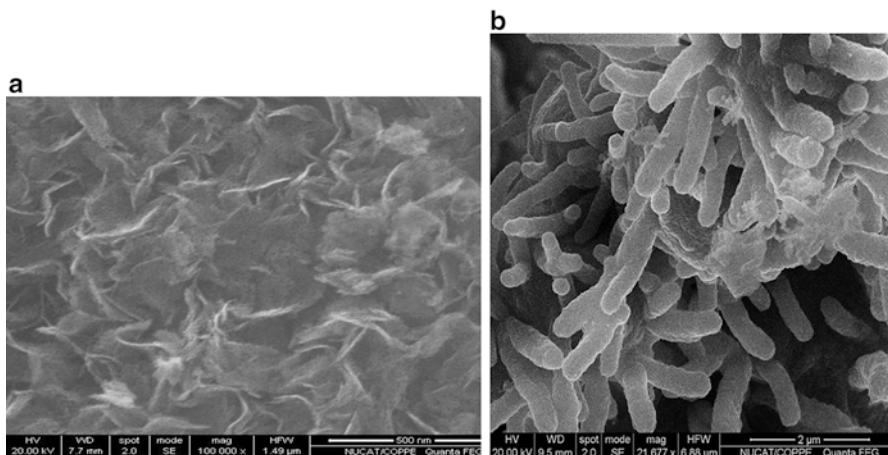
Fig. 13.22 SEM images of the NiEG sample (**a**) in oxide form: 100,000×; SEM images of the NiDMG sample (**b**) in oxide form, 20,000× [73]

- Precipitation of nickel hydroxide with sodium carbonate precursor salts dissolved in ethylene glycol (NiEG), according to Li et al. [83]
- Precipitation of nickel dimethylglyoxime as precursor (NiDMG), according to Ni et al. [84].
- NiO was obtained after hydrotreatment and calcination of β-$Ni(OH)_2$ precursor (NiHT), according to Zhu et al. [85].

Figure 13.22 shows a nanoflower-like-type morphology in tridimensional form of NiO on the NiEG sample before the reaction. This morphology was originally observed on the hydroxide before calcination and seems to be very stable after thermal pretreatment; thus removing water did not damage the structure of the precursor. The structure did not collapse or fracture, which can be attributed to the excellent contact between nanoparticles with high orientation degree [83].

Figure 13.22b shows SEM images of NiO after calcination of the NiDMG precursor, indicating the presence of bidimensional rods, which suggests made up of small particles that gather forming rods. By removing the organic molecule (DMG) during heating, the arrangement of the structure of the precursor NiDMG was not affected, and according to [87], heating probably supplies energy to maintain the NiO nanoparticles highly oriented in the structure.

The Combustion Method

The combustion method has been proposed to synthesize nanosized crystallites and is particularly useful in the production of ultrafine ceramic powders with small average sizes. This is an easy and fast method, with the advantage of using inexpensive precursors, producing homogeneous nanosized crystallites, and highly reactive materials [101]. The combustion synthesis technique consists of the contact of a saturated aqueous solution of a desired metal salt and a suitable organic

fuel boiling until the mixture ignites and a self-sustaining and fast combustion reaction takes off, resulting in dry crystalline fine oxide powder (Patil) [102, 103]. The large amount of gases released during the reaction produces a flame that can reach temperatures above 1000 °C. Kingsley et al. [105] described the preparation of aluminates with various metal nitrates (Mg, Ca, Sr, Ba, Mn, Co, Ni, Cu, and Zn) using urea or carbohydrazide as fuel. The fuel/oxidizer ratio was evaluated by Alinejad et al. [107] in the combustion synthesis of $MgAl_2O_4$ by using sucrose and PVA solution as fuels.

Nickel aluminate ($NiAl_2O_4$) is a good example of a mixed cation oxide with normal spinel structure, where Al occupies the octahedral sites and Ni occupies the tetrahedral sites [98, 113]. It can be used as support for catalysts due to its resistance to high temperatures and acidic or basic environments, providing chemical and physical stability for the catalyst.
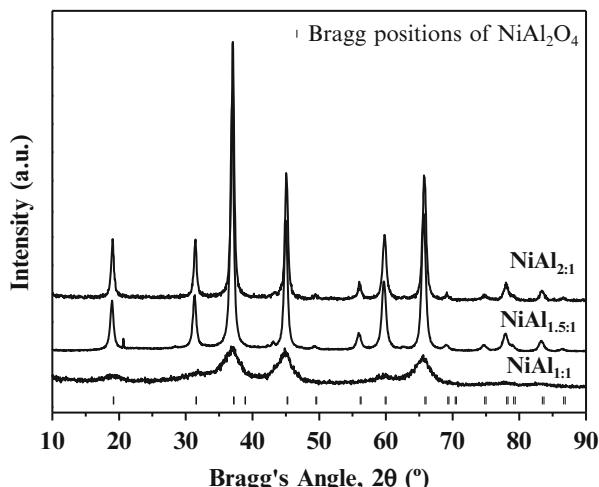
$NiAl_2O_4$ is prepared by the combustion method using urea as fuel. The stoichiometric ratio of urea to nitrate (U/N) needed to obtain $NiAl_2O_4$ powders is 2.2, assuming complete combustion, according to reaction 1 [94]:

$$3Ni(NO_3)_2 + 6Al(NO_3)_3 + 20CO(NH_2)_2$$
$$\rightarrow 3NiAl_2O_4 + 32N_2 + 20CO_2 + 40H_2O \qquad (13.3)$$

The use of a stoichiometric U/N ratio resulted in a material with high surface area and homogeneous nanocrystallites, while the excess of fuel resulted in a nonporous material with low surface area.

X-ray diffractograms of the samples (Fig. 13.23) presented only a $NiAl_2O_4$ cubic spinel-type structure (JCPDS 10-0339). All samples showed mean crystallite nanosizes. The crystallite size is strongly dependent on the fuel/oxidant ratio, which increases with increasing urea loading. Nanosized crystallites of $NiAl_2O_4$

Fig. 13.23 XRD patterns of the samples NiAl (1:1), NiAl (1.5:1) and NiAl (2:1) [94]

were obtained by Han et al. [98, 113] applying the sonochemical method, but with very poor crystallinity.

The NiAl: (1:1) catalyst showed a high surface area (186 m^2/g), similar to that reported in the literature, when using an expensive alkoxide precursor and a very long preparation time by the sol–gel method [96, 100, 111, 114]. The NiAl: (1:1) presented also unimodal pore size distribution in the range of 3–6 nm and pore volume of 0.18 mL/g, indicating mesoporous materials. On the contrary, the samples with excess of urea, NiAl: (2:1), presented lower surface area (10 m^2/g) and nonporous material crystallite sizes of 13.2 and 16.6 nm, respectively. Nanosized crystallites of $NiAl_2O_4$ were obtained by Han et al. [98, 113] applying the sonochemical method, but with very poor crystallinity.

These results can be explained mainly through the flame temperature that was reached during the preparation. The combustion process with excess of urea caused a slower ignition of the reactant mixture, and the maximum temperature was much higher. The NiAl: (1:1) sample showed maximum peak at 1318 °C with an ignition time of 86 s, while the NiAl: (2:1) samples shifted the peaks to 1237 °C and ignition of 164 s. These results show that the excess of urea favors complete combustion during the synthesis, accompanied by the evolution of a large amount of gases, which contributes to the formation of materials with good crystallinity. However, agglomeration occurred at higher temperature, lowering the surface area, increasing average crystallite sizes and forming nonporous materials [94].
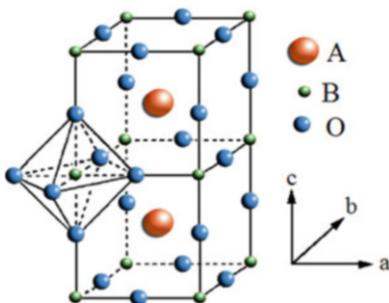
13.1.6 Mixed Oxides: Perovskite Structures Perovskites

The perovskite-type oxides have unique characteristics in response to a wide range of properties that are assigned to the cation substitution capacity in its structure, generating isostructural solid with formula $A_{1-x}A_{x'}B_{1-y}B_{y'}O_{3\pm\delta}$. These substitutions can lead to the stabilization of the structure with an unusual oxidation state for one of the cations and the creation of anionic and cationic vacancies. This has a significant influence on the catalytic activity of these materials compared to the typical supported materials. Another important feature is the thermal stability of these materials and mechanical and chemically stable reaction conditions [41, 148].

The ternary oxide of perovskite type can be divided into $A^{1+}B^{5+}O_3$, $A^{2+}B^{4+}O_3$, and $A^{3+}B^{3+}O_3$. The former is of particular interest because of their ferroelectric properties, e.g., $KNbO_3$ and $NaNbO_3$ e $KTaO_3$; $A^{2+}B^{4+}O_3$ probably forms the largest number of perovskite-type oxides, in which the cation may be an alkaline earth, cadmium, and lead, and B^{4+} includes Ce, Fe, Ti, Zr, Mo, and others. Finally, $A^{3+}B^{3+}O_3$ includes several compounds such as $LaCrO_3$, $EuFeO_3$, $LaCoO_3$, etc. [153].

The ideal structure of a perovskite-type oxide is cubic, space group *Pm3m-Oh*, and A, a cation of large size coordinated to 12 oxygen ions, while B is a smaller cation coordinated to six oxygen ion. Schematically, Fig. 13.24 shows a unit cell

Fig. 13.24 Ideal structure of perovskite ABO_3: the cation in the center of the unit cell; cation B in the center of an octahedron whose vertices are oxygen anions (Adapted from Fierro JLG, Peña MA. Chem Rev. 2001;101:1981–2018, [41])

ABO_3, where the A cation occupies the center of the cube; cations are located at the vertices B, and oxygen anions are centered on the edges of the cube. Alternatively, the structure can be displayed with the B cation occupying the center of an octahedron formed of oxygen vertices, which in turn would be inside a cube whose vertices are the A cations.

For measuring the deviation from ideality of the cubic structure ABO_3, Galasso [153] defined the tolerance factor t, according to Eq. (1). While in the ideal structure the atoms are in touch, this factor is calculated from the interatomic distances A_O and B_O, respectively, defined as $(r_A + r_O) = a/\sqrt{2}$ and $(r_B + r_O) = a/2$, which corresponds to cubic unit cell parameter.

$$t = \frac{(r_A + r_O)}{\sqrt{2}(r_B + r_O)} \tag{13.4}$$

The ideal cubic perovskite has a tolerance factor t equal to 1 and, only in some cases, approaches this factor at high temperatures. Most compounds present distortions, and the factor varies: $0.75 < t < 1.0$. However, when the tolerance factor is extrapolated beyond this range, the structure is no longer a perovskite and presents other structures, such as, limonite, calcite, and aragonite.

Besides the size of the ionic radii of A and B, there is another condition for the formation of a perovskite structure, which is electroneutrality; the sum of charge of cations must be equal to the sum of oxygen anion charge [41]. In heterogeneous catalysis, the most studied systems are those with an alkali element or alkaline earth lanthanide in position A, and a transition metal of the first set in position B (Ti, V, Cr, Mn, Fe, Co, Ni, Cu).

The structure of ABO_3 perovskite may also be modified by the partial substitution of the atoms of sites A and/or B, forming a new structure of $A_{(1-x)}A_xB_{(1-y)}B_yO_3$, in which x and y represent the degree of substitution. In general, the cation confers thermal and structural resistance, while B is responsible for the catalytic activity. However, the partial replacement of a cation can strongly affect the catalytic activity of B, due to the unusual stabilization oxidation state of this metal and due to the simultaneous formation of structural defects.

In addition, the partial substitution of the cation B can modify the catalytic activity that interferes directly the electronic state of d-orbital, the stabilization energy of the crystal field and the B–O binding energy [154]. The partial substitution represents, therefore, a fundamental tool for obtaining active, selective, and stable materials for various applications.

The nonstoichiometry, which indicates the cation deficiency in the sites A and/or B, as well as of oxygen, is a very common feature of perovskites, different from the ideal structure. In the case of oxygen site, nonstoichiometry obtained by the presence of vacancy is more common than that generated by the cationic vacancies. Therefore, the most common nonstoichiometric structures are those with a relative excess of cations due to anionic vacancies. On the other hand, the excess of oxygen is not common, probably because the extra oxygen introduced in the network is thermodynamically unfavorable.

The presence of vacancies and defects in the structure of the catalyst is largely responsible for the mobility of oxygen within the crystal lattice; the more vacancies, the greater the mobility of oxygen. The ion vacancies affect the catalytic activity to promote or not the adsorption of gas phase reactants [155].

Synthesis of Mixed Oxides Perovskite Type

The synthesis of oxide perovskite type requires a methodology that provides a homogeneous solid, maximizing the specific area. The properties of these systems, such as texture, oxidation state of the cation, stoichiometry, and structure, depend on the synthesis method. For this reason, the literature has reported a series of preparation methods, and in particular the methodologies known as sol–gel have shown promising results allowing excellent control over the properties of the synthesized perovskites.

The sol–gel technique is one of the most popular processes for powder synthesis, films, fibers, monoliths, and other materials used in engineering. It basically involves the formation of an inorganic and/or organic network via a chemical reaction in solution, generally at low temperature, followed by the transition from solution to a *colloidal sol* and a *multigel*. According to the different precursors employed, the sol–gel techniques are classified as follows:

1. Sol–gel route based on the hydrolysis–condensation of metal alkoxides
2. Chelate gel route, which is the concentration of aqueous solutions and involving chelated metals
3. Polymerizable compound route (PCR) based on the use of metal salts such as precursors, citric acid, and ethylene glycol as a chelating agent such as polyesterification

The latter route is also known as the Pechini method and has been used to prepare multicomponent metal oxides with a high homogeneity [43]. In short, the route of the polymerizable compound (PCR) process combines the formation of metal complexes and organic in situ *polymerization*. The schematic representation of this process is illustrated in Fig. 13.25.
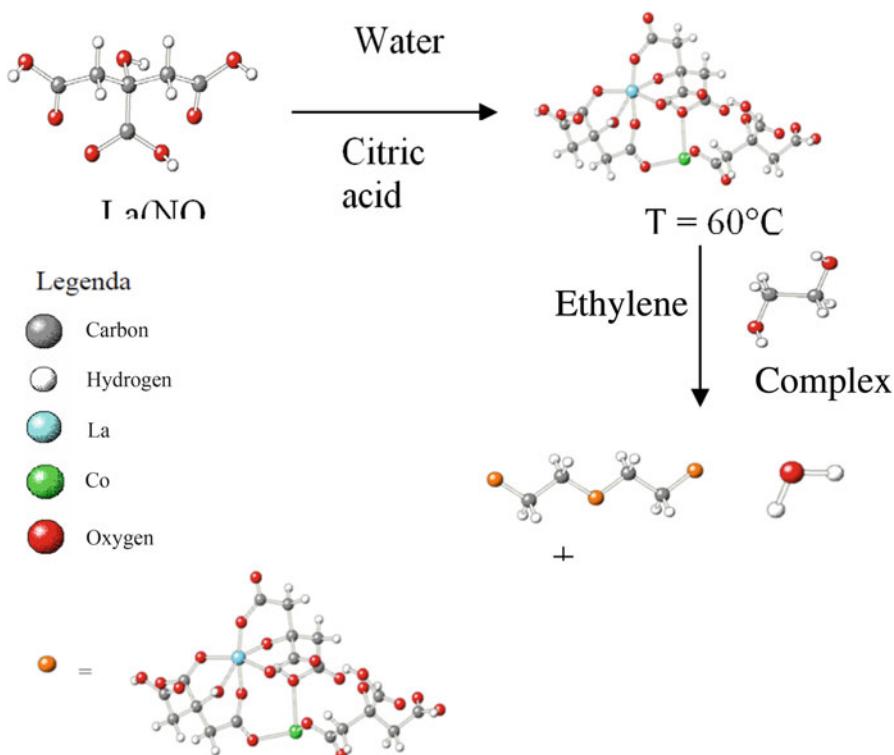
Fig. 13.25 Synthesis of LaCoO$_3$ perovskite: Pechini (Adapted from [156])

Usually an α-hydroxy-carboxylic acid, e.g., citric acid, is used to form chelates with the metal cations from the salt precursor. In the presence of a polyhydroxy alcohol, e.g., ethylene glycol, these chelates react with the alcohol to form ester and water as products. When the mixture is heated a polyesterification occurs in the liquid solution creating a homogeneous *colloidal solution* (sol), in which ions are uniformly distributed in the organic polymer matrix. Upon removal of the solvent, an intermediate resin is formed. Finally, the oxide structure is obtained by removal of organic substances by means of calcination [157].

The resin produced by PCR contains a large amount of organic material that must be totally eliminated for obtaining the perovskite. In this sense, the thermogravimetric analysis is performed in order to identify the sample decomposition temperature and thus can be properly infer the calcination temperature of the polymeric precursor.

Popa et al. [158] compared the synthesis of the perovskite LaCoO$_3$ by *PCR* with the *non-polymerizable* route, using citric acid as a complexing agent, without the use of ethylene glycol (also known as the amorphous citrate method). According to the X-ray diffraction results, the materials prepared by the amorphous citrate method showed some minor unidentified diffraction peaks, in addition to LaCoO$_3$
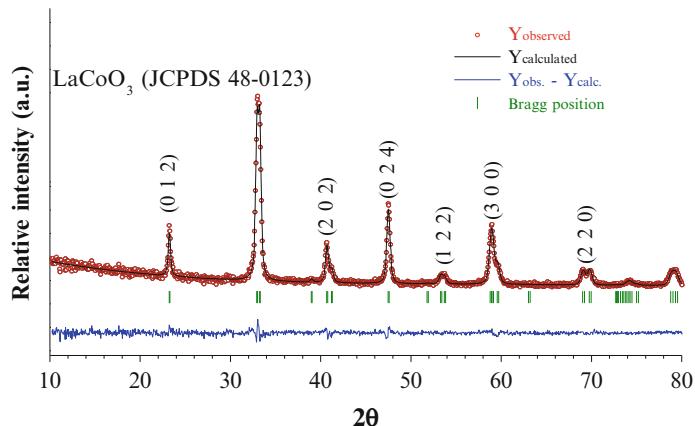
Fig. 13.26   Diffractogram of $LaCoO_3$ perovskite (JCPDS48-0123) [44]

phase for samples calcined at $T = 600$, 650 and 700 °C. Moreover, catalyst synthesized by PCR appeared pure perovskite phase after calcination even at $T = 1300$ °C.
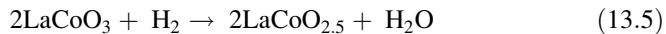
The XRD pattern of the calcined perovskite mass at 700 °C is shown in Fig. 13.26. The peaks relating to the main crystallographic planes are identified with their Miller indices [44].

The crystallographic parameters were used in the calculation of the average crystallite size resulting in 24.2 nm.
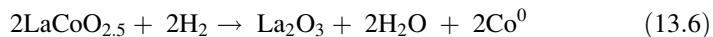
The active phase of the catalyst is obtained after the reduction of $LaCoO_3$ precursor. The appropriate reduction allows obtaining metallic cobalt catalyst (Co) dispersed in a matrix oxide La_2O_3, which confers structural stability to the material [159].

The reducibility of the perovskite $LaCoO_3$ is performed by temperature-programmed reduction and allows investigating the reduction degree. The TPR profile of this sample is shown in Fig. 13.27 and presents two reduction peaks at around 270–490 °C and 500–700 °C, respectively.

According to Villoria et al. (2011), the peak at lower temperature, centered at 426 °C, is attributed to the reduction of Co^{3+} to Co^{2+} perovskite structure, forming the structure brownmillerite $LaCoO_{2.5}$:

$$2LaCoO_3 + H_2 \rightarrow 2LaCoO_{2.5} + H_2O \tag{13.5}$$

The second peak, centered at higher temperatures, corresponds to the reduction of Co^{2+} to Co^0.

$$2LaCoO_{2.5} + 2H_2 \rightarrow La_2O_3 + 2H_2O + 2Co^0 \tag{13.6}$$
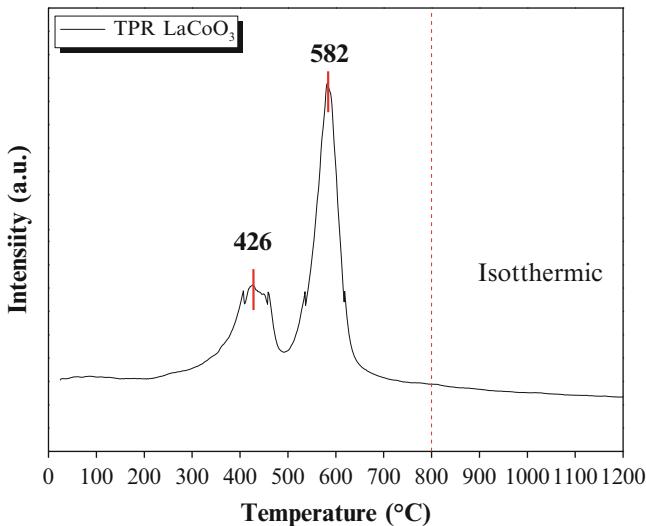
Fig. 13.27   Reducibility of the perovskite LaCoO$_3$ [37]

13.2   Part II: Graphenes

Graphenes are two-dimensional one-atom-thick planar sheet of sp^2-bonded carbon atoms, having a thickness of 0.34 nm, and are well known for electronic, mechanical, optical, thermal, and catalytic systems [5]. It has been used in the development of novel nanomaterials in various applications, such as electronic devices [4, 5, 160–162], nanoelectronics [163], composites [164], electron microscopy substrate materials [165], and catalysis [166]. While these applications have attracted attention of scientists in the nanomaterial area, the realization of potential applications is limited by difficulties in mass production of graphene.

Graphene research has expanded quickly. Andre Geim and Konstantin Novoselov at the University of Manchester won the Nobel Prize in Physics in 2010 "for groundbreaking experiments regarding the two-dimensional material graphene" [4].

Definition: The recent definition of graphene can be given as a two-dimensional monolayer of carbon atoms, which is the basic building block of graphitic materials (i.e., fullerene, nanotube, graphite) [165].

13.2.1   Syntheses of Graphenes

1. *Exfoliation and cleavage*: The mechanical exfoliation is a peeling process generating thin flakes, which are composed of monolayers or few layers of graphene. Chemical oxidation and subsequent exfoliation generate oxide

monolayers and structural defects. However, reduction or thermal treatment is impossible to regenerate graphene. Blake et al. and Hernandez et al. have demonstrated that graphite could be exfoliated in *N*-methyl-pyrrolidone to produce defect-free monolayer graphene [167, 168]. The disadvantage of this process is the high cost of the solvent and the high boiling point of the solvent.

2. *Chemical vapor deposition (CVD)*: In 2006, Novoselov and coworkers synthesized few layers of graphene films by CVD, using camphor as the precursor on Ni foils [169]. This study opened up a new graphene synthesis route. The growth mechanism of graphene on substrates mediates high carbon solubility (>0.1 atomic %) such as Co and Ni [170, 171]. The thickness of the precipitated carbon (graphene layers) is controlled by the cooling rate.

3. *Chemical process route*: This is the most important route to produce graphene for several applications in catalysis and materials, in particular for hydrogen storage in fuel cells and Fischer–Tropsch, recently. Three principal methods are developed by Brodie [172], Staudenmaier [173], and Hummers and Offeman [174], respectively.

Graphite oxide (GO) is usually synthesized through the oxidation of graphite using oxidants including concentrated sulfuric acid, nitric acid, and potassium permanganate based on Hummers method [175]. GO is highly hydrophilic and readily exfoliated in water, yielding stable dispersion consisting mostly of single-layered sheets (graphene oxide). Graphene oxide is a monolayer material produced by the exfoliation of GO. When prepared by sonication, they form homogeneous and stable sheets with uniform thickness. Exfoliation of GO was also attained for *N*, *N*-dimethylformamide (DMF), tetrahydrofuran (THF), *N*-methyl-2-pyrrolidone (NMP), and ethylene glycol [176]. Li et al. showed that the surface charges are highly negative [177]. In fact, the formation of stable graphene oxide was attributed to not only its hydrophilicity but also the electrostatic repulsion.

GO can be reduced to graphene sheets (GNS) by $NaBH_4$ [174], hydroquinone [174] and hydrogen sulfide [167]. Stankovich et al. [168] investigated the chemical reduction of exfoliated graphene oxide sheets with several reducing agents and found hydrazine hydrate ($H_2NNH_2 \cdot H_2O$) to be the best one in producing very thin graphene-like sheets. Surface area measurement of the reduced GO sheets is in the order of $460\ m^2\ g^{-1}$. However, it is still lower than the theoretical specific surface area for completely exfoliated and isolated graphene sheets []. According to Saner et al. [178], the best method for the production of mostly exfoliated (minimum number of layers) graphene nanosheets is the oxidation of the sonicated graphite flake, ultrasonic treatment of GO, and chemical reduction of sonicated GO samples (Antolini [5]).

The functionalization of graphene oxide is important for various applications. There are two approaches: covalent functionalization and non-covalent functionalization.

Functionalized GNS by surface epoxy, hydroxyl, and carboxyl groups are synthesized through simple synthesis processes. These processes include the chemical oxidation of common graphite to graphite oxide and the subsequent thermal exfoliation of the GO to GNS [165, 179]. Figure 13.28 shows an illustration of the synthetic route used to obtain the GNSs and their SEM images [180].
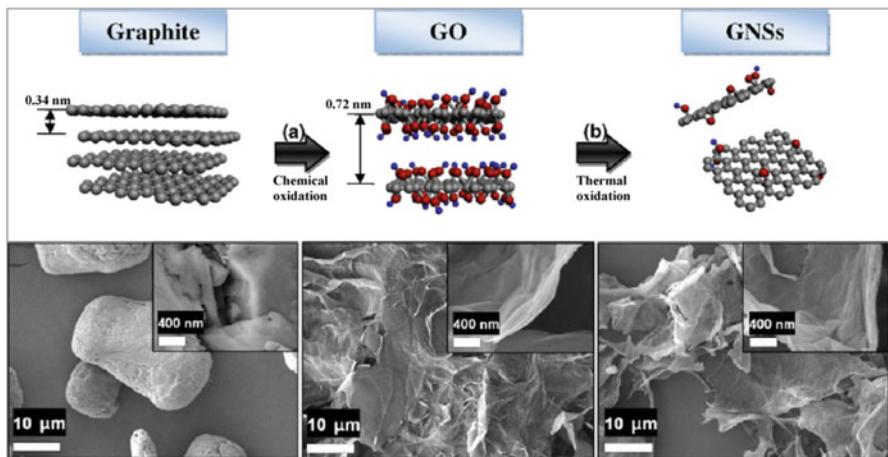
Fig. 13.28 The SEM image of graphite shows a *bulky* and *spherical* shape. After the chemical oxidation and thermal exfoliation (S.M. Choi, M.H. Seo, H.J. Kim, W.B. Kim, Carbon 49 (2011) 904–909, reproduced with permission from Elsevier) [167]

McAllister et al. [181, 181a] presented a detailed analysis of the thermal expansion mechanism of graphite oxide to produce functionalized graphene sheets.

The non-covalent functionalization of graphene oxide utilizes the weak interactions between the graphene oxide and target molecules. The network on graphene oxide provides interactions with conjugated polymers and aromatic compounds that can stabilize reduced graphene oxide resulting from chemical reduction and produce functional composite materials.

Results showed that GO reduced to few-layer level has poor dispersion in water. Zhang et al. (2004) showed an alternative method for removing epoxy and hydroxyl groups from GO with a sodium acetate trihydrate [182]. This approach may open up the new possibility for cost-effective, environment-friendly, and large-scale production of graphene. They proposed a one-step reduction of GO and demonstrated an easy efficient route to prepare graphene, employing sodium acetate trihydrate as a reducing agent.

GO was prepared from graphite powder through the modified Hummers method [183]. Graphene was synthesized via the chemical reduction of GO by sodium acetate trihydrate. A typical procedure was 1.10 g $CH_3COONa \cdot 3H_2O$ dispersed into 55 mL of GO dispersion (1 mg/mL).

13.2.2 Syntheses of Metals on Graphene Nanosheets

There are two ways to prepare Me/GNS, that is, (1) simultaneous and (2) sequential reduction of GO and metal precursors. Metal precursors are deposited on GO and then are reduced simultaneously by different methods such as ethylene glycol, [164, 169, 170, 177, 182, 184, 185], $NaBH_4$ [186, 187], PVP/hydrazine [171],

sodium citrate [188, 189] microwave heating [190], microwave polyol [191–194], and colloidal methods [195].

Pt/GNS was prepared by reduction of H_2PtCl_6 and GO suspension using $NaBH_4$ [187], as discussed before. It is difficult to prepare directly. Thus, the sequential method is overall used to prepare catalysts supported on functionalized graphene. There are two possibilities: electrochemical reduction of GO, followed by the electrochemical deposition and reduction of Pt precursor [196], and (2) in the photocatalytic reduction of GO, followed by the injection of Ag, Au, and Pd precursors on the graphene surface [197, 198].

13.2.3 Structure

The structural characteristics of GNS and Pt/GNS are shown in Figs. 13.29 and 13.30 [177, 199].

XRD analysis showed a diffraction peak of GO at $2\theta = 11.2°(0\,0\,2)$ which is consistent with interlayer space (d-spacing) of 0.7130 nm. This value is larger than the d-spacing (0.335 nm) of pristine graphite ($2\theta = 26.7°$), as a result of the intercalation of water molecules and the formation of oxygen-containing functional groups between the layers of graphite during oxidation [200]. For RGO, the $0\,0\,2$ reflection peak at $2\theta = 11.2°$ disappeared and a weak and broad diffraction peak at $2\theta = 25.4°$ appeared, consistent with d-spacing of 0.350 nm, suggesting the graphene network. This proves the formation of few layers of graphene.

Typical FETEM image of the as-synthesized RGO is shown in Fig. 13.30.
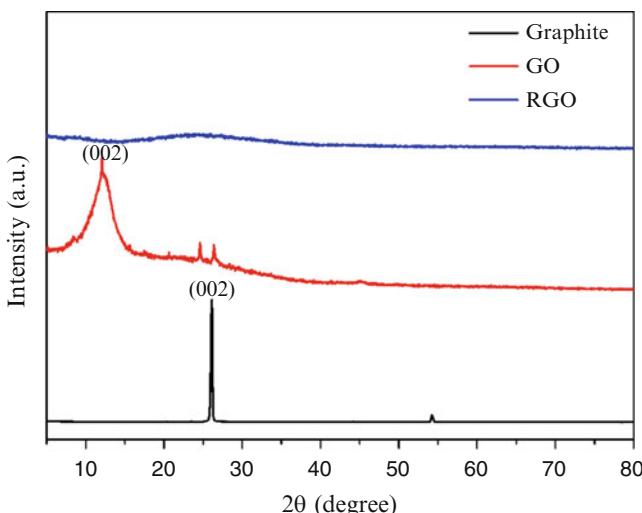
Fig. 13.29 XRD patterns of pristine graphite, GO, and RGO (Reproduced with permission from Zhang et al., Synthetic Metals 193 (2014) 132–138) [215a]

	Width [nm]	Height [nm]	Angle[deg]
—	70.49	0.80	0.65
—	155.07	1.15	0.42
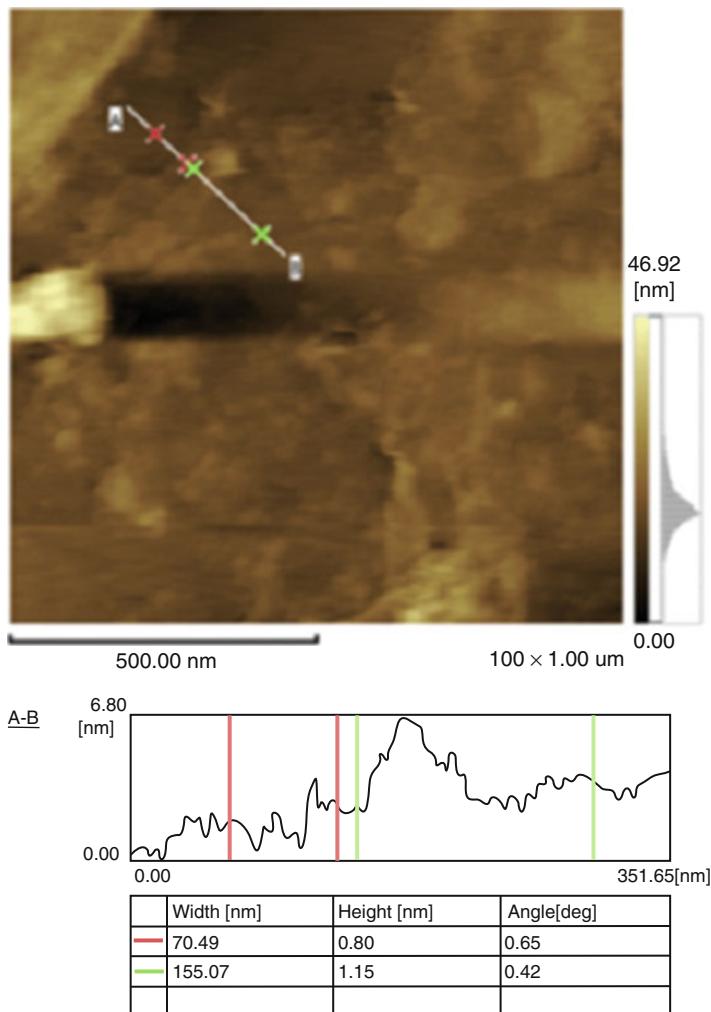
Fig. 13.30 Typical FETEM image of the as-synthesized RGO at different magnifications (X. Zhang et al., Synthetic Metals 193 (2014) 132–138, reproduced with permission) [215a]

Raman spectroscopy of GO is shown in Fig. 13.31 and indicates D, G, and 2D peaks around 1350 cm^{-1}, 1580 cm^{-1}, and 2700 cm^{-1}, which allows characterization of graphene layers in terms of number of layers present. The D band appears due to the presence of disorder in atomic arrangement or edge effect of graphene, ripples, and charge puddles. Comparison of Raman spectra between graphite and single- and few-layer graphene is shown in Fig. 13.30 [191]. There is a significant change in shape and intensity for 2D band of , graphene and graphite.

Figure 13.32 shows the XRD pattern of Pt/GNS, evidencing the disappearance of the graphite peak at 2θ about 26.4° and the appearance of a peak at 2θ at 10.4°,

Fig. 13.32 XRD patterns of graphite (*red line*, *bottom*), graphite oxide (*blue line*, *middle*) and Pt/graphene (*black line*, *top*). Reproduced with permission from Y. Li, L. Tang, J. Li, Electrochemistry Communications 11 (2009) 846–849 [160]

revealing the successful oxidation of the starting graphite (). The diffraction peaks at $2\theta = 313.13°$ and $46.2°$ correspond to the $(1\,1\,1)$, and $(2\,0\,0)$ facets of platinum crystals. As shown, GO was fully exfoliated into nanosheets with micrometer-long wrinkles by ultrasonic treatment, illustrating clearly the flake-like shapes of graphite oxide sheets.
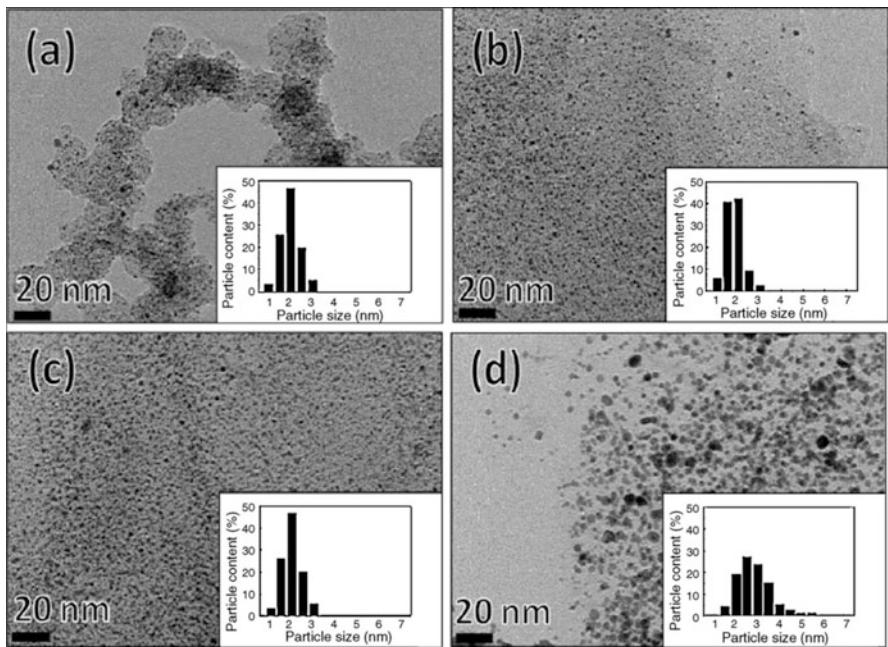
Fig. 13.33 TEM images of the (**a**) 40 wt% Pt/C, (**b**) 40 wt%, (**c**) 60 wt%, and (**d**) 80 wt% Pt/GNS catalysts (S.M. Choi, M.H. Seo, H.J. Kim, W.B. Kim, Carbon 49 (2011) 904–909, reproduced with permission) [167]

TEM images of the Pt/f-GNS catalysts revealed that for the Pt/f-GNS catalyst the Pt nanoparticles were highly dispersed even up to 80 wt% Pt/f-GNS, as shown in Fig. 13.33.

13.3   Conclusion

The literature [201–257] presents new catalysts of metallic or oxides supported on NCT and in particular on graphenes for several applications, such as hydrogen production for fuel cells and metals supported on graphenes for the Fisher–Tropsch synthesis. However, compared to the number of paper on catalytic processes, few works have been reported and tested with graphene-supported catalysts. In fact, the combination of the high surface area, high conductivity, unique graphitized basal plane structure, and potential low manufacturing cost makes graphene sheets a promising candidate as catalyst. Additional references related to this subject [201–257].

References

1. Aiken III JD, Finke RG. J Mol Catal A. 1999;135:1–44.
2. Burda C, Chen X, Narayanan R, El-Sayed MA. Chem Rev. 2005;105:1025–102.
3. Narayanan R, El-Sayed MA. Nano Lett. 2004;4:1343–8.
4. Wikipedia: the free encyclopedia.htm. file:///D:/Carbon%20nanotube%20
5. Antolini E. Appl Catal Environ. 2012;123–124:52–68.
6. Roucoux A, Schulz J, Patin H. Chem Rev. 2002;102:3757–78.
7. Moujlijn JA, van Leeuwen PWN, van Santen RA. Catalysis. In: Geus et al, editors. Studies in surface science and catalysis, Chap. 9; 1995, vol. 79, p. 339.
8. Wang X, Zhuang J, Peng Q, Li Y. Nature. 2005;437:121–4.
9. Cushing BL, Kolesnichenko VL, O'Connor CJ. Chem Rev. 2004;104:3893–946.
10. Weare WW, Reed SM, Warner MG, Hutchinson JE. Improved synthesis of small phosphine-stabilized gold nanoparticles. J Amer Chem Soc. 2000;122:12890–1.
11. Yao H, Momozawa O, Hamatami T, Kimura K. Stepwise size selective extraction of carboxylate-modified gold nanoparticles from an aqueous suspension into toluene with trioctylammonium cations. Chem Mater. 2001;13:4692–7.
12. Okitsu K, Mizukoshi Y, Bandow H, Maeda Y, Yamamoto T, Nagata Y. Formation of the noble metal nanoparticles by ultrasonic irradiation. Ultrason Sonochem. 1996;3:S249–51.
13. Okitsu K, Bandow H, Maeda Y. Sonochemical preparation of ultrafine palladium nanoparticles. Chem Mater. 1996;8:315–7.
14. Leff DV, Brandt L, Heath JR. Synthesis and characterization of hydrophobic organically soluble gold nanocrystals functionalized with primary amines. Langmuir. 1996;12:4723–30.
15. Teranishi T, Miyake M. Size control of palladium nanoparticles and their crystal structures. Chem Mater. 1998;10:594–600.
16. El-Sayed MA. Acc Chem Res. 2001;34:257–64.
17. Toniolo FS, Moya S, Schmal M. Adv Chem Lett. 2013;1:1–8.
18. Moya SF, Martins RL, Ota A, Kunkes EL, Behrens M, Schmal M. Appl Catal Gen. 2012;411–412:105–13.
19. Ota A, Kunkes EL, Kröhnert J, Schmal M, Behrens M. Appl Catal Gen. 2013;452:203–13.
20. Suslick KS, Hyeon T, Fang M, Cichowlas AA. Mater Sci Eng A. 1995;204:186–92.
21. Narayanan R, El-Sayed MA. J Phys Chem B. 2005;109:12663–76.
22. Lee MB, Yang QY, Ceyer ST. J Chem Phys. 1987;87:2724–41.
23. Valden M, Pere J, Xiang N, Pessa M. Chem Phys Lett. 1996;257:289–96.
24. Beebe Jr TP, Goodman DW, Kay BD, Yates JT. Kinetics of the activated dissociative adsorption of methane on the low index planes of Ni single crystal surfaces. J Am Chem Soc. 1987;87:2305–15.
25. Choudhary TV, Goodman DW. Top Catal. 2002;20:35–42.
26. Goodman DW. J Phys Chem. 1996;100:13090–102.
27. In YZ, Sun J, Yi J, Lin JD, Chen HB, Liao DW. J Mol Struct Theochem. 2002;587:63–71.
28. Ciobica IM, Van Santen RA. J Phys Chem B. 2002;106:6200–5.
29. Moya SF. tese de doutorado. COPPE, Universidade Federal do Rio de Janeiro, Rio de Janeiro, RJ; 2008.
30. Teranishi T, Miyake M. Chem Mat. 1999;10:594–600.
31. Thompson LH, Doraiswamy LK. Ind Eng Chem Res. 1999;38:1215–49.
32. Oh H-S, Yang KJ, Costello CK, Wang YM, Bare SR, Hung HH, Kung MC. J Catal. 2002;210:375–86.
33. Lee S-J, Gavriilidis A. J Catal. 2002;206:305–13.
34. Haruta M. J New Mater Electrochem Syst. 2004;7:163–72.
35. Wolf A, Schüth F. Appl Catal A. 2002;226:1–13.
36. Ribeiro NFP, Mendes FMT, Perez CAC, Souza MMVM, Schmal M. Appl Catal A. 2009;347:62–71.
37. Turkevich J, Stevenson PC, Killier J. Disc Faraday Soc. 1951;11:55.

38. Turkevich J. Gold Bull. 1985;18:86.
39. Duff DG, Baiker A, Edwards PP. Langmuir. 1993;9:2301–9.
40. Duff DG, Baiker A, Gameson I, Edwards PP. Langmuir. 1993;9:2310–7.
41. Fierro JLG, Peña MA. Chem Rev. 2001;101:1981–2018.
42. Tejuca LG, Fierro JLG, Tascon JMD. Adv Catal. 1989;36:237–328.
43. Lin J, Yu M, Lin C, Liu X. J Phys Chem C. 2007;111:5835.
44. Magalhães RNSH, Toniolo FS, da Silva VT, Schmal M. Appl Catal A Gen. 2010;388:216–24.
45. Ko E-Y, Park ED, Seo KW, Lee HC, Lee D, Kim S. Catal Today. 2006;116:377.
46. Białobok B, TrawczynSki J, MisTa W, Zawadzki M. Appl Catal B. 2007;72:395.
47. Oliva C, Cappelli S, Kryukov A, Chiarello GL, Vishniakov AV, Forni L. J Mol Catal A Chem. 2006;255:36.
48. Wen Y, Zhang C, He H, Yu Y, Teraoka Y. Catal Today. 2007;126:400–5.
49. Forni L, Oliva C, Vatti FP, Kandala MA, Ezerets AM, Vishniakov AV. Appl Catal B. 1996;7:269–84.
50. French SA, Catlow CRA, Oldman RJ, Rogers SC, Axon SA. Chem Commun. 2002;22:2706–7.
51. Viswanathan B, George S. React Kinet Catal Lett. 1985;27:321–4.
52. Shannon RD. Acta Crystallogr A. 1976;32:751.
53. Hadjievl VG, Ilievl MN, Vergilovs IV. J Phys C Solid State Phys. 1988;21:L199–201.
54. Wang ZL, Petroski JM, Green TC, El-Sayed MA. J Phys Chem B. 1999;102:6135–51.
55. Okitsu K, Yue A, Tanabe S, Matsumoto H. Chem Mater. 2000;12:3006–11.
56. Miyazaki A, Balint I, Nakano Y. J Nanop Res. 2003;5:69–80.
57. Duteil A, Schmid G, Meyer-Zaika W. J Chem Soc Chem Commun. 1995;31–32.
58. Kumar RV, Diamant Y, Gedanken A. Sonochemical synthesis and characterization of nanometer-size transition metal oxides form metal acetates. Chem Mater. 2000;12:2301–5.
59. Liang J, Jiang X, Liu G, Deng Z, Zhuang J, Li F, Li Y. Characterization and synthesis of pure ZrO_2 nanopowders via sonochemical methods. Mater Res Bull. 2003;38:161–8.
60. Srivastava DN, Perkas N, Zaban A, Gedanken A. Sonochemistry as a tool for preparation of porous metal oxides. Pure Appl Chem. 2002;74:1509–17.
61. Mizukoshi Y, Takagi E, Okuno H, Oshima R, Maeda Y, Nagata Y. Preparation of platinum nanoparticles by sonochemical reduction of the Pt(IV) ions: role of surfactants. Ultrason Sonochem. 2001;8:1–6.
62. Hyeon T, Fang M, Suslick KS. Nanostructure molibdenum carbide: sonochemical synthesis and catalytic properties. J Amer Chem Soc. 1996;118:5492–3.
63. Liu BS, Au CT. Appl Catal A. 2003;244:181–95.
64. Zhu J, Aruna ST, Koltypin Y, Gedanken A. A novel method for the preparation of lead selenide: pulse sonoelectrochemical synthesis of lead selenide nanoparticles. Chem Mater. 2000;12:143–7.
65. Qiu L, Wei Y, Pol VG, Gedanken A. Synthesis of a-$MoTe_2$ nanorods via annealing Te-seeded amorphous $MoTe_2$ nanoparticles. Inorg Chem. 2004;43:6061–6.
66. Thompson LH, Doraiswamy LK. Sonochemistry : science and engineering. Ind Eng Chem Res. 1999;38:1215–49.
67. Li H, Wang R, Hong Q, Chen L, Zhong Z, Koltypin Y, Calderon-Moreno J, Gedanken A. Ultrasound assisted polyol method for the preparation of SBA-15 supported ruthenium nanoparticles and the study of their catalytic activity on the partial oxidation of methane. Langmuir. 2004;20:8352–6.
68. Dhas NA, Ekhtiarzadeh A, Suslick KS. Sonochemical preparation of supported hydrodesulfurization catalysts. J Amer Chem Soc. 2001;123:8310–6.
69. Yang QY, Johnson AD, Maynard KJ, Ceyer ST. Synthesis of benzene from methane over a Ni(111) catalyst. J Am Chem Soc. 1989;111:8748–9.
70. Narayanan R, El-Sayed MA. Shape-dependent catalytic activity of platinum nanoparticles in colloidal solutions. Nano Lett. 2004;4:1343–8.

71. Narayanan R, El-Sayed MA. Changing catalytic activity during colloidal platinum nanocrystals due to the shape changes: electron transfer reactions. J Amer Chem Soc. 2004;126:7194–5.
72. Orlovskaya N, Steinmetz D, Yarmolenko S, PAI D, Sankar J, Goodenough J. Phys Rev B. 2005;72:220.
73. Martins RL, Schmal M. J Braz Chem Soc. 2013;25(12):2399–408.
74. Martins RL, Baldanza MAS, Souza MMVM, Schmal M. Appl Catal A Gen. 2007;318:207.
75. Moya SF, Martins RL, Schmal M. Appl Catal A Gen. 2011;396:159.
76. Martins RL, Baldanza MAS, Alberton AL, Vasconcelos SM, Schmal M. Appl Catal B Environ. 2011;103:326.
77. Martins RL, Schmal M. Appl Catal A Gen. 2006;308:133.
78. Muradov NZ. Energy Fuels. 1998;12:41.
79. Poirier MG, Sapundzhiev C. Int J Hydrogen Energy. 1997;22:429.
80. Choudhary TV, Goodman DW. Catal Lett. 1999;59:93.
81. Aiello R, Fiscus JE, zur Loye H-C, Amiridis MD. Appl Catal A. 2000;192:227.
82. Alberton AL, Souza MMVM, Schmal M. Appl Catal B Environ. 2011;103(3–4):326.
83. Li Y, Zhang B, Xie X, Liu J, Xu Y, Shen W. J Catal. 2006;238:412.
84. Ni X, Zhao Q, Zhou F, Zheng H, Cheng J, Li B. J Crystal Growth. 2006;289:299.
85. Zhu LP, Liao GH, Yang Y, Xiao HM, Wang JF, Fu SY. Nanoscale Res Lett. 2009;4:550.
86. Ni X, Zhang Y, Tian D, Zheng H, Wang X. J Crystal Growth. 2007;306:418.
87. Gui Z, Liv Z, Wang Z, Song L, Hu Y, Fan W, Chen D. J Phys Chem B. 2005;109:119.
88. Winslow P, Bell AT. J Catal. 1985;94:385.
89. Duncan TM, Winslow P, Bell AT. J Catal. 1985;93:1.
90. Chorkendorff I, Alstrup I, Ullmann S. Surf Sci. 1990;227:291.
91. Egeberg RC, Ullmann S, Astrup I, Mullins CB, Chorkendorff I. Surf Sci. 2002;497:183.
92. Swang O, Faegri Jr K, Gropen O, Wahlgren U, Siegbahn P. Chem Phys. 1991;156:379.
93. Xing B, Pang X-Y, Wang G-C, Shang Z-F. J Mol Catal A. 2010;315:187.
94. Ribeiro NFP, Neto RCR, Moya SF, Souza MMVM, Schmal M. Int J Hydrogen Energy. 2010;35(21):11725–32.
95. Jeevanandam P, Koltypin Y, Gedanken A. Mater Sci Eng. 2001;90:125–32.
96. Cui H, Zayat M, Levy D. J Non-Cryst Solids. 2005;351:2102–6.
97. Pompeo F, Gazzoli D, Nichio NN. Int J Hydrogen Energy. 2009;34:2260–8.
98. Han YS, Li JB, Ning XS, Yang XZ, Chi B. Mater Sci Eng A. 2004;369:241–4.
99. Guo J, Lou H, Zheng X. Carbon. 2007;45:1313–21.
100. Souza NA, Silva EB, Jardim PM, Sasaki JM. Mater Lett. 2007;61:4743–6.
101. Avgouropoulos G, Ioannides T, Matralis H. Appl Catal B Environ. 2005;56:87–93.
102. Patil KC, Aruna ST, Ekambaram S. Combustion synthesis. Curr Opin Solid State Mater. 1997;2:158–65.
103. Patil KC, Aruna ST, Mimani T. Solid State Mater. 2002;6:505–12.
104. Varma A, Rogachev AS, Mukasyan AS, Hwang S. Adv Chem Eng. 1998;24:79–226.
105. Kingsley JJ, Suresh K, Patil KC. J Mater Sci. 1990;25:1305–12.
106. Minami T. J Alloy Compd. 2001;315:123–8.
107. Alinejad B, Sarpoolaky H, Beitollahi A, Saberi A, Afshar S. Mater Res Bull. 2008;43:1188–94.
108. Chen Y, Zhou W, Shao Z, Xu N. Catal Commun. 2008;9:1318–25.
109. Ringuedé A, Labrincha JA, Frade JR. Solid State Ion. 2001;131:549–57.
110. Avgouropoulos G, Ioannides T. Appl Catal A. 2003;244:155–67.
111. Areán CO, Mentruit MP, López AJL, Parra JB. Colloids Surf A. 2001;180:253–8.
112. Sahli N, Roger AC, Kiennemann A, Libs S, Bettahar MM. Catal Today. 2006;113:187–93.
113. Han YS, Li JB, Ning XS, Chi B. J Am Ceram Soc. 2004;87:1347–9.
114. Hoffer BH, van Langeveld AD, Jannssens J-P, Bonné RLC, Martin C, Moulijn JA. J Catal. 2000;192:432–40.
115. Neto CRR, Schmal M. Appl Catal A Gen. 2013;450:131–2.

116. Mamontov E, Egami T, Brezny R, Koranne M, Tyagi S. J Phys Chem B. 2000;104:11110–6.
117. Khaodee W, Jongsomjit B, Assabumrungrat S, Praserthdam P, Goto S. Catal Commun. 2009;10:494–501.
118. Reddy BM, Khan A. Catal Surv. 2005;9:155–71.
119. Su C, Li J, He D, Cheng Z, Zhu Q. Appl Catal A. 2000;202:81–9.
120. Postula WS, Feng Z, Philip CV, Akgerman A, Anthony RG. J Catal. 1994;135:126–31.
121. Feng Z, Postula WS, Akgerman A, Anthony RG. Ind Eng Chem Res. 1995;34:78–82.
122. Lu L, Hayakawa T, Ueda T, Hara M, Domen K, Maruya K. Chem Lett. 1998;1:65–6.
123. Maruya K, Takasawa A, Aikawa M, Haraoka T, Omen K. J Chem Soc Faraday Trans. 1994;90:911–7.
124. Zhu Z, He D. Fuel. 2008;87:2229–35.
125. Trovarelli A. J Inorg Chem. 1999;20:263–84.
126. Sun C, Li H, Chen L. J Phys Chem Solids. 2007;68:1785–90.
127. Sun C, Sun J, Xiao G, Zhang H, Qiu X, Li H, Chen L. J Phys Chem B. 2006;110:13445–52.
128. Sing KSW, Everett DH, Haul RAW, Moscou L, Pierotti RA, Rouquerol J, Siemieniewska T. Pure Appl Chem. 1985;57:603–19.
129. Nguyen C, Do DD. Langmuir. 1999;15:3608–15.
130. Donohue MD, Aranovich GL. J Colloids Interf Sci. 1998;205:121–30.
131. Leofanti G, Padovan M, Tozzola G, Venturelli B. Catal Today. 1998;41:207–19.
132. Burgess CGV, Everett DH, Nuttall S. Pure Appl Chem. 1989;61(11):1845–52.
133. Yuan Z, Idakiev V, Vantomme A, Tabakova T, Ren T, Su BL. Catal Today. 2008;131:203–10.
134. Bonnetot B, Rakic V, Yuzhakova T, Guimon C, Auroux A. Chem Mater. 2008;20:1585–96.
135. Aguila G, Guerrero S, Gracia F, Araya P. Appl Catal A. 2006;305:219–32.
136. Pérez-Hernández R, Aguilar F, Gómez-Cortés A, Díaz G. Catal Today. 2005;107:175–80.
137. Zawadzki M. J Alloys Compd. 2008;454:347–51.
138. Tartaj P, Bomatí-Miguel O, Rebolledo AF, Valdes-Solis T. J Mater Chem. 2007;17:1958–63.
139. Bumajdad A, Zaki MI, Eastoe J, Pasupulety L. Langmuir. 2004;20:11223–33.
140. Inoue M, Sato K, Nakamura T, Inui T. Catal Lett. 2000;65:79–83.
141. Stagg-Williams SM, Noronha FB, Fendley G, Resasco DE. J Catal. 2000;194:240–9.
142. Wang ZL, Feng X. J Phys Chem B. 2003;107:13563–6.
143. Giamello E. Catal Today. 1998;41:239–49.
144. Abi-aad E, Bechara R, Grimblot J, Aboukais A. Chem Mater. 1993;5:793–7.
145. Adamski A, Djéga-Mariadassou G, Sojka Z. Catal Today. 2007;119:120–4.
146. Wang JB, Tai YL, Dow WP, Huang T-J. Appl Catal A. 2001;218:69–79.
147. Appel LG, Eon JG, Schmal M. Physica Status Solidi. 1997;163:107–20.
148. Voorhoeve RJH, Johnson DW, Remeika JP, Gallagher PK. Science. 1977;195:827–33.
149. Vaz T, Salker AV. Mater Sci Eng B. 2007;133:81–4.
150. Tascón JMD, González-Tejuca L. Z Phys Chem-Wiesbaden. 1980;121:63–78.
151. Tascón JMD, González-Tejuca L. Z Phys Chem-Wiesbaden. 1980;121:79–93.
152. Royer S, Duprez D, Kaliaguine S. Catal Today. 2006;112:99–102.
153. Galasso FS. Perovskites and high TC superconductors. 1st ed. Chap. 1. Amsterdam: Gordon and Breach Sc. Publ.; 1990.
154. Nitadori T, Muramatsu M, Misono M. The valence control and catalytic properties of La$_2$−xSrxNiO$_4$. Bull Chem Soc Jpn. 1988;61:3831–7.
155. Ferri D, Forni L. Methane combustion on some perovskite-like mixed oxides. Appl Catal B. 1998;16(2):119–26.
156. Spinicci R, Tofanari A, Faticanti M, et al. Hexane total oxidation on LaMO$_3$ (M = Mn, Co, Fe) perovskite-type oxides. J Mol Catal A Chem. 2001;176:247–52.
157. Quinelato AL, Longo ER, Leite MI, et al. Synthesis and sintering of ZrO$_2$CeO$_2$ powder by use of polymeric precursor based on Pechini process. J Mater Sci. 2001;36:3825–30.
158. Popa M, Kakihana M. Synthesis of lanthanum cobaltite (LaCoO$_3$) by the polymerizable complex route. Solid State Ion. 2002;151(1–4):251–7.

159. Villoria JA, Alvarez-Galvan MC, Navarro RM, et al. Zirconia-supported LaCoO$_3$ catalysts for hydrogen production by oxidative reforming of diesel: optimization of preparation conditions. Catal Today. 2008;138(3–4):135–40.

160. Machado BF, Serp P. Catal Sci Technol. 2012;2:54–75.

161. Geim AK, Novoselov KS. Nat Mater. 2007;6:183–91.

162. Chen D, Tang L, Li J. Chem Soc Rev. 2010;313:3157–80.

163. Brownson DAC, Kampouris DK, Banks CE. J Power Sources. 2011;1136:4873–85.

164. Novoselov KS, Geim AK, Morozov SV, Jiang D, Zhang Y, Dubonos SV, Grigorieva IV, Firsov AA. Science. 2004;306:666–9.

165. Singh V, Joung D, Zhai L, Das S, Khondaker SI, Seal S. Prog Mater Sci. 2011;56:1178–271.

166. Moussa SO, Panchakarla LS, Ho MQ, El-Shall MS. ACS Catal. 2013;4:535–45.

167. Hofmann U, Frenzel A. Kolloid-Zeitschrift and Zeitschrift fur Polymere. 1934;68:99–151.

168. Stankovich S, Dikin DA, Piner RD, Kohlhaas KA, Kleinhammes A, Jia Y, Wu Y, Nguyen ST, Ruoff RS. Carbon. 2007;45:1558–65.

169. Novoselov KS, Geim AK, Morozov SV, Jiang D, Katsnelson MI, Grigorieva IV, Dubonos SV, Firsov AA. Nature. 2005;438:197–200.

170. Lee C, Wei X, Kysar JW, Hone J. Measurement of the elastic properties and intrinsic strength of monolayer graphene. Science. 2008;321:385.

171. Ubbelohde AR, Lewis LA. Graphite and its crystal compounds. London: Oxford University Press; 1960.

172. Brodie BC. Annales de Chime et de Physique. 1860;513:466–72.

173. Staudenmaier L. Chemische Berichte. 1898;31:981–99.

174. Hummers WS, Offeman RE. J Am Chem Soc. 1958;80:939.

175. Hummers WS, Offeman RE. J Am Chem Soc. 1958;6:1339.

176. Salavagione HJ, Martínez G, Ellis G. Macromol Rapid Commun. 2011;32:1771–89.

177. Li X, Wang X, Zhang L, Lee S, Dai H. Chemically derived, ultrasmooth graphene nanoribbon semiconductors. Science. 2008;319:1229.

178. Saner B, Okyay F, Yürüm Y. Fuel. 2010;89:1903–10.

179. Schniepp HC, Li J-L, McAllister MJ, Sai H, Herrera-Alonso M, Adamson DH, Prud'homme RK, Car R, Saville DA, Aksay IA. J Phys Chem B. 2006;110:8535–9.

180. Slonczewski JC, Weiss PR. Band structure of graphite. Phys Rev. 1958;109:272.

181. McAllister MJ, Li JL, Adamson DH, Schniepp HC, Abdala AA, Liu J, Alonso MH, Milius DL, Car R, Prud'homme RK, Aksay IA. Chem Mater. 2007;19:4396–404.

181a. Schniepp HC, Abdala AA, Liu J, Alonso MH, Milius DL, Car R, Prud'homme RK, Aksay IA. Chem Mater. 2007;19:4396–404.

182. Zhang YB, Tan YW, Stormer HL, Kim P. Experimental observation of the quantum Hall effect and Berry's phase in graphene. Nature. 2005;438:201.

183. Alanyalıoglu M, Segura JJ, Oró-Solè J, Casan-Pastor N. Carbon. 2012;50:92–152.

184. Balandin AA, Ghosh S, Bao W, Calizo I, Teweldebrhan D, Miao F, et al. Superior thermal conductivity of single-layer graphene. Nano Lett. 2008;8:1302.

185. Wu J, Becerril HA, Bao Z, Liu Z, Chen Y, Peumans P. Organic solar cells with solution-processed graphene transparent electrodes. Appl Phys Lett. 2008;92:263–302.

186. Li Y, Tang L, Li J. Electrochem Commun. 2009;11:846–9.

187. Ritter KA, Lyding JW. The influence of edge structure on the electronic properties of graphene quantum dots and nanoribbons. Nat Mater. 2009;8:235.

188. Thompson TE, Falardeau ER, Hanlon LR. The electrical conductivity and optical reflectance of graphite–SbF5 compounds. Carbon. 1977;15:39.

189. Fuzellier H, Melin J, Herold A. Conductibilité électrique des composés lamellaires graphite–SbF5 et graphite–SbCl5. Carbon. 1977;15:45.

190. Shenderova OA, Zhirnov VV, Brenner DW. Carbon nanostructures. Crit Rev Solid State Mater Sci. 2002;27:227.

191. Krishnan A, Dujardin E, Treacy MMJ, Hugdahl J, Lynum S, Ebbesen TW. Graphitic cones and the nucleation of curved carbon surfaces. Nature. 1997;388:451.

192. Emtsev KV, Bostwick A, Horn K, Jobst J, Kellogg GL, Ley L, et al. Towards wafer-size graphene layers by atmospheric pressure graphitization of silicon carbide. Nat Mater. 2009;8:203.
193. Choi SM, Seo MH, Kim HJ, Kim WB. Carbon. 2011;49:904–9.
194. Sprinkle M, Siegel D, Yu Y, Hicks J, Tejeda A, Taleb-Ibrahimi A, et al. First direct observation of a nearly ideal graphene band structure. Phys Rev Lett. 2009;103:226–803.
195. de Parga ALV, Calleja F, Borca BMCG, Passeggi J, Hinarejos JJ, Guinea F, et al. Periodically rippled graphene: growth and spatially resolved electronic structure. Phys Rev Lett. 2008;100:056807.
196. Zhang X, Li K, Li H, Lu J, Qiangang F, Chu Y. Graphene nanosheets synthesis via chemical reduction of grapheneoxide using sodium acetate trihydrate solution. Synt Met. 2013;193:132–8.
197. Park J, Mitchel WC, Grazulis L, Smith HE, Eyink KG, Boeckl JJ, Tomich DH, Pacley SD, Hoelscher JE. Adv Mater. 2010;2:4130–5.
198. Park J, Mitchel WC, Grazulis L, Smith HE, Eyink KG, Boeckl JJ, Tomich DH, Pacley SD, Hoelscher JE. Adv Mater. 2010;2:4140–5.
199. Li D, Muller MB, Gilje S, Kaner RB, Wallace GG. Processable aqueous dispersions of graphene nanosheets. Nat Nanotechnol. 2008;3:101.
200. He H, Riedl T, Lerf A, Klinowski J. J Phys Chem. 1996;100:19954–8.
201. Murray CB, Kagan CR, Bawendi MG. Ann Rev Mater Sci. 2000;30:545–610.
202. Araujo GC, Lima S, Rangel MC, Parola V, Peña MA, Fierro JLG. Catal Today. 2005;107:906–12.
203. Lee DW, Won JH, Shim KB. Mat Lett. 2003;57:3346–51.
204. Gajbhiye NS, Bhattacharya UE, Darshane VS. Thermoc Acta. 1995;264:219–30.
205. Ponce S, Peña MA, Fierro JLG. Appl Catal B. 2000;24:193–205.
206. Sis LB, Wirtz GP. J Appl Phys. 1973;44:5553–9.
207. Antolini E. Mater Chem Phys. 2003;78:563–73.
208. Antolini E. Appl Catal B. 2013;88:1–24.
209. Stankovic S, Dikin DA, Dommett GHB, Kohlhass KM, Zimney EJ, Stach EA, Piner RD, Nguyen ST, Ruoff RS. Nature. 2006;442:282–6.
210. Sun Y, Wu Q, Shi G. Energy Environ Sci. 2011;4:1113–32.
211. Huang X, Yin Z, Wu S, Qi X, He Q, Zhang Q, Yan Q, Boey F, Zhang H. Small. 2011;7:1876–902.
212. Berger C, Song ZM, Li XB, Wu XS, Brown N, Naud C, Mayou D, Li T, Hass J, Marchenkov AN, Conrad EH, First PN, de Heer WA. Science. 2006;312:1191–8.
213. Dato A, Radmilovic V, Lee Z, Phillips J, Frenklach M. Nano Lett. 2008;8:2012–6.
214. Choucair M, Thordarson P, Stride JA. Nat Nanotechnol. 2009;4:30–3.
215. Liu N, Luo F, Wu H, Liu Y, Zhang C, Chen J. Adv Funct Mater. 2008;18:1518–25.
215a. Zhang X, Li K, Li H, Lu J, Qiangang F, Chu Y. Synth Met. 2014;193:132–8.
216. Wang G, Wang B, Park J, Wang Y, Sun B, Yao J. Carbon. 2009;47:3242–6.
217. Lee SH, Seo SD, Jin YH, Shim HW, Kim DW. Electrochem Commun. 2010;12:1319–22.
218. Lerf A, He H, Riedl T, Forster M, Klinowski J. Solid State Ionics. 1997;101–103:857–62.
219. Hontoria-Lucas C, Lopez-Peinado AJ, Lopez-Gonzalez JD, Rojas-Cervantes ML, Martin-Aranda RM. Carbon. 1995;33:1585–92.
220. Ramesha GK, Sampath S. J Phys Chem C. 2009;113:7985–9.
221. Wang Z, Zhou X, Zhang J, Boey F, Zhang H. J Phys Chem C. 2009;19:9071–5.
222. Dilimon VS, Sampath S. Thin Solid Films. 2011;519:2323–7.
223. Novoselov KS, Jiang Z, Zhang Y, Morozov SV, Stormer HL, Zeitler U, et al. Room-temperature quantum Hall effect in graphene. Science. 2007;315:979.
224. Sutter PW, Flege J, Sutter EA. Epitaxial graphene on ruthenium. Nat Mater. 2008;7:406.
225. Wintterlin J, Bocquet M-L. Graphene on metal surfaces. Surf Sci. 2013;603:1841.
226. Stankovich S, Dikin DA, Dommett GHB, Kohlhaas KM, Zimney EJ, Stach EA, et al. Graphene-based composite materials. Nature. 2006;442:282.

227. Verdejo R, Barroso-Bujans F, Rodriguez-Perez MA, de Saja JA, Lopez-Manchado MA. Functionalized graphene sheet filled silicone foam nanocomposites. J Mater Chem. 2008;18:2221.
228. Gilje S, Han S, Wang M, Wang KL, Kaner RB. A chemical route to graphene for device applications. Nano Lett. 2007;7:3394.
229. Gomez-Navarro C, Weitz RT, Bittner AM, Scolari M, Mews A, Burghard M, et al. Electronic transport properties of individual chemically reduced graphene oxide sheets. Nano Lett. 2007;7:3499.
230. Hummers WOR. Preparation of graphite oxide. J Am Chem Soc. 1958;80:939.
231. Paredes JI, Villar-Rodil S, Martinez-Alonso A, Tascon JMD. Graphene oxide dispersions in organic solvents. Langmuir. 2008;24:10560.
232. Negishi R, Hirano H, Ohno Y, Maehashi K, Matsumoto K, Kobayashi Y. Thin Solid Films. 2011;519:6447–52.
233. Jiao L, Zhang L, Wang X, Diankov G, Dai H. Nature. 2009;458:877–80.
234. Lotya M, Hernandez Y, King PJ, Smith RJ, Nicolosi V, Karlsson LS, Blighe FM, De S, Wang Z, McGovern IT, Duesberg GS, Coleman JN. J Am Chem Soc. 2009;131:3611–20.
235. Guo J, Ren L, Wang R, Zhang C, Yang Y, Liu T. Compos B Eng. 2011;42:290–5.
236. Liao KA, Mittal KA, Bose S, Leighton C, Mkhoyan K, Macosko CW. ACS Nano. 2011;5:1253–8.
237. Fan Z, Wang K, Wei T, Yan J, Song L, Shao B. Carbon. 2010;48:1686–9.
238. Mei X, Ouyang J. Carbon. 2011;49:5389–97.
239. Thakur S, Karak N. Carbon. 2012;50:5331–9.
240. Zhu C, Guo S, Fang Y, Dong S. ACS Nano. 2010;4:2429–37.
241. Shen J, Li T, Long Y, Shi M, Li N, Ye M. Carbon. 2012;50:2134–40.
242. Zangmeister CD. Chem Mater. 2010;22:5625–9.
243. Chen W, Yan L, Bangal PR. J Phys Chem C. 2010;113:19885–90.
244. Wang G, Shen X, Wang B, Yao J, Park J. Carbon. 2013;47:1359–64.
245. Zhu Y, Stoller MD, Cai W, Velamakanni A, Piner RD, David C, Ruoff RS. ACS Nano. 2010;2:1227–33.
246. Fan X, Peng W, Li Y, Li X, Wang S, Zhang G, Zhang F. Adv Mater. 2008;20:4490–3.
247. Lian P, Zhu X, Xiang H, Li Z, Yang W, Wang H. Electrochim Acta. 2010;56:834–40.
248. Kang X, Wang J, Wu H, Liu J, Aksay IA, Lin Y. Talanta. 2010;81:754–9.
249. Le LT, Ervin MH, Qiu HW, Fuchs BE, Lee WY. Electrochem Commun. 2011;13:355–8.
250. Xue X, Ma C, Cui C, Xing L. Solid State Sci. 2011;13:1526–30.
251. Liu C, Alwarappan S, Chen Z, Kong X, Li C. Biosens Bioelectron. 2010;25:1829–33.
252. Lemme MC, Echtermeyer TJ, Baus M, Szafranek BN, Bolten J, Schmidt M, Wahlbrink T, Kurz H. Solid-State Electron. 2008;52:514–8.
253. Zhang H, Zheng W, Yan Q, Yang Y, Wang J, Lu Z, Ji G, Yu Z. Polymer. 2010;51:1191–6.
254. Grande L, Chundi VT, Wei D, Bower C, Andrew P, Ryhänen T. Particuology. 2012;10:1–8.
255. Pantelic RS, Meyer JC, Kaiser U, Baumeister WF, Plitzko JM. J Struct Biol. 2010;170:152–6.
256. Chen W, Yan L, Bangal PR. J Phys Chem C. 2010;114:19885–90.
257. Wang G, Shen X, Wang B, Yao J, Park J. Carbon. 2009;47:1359–64.
258. Salas EC, Sun ZZ, Lüttge A, Tour JM. ACS Nano. 2010;4:4852–6.

Chapter 14
Kinetics and Mechanisms

Abstract The classical kinetics uses specific models for determining the kinetic parameters, the rate constants and reaction orders. We will present some specific cases in order to determine quantitatively the kinetic parameters of the reaction rates and suggest mechanisms, based on the identification of intermediate species.

The classical kinetics uses specific models for determining the kinetic parameters, the rate constants, and reaction orders, for reactions in the homogeneous phase. When the reaction is heterogeneous, there are additional adsorptions and desorption parameters, which can be represented by the conventional power low or Langmuir–Hinshelwood Anderson models. The goal is to find out a complete kinetic equation with defined numerical parameters. One resorts to the usual methods, measuring the kinetic constants in a differential reactor, varying temperatures, partial pressures, and space velocities, namely, macroscopic variables [1–3].

On the other hand, we have seen that the true rate is expressed by the turnover frequency (TOF), which takes into account the surface properties, or active sites, which require the knowledge and the determination of surface properties. That allows us to determine the real reaction rate and the reaction mechanism. Without this understanding, the rates will be always empirical. Understanding this true rate is crucial for heterogeneous reactions, whatever their nature.

There are two ways for determining the true kinetics. One, according to van Santen and Niemantsverdriet [4], it is possible to predict or calculate the rate constants, based on the kinetic theory, transition state, or collision theory. On the other hand, characterization techniques in situ allow verifying the surface properties changes occurring during the reaction, modification of particle sizes, and nature of the surface sites, caused by temperature and reactants or products. Also, during the reduction and oxidation, for example, there are structural changes, formation of intermediate oxidation states, agglomeration, and re-dispersions of particles. Indeed, these changes affect the surface reaction mechanisms. In summary, Fig. 14.1 shows a general scheme:

The challenge is to know the reaction mechanism, composed of several steps and intermediate species or complexes, which are unknown. These species may be radicals or intermediate compounds, joining to form a reaction mechanism.
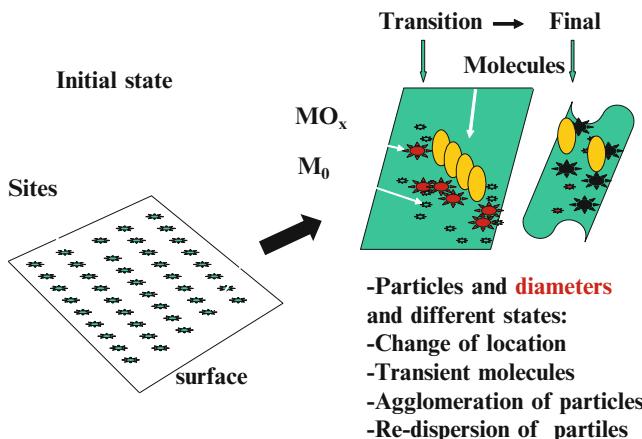
Fig. 14.1 Scheme of the surface transition state before and after reaction [4]

The radicals are very active, have very short life times and very small concentrations, but react easily in this form on the surface and in the gas phase. In most cases, gas molecules are inert, but as radicals can react violently.

The difference between the reaction in the gas phase and on the surface is that the reactive species are linked to the surface, forming radicals or intermediates with bindings having a lower degree of freedom movement than in the gas phase. However, the reaction mechanism may not be similar to reactions with radicals in the gas phase, because they involve additional phenomena and many exceptions.

The intermediate species and radicals in the gas phase are unstable. However, when adsorbed they have limited move and are strongly (irreversibly) or weakly (reversible) adsorbed on the surface. In this case, the reactivity depends on the adsorption strengths, residence times, and forms of adsorption, as well as of the types of sites on the surface.

Boudart and Djega-Mariadassou [1] showed for the ozone transformation reaction that the catalyzed reaction is much higher than the non-catalyzed reaction. Thus, for the reaction:

$$O + O_3 \rightarrow 2O_2 \tag{14.1}$$

The ratio of the catalyzed and non-catalyzed reaction rates is [2]:
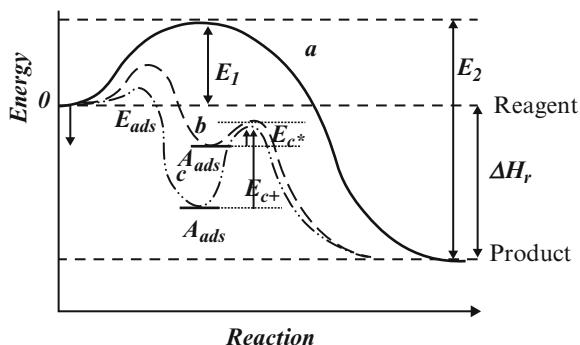
$$\frac{r_c}{r_{nc}} = 5.79 \times 10^{-3} e^{-(2080/T)} \tag{14.2}$$

In fact, at 200 K the catalyzed reaction rate is 190 times greater than the non-catalyzed reaction, which is very significant.

Boudart and Djega-Mariadassou [1] presented the catalytic reaction mechanism in terms of energy or enthalpy of adsorption reaction, as shown in Fig. 14.2.

Fig. 14.2 Energy diagram
showing the intermediate
mechanism [1–4]

a _ non-catalyzed
b - Catalyzed - good catalyst
c - Catalyzed - worse catalyst

The adsorbed species, radicals, or intermediate complexes need to surpass the energy barrier E_c^* or E_c^+ to be transformed in products, which are facilitated the smaller they are. The energy of adsorbed species is negative or exothermic and thus thermodynamically favorable.

There are several studies related to the formation of intermediate species. Calculations of the binding energies of species and surfaces can help verifying the possible formation of species during the chemical reaction. In particular, Van Santen et al. [4] showed in this way the dissociation of methane (intermediates CH_x, where $x = 4$ nH) on ruthenium surface (1120) by applying the density functional theory (DFT) [4].

The energy barrier of each step of the process must be surpassed successively, and the smaller the binding energy is, the easier the transposition of each intermediary is. The bond energies of the intermediates were calculated, based on the more stable species, as shown in Fig. 14.3, which indicates the most feasible energetic pathway [5].

In fact, calculations based on DFT allowed proposing a surface reaction mechanism and identifying the intermediate species, which can be correlated with experimental data, and thus elucidate the reaction mechanism [2, 3, 5].

There are many possibilities which may represent kinetics of surface mechanisms, but in general, the simplest kinetic models are represented by the Langmuir–Hinshelwood and Rideal–Eley equations [6], including the intermediates, as shown in Fig. 14.4.

These models have been suggested or guessed for a long time, for surface reaction rates and possible mechanisms; however, the surface parameters are yet unknown. Therefore, characterization techniques in situ are essential to monitor surface reactions.

We will present some specific cases in order to determine quantitatively the kinetic parameters of the reaction rates and suggest mechanisms, based on the identification of intermediate species. Noteworthy is that the methodologies here have an objective in each case, which requires only specific characterizations and not any characterization as usually done.
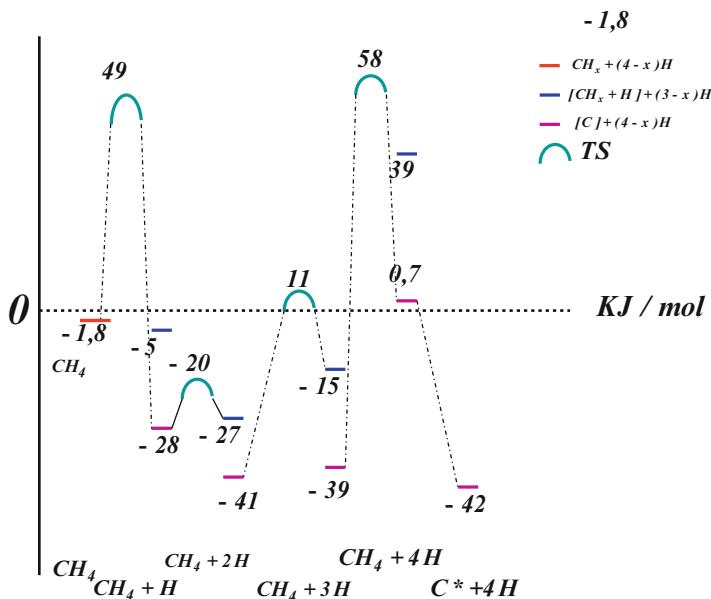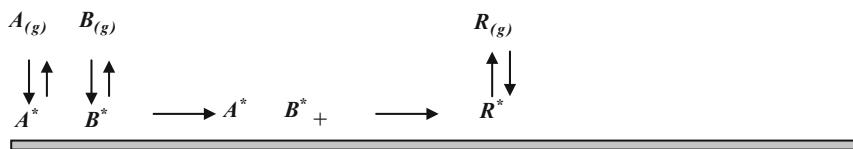
Fig. 14.3 Reaction path of methane activation on the surface Ru (1120) (Adapted with permission from CIOBICA, J. Phys. Chem. B, vol. 106, pp. 6200–6205)
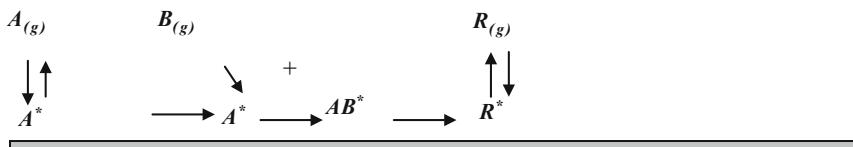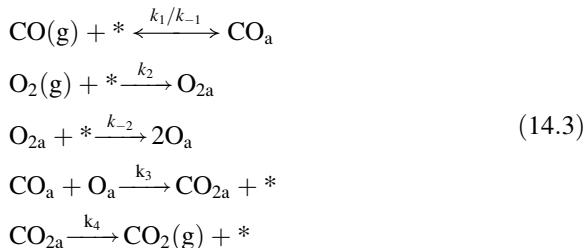
Fig. 14.4 Kinetic model [2]

14.1 Kinetics of the Carbon Monoxide Oxidation on Pt/TiO$_2$ Catalyst

In general, the mechanism is well known and has been described by the classical Langmuir–Hinshelwood (LH) model [7–10], based on adsorption of oxygen in competition with adsorbed carbon monoxide. This mechanism was presented by Engel et al. [9]:

$$
\begin{aligned}
&CO(g) + * \xleftrightarrow{k_1/k_{-1}} CO_a \\
&O_2(g) + * \xrightarrow{k_2} O_{2a} \\
&O_{2a} + * \xrightarrow{k_{-2}} 2O_a \\
&CO_a + O_a \xrightarrow{k_3} CO_{2a} + * \\
&CO_{2a} \xrightarrow{k_4} CO_2(g) + *
\end{aligned}
\tag{14.3}
$$

where * represents the sites and (g) the gas phase.

Assuming step 4 is the limiting step, we calculate the rate of CO_2 formation, assuming the Langmuir–Hinshelwood model, which was deduced and expressed in turnover frequency as follows [2, 11]:

$$
\text{TOF} = \frac{r}{N} = \frac{k_3 K_1 \sqrt{K_2} \cdot p_{CO} \cdot \sqrt{p_{O_2}}}{\left(1 + K_1 p_{CO} + \sqrt{K_2 p_{O_2}} + K_4 p_{CO_2}\right)^2}
\tag{14.4}
$$

where

$$
K_1 = \frac{k_1}{k_{-1}}, K_2 = \frac{k_2}{k_{-2}}, K_4 = \frac{k_4}{k_{-4}}
$$

Figure 14.5 shows the Arrhenius plot of the experimental results for Pt/Al$_2$O$_3$ and Pt/TiO$_2$ and for a feed ratio of CO/O$_2$ = 3.014. The TOF, "turnover frequency," was obtained by normalizing the reaction rates with the total number of surface atoms, measured by CO chemisorption at room temperature after reduction at 573 K [11].

The activation energy was found equal to 12.1 Kcal/mol and is consistent with this reaction mixtures (CO/O$_2$ = 3.014) with CO in excess, showing that the oxygen adsorption is the slow step [4, 11–15].

However, how can we determine the adsorption parameters and estimate the influence of the CO and O$_2$ adsorption on the reaction rate? There are many studies [10–15] suggesting the infrared spectrometry with Fourier transform in situ, which allows to identify the adsorbed surface species relevant to this reaction. The sample is placed in a reaction chamber and then reduced at 573 K for 1 h. After vacuum the mixture CO + O$_2$ at 1: 1 is introduced at room temperature. After vacuum was
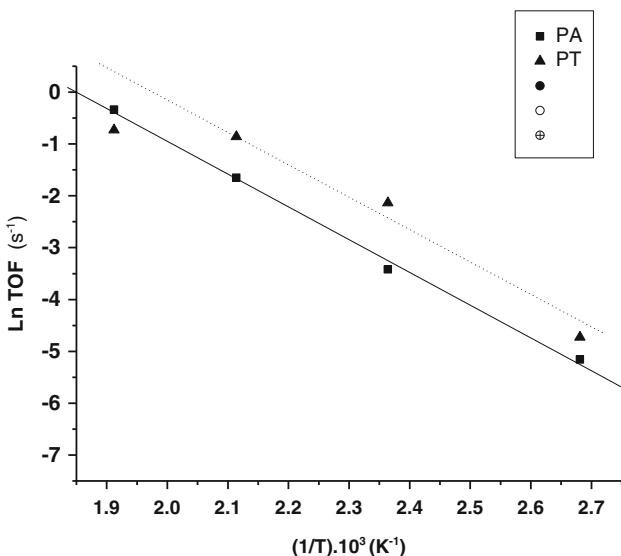
Fig. 14.5 Arrhenius plot of CO oxidation on Pt/Al$_2$O$_3$ and Pt/TiO$_2$ for feed conditions of 7.6 % CO:2.46 % O$_2$ balanced in He and space velocity of 25,000 h^{-1} [11]
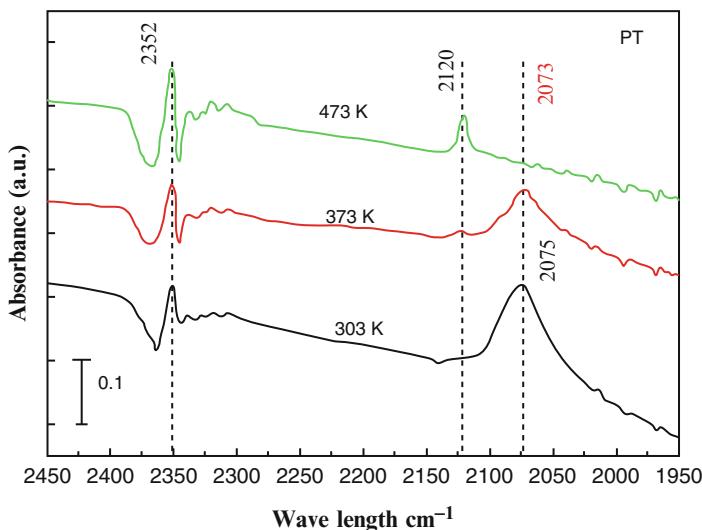
Fig. 14.6 IR spectra of CO + O$_2$ mixture adsorption at RT; desorption at de 303, 373 and 473 K (CO/O$_2$ = 1, P$_{CO+O2}$ = 22 Torr), on Pt/TiO$_2$ reduced at 573 K [10]

desorbed at different temperatures and analyzed by infrared spectroscopy FTIR. The spectra are shown in Fig. 14.6 [11].

Reduced platinum catalysts exhibited an intense band near 2072 cm^{-1}, which is attributed to the linear stretching vibration of CO molecule adsorbed on metallic platinum [16].

Simulation of the reaction by infrared analysis shows that by increasing temperature up to 573 K, the CO_{ads} band on the reduced platinum (2070 cm^{-1}) gradually decreases with the appearance of band 2120 cm^{-1}, related to the CO adsorption on platinum oxide [17, 18]. At 573 K, the band observed at 2072 cm^{-1} disappeared, remaining only the band at 2120 cm^{-1} [15, 17].

Based on these results, it seems that the oxygen adsorption is the limiting step, since $K_1 p_{CO} > 1 + \sqrt{K_2 p_{O_2}}$. Thus, Eq. (14.4) is simplified as follows [11]:

$$TOF = \frac{k_0 e^{\left(-\frac{E}{RT}\right)} . \sqrt{K_2} . \sqrt{p_O}}{K_1 p_{CO}} \tag{14.5}$$

where $K_1 = \frac{k_1}{k_{-1}}, K_2 = \frac{k_2}{k_{-2}}$ are the adsorption–desorption equilibrium constants.

The reaction rate constant k_3 can be calculated for platinum according to Van Santen and Niemantsverdriet [4]:

$$k_3 = 10^5 e^{-5.4 \times 10^3 / T} \tag{14.6}$$

This energy value is similar to the found experimental value.

Substituting the experimental TOF value (0.175 s^{-1}) at 473 K (Fig. 14.5), we obtain the following equation:

$$TOF = 7.1 \times 10^4 e^{\left(-\frac{6.1 \times 10^3}{T}\right)} \frac{\sqrt{p_O}}{p_{CO}} \tag{14.7}$$

14.2 Kinetics of a Bifunctional Model: Methane Dry Reforming with CO_2

Can support influence the kinetic rates and reaction mechanism; that means, is it a bifunctional site system? O'Connor [19] demonstrated the involvement of the oxygen of the zirconia network in the dry reforming of methane on Pt/ZrO_2 catalysts. DRIFTS results showed that the presence of carbonate during the reaction, due to the oxygen in the network of zirconia, was replaced by CO_2 [20].

Dilara and Vohs [21] observed the adsorption of CO on $Pt–ZrO_2$ interfaces, after depositing platinum on ZrO_2 (100) and proposed a model for carbon of CO molecule linked to platinum, while oxygen interacts with Zr^{n+} ions at the surface of zirconia, as shown in Fig. 14.7. The interaction of platinum with Zr^{4+} ions present on the support has been demonstrated by TPD of CO [22].

It is not possible to verify the reduction of zirconia oxide by XPS. However, ISS, which is more sensitive and permits to analyze only the first atomic layer, showed (Fig. 11.12) that there are zirconia cations exposed at the surface interacting

Fig. 14.7 Schematic representation of the interaction of CO on Pt–ZrO$_2$ interface (adapted from Dilara and Vohs [21])
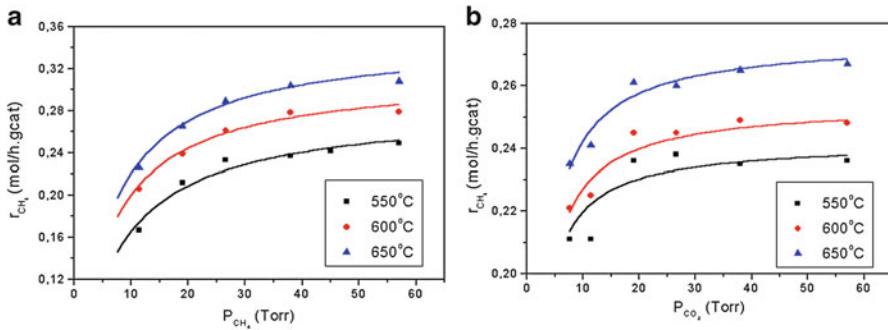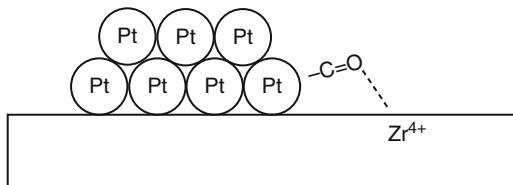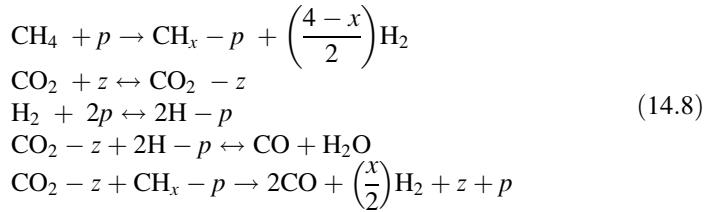
Fig. 14.8 Experiments and model for the Pt10Zr catalyst as a function of (**a**) partial pressure of CH$_4$ and (**b**) partial pressure of CO$_2$ [20, 23]

strongly with CO. Thus, CO adsorbs on both the platinum and on cationic sites Zr^{n+}, at the interface of ZrO$_x$, indicating a bifunctional adsorption process.

Therefore, we can propose the following reaction mechanism [20, 23]:

$$
\begin{aligned}
&CH_4 + p \rightarrow CH_x - p + \left(\frac{4-x}{2}\right)H_2 \\
&CO_2 + z \leftrightarrow CO_2 - z \\
&H_2 + 2p \leftrightarrow 2H - p \\
&CO_2 - z + 2H - p \leftrightarrow CO + H_2O \\
&CO_2 - z + CH_x - p \rightarrow 2CO + \left(\frac{x}{2}\right)H_2 + z + p
\end{aligned}
\tag{14.8}
$$

The reaction rate was determined based on this model and resulted in the following expression [20]:

$$
r_{CH4} = \frac{k.K_{CO2}.k_{CH4}.P_{CO2}.P_{CH4}}{k.K_{CO2}.P_{CO2} + (1 + K_{CO2}.P_{CO2}) \times \left(k_{CH4}.P_{CH4} + k_{CH4}^1.P_{H2}^{(4x)/2}\right)}
\tag{14.9}
$$

where

k_i are specific rate constants and K_i adsorption–desorption equilibrium constants of I components.

The experiments were performed as usual and results are presented in Fig. 14.8. The experimental results adapted very well the kinetic model.

14.3   Mathematical Modeling of Microkinetics

Extended microkinetic models for a reactions, including so-called catalyst descriptors have been studied for the simulation of experimental data on various catalysts. The good agreement between experimental data and calculated results over a large range of operatingconditions proves the capability of the model being incorporated in a high throughput workflow for catalyst development. The model allows the selection of the optimal operating conditions for catalyst evaluation. With this microkinetic model the yield of products are optimized using a generic algorithm followed by the Rosenbrock and the Levenberg–Marquardt method.

Special attention has been devoted to the reduction of the number of adjustable parameters in the model and the a priori determination of thermodynamic as well as kinetic parameters.

Thybaut et al [35] studied the microkinetic model, using the simulation of experimental results for various catalyst. Alexiadis et al [36] and Vatani [37] presented a microkinetic model of a heterogeneous reaction of the oxidative coupling of methane which has been used in the assessment of kinetic data. Kechagiopoulos et al [38] studied in similar way the microkinetics of this reaction based on reaction mechanism. The main contribution was to elucidate the reaction pathway leading to the desired products.

14.3.1   Statistical Analyses: Influence of Independent Variables on Reaction Rates

Literature presents also statistical analyses for determining the Influence of independent variables on reaction rates. Statistical analysis of the experimental results was performed by evaluating the experimental errors associated to each input variable of the system. After calculation of errors, a model can be proposed for evaluating the influence of the independent variables on the reaction rates of reactions. The theoretical bases of the parameter estimation and statistical analysis are described elsewhere [39]. Each variable output, representing the uncertainty of measured values, input variables which are nearest to the experimental data are calculated. It is important to emphasize that uncertainty measurements influence model parameters.

14.4   Conclusions

These examples of surface characterization of real catalyst and real conditions attempt to explain the phenomena occurring at higher temperatures and pressures, which affect the activity, stability, and selectivity of a chemical process. The main

properties, mainly, electronic and structural, besides morphological which have been determined using spectroscopy at ultrahigh vacuum, are of course the same with real catalyst; however, these catalysts differ from the well-controlled structures, presenting defects and interfaces and nonhomogeneous or uncontrolled features, causing different results as expected for the ideal systems. There are many books describing different experiences for specific problems, as presented in the references [6, 24–34].

References

1. Boudart M, Djega-Mariadassou G. Kinetics of heterogeneous catalytic reactions. Princeton, NJ: Princeton University Press; 1984.
2. Satterfield CN. Heterogeneous catalysis in practice. New York: McGraw Hill; 1980.
3. Masel RI. Principles of adsorption and reaction on solid surfaces. New York: Wiley; 1996.
4. van Santen RA, Niemantsverdriet JW. Chemical kinetics and catalysis. New York: Plenum; 1995.
5. Ciobica IM, Van Santen RA. A DFT study of CHx Chemisorption and transition states for C–H activation on the Ru(1120) surface. J Phys Chem B. 2002;106:6200–5.
6. Vannice MA. Kinetics of catalytic reactions. Berlin: Springer; 2005. ISBN 978-0-387-25972-7.
7. Koerts T, Deelen MJA, Van Santen RA. Hydrocarbon formation from methane by a low-temperature 2-step process reaction sequence. J Catal. 1992;138:101.
8. Martins RL, Schmal M. Methane activation on superacidic catalysts based on oxoanion modified zirconium oxide. Appl Catal A. 2006;308:143D.
9. Engel T, Ertl G. Elementary steps in the catalytic oxidation of carbon monoxide on platinum metals. Adv Catal. 1979;28:1.
10. Wootsch A, Descorme C, Rousselet S, Duprez D, Templier C. Appl Surf Sci. 2006;253:1310.
11. Resende NS, Perez CA, Eon J-G, Schmal M. The effect of coating TiO_2 on the CO oxidation of the Pt/c-alumina catalysts. Catal Lett. 2011;141:1685–92.
12. Sarkany J, Gonzalez RD. Support and dispersion effects on silica- and alumina-supported platinum catalysts: II. Effect on the $CO-O_2$ reaction. Appl Catal. 1983;5:85.
13. McCabe RW, Schmidt LD. Binding states of CO on single crystal planes of Pt. Surf Sci. 1977;66:101.
14. Primet M, Basset JM, Mathieu MV, Prettre M. Infrared study of CO adsorbed on $PtAl_2O_3$. A method for determining metal-adsorbate interactions. J Catal. 1973;29:213.
15. Primet M. Electronic transfer and ligand effects in the infrared spectra of adsorbed carbon monoxide. J Catal. 1984;88:273.
16. Bradford MCJ, Vannice MA. Methane conversion to synthesis gas by partial oxidation and CO_2 reforming over supported platinum catalysts. Appl Catal A Gen. 1996;142:97.
17. Hadjiivanov K, Saint-Just J, Che M, Tatibouet JM, Lamotte J, Lavalley JC. Preparation and characterization of multiple ion-exchanged Pt/TiO_2 catalysts. J Chem Soc Faraday Trans. 1994;90(15):2277.
18. Matsushima T, Almy DB, White JM. The reactivity and auger chemical shift of oxygen adsorbed on platinum. Surf Sci. 1977;67:89.
19. O'Connor AM. Carbon dioxide reforming of methane over Pt/ZrO2 catalysts. Ph.D. Thesis, University of Limerick, Irland, 1998.
20. Souza MMVM, Aranda DAG, Schmal M. The reactivity and auger chemical shift of oxygen adsorbed on platinum. J Catal. 2001;204(2):498.

21. Dilara PA, Vohs JM. Interaction of CO with Pt supported on $ZrO_2(100)$: evidence for CO adsorbed at the Pt-ZrO_2 interface. J Phys Chem. 1995;99(47):17259.
22. Schmal M, Souza MMVM, Aranda DAG, Perez CAC. Promoting effect of zirconia coated on alumina on the formation of platinum nanoparticles – application on CO_2 reforming of methane. Stud Surf Sci Catal. 2001;132:695–700.
23. Souza MMVM, Schmal M. Methane conversion to synthesis gas by partial oxidation and CO_2 reforming over supported platinum catalysts. Catal Lett. 2003;91:13–7.
24. Akubuiro EC, Verykios XE, Lesnick L. Dispersion and support effects in carbon monoxide oxidation over platinum. Appl Catal. 1985;14:215.
25. McCarthy E, Zahradnik J, Kuczynski GC, Carberry JJ. Some unique aspects of CO oxidation on supported Pt. J Catal. 1975;39:29.
26. Cant NW. Metal crystallite size effects and low-temperature deactivation in carbon monoxide oxidation over platinum. J Catal. 1980;62:173.
27. Anderson JA. Infrared study of the oxidation of carbon monoxide over Pt/Al_2O_3. J Chem Soc Faraday Trans. 1992;88(8):1197.
28. Barth R, Pitchai R, Anderson RL, Verykios XE. Thermal desorption-infrared study of carbon monoxide adsorption by alumina-supported platinum. J Catal. 1989;116:61.
29. Passos FB, Aranda DAG, Schmal M. J Catal. 1998;178:478.
30. Bitter JH, Seshan K, Lercher JA. The state of zirconia supported platinum catalysts for CO_2/CH_4 reforming. J Catal. 1997;171:279.
31. van Keulen ANJ, Seshan K, Hoebink JH, Ross JRH. TAP investigations of the CO_2 reforming of CH_4 over Pt/ZrO_2. J Catal. 1997;166:306.
32. Stagg SM, Romeo E, Padro C, Resasco DE. Effect of promotion with Sn on supported Pt catalysts for CO_2 reforming of CH_4. J Catal. 1998;178:137.
33. Stagg-Williams SM, Soares R, Romero E, Alvarez WE, Resasco DE. Novel catalyst development and process optimization for COZ Reforming of CH_4. Stud Surf Sci Catal. 2000;130:3663.
34. Bradford MCJ, Vannice MA. CO_2 reforming of CH_4 over supported Pt catalysts. J Catal. 1998;173:157.
35. Thybaut JW, Sun J, Olivier L, Van Veen AC, Mirodatos C, Marin GB. Catalyst design based on microkinetic models: oxidative coupling of methane. Catal Today. 2011;159:29–36.
36. Alexiadis VI, Thybaut JW, Kechagiopoulos PN, Chaar M, Van Veen AC, Muhler M, Marin GB. Oxidative coupling of methane: a microkinetic model accounting for intraparticle surface-intermediates concentration profiles. Appl Catal B Environ. 2014;150:496–505.
37. Vatani A, Jabbari E, Askarieh M, Torangi MA. Kinetic modeling of oxidative coupling of methane over Li/MgO catalyst by genetic algorithm. J Nat Gas Sci Eng. 2014;20:347–56.
38. Kechagiopoulos PN, Thuybaut JW, Marin GB. Oxidative coupling of methane: a microkinetic model accounting for intraparticle surface-intermediates concentration profiles. Ind Eng Chem Res. 2014;53:1825–40.
39. Alberton AL, Schwaab M, Lobão MWN, Pinto JC, Alberton AL, Schwaab M, Lobão MWN, Pinto JC. Chem Eng Sci. 2011;66:1940–52.

Chapter 15
Evaluation of Industrial Catalysts

Abstract Industrial catalysts are often subjected to drastic conditions affecting its performance and modifying their properties. It is aimed to describe the catalysts of industrial processes, but understanding the changes undergone during the process and caused by different thermal treatments or chemical and the possible causes of changes that cause disabling, poisoning and sintering. Being impossible to test in real conditions is suggested here to test the catalyst in a process similar industrial conditions in a system "scale down", using the same variables, forced or not. Here are some examples of typical catalysts and industrial processes.

Keywords Deactivation • Hydrogenation • Pyrolysis • Regeneration

15.1 Hydrogenation in Petrol Pyrolysis Unit

15.1.1 Introduction

The selective hydrogenation of pyrolysis gasoline is a conventional process vapor under high-pressure reaction conditions and temperatures around 100 °C. The process aims to hydrogenate the unsaturated chains of a load containing compounds such as styrene, olefins and diolefins, and other aromatic compounds.

In industrial processes supported metal catalysts are used, especially nickel with high concentration and consequently low dispersion, and palladium, which instead has a low concentration of metal and higher dispersion. High conversions and selectivities are obtained; however, due to coke formation and the presence of gums in the load, the catalysts suffer marked deactivation. The coke deposited is preferably metal, impairing the hydrogenation, while the gum can be deposited either on the metal and the support, deactivating the catalyst more quickly. Hence, it is very important to study the stability of the catalyst in industrial conditions, both the degree of deactivation due to coke formation or gums and its possible regeneration [1].

To assess the industrial catalyst under the same conditions in laboratory, one makes "scale down," using the same space velocity, pressure, and temperature but with a catalyst mass in bench scale. In addition, to evaluate catalysts under kinetic regime conditions, the diffusion and mass effects are minimized. These conditions

can be made benchmarking between the results of bench and produced by manufacturing. In addition, the deactivation process is forced to simulate operating conditions, requiring more drastic conditions than in the industrial process and in a shorter time.

The choice of the most appropriate commercial catalyst passes necessarily by the determination of higher stability, i.e., lower deactivation, and thus, higher activity and selectivity. To this end a catalytic testing study was proposed to meet these key requirements.

As expected the catalysts exhibit high conversions; however, some results presented accentuate differences that allowed classifying the selected samples. As had been established in the original scope, there were selected catalysts that showed better overall performance: one based on palladium and nickel base.

This study aims to evaluate samples of commercial catalysts based on palladium or nickel, selected by the Petrochemical Company (COPESUL), comparing them for activity and selectivity for use in industrial drive pyrolysis gasoline hydrogenation.

The actions developed follow the goals:

1. Evaluation of the activity and selectivity of nickel and palladium catalysts
2. Evaluation of aromatic loss
3. Evaluation of the performance of catalysts with forced aging
4. Evaluation of the recovery of activity of the catalysts after regeneration
5. Specific characterizations before and after reaction

Performance tests were initially divided into two stages:

Step 1. Preselection: tests with synthetic load of catalysts samples.
Step 2. Final test: three samples of activity test of Ni and Pd catalysts with gasoline pyrolysis.

15.1.1.1   Coke and Sintering Evaluation of the Used Samples

Because this is a study with limited time, a short-term test was proposed for each sample (about 8 h) with temperature steps covering the entire range used as a standard campaign (60–120 C).

The forced shutdown test simulation intended to high temperatures, quickly, wears to which the catalyst is subjected during a campaign. For this we determine the conditions under which there was a drastic reduction of activity, to then be tested using the regeneration procedure, according to each manufacturer.

In order to reduce the time of analysis and identification of products, and reduce the effects of deactivation by deposition of polymeric compounds, a first batch of tests was performed with synthetic load, which favored the presence of the most interesting components of the process. The catalysts which have worked best were submitted to actual load.

Table 15.1 Average composition of loads used in the catalytic tests

Composition	% (area)	
	Synthetic	Real
Toluene	86	15.7
Styrene	5	4.0
Isopren	5	3.8
DCPD (dicyclopentadiene)	2	3.3
Indene	1	1.7
Ciclohexene	1	0.5
Tiophene	0.02	–

Table 15.2 Operating parameters used in catalytic tests

Space velocity	$4.5\ h^{-1}$
Internal diameter of the reaction	1.9 cm
Length of catalytic bed	9.5 cm
Molar ratio of H_2/hydrocarbons (HC)	0.45

Table 15.3 Mass of catalysts

Sample	d (g/cm^3)	Mass (g)
Pd1	0.66	17.79
Ni2	0.55	14.79
Ni4	0.71	19.15

At the conclusion of step 1 with synthetic load are selected catalysts with improved performance. The selected catalysts are submitted to performance test under the same operating conditions of step 1, but with actual load, provided by the company.

The synthetic and real load composition sets are presented in Table 15.1.

The catalytic tests were carried out on steel reactor with upward flow and volume of the catalyst bed set at 27 cm^3. The operating parameters established in accordance with the plant are presented in Table 15.2.

The samples chosen for testing and the mass used are shown in Table 15.3.

Testing Fresh Catalysts

Temperatures: 60, 80, 100, and 120 °C and back to 60 °C

Forced Deactivation

The conditions laid down in step 1 were used: the temperature was 350 °C for accelerated deactivation of the catalysts for 3 h with N_2 flow and load. The load flow was reduced to half that used in the catalytic test.

Table 15.4 Specific surface area of fresh and used catalysts

Catalyst	Content Pd/NiO (%)[b]	S^a_{BET} (m²/g) Fresh	S^a_{BET} (m²/g) Used	Difference (%)
Pd1	0.35	56	56	–
Ni4	17.3	105	89	15
Ni4′	17.3	105	65	38
Ni2	21.7	120	117	–

[a]BET analyses with N_2
[b]X-ray fluorescence analyses (FRX)

Table 15.5 Dispersions and metal area

Catalyst	Content %Pd (%Ni)[a]	Dispersion[b] %D	Metalllic area[b] (m²/g)	Metal area[b] (m²/g metal)
Pd1	0.35	39.9	0.53	151
Ni2	17.08	Zero*	–	–
Ni4	13.63	1.9	1.7	13
Pd1-used	0.35	23.9	0.32	107

[a]FRX
[b]Chemisorption of H_2

Product Analysis

The gas and the liquid phase of the reactor effluent were analyzed by gas chromatography, with at least the following identified compounds: CPD, cyclopentene, cyclopentane, isoprene, pentadiene, styrene, benzene, toluene, xylene, indene, indane, aromatic C9 DCPD, 4.7 1indeno hexahydro-methane, 4,7-methanooctahydro indeno 1.

Evaluation

The selected catalysts, Ni4, Ni2, and Pd1, were evaluated, and the textural analyses of Ni2, Ni4, and Pd1 and fresh and used catalysts are presented in Table 15.4.

The specific surface areas of the fresh and used Pd1 and Ni2 catalysts didn't change. The surface area of the used Ni4 catalyst decreased approximately 15 %. After deactivation at 350 °C, it decreased 38 % when compared to first test (15 %). The textural change which occurred with the NI4 after use is probably due to the blocking of pores by organic wastes, justifying loss of activity.

The metal dispersions, obtained by hydrogen chemisorption of the fresh and used catalysts, are presented in Table 15.5.

Styrene Conversion

The conversion of styrene on the fresh is presented in Table 15.6 and showed differences in temperatures below 100 °C; at 120 °C all the catalysts have reached conversions higher than 90 %.

Table 15.6 Styrene conversion data for pyrolysis gasoline hydrogenation catalysts for commercial virgin nickel and palladium
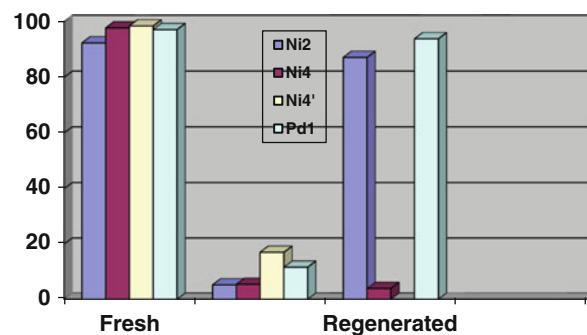
| Catalyst/temperature (°C) | Conversion of styrene (%) fresh catalysts | | | | | Deactivation degree |
	60°	80°	100°	120°	60°	%
Ni2	34.6	55.9	84.5	92.3	**75.7**	–
Ni4	81.5	90.1	90.2	97.7	**77.5**	5
Pd1	88.7	95.8	97.0	97.1	**86.6**	2

Table 15.7 Styrene conversion data for pyrolysis gasoline hydrogenation and synthetic load of commercial nickel and palladium catalysts after forced regeneration and shutdown

| Catalyst/ temperature | Conversion of styrene (%) | | | | | |
| | After deactivation[a] | Deactivation degree | After regeneration | | | |
	120 °C	%	60 °C	100 °C	120 °C	60 °C
Ni2 gasoline	5.2	**94.3**	51.7	77.1	87.1	60.8
Synthetic	34.5	**65.2**	42.8	90.9	98.5	–
Ni4 gasoline	5.4	**94.4**	6.6	8.6	3.9	–
Synthetic	96.5	**3.6**	78.1	98.9	99.3	–
Pd1 gasoline	11.6	**88.1**	52.6	82.8	93.8	83.5
Carga sintética	45.7	**54.2**	97.2	–	99.7	–

[a]A 350 °C

Fig. 15.1 Conversion of styrene (%) at 120 °C, for Ni2, and Ni4 catalysts Pd 1: blank after deactivation forced to 350 °C and after regeneration treatment
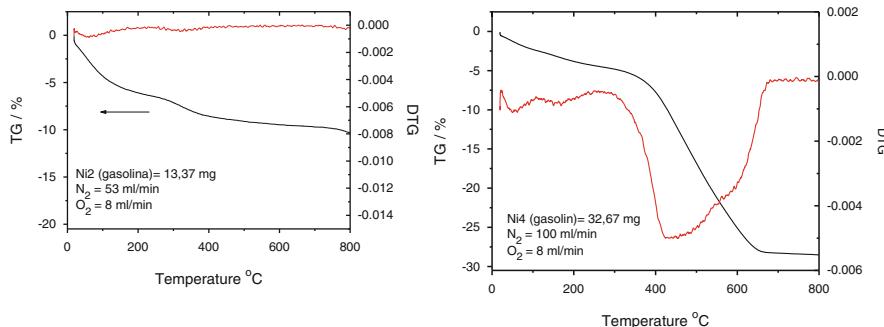
In this step, the Pd Ni4 presents higher conversions at low temperatures. Regarding deactivation in returning to the first point at 60 °C, the Ni2 catalysts was 2 times more active. This confirms that the catalyst Ni2 requires a much longer time than others to stabilize.

Table 15.7 shows the results obtained with gasoline for the reaction tests after forced off with a single point 120 °C and after regeneration at temperatures 60, 100, and 120 °C. For comparison, the results in step 1 with synthetic load are also presented.

The activity results in pyrolysis gasoline conversion of styrene, measured at 120 °C for the three selected samples, are shown in Fig. 15.1.

Table 15.8 Thermogravimetric and thermodifferential analyses of used catalysts

Used catalysts	Oxidizing flow up to 800 °C	
	Mass loss %	Temperature range
Pd1	2.4	até 100
Ni2	10.3	250–400
Ni4	28.1	300–650

Fig. 15.2 Thermograms of Ni2 and Ni4 catalyst after use (real load)

Thermogravimetric Results

The thermogravimetric analysis (TGA) and differential thermal analysis (DTA) were performed after activity tests, with increasing temperature up to 800 °C and under oxidizing mixture flow (8 % O_2/N_2) as shown in Table 15.8.

Figure 15.2 shows the thermograms of Ni2 and Ni4 catalyst. For the sample used, two small endotherms at low-temperature region and a broad, intense peak between 300 °C and 650 °C have been observed, which corresponds to 10.3 and 28 % mass loss, respectively.

At this stage, there has been a large increase in the level of deactivation with respect to step 1, with a synthetic load. This is mainly found with NI4 catalyst, which had hardly been off earlier (around 4 %) after severe treatment to 350 °C. This result is corroborated with those obtained by ATG (Table 15.8), in which the catalyst has Ni4 with longer Tmax and higher mass loss. For the other two catalysts, Ni2 and Pd1, which also suffer an increase in deactivation of 65–94 % and from 54 to 88 %, respectively, a recovery is observed in the activity of these catalysts after the regeneration step.

15.2   1,3-Butadiene Conversion at High Pressure

Purification of olefin-rich C_4 cuts, particularly from FCC, is usually performed by selective hydrogenation of undesirable amounts of 1,3-butadiene and acetylene compounds. The use of butene-1 as a monomer in the production of polybutene and comonomer in low-density polyethylene production has high technological appeal and has been the object of recent studies in the literature [2–4]. To this end a C_4 stream needs to be rich in butene-1 and free from the presence of 1,3-butadiene and acetylenic compounds (content of < than 10 ppm).

The 1,3-butadiene in charge leads to poisoning and therefore reduction in the quality of the polymers produced; therefore, its removal is considered essential. Thus, the improvement in selectivity to butene-1 may be considered a "key point" of the process, and any small contribution achieved very valuable from the viewpoint of process economy.

On an industrial scale, this purification is usually carried out in a fixed bed reactor, with a mixture of liquid hydrocarbons and H_2 flow and countercurrent at temperatures between 50 and 60 °C and the total pressure high enough to maintain the hydrocarbons in liquid phase [2].

Commercially, palladium is used as catalyst in the active phase, with or without the addition of promoters [5–9]. Pd is known to be very effective for the selective hydrogenation, due to the fact that olefins reactions are inhibited by strong adsorption of acetylenic compounds and 1,3-butadiene in the catalyst.

However, due to existing diffusional limitations, the concentration of these contaminants increases rapidly within the catalyst, which provides the reaction of olefins. In order to overcome these diffusional limitations, the catalysts of the "egg shell" [10] are usually the most used.

COPESUL provided a stream with approximately 58 mol% of butadiene exiting the reactor with a concentration of between 1 and 1.5 % and in the second stage. The output current should reduce the butadiene content to 10 mol ppm. For testing commercial catalyst LD 271 was also provided by COPESUL.

The tests were conducted between 30 and 80 °C and varied butadiene/H_2 ratio in the inlet stream and the reaction pressure, 4 and 25 atm, using a real load.

The actual net charge was introduced into the input stream by a piston pump (Isco model 500D) high accuracy, at a flow rate of 0.01 mL/min, and joined to a gas mixture in which the H_2 content was varied and the total flow maintained by adding inert gas (nitrogen). The catalyst was previously reduced with a mixture of 10 % H_2/N_2 at 300 °C for 1 h.

The real load from COPESUL is specified in Table 15.9.

Table 15.10 shows the values of butadiene conversion and mole fractions of the products obtained from the butadiene hydrogenation reaction at constant temperature and pressure of 30 °C and 4 atm, respectively, varying the H_2/butadiene ratio.
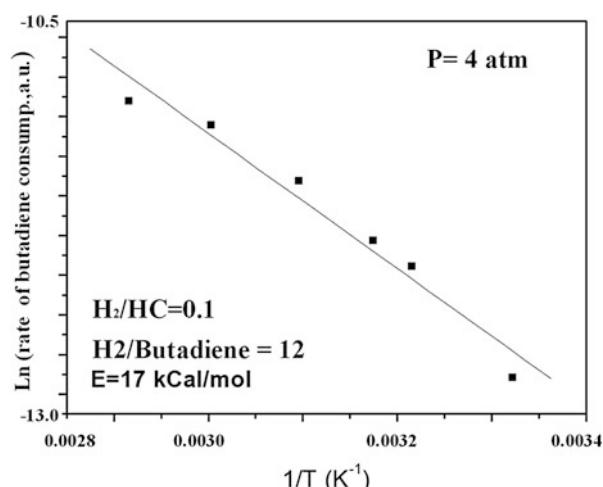
The Arrhenius plot is presented in Fig. 15.3, assuming a first-order reaction, and the energy of activation was found equal to 22 kcal/mol.

Table 15.9 Actual load stream

Actual load (%)	
Others	0.16
1-Butene	1.22
n-Butane	7.16
Trans-2-butene	18.05
1-Butene	32.26
Isobutene	34.40
Cis-butene	5.48
1-Pentene	0.10
n-Pentane	0.04
Butadiene	1.13
n-Hexane	0.004
Temperature (°C)	Between 30 and 80
Pressure (atm)	4 and 25

Table 15.10 Butadiene conversion and molar fractions obtained for different H_2/butadiene ratios

	Molar fraction (%)						
H_2/butadiene (H_2/HC)	12 (0.1)	24 (0.3)	36 (0.4)	61 (0.7)	97 (1.1)	113 (1.3)	182 (2.1)
1-Butane	1.11	1.10	1.12	1.09	1.16	1.15	1.13
n-Butane	6.91	7.13	6.94	6.86	7.17	7.28	7.21
Trans-2-butene	18.49	18.56	18.33	19.09	18.51	19.22	19.61
1-Butene	32.09	31.97	32.31	31.82	32.27	31.37	30.45
Iso-butane	34.45	34.45	34.53	34.59	34.49	34.42	34.64
Cis-butene	5.55	5.57	5.59	5.70	5.68	6.04	6.81
Butadiene	1.11	0.97	0.94	0.58	0.42	0.21	0.04
Conversion (%)	5.60	17.6	19.7	50.5	64.0	82.5	96.8

Fig. 15.3 Determination of activation energy from the Arrhenius plot ($P = 4$ atm, H_2/butadiene $= 12$)

15.2.1   Butadiene Hydrogenation Reaction at 25 atm

Table 15.11 presents the variation of the molar fractions of the main product at the reaction temperature in the tests carried out at 25 atm.

Figure 15.4 shows the results for the butadiene conversion as a function of the temperature for 25 atm, compared to the test performed at 4 atm (both to the same H_2/butadiene $= 12$). It shows that with increasing pressure, the hydrogenation reaction of butadiene increased, reaching 100 % conversion at a lower temperature (around 20 °C). Figure 15.5 displays Arrhenius plot and the activation energy, assuming first-order reaction resulted in $E = 12$ kcal/mol, which compared to the 22 kcal/mol at 4 atm pressure suggests the existence of diffusional resistance within the pores of the catalyst [3, 11, 12].

Table 15.11 Butadiene conversion and molar fractions for different temperatures and at 25 atm

Compounds	Molar fraction (%)				
Temperature (°C)	30	38	50	60	30
1 Butane	1.09	1.11	1.09	1.12	1.10
n-Butane	6.80	6.85	6.82	7.13	6.82
Trans-2-butene	16.9	16.74	17.16	19.77	17.03
1-Butene	33.66	33.98	33.61	29.32	33.51
Iso-butane	34.68	34.72	34.58	34.77	34.65
Cis-butene	5.73	5.70	6.06	7.89	5.77
Butadiene	1.00	0.76	0.55	0.00	1.01
Conversion (%)	14.68	34.88	53.31	100.0	14.12
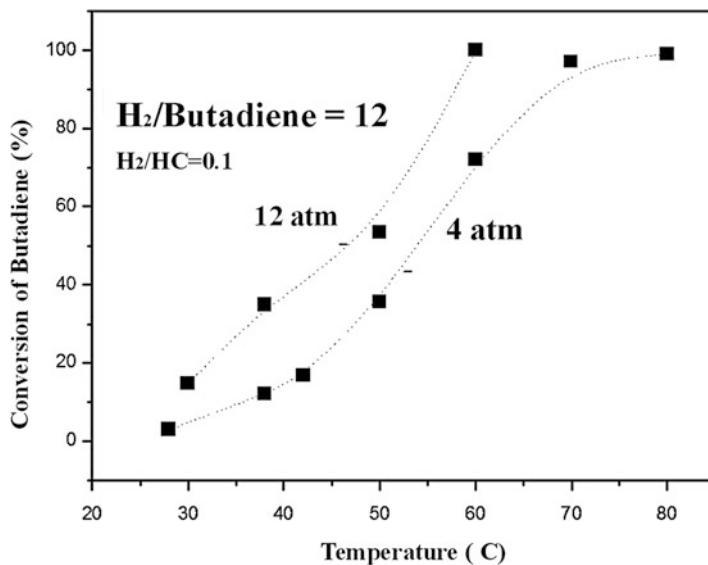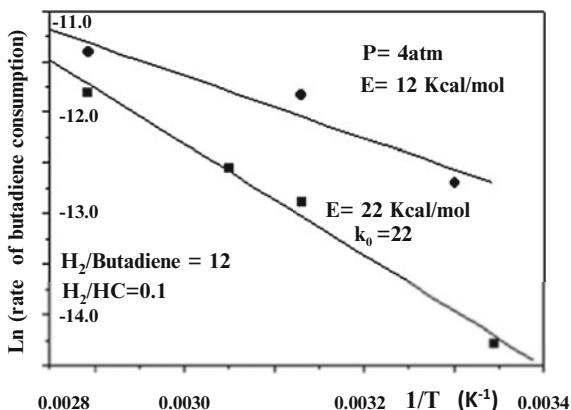
Fig. 15.4   Butadiene conversion against temperature (H_2/butadiene $= 12$)

Fig. 15.5 Arrhenius plot
(25 atm and $P = 4$ atm,
H_2/butadiene $= 12$)

With respect to product formation, Table 15.5 lists the variation of the molar fractions of the main product at the reaction temperature in the tests carried out at 25 atm.

15.3   Production of Polyalcohol at High-Pressure Hydrogenation of Cane Sugar and Hydrolyzed Amides

15.3.1   Introduction

Sorbitol is one of the main products of hydrogenation of glucose, and it is an important natural sweetener, largely used in the industry as additive in food, pharmaceutics, and cosmetics. In particular, GETEC (Guanabara Química Industrial S.A.) uses hydrolyzed amides and cane sugar as raw material for the production of sorbitol and other important pharmaceutical products. A classical slurry pressurized batch reactor is used, employing Raney-Ni catalysts. The yield in sorbitol was increased with promoted catalysts. However, besides yield, high conversion is required in this process.

The catalytic performance of nickel in the hydrogenation process can be associated to the adsorption of hydrogen at the surface, which enhances the hydrogenation of complex molecules. Raney-Ni catalysts are basically leached Al–Ni alloys, which are prepared by attacking the alloy with soda, removing Al as much as possible, resulting in a highly porous material with metallic nickel at the surface. The addition of promoters in small amounts affects the hydrogenation process and although very effective it is not yet clear.

Glucose hydrogenation has been studied in a well-stirred, high-pressure batch reactor on promoted Raney-Ni catalysts [13]. Mo, Cr, Sn, and Fe were reported to

be good promoters for this reaction. For an optimal promoter concentration, the catalysts are up to seven fold more active than the non-promoted ones. The activities of Mo- and Cr-promoted catalysts decrease slightly after several recycling in successive hydrogenation experiments. This behavior is mostly attributed to surface poisons by cracking products formed in side reactions. Fe- and Sn-promoted Raney-Ni catalysts deactivated quickly.

This work intends to provide a clue of the nature of the promoter and their influence in the hydrogenation performance of Raney-Ni catalysts.

15.3.2   Experimental

The preparation of the Raney-Ni catalysts follows the conventional method [14]. Pure metallic cobalt, chromium, iron, and molybdenum as fine powders were added to nickel and aluminum powders, with a Ni/Me molar ratio around 0.02. Then, the alloy powders were submitted to a leaching process with soda under different temperatures to obtain promoted Raney-Ni catalysts. Besides the prepared samples, a commercial Raney-Ni catalyst (GETEC) was also tested [15]. The industrial leaching process from GETEC was adopted: sodium hydroxide solution (6 M) was added to the alloy and the mixture was heated at 100 and 120 °C for 2 h and stirred at 1200 rpm.

The reaction was performed in an autoclave reactor with 450 mL capacity (Parr Instrument Co.) equipped with variable stirring and temperature controller. The reactant, supplied by GETEC, was obtained by amides and cane sugar hydrolysis containing 50 % of solids (0.57 % sacarose, 25.86 % glucose, 23.57 % fructose) diluted in deionized water, called HD. A mass of 11 g of catalyst and 290 mL reactant solution (HD) was introduced with hydrogen at 580 psig, and then the temperature was raised up to the final reaction temperature. At this moment, the hydrogen flow was stopped and the reactor was cooled in ice bath until room temperature. Products (non-converted reactants, sorbitol and manitol) were analyzed in a liquid chromatograph (HPLC–Waters) with movable water phase at 0.9 mL/min, equipped with a cationic column (Ca^+) Shodex SCI 011.

The conversion and selectivity were defined as follows:

$$X_{\text{fructose+glucose}} = \left[\left\{ \text{Initial Conc}_{\text{fructose+glucose}} - \text{Conc}(t)_{\text{fructose+glucose}} \right\} \middle/ \text{Initial Conc}_{\text{fructose+glucose}} \right]$$

$$S_{\text{sorbitol+manitol}} = \left[\text{Conc}(t)_{\text{sorbitol+mannitol}} \middle/ \left\{ \text{Initial Conc}_{\text{fructose+glucose}} - \text{Conc}(t)_{\text{fructose + glucose}} \right\} \right]$$

The important criterion for comparison was the industrial performance. They reached 90 % conversion for a reaction time of 65 min and final temperature of 140 °C. These data were reproducible.

Fig. 15.6 Conversion
and selectivity for the HD
hydrogenation at 140 °C,
for catalysts leached at
120 °C
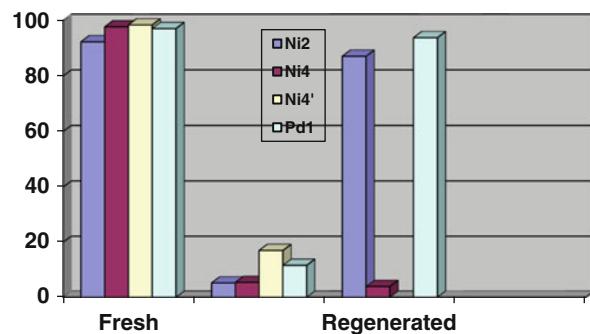
Table 15.12 Results of chemical analyses by X-ray fluorescence of different catalysts[1]

Element	Bulk content before leaching (weight %)			Element amount after leaching (weight %)			
	Ni–Al	Ni–Al–Cr	Ni–Al–Mo	Ni–Al	Ni–Al–Cr	Ni–Al–Mo	Commercial
Ni	44.43	54.44	54.44	78.50	77.42	76.07	89.39
Al	55.25	43.17	41.74	19.09	18.01	21.36	9.98
Cr		1.51		–	1.99	–	–
Mo			2.19	–	–	0.98	–

The catalysts were tested at 140 °C (65 min). The effect of leaching time was not significant as shown in Fig. 15.6 [16].

The quantitative analysis of the elements in the alloy and the resulting catalysts after leaching at 120 °C is listed in Table 15.12. The results show that the leached prepared samples contain a residual aluminum level of 20 % in weight, while there was 10 % in the commercial catalyst. This indicates that the leaching process of the alloys is important.
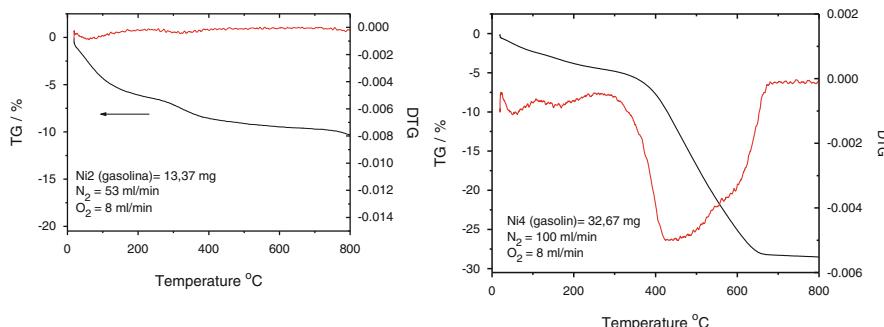
15.3.2.1   Influence of the Reaction Temperature

The results of conversion and sorbitol selectivity obtained at different temperatures are shown in Table 15.13. They show clearly the effect of the promoter on the conversion. Cr and Mo exhibited the highest conversion compared to the non-promoted Raney-Ni catalyst and the commercial GETEC catalyst. These results indicate that the addition of Cr or Mo improves the Raney-Ni catalyst performance and under similar conditions presented 23 % more sugar conversion, although the selectivity was the same.

The difference in activity between non-promoted catalysts (prepared and commercial) can be related to residual aluminum amount as shown in Table 15.12. The sorbitol selectivity was not altered with the promoter and the framework residual aluminum content. It was around 75 % between 90 and 110 °C and 80 % for 130 and 140 °C (Table 15.13).

Table 15.13 HD hydrogenation at different temperatures

Raney-Ni	Reaction Temperature (°C)							
	90		110		130		140	
Catalyst	Conv. (%)	sel. (%)	Conv. (%)	sel. (%)	Conv. (%)	sel. (%)	Conv (%)	sel. (%)
Commercial	24.03	77.64	41.45	77.64	76.10	80.58	90.71	81.89
NiAl	14.28	73.91	26.45	75.33	56.22	81.41	77.34	80.93
NiAlCr	26.15	76.81	38.96	76.806	83.20	80.79	94.90	81.75
NiAlMo	22.63	76.08	48.16	76.08	76.35	79.33	95.04	81.48

Fig. 15.7 Diffractograms of Raney-Ni catalysts

15.3.2.2   Influence of Crystallite Size

The diffractograms of the Raney-Nickel catalysts are presented in Fig. 15.7. The results indicate the presence of four different crystalline phases in the catalysts. Predominance of Ni phase was found on all three samples. This Ni phase can be related to the reaction active Ni sites. Besides, our catalysts presented small quantities of non-leached Ni–Al alloy (Al_3Ni_2) and traces of a nickel aluminum oxide ($Ni_5Al_4O_{11}.18H_2O$). The presence of Ni–Al phase is supported by X-ray fluorescence data, indicating incomplete leaching. The commercial catalyst presented besides the Ni phase, traces of a nickel oxide, is identified as Ni_xO_y.xH_2O.

The full width at half maximum of the Ni (111) peak, correrponding to $2\theta = 44.4°$, was used to determine the crystallite size of nickel [17]. The results are listed in Table 15.14, which shows that the presence of Cr and Mo metals caused decrease in the average crystallite size of the nickel particles of about 30 %.

The great difference in the conversions of promoted and non-promoted catalysts can be attributed, firstly, to the leaching procedure and to the nickel particle size distribution. Using the same leaching procedure for different alloys the difference was marked.

Table 15.14 Crystallite size of the Ni phase

Sample	Ni crystallite size (Å)
Commercial Raney Ni	120
Cr promoted Raney Ni	33
Mo promoted Raney Ni	43

Although the promoter contents are low, the conversions were very similar. It seems that the activity depends on the promoter Cr or Mo and not on the surface area but on the formation of smaller Ni particle sizes affected by the addition of these promoters, which enhances the activity and the stability of the catalysts.

Nevertheless, the results showed that the selectivity was not altered for different conditions. This fact indicates that the reaction was not influenced by electronic effects but by geometric effects. The main factor of distinction of the catalysts was the nickel particle size, which for the promoted catalysts were about threefold smaller. Indeed, the reduction of the Nickel crystallite size with the introduction of Cr or Mo in the Raney-Ni catalyst increased the Ni metallic superficial area, which is effectively the active phase for hydrogenation reaction. Despite of the less total nickel amount of prepared samples compared to commercial sample, the available nickel amount for reaction is larger than in the promoted catalysts.

15.3.3   Conclusions

Results showed that high yields were obtained either on promoted or non-promoted Raney-Ni catalysts. However, the activity depends on the promoter. The most important factor is the leaching process during the alloying activation, which depends on the Al and the promoters' extracted amounts. The surface area increases improving the leaching process.

The increased activity of the catalysts can probably be related to the small Nickel particles size formation at the surface with the promoter. The XRD results showed Ni crystallite size rather smaller than the non-promoted Raney Ni.

References

1. Ali J. The hydrogenation of pyrolysis gasoline (PyGas) over nickel and palladium catalysts; 2012. PhD thesis. School of Chemistry University of Glasgow. http://theses.gla.ac.uk/3542/
2. Derrien ML. Selective hydrogenation applied to the refinging of petrochemical raw materials produced by steam cracking. Stud Surf Sci Catal. 1986;27:613.
3. Schmal M. Chemical reaction engineering: essentials, exercises and examples. Boca Raton, FL: Taylor and Fracis; 2014. ISBN 978041569538.
4. Lee DC, Kim JH, Kim WJ, Kang JH, Moon SH. Selective hydrogenation of 1,3-butadiene on TiO_2-modified Pd/SiO2 catalysts. Appl Catal A Gen. 2003;244:83.

5. Furlong B, Hightower JW, Chan TY-L, Sarkany A, Guczi L. 1,3-Butadiene selective hydrogenation over Pd/alumina and CuPd/alumina catalysts. Appl Catal A Gen. 1994;117:41.

6. Borgna A, Moraweck B, Massadier J, Renouprez AJ. New supported palladium-chromium catalysts: characterization and catalytic properties. J Catal. 1991;128:99.

7. Pereira MM, Noronha FB, Schmal M. SMSI effect in the butadiene hydrogenation on Pd-Cu bimetallic catalysts. Catal Today. 1993;16:407.

8. Sarkany A, Zsoldos Z, Stefler G, Hightower JW, Guczi L. New supported palladium-chromium catalysts: characterization and catalytic properties. J Catal. 1995;157:179.

9. Schmal M, Aranda DAG, Soares RR, Noronha FB, Frydman A. SMSI effect in the butadiene hydrogenation on Pd-Cu bimetallic catalysts. Catal Today. 2000;57:169.

10. Krishma R, Sie ST. Chem Eng Sci. 1994;49:4029.

11. Alves JA, Bressa SP, Martínez OM, Barreto GF. Selective hydrogenation of 1,3-butadiene: improvement of selectivity by using additives. Chem Eng J. 2004;99:45–51.

12. Ramos ALD, Silva Alves P, Aranda DAG, Schmal M. Characterization of carbon supported palladium catalysts: inference of electronic and particle size effects using reaction probes. Appl Catal A Gen. 2004;277:71–81.

13. Gallezot P, Cerino PJ, Blanc B, Fleche G, Fuertes P. Glucose hydrogenation on promoted Raney-nickel catalysts. J Catal. 1994;146:93.

14. Adkins H, Billica HR. The preparation of Raney nickel catalysts and their use under conditions comparable with those for platinum and palladium catalysts. J Am Chem Soc. 1948;70:695.

15. Final Report - Fundação COPPETEC - ET-110251, Pesquisa e Desenvolvimento de um novo catalisador para a fabricação de Polialcoois por Hidrogenação sob pressão de Açucares ou Xarope de Amido Hidrolisado, 2000, PADCT/ FINEP no 65.95.0252.00 and GETEC - Guanabara Química Industrial S.A.

16. Carvalho M, Perez CA, Schmal M. Production of polyalcohol at high-pressure hydrogenation of cane sugar and hydrolyzed amides. Appl Catal A Gen. 2004;264:111–6.

17. Klug HP, Alexander LE. X-ray diffraction procedures for polycrystalline and amorphous materials. New York: Wiley; 1974.

Nomenclature

Symbols	Meaning	Units
a, b, c	Stoichiometric coefficients	
a', b', c'	Reaction order	
$Ai, Bi \ldots$	Components, reactants, and products	
C	Concentration	gmol/l
C_A	Concentration of reactant A	gmol/l
C_{AO}	Initial concentration of reactant A	gmol/l
C_P	Specific heat at constant pressure	cal/g°
E	Activation Energy	cal/gmol
E_C	Kinetic energy	cal/gmol
$\boldsymbol{F, F_0}$	Molar flow, initial	moles/h
F_A	Molar flow of reactant A	moles/h
F_{Ao}	Initial molar flow of reactant A	moles/h
$\dot{G}_j$	Mass flow of component j	Kg/h
ΔG^0	Gibbs free energy	Kcal/gmol
H_T	Enthalpy of reaction at T	Kcal/gmol
$H°$	Enthalpy of reaction at 25 °C	Kcal/gmol
K	Equilibrium constant	Kcal/gmol
K_c	Concentration equilibrium constant	Kcal/gmol
K_p	Equilibrium constant at pressure P	atm^{-1}
k, k'	Specific reaction rates, direct and reverse	eq. 3.19
k_0	Frequency factor of Arrhenius equation	
L	Reactor length	cm (m)
m	Mass	g (Kg)
M	Molecular weight	
n	Global reaction order	
n	Number of moles	moles
$n_{A, B}$	Number of mols of reactants A, B $\ldots$	moles

(continued)

Symbols	Meaning	Units
n_0	Initial total number of mols	moles
n_T	Total number of mols	moles
P	Pressure	atm^{-1}
P_0	Initial pressure	atm
q	Heat transfer rate	Kcal/h
$\dot{Q}_T$	Total heat transfer	Kcal/h
r	Reaction rate	mol/L h
$(-r_A), (-r_B)$	Disappearance rate of A, B	mol/L h
r_i	Rate of formation of component j	mol/L h
R	Gas constant	Atm l/mol K
S	Selectivity	
s	Space velocity	s^{-1}
t	Time	s
t_f	Final time	s
$\bar{t}$	Mean residence time	s
T	Temperature	°C (°K)
v	Linear velocity	cm/s
v_0	Volumetric flow rate	cm^3/s
V_R	Reactor volume	cm^3 (L)
V	Reaction volume	cm^3
X	Conversion	
X_A	Conversion of reactant A	
y	Molar fraction	
Symbols		
α	Degree of extension	
β	Kinetic parameter	
γ	Kinetic parameter	
ε	Porosity	
εA	Expansion or contraction parameter	
μ	Viscosity; potential, reduced mass	
ν	Stoichiometric coefficient; Kinematic viscosity	
ρ	Density	g/cm^3
τ	Space time	s
Subscripts		
A, R	Reactant or products	
e	Equilibrium	
f	Final	
g	Gas	
j	Component	
i	Reaction number	
r	Reaction	
o	Initial	

Other General Nomenclatures

ρ	Density of gas
$\bar{u}$	Mean velocity; collision velocity
D_e	Effective diffusivity
ρ_s	Particle density of solids
ρ_f	Fluid density
d_p	Particle diameter
g	Gravity
ρ_s	Solid density
$\overline{d_p}$	Mean particle size
ρ_s	Solid density (kg/m^3)
r''	Reaction rate (mole/g s)
d_t, d_p	Diameter (tube and particles)
k_l	Mass transfer coefficient (cm/s)
m_p	Mass of particles (g)
pi	Partial pressure
k_d	Deactivation constant
S	Selectivity
E_j	Energy of component j
F_j	Molar flow rate of component j
W	Work
Q	Heat (J/mol)
k^*	Apparent specific constant
ΔS^0	Entropy
$V_{ads}; V_{des}$	Adsorption or desorption volume

MeO	Metal oxide
M^0	Metal
$k_B(k)$	Boltzmann constant
O^{2-}	Oxygen anions
RSS	Structure-sensitive reaction
RIS	Structure-insensitive reaction
BET	Surface area (m^2/g)
TOF	Rate (frequency factor) (s^{-1})
DRX	X-ray diffraction
TPR	Temperature-programmed reaction
SEM	Scanning electronic microscopy
TEM	Transmission electronic microscopy

Chapter 4

γ	Surface tension
V	Molar volume
r	Pore radius
γ	Surface tension
φ	Contact angle
θ_A	Occupied fraction
r_{ads}	Adsorption rate
k_a	Adsorption constant
r_{des}	Desorption rate
k_d	Desorption constant
K_A	Equilibrium adsorption–desorption constant
$*$	Site
θ_i	Occupied fraction of component i
θ_v	Vacant sites
K_i	Adsorption–desorption equilibrium constant of component i
ΔH^0	Enthalpy
ΔS^0	Entropy
ΔH_{ads}	Enthalpy of adsorption
θ	Surface coverage
ΔH_f	Enthalpy of formation
E_c	Energy barrier
χ_A, χ_B	The electronegativity
γ_{Pa}	The universal Pauling constant
$D(A - B)$	Binding energies between A and B
ΔH_{MX}	Bond enthalpy M–X
D_{XX}	Enthalpy of diatomic molecule
D	is the dispersion (%)
d_p	The particle diameter (nm)
M^{2+}	Metal ion
O^{2-}	Oxygen ion
M^0	Metal

Chapter 5

E_T	Total energy
$N(E)$	Electron density
E_F	Fermi energy
d	Electron d band—orbital
γ_P	Transfer coefficient
E_a^0	Intrinsic energy barrier
σ, π	Covalent binding
σ^*, π^*	Anti-ligands

ΔH_r	The enthalpy of reaction
s, p, d	Electron distribution in layers
d_{z^2} and $d_{x^2-y^2}, d_{xy}, d_{yz}, d_{xz}$	Electron densities

Chapter 6

V_p and V_t	Pore volume (cm^3/g) and the total volume of the pores in the solid
S	Specific surface area (m^2/g)
n_m	Maximum moles for a complete monolayer (moles/g$_{cat}$)
N_A	The number of Avogadro (6.023×10^{23} mol^{-1})
n	Number of moles adsorbed per gram of catalyst (moles/g$_{cat}$)
p	Partial pressure
M	Molecular weight
R	Gas constant
H_1	Enthalpy of the formation of the first layer
H_2	Condensation heat of the gas
P_A	Pressure of gas A on gas–solid interface
P_o	Vapor pressure of gas A at constant temperature T
V_m	Volume of a monolayer at NTP
V_M	Molar volume at NTP
S_g	Specific area of the solid $\left(\text{m}^2 \big/ \text{g}_{cat} \right)$
r_K	is called the Kelvin radius

TPD	Temperature-programmed desorption
TPR	Temperature-programmed reduction
TPO	Temperature-programmed oxidation
DSC	Differential scanning calorimetry
TG-DT	Thermo-gravimetric and thermo-differential
TPSR	Temperature-programmed surface reaction

r_d	Desorption rate of A (molecules/cm^2)
N_s	Concentration of sites (number/cm^2)
θ_A	Fraction of surface coverage of species A
n	Desorption order
k_0	Pre-exponential factor
E_A	Activation energy of desorption
T_m	Maximum peak temperature
θ_m	Fraction coverage for maximum temperature peak
k_A	Adsorption constant
k'_A	Desorption constant
K	Equilibrium adsorption–desorption constant

E_A	Activation energy of adsorption
E'_A	Activation energy of desorption
ΔH_A	Enthalpy of adsorption
$\alpha = \frac{n_{H_2}}{n_{H_2(\text{teórico})}} \times 100 (\%)$	Degree of reduction
S	Rate of reduction of the solid (μmol)
$\frac{dn_H}{dt}$	Rate of H_2 consumption (μmol/s)
k	Specific rate constant
$\overline{C}$	Mean concentration of H_2 (μmol/cm^3) $= \overline{C} = \frac{C+C_0}{2}$
C_0, C	Input and output concentrations
k_0	Pre-exponential factor (min^{-1})
α	Reduction degree
n	Reaction order
E	Activation energy (J/mol)
T	Temperature (K)
R	Gas constant
$\beta = \frac{dT}{dt}$	Heating rate (K/s)

Chapter 7

r_c	Critical nuclei size
$\Delta G^0_{\text{nucleation}}$	Nucleation free energy
$\Delta G^0_{\text{superficial}}$	Superficial free energy
$\Delta G^0_{\text{volume}}$	Volume energy
C_{s0}	Saturation concentration
$s = \frac{C}{C_{s0}}$	Concentration
r_c	Growth rate
C	Concentration of the solute
ΔG^*	The nucleation free energy
C_{s0}	The initial concentration of the solute
r_{c0}	is the initial rate
s^*	The super-saturation concentration
N^*	The number of critical nuclei
r_{ch}	Rate growth around the core
ψ	Electrostatic potential
δ	Layer thickness
$V_{\text{pores}} = V_{\text{solution}}$	Dry impregnation
$V_{\text{solution}} >> V_{\text{pores}}$	Wet impregnation
$t_{\text{diffusion}} = t_d$	Diffusion time
PI	Isoelectric point
H^+	Proton
OH^-	Hydroxyl

Chapter 8

$\dot{m} = a k_m (p_s - p_g)$ Mass transfer
$\dot{q} = a' h (T_g - T_s)$ Heat transfer
k_m Mass transfer coefficient
h Heat transfer coefficient
GHSV   Space velocity
SMSI   Strong metal support interaction

Chapter 9

E_y Amplitude
E(r)   Amplitude of the electric field
S   Unit vector
R   Position
$s = (\mathbf{S} - \mathbf{S_o})/\lambda$ Scattering vector
φ   Angle
M   Mass
$I(s)$ is called intensity of diffractogram
$\rho(r)$ Distribution of electrons
F m 3 m   Spatial Symmetry Group
$h\ k\ l$ Miller indexes
K Scherrer constant
FWHM   Full width at half maximum
$\overline{d} = \frac{\lambda}{\beta \cos(\theta)}$ Scherrer equation
$\overline{d}$ Average crystal diameter
a, b, c   Unit cell parameters (Å)
L_{hkl}(nm)   Crystallite size

Chapter 10

IR   Infrared
UV visible   Ultraviolet
ν Frequency
λ Wavelength
$\overline{\nu}$ Wavenumber
c Propagation velocity
$\hbar$ Planck constant $= 6.63 \times 10^{-34}$ J/s
$\frac{1}{\lambda} = \frac{1}{2\pi c} \left(\frac{k}{\mu} \right)^{1/2} = \overline{\nu}$ Schrödinger equation
k Force constant
m_i Reduced mass, equivalent to: $\mu = \frac{m_1 m_2}{m_1 + m_2}$
$A = a \cdot b \cdot c$ Lambert–Beer law
a Absorptivity (L g^{-1} cm^{-1})

b	Optical pathway covered by the radiation (cm)
c	Species concentration (g/L)
A	Absorbance
ν_i	Vibrational mode
B^-	Brönsted acidic sites
L	Lewis acidic sites
ε	Extinction coefficients
T	Transmittance (%)
IS	Intensity of infrared radiation reflected by the sample
IB	Intensity of infrared radiation reflected by a reference
A	Absorbance (%)
% R	Quantity of energy reflected
K–M	Kubelka–Munk
$F(R_\infty) = k \cdot c$	
k	Scattering coefficient
R_∞	Reflectance

Chapter 11

XPS	X-ray photoelectron spectroscopy
h_ν	Photon energy
E_c	Kinetic energy
E_b	Binding energy
BE	Binding energy
$N(E)$	Intensity of the photoelectrons
FWHM	Full width at half maximum
1s, $2p_{3/2}$, $2p_{1/2}$, $3d_{5/2}$, $3d_{3/2}$	Spin–orbit component
I_{Al}/I_{Zr}	Relative intensities

Chapter 12

EM	Electronic microscopy
SEM	Scanning electronic microscopy
TEM	Transmission electronic microscopy
SE	Secondary electrons
EDS	Energy-Dispersive X-Ray Spectroscopy

Chapter 13

S/V	Surface/volume ratio
Ns	Number of atoms per layer
N	Total number of atoms
ψ	Electric potential
κ	Boltzmann constant ($\kappa = 1.38 \times 10^{-23}$ J/K)

Chapter 14

E_c^* or E_c^+	Energy barrier
DFT	Density functional theory
*	Represents the sites
g	Sub-index gas phase
TOF	Turnover frequency
k_i	Specific rate constants
K_i	Adsorption–desorption equilibrium constants of I components

Chapter 15

	Deactivation degree (%)
COPESUL	Petrochemical industry—Brazil
SV	Space velocity (h−1)
D	Reactor diameter (cm)
L	Lenght (cm)
H/C	Molar ratio
NiI	Nickel catalysts sample I (1,2,4)
Pd1	Palladium catalysts sample 1
E	Activation Energy Kcal/mol

Book References—Principal

1. Anderson JR. Structure of metallic catalysts. London: Academic; 1975.
2. Anderson JR, Boudart M. Catalysis, science and technology, vol. 7. Berlin: Springer; 1985.
3. Amarendra G, Raj B, Manghanani MH. Advances in materials characterization. Hyderabad: University Press India; 2007.
4. Barret P, editor. Reaction kinetics in heterogeneous chemical systems. Amsterdam: Elsevier; 1975.
5. Boudart M, Djega-Mariadassou G. Cinétique des Réactions en catalyse hétérogêne. Paris: Masson; 1982.
6. Boudart M. Kinetics of chemical processes. Englewood Cliffs, NJ: Printice-Hall; 1968.
7. Carley AF, Davies PR, Hutchings GJ, Spencer MS. Surface chemistry and catalysis. New York: Kluwer Academic/Plenum; 2002.
8. Froment GF, Waugh KC, editors. Reaction kinetics and the development of catalytic processes. Amsterdam: Elsevier; 1999.
9. Bond GC. Heterogeneous catalysis, principles and applications. Oxford: Oxford University Press; 1987.
10. Gates BC, Katzer JR, Shuit GC. Chemistry of catalytic processes. New York: McGraw-Hill; 1978.
11. Ertl G, Knözinger H, Schüth F, Weitkamp J, editors. Handbook of heterogeneous catalysis, 8 Volumes. 2nd ed. New York: Wiley; 2008. Hardcover—March 31, ISBN-13: 978-3527312412, ISBN-10: 3527312412.
12. Faith WL, Keyes DB, Clark LR. Industrial chemicals. 3rd ed. New York: Wiley; 1965.
13. Fukui K. Theory of orientation and stereoselection. Berlin: Springer; 1975.
14. Krylov OV. Catalysis by nonmetals. New York: Academic; 1970.
15. Le Page JF, editor. Applied heterogeneous catalysis. Paris: Editins Technip; 1987.
16. Lewis ES, editor. Investigation of rates and mechanisms of reactions, vol. VI. 3rd ed. - New York: Wiley; 1974.
17. Masel IR. Principles of adsorption and reaction on solid surfaces. New York: Wiley; 1996.
18. Machado BF, Serp P. Catalysis Science & Technology, Minireview. Catal Sci Technol. 2012;2:54–75.
19. Moulijn JA, van Leeuwen PWNM, van Santen RA. Catalysis. 2nd ed. Amsterdam: Elsevier; 1995.
20. Moulijn JA, Makee M, van Diepen A. Chemical process technology. New York: Wiley; 2001.
21. Moulijn AJ, Cybylski A. Structural catalysts and reactors. 2nd ed. Boca Raton, FL: CRC, Taylor and Francis; 2006.
22. Patat F, Kirchner K. Praktikum der Teschnishen Chemie. 3rd ed. Berlin: W.dGruyter; 1975.

23. Rudd DF, Dumesic JA. The microkinetics of heterogeneous catalysis. Oxford: Oxford University Press; 1993.
24. Satterfield CN. Mass transfer in heterogeneous catalysis. Cambridge, MA: M.I.T. Press; 1970.
25. Satterfield CN, Sherwood TK. The role of diffusion in catalysis. Reading, MA: Addison-Wesley; 1963.
26. Satterfield CN. Heterogeneous catalysis in industrial practice. 2nd ed. New York: McGraw-Hill; 1991.
27. Schmal M. Chemical reaction engineering: essentials, exercises and examples. Boca Raton, FL: CRC, Taylor and Francis; 2014. ISBN 9780415695381.
28. Somorjai GA. Introduction to surface chemistry and catalysis. New York: Wiley; 1994.
29. van Santen RA, Niemanstverdriet JW. Chemical kinetics and catalysis—fundamental and applied catalysis. New York: Plenum Press; 1995.
30. Serp P, Figueiredo JL. Carbon materials for catalysis. New York: Wiley; 2009.
31. Trimm DL. Design of industrial catalysis. Amsterdam: Elsevier Scientific Publishing Company; 1980.
32. Tanabe K. Solid acids and bases. New York: Academic; 1970.
33. Vannice MA. Kinetics of catalytic reactions. New York: Springer; 2005.
34. Wikipedia: the free encyclopedia. htm :file:///D:/Carbon%20nanotube%20
35. Young DM, Crowell AD. Physical adsorption of gases. New York: Butterworth; 1962.

Index